Impedimetric CRISPR-dCas9 Based Biosensor System for Sickle Cell Anemia Mutation

Hilmiye Deniz ERTUĞRUL UYGUN[1]* iD

[1] Dokuz Eylül University, Center for Fabrication and Application of Electronic Materials, Izmir 35390, Turkey

Abstract: Sickle cell anemia is one of the single point mutation diseases with symptoms such as stroke, lethargy, chronic anemia, and increased mortality, and it causes red blood cells to become sickle-shaped. In the study, a biosensor system was developed to detect this mutation quickly and cost-effectively. This biosensor system was prepared by forming a SAM layer with 4-Aminothiophenol (4-ATP) on the gold electrode, and coating it with amino graphene. It was then modified with SG-RNA with the sequence of the target mutation after CRISPR-dCas9 immobilization. The nanomaterial used in the preparation of the biosensor increased the sensitivity of the method by increasing the surface area. The biosensor prepared in this way was optimized and made to perform DNA analysis. As a measurement method, electrochemical impedance spectroscopy (EIS) was used. Electrochemical measurements were carried out in 50 mM pH 7.0 phosphate buffer solution, which includes 5 mM $Fe(CN)_6^{4-/3-}$ and 10 mM KCl, as redox probe solution by CV and EIS in this redox probe solution. EIS parameters were 10,000–0.05 Hz frequency, 10 mV AC and 180 mV DC potentials, and CV parameters were between - 0.2 to 0.5 V potential, 100 mV/s scan rate for 5 cycles. The DNA measurement time of the biosensor system was determined by the chronoimpedance measurements taken by applying a frequency of 500 Hz under 200 mV DC current. Measurement time of the biosensor was found to be 100 seconds. With the CRISPR-Cas9 based electrochemical biosensor system, which gives faster results compared to the measurement methods in the literature, a linear measurement between 40 pM and 1000 pM with a length of 400 base pairs was taken.

Keywords: Sickle cell anemia, CRISPR-dCas9, biosensor, electrochemical impedance spectroscopy.

INTRODUCTION

Sickle cell anemia (SCA) is an inherited disease that occurs when an abnormal form of hemoglobin, called Hemoglobin S (HbS), replaces the normal protein hemoglobin A (HbA) (1). The causative agent of HbS formation in SCA is a point (nucleotide) mutation in the beta globin gene (2). This mutation occurs in the beta globin gene, where the GAG triplet in the sixth position is transformed into GTG triplet, and valine is encoded instead of glutamine (3). When the amount of oxygen in the environment is low, HbS becomes insoluble and the polymeric structures they form by bonding to each other cause the deformation of red blood cells from circular to sickle shape. If the red blood cell membrane is not too damaged, this deformation can be reversed by oxygenation, but this cycle damages the red blood cells, shortening their lifespan, and leading to anemia (4). Diagnosis of this mutation is made by conventional techniques such as polymerase chain reaction (5), liquid chromatography (6), and electrophoresis (7). Although these methods show high sensitivity, they are time-consuming and costly (4). In this study, a CRISPR-dCas9-based electrochemical biosensor system was developed to detect this mutation quickly and cost-effectively.

Biosensors are systems that are developed by the immobilization of highly selective biomolecules such as enzymes, receptors, antibodies, DNA, or proteins (biorecognition agents) produced by living systems on a physicochemical transducer and that allow measurement of complex substances (8). The CRISPR-dCas9 system is also used as a biorecognition agent in biosensor systems (9). dCas9 and synthetic guide RNA (sgRNA) have the capacity to specifically bind DNA sequences, and this binding can be used to detect DNAs (10). Biosensors are divided into two categories: bioaffinity and biocatalytic, according to the interaction feature between the biorecognition agent and the analyte molecule. Bioaffinity-based biosensors are based on the affinity between the biorecognition molecule and the analyte molecule. With this affinity, the measurement system is realized by measuring the affinity of the analyte molecule to the biorecognition molecule (11). Electrochemical systems precede other measurement methods (Optical, Piezoelectric) as they are cheap, fast, practical, and economical systems. Electrochemical systems with simplicity of transducers and easy measurement method can reach very low detection limits in biosensor systems modified with a suitable bioreceptor (12). Electrochemical biosensors can be classified as amperometric, voltammetric, or impedimetric.

Electrochemical impedance spectroscopy (EIS) is an electrochemical surface characterization technique and is widely used in sensors because it provides the advantage of label-free detection. EIS offers inexpensive measurement at low concentrations without sample pretreatment (13). Impedimetric measurement is well suited for affinity-based biosensor systems because the system does not require label, an electroactive secondary molecule, or biochemical reaction. With this method, quantitative analysis is possible only by determining the surface binding kinetics of the analyte molecule (13).

In the presented study, deactivated Cas 9 was immobilized by forming self-assembled monolayers on the gold electrode for the determination of sickle cell anemia and electrochemical impedance spectroscopy was used as the measurement method. SAM surfaces formed by the strong bond between gold and sulfur are very preferred in biosensor fabrication and provide stable surfaces (14). The sensitivity of the method was increased by obtaining a larger surface area with ammonium-functionalized graphene used in electrode immobilization.

EXPERIMENTAL SECTION

Chemicals and Equipment
dCas9 proteins were obtained from Applied Biological Materials (ABM) Inc. (Richmond, BC, Canada), sgRNA sequences were obtained from Synthego Corp. Other chemicals were obtained from Sigma Aldrich (USA). Electrodes (Reference, Working, and Counter) were obtained from BASi. PalmSens 3 potentiostat system was used for electrochemical techniques (EIS and cyclic voltammetry (CV)) and PSTrace 5.6 was used as electrochemical interface software. Scanning Electron Microscopy (SEM) images obtained from COXEM EM-30 Plus (Daejeon, Korea). For FT-IR analysis, a Thermo Scientific NICOLET iS10 spectrometer was used.

Method
Experimental parameters
All electrode modification steps were monitored by scanning electron microscopy (SEM), FT-IR, CV, and EIS. EIS and CV measurements were carried out in a solution of redox probe, which includes 5 mM $Fe(CN)_6^{4-/3-}$ redox couple and 100 mM KCl in 50 mM pH 7.0 phosphate buffer. All modifications and measurements were carried out at 37°C. EIS signals showed that the electrical circuit for EIS calculation was constructed as shown in Figure 1.

Preparation of the electrode surface
Prior to use, gold electrode (AuE) was polished 0.05 µm alumina slurry for 2 minutes. Then, to remove any adsorbents, the electrode was washed ultrasonically with pure ethanol and pure water, respectively. EIS and CV were performed to obtain bare gold electrode as baseline. After each modification step, the electrode was washed by soaking in pure water and dried under nitrogen stream, gently. Subsequently, AuE was soaked in 50 mM 4-aminothiophenol (4-ATP) solution in ethanol for overnight to form Self-assembly Monolayer (SAM) for further immobilization via amino bonds (15). Then electrode was washed with ethanol and water to remove unbonded 4-ATP from AuE surface. In the next step, the electrode was incubated in 5% glutaraldehyde solution for 30 minutes to activate amino groups on the 4-ATPs. The ammonium functionalized graphene oxide (1 mg/mL) was sonicated until the particles dispersed homogenously and dropped on the AuE/4ATP electrode and incubated for one hour. The glutaraldehyde step was performed again, and the modified electrode was incubated with dCas9 (250 pmol) protein for one hour. Then the electrode was incubated with sgRNA for 30 minutes. After the biosensor was successfully produced, the optimization of modification steps, preparation of the calibration curve, determination of LOD and LOQ, reproducibility and repeatability optimization studies were carried out.

Biosensor optimization
The first of the biosensor optimization steps was to determine the exact incubation time for modification and then measurement time. Chronoimpedance was used for obtaining the DNA detection time.

Chronoimpedimetric measurement is optimized in buffer solution and frequency was obtained from the Bode plot of impedimetric detection of the prepared biosensor (AuE-4ATP-GPH-dCas9-sgRNA) (16). The frequency is selected on Bode-Plot where the impedance shows an increasing character and the phase angle becomes constant. The applied potential should be low in order to prevent the oxidation of other compounds in real samples (17). After obtaining the exact DNA detection time, a calibration curve was performed by incubating the biosensor with DNA. The calibration curve was prepared with DNA standards against obtained EIS signals in redox probe solution. The LOQ was calculated by using 10 S/m and LOD 3.3 S/m. S is the standard deviation of EIS data at the lowest concentration of the calibration curve, seven times the obtained standard deviation, and m is the slope of the calibration curve. Reproducibility was obtained by preparing the calibration curves for six time and R^2 results of the calibration curves with C.V%. Repeatability was also tested on three different DNA samples (80, 200, and 900 pM) with added artificial serums.

RESULTS AND DISCUSSION

Preparation of the Electrode Surface

In order to develop a new generation genetic biosensor technology, CRISPR technology has been used with good accuracy. In this study, accuracy was increased by using nanomaterials with high sensitivity. AuE electrode modification steps were observed by EIS and in redox probe solution (Figures 1 and 2). AuE was chosen for its easy modification capabilities with SAM and observed as baseline in developing biosensors. The SAM layer was formed by 4-ATP, because of the benzene ring. Electrical conductivity is provided, and that increases the sensitivity with stability. The modification showed an increase in CV and decrease in EIS because the positively charged 4ATP groups attract the negatively charged redox probes, resulting in the release of more electrons that move towards electrode surface, which decreases the electron transfer resistance by increasing current. Afterwards, the amino graphene modification, the same results were observed. dCas9 and sgRNA modifications increased the EIS and decreased the CV peaks by forming insulation layers. The modification layers were also observed in Figure 3 as AFM and SEM images. There, it can be seen as topographic changes and changes in the surface characteristics can be seen (Figure 3).
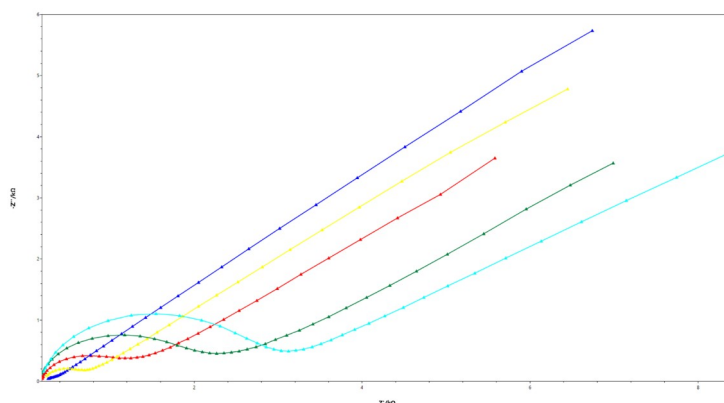

Figure 1: EIS representation of the modification steps. a) Red EIS: AuE, blue EIS: AuE/4-ATP, yellow EIS: AuE/4-ATP/GPH, green EIS: AuE/4-ATP/GPH/dCas9, light blue EIS: AuE/4-ATP/GPH/dCas9/sgRNA.

Figure 2: CV representation of the modification steps. a) Red EIS: AuE, blue EIS: AuE/4-ATP, yellow EIS: AuE/4-ATP/GPH, green EIS: AuE/4-ATP/GPH/dCas9, light blue EIS: AuE/4-ATP/GPH/dCas9/sgRNA.
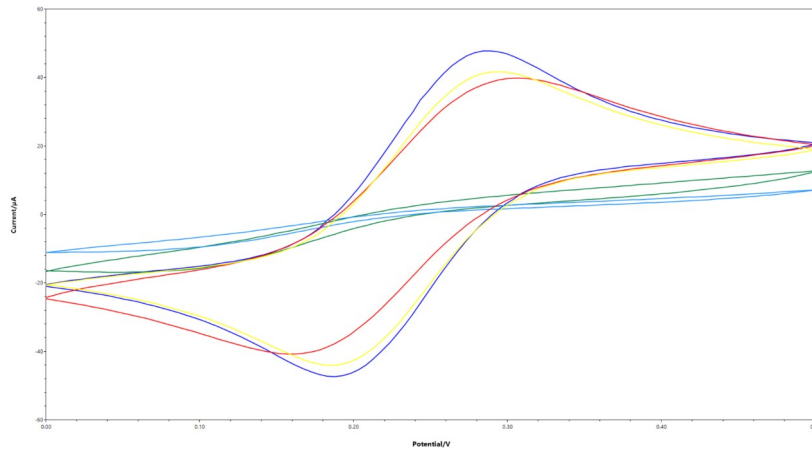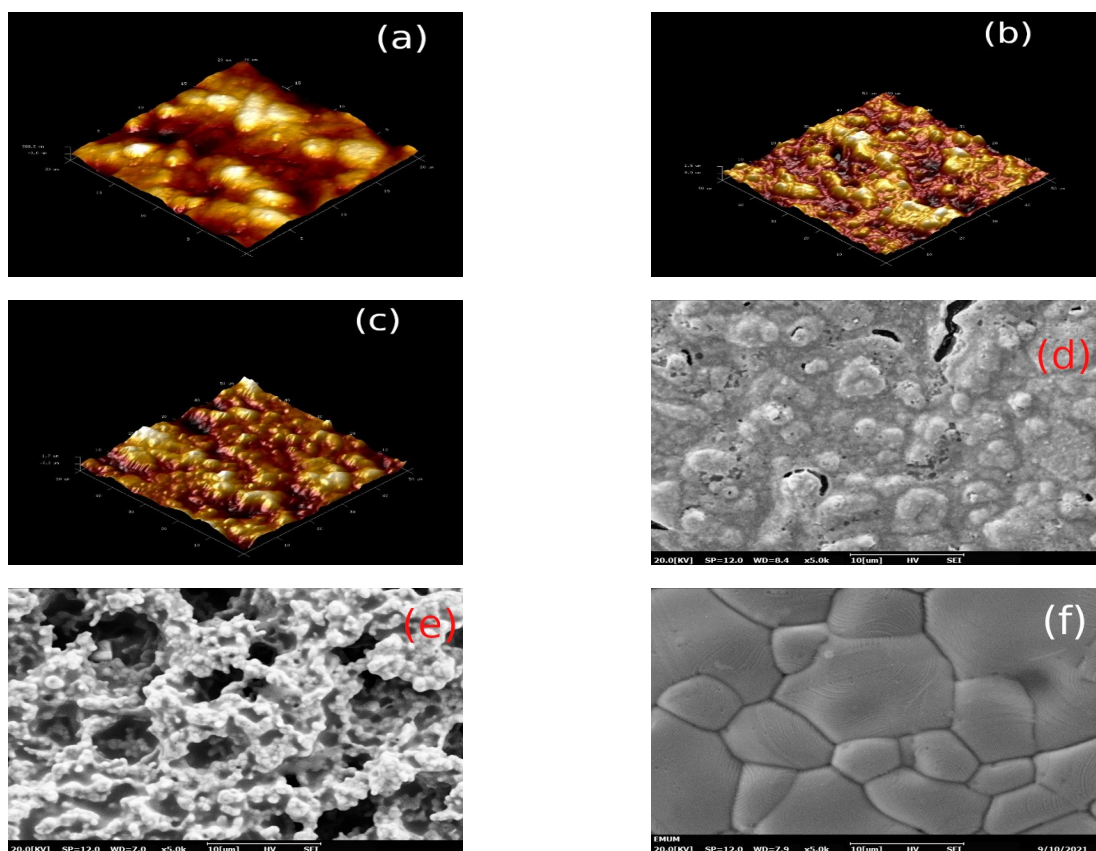

Figure 3: Atomic force microscopy and SEM images of the biosensor modifications. AFM images A; AuE, B; AuE-Cys-GPH-Cas9-sgRNA, C; AuE-Cys-GPH-dCas9-sgRNA-DNA, SEM images D; AuE, E; AuE-Cys-GPH-Cas9-sgRNA, F; AuE-Cys-GPH-dCas9-sgRNA-DNA.

Biosensor Optimization

The first of the optimization steps was to determine the measurement time with chronoimpedance. The first linear increase was observed at 105 seconds, and biosensor saturation was observed at around 800 seconds (Figure 4). Therefore, detection time was determined to be 100 seconds, and this time was chosen for the determination of the DNA detection time.
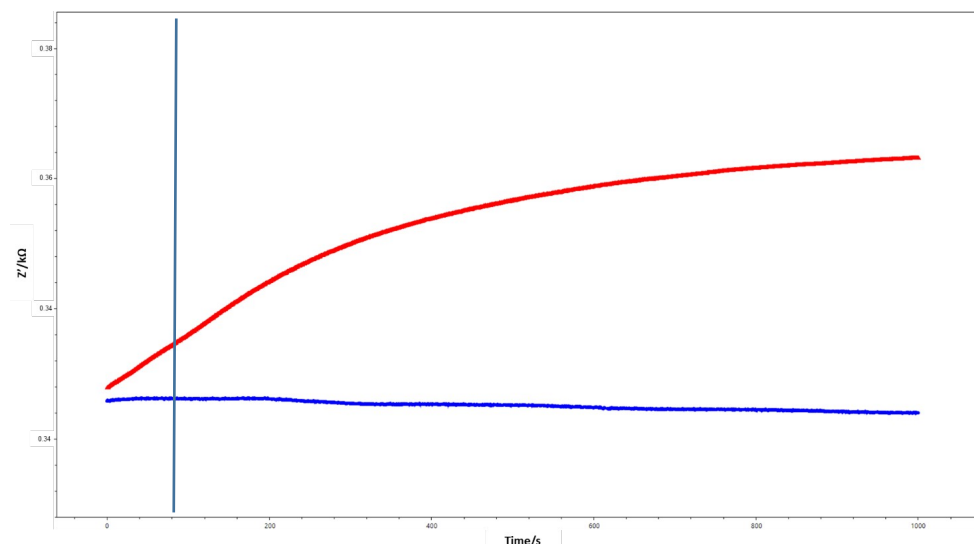
Figure 4: Chronoimpedance curves of detection of the sickle cell anemia DNA. Red sickle cell anemia, blue blank solution (PBS).

Afterwards, the calibration curve was prepared with the data of the electron transfer resistance of the biosensor, which was calculated by fitting EIS data onto a proper circuit model (9). The biosensor showed good linearity between 40-1000 pM DNA (400 bp) and $R^2=0.9930$.

Figure 5: Representation of the calibration curve with CV.

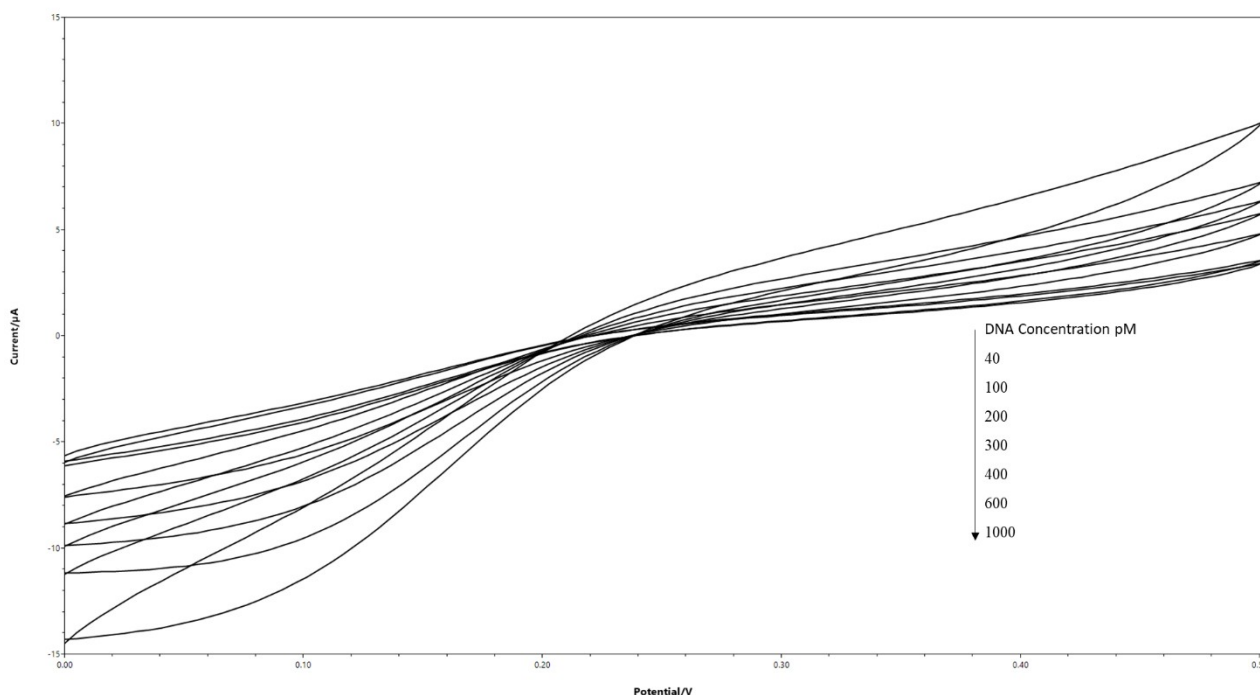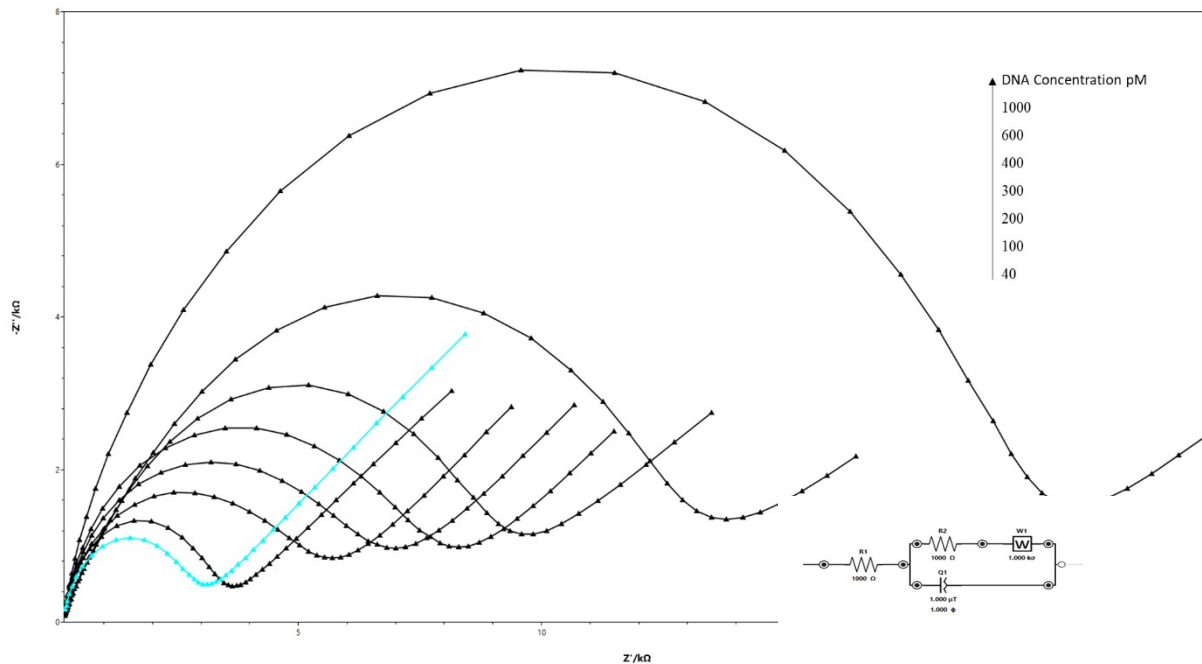**Figure 6:** Representation of the calibration curve with EIS.

Equation   Y = 17.05*X + 2935

Goodness of Fit
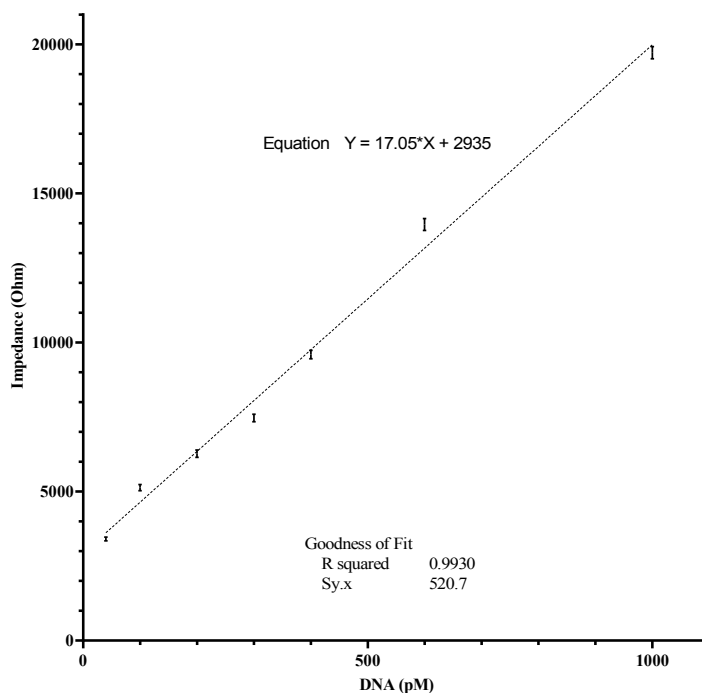R squared   0.9930
Sy.x   520.7

Figure 7: Calibration curve of the biosensor (y-axis impedance, x-axis concentration of the DNA).

Sy.x, given in Figure 7, is the abbreviation of the Standard Error of Estimate. If this value is large, it indicates the goodness of fit value. It shows the agreement between the measured values and the theoretical values.

Optimization and characterizations are all performed using EIS in a redox probe solution. Reproducibility was also tested with different calibration curves and $R^2=0.9930\pm0.0027$. Therefore, reproducibility is high because of the stability of self-assembly monolayer and the graphene layers. In order to find out the lower limit of detection (LOD) and lower limit of quantification, 40 pM concentration was tested and calculated as 3412 ± 64.59 ohm. LOD and LOQ were calculated as 12.50 pM and 37.88 pM, respectively. Performance parameters were shown in Table 1.

Table 1: Sickle cell anemia biosensor performance parameters.

Parameter	Performance		
Linearity	40-1000 pM		
LOD	12.50 pM		
LOQ	37.88 pM		
Reproducibility	R^2=0.9930±0.0027 (2.7%)		
Repeatability and Recovery	Added	Found	C.V %
	80 pM	87 ± 6 pM	6.90
	200 pM	224 ± 11 pM	7.74
	900 pM	940 ± 21 pM	10.11

Methods such as Complete Blood Cell Count, Peripheral Blood Smear, Hemoglobin Electrophoresis, Isoelectric Focusing, High Performance Liquid Chromatography, and Polymerase Chain Reaction (PCR) are used to determine sickle cell anemia (18). These methods are time consuming and expensive. Also, the prepared biosensor is more feasible and sensitive than PCR to diagnose sickle cell anemia.

CONCLUSION

In conclusion, in this study, a biosensor system was developed to detect the point mutation that causes sickle cell anemia. A gold electrode was used as working electrode and modified with 4-ATP and ammonium functionalized graphene oxide for sensitive measurement of the point mutation. Detection time was determined with chronoimpedimetric measurement. The biosensor showed good linearity between 40 and 1000 pM. As a result, a very selective and specific CRISPR-dCas9 based biosensor system for the determination of sickle cell anemia point mutation was developed and reported successfully. This study represents the easy to use, low cost and selective Sickle Cell DNA detection method. Moreover, there is no need for pre-sample applications and modifications. It can easily be used to detect sickle cell anemia.

CONFLICT OF INTEREST

The author declares no conflict of interest.

REFERENCES

1. Breveglieri G, D'Aversa E, Cosenza LC, Boutou E, Balassopoulou A, Voskaridou E, et al. Detection of the sickle hemoglobin allele using a surface plasmon resonance based biosensor. Sensors and Actuators B: Chemical. 2019 Oct;296:126604. <DOI>.

2. Kasiri M, Rahaie M. A visible and colorimetric nanobiosensor based on DNA-CuO nanoparticle for detection of single nucleotide polymorphism involved in sickle cell anemia disease. Materials Today Communications. 2021 Jun;27:102423. <DOI>.

3. Sahu M, Biswas AK, Uma K. Detection of Sickle Cell Anemia in Red Blood Cell. A International Journal of Engineering and Applied Sciences (IJEAS). 2015;2(3).

4. Brazaca LC, Bramorski CB, Cancino-Bernardi J, Janegitz BC, Zucolotto V. A Genosensor for Sickle Cell Anemia Trait Determination. Electroanalysis. 2017 Mar;29(3):773–7. <DOI>.

5. Barrett AN, McDonnell TCR, Chan KCA, Chitty LS. Digital PCR Analysis of Maternal Plasma for Noninvasive Detection of Sickle Cell Anemia. Clinical Chemistry. 2012 Jun 1;58(6):1026–32. <DOI>.

6. Galvão AF, Petta T, Flamand N, Bollela VR, Silva CL, Jarduli LR, et al. Plasma eicosanoid profiles determined by high-performance liquid chromatography coupled with tandem mass spectrometry in stimulated peripheral blood from healthy individuals and sickle cell anemia patients in treatment. Analytical and Bioanalytical Chemistry. 2016 May;408(13):3613–23. <DOI>.

7. Ali TH, Alamiry AAN, Majeed MN. Detection of hemoglobinopathies in hypochromic, microcytic and sickled cell blood films by hemoglobin electrophoresis. University of Thi-Qar Journal Of Medicine. 2011;5(1):139–48.

8. Tothill IE. Biosensors for cancer markers diagnosis. Seminars in Cell & Developmental Biology. 2009 Feb;20(1):55–62. <DOI>.

9. Uygun ZO, Yeniay L, Girgin Sağın F. CRISPR-dCas9 powered impedimetric biosensor for label-free detection of circulating tumor DNAs. Analytica Chimica Acta. 2020 Jul;1121:35–41. <DOI>.

10. Huang M, Zhou X, Wang H, Xing D. Clustered Regularly Interspaced Short Palindromic Repeats/Cas9 Triggered Isothermal Amplification for Site-Specific Nucleic

Acid Detection. Analytical Chemistry 2018 Feb 6;90(3):2193–200. <DOI>.

11. Mehrotra P. Biosensors and their applications – A review. Journal of Oral Biology and Craniofacial Research. 2016 May;6(2):153–9. <DOI>.

12. Uygun ZO, Sezgintürk MK. A novel, ultra sensible biosensor built by layer-by-layer covalent attachment of a receptor for diagnosis of tumor growth. Analytica Chimica Acta. 2011 Nov 14;706(2):343–8. <DOI>.

13. Uygun ZO, Ertuğrul Uygun HD. A short footnote: Circuit design for faradaic impedimetric sensors and biosensors. Sensors and Actuators B: Chemical. 2014 Oct;202:448–53. <DOI>.

14. Chaki NK, Vijayamohanan K. Self-assembled monolayers as a tunable platform for biosensor applications. Biosensors and Bioelectronics. 2002 Jan;17(1–2):1–12. <DOI>.

15. Uygun ZO, Şahin Ç, Yılmaz M, Akçay Y, Akdemir A, Sağın F. Fullerene-PAMAM(G5) composite modified impedimetric biosensor to detect Fetuin-A in real blood samples. Analytical Biochemistry. 2018 Feb;542:11–5. <DOI>.

16. Ertuğrul Uygun HD, Uygun ZO, Canbay E, Gїrgїn Sağın F, Sezer E. Non-invasive cortisol detection in saliva by using molecularly cortisol imprinted fullerene-acrylamide modified screen printed electrodes. Talanta. 2020 Jan;206:120225. <DOI>.

17. Uygun ZO, Atay S. Label-free highly sensitive detection of DNA approximate length and concentration by impedimetric CRISPR-dCas9 based biosensor technology. Bioelectrochemistry. 2021 Aug;140:107812. <DOI>.

18. Arishi WA, Alhadrami HA, Zourob M. Techniques for the Detection of Sickle Cell Disease: A Review. Micromachines. 2021 May 5;12(5):519. <DOI>.

Impact of Irrigation Water On the Quality Attributes of Selected Indigenous Plants

Sami Ullah¹, Aiman Shahbaz¹* iD, Muhammad Zeeshan Aslam¹

¹University of Lahore, Department of Chemistry, Sargodha Campus, 40100, Pakistan.

Abstract: The present study was carried out to study the effects of irrigation water on the quality attributes of mango, banana, and mulberry collected from the nearby orchards located in peri-urban areas of Sahiwal (Pakistan). Due to freshwater scarcity in peri-urban areas, wastewater is used as a source of irrigation for orchards, which consequently increases heavy metal accumulation in the soil, leaves, and fruits. The physio-chemical attributes and accumulation of heavy metals were analyzed in different soil layers and fruit cultivars. Among the heavy metals, copper, lead, chromium, and cadmium contents were found to be in greater amounts in the effluent sample than in freshwater samples, according to WHO. Heavy metals such as copper, lead, and chromium were found to be in higher concentrations in soil and effluent samples. The concentration levels of copper in mango and mulberry were 0.005 and 0.002 mg/kg, respectively. The concentration levels of lead in banana and mulberry were 0.231 and 1.248 mg/kg, and the concentration of chromium in banana was found to be 1.203 mg/kg, which is higher than the allowed limit given by WHO. The interaction among the sources of irrigation and fruit cultivars was significant for copper accumulation in different soil layers, lead, and copper accumulation in fruit cultivars. The irrigation water quality index (WQI) of all effluent samples ranged from 63.5 to 63.57, which, according to WHO, can be used for irrigation purposes as it is non-drinkable water.

INTRODUCTION

Freshwater scarcity is a major issue worldwide, which is due to rapid urbanization and anthropogenic activities. In developing countries, due to the non-existence of industrial and environmental standards, the dumping of waste such as pharmaceuticals, industrial and sewage into rivers, streams, and lagoons has become a threat to ecological life which unfortunately causes long term health effects such as gene mutation, lung cancer, and kidney diseases, etc. ([1]). Water is polluted due to non-conservative materials, conservative pollutants, and accumulation of heavy metals by different sources like pharmaceutical industries, chemical industries, metal fishing and plating operations. Some of the sources of trace metal pollution in rivers and oceans include thermal power plants ([2], [3]).

Heavy metals' accumulation in the surroundings is deleterious for living organisms as they are non-biodegradable and intensive through the food chain, which causes numerous known health effects such as gastrointestinal and respiratory diseases ([4-6]), nausea, vomiting, and several diseases ([7]). Toxic metals are accumulated in the

aquatic environment from plastic manufacturing, fertilizers, and metallurgy processing. This wastewater causes a big threat to the ecosystem and causes environmental pollution. Heavy metals when combined with organic matter in the presence of bacteria yield monomethyl mercury and dimethyl cadmium, which are highly toxic compounds (8). Due to the non-availability of fresh water in the peri-urban areas, wastewater is commonly used to irrigate vegetable crops and orchards. Sewage water is mostly used by farmers as it increases the nutrient concentration, but the drawbacks are completely ignored by them, which leads to heavy metal accumulation in the soil, causing contamination and spoiling fruit quality. Contaminants of emerging concerns (CECs) such as pharmaceutical effluents are introduced into the agroecosystem through reclaimed wastewater irrigation. However, the effects of reclaimed wastewater irrigated crops have not caught the attention of the population. Therefore, they are being sold and consumed (9). However, recent studies show that 65% of all the irrigated core plants rely on treated wastewater flow, which causes serious health issues to the patrons (10). The mechanism of bio-chemo-physical properties of the molecule and in-planta processes such as uptake, translocation, accumulation, and transformation, influenced the fate of the pharmaceuticals in the water-soil-plant continuum (11). Numerous studies have shown the consequences of heavy metals in the streams which otherwise would have endured as conventional. This leads to the identification of wastewater treatment plants (WWT) as a substantial source of these compounds for the environment (12). The innovation in modern technology improved the analytical capabilities, which manifested the wide range of pharmaceuticals in the environment. Wastewater has long-term effects on the ecological health of human beings, such as acute and chronic effects (13), behavioral changes (14), and reproductive damage (15). Current studies indicate that pharmaceuticals have also affected aquatic life. The high level of concentration of pharmaceuticals in freshwater causes hormonal changes in fish, which can be a life-altering phenomenon (16). Assessment of risk associated with pharmaceutical effluents in irrigating fruit plants can be studied by checking water quality parameters and formulating a hypothesis on how the chemical composition of fruits has been affected by pharmaceutical effluents (17). Most of the pharmaceutical industries' effluents contain heavy metals (18), solids, organic compounds, and solvents which play a vital role in identifying potential ecological effects. The biological oxygen demand (BOD) (19),

chemical oxygen demand (COD) (20), suspended solid (SS) and pH of the pharmaceutical effluent also contribute to checking the quality attributes of the irrigation water (21).

Accumulation of heavy metals in the soil and their effects on the quality attributes of fruits have not been widely studied. However, recent advancements in green chemistry and sustainability have shifted the attention of scientists to studying every aspect of the irrigation source, as improving water quality is beneficial for the environment. Re-use of water for irrigation purposes follows the green chemistry principle, but what if it is affecting the consumers on the other side. Therefore, in the current study, we compared the heavy metal accumulation in the mango, banana, and mulberry cultivars under different pharmaceutical irrigation water. The water quality index of the pharmaceutical effluent samples along with statistical analysis is being studied. The physiochemical attributes and heavy metals' accumulation in water, soil, and fruit samples were studied. Recently, heavy metal contamination in wastewater-irrigated soil and fruits has been studied by scientists from China, India, and other countries. A few papers have been reported, covering the aspect of vegetable crops. This research article is based on the heavy metal contamination in different fruits observed in Sahiwal, Pakistan, along with the wastewater-irrigated soil. Comparison with the determined hazardous elements with standard values gives us a clear idea of the contamination.

MATERIAL AND METHOD

Heavy metal concentration in pharmaceutical water and soil

To determine the concentration of heavy metals in pharmaceutical water, samples from each irrigation source were collected and filtered in the laboratory. Samples of effluent from different locations in Sahiwal at different depths were collected, i.e. Sample A from upper surface discharge wastewater into the drain, a) upper surface, b) 0-5 cm, c) 5-10 cm labeled as ES-1, ES-2, and ES-3, respectively. Sample B, 1 km away from the sample A location and collected from three depths: a) Upper surface, b) 0-5 cm, c) 5-10 cm labeled as ES-4, ES-5, and ES-6, respectively. Sample C, 2 km away from sample B location and collected from three depths: a) upper surface, b) 0-5 cm, c) 5-10 cm labeled as ES-7, ES-8, and ES-9, respectively. Samples of soil from 3 different depths i.e. 0–15 cm were obtained from the same orchards irrigated with water from these irrigation sources. A fruit sample was taken from the nearby orchards irrigated with pharmaceutical effluent. The collected samples were washed, dried, crushed, sieved, and labeled.
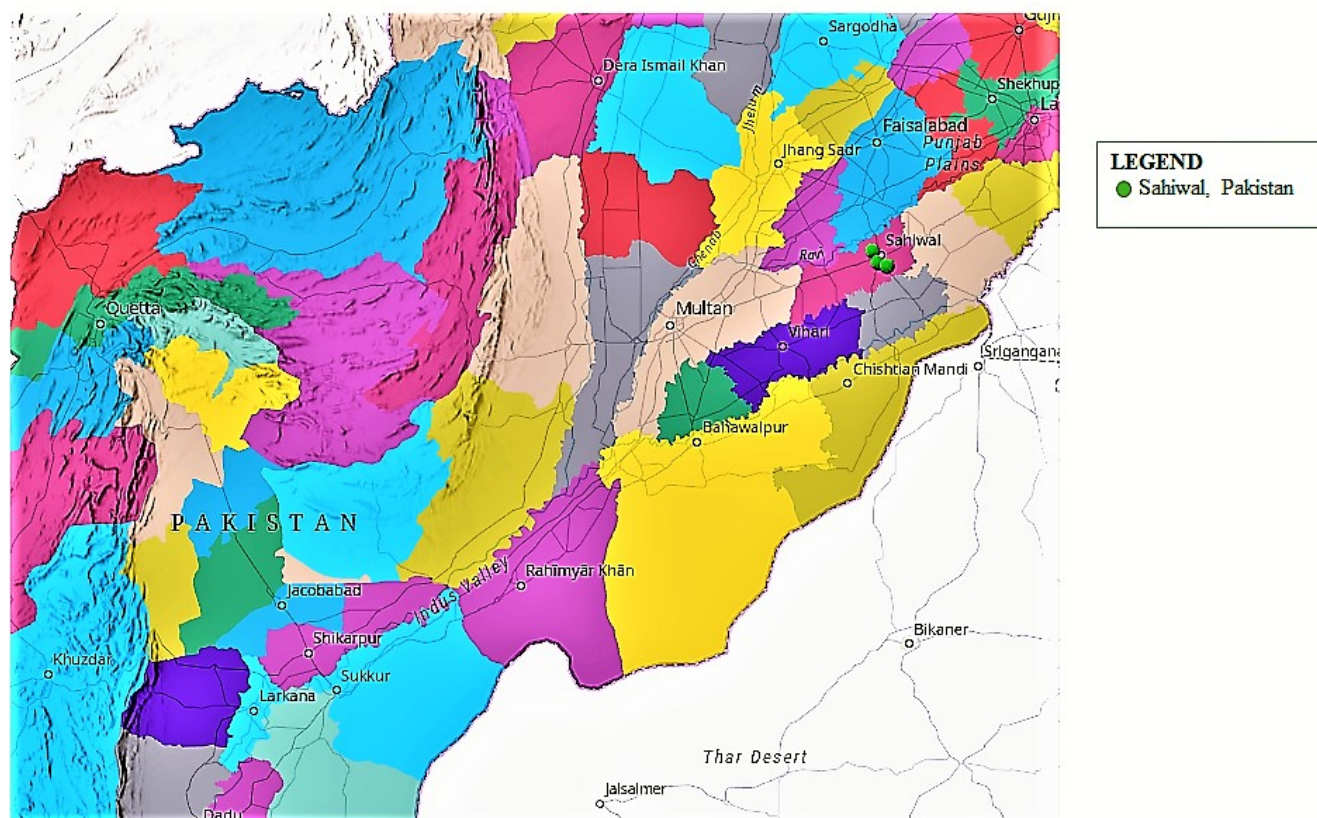
Figure 1: Location of different irrigation water samples collected from Sahiwal near and the natural regions of Pakistan. Source: DIVA GIS 7.5.0 (2015).

Preparation of soil samples

The soil sample was prepared by drying it as it is available from three different sites. The most convenient state is to perform chemical tests on dry soil, so microwave drying was done to remove excess moisture in the soil. Due to the presence of concretions and rocks, crushing of sample into fine powder was done, which was afterwards designated for mechanical analysis with a wooden rolling pin. Samples were sieved by using a set of sieves that have progressively smaller openings, and the grain size was ≤ 0.075 mm. The prepared soil sample was soaked in DPTA solution and then shaken for 3 hours on an orbital shaker. After removing them from the shaker, the flasks were rested for 2-3 minutes and then filtered using the standard method. The sample was saved in the test tube for heavy metal content analysis and labeled as SOR-1, SOR-2, and SOR-3.

Preparation of fruit samples

The samples of mango, banana, and mulberry were collected from the nearby orchard where the irrigation source was the pharmaceutical effluent. The fruit samples were washed to remove any contamination and, after careful sorting of fruits, they were subjected to hot water treatment in cotton bags at 60°C for 4 minutes, then removed and cooled at 25°C. Then it was dried in a desiccator at 60°C for 3 hours. After that, it was crushed into a fine paste and the sample was digested with 30% hydrogen peroxide (H_2O_2) and 50% nitric acid solution (22).

The labeled fruit samples were filtered and diluted with 20 mL of distilled water and saved in a test tube for heavy metal detection by atomic absorption spectrophotometer (Buck model 210VGP HACH). Fresh juice from fruit samples was extracted and filtered twice to remove any excess pulp. The sample was labeled and saved for further chemical analysis (23).

Fruit weight and shelf life

The fruit weights of mango, banana, and mulberry cultivars were noted by a digital weighing balance. Shelf life is regarded as the period during which fruits can be marketed after ripening. It is called shelf life.

Metal Analyses by Atomic absorption spectrophotometer

Before running the samples, calibration curves for each sample were prepared using de-ionized water in the range of 0-100 mg/L. The blank was also prepared, which was free of CECs. The calibration curves were plotted by using absorbance vs

concentration and the linearity of the curves was demonstrated by the coefficient of determination (R^2), which ranged from (0.91-to 0.99) with a mean value of 0.95. The operating conditions for the analysis of heavy metals by AAS are given in table 1.

Physiochemical parameters Analyses
Physiochemical parameters such as pH, total suspended solids (TSS), dissolved oxygen, biochemical oxygen demand (BOD), chemical oxygen demand (COD), electrical conductivity, the concentration of ions (Na^+, K^+, Ca^{2+}, CO_3^{2-} /HCO_3^-, Cl^-, Mg^{2+} and SO_4^{2-}, residual sodium carbonate (RSC), and metal ion concentration were checked in the pharmaceutical effluent samples following standard procedures and methods. The pH was determined using a potentiometer. Total dissolved solids in the effluent sample were measured using TDS meter. The dissolved oxygen concentration in the unit (mg/L) was measured by DO meter (Jenway970/HACH Method 8215 & 8043 resp). Biochemical oxygen demand was measured using (BOD) monometer. Chemical oxygen demand was measured using potassium dichromate in 50% sulphuric acid solution and COD meter (Lovi bond RD 125/HACH Method 8000). The sodium ion concentration was analyzed by flame photometer and metal ion concentration by using titration and Schott instrument.

Statistical Analysis
Using IBM SPSS 21, the mean and standard deviation of the heavy metals in the effluent samples, soil samples and fruits were calculated. All calculated results were then subjected to one-way ANOVA with 0.05 probability levels.

RESULTS AND DISCUSSION

Measurement of physicochemical parameters of the effluent sample
All physicochemical parameters, such as TSS, titratable acidity, chemical oxygen demand, TDS, shelf life, biological oxygen demand, ascorbic acid, mineral content, and heavy metal concentration were significantly affected by the irrigation of pharmaceutical effluent. The physiochemical parameters were analyzed separately for each effluent sample, and then the water quality index was calculated. All effluent samples were assessed for these physicochemical parameters (Table 2-4). The pH ranged from 7.8 to 8.8, BOD ranged from 128-142 mg/L, and COD ranged from 279-292 mg/L in the three samples collected from the initial point as listed in table 2. The pH ranged from 8.1-9.1, BOD ranged from 161 to 168 mg/L, and COD ranged from 260 to 276 mg/L in the three samples collected from the initial point as listed in table 3. The pH ranged from 8.3-9.2, BOD ranged from 291-95 mg/L, and COD ranged from 151-169 mg/L in the three samples collected from the initial point as listed in table 4. Irrigation of wastewater improves the biochemical attributes such as flavonoids, antioxidants, and total phenolic of the crops. Literature reported findings concluded that total suspended solids in fruits increased when irrigated with wastewater than with well water (24). Fruit weight and shelf life remain unaffected by the irrigation water.

Among the cultivars, mango resulted in the maximum fruit weight (350.1 g), while the minimum fruit weight was attained in mango (562.5 g). The rate of chemical and biological processes is dependent on the temperature. The optimal temperature for fruits depends on the survival life and good growth of fruits, whereas others prefer warmer water. If the temperature of the water becomes higher than the allowed range of NEQs and WHO for a longer period, then this irrigation water becomes harmful to soil and fruits that are growing by the irrigation of these effluents. Temperature directly affects the concentration of oxygen in the water. By increasing the temperature of effluents, the concentration of oxygen decreases. pH directly affects the concentration of oxygen in the water. By increasing the pH of effluents, the concentration of oxygen decreases. These effluents, which have a high pH from the range of MAC are not good for the growth of fruits and vegetables.

Table 1: Operating conditions for the analysis of heavy metals using AAS.

Element	Cd	Cr	Cu	Pb
Wavelength (nm)	288.8	357.9	324.8	283.3
Burner height (mm)	9	7	7	9
Lamp current (mA)	12	12	8	10
Acetylene flow rate (L/min)	2	1.8	2	1.8
Air flow rate	15	17	17	15

Table 2: Results of pharmaceutical effluents analysis from the initial point.

Sr No.	Parameters	[1]Mean±SD	[2]Mean±SD	[3]Mean±SD	[4]NEQS	[5]WHO
1	Temperature (^{0}C)	34±1.44	35 ± 1.42	33±1.45	37	40
2	pH	7.8±0.34	8.2 ± 0.34	8.8±0.34	8.4	6-9
3	DO (mg/L)	0.7±0.04	0.8±0.03	0.6±0.02	NA	5-9
4	COD (mg/L)	279±13.4	281±12.6	292±14.1	150	150
5	BOD (mg/L)	128±5.68	137±5.28	142±5.27	80	50
6	TDS (mg/L)	3140±114.8	3210±114.9	3302±115.2	3500	2000
7	TSS (mg/L)	641±24	560±23	595±23	200	150
8	Na^+ (mg/L)	3.92±0.14	4.75±0.15	5.42±0.12	9	9
9	K^+ (mg/L)	0.41±0.24	0.49±0.22	0.62±0.31	9	9
10	Ca^{2+} (mg/L)	0.93±0.31	0.81±0.32	0.46±0.33	9	9
11	CO_3^{2-} (mg/L)	6.9±0.29	7.2±0.31	7.3±0.26	9	9
12	HCO_3^- (mg/L)	0.41±0.32	0.39±0.22	0.49±0.38	8.5	8.5
13	Cl^- (mg/L)	21.69±0.48	22.42±0.41	22.93±0.39	10	10
14	Mg^{2+}(mg/L)	2.42±0.21	2.39±0.28	3.10±0.30	3	9
15	SO_4^{2-} (mg/L)	560±18.02	662±17.09	570±17.95	500	500
16	SAR (mg/L)	4.36±0.19	4.21±0.22	3.92±0.23	-	<6
17	RSC (mg/L)	1.92±1.01	1.31±1.22	1.62±1.08	-	<40

[1]Mean±SD= Mean ± SD (standard deviation) from the upper surface of the water (ES-1).
[2]Mean±SD= Mean ± SD (standard deviation) from the center surface of the water (ES-2).
[3]Mean±SD= Mean ± SD (standard deviation) from the bottom surface of the water (ES-3).
[4]NEQS= National Environmental Quality Standards.
[5]WHO= World Health Organization

Table 3: Results of pharmaceutical effluents analysis from the initial point to 500 (meters) away.

Sr No.	Parameters	[1]Mean±SD	[2]Mean±SD	[3]Mean±SD	[4]NEQS	[5]WHO
1	Temperature (^{0}C)	38±1.41	37±1.41	39±1.42	37	40
2	pH	8.1±0.32	8.4±0.32	9.1±0.31	8.4	6-9
3	DO (mg/L)	0.7±0.01	0.9±0.09	0.6±0.07	NA	5-9
4	COD (mg/L)	276±13.2	242±12.3	260±14.	150	150
5	BOD (mg/L)	161±5.64	157±5.21	168±5.21	80	50
6	TDS (mg/L)	2960±114.7	3161±114.1	3202±115.2	3500	2000
7	TSS (mg/L)	494±22	520±21	563±22	200	150
8	Na^+ (mg/L)	4.93±0.11	4.41±0.11	5.21±0.17	9	9
9	K^+ (mg/L)	0.92±0.22	1.21±0.23	1.31±0.32	9	9
10	Ca^{2+} (mg/L)	0.88±0.36	0.99±0.36	0.93±0.35	9	9
11	CO_3^{2-} (mg/L)	6.4±0.21	6.9±0.33	7.1±0.22	9	9
12	HCO_3^- (mg/L)	0.41±0.33	0.32±0.23	0.64±0.35	8.5	8.5
13	Cl^- (mg/L)	22.72±0.42	22.31±0.45	21.92±0.31	10	10
14	Mg^{2+}(mg/L)	2.92±0.22	3.21±0.21	3.42±0.34	3	9

15	SO_4^{2-} (mg/L)	602±18.01	590±17.00	660±17.96	500	500
16	SAR (mg/L)	4.92±0.13	4.12±0.28	3.99±0.21	-	<6
17	RSC (mg/L)	2.01±1.07	2.12±1.27	1.99±1.03	-	<40

[1]Mean±SD = Mean±SD (standard deviation) from the upper surface of the water (ES-4).
[2]Mean±SD= Mean±SD (standard deviation) from the center surface of the water (ES-5).
[3]Mean±SD= Mean±SD (standard deviation) from the bottom surface of the water (ES-6).
[4]NEQS= National Environmental Quality Standards.
[5]WHO= World Health Organization.

Table 4: Results of effluents analysis from the initial point to 1000 meters.

Sr No.	Parameters	[1]Mean±SD	[2]Mean±SD	[3]Mean±SD	[4]NEQS	[5]WHO
1	Temperature (°C)	39±1.41	38±1.32	41±1.46	37	40
2	pH	8.3±0.37	9.2±0.34	8.3±0.39	8.4	6-9
3	DO (mg/L)	0.8±0.01	0.5±0.04	0.2±0.04	NA	5-9
4	COD (mg/L)	291±13.9	263±12.5	295±14.4	150	150
5	BOD (mg/L)	169±5.62	182±5.22	151±5.21	80	50
6	TDS (mg/L)	3466±114.1	3342 ±114.2	3240 ±115.5	3500	2000
7	TSS (mg/L)	602±22	660±24	720±24	200	150
8	Na^+ (mg/L)	4.66±0.12	4.84±0.12	4.66±0.11	9	9
9	K^+ (mg/L)	1.10±0.22	2.0±0.21	1.01±0.34	9	9
10	Ca^{2+} (mg/L)	0.72±0.33	0.32±0.32	0.91±0.33	9	9
11	CO_3^{2-} (mg/L)	7.6±0.22	6.1±0.34	7.1±0.22	9	9
12	HCO_3^{-} (mg/L)	0.42±0.31	1.0±0.27	0.39±0.37	8.5	8.5
13	Cl^- (mg/L)	22.93±0.38	22.42±0.31	21.90±0.29	10	10
14	Mg^{2+}(mg/L)	3.21±0.28	3.22±0.24	3.93±0.39	3	9
15	SO_4^{2-} (mg/L)	593±18.12	522±17.	595±17.92	500	500
16	SAR (mg/L)	3.98±0.19	4.21±1.2.	4.21±0.23	-	<6
17	RSC (mg/L)	1.91±1.01	1.81±0.013	1.21±1.04	-	<40

[1]Mean±SD= Mean±SD (standard deviation) from the upper surface of the water (ES-7).
[2]Mean±SD= Mean±SD (standard deviation) from the canter surface of the water (ES-8).
[3]Mean±SD= Mean±SD (standard deviation) from the bottom surface of the water (ES-9).
[4]NEQS= National Environmental Quality Standards.
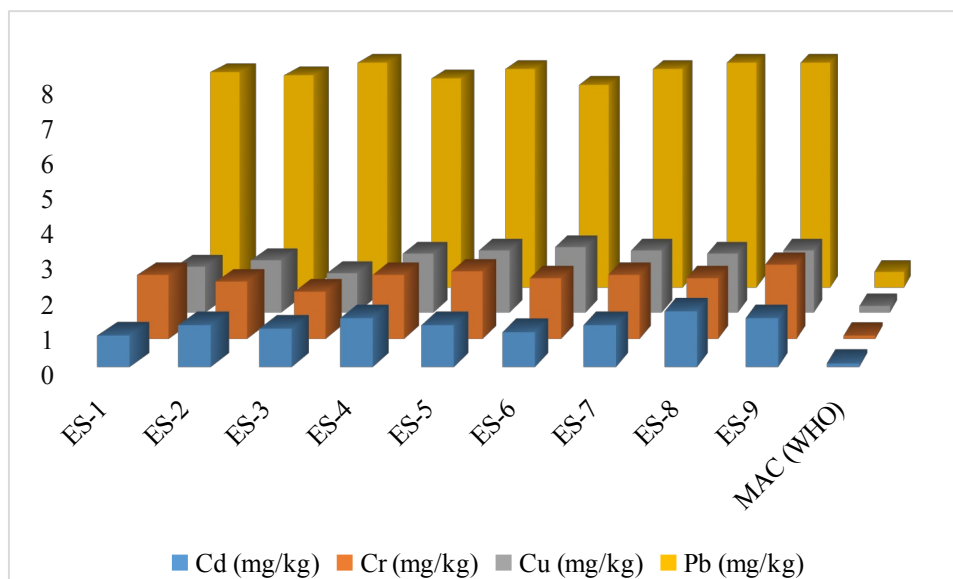[5]WHO= World Health Organization.

Figure 2: Heavy metal concentration (mg/Kg) in the effluent samples collected from nine sites of Sahiwal and comparison with WHO values.

Water Quality Index of irrigated water

The water quality index is not linked to a single parameter. The physiochemical analysis, as shown in tables 2-4, helps us to study the water quality parameters one by one. However, the water quality index gives us a combined quality index of all parameters. The irrigation water quality index (WQI) of all effluent samples ranged from 63.5- to 63.57 which according to WHO can be used for irrigation purposes as it is non-drinkable water. Thus, the irrigation water quality index (IWQI) is used to assess the quality of irrigation water. The application of this method is carried out based on the criteria specified in FAO 29. Regional characteristics were also investigated in this study. The advantage of IWQI is that it generalizes different quality parameters.

Table 4: Water standards and WQI calculations of effluent sample 1(ES-1 to ES-3), sample 2 (ES-4 to ES-6), and sample 3 (ES-6 to ES-9).

Sr. no	Parameters	Wn = K/Sn (Sample 1)	Wq_n = Wn* qn [b]	W_n = K/Sn (Sample 2)	Wqn = Wn * qn	Wn = K/Sn (Sample 3)	Wqn = Wn * qn
1	pH	0.093875459	8.579347	0.093952	8.626309431	0.093951761	8.626309431
2	DO (mg/L)	0.090514486	0.737525	0.090507	0.737463332	0.090506863	0.737463332
3	COD (mg/L)	0.005430869	0.938937	0.00543	0.938857864	0.005430412	0.938857864
4	BOD (mg/L)	0.016292607	5.278805	0.016291	5.278360279	0.016291235	5.278360279
5	TDS [a] (mg/L)	0.00081463	0.25316	0.000815	0.253138646	0.000814562	0.253138646
6	TSS (mg/L)	0.005430869	1.903218	0.00543	1.90305765	0.005430412	1.90305765
7	Na^+ (mg/L)	0.090514486	4.877725	0.090507	4.87731431	0.090506863	4.87731431
8	K^+ (mg/L)	0.090514486	1.153222	0.090507	1.153124483	0.090506863	1.153124483
9	Ca^{2+} (mg/L)	0.090514486	0.938669	0.090507	0.938589695	0.090506863	0.938589695
10	CO_3^{2-} (mg/L)	0.090514486	6.838872	0.090507	6.838296353	0.090506863	6.838296353
11	HCO_3^- (mg/L)	0.095838867	0.514899	0.095831	0.514855653	0.095830797	0.514855653

12	Cl$^-$ (mg/L)	0.081463037	18.17983	0.081456	18.17830353	0.081456177	18.17830353
13	Mg^{2+}(mg/L)	0.090514486	3.201531	0.090507	3.201261283	0.090506863	3.201261283
14	SO$_4^{2-}$ (mg/L)	0.001629261	0.201159	0.001629	0.201142453	0.001629124	0.201142453
15	SAR (mg/L)	0.135771728	9.828365	0.13576	9.827536927	0.135760295	9.827536927
16	RSC (mg/L)	0.020365759	0.103865	0.020364	0.103856626	0.020364044	0.103856626
	Total	ΣWn = 1	ΣWqn = 63.52913284	ΣWn= 1	ΣWqn= 63.57147	ΣWn= 1	ΣWqn = 63.57146852

^{a} total dissolved solid ^{b} quality rating values

Values for quality rating were calculated by using the formula:

$$q_{ni} = \left[\frac{(V_{actual} - V_{ideal})}{(V_{standard} - V_{ideal})} \right] \times 100$$

V_{actual} = value of parameter of sample
V_{ideal} = value of parameter ideally
$V_{standard}$ = value of parameter as standard

Water quality index WQI (Sample 1) = $\dfrac{\Sigma W_n qn}{\Sigma W}$

= 63.5291 / 1
= 63.5291

WQI (Sample 2) = $\dfrac{\Sigma W_n qn}{\Sigma W}$

    = 63.57147/ 1
    = 63.57147

WQI (Sample 2) = $\dfrac{\Sigma W_n qn}{\Sigma W}$

    = 64.50654/ 1
    = 64.50654

Heavy metals in soil layers and fruits
The soil sample taken from the areas which were irrigated with pharmaceutical water was investigated and found to have varying concentrations of heavy metal content (Cu, Cd, Cr, and Pb), which is shown in table 6. The results showed noticeable differences in the concentration of each sample, which was later analyzed by comparing them with the neutral soil sample as a reference and found to have the higher heavy metal concentration due to the variant pH values and the concentration of organic matter. We employed statistical analysis to check for significant differences in the values of the different samples. Table 5 indicated the statistical analysis of soil samples from different sites, which showed that the data for SOR-1 and SOR-3 is highly skewed. The present study indicates that the pharmaceutical irrigated soil has a higher concentration of cadmium (mg/kg) when compared with the WHO value, which is shown in Fig. 2. However, the present study results are compared with those of Anjum *et.al.,* who analyzed the different areas of Sahiwal, and noted that nickel accumulation in soil was non-significant. Heavy metal accumulation varied significantly between soil layers. The copper concentration was found to be highest in the 1st soil layer, labeled as SOR-1. As we predicted, the concentration of heavy metals in soil should gradually decrease from the top layer to the bottom layer irrigated with pharmaceutical wastewater. However, the scenario was a bit different and the copper content significantly increased down the layer. The main reason behind this is that the heavy metals sometimes leach from the top layer of the soil to the bottom resulting in increased concentration of copper and also variable conditions such as pH of the soil, contaminants, and composition of the soil. Cd, Cr, and Pb. Zinc was not detected in the soil sample. Therefore, it has not been discussed in these sections. The purpose of studying soil irrigated with pharmaceutical wastewater is to see the effect of heavy metals' accumulation in the soil on the fruit.
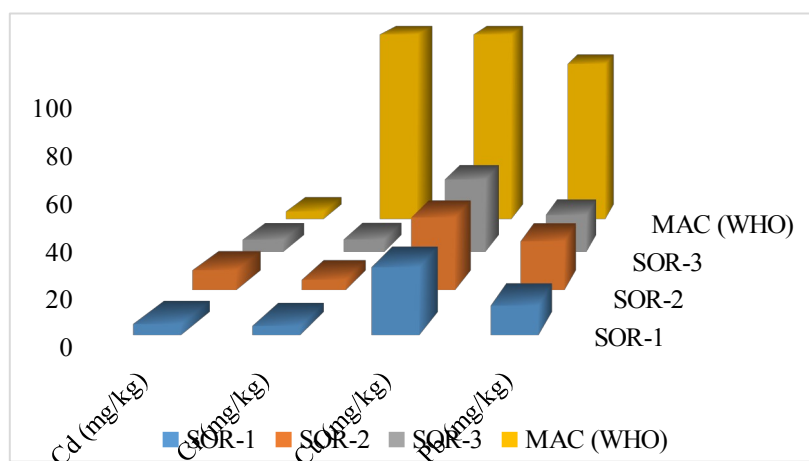
Figure 3: Heavy metal contents (mg/kg) in soil layers irrigated with pharmaceutical effluent.

Table 5: Statistical analysis of metal content mg/kg in the soil; standard deviation, variance, skewness, and kurtosis.

Descriptive Statistics

	N	Range	Mean		Std. Deviation	Variance	Skewness		Kurtosis	
	Statistic	Statistic	Statistic	Std. Error	Statistic	Statistic	Statistic	Std. Error	Statistic	Std. Error
SOR-1*	4	25	12.58	5.813	11.626	135.163	1.404	1.014	1.480	2.619
SOR-2**	4	29	17.63	6.601	13.202	174.283	.480	1.014	-2.393	2.619
SOR-3***	4	30	16.80	7.153	14.305	204.633	1.166	1.014	.297	2.619
Valid N (list wise)	4									

*SOR-1 = Soil Samples from the upper surface, which is irrigated by pharmaceutical effluents.
**SOR-2 =Soil Sample from the upper surface at 5 cm depth, which was irrigated by pharmaceutical effluents.
***SOR-3 =Soil Sample from the upper surface 10 cm depth, which is irrigated by pharmaceutical effluents

Table 6: Detection of heavy metals (Cu, Pb, Cr and Cd) in various sources of irrigation water and its effects on heavy metal accumulation on soils and fruits.

Effluent sample	Cd	Cr	Cu	Pb
	(mg/kg)	(mg/kg)	(mg/kg)	(mg/kg)
ES-1	0.9	1.9	1.4	6.8
ES-2	1.2	1.7	1.6	6.7
ES-3	1.1	1.4	1.2	7.1
ES-4	1.4	1.9	1.8	6.6

ES-5	1.2	2	1.9	6.9
ES-6	1	1.8	2	6.4
ES-7	1.2	1.9	1.9	6.9
ES-8	1.6	1.8	1.8	7.1
ES-9	1.4	2.2	1.9	7.1
SOR-1	4.8	3.9	29	12.6
SOR-2	9.2	4.8	33.8	22.7
SOR-3	6.1	6.2	36.4	18.5
Banana	0	1.203	0	0.231
Mango	0.005	0.891	0.005	0.189
Mulberry	0.002	0.769	0.002	1.248

Table 7: ANOVA analysis of effluents, soil, and fruits.

	Sum of Squares	df	Mean Square	F
Between Groups	965.167	36	26.810	3.983
Within Groups	154.833	23	6.732	
Total	1120.00	59		

The value of F obtained (F= 3.98) experimentally is higher than the theoretical value, so the null hypothesis prediction is dismissed, which means that the value of F is a statistically significant value, and therefore, the null hypothesis is rejected, which means there is a difference between the average value of the soil, fruits, and effluent sample group.

CONCLUSION

Pharmaceutical irrigation water affects the quality attributes of mango, banana, and mulberry. Farmers are attracted to sewage water irrigation as it increases organic matter, but in comparison to canal water, it contaminates the soil, leaves, and fruits with heavy metals. The physiochemical attributes and water quality index show that irrigation water is safe, but still, the risk of contamination can be reduced by educating the farmers to use canal water or treated sewage water by using efficient and low-cost adsorbents. The current study gives an overview of how heavy metals accumulate in the fruit through irrigation water, which has an adverse effect on the living standards of human health. This research article is based on the hazardous element contamination in different fruits observed in Sahiwal, Pakistan, along with the wastewater-irrigated soil. Literature articles focused on either effluent or fruit samples, but this article targeted the heavy metal accumulation in wastewater, soil, and irrigated orchards. Bioaccumulation variables, physicochemical factors, possible dangers, and enrichment factors were evaluated by comparing them to the identified hazardous materials.

CONFLICT OF INTEREST

The authors declare that they have no known competing financial interests that could have appeared to influence the work reported in this paper.

REFERENCES

1. Chidozie K, Nwakanma C. Assessment of saclux paint industrial effluents on Nkoho River in Abia State, Nigeria. J Ecosyst Ecography. 2017;7(2).

2. Nriagu JO, Pacyna JM. Quantitative assessment of worldwide contamination of air, water and soils by trace metals. Nature. 1988 May;333(6169):134–9. <DOI>.

3. Mohammed AS, Kapri A, Goel R. Heavy Metal Pollution: Source, Impact, and Remedies. In: Khan MS, Zaidi A, Goel R, Musarrat J, editors. Biomanagement of Metal-Contaminated Soils [Internet]. Dordrecht: Springer Netherlands; 2011 [cited 2022 Apr 27]. p. 1–28. (Environmental Pollution; vol. 20). <URL>.

4. Dayan AD, Paine AJ. Mechanisms of chromium toxicity, carcinogenicity and allergenicity: Review of the literature

from 1985 to 2000. Hum Exp Toxicol. 2001 Sep;20(9):439–51. <DOI>.

5. Costa M, Klein CB. Toxicity and Carcinogenicity of Chromium Compounds in Humans. Critical Reviews in Toxicology. 2006 Jan;36(2):155–63. <DOI>.

6. An H. Crab shell for the removal of heavy metals from aqueous solution. Water Research. 2001 Oct;35(15):3551–6. <DOI>.

7. Imaga C, Abia A. c A comparative study of adsorption kinetics and mechanisms of zinc (II) ion sorption using carbonized and modified sorghum (Sorghum bicolor) hull of two pore sizes (150 μm and 250 μm). Global Journal of Science Frontier Research. 2015;15(1):1–15.

8. Duruibe JO, Ogwuegbu M, Egwurugwu J. Heavy metal pollution and human biotoxic effects. International Journal of physical sciences. 2007;2(5):112–8.

9. Ben Mordechay E, Mordehay V, Tarchitzky J, Chefetz B. Pharmaceuticals in edible crops irrigated with reclaimed wastewater: Evidence from a large survey in Israel. Journal of Hazardous Materials. 2021 Aug;416:126184. <DOI>.

10. Krzeminski P, Tomei MC, Karaolia P, Langenhoff A, Almeida CMR, Felis E, et al. Performance of secondary wastewater treatment methods for the removal of contaminants of emerging concern implicated in crop uptake and antibiotic resistance spread: A review. Science of The Total Environment. 2019 Jan;648:1052–81. <DOI>.

11. Carter LJ, Chefetz B, Abdeen Z, Boxall ABA. Emerging investigator series: towards a framework for establishing the impacts of pharmaceuticals in wastewater irrigation systems on agro-ecosystems and human health. Environ Sci: Processes Impacts. 2019;21(4):605–22. <DOI>.

12. Hoerger CC, Dörr B, Schlienger C, Straub JO. Environmental Risk Assessment for the Galenical Formulation of Solid Medicinal Products at Roche Basle, Switzerland. Integr Environ Assess Manag. 2009;5(2):331. <DOI>.

13. Lee AH, Fraz S, Purohit U, Campos AR, Wilson JY. Chronic exposure of Brown (Hydra oligactis) and green Hydra (Hydra viridissima) to environmentally relevant concentrations of pharmaceuticals. Science of The Total Environment. 2020 Aug;732:139232. <DOI>.

14. Stoczynski L, van den Hurk P. Effects of selective serotonin reuptake inhibitor sertraline on hybrid striped bass predatory behavior and brain chemistry. Aquatic Toxicology. 2020 Sep;226:105564. <DOI>.

15. Nentwig G. Effects of Pharmaceuticals on Aquatic Invertebrates. Part II: The Antidepressant Drug Fluoxetine. Arch Environ Contam Toxicol. 2007 Feb;52(2):163–70. <DOI>.

16. Burkina V, Zlabek V, Zamaratskaia G. Effects of pharmaceuticals present in aquatic environment on Phase I metabolism in fish. Environmental Toxicology and Pharmacology. 2015 Sep;40(2):430–44. <DOI>.

17. Khalil N, Ashour M, Fikry S, Singab AN, Salama O. Chemical composition and antimicrobial activity of the essential oils of selected Apiaceous fruits. Future Journal of Pharmaceutical Sciences. 2018 Jun;4(1):88–92. <DOI>.

18. Shahsavan-Davoudi M hossein, Ziarati P. Green Method for Cadmium Removal from Pharmaceutical Effluent Laboratories by Grapefruit Peel. Journal of Medical Discovery. 2020;5(3):1–13.

19. Abdullahi A, Ighalo J, Ajala O, Ayika S. Physicochemical Analysis and Heavy Metals Remediation of Pharmaceutical Industry Effluent Using Bentonite Clay Modified by H2SO4 and HCl. Journal of the Turkish Chemical Society Section A: Chemistry. 2020 Oct 30;7(3):727–44. <DOI>.

20. Hamaidi-Chergui F, Brahim Errahmani M. Water quality and physicochemical parameters of outgoing waters in a pharmaceutical plant. Appl Water Sci. 2019 Oct;9(7):165. <DOI>.

21. Vanitha M, Thatheyus AJ. Assessment of Pollution by Physico-Chemical Parameters of Sathiyar River in Madurai District. International Journal of Multidisciplinary Researches. :82.

22. Yaqub G, Khan A, Zishan Ahmad M, Irshad U. Determination of Concentration of Heavy Metals in Fruits, Vegetables, Groundwater, and Soil Samples of the Cement Industry and Nearby Communities and Assessment of Associated Health Risks. Faisal Manzoor M, editor. Journal of Food Quality. 2021 Sep 30;2021:1–9. <DOI>.

23. Anastácio M, dos Santos APM, Aschner M, Mateus L. Determination of trace metals in fruit juices in the Portuguese market. Toxicology Reports. 2018;5:434–9. <DOI>.

24. Parsons LR. Agricultural Use of Reclaimed Water in Florida: Food for Thought. Journal of Contemporary Water Research & Education. 2018 Dec;165(1):20–7. <DOI>.

A Novel Potentiometric Sensor for the Determination of Pb(II) Ions Based on a Carbothioamide Derivative in PVC Matrix

Oguz Özbek[1*] iD

Zonguldak Bülent Ecevit University, Science and Technology, Application and Research Center, Zonguldak, 67600, Turkey

Abstract: In this research, a carbotioamide derivative molecule was synthesized to be used as an electroactive material, and poly (vinyl chloride) (PVC) membrane lead(II)–selective potentiometric sensors with different components were prepared. Among various compositions, the best potentiometric performance was exhibited by the membrane having the electroactive material, bis(2–ethylhexyl)sebacate (BEHS), PVC, and potassium tetrakis(*p*–chlorophenyl)borate (KT*p*ClPB) in the ratio of 4.0:63.0:32.0:1.0 (*w/w*). The proposed sensor exhibited a Nernstian response in the concentration range of 1.0×10^{-5}– 1.0×10^{-1} mol L^{-1} with a slope of 29.5 ± 1.6 mV/decade. The detection limit of the sensor was 3.96×10^{-6} mol L^{-1}. The potentiometric response of the lead(II)–selective sensor was independent of pH of test solution in the pH range of 5.0–9.0. The developed sensor had very good repeatability, stability, and selectivity, as well as a response time of 5s. These novel lead(II)–selective sensors, produced cost–efficiently, have been successfully used as an indicator electrode for the potentiometric titration of Pb(II) against EDTA and for the determination of Pb(II) ions in different water samples.

INTRODUCTION

The determination of heavy metal ions in various environmental samples has become very important due to the increasing interest in monitoring environmental pollution (1). Lead, one of the toxic heavy metal ions, can be found in various sources such as industrial emissions, car exhaust, drinking water, soil, contaminated food and beverages (2). These and similar sources can lead to an accumulation of lead in the body, and excessive lead can cause certain health problems, including those in synthesis of hemoglobin, in digestive, reproductive, and nervous systems, joints, and kidneys (3). Therefore, it is highly important to determine its concentration in various

environmental and biological samples. Lead concentration is commonly determined using various analytical methods such as inductively coupled plasma mass spectroscopy (ICP–MS) (4), liquid chromatography (5), and atomic absorption spectrometry (AAS) (6). However, these methods are expensive, involve complex procedures, require experienced personnel, are time consuming and often require pre–treatment.

The ion–selective electrodes (ISEs) developed using the potentiometry technique have very important advantages, such as the ease of preparation and use, short response time, low cost, wide linear concentration range, high selectivity, and low detection limit (7–10). These electrodes are widely

used in areas such as environmental, food, drug, clinical, and industrial analyses (11, 12).

The molecular structure of ionophores, which are in the composition of ion–selective electrodes and interact directly with the analyte, is very important in the design of potentiometric sensors. Ionophores, which contain various functional groups in their structure, are important components due to their interaction with ions. The use of non–commercial ionophores is an important factor that makes the sensors produced very cost–effective. In this study, a carbothioamide derivative molecule was synthesized, and lead(II)–selective sensors were prepared. The potentiometric performance characteristics and applications of these sensors were investigated.

EXPERIMENTAL

Reagents and chemicals
All reagents used in the ionophore synthesis were obtained from Sigma Aldrich. All reagents used were of analytical grade. High molecular weight PVC, BEHS, KTpClPB, bis(2–ethylhexyl)adipate (DEHA), o–nitrophenyloctyl ether (o–NPOE), tetrahydrofuran (THF), graphite and ethylenediaminetetraacetic acid (EDTA) were purchased from Sigma Aldrich. Sodium hydroxide (NaOH) and nitric acid (HNO₃) used for pH adjustment were obtained from Merck. Nitrate salts of the cations used in selectivity studies were obtained from Sigma Aldrich and Merck. Epoxy (Macroplast Su 2227) and hardener (Desmodur RFE) were obtained from Henkel (Istanbul, Turkey) and Bayer AG (Darmstadt, Germany), respectively.

Apparatus
Potentiometric measurement were obtained by using a computer–controlled multichannel potentiometric system (Medisen Medical Ltd. Sti., Turkey). In this system, a laboratory–made software was used. Ag/AgCl electrode used as reference electrode was purchased from Thermo–Orion. ^{1}H– and ^{13}C– NMR spectra were recorded on a Bruker Advance DPX–400 instrument. Melting points were measured on an Electrothermal 9100.

Method
Synthesis of (E)-2-((1H-pyrrol-2-yl)methylene) hydrazinecarbothioamide
(E)-2-((1H-pyrrol-2-yl)methylene)hydrazine carbo-thioamide was synthesized as previously reported in the literature (13). The 1H-pyrrole-2-carbaldehyde **(1)** (1 mmol) was dissolved in warm ethanol (15 mL). Thiosemicarbazide **(2)** (1 mmol) was dissolved in warm water (15 mL) and then added to this solution. Five drops of acetic acid were subsequently added to the mixture. The reaction was stirred magnetically for 4 hours at room conditions. The precipitate formed at the end of the reaction was filtered off. After washing with ethanol several

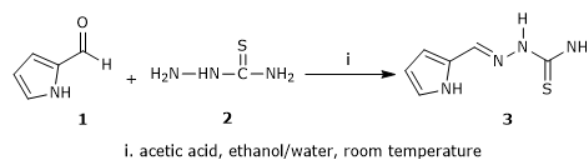times, (E)-2-((1H-pyrrol-2-yl)methylene) hydrazine-carbothioamide **(3)** was synthesized (Figure 1).

i. acetic acid, ethanol/water, room temperature

Figure 1: Synthesis schema of ionophore **(3)**.

Preparation of PVC membrane lead(II)–selective sensors
Lead(II)–selective PVC membrane sensors based on the synthesized carbothioamide derivative molecule (ionophore) were prepared by the method we previously reported (14–17). First, all solid state contact consisting of graphite, epoxy and hardener was taken at 50% (w/w), 35% (w/w) and 15% (w/w) ratios, respectively, and completely dissolved in approximately 3 mL of THF. After obtaining the appropriate viscosity, the ends of the copper wires were coated by dipping them into this mixture several times, and were kept in the dark at room temperature for about 24 hours. Then, different ratios of ionophore, plasticizer, PVC and KTpClPB were dissolved in THF and mixed homogeneously. Finally, the surface of the conductive solid contact was covered with PVC membrane by dipping it several times into the prepared membrane mixture. The coated electrodes were left to dry in the dark at room temperature. The prepared sensors and their potentiometric properties are given in Table 1.

Potential measurements
Potentials were measured using an Ag/AgCl reference electrode. All potential studies were carried out at 25 ± 1.0 °C temperature by using the following cell assembly:
Ag/AgCl; KCl (saturated) ‖ Pb²⁺ sample solution│lead(II)–selective sensor │conductive solid contact│Cu wire
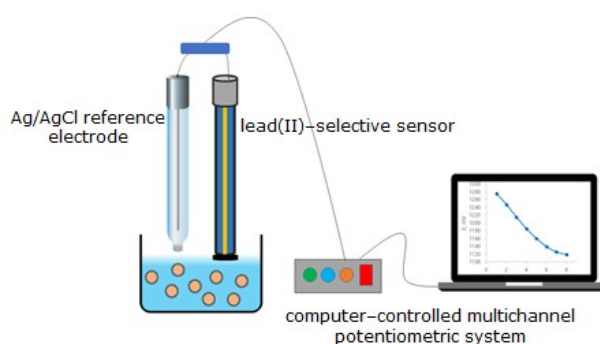The schema of the potentiometric measurement system is given in Figure 2.

Figure 2: Potentiometric measurement system.

RESULTS AND DISCUSSION

The synthesis of the ionophore used in this study was carried out in the laboratory. The synthesized molecule was characterized by ^{1}H− and ^{13}C− NMR (Figures 3 and 4). After the molecular structure was verified, PVC membrane sensors were prepared directly, and potentiometric measurements were taken.

(*E*)-2-((1*H*-pyrrol-2-yl)methylene)hydrazine-carbothioamide: Yellow solid. Yield 93%. M.p. 158–160 °C. ^{1}H NMR (400 MHz, δ, ppm, DMSO-*d6*): δ 11.36 (s, 1H), 11.26 (s, 1H), 8.05 (s, 1H), 7.95 (s, 1H), 7.83 (s, 1H), 6.98 (s, 1H), 6.40 (s, 1H), 6.11–6.09 (m, 1H); ^{13}C NMR (101 MHz, δ, ppm, DMSO−*d6*): 177.74, 134.17, 128.09, 122.23, 113.28, 109.66. The peaks of the protons in the structure are shown in Figure 3.

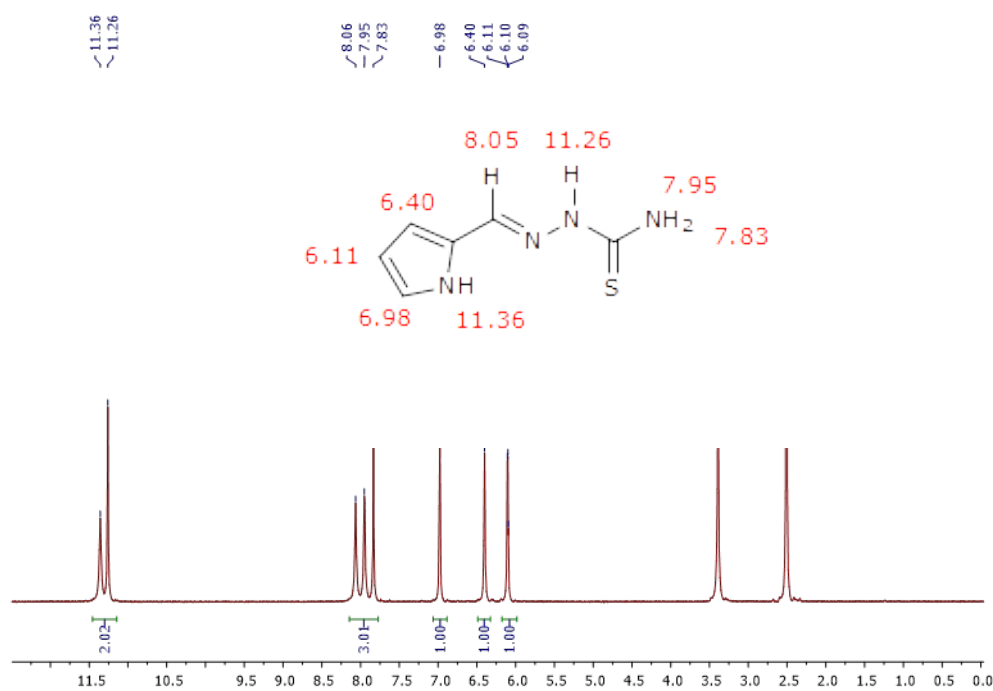**Figure 3:** ^{1}H NMR of the synthesized carbothioamide derivative molecule.
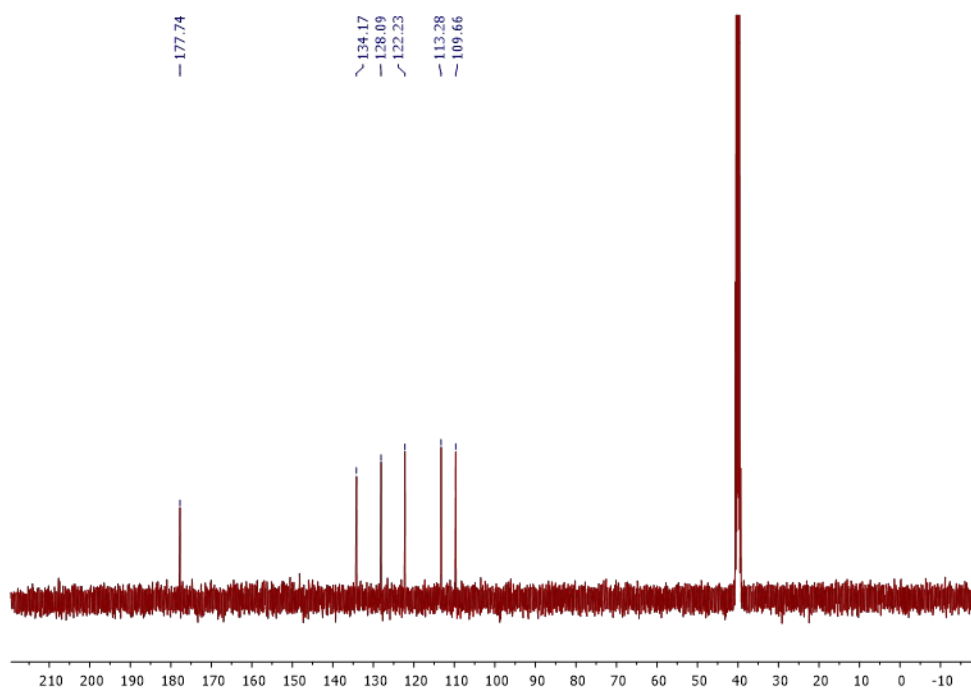

Figure 4: ^{13}C NMR of the synthesized carbothioamide derivative molecule.

Membrane components and their ratios are the most important factors that determine the potentiometric performance. In this study, PVC membranes with six different compositions were prepared using three different plasticizers (BEHS, DEHA, *o*−NPOE), and their potentiometric performance properties such as linear operating range, limit of detection, and slope were evaluated. The prepared membranes and their potentiometric properties are given in Table 1. As can be seen, sensor no 2 has the lowest detection limit (3.96×10^{-6} mol L^{-1}) over a wide linear working range. In addition, this sensor exhibited the most ideal Nernstian behavior in the concentration range of 1.0×10^{-1} – 1.0×10^{-5} mol L^{-1}. While the sensor prepared with *o*−NPOE does not exhibit Nernstian behavior, the sensors prepared with DEHA have a lower R^2 value. Therefore, sensor no 2 exhibited the best potentiometric performance, and sensors with

these components were used in the later stages of the study.

In this study, the potentiometric behavior of the proposed novel lead(II)−selective sensor aganist lead(II) ions was investigated in a concentration range of 1.0×10^{-1} – 1.0×10^{-7} mol L^{-1}. In this range, the sensor exhibited linear behavior in the concentration range of 1.0×10^{-1} – 1.0×10^{-5} mol L^{-1}. The potentiometric behavior of the developed sensor is given in Figure 5. The detection limit was calculated by substituting the potential value (916.0 mV) corresponding to the intersection point of the extrapolations of the two linear regions on the calibration curve (Figure 6) in the linear equation ($E = -29.487 (-\log[Pb^{2+}]) + 1075.3$). Thus, the detection limit of the sensor was calculated as 3.96×10^{-6} mol L^{-1}.

Table 1: The prepared PVC membrane components and its potentiometric characteristics.

No	Composition (% *w/w*)						R^2	Linear working concentration (mol L^{-1})	Limit of detection (mol L^{-1})	Slope (mV dec^{-1})
	Ionophore	PVC	KT*p*ClPB	BEHS	DEHA	*o*−NPOE				
1	3.0	30.0	1.0	66.0			0.9767	1.0×10^{-1} – 1.0×10^{-5}	5.2×10^{-6}	20.5±3.7
2	4.0	32.0	1.0	63.0			0.9949	1.0×10^{-1} – 1.0×10^{-5}	3.9×10^{-6}	29.5±1.6
3	5.0	30.0	1.0	64.0			0.9624	1.0×10^{-2} – 1.0×10^{-5}	7.9×10^{-6}	23.6±2.5
4	4.0	32.0	1.0		63.0		0.9901	1.0×10^{-1} – 1.0×10^{-5}	7.8×10^{-6}	27.5±2.2
5	5.0	32.0	1.0		62.0		0.9816	1.0×10^{-1} – 1.0×10^{-5}	1.3×10^{-5}	31.5±3.0
6	4.0	32.0	1.0			63.0	0.9912	1.0×10^{-2} – 1.0×10^{-5}	9.1×10^{-6}	14.5±1.2

The response time of the developed lead(II)−selective sensor was determined according to IUPAC recommendations (18). The time it takes the sensor to reach equilibrium at each 10−fold concentration change was examined. The developed sensor has a very fast response time of 5 seconds.

The repeatability study was performed with repeated measurements in three different

concentration ranges (1.0×10^{-2}, 1.0×10^{-3} and 1.0×10^{-4} mol L^{-1}). The repeatability of the measurements can also give information about the stability of the sensor. The return of signals for the 1.0×10^{-3} mol L^{-1} is more unstable than for the 1.0×10^{-2} mol L^{-1} and 1.0×10^{-4} mol L^{-1}. This may be due to the late arrival of the electrode to equilibrium. The experimental measurements in Figure 7 and Table 2 clearly show that the proposed sensor gives reproducible results.
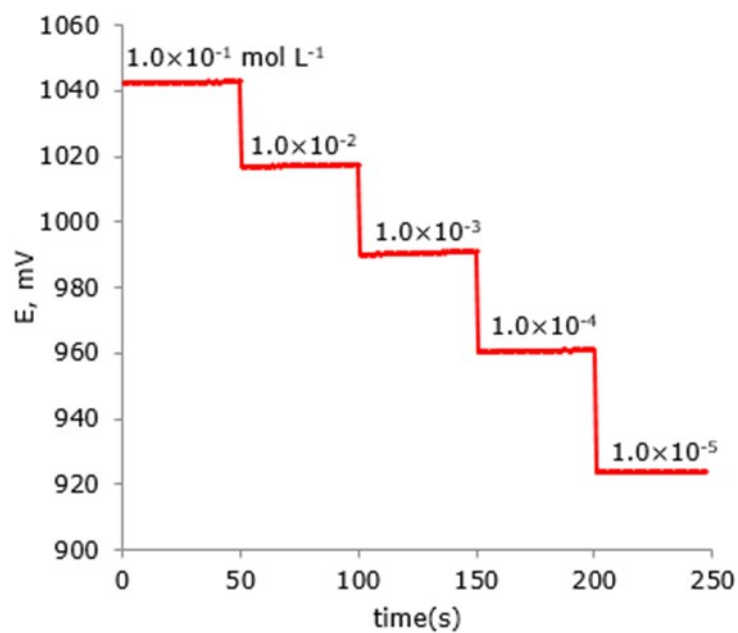
Figure 5: Potentiometric behavior of the developed lead(II)–selective sensor.
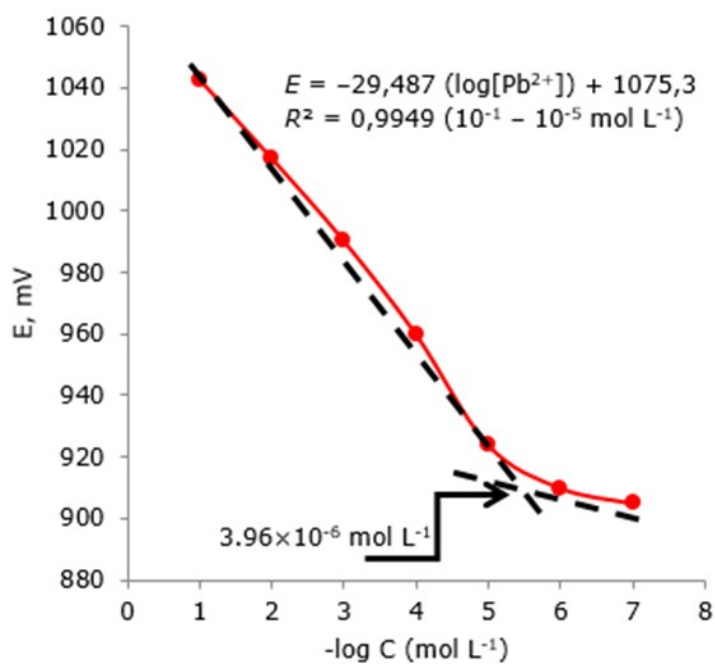

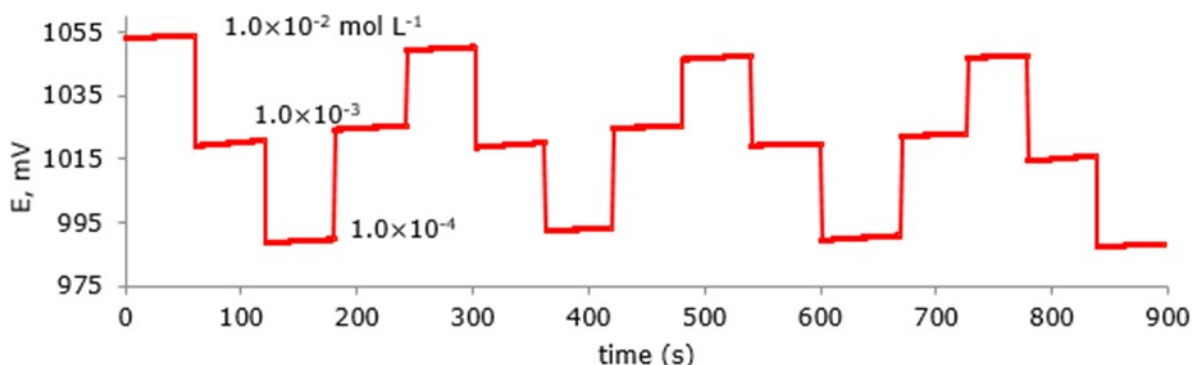**Figure 6:** Calibration curve of the developed lead(II)–selective sensor.

655

Figure 7: Repeatability of the developed lead(II)–selective sensor.

Table 2: The repeatability data of the lead(II)–selective sensor.

Pb(II) solution (mol L^{-1})	Potential (mV)				
	I	II	III	IV	Average (± SD)
1.0×10^{-2}	1053	1050	1047	1048	1049.5 (± 2.3)
1.0×10^{-3}	1021	1020	1019	1016	1019.0 (± 1.8)
1.0×10^{-4}	988	992	990	987	989.3 (± 1.92)

The selectivity of an ion–selective sensor is its specific behavior towards the main ion in the presence of different ionic species. The selectivity study of the sensor with optimum properties was performed using different cationic species. With the developed lead(II)–selective sensor, the potentiometric behavior of ions with different charges was investigated in the concentration range of 1.0×10^{-1} – 1.0×10^{-5} mol L^{-1}. Obtained test results are given in Figure 8. As can be seen here, there is a selectivity towards lead ions. On the other hand, the selectivity coefficients were determined by the separate solution method as suggested by IUPAC (19) and are given in Table 3. The values in Table 3 were calculated using the potential values of the ions at 1.0×10^{-1} mol L^{-1}.

Table 3: The calculated potentiometric selectivity coefficients of the lead(II)–selective sensor.

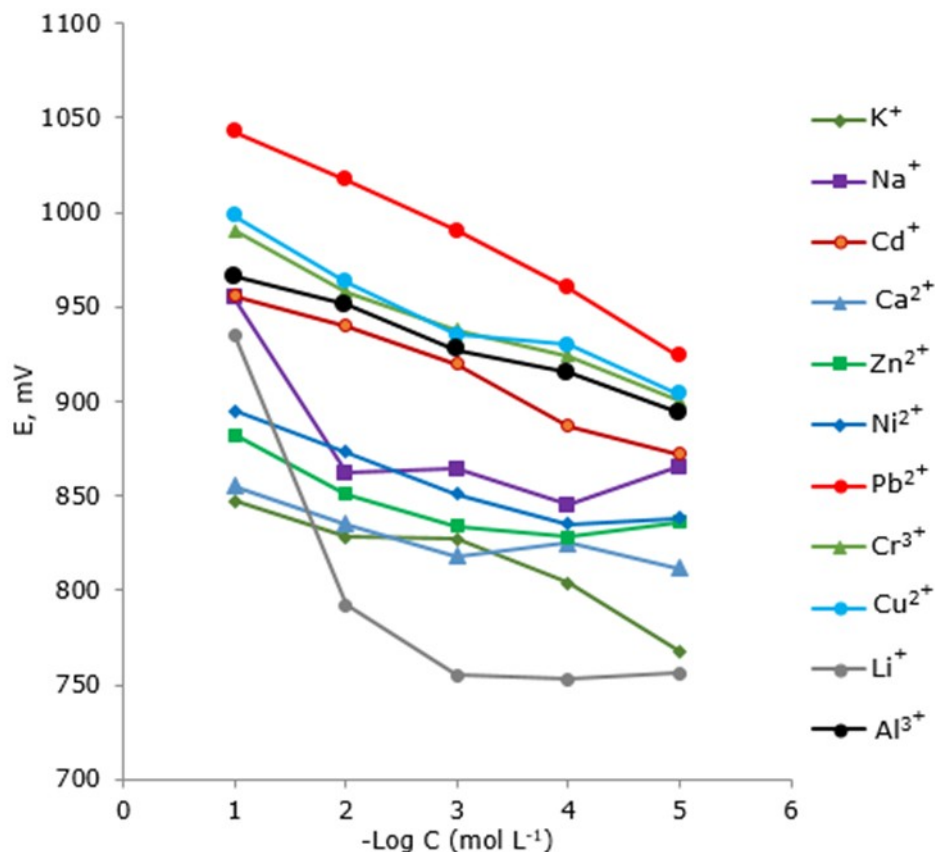| Interfering ions	Selectivity coefficient		Interfering ions	Selectivity coefficient	
	$\log K^{pot}_{Pb(2+), M(n+)}$	$K^{pot}_{Pb(2+), M(n+)}$		$\log K^{pot}_{Pb(2+), M(n+)}$	$K^{pot}_{Pb(2+), M(n+)}$
Cu^{2+}	−1.515	3.05×10^{-2}	Li$^+$	−3.644	2.27×10^{-4}
Cr^{3+}	−1.787	1.63×10^{-2}	Ni^{2+}	−4.999	1.00×10^{-5}
Al^{3+}	−2.598	2.52×10^{-3}	Zn^{2+}	−5.438	3.65×10^{-6}
Cd^{2+}	−2.936	1.16×10^{-3}	Ca^{2+}	−6.351	4.46×10^{-7}
Na$^+$	−2.968	1.08×10^{-3}	K$^+$	−6.620	2.40×10^{-7}

Figure 8: Potentiometric selectivity of the developed lead(II)–selective sensor.

When Table 3 is evaluated, it can be seen that Cu^{2+} has the highest selectivity coefficient. However, the developed sensor is approximately 100 times more selective for Pb^{2+} ions compared to Cu^{2+} ions.

The pH effect of the sensor was investigated at two concentrations of Pb^{2+} (1.0×10^{-2} and 1.0×10^{-3} mol L^{-1}). For this purpose, the solutions used in the pH working range of the sensor were prepared with HNO_3 for the pH range of 2.0–7.0, and NaOH for the pH range of 8.0–12.0. 1.0×10^{-2} mol L^{-1} Pb^{2+} solution was added to these solutions, and direct potentiometric measurements were taken. The potentiometric measurement results are shown in Figure 9. As can be seen in this figure, the developed sensor works independently of the pH of the test solution in the pH range of 5.0–9.0 at both concentrations. The high potential observed at low pH values (< 5.0) shows that the sensor can respond to hydrogen ions, while the low potential observed at high pH (>9.0) values may be due to the formation of $Pb(OH)_2$ in the solution.
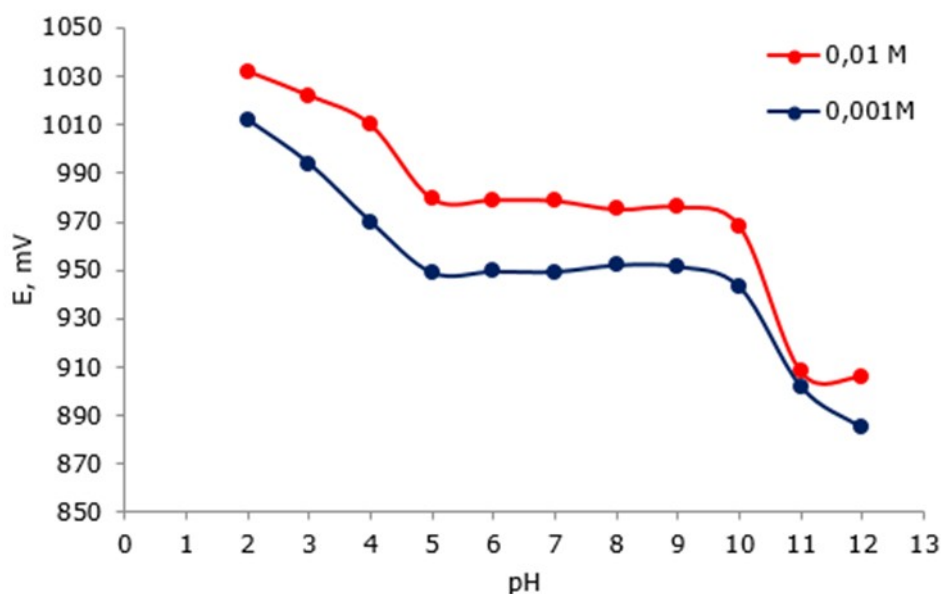
Figure 9: The effect of pH on the developed lead(II)−selective sensor.

Analytical applications of the sensor, whose potentiometric performance features were successfully completed, were carried out. The usability of the developed lead(II)−selective sensor as an indicator electrode by potentiometric titration was investigated. For this purpose, 1.0×10^{-2} mol L^{-1} EDTA solution was added to 10 mL of 1.0×10^{-3} mol L^{-1} Pb^{2+} solution and the potential obtained after each addition was recorded. A total of 2.0 mL of EDTA was added and, the titration end point was determined as 1.2. The potential (*E*)−added EDTA (mL) graph in Figure 10 was drawn with the obtained data. As a result, it is clear that the developed sensor can be used as an indicator electrode.
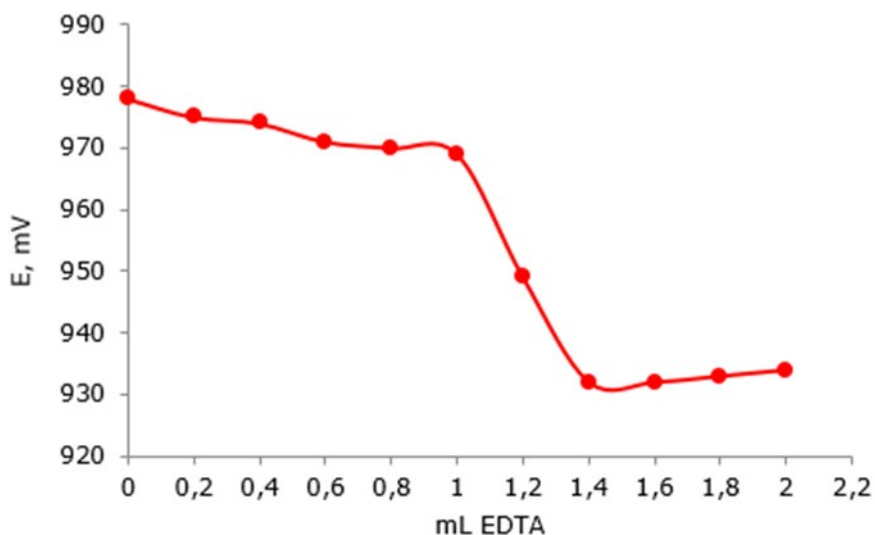

Figure 10: Potentiometric titration curve of Pb^{2+} ion with EDTA.

The standard addition method was used for the applications of the developed sensor in real samples. Herein, known concentrations of Pb(II) were added to different water samples. Then, direct potentiometric measurements were carried out with the developed sensor. The potential values thus obtained were substituted in the linear equation obtained from the calibration curve. Finally, the Pb^{2+} concentrations in the solution were determined by the sensor. The data of the measurements

performed in triplicate are given in Table 4, which shows that the developed sensor can be used successfully for lead determination in real samples.

Table 4: Analysis of Pb(II) in different water samples by use of the proposed sensor.

Real Sample	Pb(II) quantity, (mol L^{-1})		
	Added Pb(II)	Mean (± SD) found with sensor (average=3)*	% Recovery
Purification drinking water	1.00×10^{-2}	$9.71(\pm 0.15)\times10^{-3}$	97.1
Tap water (Zonguldak, Turkey)	1.00×10^{-3}	$9.60(\pm 0.21)\times10^{-4}$	96.0
Commercial drinking water	1.00×10^{-4}	$9.56(\pm 0.19)\times10^{-5}$	95.6

Comparison of the developed sensor with other potentiometric lead(II)–selective sensors is given in Table 5. When compared to other potentiometry–based sensors in the literature, the developed lead(II)–selective sensor has a relatively better linear concentration range, pH working range, and low detection limit. This developed sensor has a faster response time than existing lead(II)–selective sensors.

Table 5: The comparison of the proposed sensor with other lead(II)-selective sensors.

Ionophore	concentration range (mol L^{-1})	limit of detection (mol L^{-1})	pH working range	response time (s)	Slope (mV dec^{-1})	Ref.
acridono-crown ether	1.0×10^{-4} – 8.0×10^{-2}	7.9×10^{-6}	4.0–7.0	5	26.9	(20)
1,4,8,11-tetrathia cyclotetradecane	1.0×10^{-5} – 1.0×10^{-2}	2.2×10^{-6}	3.0–6.5	15	29.9	(21)
PbS nanoparticles	1.0×10^{-5} – 1.0×10^{-2}	Not reported	3.0–7.0	10	Not reported	(22)
amide-linked diporphyrin xanthene	2.6×10^{-6} – 1.0×10^{-1}	Not reported	4.5–7.5	<30	28.2	(23)
poly(m-phenylene diamine) microparticles	3.16×10^{-6} – 3.16×10^{-1}	6.31×10^{-6}	3.0–5.0	14	29.8	(24)
Schiff base complex [Co(L)$_2$] (ClO$_4$)·(C$_3$H$_6$O)·(H$_2$O)	1.0×10^{-5} – 1.0×10^{-2}	4.6×10^{-6}	4.0–13.0	10	23.9	(25)
(*E*)-2-((1*H*-pyrrol-2-yl)methylene)hydrazinecarbo thioamide	1.0×10^{-5} – 1.0×10^{-1}	3.96×10^{-6}	5.0–9.0	5	29.5±1.6	This work

CONCLUSION

In this study, the usability of a carbothioamide derivative molecule as an ionophore was investigated. Using the synthesized molecule, PVC membrane sensors were prepared at different rates, and high selectivity against Pb^{2+} ions was obtained. The new lead(II)–selective sensors, which can be produced very economically, have Nernstian behavior over a wide concentration range. The developed sensor has a very fast response time compared to other potentiometric lead(II)–selective sensors in the literature. Besides having a fast response time, this developed sensor can operate in a wide pH range without being affected by the changes in pH. The sensor, which performs very well in analytical applications, could be a new alternative for the determination of lead(II) ions in various samples considering the advantages it provides.

REFERENCES

1.   Esmailzadeh A, Afzali D, Fayazi M. Determination of lead (II) in environmental water samples by solid-phase extraction using a novel modified carbon hybridised sepiolite combined with flame atomic absorption spectrometry. Int. J. Environ. Anal. Chem. 2020; 1-13. <DOI>.

2.   Wuilloud RG, Acevedo HA, Vazquez FA, Martinez LD. Determination of lead in drinking water by ICP-AES with ultrasonic nebulization and flow-injection on-line preconcentration using an amberlite XAD-16 resin. Anal. Lett. 2002; 35(10): 1649-1665. <DOI>.

3.   Kendüzler E, Dinç MD, Trak D, Kabak B, Arslan Y. Separation/preconcentration and determination of lead (II) in drinking, spring and lake water samples. J. Anal. Chem. 2020; 75(10): 1264-1269. <DOI>.

4.   Rapp I, Schlosser C, Rusiecka D, Gledhill M, Achterberg EP. Automated preconcentration of Fe, Zn, Cu, Ni, Cd, Pb, Co, and Mn in seawater with analysis using high-resolution sector field inductively coupled plasma mass spectrometry. Anal. Chim. Acta 2017; 976: 1–13. <DOI>.

5.   Yang G, Hu Q, Huang Z, Yin J. Study on the determination of lead, cadmium, mercury, nickel and zinc by a rapid column high-performance liquid chromatographyatography. J. Braz. Chem. Soc. 2005; 16: 1154–1159. <DOI>.

6.   Tinas H, Ozbek N, Akman S. Determination of lead in flour samples directly by solid sampling high resolution continuum source graphite furnace atomic absorption spectrometry. Spectrochim. Acta Part B 2018; 140: 73–75. <DOI>.

7.   Özbek O, Isildak Ö, Isildak I. A potentiometric biosensor for the determination of valproic acid: human blood–based study of an anti–epileptic drug. Biochem. Eng. J. 2021; 176: 108181. <DOI>.

8.   Isildak Ö, Özbek O. Silver(I)-selective PVC membrane potentiometric sensor based on 5,10,15,20-tetra(4-pyridyl)-21H,23H-porphine and potentiometric applications. J. Chem. Sci. 2020; 132: 29. <DOI>.

9.   Isildak Ö, Özbek O. Yigit KM. Zinc(II)-selective PVC membrane potentiometric sensor for analysis of Zn2+ in drug sample and different environmental samples. Int. J. Environ. Anal. Chem. 101 (2021) 2035–2045. <DOI>.

10.   Özbek O, Isildak Ö, Berkel C. The use of porphyrins in potentiometric sensors as ionophores.

J. Incl. Phenom. Macrocycl. Chem. 2020; 98: 1–9. <DOI>.

11.   Isildak Ö, Özbek O. Application of potentiometric sensors in real samples. Crit. Rev. Anal. Chem. 2021; 51: 218–231. <DOI>.

12.   Özbek O, Berkel C, Isildak Ö, Isildak I. Potentiometric urea biosensors. Clin. Chim. Acta 2022; 524: 154–163. <DOI>.

13.   Alam MS, Liu L, Lee DU. Cytotoxicity of new 5-phenyl-4, 5-dihydro-1, 3, 4-thiadiazole analogues. Chem. Pharm. Bull. 2011; 59(11): 1413-1416. <DOI>.

14.   Özbek O, Isildak Ö. Potentiometric PVC membrane sensor for the determination of anti-epileptic drug levetiracetam in pharmaceutical formulations. ChemistrySelect, 2022; 7(3): e202103988. <DOI>.

15.   Isildak Ö, Özbek O, Gürdere MB. Development of chromium(III)-selective potentiometric sensor by using synthesized pyrazole derivative as an ionophore in PVC matrix and its applications. J. Anal. Test. 2020; 4: 273–280. <DOI>.

16.   Işıldak Ö, Deligönül N, Özbek O. A novel silver(I)-selective PVC membrane sensor and its potentiometric applications. Turk. J. Chem. 2019; 43: 1149–1158. <DOI>.

17.   Topcu C. Highly selective direct determination of chlorate ions by using a newly developed potentiometric electrode based on modified smectite. Talanta 2016; 161: 623–631. <DOI>.

18.   Buck RP, Lindner E. Recommendations for nomenclature of ion-selective electrodes. Pure Appl. Chem. 1994; 66: 2527–2536. <DOI>.

19.   Umezawa Y, Bühlmann P, Umezawa K, Tohda K, Amemiya AS. Potentiometric selectivity coefficention of ion-selective electrodes, Part I. Inorganic Cations. Pure Appl. Chem. 2000; 72: 1851–2082. <DOI>.

20.   Golcs Á, Horváth V, Huszthy P, Tóth T. Fast potentiometric analysis of lead in aqueous medium under competitive conditions using an acridono-crown ether neutral ionophore. Sensors 2018; 18(5): 1407. <DOI>.

21.   Elmosallamy MA, Fathy AM, Ghoneim AK. Lead (II) potentiometric sensor based on 1,4,8,11-tetrathiacyclotetradecane neutral carrier and lipophilic additives. Electroanal. 2008; 20: 1241–1245. <DOI>.

22.   Song W, Wu C, Yin H, Liu X, Sa P, Hu J. Preparation of PbS nanoparticles by phase-transfer method and application to Pb^{2+}-selective electrode based on PVC membrane. Anal. Lett. 2008; 41: 2844–2859. <DOI>.

23.   Zhang WJ, Li CY, Zhang XB, Jin Z. Synthesis of an amide-linked diporphyrin xanthene as a neutral carrier for a lead(II)-sensitive electrode. Anal. Lett. 2007; 40: 1023–1035. <DOI>.

24.   Huang MR, Rao XW, Li XG, Ding YB. Lead ion-selective electrodes based on polyphenylenediamine as unique solid ionophores. Talanta, 2011; 85: 1575–1584. <DOI>.

25.   Yuan X-J, Wang R-Y, Mao C-B, Wu L, Chu, C-Q, Yao R, Gao Z-Y, Wu B-L, Zhang H-Y. New Pb(II)-selective membrane electrode based on a new Schiff base complex. Inorg. Chem. Commun. 2012; 15: 29–32. <DOI>.

0

A Comprehensive Review on Analytical Applications of Hydrazone Derivatives

Mussarat Jabeen (iD)

Department of Chemistry, Government Sadiq College Women University Bahawalpur, 63100 Pakistan

Abstract: This review covers a summary of analytical applications of hydrazone derivatives in a systematic manner (1961-2021), which will help researchers in the design and development of hydrazone derivatives as potential candidates in medicinal, pharmaceutical, catalytic, and analytical chemistry, especially in the separation, identification, and detection of several metal ions, anions, organic molecules, and water in various real and synthetic samples. In addition to these, hydrazone derivatives may be used as light emitting diodes, for synthesis of dye-sensitized solar cells (DSSC), nanoparticles and polymers, as corrosion inhibitors, as dyes, etc. This review does not include all papers in this field, but it does synthesize all significant works on the subject.

INTRODUCTION

Hydrazones are a class of azomethine with a -C=N-N- linkage, prepared by the reaction of hydrazide and aldehydes or ketones (1). In hydrazones, azomethine group gained much importance as compared to other organic compounds because carbon has both electrophilic and nucleophilic nature while both nitrogen atoms are in nucleophilic nature (2,3). All the hydrazone derivatives exist in *keto-enol* tautomerism via intermolecular proton transfer (4) and cis-trans form depends on azomethine bond, solvent, pH, and concentration. Hydrazone derivatives are considered as both proton donor and proton acceptor species and show intermolecular and intermolecular hydrogen bonding (5). This unique characteristic of hydrazone derivatives makes a them very important class of compounds.

In the past few decades, hydrazone and their derivatives possessed many biological applications (6) (Figure 1,2) like antifungal ((E)-N'-[(5-Methyl-7-

nitrobenzofuran-2-yl)methylene]-benzo-hydrazide, **1**) (7), antibacterial (2,3,4 pentanetrione-3-[4-[[(5-nitro-2-furyl)methylene]-hydrazino]-carbonyl]phenyl]-hydrazone, **2**) (8), intestinal antiseptic (4-hydroxybenzoic acid[(5-nitro-2-furyl)-methylene]-hydrazide, **3**) (9), anticonvulsant (N'-(4-chloro-benzylidene)-nicotinohydrazide, **4**) (10), analgesic (Decanoic acid (4-methoxy benzylidene)hydrazide, **5**) (11), anti-cancer (1H-pyrazole-5-carbohydrazide hydrazone, **6**) (12), anti-inflammatory (Salicylaldehyde-2-(4-isobutyl-phenyl)-propionyl hydrazone, **7**) (13), anti-platelet *(*Indole-3-carboxaldehyde 4-methoxyphenyl-hydrazone*,* **8**) (14), anti-viral (N'-benzylidene-2-((4,4-dimethyl-6-oxocyclohex-1-en-1-yl)-amino)acetohydrazide, **9**) (15), anti-proliferative (2-(2-(2,4,6-trioxotetrahydro-pyrimidin-5(2H)-ylidene) hydrazinyl) benzoic acid, **10)** (16), anti-malarial (4-((2-(benzo[d]thiazol-2-yl)hydrazineylidene)-methyl)benzene-1,2-diol, **11**) (17), and anti-tuberculosis (N-isopropylisonicotino-hydrazide, **12**)

(18), they were also used as organic, inorganic, and   analytical reagents.
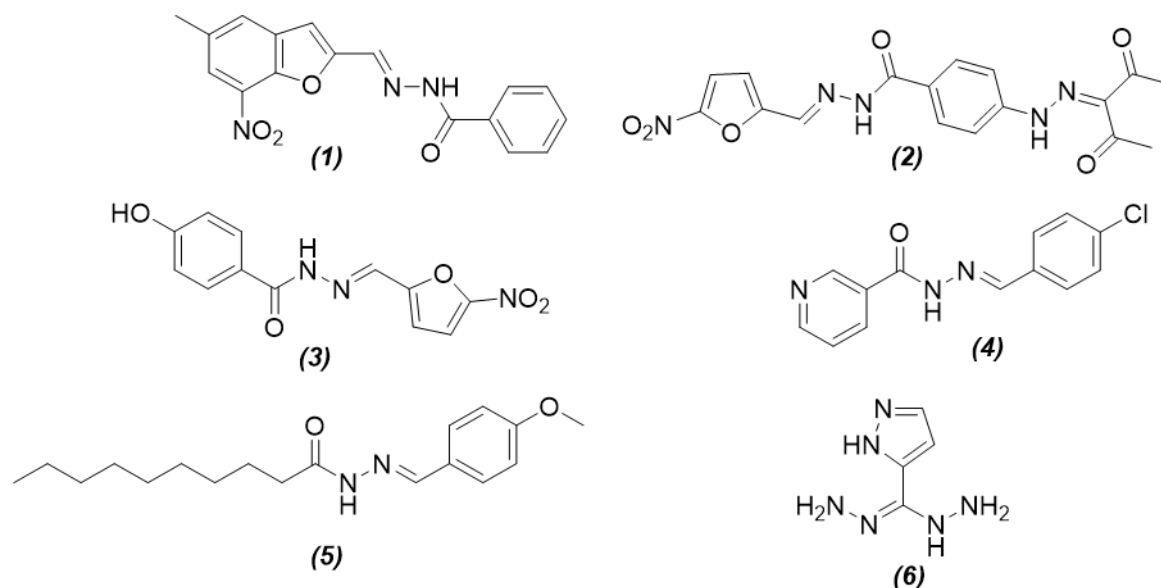

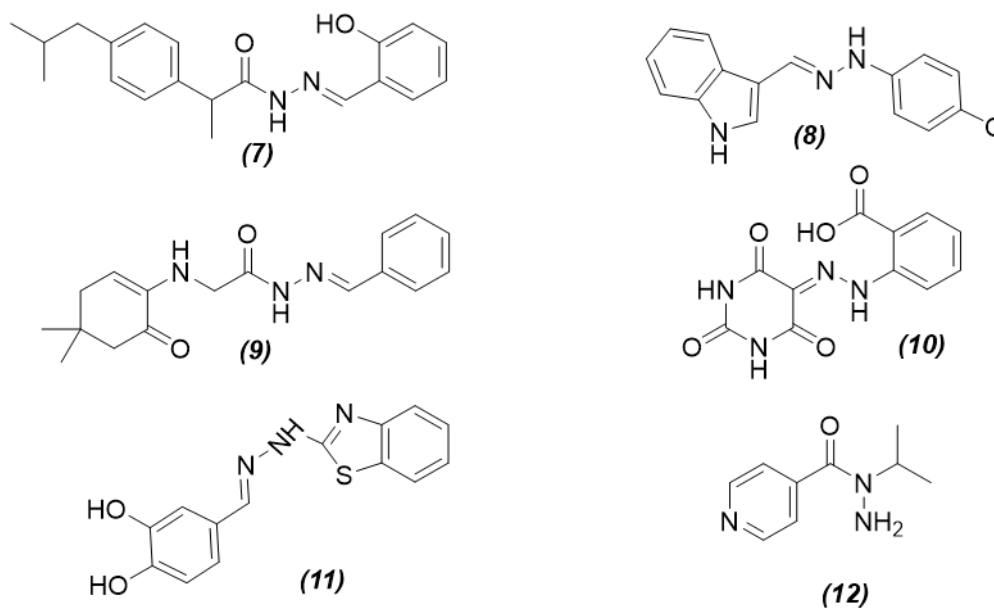**Figure 1:** Some biologically important hydrazone derivatives

Figure 2: Biologically active hydrazone derivatives

Hydrazones are also used as plant growth regulators (2-((2-(benzo[d]oxazol-2-yl)-2-methyl-hydrazineylidene)methyl)benzoic acid, **13**) (19), insecticides (podophyllotoxin-based hydrazone, **14**) (20), pesticides (substituted nalidixic acid based hydrazones, **15**) (21), corrosion inhibitors (ethylacetoacetate-[N-(3-hydroxy-2-naphthoyl)] hydrazone, **16**) (22) etc. They are important an class of compounds for the synthesis of other heterocyclic compounds like Coumarin, Pyridine, Thiazole and Thiophene Derivatives (2-cyano-N'-(1-(pyridin-3-yl)ethyl-idene)acetohydrazide **(17)** (23), and polymer initiators (acetophenone *t*-butylhydrazone, *(18)* (24).
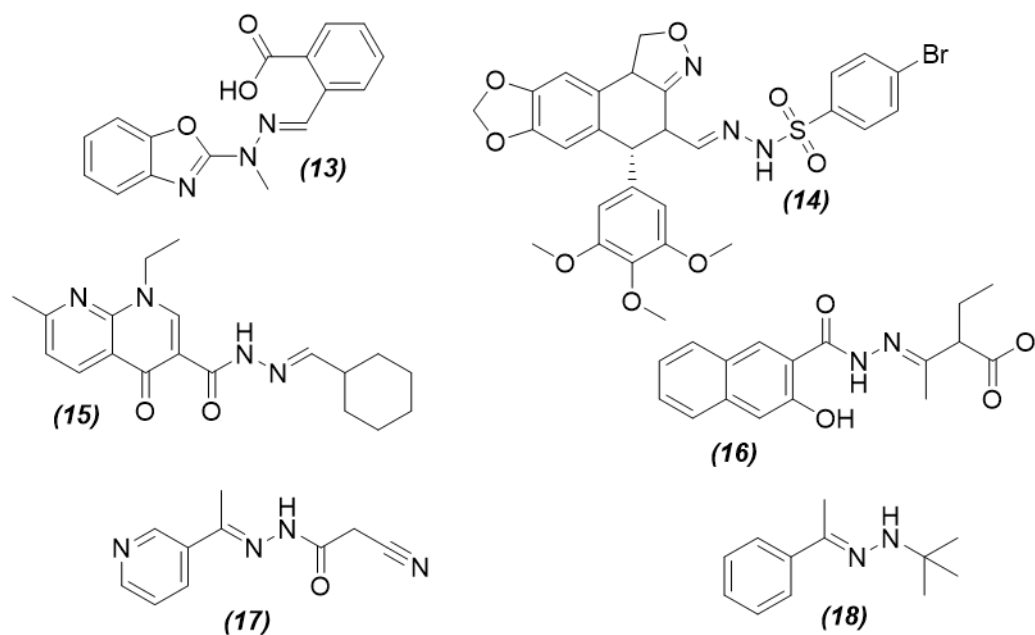
Figure 3: Hydrazone derivatives as polymer initials, corrosion inhibitor, pesticidal, insecticidal

ANALYTICAL APPLICATIONS

Hydrazone is very important class of analytical reagents used for the spectroscopic determination of different metal ions in food, environmental, pharmaceutical, and biological samples. These are also used for organic compounds' determination like glucose, carbonyl compounds, estrogen, etc. in blood, urine, cell culture, and pharmaceutical samples. Hydrazone derivatives are also used as corrosion inhibitors for nickel, copper, and many others in acidic and basic media. They are widely used for dyeing purposes for cotton, nylon, etc., chemosensors, polymer initiators, sensitizers, pH sensors for detection of microbes, and waste water treatment.

Spectrophotometric Agents

Hydrazone derivatives are not only extensively used for the detection of metal ions in water, alloys, soil and pharmacological samples but are also used for determination of anions like cyanide ion, fluoride ions, etc. via spectrophometric method. Hydrazone containing different heteroatom like S, O, N or presence of -OH, -C=O, -N-H, -COOH groups form stable compounds with metal ions and anions as compared to others. Hydrazone derivatives form soluble metal complexes when worked on in very small amounts and are capable of detecting metal ions in micro or nanograms.
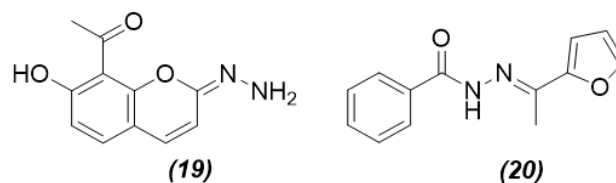

Figure 4: Hydrazone derivatives for spectrophotometric determination of metals.

Spectrophotometric determination of Cu (II) and Ni (II) in pharmaceutical samples was performed by 7-Hydroxy-8-aceto-coumarin hydrazone **(19)** at pH 4.5 and 5.5, respectively (25). 2-acetylfuran benzoyl-hydrazone **(20)** was prepared by Saleem Basha in 2017 and used for spectrophotometric Cu (II) determination in liver cells, vegetable oil, soil, cauliflower, and water samples as a greenish yellow colored complex at pH 6.5 with a detection limit ranging between 1.02 and 10.2 µg/mL (26, see Figure 4).

All the hydrazone derivatives that were used as spectrophotometric agents and the established conditions like color of complex, pH range, λ_{max} and detection limit in ppm are presented in **Table 1**. In this table, hydrazone reagents used for the detection of metals or anions via spectroscopic methods from the period of 1971 to 2021 were described.

Table 1: Important Hydrazone derivatives worked as Spectrophotometric Agents.

Spectrophotometric reagent	Sample	Metal-containing entity	pH	Color of complex	Detection range (ppm)	λ_{max} (nm)	Ref
3,5-Dimethoxy-4-hydroxybenzaldehyde isonicotinoyl-hydrazone	Alloy	Ni(II)	8.5-9.5	Yellow		386	(27)
	Alloy samples, hydrogenation catalyst samples and real water samples	Pd(II)	5.5	Bright yellow	0.1064-2.1284	382	(28)
	Monazite sand	Th(IV)	3.0	Yellow	0.580-5.80	390	(29)
	Synthetic mixtures, certified reference materials, water samples and pharmaceutical samples	Au(III)	4.0	Orange	0.197-1.97	386	(30)
	Beer, wine, vegetables and milk	Cu(II)	8.0-9.5	Bright yellow	0.317-3.17	494	(31)
Diacetylmonoxime-4-hydroxybenzoyl-hydrazone	Synthetic alloy	Pb(II)	10.0	Bright yellow	0.414-10.360	440	(32)
2-pyridinecarb-aldehyde 2-(5-nitro)pyridyl-hydrazone	Steel	Ni(II)	6.0	Red	0.05	475 & 507	(33)
	----	Fe(III)	7.0	Yellow	0.20–1.45	420	(34)
2,4-dihydroxy-benzaldehyde isonicotinoyl hydrazone	Alloy sample, zirconium sand and micro granite rock sample	Zr(IV)	1.5	Golden yellow	0.4-4.0	410	(35)
	Alloys and steel samples	Ti(IV)	1.0-7.0	Reddish brown	0.09- 2.15	430	(36)
	Synthetic samples and ores	Os (VIII)	5.0	yellow	0.95- 11.41	393	(37)
	Water and pharmaceutical samples	Zn(II)	6.0-8.0	greenish yellow	0.06- 1.6	390	(38)
	Monazite sand	Th(IV)	2.0-8.0	yellowish orange	0.3- 7.0	415	(39)
	Portable water samples	Fe(II)	7.0	Yellow	0.1-1.5	395	(40)

Spectrophotometric reagent	Sample	Metal-containing entity	pH	Color of complex	Detection range (ppm)	λ_{max} (nm)	Ref
	Steel samples & in alloys	Ti(IV)	1.5	Red	0.36-3.8	560	(41)
		Mo(VI)	1.5	Golden yellow	0.3- 6.0	445	
	Silicate and carbonate minerals	Al(III)	5.5	Yellow	0.03-0.40	395	(42)
o-hydroxybenz-aldehyde isonicotinoyl hydrazone	---	Ga(III)		Yellow	0.2-1.6	390	
	---	In(III)	6.2	Yellow	0.3-2.5	380	(43)
	---	Co(II), Zn(II), Mn(II), Ni(II) Cd(II)	8.4	Yellow	---	390-420	(44)
3,4-dihydroxybenz-aldehyde isonicotinoyl hydrazone	Water	V(V)		Yellow	0.5-5.3	400	
		Cr(IV)	5.5		0.7-7.7	360	(45)
		Ti(IV)	3.5	Yellow	0.5-4.2	370	(46)
5-bromo-salicylaldehyde isonocotinoyl hydrazone	Water, hydrogenation catalyst and alloy	Pd(II)	1.0-5.0	Brown	0.4-11	445	(47)
	Soil and steel	Cr(VI)	6.0	Brown	0.16-3.90	430	(48)
	Eenvironmental, phosphate rocks and fertilizer samples	U(VI)	5.0	Yellow	0.119-1.071	395	(49)
N'-(2-hydroxybenz-ylidene)-3-oxobutane-hydrazide	Synthetic mixtures and alloys	Ti(IV)	2.0	Reddish orange	1.75- 17.57	500	(50)
Diacetylmonoxime benzoylhydrazone	Alloys and synthetic mixtures	Ni(II)	8.0-10.0	---	0.12-2.58	362	(51,52)
		Cu(II)	8.0-11.0	---	0.2-2.54	346	
		Fe(II)	6.25	yellow	0.11-2.24	360	(53)
		Hg(II)	10.5	Orange	1-12	361	(54,55)
o-hydroxypropio-phenone isonicotinoyl hydrazone	---	U(IV)	3.0	Yellow	0.47-17	380	(56)
2-hydroxy-l-naphthaldehyde isonicotinoyl hydrazone	Synthetic mixtures	U(IV)	3.0	Orange red	0.2-33	430	(57)
2-Hydroxy-1-naphthalene carboxaldehyde phenyl hydrazone	Synthetic and commercial samples of alloy or ores (Hematite, steel, Fefol, Autrin, binary mixtures of Fe+Mg and Fe+Zn),	Fe(III)	6.0	Orange red	1-7	510	(58)

Spectrophotometric reagent	Sample	Metal-containing entity	pH	Color of complex	Detection range (ppm)	λ_{max} (nm)	Ref
	Synthetic and commercial samples	Cu(II)	9.2	Yellow	1-10	360	(59)
	Alloys, steel, synthetic mixtures	Co(II)	8.4		1-10		(60)
2,5-Dihydroxyacetophenone benzoic hydrazone	Alloy and plant leaves	Cu(II)	Acidic	Yellow	0.3-6.0	400	(61)
1-((1E,4E)-4-((2-aminoethyl)imino)naphthalen-1(4H)-ylidene)-2-(2,4-dinitro-1λ^5-phenyl)hydrazin-1-ium	Soil, water, urine, human hair, goat liver, plant material, steel and alloy samples	V(V)	Basic	Red	0.02 - 3.5	495	(62)
2-hydroxy-1-naphthaldehyde-p-hydroxybenzoichydrazone	Water (river, tap, and rain), soil, pharmaceutical samples, wheat, orange, rice, tomato, banana, blood and urine	Fe(II)	5.0	Reddish brown	0.055-1.373	405	(63)
		Co(II)	6.0	Yellow	0.118-3.534	425	
	Environmental, Leafy vegetable, and Biological Samples	V(V)	4.0	Deep yellow	0.101-1.121	430	(64)
	Water, ore, fertilizer, and gas mantle samples	Th(IV)	6.0	Yellow	0.464-6.961	415	(65)
		U(IV)	6.0	Reddish brown	0.476-7.14	410	
	Nickel based alloy samples and geological samples	Y(III)	8.5	Yellow	0.044-2.222	410	(66)
	Plant, pharmaceutical, water and alloy samples.	V(V)	4.0	Deep yellow	0.050-1.935	430	(67)
		Pd(II)	4.0	Greenish yellow	0.022-2.021	430	
Diacetyl monoxime	Rock, in	U(VI)	3.25	Yellow	1.19-14.28	364	(68)

Spectrophotometric reagent	Sample	Metal-containing entity	pH	Color of complex	Detection range (ppm)	λ_{max} (nm)	Ref
isonicotinoyl hydrazone	pitchblende ore samples and synthetic samples						
	Synthetic alloys	Au(III)	4.5	Yellow	1.97-9.85	361	(69)
	Synthetic samples of alloy and in Monazite sand sample	Th (IV)	4.0-6.0	Yellow	1.16-13.12	352	(70)
	Synthetic alloys	Hg(II)	5.5	Yellow	1.003-12.3	351	(71)
	Synthetic mixtures,	Ga(III)	3.0-6.0	Green	0.002002	376	(72)
	biological samples	Ni(II)	8.0-9.0	Yellow	0.495-3.09	387	
	and alloys	Al(III)	7.0-8.0	Yellow	0.392-2.452	370	
	Alloys	Mo(VI)	5.0	Greenish yellow	0.48-5.76	346	(73)
pyridine-2-acetaldehyde salicyloylhydrazone	Synthetic samples, pharmaceutical samples and in high speed steel	Co(II)	1-4	Yellow	0.5-7.0	415	(74)
	Beer, wine, garlic, Tobacco and water samples	Fe(III)	2.5-3.0	Green	2.7-16.0	640	(75)
	Steel and alloys	V(V)	4.7	Yellow	0.5-2.0	415	(76)
	Synthetic mixtures, alloys, water and soil samples	Pb(II)	8.6-9.3	Yellow green	1.5-6.2	380	(77)
	Synthetic mixtures, catalysts and in ores	Pd(II)	2.0-4.25	Yellow	0.5-3.0	425	(78)
	Synthetic mixtures alloys and a pharmaceutical sample.	Sb(III)	2.9	Yellow	1.5-5.0	405	(79)
pyridine-2-carboxaldehyde 2-	Binary mixtures,	U(VI)	3.5-4.6	Yellow	1.0-5.6	375	(80)

Spectrophotometric reagent	Sample	Metal-containing entity	pH	Color of complex	Detection range (ppm)	λ_{max} (nm)	Ref
hydroxybenzoylhydrazone	multicomponent mixtures and in monazite sand						
	Eye Drops and Ayurvedic Medicines	Hg(II)	8.8-10.0	Yellow	0.5-5.8	385	(81)
	Alloys and drug samples	Bi(III)	2.0-3.0	Yellow	0.7-4.3	380	(82)
N',N''E,N',N''E)-N',N''-(2,2'-(propane-1,3-diylbis(sulfanediyl))bis(1-(4-chlorophenyl)-ethan-2-yl-1ylidene))bis(2hydroxybenzohydrazide)	Water, food, medicinal plants and in synthetic samples	Co(II)	7.0	Orange	0.059-0.59	380	(83)
5-Bromosalicyl-aldehyde Thiosemicar-bazone	Grape leaves and aluminum based alloy samples	Cu(II)	4.5	Greenish yellow	0.31 – 6.35	390	(84)
phenylglyoxal mono(2-pyridyl)hydrazone	Tap water, mineral water and in cooking salt	Zn(II)	7.2-8.5	yellow-orange	0.05-0.6	464-470	(85)
N-oxalylamine-(salicylaldehyde hydrazone)	Aluminum and nickel alloy	Ga(III)	3.8	greenish yellow	0.003- 0.227	382	(86)
	Mineral water	Al(III)	3.7	---	0.005- 0.16	387 & 474	(87)
4-Hydroxy 3, 5-dimethoxy benzaldehyde-4-hydroxybenzoyl-hydrazone	Synthetic alloy sample	Fe(II) Fe(III)	4.0 5.0	Yellow Yellow	0.139-1.396 0.279-2.79	400 380	(88)
	Edible oil, plant sample and in alloy samples	Ni(II)	9.0	Yellow	0.117-0.528	408	(89)
	Hydrogenation catalyst, synthetic alloy and in water samples	Pd(II)	3.0-4.0	Brown	0.106-1.06	373	(90)
	Beer, Wine, Biological materials and alloy samples	Cu(II)	8.0-9.0	Yellow	0.063-0.635	382	(91)
3-Methoxy-salcilaldehyde-4-	Synthetic matrix,	Cu(II)	5.0-6.0	Yellow	0.1271 – 2.5418	390	(92)

Spectrophotometric reagent	Sample	Metal-containing entity	pH	Color of complex	Detection range (ppm)	λ_max (nm)	Ref
hydroxybenzoylhydrazone	alloy samples and edible oils	Ni(II)	5.0-6.5	Yellow	0.1174 – 2.9410	425	
Cinnamaldehyde-4-hydroxybenzoylhydrazone	Tealeaves, vehicle exhaust, vitamin B_{12} and in some alloy samples	Co(II)	9.0	Yellow	0.029-0.294	393	(93)
	Plant sample, edible oil and in alloys	Ni(II)	8.0-9.0	Yellow	0.146-1.46	400	(89)
	Tannery effluent, synthetic water and chrome liquor samples	Cr(VI)	4.0	Brown	0.078-0.780	440	(94)
	Food stuffs, pharmaceutical samples and alloys	Mo(VI)	3.0-4.0	Green	0.047-0.479	404	(95)
	Hydrogenation catalyst samples, synthetic alloy samples and in water samples.	Pd(II)	4.0-5.0	Brown	0.106-1.064	375	(90)
benzil-α-monoxime isonicotinoyl hydrazone	Pipe water, bore water and municipal water samples	Pb(II)	10.0-11.0	Yellow	0.41-13.26	405	(96)
dipyridylglyoxal mono(2-pyridyl)-hydrazone	Pharmaceutical samples, multivitamins, hormones and Hidropolivit mineral	Co(II)	3.0-7.0	Orange red	0.15-2.0	510	(97,98)
salicylaldehyde benzoyl hydrazone	Steel, alloys, water,	Cu(II)	1.21-2.58	Greenish yellow	0.001-10	404	(99)

Spectrophotometric reagent	Sample	Metal-containing entity	pH	Color of complex	Detection range (ppm)	λ$_{max}$ (nm)	Ref
	human blood, urine, apple, egg, soil and synthetic mixtures						
benzil mono-(2-pyridyl) hydrazone	Steel and alloy samples	Co(II)	Basic	Red	0.0061-0.061	535	(100)
Benzil mono(2-quinolyl)hydrazone	---	Cu(II)	6.0	Red	0.3-3.0	520	(101,102)
2,4-dimethoxy benzaldehyde-4-hydroxy benzoylhydrazone	Pharmaceutical samples (Zingisol, Insulin Zinc Suspension and in Biocosules Z)	Zn(II)	10.0-11.0	Yellow	0.163-1.96	466	(103)
2,4-dihydroxy benzophenone benzoic hydrazone	Simulated rock samples	Ce(IV)	10.0	Orange red	0.7-7.0	400	(104)
5-Bromo-2-hydroxy-3-methoxybenzaldehyde-p-hydroxybenzoic hydrazone	Alloy samples, industrial water, drinking water, plant samples and in vegetable oil	Ni(II)	5.5-7.5	Green	0.117-2.64	440	(105)
	In alloys, steel and in water	Ti(II)	2.0-7.0	Orange	0.241-2.87	390	(106)
2-(3'-sulfobenzoyl)-pyridine benzoyl-hydrazone	Natural water	Fe(II)	7.0-9.0	Blue	0-4	646	(107)
N,N'-Oxalyl-bis(salicylaldehyde Hydrazone)	Water	Al(III)	4.7	Yellow	0-0.2	390	(108)
N-cyanoacylacet-aldehyde hydrazone	Water	Au(III)	3.0-7.0	Blue	1-30	550	(109)
p-dimethylaminoben-zaldehyde isonicotinoyl hydrazone	---	Hg(I) Hg(II)	3.5	Orange yellow	---	---	(110)
4-Hydroxy benzaldehyde-4-bromophenyl hydrazone	Water and alloy sample	Ni(II)	4.0	Red	0.01-1.0	497	(111)
3-methylbenzothiazolin-2-one hydrazone	Drugs	Ce(IV)	4.2	Orange	4.0-80.0	450	(112)
2-(4-biphenyl)-imidazo[1,2-]pyrimidine-3-hydrazone	---	Cu(II)	4	Green	---	430	(113)

Spectrophotometric reagent	Sample	Metal-containing entity	pH	Color of complex	Detection range (ppm)	λmax (nm)	Ref
Glutaraldehyde phenyl hydrazone	Water, soil, biological samples	Pb, Cr, Cd, As	5.6-7.5	---	---	387 (Cd) 395 (As) 395 (Pb) 360 (Cr)	(114)

Chemosensors

Chemosensors are non-toxic nano-sized organic molecules or receptors that produced a detectable change for sensoring analyte (usually metal ions or small molecules) using fluorescence spectroscopy (115). These chemosensors not only detect toxic and dangerous chemicals in the external and internal environment of the human body but also transmit that information to the nervous system to expel these toxins from body. For this purpose, a large number of organic molecules can be used but hydrazone derivatives containing thiol, carboxylic group gained more importance. Some important hydrazone derivatives used as chemosensors are presented below in **Table 2.**

Organic Compound Detector

Hydrazone derivatives are efficiently used for detection of organic compounds (Figure 5) like glucose, aromatic amines, hetero-atomic compounds, azo dyes, active methylene compounds, etc., in blood, urine, and pharmaceutical samples via spectroscopic and chromatographic methods.

Alzweiri and coworkers established a unique method for the spectrophotometric determination of glucose in biological samples by derivatization of glucose with 2,4-dintrophenyl hydrazine *(21)* (154).
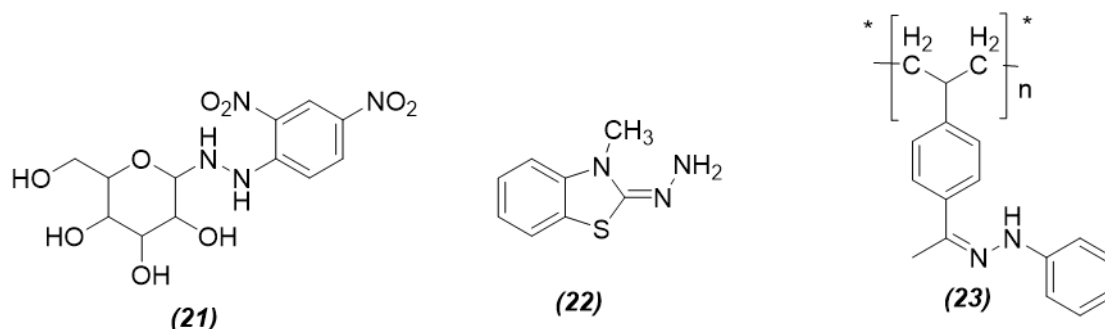
Figure 5: Hydrazone derivatives as organic compounds detector.

3-Methylbenzthiazolinone-2-hydrazone *(22)* was used as an analytical reagent for determination of phenols (155), azo dyes, Schiff bases, stilbenes (156), aliphatic aldehydes from fumes and polluted air (157), carbazole in air (156), aromatic amines (158), imino heteroaromatic compounds (158), heterocyclic bases, heteroaromatic compounds, compounds with active methylene groups (159), Rutin (160), glyoxal (161), phenolphthalein in pharmaceutical products (162), metaxalone (163), dabigatran etexilate mesylate (163), total estrogens in urine (164), determination of formaldehyde and acetaldehyde in methanol and ethanol (165), oxcarbazepine in pharmaceuticals, sulpha drugs in blood and urine samples (166,167), cannabinoids on thin-layer chromatography plates (168), free salicylic acid in aspirin (169), dobutamine hydrochloride (170) and carbonyl compounds in pharmaceutical samples (159) via different spectroscopic and chromatographic techniques.

By this method, 99.93% of phenol from waste water was removed by polystyrene hydrazone *(23)* by solid-phase extraction method prepared by acetylation of waste polystyrene with phenyl hydrazine (171).

For the determination of atmospheric ozone in very low concentrations up to 0.02 ppm and carbonyl compounds from mixtures, 2-Diphenylacety-1,3-indandione-1-hydrazone *(24)* was used as a spectrofluorometric reagent (172,173).
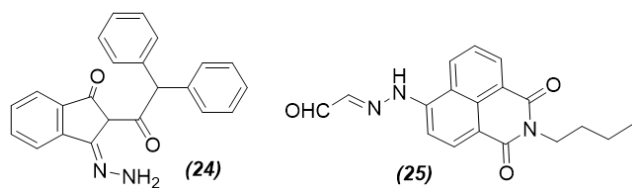
Figure 6: Fluorescence detecting hydrazone derivatives

Naphthalimide-based glyoxal hydrazone **(25)** is used for biological imaging of cysteine and homocysteine inside living cells via fluoresce spectroscopy with a color change from dark to green (174).

Table 2: Some Important Hydrazone reagents used as chemosensors

Chemosensor Name	Sample	Analyte	LOD (M)	Color change	Fluorescence color	Tested media	Em/ ex (nm)	Ref
1-phenyl-3-methyl-5-hydroxy-pyrazole-4 benzoyl(fluorescein)-hydrazone	---	Cu^{2+}	2.0×10^{-3}	Colorless → Yellow		DMSO/ H_2O	337/287	(116)
Benzil mono(2-phen-yl)hydrazone	Biomedical & environmental	Cu^{2+}	8.25×10^{-8}	Colorless → Pink		THF/H_2O	490	(117)
Salicylaldehyde hydrazone derivatives	Living cells (MCF-7 calls)	Al^{3+}	1.5×10^{-7}	Colorless → blue		DMF/H_2O	450/390	(118)
2-((E)-(((E)-2-hydr-oxybenzylidene)hydrazineylidene)methyl)-6-methoxy-4-nitrophenol	Liver cells	Cu^{2+}	18×10^{-8}	Colorless → light yellow	Green	H_2O	570/400	(119)
	Biological system	Al^{3+}	7.45×10^{-8}	Yellow → colorless	Green	CH_3OH	545/400	
ethyl (E)-5-((2-(2-(2-hydroxyethyl)-1,3-dioxo-2,3-dihydro-1H-3a1λ5-benzo-[de]isoquinolin-6-yl)hydrazineylidene)methyl)-2,4-dimethyl-1l2-pyrrole-3-carboxylate	HeLa cells	Cu^{2+}	3×10^{-6}	Yellow → red		CH_3CN/ H_2O	620/480	(120)
(3a^{1}S)-2-butyl-7-(2-((Z)-1-(4-hydroxy-6-methyl-2-oxo-2H-pyran-3-yl)ethylidene)-hydrazineyl)-3a,3a^1-dihydro-1H-benzo[de]isoquinoline-1,3(2H)-dione	Real sample	Cu^{2+}	1.58	Yellow → Colorless		THF/H_2O	520/412	(121)
4-methyl-N'-(ferrocene-2-ylidene)benzenesulfonohydrazide		Cu^{2+}	2.66×10^{-5}	Pale yellow → yellow green		CH_3CN		(122)
		Hg^{2+}	7.60×10^{-6}	Pale yellow → Red		CH_3CN		
(E)-3-(1-(2-(benzo[d]thiazol-2-yl)hydrazineylidene)ethyl)-7-(diethylamino)-2H-chromen-2-one	HeLa tumor cells (Cervical cancer cells)	Cu^{2+}	4×10^{-8}	Yellow → wine red		1%DMSO	572/420	(123)
7-(diethylamino)-3-((E)-(((E)-(2-hydroxynaphthalen-1-yl)methylene)hydrazineylidene)methyl)-2H-chromen-2-one	human breast adenocarcinoma	Cu^{2+}	2×10^{-4}		Green	CH_3OH/ H_2O	574/487	(124)

Chemosensor Name	Sample	Analyte	LOD (M)	Color change	Fluorescence color	Tested media	Em/ ex (nm)	Ref
	cells (MCF-7 cells)							
3-(2-((3-Hydroxy-5-(hydroxymethyl)-2-methylpyridin-4-yl)methylene)hydrazinyl)-1,2-benzothiazole 1,1-dioxide	Biological system	Al^{3+}	$6x10^{-7}$	White → yellow	Blue	DMSO/ H_2O	468/399	(125)
2-(3a,7a-dihydro-1H-benzo[d][1,2,3]triazol-1-yl)-N'-((8-hydroxyquinolin-5-yl)methylene)-2λ^2-ethanehydrazide	Biological system	Mg^{2+}	$6.9x10^{-3}$	Blue → green	bright yellow	CH_3CN	525/395	(126)
2- aminoquinolin-3-yl-phenyl hydrazone	---	Fe^{3+}	8.22×10^{-6}	---		C_2H_5OH	423/246	(127)
N-(quinolin-8-ylmethylene)acetohydrazide	In HeLa cells	Zn^{2+}	$8.93x10^{-2}$		bright yellow	C_2H_5OH	525/360	(128)
N-((8-hydroxy-5-quinoline aldehyde acetylhydrazone)-benzoaza-15-crown-5	Biological system	Mg^{2+}	$7.87x10^{-5}$	Colorless → Yellow		C_2H_5OH	520/370	(129)
	germinated potato, bitter almond and in tap water	CN^-	$3.57x10^{-7}$	Colorless → Yellow	bright yellow	DMSO/ H2O	498/355	
3',6'-bis(diethylamino)-2-(((3-hydroxypyridin-2-yl)methylene)amino)spiro[isoindoline-1,9'-xanthen]-3-one	Biological system	Cu^{2+}	$3.63x10^{-7}$	Colorless → purple	White	DMSO/ H2O	492/373	(130)
		Cu^{2+}	$2.5x10^{-8}$	Colorless → pink		H_2O/ CH_3CN	585/520	(131)
3',6'-bis(diethylamino)-2-((2-(2-(2-methoxyethoxy)-ethoxy)benzylidene)amino)spiro[isoindoline-1,9'-xanthen]-3-one	HeLa cells	Hg^{2+}	$1.5x10^{-7}$	Colorless → purple	Orange	CH_3CN	590/558	(132)
(Z)-N'-(1-(2,4-dihydroxy-phenyl)ethylidene)-2,2,2-trifluoroacetohydrazide		Cu^{2+}	$1x10^{-5}$	Colorless → yellow	Bright green	DMF	500/400	(133)
2-(((3H,4'H-1l3,1'l3-[2,2'-bithiophen]-5-yl)methyle-ne)amino)-3',6'-bis(diethyl-amino)spiro[isoindoline-1,9'-xanthen]-3-one	Human epithelial	Hg^{2+}	$2.31x10^{-8}$	Colorless → purple	Blue	EtOH/ H2O	590/544	(134)

Chemosensor Name	Sample	Analyte	LOD (M)	Color change	Fluorescence color	Tested media	Em/ ex (nm)	Ref
3',6'-bis(diethylamino)-2-((2-hydroxy-5-(1,2,2-triphen-ylvinyl)benzylidene)amino)spiro[isoindoline-1,9'-xanthen]-3-one	adenocarcinoma (HeLa) cells ---	Cu^{2+}	10^{-6}	Colorless → purple		$EtOH/H_2O$	550/-	(135)
2-(((3H,4'H-1l3,1'l3-[2,2'-bithiophen]-5-yl)methylene)-amino)-3',6'-bis(diethyl-amino)spiro[isoindoline-1,9'-xanthene]-3-thione	Human epithelial adenocarcinoma (HeLa) cells	Hg^{2+}	3.10×10^{-9}	Colorless → purple	Pink	EtOH	593/390	(136)
3',6'-bis(diethylamino)-2-((piperidin-2-ylmethyl)-amino)spiro[isoindoline-1,9'-xanthen]-3-one	Caco-2 cells	Cu^{2+}	0.137	Colorless → red	Orange	CH_3CN	573/520	(137)
N-(3',6'bis(diethylamino)-3-oxospiro[isoindoline-1,9'-xanthen]-2-yl)-3-oxo-3-ferrocenylpropanamide	HeLa cells	Cu^{2+}	1.0×10^{-6}	Colorless → purple	Orange red	ethanol/ H2O	595/550	(138)
2-(hydrazineylidenem-ethyl)pyren-1-ol	HeCaT cells	Zn^{2+}	3×10^{-4}	Colorless → yellow	Green	CH_3CN	527/450	(139)
3',6'-bis(diethylamino)-2-((2-mercaptobenzylidene)amino)spiro[isoindoline-1,9'-xanthen]-3-one	Nematode *Caenorhabditis elegans*	Hg^{2+}	1×10^{-9}	Colorless → pink	Red	CH_3CN/ H_2O	580/510	(140)
1-phenyl-3-methyl-5-hydroxypyrazole-4-carbalde-hyde(benzoyl)hydrazone		Cu^{2+}	1.0×10^{-6}			CH_3CN	305/406	(141)
3',6'-bis(diethylamino)-2-((furan-2-ylmethylene)-amino)spiro[isoindoline-1,9'-xanthene]-3-thione	Rat Schwann cells	Hg^{2+}	5×10^{-4}	Colorless → pink	Orange	H_2O-DMF	564/500	(142)
4-nitro-2-[(phenylhydra-zoimino)methyl]phenol		F^-	$0.02-0.2 \times 10^{-4}$	Colorless → yellow	Yellow	CH_3CN		(143)
4-nitro-2-[(4-nitrophenylhydra-		F^-	$0.02-0.2$	Colorless	Yellow	CH_3CN		

Chemosensor Name	Sample	Analyte	LOD (M)	Color change	Fluorescence color	Tested media	Em/ ex (nm)	Ref
zoimino)methyl]phenol			x10^{-4}	→ orange				
N',N'''-((1E,1'E)-(((4-((E)-(2-(1-hydroxy-2-naphthoyl)-hydrazineylidene)methyl)phenyl)azanediyl)bis(4,1-phenylene))bis(methaneylylidene))bis(3-hydroxy-2-naphthohydrazide)	Human cervical cancer (HeLa) cancer cell lines	Cu^{2+}	---	---	---	H$_2$O/ CH$_3$CN	470/450	(144)
3,3'-((1E,1'E)-(((1E,1'E)-(((4-((E)-(((E)-(1-hydroxy-naphthalen-2-yl)methylene)-hydrazineylidene)methyl)phenyl)azanediyl)bis(4,1-phenylene))bis(methaneylylidene))bis(hydrazine-2,1-diylidene))bis(methaneylylidene))bis(naphthalen-2-ol)	Human cervical cancer (HeLa) cancer cell lines	Cu^{2+}	---	---	---	H$_2$O/ CH$_3$CN	430/405	(144)
2-(((1E,2E)-but-2-en-1-ylidene)amino)-3',6'-bis-(ethylamino)spiro[isoindoline-1,9'-xanthen]-3-one	Water, soil biological and environmental sample	Pd^{2+}	1.80x10^{-7}	Colorless → pink	Yellow	EtOH/H$_2$O	555/505	(145)
2-hydroxy-benzaldehyde benzoyl-hydrazone		Cu^{2+}	5.6x10^{-6}	---	---	MeOH/ H$_2$O	490/424	(146)
Methyl Pyrazinylketone Benzoyl Hydrazone	---	Al^{3+}	10^{-7}		Green	Ethanol	506/390	(147)
3',6'-bis(diethylamino)-2-((2-hydroxybenzylidene)amino)spiro[isoindoline-1,9'-xanthen]-3-one	---	Cu^{2+}	---	Colorless → pink		CH$_3$CN	576/520	(148)
(E)-(2-((2-(2,4-dinitrophenyl)hydrazineylidene)methyl)phenyl)diphenylphosphine oxide	----	F$^-$	2 × 10^{-5}	Yellow → pink		CH$_3$CN	514/379	(149)
N-(2-(-(2-(-3,4-dihydroxy-6-(hydroxymethyl)-5-(-3,4,5-trihydroxy-6-(hydroxymethyl) tetrahydro-2H-pyran-2-yloxy) tetrahydro-2H-pyran-2-yl) hydrazono) methyl)-4-(-phenyldiazenyl) phenyl) acetamide	Water	CN$^-$	1.29x10^{-6}	Colorless → purple		MeOH/ H$_2$O	----	(150)
(E)-2-(2-(2,4-dinitrophenyl)hydrazineylidene)-1,2-diphenylethan-1-one	Real water and simulated urine samples	CN$^-$	10^{-7}	Yellow → Red		CH$_3$CN/ H$_2$O		(151)
1-((Anthracene-9-yl)-methylene)-2-(4-nitrophenyl)hydrazine		F$^-$	4x10^{-5}	Yellow → green		DMSO	571/493	(152)
N, N-diethylamino-3-acetyl coumarin with 2-	HeLa cells	Cu^{2+}		Yellow →	Green	DMF	536/420	(123)

Chemosensor Name	Sample	Analyte	LOD (M)	Color change	Fluorescence color	Tested media	Em/ ex (nm)	Ref
hydrazinobenzothiazole *N*-(3-methoxy-2-hydroxybenzylidene)-3-hydroxy-2-naphthahydrazone	Water	Zn^{2+} Cd^{2+}	Zn (9.85 $\times 10^{-9}$ M) Cd (1.27 $\times 10^{-7}$ M)	orange ---	Yellow (Zn) Red (Cd)	THF/H_2O	365/440 645/430	(153)

LOD= limit of detection; Em= emission; Ex= excitation.

Water Detectors

Hydrazone – acetate derivatives **(26)** derived from 9-anthracenealdehyde and 7-hydroxy-coumarin-8-carboxaldehyde were used as for Chromogenic signaling (detection) of water contents in water miscible organic solvents like THF and acetonitrile by Y.H. Kim *et al* in 2012 (175). Anthracene-based hydrazone **(27)** was found to be more sensitive to water content as compared to 7-hydroxycoumarin hydrazone and showed a visible color change from red to yellow with a detection limit of 0.037 and 0.071% in both solvents (175).
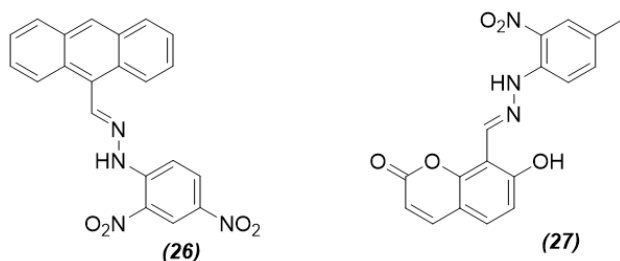
Figure 7: Water-monitoring hydrazone derivatives.

Microbes Detectors

Most of the hydrazone derivatives have different colors in acidic and basic media as well as in neutral ones. This property of hydrazones is very useful for microbe detection in food and pharmaceutical samples (Figure 8).

Recently, Khattab and coworkers introduced Tricyanofuran hydrazone derivatives **(28)** as pH sensors for detection of microbes which alkalize the environment, like *S. aureus, B. subtilis, E. coli, and P. aeuroginosa*. The color change from yellow to blue to red indicates the pH change from acidic to neutral to basic. These pH sensors were also used to detect microbes in food packages and pharmaceutical samples (176-178).
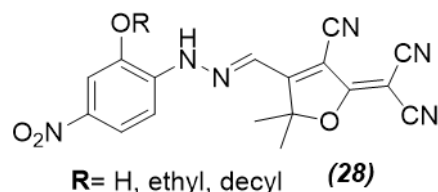
Figure 8: Microbe detecting hydrazone derivatives.

Sorbents

Some modified hydrazone derivatives are widely used as sorbents in ion exchange chromatography or in Sol-gel process for separation of ions in synthetic mixtures, natural water, ash coal, petroleum products, and pharmaceutical samples. Such hydrazones work as low cost resins with high productivity, are highly stable and can be used many times with the same sorption capacity listed in **Table 3.**

Organic Collectors in Flotation

Flotation is the separation process of toxic metal ions in trace amounts, for this purpose many hydrazone derivatives worked as organic collectors. These form hydrophobic aggregates with metal ions that float with the help of air bubbles produced on the surface of solution by slight shaking of floatation cell. Many important hydrazones used as organic collectors are summarized in **Table 4.**

Sewage Water Treatment

Sewage water is commonly known as wastewater, which contains a large amount of contamination mainly coming from household and industrial waste. This wastewater contains several heavy metals like mercury, arsenic, cadmium, chromium, lead, thallium, and nitrogen compounds like ammonia, nitrite, and nitrates. Many physical, chemical, and biological processes are now used for sewage water treatment, but most of these are very costly and time consuming.

Cellulose hydrazone derivatives were obtained by the reaction of dialdehyde cellulose and 2-hydrazino- 3,5,6,7-tetrahydrocyclopentanethieno[2,3-d]-pyrimidin-4(4H)-one **(29)** used as a polymer for sewage water treatment and the removal of several heavy metal ions. The synthesized derivatives were used for production of clean water with less side effects. These derivatives not only had ability to remove iron and chromium up to 73.91 % but also chlorine up to 50 % **(192).**
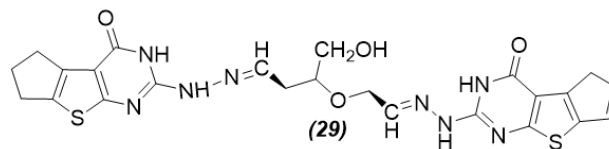
Figure 9: Hydrazone for sewage water treatment.

Table 3: Some widely used hydrazones as sorbents.

Sorbent	Separated Ion	Sample	pH	LOD (ppb)	Eluent	Recovery %	Ref
1-(3,4-Dihydroxy-benzylidine)-2-acetylpyridinium chloride hydrazone	Fe^{3+}	Waste water, sea water, lake water, food oil, petroleum products, pharmaceutical sample	3.0	1.0	0.5 M HCl	~100	(179)
	Cr^{3+}	Waste water	6.0	13.3	0.1 M HCl	~100	(180)
	Cr^{6+}	Waste water	2.0	10.0	3.0 M HCl	~100	(180)
	Ga^{3+}	Synthetic mixture of mercury, aluminum, cobalt, copper, zinc & lead	2.5-3.0	20	0.5 M HCl	98	(181)
	In^{3+}		2.5-3.0	13	5.0 M HCl	98	(181)
	Tl^{3+}		2.0	20	2.0 M HCl	95	(181)
acenaphthenequinone-[N-[(2,4-dinitrophenyl)]-hydrazone	La^{3+}	Lake water, rain water, river water	4.0	---	0.1 M HNO$_3$	97	(182)
1-[(bromomethyl)-(phenyl)methyl]-2-(2,4-dinitrophenyl) hydrazine	Ag^+	Tap water, drain water	5.0			99	(183)
4-hydroxy-N'-[(E)-(2-hydroxyphenyl)methylidene]benzohydrazide	Biogenic amines	Orange juice, ketchup, budu, soy sauce.	9.0	20-60	---	99.7	(184)

Polymer Initiators

Polymer synthesis is the process in which small molecules (monomers) covalently combined to form giant molecules that are more stable as compared to initiators. Many organic molecules are used for this purpose, but hydrazone derivatives gave the highest yields and the best results among them (Figure 10).

Nakanishi et al. and Masuda et al. used pyridine hydrazone derivatives *(30)* as a suitable and useful initiator or starting material for the synthesis of synthetic polymers or hydrazone polymers (193,194).

Hydrazone derivatives *(31)* were used as initiators for high yield polymerization of acrylamide, acrylic acid or styrene at a temperature -10-98°C with yield

A series of six hydrazone derivatives *(32)* were prepared by Singh and coworkers and used for the synthesis of hydrazone functionalized epoxy polymers by the conversion of hydrazone derivatives into epoxide to form hydrazone polymer (Figure 11). These polymers showed high nonlinear optical properties (196).

Indicators

Salicylaldehyde phenylhydrazone **(33)** prepared by Love and Jones from simple and cheap starting
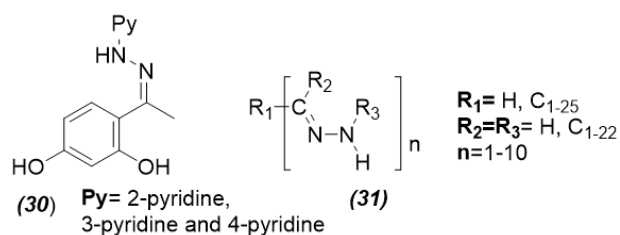
Figure 10: Polymer initiating hydrazone derivatives
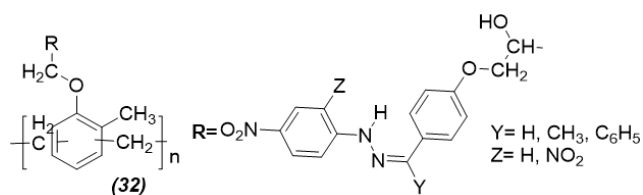
up to 77% (24). Similarly, acylhydrazone derivatives were also used as starting materials for acylhydrazone polymers (195).

material was used as an indicator for the titration of organometallics, including Grignard reagent, providing a clear and accurate end point from yellow to golden orange or red (Figure 12) (197).
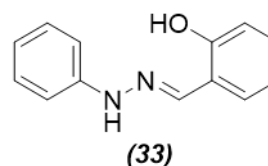
Figure 12: Hydrazone as indicator.
Figure 11: Hydrazone as epoxy polymer

Table 4: Hydrazones used as organic collectors in flotation.

Organic collector	Surfactant	Metal ion	Tested Sample	pH	Recovery percentage	HOL	Ref
1-acetylpyridinium chloride-4-phenylthio-semicarbazide	Oleic acid	Hg^{2+}	Natural water samples of Mansoura city	6.8	~100	$1x10^{-3}$	(185)
4-acetylpyridine-[N-(3-hydroxy-2-naphthoyl)]hydrazone	Oleic acid	Ni^{2+}	Water	7.0	~100	$4x10^{-4}$	(186)
1-(amino-N-(pyridine-3-yl)methanethio)-4-(pyridine-2-yl)thiosemi-carbazide	Oleic acid	Hg^{2+}	Sea water, lake water, Nile water, distilled water	5.0	~100	$1x10^{-3}$	(187)
thiophene-2-carboxaldehyde-[N-(3-hydroxy-2-naphthoyl)]-hydrazone	Oleic acid	Ni^{2+}	Water	7.0	~100	$4x10^{-4}$	(186)
salicylaldehyde-[N-(3-hydroxy-2-naphthoyl)]-hydrazone	Oleic acid	Ni^{2+}	Water	7.0	ˆ100	$4x10^{-4}$	(186)
p-anisaldehyde-[N-(3-hydroxy-2-naphthoyl)]hydrazone	Oleic acid	Ni^{2+}	Water	7.0	ˆ100	$4x10^{-4}$	
ethylacetoacetate-[N-(3-hydroxy-2naphthoyl)]-hydrazone	Oleic acid	Ni^{2+}	Water	7.0	ˆ100	$4x10^{-4}$	
(E)-2-(2-(dimethylamino)-1λ³,3λ²-thiazol-4-yl)-N'-(2-hydroxybenzylidene)acetohydrazide	Oleic acid	Zn^{2+}	Water	7.0	96	$1x10^{-3}$	(188)
4-(2-pyridyl-azo) resorcinol mono sodium mono hydrate	Oleic acid	Cu^{2+}	Water, drug	3-5	95	$2x10^{-5}$	(189)
Oxalyl-bis(3,4-di-hydroxy-benzylidene) hydrazone	Oleic acid	ZrO^{2+}	Sea water, underground water, lake water, tap water, Nile water	3.0	99.7	$1x10^{-5}$	(190)
2-(2-(4-hydroxy-3-methoxybenzylidene) hydrazinyl)-2-oxo-N-phenylacetamide	Oleic acid	Cu^{2+}	---	7.0	98	$1x10^{-3}$	(191)
2-(2-(2-hydroxy-3-methoxybenzylidene) hydrazinyl)-2-oxo-N-phenylacetamide	Oleic acid	Cu^{2+}	---	7.0	99	$1x10^{-3}$	(191)

Catalyst

2-Carboxybenzaldehyde-p-Toluenesulfonyl Hydrazone **(34)** was used as an efficient catalyst in coupling reaction (Figure 13) of benzaldehyde, piperidine, and phenylacetylene with 1,4 dioxane as a solvent for the preparation of 1-(1,3-diphenylprop-2-yn-1-yl)piperidine at 120 °C (198).
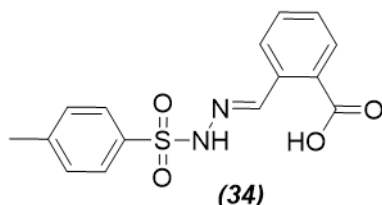
Figure 13: Hydrazone as catalyst for organic coupling reaction.

Corrosion Inhibitors

Corrosion is the degradation process of metals to form oxides, sulfides, or hydroxides. Many organic compounds like pyrimidine, imidazole, oxazole, triazole, amino acids and hydrazone are common organic corrosion inhibitors used to prevent or delay corrosion process of metals like copper, nickel, iron, and tin. Among all the organic compounds hydrazone gained much importance due to heteroatom nitrogen and oxygen. Some important hydrazone derivatives that worked as good corrosion inhibitors are presented in **Table 5.**

Ionophores

Ionophores are ion carriers and have tendency to bind, shield, and facilitate transportation of metal ions across the membrane (Figure 14). Ganjali and coworkers used pyridine-2-carbaldehyde-2-(4-methyl-1,3-benzothiazol-2-yl) hydrazone **(35)** and thiophene-2-carbaldehyde-(7-methyl-1,3-benzothiazol-2-yl)hydrazone **(36)** as suitable neutral ionophore for the preparation of Er (III) and Tm (III) membrane sensor at pH 2.5-12.0 and 3.0 - 12.0, respectively, with lower detection limits 5.0 $\times 10^{-6}$ M and 8.0×10^{-6} M. (218,219).

Dyes and Pigments

Nowadays, various hydrazones are used as stable dyes and pigments with a visible color change at different pH levels due to C=N-N linkage or presence of carbonyl group. Such dyes are not only used for dying polyester, silk, cotton, or nylon but are also used as sensitizers or for dying purposes in dye sensitized solar cells due to their broad absorption band.
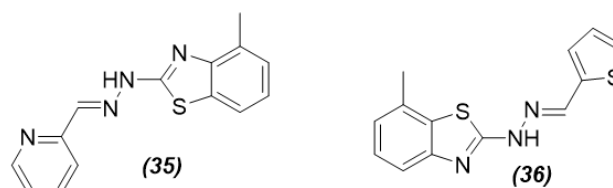
Figure 14: Hydrazone derivatives as ionophore for inner transition metals

Tricyanofuran hydrazone derivatives *(37)* were tested as pigments on polyester fibers to give orange-red, yellow and orange shades with λ_{max} 485 nm, 478 nm, and 463 nm, respectively, by Khattab and coworkers (220).

A series of heterocyclic hydrazone dyes **(38-44)** (Figure 15) were prepared from 2-amino-3-cyano-4-chloro-5 formyl-thiophene and five pyridine-2,6-dione based coupling components by Qian and coworkers. These hydrazone derivatives display distinct colors: yellow, purple, pink, and grey on five common fibers like Polyester, Nylon, Silk, Wool, and Cotton at pH 7.0 and 8.5 (221).

Al-Sehemi and coworkers synthesized different hydrazone dyes **(45)** (Figure 16) by the reaction of aromatic aldehydes with phenyl hydrazine. These hydrazones were further reacted with tetracyanoethylene to obtain violet colored dyes and supposed to be low-cost, efficient, and stable DSSC due to their smaller HOMO-LUMO energy gaps (222,223). Percentage efficiency for **45** was increased by 3.12 % at incident power 50 mW/cm^2. Due to high EA, it had high tendency to generate free electrons and holes (222,224-226).
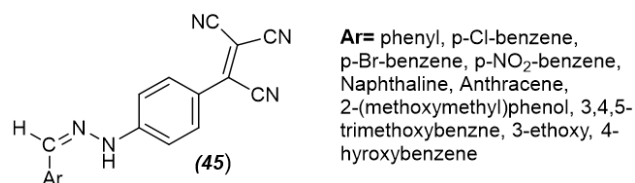
Figure 16: Hydrazone derivatives as dyes in DSSC

Ping Shen at el synthesized and used a series of N, N-diphenyl-hydrazone dye as efficient sensitizers (Figure 17) for production of DSSC with maximum conversion efficiency of up to 5.83 % (227). A series of metal free hydrazone based dyes *(46)* were synthesized from cheap materials without any expensive catalyst and used as DSSC by Urnikaite at el. The highest solid-state device conversion efficiency for these hydrazone dyes was 3.8-4.5 % with FF % 64-72% under 100 mW cm^{-2}, AM 1.5G (228-230). In 2020, Al-Sehemi et al. synthesized some promising dyes CHMA, CDBA, and AMCH *(47)* for DSSC (231).
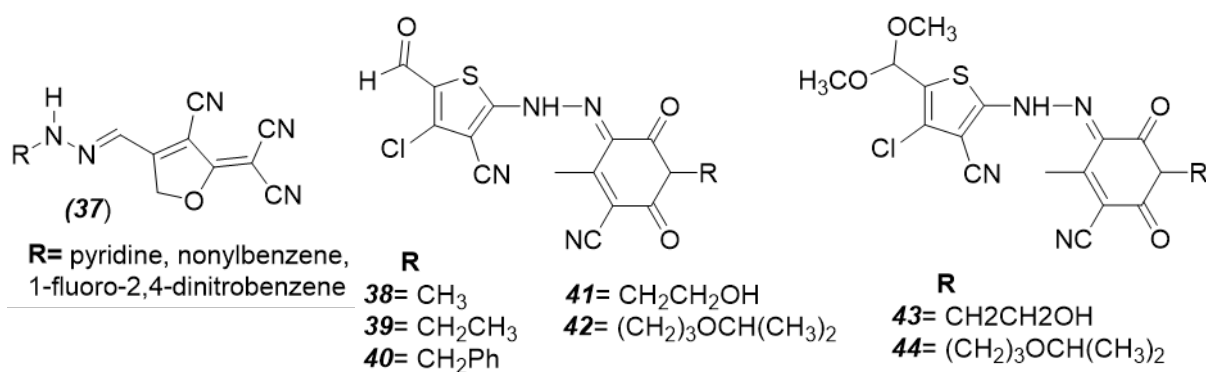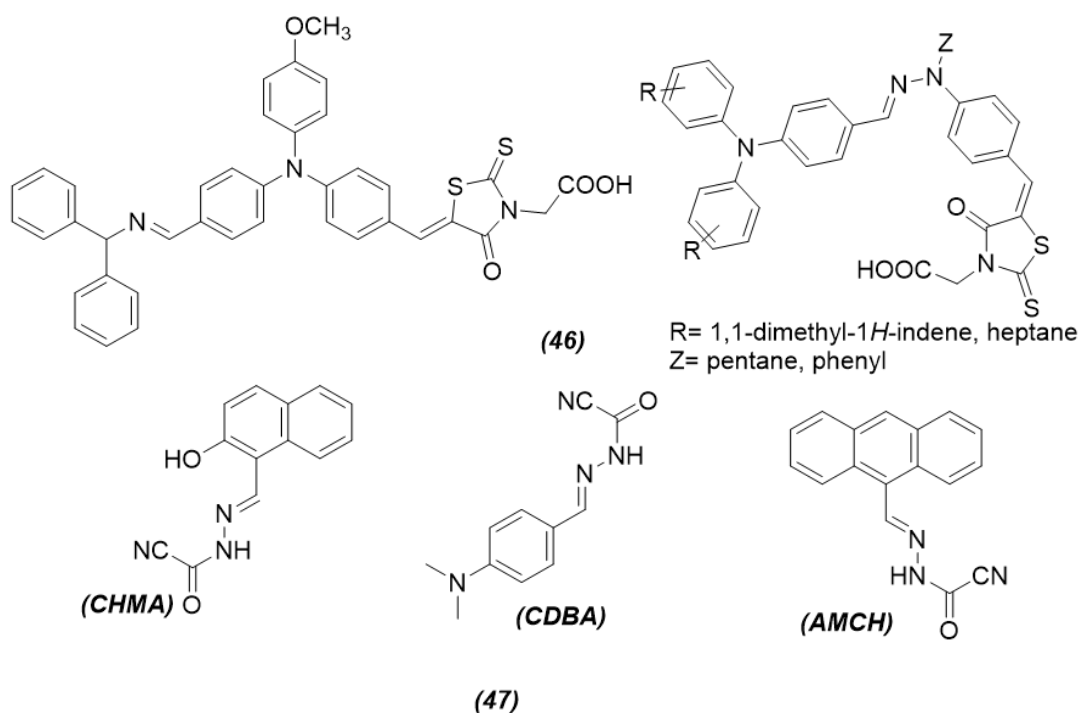
Figure 15: Hydrazone derivatives as dyes.

Figure 17: Hydrazone based dye sensitizers.

Nanoparticle Synthesizer

3-thiopropionylhydrazones **(48)** of mono and di-saccharides were prepared by Vasileva *et al.* and used for the synthesis of silver glycol-nanoparticles in ultrasonic bath with average particle size of 15–40 nm while hydrazine hydrate was used as reductant (232).
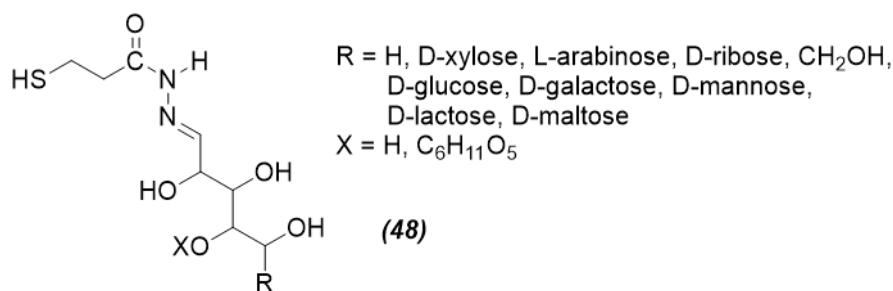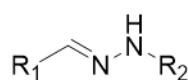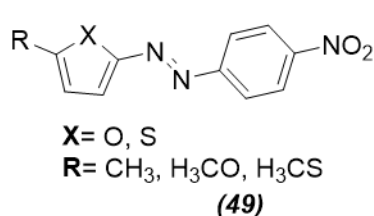

Figure 18: Hydrazone derivatives as nanoparticle synthesizer.

Table 5: Some important hydrazones that worked as good corrosion inhibitors

Corrosion inhibitors	Material	Medium	Conc. of inhibitor (M)	Inhibition efficiency (%)	Ref
(9H-fluoren-9-ylidene)hydrazine	Carbon steel	1.0 M H_2SO_4	10^{-1}	95.08	(199)
(2,7-dichloro-9H-fluoren-9-ylidene)hydrazine	Carbon steel	1.0 M H_2SO_4	10^{-1}	93.44	(199)
3-[8-(trlfluoromethyl)quinolin-4-yl]thlo]-N'-(2,3,4-trihydroxy-benzylidene)propano hydrazide	Mild steel	0.5 M H_2SO_4	$11.1x10^{-4}$	97.6	(200)
2,7-dibromo-9H-fluoren-9-ylidene)hydrazine	Carbon steel	1.0 M H_2SO_4	10^{-1}	89.34	(199)
(2,7-dinitro-9H-fluoren-9-ylidene)hydrazine	Carbon steel	1.0 M H_2SO_4	10^{-1}	84.42	(199)
2-hydroxyacetophenone-3-aminobenzoyl hydrazone	Copper	3N HNO_3	10^{-5}	70.0	(201)
3-hydroxybenzalde-hyde, 2-hydroxy-benzoyl hydrazone	Aluminum	2N HCl	$5x10^{-4}$	92.0	(202)
benzyl monophenyl hydrazone-N-cetyloxycarbonyl-ethyltaurate	Carbon steel	5% H_2S	$1x10^{-4}$	56	(203)
4-bromobenzalde-hyde, 2-hydroxy-benzoyl hydrazone	Aluminum	2N HCl	$5x10^{-4}$	92.0	(202)
Nitrobenzaldehyde G-T	C-steel	2 M HCl	$5x10^{-4}$	95.21	(204)
p-Hydroxybenzaldehyde G-T	C-steel	2 M HCl	$5x10^{-4}$	84.15	(204)
Thiophen-2-carboxaldehyde-[N-(3-hydroxy-2-naphthoyl)]-hydrazone	Nickel	2 M HCl	$1.5x10^{-5}$	59.3	(22)
bis-(o-methoxybenzaldehyde)-thiocarbodihydrazone	Copper	3.5% NaCl	$1.5X10^{-3}$	61	(205)
2-Acetophenone [N-3-hydroxyl-2-naphthoyl hydrazone]	Carbon steel	0.5 M H_2SO_4	$7X10^{-5}$	59	(206)
Furfural-isobutroyl hydrazone	Carbon steel	3 M H_3PO_4	$11x10^{-6}$	79.5	(207)
Furfural 4-methoxybenzoyl-hydrazone	Carbon steel	1 M H_3PO_4	$11x10^{-6}$	47	(208)
4-(N,N-dimethylamino) benzaldehyde nicotinic acid hydrazone	Mild steel	1M HCl	$6x10^3$	94.91	(209)
(E)-2-((2,3-dimethylphenyl)-amino)-N'-(thiophen-2-ylmethylene)-benzohydrazide	Mild steel	1M HCl	$5x10^{-3}$	92	(210)
(E)-2-((2,3-dimethylphenyl)-amino)-N'-(furan-2-ylmethylene)benzohydrazide	Mild steel	1M HCl	$5x10^{-3}$	88	(210)
2-((2,3-dimethylphenyl)amino)-N'-((1E,2E)-3-phenylallylidene)-benzohydrazide	Mild steel	1 M HCl	$5x10^{-3}$	97	(211)
(E)-2-((2,3-dimethylphenyl)-amino)-N'-(4-hydroxybenzy-lidene)benzohy-drazide	Mild steel	1 M HCl	$5x10^{-3}$	94	(211)
N'-(3-phenylallylidene) benzohydrazide	Mild steel	1 M HCl	$2x10^{-3}$	97.43	(212)
2-heterocarboxaldehyde-2'-pyridyl-hydrazones	Aluminum	2 M HCl	---	85	(213)
N-benzylidene-benzohydrazide	Mild steel	1 M HCl	$2.23x10^{-3}$	97.32	(212)
3-(cyano-dimethyl-methyl)-benzoic acid thio-phen-2-ylmethylene-hydrazide	Mild steel	0.5 M HCl	$2x10^{-3}$	91.2	(214)
3-(cyano-dimethyl-methyl)-benzoic acid furan-2-ylmethylene-hydrazide	Mild steel	0.5 M HCl	$2x10^{-3}$	86.7	(214)
2-(2-[2-(4-Pyridylcabonyl)-hydrazono]methyl-phenoxy)-acetic acid	Mild steel	Sea water	2.8×10^{-4}	85.4	(215)
4-(4'-benzoylhydrazine)-pyridine-carboxaldehyde hydrazone	N80 Steel	1 M HCl	$1x10^{-3}$	93.6	(216)
N'-[4-(diethylamino)-benzylidine]-3-[8-(trifluoromethyl)-quinolin-4-yl]thio-propano hydrazide	Mild steel	0.5 M H_2SO_4	$2x10^{-4}$	94.7	(217)

Nonlinear Optical Devices

Nonlinear optical materials are those materials or organic compounds that describe the behavior of light in nonlinear medium (Figure 19). Such materials play a major role in modern technology in telecommunication, optical switching, data processing, ultra-short pulsed lasers, laser amplifiers, sensors, and many more.

Shing Wong et al. synthesized various hydrazone derivatives *(49)* from aromatic aldehydes and 4-methoxy-phenylhydrazine or 4-tolylhydrazine or 4-nitrophenylhydrazine and used them with powder test for second or third order nonlinear optical devices (233).

X= O, S
R= CH_3, H_3CO, H_3CS
(49)

R₁= pyrene, anthracene
R₂= 4-flurobenzene, 2,4-difluorobenzene, 2,3,5,5-terafluorobenzene, 2,3,4,5,6-pentafluorobenzene
(50)

Figure 19: Hydrazone compounds used in nonlinear optical devices.

A series of eight anthracene hydrazone derivatives *(50)* were prepared and their third-order NLO performance was studied using the standard picosecond Z-scan technique in the open aperture mode by Wenjuan Xu at el. in 2018 (234). Similarly, 4-dimethylaminobenzaldehyde-4-nitrophenylhydrazone had promising non-liner optical properties (235).

Light Emitting Diodes

6-Alkyl-3-chromonealdehyde (2,2-dialkyl)hydrazone derivatives *(51)* were synthesized from 6-alkyl-3-chromonealdehydes and 2,2-dialkylhydrazones by Chung and Chang and were used as light-emitting diodes due to their green light emission (236).

R= CH_3, $CH(CH_3)_2$
R'= CH_3, C_6H_5
(51)
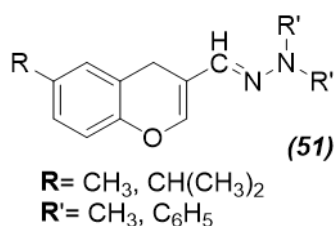
Figure 20: Hydrazone based light emitting diodes.

CONCLUSION

This review summarizes the analytical applications of hydrazone derivatives. These hydrazone derivatives are widely used as spectrophotometric agents not only for detection of metals in sand, soil, water, pharmaceutical samples, alloys, wine, beer, bread, oil, fruits, and vegetables, but also for the detection of organic compounds like carbazoles, aldehydes, ketones, carboxylic acids, salicylic acid, aspirin, aromatic amines, heterocyclic bases, and many more in drugs, food, air, blood, and urine samples. These are also used as organic collectors in flotation for collecting different metals from water, where oleic acid is used as surfactant. Nowadays, they are used as dyes in DSSC due to their broad absorption band, as chemosensors, especially in tumor cells due to their florescence property, as indicators and as microbe detectors due to their pH sensing properties. Hydrazone derivatives are also used as corrosion inhibitors for nickel, iron, steel, copper, etc. Hydrazone derivatives have many binding sites due to which they have ability to bind metals via coordinate covalent bond and anions via covalent bond. This property makes them a unique class of compounds among all organic compounds. These types of compounds are used in light emitting diodes and due to nonlinear optical properties, are also used in lasers, telecommunication devices, and optical switching. Hydrazone derivatives produce stable colors that can't fade after long washing and are used as dying reagents for the dying of nylon, cotton, polyester, and silk. This review covers approximately 61 years of work on hydrazone's analytical applications with 236 references.

REFERENCES

1. Abd El-Wahab H, Abd El-Fattah M, Ahmed AH, Elhenawy AA, Alian NA. Synthesis and characterization of some arylhydrazone ligand and its metal complexes and their potential application as flame retardant and antimicrobial additives in polyurethane for surface coating. Journal of Organometallic Chemistry. 2015 Aug;791:99–106. <DOI>.

2. Xavier A, Thakur M, Marie JM. Synthesis and spectral characterisation of hydrazone based 14-membered octaaza macrocyclic Ni (II) complexes. J Chem Pharm Res. 2012;4(2):986–90.

3. Belskaya NP, Dehaen W, Bakulev VA. Synthesis and properties of hydrazones bearing amide, thioamide and amidine functions. Zhdankin VV, editor. Arkivoc. 2010 Jul 30;2010(1):275–332. <DOI>.

4. Ray A, Banerjee S, Sen S, Butcher RJ, Rosair GM, Garland MT, et al. Two Zn(II) and one Mn(II) complexes using two different hydrazone ligands: spectroscopic studies and structural aspects. Struct Chem. 2008 Apr;19(2):209–17. <DOI>.

5. Balakrishnan KP, Krishnan V. Studies on ß-arylhydrazone-imine nickel(II) complexes—Examples of metal template syntheses. Journal of Inorganic and Nuclear Chemistry. 1979 Jan;41(1):37–40. <DOI>.

6. Mermer A, Demirbas N, Uslu H, Demirbas A, Ceylan S, Sirin Y. Synthesis of novel Schiff bases using green chemistry techniques; antimicrobial, antioxidant, antiurease activity screening and molecular docking studies. Journal of Molecular Structure. 2019 Apr;1181:412–22. <DOI>.

7. Subhashini NJP, Janaki P, Bhadraiah B. Synthesis of hydrazone derivatives of benzofuran and their antibacterial and antifungal activity. Russ J Gen Chem. 2017 Sep;87(9):2021–6. <DOI>.

8. Küçükgüzel ŞG, Rollas S, Küçükgüzel I, Kiraz M. Synthesis and antimycobacterial activity of some coupling products from 4-aminobenzoic acid hydrazones. European Journal of Medicinal Chemistry. 1999 Dec;34(12):1093–100. <DOI>.

9. Bouree P. Effet du nifuroxazide sur Giardia intestinalis. Médecine et Maladies Infectieuses. 1991 Jul;21(7):424–6. <DOI>.

10. Sinha R, Sara UVS, Khosa RL, Stables J, Jain J. Nicotinic acid hydrazones: a novel anticonvulsant pharmacophore. Med Chem Res. 2011 Dec;20(9):1499–504. <DOI>.

11. Sharma A, Kumar V, Jain S, Sharma PC. Thiazolidin-4-one and hydrazone derivatives of capric acid as possible anti-inflammatory, analgesic and hydrogen peroxide-scavenging agents. Journal of Enzyme Inhibition and Medicinal Chemistry. 2011 Aug 1;26(4):546–52. <DOI>.

12. Zheng LW, Wu LL, Zhao BX, Dong WL, Miao JY. Synthesis of novel substituted pyrazole-5-carbohydrazide hydrazone derivatives and discovery of a potent apoptosis inducer in A549 lung cancer cells. Bioorganic & Medicinal Chemistry. 2009 Mar;17(5):1957–62. <DOI>.

13. Mei WL, Qian L, Fei JL, Qiang ZZ. Synthesis and structure of the acylhydrazone Schiff base. Chin J Struc Chem. 2010;29(9):1399–403.

14. Haj Mohammad Ebrahim Tehrani K, Esfahani Zadeh M, Mashayekhi V, Hashemi M, Kobarfard F, Gharebaghi F, et al. Synthesis, Antiplatelet Activity and Cytotoxicity Assessment of Indole-Based Hydrazone Derivatives. Iran J Pharm Res. 2015;14(4):1077–86.

15. El-Sabbagh OI, Rady HM. Synthesis of new acridines and hydrazones derived from cyclic β-diketone for cytotoxic and antiviral evaluation. European Journal of Medicinal Chemistry. 2009 Sep;44(9):3680–6. <DOI>.

16. Mahmudov KT, Guedes da Silva MFC, Kopylovich MN, Fernandes AR, Silva A, Mizar A, et al. Di- and tri-organotin(IV) complexes of arylhydrazones of methylene active compounds and their antiproliferative activity. Journal of Organometallic Chemistry. 2014 Jun;760:67–73. <DOI>.

17. Hedrich L W, Patel N R, Kirkpatrick J L. Heterocyclic-Substituted Hydrazides and Hydrazones as Plant Growth Regulators 1982. US patent US4,319,026A. <URL>.

18. Wang Y, Yu X, Zhi X, Xiao X, Yang C, Xu H. Synthesis and insecticidal activity of novel hydrazone compounds derived from a naturally occurring lignan podophyllotoxin against Mythimna separata (Walker). Bioorganic & Medicinal Chemistry Letters. 2014 Jun;24(12):2621–4. <DOI>.

19. Aggarwal N, Kumar R, Srivastva C, Dureja P, Khurana JM. Synthesis of Nalidixic Acid Based Hydrazones as Novel Pesticides. J Agric Food Chem. 2010 Mar 10;58(5):3056–61. <DOI>.

20. Fouda A, Mostafa H, Ghazy S, Farah S. Use of hydrazone derivates as inhibitors for the corrosion of nickel in hydrochloric acid solution. Int J Electrochem Sci. 2007;2:182–94.

21. Mohareb RM, Fleita DH, Sakka OK. Novel Synthesis of Hydrazide-Hydrazone Derivatives and Their Utilization in the Synthesis of Coumarin, Pyridine, Thiazole and Thiophene Derivatives with Antitumor Activity. Molecules. 2010 Dec 23;16(1):16–27. <DOI>.

22. Wolf R A, Warakomski J M. Hydrazone initiated polymerization process. 1993. US patent US5218066A. <URL>.

23. Jani G, Vyas K, Nimavat K, Franco J. synthesis and spectrophotometric studies of metal (II) complexes of hydrazone derivatives. Int J Chem Sci. 2010;8(1):139–45.

24. Basha VS. Synthesis and Characterization of 2- Acetyl Furan Benzoyl Hydrazone and its Applications in the Spectrophotometric Determination of Cu (II). MOJBOC [Internet]. 2017 Aug 1 [cited 2022 Apr 29];1(3). Available from: <DOI>.

25. Bai KA, Vallinath G, Chandrasekhar K, Devanna N. Derivative spectrophotometric determination of nickel (II) using 3, 5-dimethoxy-4-hydroxy benzaldehyde isonicotinoyl hydrazine (DMHBIH). Rasayan Journal of Chemistry. 2010;3(3):467–72.

26. Rao MR, Chandrasekhar K. Sensitive Derivative Spectrophotometric Determination of Palladium (II) Using 3, 5-Dimethoxy-4-hydroxybenzaldehydeisonicotinoylhydrazone in presence of Micellar medium. Chem. 2011;3:358–66.

27. Vallinath G, Chandrasekhar K, Devanna N. Determination of thorium (IV) by derivative spectrophotometric technique. Int J Pharm Qual Assur. 2010;2:67–72.

28. Vallinath G, Chandrasekhar K, Devanna N. Sensitive derivative spectrophotometric determination of gold (III) using 3, 5-dimethoxy-4-hydroxybenzaldehyde isonicotinoyl hydrazone (DMHBIH) in presence of micellar medium. Chemistry of metals and alloys. 2011;(4,№ 1-2):143–51.

29. Bai KA, Vallinath G, Chandrasekhar K, Devanna N. Derivative spectrophotometric determination of nickel (II) using 3, 5-dimethoxy-4-hydroxy benzaldehyde isonicotinoyl hydrazine (DMHBIH). Rasayan Journal of Chemistry. 2010;3(3):467–72.

30. Devanna N, Reddy G, Bannoth C, Jayaveera K. Derivative Spectrophotometric determination of Lead(II) using diacetylmonoxime 4-hydroxyl hydrazone reagent. Asian J Chem. 2008;20(3):2257–63.

31. Ishii H, Odashima T, Hashimoto T. Synthesis of sensitive pyridylhydrazone reagents and extraction-spectrophotometric determination of trace nickel with 2-pyridinecarbaldehyde 2-(5-nitro)pyridylhydrazone. Anal Sci. 1987;3(4):347–52. <DOI>.

32. Cha K, Park C. Spectrofluorimetric determination of iron(III) with 2-pyridinecarbaldhyde-5-nitro-pyridylhydrazone in the presence of hexadecyltrimethylammonium bromide surfactant. Talanta. 1996 Aug;43(8):1335–40. <DOI>.

33. Sivaramaiah S, Reddy PR, Reddy V, Reddy T. Direct and derivative spectrophotometric determination of zirconium(IV) with 2,4-dihydroxy benzaldehyde isonicotinoyl hydrazone. Indian J Chem. 2003;42A:109–11. <URL>.

34. Babaiah O, Kesavarao C, Sreenivasulureddy T, Krishnareddy V. Rapid, selective, direct and derivative spectrophotometric determination of titanium with 2,4-dihydroxybenzaldehyde isonicotinoyl hydrazone. Talanta. 1996 Apr;43(4):551–8. <DOI>.

35. Bai K, Chandrasekhar K. Spectrophotometric Determination of Osmium (VIII) using 2,4-Dimethoxybenzaldehyde Isonicotinoyl Hydrazone (Dmbih) in presence of Surfactant Triton X-100. RJPBCS. 2011;2(3):174–82.

36. Sivaramaiah S, Raveendra Reddy P. Direct and Derivative Spectrophotometric Determination of Zinc with 2,4-Dihydroxybenzaldehyde Isonicotinoyl Hydrazone in Potable Water and Pharmaceutical Samples. J Anal Chem. 2005 Sep;60(9):828–32. <DOI>.

37. Sivaramaiah S, Raveendra Reddy P, Krishna Reddy V, Sreenivasulu Reddy T. Direct and Derivative Spectrophotometric Determination of Thorium with 2,4-dihydroxybenzaldehyde Isonicotinoyl Hydrazone. Journal of Radioanalytical and Nuclear Chemistry. 2000;245(2):367–70. <DOI>.

38. Borhade S. Synthesis, characterisation and spectrophotometric determination of Fe (II) complex of 2, 4-dihydroxybenzaldehyde isonicotinoyl hydrazone (E)-N'-(2, 4-dihydroxybenzylidene) isonicotinohydrazide, it's application & biological activity. Der Chemica Sinica. 2011;2(4):64–71.

39. Babaiah O, Reddy P, Reddy V, Reddy T. Simultaneous spectrophotometric determination of Molybdium (VI) and titanium (IV) using 2,4-dihydroxybenzaldehyde isonicotinoyl hydrazone. Indian J Chem. 1999;38A:1035–8. <URL>.

40. Sivaramaiah S, Raveendra Reddy P, Krishna Reddy V, Sreenivasulu Reddy T. Derivative spectrophotometric determination of aluminium using 2,4-dihydroxybenzaldehyde isonicotinoyl hydrazone as a complexing agent. Chemia Analityczna. 2004;49(1):101–9. <URL>.

41. Vasilikiotis GS, Kouimtzis TA, Vasiliades VC. Spectrophotometric and solvent extraction study of o-hydroxybenzaldehyde isonicotinoyl hydrazone complexes with gallium and indium. Microchem Journal. 1975 Jun;20(2):173–9. <DOI>.

42. Vasilikiotis GS, Kouimtzis ThA. Spectrophotometric and solvent extraction studies of metal complexes of some hydrazones. Microchem Journal. 1973 Feb;18(1):85–94. <DOI>.

43. Narayana L, Suvarapu, Somala AR, Bobbala P, Inseong H, Ammireddy VR. Simultaneous Spectrophotometric Determination of Chromium(VI) and Vanadium(V) by using 3,4-Dihydroxybenzaldehyde isonicotinoyl hydrazone (3,4-DHBINH). E-Journal of Chemistry. 2009;6(s1):S459–65. <DOI>.

44. Suvarapu LN, Seo YK, Baek SO. Spectrophotometric Determination of Titanium(IV) by Using 3,4-Dihydroxybenzaldehydeisonicotinoyl-hydrazone(3,4-DHBINH) as a Chromogenic Agent. Chem Sci Trans. 2012 May 26;1(1):171–9. <DOI>.

45. Swetha M, Raveendra Reddy P, Krishna Reddy V. Direct, derivative spectrophotometric determination of micro amounts of Palladium (II) by 5-bromo salicylaldehyde isonocotinoyl hydrazone (5-BrSAINH). Adv Appl Sci Res. 2013;4(2):298–304.

46. Sobha S, Swetha M, Reddy PR, Reddy VK. Direct and Derivative Spectrophotometric Determination of Chromium (VI) in Microgram Quantities Using 5-Bromo Salicylaldehyde Isonocotinoyl Hydrazone (5-BrSAINH). Asian Journal of Research in Chemistry. 2013;6(7):667–70.

47. Swetha M, Reddy PR, Reddy VK. Non-Extractive Spectrophotometric Determination of U (VI) Using 5-Bromo Salicylaldehyde Isonicotinoyl Hydrazone in Environmental, Phosphate Rocks and Fertilizer Samples. International Journal of Scientific and Research Publications. 2013;3(8):1–5.

48. Srilalitha V, Prasad G, Kumar R, Seshagiri V, Ravindranath R. A new spectrophotometric method for the determination of trace amounts of titanium(IV). Facta Univ, Phys Chem Technol. 2010;8(1):15–24. <DOI>.

49. Reddy KH, Chandrasekhar K. Simultaneous first derivative spectrophotometric determination of nickel (II)

and copper (II) in alloys with diacetylmonoxime benzoylhydrazone. Indian J Chem. 2001;40A: 727-32.

50. Chandrasekhar K, Hussain Reddy K, Sreenivasulu Reddy T. Simultaneous second derivative Spectrophotometric determination of nickel (II) and copper (II) in alloys using diacetylmonoxime benzoylhydrazone (DMBH). J Ind Chem Soc. 2003;80(10):930–3.

51. Devanna N, Satheesh K, Sekhar KC. Derivative spectrophotometric determination of iron (II) using diacetylmonoxime benzoyl hydrazone. Asian J Chem. 2005;17(3):1767-72.

52. Devanna N, Direct and Derivative Spectrophotometric Determination of Mercury (II) using Diacetyl Monoxime Benzoylhydrazone (DMBH). Int J Chem. 2011;3(2):754-61. <DOI>.

53. Reddy KR, Devanna N, Sekhar K, Vallinath G. Direct and derivative spectrophotometric determination of mercury (II) using diacetylmonoxime benzoylhydrazone (DMBH). 2010;1(3): 754-61.

54. Ramachandraiah C, Vijayakumari D, Lakshminarayana K. A sensitive spectrophotometric method for the determination of trace amounts of uranium (VI) using o-hydroxypropiophenone isonicotinoyl hydrazone. J Radioanal Nucl Chem Lett. 1993 Mar;175(3):185–90. <DOI>.

55. Vijayakumari D, Lakshiminarayana K. A sensitive spectrophotometric method for the determination of trace amounts of uranium(VI) using 2-hydroxy-1-naphthaldehyde isonicotinoyl hydrazone. J Radioanal Nucl Chem Lett. 1993 Jan;175(1):1–7. <DOI>.

56. Sonawane RP, Lokhande RS, Chavan UM. Development of Method for Extractive Spectrophotometric Determination of Fe(III) with 2-Hydroxy-1-Naphthalene Carboxaldehyde Phenyl Hydrazone as an Analytical Reagent. ILCPA. 2013 Sep;14:7–12. <DOI>.

57. Sonawane RP, Lokhande RS, Chavan UM. Development of Method for Extractive Spectrophotometric Determination of Cu(II) with 2-Hydroxy-1-Naphthalene Carboxaldehyde Phenyl Hydrazone as an Analytical Reagent. ILCPA. 2013 Sep;14:1–6. <DOI>.

58. Sonawane P, Lokhande RS, Chavan UM, Development Of Method For Extractive Spectrophotometric Determination Of Co(II) With 2-Hydroxy-1-Naphthalene Carboxaldehyde Phenyl Hydrazone As An Analytical Reagent. Int J Chem Sci. 2013; 11(1): 436-42.

59. Kudapalia Y, Suresh T. Spectrophotometric Determination of Copper (Ii) with 2, 5-Dihydroxyacetophenone Benzoic Hydrazone. Orient J Chem. 2004;20(2):18625. <URL>.

60. Priya BK, Subrahmanyam P, Kumar JD, Chiranjeevi P. Simple Sensitive Spectrophotometric Determination of Vanadium in Biological and Environmental Samples. E-Journal of Chemistry. 2006;3(4):286–97. <DOI>.

61. Devi VSA, Reddy VK. Spectrophotometric Determination of Iron(II) and Cobalt(II) by Direct, Derivative, and Simultaneous Methods Using 2-Hydroxy-1-Naphthaldehyde-p-Hydroxybenzoichydrazone. Int J Anal Chem. 2012;2012:1–12. <DOI>.

62. Chowdary P, Basha V. Determination of vanadium in different environmental, Leafy vegetable and biological samples using 2-hydroxy-1-naphthaldehyde-p-hydroxybenzoichydrazone (HNHBH) spectrophotometrically. Der Pharma Chem. 2015;7(12):338–45.

63. Devi VSA, Reddy VK. 2-Hydroxy-1-naphthaldehyde-P-hydroxybenzoichydrazone: A New Chromogenic Reagent for the Determination of Thorium(IV) and Uranium(VI). Journal of Chemistry. 2013;2013:1–10. <DOI>.

64. Chowdary PG, Basha VS. Direct and derivative spectrophotometric determination of Yttrium (III) using 2-hydroxy-1-naphthaldehyde-p-hydroxybenzoichydrazone (HNHBH) in alloy and geological samples. Der Pharm Lett. 2014;6(6):373–9.

65. Chowdary PG, Basha VS, Devi VSA. Simultaneous Third order derivative Spectrophotometric Determination of Vanadium and Palladium Using 2-Hydroxy-1-Naphthaldehyde-P-hydroxy Benzoichydrazone (HNHBH). IOSR. 2016 Apr;08(04):55–9. <DOI>.

66. Reddy G, Devanna N, Chandrasekhar K. Derivative spectrophotometric determination of uranium (VI) using diacetyl monoxime isonicotinoyl hydrazone (DMIH). Orbital Elec J Chem. 2011;3(1):24–31.

67. Reddy GC, Devanna N, Chandrasekhar K. Sensitive method of determination of gold (III) using diacetyl monoxime isonicotinoyl hydrazone (DMIH). Orbital: The Electronic Journal of Chemistry. 2011;3(3):125–32.

68. Reddy GC, Devanna N, Chandrasekhar K. SENSITIVE SPECTROPHOTOMETRIC DETERMINATION OF THORIUM (IV) USING DIACETYL MONOXIME ISONICOTINOYL HYDRAZONE (DMIH). Int J App Bio Pharm Tech. 2011;2(2):133–9.

69. Gadikota CR, Devanna N, Chandrasekhar K. Sensitive method of determination of gold (III) using diacetyl monoxime isonicotinoyl hydrazone (DMIH). Orbital Elec J Chem. 2011;3(3):125–32. <DOI>.

70. Mallikarjuna P, Mastanaiah T, Narayana BV, Varma MP, Rao VS. Research Journal of Pharmaceutical, Biological and Chemical Sciences. 2012;3(3):1140–49.

71. Gadikota CR, Devanna N, Chandrasekhar KB. Derivative Spectrophotometric Determination of Molybdenum (VI) using Diacetyl Monoxime Isonicotinoyl Hydrazone (DMIH). Asian J Res Chem. 2011;4(2):282-84. doi: <DOI>.

72. Patil SS, Sawant AD. Pyridine-2-acetaldehyde salicyloyl hydrazone as reagent for extractive and spectrophotometric determination of cobalt(II) at trace level. Indian J Chem Technol. 2001;8:88–91.

73. Garcia-Vargas M, Rodriguez JMB, Novás SA, Coy-Yll R. Absorptiometric determination of micro- and submicroamounts of iron using an extractive method with pyridine-2-acetaldehyde salicyloylhydrazone. Microchemical Journal. 1982 Dec;27(4):519–29.

74. Vargas M, Gallego M, Guardiat M. Pyridine-2-acetaldehyde SalicyloyI hydrazone as an Analytical Reagent and its Application to the Determination of Vanadium. Analyst. 1980;105:965–73.

75. Bale MN, Dave DP, Sawant AD. Extraction and spectrophotometric determination of lead(II) with pyridine-2-acetaldehyde salicyloylhydrazone. Talanta. 1995 Sep;42(9):1291–6.

76. Sinha SH, Sawant AD. Extraction and Spectrophotometric Determination of Palladium with Pyridine-2-acetaldehyde Salicyloylhydrazone. Bull Chem Soc Jpn. 1992 Jun;65(6):1622–5.

77. Patil S, Sawant A. Solvent extraction and spectrophotometric determination of Sb (lll) with pyridine-2-acetaldehyde salicyloylhydrazone. 1998; 37:1038-40.

78. Bale MN, Sawant AD. Solvent Extraction and Spectroscopic determination of Uranium (VI) with pyridine-2-carboxaldehyde 2-hydroxybenzoylhydrazone. J Radioanal Nucl Chem. 2001;247(3):531–4.

79. Bale MN, Sawant AD, Shaikh H, Garole DJ. Extractive Spectrophotometric Determination of Trace Hg (II) in Eye Drops and Ayurvedic Medicines Using Pyridine 2-Carboxaldehyde 2-Hydroxybenzoylhydrazone. IOSR JAC. 2017 Feb;10(01):24–31.

80. Bale MN, Sawant AD, Shaikh H, Garole DJ. Spectrophotometric Determination of Bi(III) from Alloys and Drugs Samples Using Pyridine-2-carboxaldehyde-2-hydroxybenzoylhydrazone. Asian J Chem. 2017 Apr 30;29(6):1328–32.

81. Reddy PNK, Reddy GT, Kumar SD, Reddy AVR, Parveen SN, Reddy NCG. A New Hydrazone Derivative as a Sensitive Analytical Reagent for The Determination of Co(II) in Food, Water and Synthetic Samples. IJPSR. 2016;7(1): 153-62.

82. Ramanjaneyulu G, Reddy PR, Reddy VK, Reddy TS. Direct and Derivative Spectrophotometric Determination of Copper(II) with 5-Bromosalicylaldehyde Thiosemicarbazone. TOACJ. 2009 Jan 2;2(1):78–82.

83. Asuero AG, Marques ML, Herrador MA. Spectrophotometric determinationof zinc in cooking salts, tap and mineral waters with phenylglyoxal mono(2-pyridyl)hydrazone. Analytica Chimica Acta. 1987;196:311–6.

84. de Pablos F, Galan G, Ariza JG. Fluorimetric determination of gallium in a nickel alloy and aluminium with N-oxalylamine(salicylaldehyde hydrazone). Talanta. 1987 Oct;34(10):835–8.

85. de Pablos F, Ariza JLG, Pino F. N-oxalylamine(salicylaldehyde hydrazone) as an analytical fluorimetric reagent for the determination of nanogram amounts of aluminium. Analyst. 1986;111(10):1159-1162.

86. Krishna D, Devi C. Determination of Iron (II) and Iron (III) in Presence of Micellar Medium Using 4-Hydroxy 3, 5 Dimethoxy Benzaldehyde 4-Hydroxy Benzoyl hydrazone by Spectrophotometry. IJGHC. 2012;1(3):256–63.

87. Krishna D, Devanna N, Chandrasekhar K. A Comparative study of Nickel (II) using 4-Hydroxy 3,5 dimethoxy benzaldehyde 4-hydroxy benzoylhydrazone and Cinnamaldehyde 4-hydroxybenzoyl hydrazone in presence of micellar medium by Spectrophotometry. Int J ChemTech Res. 2011;3(1):506–15.

88. Krishna DG, Devanna N, Chandrasekhar KB. Comparative study of Palladium (II) using 4-Hydroxy 3, 5 dimethoxy benzaldehyde-4-hydroxy benzoyl hydrazone and Cinnamaldehyde 4-hydroxy benzoylhydrazone in presence of micellar medium by Spectrophotometry. Int J Pharm Sci Res. 2010;1(8):301-11.

89. Krishna D, Devanna N, Chandrasekhar K. Comparative study of Copper (II) using 4-Hydroxy 3, 5 dimethoxy benzaldehyde 4-hydroxy benzoyl hydrazone and Cinnamaldehyde 4-hydroxy benzoylhydrazone in presence of micellar medium by Spectrophotometry. Res J Pharm Biol. 2011;2(1):252–4.

90. Rao MR, Chandrasekhar K, Devanna N. Simultaneous determination of nickel (II) and copper (II) using 3-methoxysalcilaldehyde-4-hydroxybenzoylhydrazone (MSHBH) by first order derivative spectrophotometric technique. Archives of Applied Science Research. 2011;3(1):462–71.

91. Krishna G, Chan D, Drasekhar B. Direct and Derivative Spectrophotometric Determination of Cobalt (II) in presence of Micellar Medium in Real Samples using Cinnamaldehyde-4-Hydroxy Benzoyl Hydrazone (CMHBH). International Journal of Organic and Bio Organic Chemistry. 2011;1:1–7.

92. Krishna D, Devi C. Determination of Chromium (VI) In Presence of Micellar Medium Using Cinnamaldehyde-4-Hydroxybenzoylhydrazone by Spectrophotometry. Int J Anal Bioanal Chem. 2011;1(3):107–9.

93. Devi C, Krishna D, Devanna N, Chandrasekhar K. Direct and derivative spectrophotometric determination of Molybdenum (VI) in presence of micellar medium in food stuffs, pharmaceutical samples and in alloys using cinnamaldehyde-4-hydroxy benzoylhydrazone (CHBH). Research Journal of Pharmaceutical Biological and Chemical Sciences. 2010;1(3):808–25.

94. Ramesh M, Chandrasekhar K, Reddy KH. Spectrophotometric determination of lead (II) in water samples using benzil α-monoxime isonicotinoyl hydrazone. Indian J Chem. 2000; 39A:1337-39.

95. Asuero AG, Marques ML, Navas MJ. Spectrophotometric determination of cobalt in multivitaminic preparations with dipyridylglyoxal mono (2-pyridyl) hydrazone. International Journal of Pharmaceutics. 1987 Nov;40(1–2):43–9.

96. Asuero AG, Marques ML, Navas MJ. Spectrophotometric determination of cobalt with dipyridylglyoxal mono(2-pyridyl)hydrazone. Microchemical Journal. 1987 Oct;36(2):216–21.

97. Ahmed MJ, Zannat T. Simple Spectrophotometric Method for the Determination of Copper in Some Real, Environmental, Biological, Food and Soil Samples Using

Salicylaldehyde Benzoyl Hydrazone. Pakistan Journal of Analytical & Environmental Chemistry. 2012;13(1):22-35.

98. Pflaum RT, Tucker EScott. Spectrophotometric determination of cobalt with benzil mono-(2-pyridyl)hydrazone. Anal Chem. 1971 Mar 1;43(3):458–9.

99. Berger SA. Benzil-mono- (2-quinolyl) -hydrazone as a chelating agent for copper. Microchem Acta. 1979 May;71(3–4):311–6.

100. Berger S. The solvent extraction of Cu(II), Ni(II) and Co(II) with benzil mono(2-quinolyl)hydrazone. Talanta. 1982 Aug;29(8):718–20.

101. Radhakrishna N, Viswanatha C, Reddy KR, Devanna N. A Sensitive and Selective Chromogenic Organic Reagent 4-hydroxy-3,5-dimethoxy benzaldehyde-4-hydroxy benzoyl hydrazone (HDMBHBH) for the Direct and Derivative Spectrophotometric Determination of Lead (II). European Reviews of Chemical Research. 2015 Mar 11;3(1):43–50.

102. Rao CK, Reddy VK, Reddy TS. Rapid and sensitive spectrophotometric determination of cerium(IV) with 2,4-dihydroxy benzophenone benzoic hydrazone. Talanta. 1994 Feb;41(2):237–41.

103. Saritha B, Reddy TS. Direct Spectrophotometric Determination of Ni (II) Using 5- Bromo-2- hydroxyl -3-methoxybenzaldehyde-4-hydroxy benzoichydrazone. IOSR-JAC. 2014;7(3):22–6.

104. Devireddy M, Saritha B, Giri A, Reddy TS. Direct spectrophotometric determination of titanium (IV) with 5-bromo-2-hydroxy-3-methoxybenzaldehyde-p-hydroxybenzoic hydrazine. J Chem Pharm Res. 2014;6(6):1145–50.

105. Nakanishi T, Otomo M. Spectrophotometric determination of iron(II) with 2-(3'-sulfobenzoyl)pyridine benzoylhydrazone. Microchemical Journal. 1987 Aug;36(1):128–34.

106. Ariza JLG, González MLM, González MTM. N,N'-oxalylbis(salicylaldehyde hydrazone) as an analytical spectrophotometric and fluorimetric reagent. Part I. Study of the metal reactivity and application to the determination of aluminium. Analyst. 1984;109(7):885–9.

107. Kabil MA, Ghazy SE, Mostafa MA, El-Asmy AA. Micro-determination of gold using N-cyanoacylacetaldehyde hydrazone. Fresenius J Anal Chem. 1994;349(10–11):775–6.

108. Vasilikiotis GS. Analytical applications of isonicotinoyl hydrazones. Microchemical Journal. 1968 Dec;13(4):526–8.

109. Rekha D, Kumar JD, Jayaraj B, Lingappa Y, Chiranjeevi P. Nickel(II) Determination by Spectrophotometry Coupled with Preconcentration Technique in Water and Alloy Samples. Bulletin of the Korean Chemical Society. 2007 Mar 20;28(3):373–8.

110. Rajendraprasad N, Basavaiah K, Vinay KB. Application of 3-methylbenzothiazolin-2-one hydrazone for the quantitative spectrophotometric determination of oxcarbazepine in pharmaceuticals with cerium(IV) and periodate. J Appl Spectrosc. 2012 Sep;79(4):616–25.

111. Yaseen S, Qasim B, Al-lame N. Spectrophotometric Determination of Cu (+II) by Complexation with 2-(4-biphenyl) Imidazo [1,2-] Pyrimidine-3-Hydrazone and Studying Characteristics of prepared complex. Egypt J Chem. 2021 Oct 5;64(2):673-691.

112. Echioda S, Ogunieye AO, Salisu S, Abdulrasheed AA, Chindo IY, Kolo AM. UV-Vis Spectrophotometric Determination of Selected Heavy Metals (Pb, Cr, Cd and As) in Environmental, Water and Biological Samples with Synthesized Glutaraldehyde Phenyl Hydrazone as the Chromogenic Reagent. EJCHEM. 2021 Jul 13;2(3):1–5.

113. Tümay SO, Şenocak A, Mermer A. A "turn-on" small molecule fluorescent sensor for the determination of Al 3+ ion in real samples: theoretical calculations, and photophysical and electrochemical properties. New J Chem. 2021;45(39):18400–11.

114. Li T, Yang Z, Li Y, Liu Z, Qi G, Wang B. A novel fluorescein derivative as a colorimetric chemosensor fordetecting copper(II) ion. Dyes and Pigments. 2011 Jan;88(1):103–8.

115. Hu S, Song J, Zhao F, Meng X, Wu G. Highly sensitive and selective colorimetric naked-eye detection of Cu2+ in aqueous medium using a hydrazone chemosensor. Sensors and Actuators B: Chemical. 2015 Aug;215:241–8.

116. Rahman FU, Ali A, Khalil SK, Guo R, Zhang P, Wang H, et al. Tuning sensitivity of a simple hydrazone for selective fluorescent "turn on" chemo-sensing of Al3+ and its application in living cells imaging. Talanta. 2017 Mar;164:307–13.

117. Xu ZH, Wang Y, Wang Y, Li JY, Luo WF, Wu WN, et al. AIE active salicylaldehyde-based hydrazone: A novel single-molecule multianalyte (Al3+ or Cu2+) sensor in different solvents. Spectrochimica Acta Part A: Molecular and Biomolecular Spectroscopy. 2019 Apr;212:146–54.

118. Wang Y, Mao PD, Wu WN, Mao XJ, Zhao XL, Xu ZQ, et al. A novel colorimetric and ratiometric fluorescent Cu2+ sensor based on hydrazone bearing 1,8-naphthalimide and pyrrole moieties. Sensors and Actuators B: Chemical. 2017 Nov;251:813–20.

119. Saini N, Prigyai N, Wannasiri C, Ervithayasuporn V, Kiatkamjornwong S. Green synthesis of fluorescent N,O-chelating hydrazone Schiff base for multi-analyte sensing in Cu2+, F− and CN− ions. Journal of Photochemistry and Photobiology A: Chemistry. 2018 May;358:215–25.

120. Ling L, Hu J, Zhang H. Ferrocene containing N-tosyl hydrazones as optical and electrochemical sensors for Hg2+, Cu2+ and F− ions. Tetrahedron. 2019 Apr;75(17):2472–81.

121. Mani KS, Rajamanikandan R, Murugesapandian B, Shankar R, Sivaraman G, Ilanchelian M, et al. Coumarin based hydrazone as an ICT-based fluorescence chemosensor for the detection of Cu2+ ions and the application in HeLa cells. Spectrochimica Acta Part A: Molecular and Biomolecular Spectroscopy. 2019 May;214:170–6.

122. Xu H, Wang X, Zhang C, Wu Y, Liu Z. Coumarin-hydrazone based high selective fluorescence sensor for copper(II) detection in aqueous solution. Inorganic Chemistry Communications. 2013 Aug;34:8–11.

123. Kejík Z, Kaplánek R, Havlík M, Bříza T, Vavřinová D, Dolenský B, et al. Aluminium(III) sensing by pyridoxal hydrazone utilising the chelation enhanced fluorescence effect. Journal of Luminescence. 2016 Dec;180:269–77.

124. Jin X, Yang Z, Li T, Wang B, Li Y, Yan M, et al. 8-hydroxyquinoline-5-carbaldehyde-(benzotriazol-1'-acetyl)hydrazone as a potential Mg 2+ fluorescent chemosensor. Journal of Coordination Chemistry. 2013 Jan 1;66(2):300–5.

125. Patil DY, Patil AA, Khadke NB, Borhade AV. Highly selective and sensitive colorimetric probe for Al3+ and Fe3+ metal ions based on 2-aminoquinolin-3-yl phenyl hydrazone Schiff base. Inorganica Chimica Acta. 2019 Jun;492:167–76.

126. Wu WN, Mao PD, Wang Y, Zhao XL, Xu ZQ, Xu ZH, et al. Quinoline containing acetyl hydrazone: An easily accessible switch-on optical chemosensor for Zn2+. Spectrochimica Acta Part A: Molecular and Biomolecular Spectroscopy. 2018 Jan;188:324–31.

127. Ma R, Li Q, Zhang Q. A novel selective chemosensor for Mg 2+ detection based on quinoline-hydrazone-crown ether. Indian J Chem. 2018;57B:120–6.

128. Long C, Hu JH, Fu QQ, Ni PW. A new colorimetric and fluorescent probe based on Rhodamine B hydrazone derivatives for cyanide and Cu2+ in aqueous media and its application in real life. Spectrochimica Acta Part A: Molecular and Biomolecular Spectroscopy. 2019 Aug;219:297–306.

129. Xiang Y, Tong A, Jin P, Ju Y. New Fluorescent Rhodamine Hydrazone Chemosensor for Cu(II) with High Selectivity and Sensitivity. Org Lett. 2006 Jun 1;8(13):2863–6.

130. Lee HY, Swamy KMK, Jung JY, Kim G, Yoon J. Rhodamine hydrazone derivatives based selective fluorescent and colorimetric chemodosimeters for Hg2+ and selective colorimetric chemosensor for Cu2+. Sensors and Actuators B: Chemical. 2013 Jun;182:530–7.

131. Said AI, Georgiev NI, Bojinov VB. Sensor activity and logic behavior of dihydroxyphenyl hydrazone derivative as a chemosensor for Cu 2+ determination in alkaline aqueous solutions. Journal of Photochemistry and Photobiology A: Chemistry. 2015 Oct;311:16–24.

132. Park S, Kim W, Swamy KMK, Lee HY, Jung JY, Kim G, et al. Rhodamine hydrazone derivatives bearing thiophene group as fluorescent chemosensors for Hg2+. Dyes and Pigments. 2013 Nov;99(2):323–8.

133. Yang Y, Gao CY, Li T, Chen J. A Tetraphenylethene-Based Rhodamine Hydrazone Chemosensor for Colorimetric and Reversible Detection of Cu 2+. ChemistrySelect. 2016 Sep 16;1(15):4577–81.

134. Fang Y, Li X, Li JY, Wang GY, Zhou Y, Xu NZ, et al. Thiooxo-Rhodamine B hydrazone derivatives bearing bithiophene group as fluorescent chemosensors for detecting mercury(II) in aqueous media and living HeLa cells. Sensors and Actuators B: Chemical. 2018 Feb;255:1182–90.

135. Jiang Z, Tian S, Wei C, Ni T, Li Y, Dai L, et al. A novel selective and sensitive fluorescent turn-on chemodosimeter based on rhodamine hydrazone for copper ions and its application to bioimaging. Sensors and Actuators B: Chemical. 2013 Jul;184:106–12.

136. Ge F, Ye H, Luo JZ, Wang S, Sun YJ, Zhao BX, et al. A new fluorescent and colorimetric chemosensor for Cu(II) based on rhodamine hydrazone and ferrocene unit. Sensors and Actuators B: Chemical. 2013 May;181:215–20.

137. Zhou Y, Kim HN, Yoon J. A selective 'Off–On' fluorescent sensor for Zn2+ based on hydrazone–pyrene derivative and its application for imaging of intracellular Zn2+. Bioorganic & Medicinal Chemistry Letters. 2010 Jan;20(1):125–8.

138. Kim HN, Nam SW, Swamy KMK, Jin Y, Chen X, Kim Y, et al. Rhodamine hydrazone derivatives as Hg2+ selective fluorescent and colorimetric chemosensors and their applications to bioimaging and microfluidic system. Analyst. 2011;136(7):1339-43.

139. Han F, Bao Y, Yang Z, Fyles TM, Zhao J, Peng X, et al. Simple Bisthiocarbonohydrazones as Sensitive, Selective, Colorimetric, and Switch-On Fluorescent Chemosensors for Fluoride Anions. Chem Eur J. 2007 Mar 26;13(10):2880–92.

140. Wang H, Li Y, Xu S, Li Y, Zhou C, Fei X, et al. Rhodamine-based highly sensitive colorimetric off-on fluorescent chemosensor for Hg2+ in aqueous solution and for live cell imaging. Org Biomol Chem. 2011;9(8):2850-55.

141. Saravanakumar D, Devaraj S, Iyyampillai S, Mohandoss K, Kandaswamy M. Schiff's base phenol–hydrazone derivatives as colorimetric chemosensors for fluoride ions. Tetrahedron Letters. 2008 Jan;49(1):127–32.

142. Anbu S, Shanmugaraju S, Ravishankaran R, Karande AA, Mukherjee PS. Naphthylhydrazone based selective and sensitive chemosensors for Cu2+ and their application in bioimaging. Dalton Trans. 2012;41(43):13330-37.

143. Li H, Fan J, Song F, Zhu H, Du J, Sun S, et al. Fluorescent Probes for Pd 2+ Detection by Allylidene–Hydrazone Ligands with Excellent Selectivity and Large Fluorescence Enhancement. Chem Eur J. 2010 Nov 2;16(41):12349–56.

144. Espada-Bellido E, Galindo-Riaño MD, García-Vargas M, Narayanaswamy R. Selective Chemosensor for Copper Ions Based on Fluorescence Quenching of a Schiff-Base Fluorophore. Appl Spectrosc. 2010 Jul;64(7):727–32.

145. Liao ZC, Yang ZY, Li Y, Wang BD, Zhou QX. A simple structure fluorescent chemosensor for high selectivity and

sensitivity of aluminum ions. Dyes and Pigments. 2013 Apr;97(1):124–8.

146. Tang R, Lei K, Chen K, Zhao H, Chen J. A Rhodamine-Based Off–On Fluorescent Chemosensor for Selectively Sensing Cu(II) in Aqueous Solution. J Fluoresc. 2011 Jan;21(1):141–8.

147. Kumaravel M, Mague JT, Balakrishna MS. Hydrazone derivatives appended to diphenylphosphine oxide as anion sensors. J Chem Sci. 2017 Apr;129(4):471–81.

148. Isaad J, Achari AE. A novel glycoconjugated N-acetylamino aldehyde hydrazone azo dye as chromogenic probe for cyanide detection in water. Analytica Chimica Acta. 2011 May;694(1–2):120–7.

149. Mondal J, Manna AK, Patra GK. Highly selective hydrazone based reversible colorimetric chemosensors for expeditious detection of CN− in aqueous media. Inorganica Chimica Acta. 2018 Apr;474:22–9.

150. Shang XF, Xu XF. The anion recognition properties of hydrazone derivatives containing anthracene. Biosystems. 2009 May;96(2):165–71.

151. Wu M, Yang DD, Zheng HW, Liang QF, Li JB, Kang Y, et al. A multi-binding site hydrazone-based chemosensor for Zn(II) and Cd(II): a new strategy for the detection of metal ions in aqueous media based on aggregation-induced emission. Dalton Trans. 2021;50(4):1507–13.

152. Alzweiri M, Al-Marabeh S, Bardaweel SK, Alfar R, Al-Hiari YM. Stability determination for cyclized 2,4-dinitrophenyl hydrazone derivative of glucose. J Anal Sci Technol. 2017 Dec;8(9):1-8.

153. Friestad HO, Ott DE, Gunther FA. Automated colorimetric microdetermination of phenols by oxidative coupling with 3-methyl-2-benzothiazolinone hydrazone. Anal Chem. 1969 Nov 1;41(13):1750–4.

154. Sawicki E, Hauser TR, Stanley TW, Elbert W, Fox FT. Spot Test Detection and Spectrophotometric Characterization and Determination of Carbazoles, Azo Dyes, Stilbenes, and Schiff Bases. Application of 3-Methyl-2-benzothiazolone Hydrazone, p -Nitrosophenol, and Fluorometric Methods to the Determination of Carbazole in Air. Anal Chem. 1961 Oct 1;33(11):1574–9.

155. Nebel GJ. Determination of total aliphatic aldehydes in auto exhaust by a modified 3-methyl-2-benzothiazolinone hydrazone method. Anal Chem. 1981 Sep 1;53(11):1708–9.

156. Cohen IR, Altschuller AP. Spot Test Detection and Colorimetric Determination of Aromatic Amines and Imino Heteroaromatic Compounds with 3-Methyl-2benzothiazolone Hydrazone. Anal Chem. 1961 May 1;33(6):722–5.

157. John M. Utilization of 3-Methylbenzthiazolinone-2(3H)-Hydrazone as a Chromogenic Reagent in Pharmaceutical Analysis. ASPS. 2018;2(7):1–2.

158. Lavanya K, Baggi TR. Spectrophotometric determination of rutin in pharmaceutical preparations using 3-methylbenzthiazolinone-2-hydrazone. Microchemical Journal. 1990 Apr;41(2):126–31.

159. Neumann FW. Spectrophotometric determination of glyoxal with 3-methyl-2-benzothiazolinone hydrazone. Anal Chem. 1969 Dec 1;41(14):2077–8.

160. Geeta N, Veena AP, Baggi TR. Spectrophotometric determination of phenolphthalein in pharmaceutical products using 3-methylbenzthiazolinone-2-hydrazone. Microchemical Journal. 1989 Dec;40(3):304–10.

161. Kumar D, Archana G, Sunitha G, Paul K, Harika R, Sowndarya N. Simplistic Application of 3-Methy-2-Benzothiazoline Hydrazone (MBTH),an Oxidative Coupling Chromogenic Reagent for Quantification of Metaxalone and Dabigatran Etexilate Mesylate Bulk Drug and Their Dosage Forms. Pharm Anal Acta. 2015;06(05):362–7.

162. Yee HY, Jackson Bobette. Determination of total estrogens in urine with 3-methyl-2-benzothiazolinone hydrazone. Anal Chem. 1976 Oct 1;48(12):1704–7.

163. Oliveira FS de, Leite BCO, Andrade MVAS de, Korn M. Determination of total aldehydes in fuel ethanol by MBTH method: sequential injection analysis. J Braz Chem Soc. 2005 Feb;16(1):87–92.

164. El-Kommos ME, Emara KM. Application of 3-methylbenzothiazolin-2-one hydrazone as a chromogenic reagent for the spectrophotometric determination of certain sulpha drugs. Analyst. 1988;113(1):133-37.

165. Baggi TR. 3-Methylbenzthiazolinone-2-Hydrazone (MBTH) as a New Visualization Reagent for the Detection of Cannabinoids on Thin-Layer Chromatography Plates. J Forensic Sci. 1980 Jul 1;25(3):691-94.

166. Geeta N, Baggi TR. A new spectrophotometric method for the determination of free salicylic acid in aspirin and its formulations based on oxidative coupling of 3-methylbenzthiazolinone-2-hydrazone with salicylic acid. Microchemical Journal. 1988 Oct;38(2):236–40.

167. El-Kommos ME. Spectrophotometric determination of dobutamine hydrochloride using 3-methylbenzothiazolin-2-one hydrazone. Analyst. 1987;112(1):101-3.

168. Siyal AN, Memon SQ, Parveen S, Soomro A, Khaskheli MI, Khuhawar MY. Chemical Recycling of Expanded Polystyrene Waste: Synthesis of Novel Functional Polystyrene-Hydrazone Surface for Phenol Removal. Journal of Chemistry. 2013;2013:1–8.

169. Amos D. Specific spectrofluorometric determination of atmospheric ozone using 2-diphenylacetyl-1,3-indandione-1-hydrazone. Anal Chem. 1970 Jul 1;42(8):842–4.

170. Pietrzyk DJ, Chan EP. Determination of carbonyl compounds by 2-diphenylacetyl-1,3-indandione-1-hydrazone. Anal Chem. 1970 Jan 1;42(1):37–43.

171. Wang P, Liu J, Lv X, Liu Y, Zhao Y, Guo W. A Naphthalimide-Based Glyoxal Hydrazone for Selective Fluorescence Turn-On Sensing of Cys and Hcy. Org Lett. 2012 Jan 20;14(2):520–3.

172. Kim YH, Choi MG, Im HG, Ahn S, Shim IW, Chang SK. Chromogenic signalling of water content in organic solvents by hydrazone–acetate complexes. Dyes and Pigments. 2012 Mar;92(3):1199–203.

173. Khattab TA, Gaffer HE. Synthesis and application of novel tricyanofuran hydrazone dyes as sensors for detection of microbes. Coloration Technol. 2016 Dec;132(6):460–5.

174. Abdelmoez S, Abdelrahman M, Khattab T. Synthesis, solvatochromic properties and pH sensory of novel symmetrical bis(tricyanofuran)hydrazone chromophore. Egypt J Chem. 2019 Jan 14;62(7):1197–206.

175. Kenawy I, Geragh B, El-Menshawy A, El-Asmy A. Separation and Preconcentration of Fe(III) from Aqueous and Nonaqueous Media using 1-(3,4-Dihydroxybenzylidine)-2-acetylpyridinium chloride Hydrazone Modified Resin. Can Chem Trans. 2013 Nov 20;1(4):338–52.

176. Hassanien MM, Kenawy IM, El-Menshawy AM, El-Asmy AA. A novel method for speciation of Cr(III) and Cr(VI) and individual determination using Duolite C20 modified with active hydrazone. Journal of Hazardous Materials. 2008 Oct;158(1):170–6.

177. Hassanien MM, Kenawy IM, El-Menshawy AM, El-Asmy AA. Separation and Preconcentration of Gallium(III), Indium(III), and Thallium(III) Using New Hydrazone-modified Resin. Anal Sci. 2007;23(12):1403–8.

178. Ali A, Khzam A, Alhony M, Bin S, Salleh B. Acenaphthenequinone Hydrazone Derivative Based Sol-Gel In Solid-Phase Extraction of Lanthanum (III) in Aqueous. World Appl Sci J. 2013;21(3):433–41.

179. Mohamad Ali AS, Abdul Razak N, Ab Rahman I. Bach Adsorption Study for the Extraction of Silver Ions by Hydrazone Compounds from Aqueous Solution. The Scientific World Journal. 2012;2012:1–10.

180. Tameem AA, Saad B, Makahleh A, Salhin A, Saleh MI. A 4-hydroxy-N'-[(E)-(2-hydroxyphenyl)methylidene] benzohydrazide-based sorbent material for the extraction-HPLC determination of biogenic amines in food samples. Talanta. 2010 Sep 15;82(4):1385–91.

181. Ghazy S, Rakha T, EI-Kady E, El-Asmy A. Use of some hydrazine derivatives for the separation of mercury(II) from aqueous solutions by flotation technique. Indian J Chem Technol. 2000;7(4):178–82.

182. Ghazy S, Mostafa H, El-Farra S, Fouda A. Flotation-separation of nickel from aqueous media using some hydrazone derivatives as organic collectors and oleic acid as surfactant. IJCT. 2004;11(6):787–92.

183. Ghazy SE, Abu El-Reash GM, Al-Gammal OA, Yousef T. Flotation separation of mercury(II) from environmental water samples using thiosemicarbazide derivatives as chelating agents and oleic acid as surfactant. Chemical Speciation & Bioavailability. 2010 Jan;22(2):127–34.

184. Khalifa, Youssef H, Majeed A, El-Reash G. Structural investigation, biological and flotation studies of Co(II) and

Zn(II) complexes of salicoyl hydrazone ending by thiazole ring. IJARBS. 2016;3(6):235–54.

185. Magdy M Bekheit MAA, Mezban Salih Q. Surfactant Assisted Separation Spectrophotometric Procedure for the Trace Analysis of Copper (II) in Drug and Water Samples Using a Heterocyclic Pyridyl Azo Dye. Pharm Anal Acta. 2015;6(9):1-7. <DOI> .

186. El-Asmy AA, El-Gammal OA, Radwan HA, Ghazy SE. Ligational, analytical and biological applications on oxalyl bis(3,4-dihydroxybenzylidene) hydrazone. Spectrochimica Acta Part A: Molecular and Biomolecular Spectroscopy. 2010 Sep;77(1):297–303.

187. Shah R. Ligational, potentiometric and floatation studies on Cu(II) complexes of hydrazones derived from p and o-vanillin condensed with diketo hydrazide. Journal of Molecular Liquids. 2016 Aug;220:939–53.

188. El Meligy MG, El Rafie Sh, Abu-Zied KM. Preparation of dialdehyde cellulose hydrazone derivatives andevaluating their efficiency for sewage wastewater treatment. Desalination. 2005 Mar;173(1):33–44.

189. Masuda H, Fujii T, Nakanishi H, Matsumoto S, Arikawa H. Catalyst using hydrazone compound, hydrazone polymer compound, and catalyst using hydrazone polymer compound. 2011. Japan patent US7960501 B2. <URL> .

190. Nakanishi H, Matsumoto S, Arikawa H, Kllmagais H. Hydrazone Compound, Hydrazone Compound for Forming Complex, Ligand for Forming Metal Complex, and Monomer for Manufacturing Polymer Compound 2011. US patent US7,951,903 B2. <URL>.

191. Gao S, Li L, Vohra I, Zha D, You L. Differential metal-binding properties of dynamic acylhydrazone polymers and their sensing applications. R Soc open sci. 2017 Aug;4(8):1-10.

192. Singh RK, Stoffer JO, Flaim TD, Hall DB, Torkelson JM. Monohydroxy-hydrazone-functionalized thermally crosslinked polymers for nonlinear optics. J Appl Polym Sci. 2004 Apr 15;92(2):770–81.

193. Love BE, Jones EG. The Use of Salicylaldehyde Phenylhydrazone as an Indicator for the Titration of Organometallic Reagents. J Org Chem. 1999 May 1;64(10):3755–6.

194. Tai XS, Li PF, Liu LL. Preparation, Characterization, and Catalytic Property of a Cu(II) Complex with 2-Carboxybenzaldehyde-p-Toluenesulfonyl Hydrazone Ligand. Bull Chem React Eng Catal. 2018 Apr 2;13(1):7-13.

195. Jahdaly B, Althagafi I, Abdallah M, Khairou K, Ahmed S. Fluorenone Hydrazone Derivatives as efficient Inhibitors of Acidic and Pitting Corrosion of Carbon Steel. J Mater Environ Sci. 2016;7(5):1798–809.

196. Saliyan, Adhikari A. Corrosion inhibition of mild steel in acid media by quinolinyl thiopropano hydrazone. Indian J Chem Technol. 2009;16:162–74.

197. Fouda A, Gouda M, El-Rahman S. 2-Hydroxyacetophenone-aroyl Hydrazone Derivatives as Corrosion Inhibitors for Copper Dissolution in Nitric Acid Solution. B K Chem Soc. 2000;21(11):1085–9.

198. Fouda AS, Gouda MM, El-Rahman SIA. Benzaldehyde, 2-Hydroxybenzoyl Hydrazone Derivatives as Inhibitors of the Corrosion of Aluminium in Hydrochloric Acid. Chem Pharm Bull. 2000;48(5):636–40.

199. Negm NA, Morsy SMI, Said MM. Corrosion inhibition of some novel hydrazone derivatives. J Surfact Deterg. 2005 Jan;8(1):95–8.

200. Moussa MNH, El-Far AA, El-Shafei AA. The use of water-soluble hydrazones as inhibitors for the corrosion of C-steel in acidic medium. Materials Chemistry and Physics. 2007 Sep;105(1):105–13.

201. Sherif ESM, Ahmed AH. Synthesizing New Hydrazone Derivatives and Studying their Effects on the Inhibition of Copper Corrosion in Sodium Chloride Solutions. Synthesis and Reactivity in Inorganic, Metal-Organic, and Nano-Metal Chemistry. 2010 Jul 19;40(6):365–72.

202. Fouda AS, EL-Sayyad SA, Abdallah M. N-3-hydroxyl-2-naphthoyl hydrazone derivatives as inhibitors for corrosion of carbon steel in H 2 SO 4 acid solution. Anti-Corrosion Methods and Materials. 2011 Mar 22;58(2):63–9.

203. Fouda AS, Badr GE, El-Haddad MN. The Inhibition of C-steel Corrosion in H3PO4 Solution by Some Furfural Hydrazone Derivatives. Journal of the Korean Chemical Society. 2008 Apr 20;52(2):124–32.

204. Fouda AEAS, Al-Sarawy AA, Radwan MS. Some Aromatic Hydrazone Derivatives as Inhibitors for the Corrosion of C-Steel in Phosphoric Acid Solution. Annali di Chimica. 2006 Jan;96(1–2):85–96.

205. Singh DK, Kumar S, Udayabhanu G, John RP. 4(N,N-dimethylamino) benzaldehyde nicotinic hydrazone as corrosion inhibitor for mild steel in 1 M HCl solution: An experimental and theoretical study. Journal of Molecular Liquids. 2016 Apr;216:738–46.

206. Lgaz H, Zehra S, Albayati M, Toumiat K, Aoufir Y, Chaouiki A, et al. Corrosion Inhibition of Mild Steel in 1.0 M HCl by two Hydrazone Derivatives. Int J Electrochem Sci. 2019 Jul;14:6667–81.

207. Lgaz H, Chaouiki A, Albayati MR, Salghi R, El Aoufir Y, Ali IH, et al. Synthesis and evaluation of some new hydrazones as corrosion inhibitors for mild steel in acidic media. Res Chem Intermed. 2019 Apr;45(4):2269–86.

208. Mohan P, Usha R, Kalaignan GP, Muralidharan VS. Inhibition Effect of Benzohydrazide Derivatives on Corrosion Behaviour of Mild Steel in 1 M HCl. Journal of Chemistry. 2013;2013:1–7.

209. El-Tagouri MM, Mostafa MR, Abu El-Nader HM, Abu El-Reash GM. Efficiency of some 2-heterocarboxaldehyde-2'-pyridyl-hydrazones as corrosion inhibitors for Al dissolution in HCl solution. Anti-Corrosion Methods and Materials. 1989 Sep 1;36(9):10–4.

210. Chaitra TK, Mohana KN, Tandon HC. Evaluation of newly synthesized hydrazones as mild steel corrosion inhibitors by adsorption, electrochemical, quantum chemical and morphological studies. Arab Journal of Basic and Applied Sciences. 2018 May 4;25(2):45–55.

211. Liu B, Xi H, Li Z, Xia Q. Adsorption and corrosion-inhibiting effect of 2-(2-{[2-(4-Pyridylcarbonyl)hydrazono]methyl}phenoxy)acetic acid on mild steel surface in seawater. Applied Surface Science. 2012 Jun;258(17):6679–87.

212. Liu H, Zhu L, Zhao Q. Schiff base compound as a corrosion inhibitor for mild steel in 1 M HCl. Res Chem Intermed. 2015 Jul;41(7):4943–60.

213. Ramesh SV, Adhikari AV. N'-[4-(diethylamino)benzylidine]-3-{[8-(trifluoromethyl) quinolin-4-yl]thio}propano hydrazide) as an effective inhibitor of mild steel corrosion in acid media. Materials Chemistry and Physics. 2009 Jun;115(2–3):618–27.

214. Ganjali MR, Rezapour M, Rasoolipour S, Norouzi P, Adib M. Application of pyridine-2-carbaldehyde-2-(4-methyl-1,3-benzo thiazol-2-yl)hydrazone as a neutral ionophore in the construction of a novel Er(III) sensor. J Braz Chem Soc. 2007 Apr;18(2):352–8.

215. Ganjali MR, Rasoolipour S, Rezapour M, Norouzi P, Adib M. Synthesis of thiophene-2-carbaldehyde-(7-methyl-1,3-benzothiazol-2-yl)hydrazone and its application as an ionophore in the construction of a novel thulium(III) selective membrane sensor. Electrochemistry Communications. 2005 Oct;7(10):989–94.

216. Khattab TA, Allam AA, Othman SI, Bin-Jumah M, Al-Harbi HM, Fouda MMG. Synthesis, Solvatochromic Performance, pH Sensing, Dyeing Ability, and Antimicrobial Activity of Novel Hydrazone Dyestuffs. Journal of Chemistry. 2019 Feb 5;2019:1–10.

217. Qian HF, Zhao XL, Dai Y, Huang W. Visualized fabric discoloration of bi-heterocyclic hydrazone dyes. Dyes and Pigments. 2017 Aug;143:223–31.

218. G. Al-Sehemi A, Irfan A, M. Asiri A, A. Ammar Y. Synthesis, characterization and density functional theory study of low cost hydrazone sensitizers. Bull Chem Soc Eth. 2015 Jan 18;29(1):137-48.

219. Al-Sehemi AG, Irfan A, Asiri AM. The DFT investigations of the electron injection in hydrazone-based sensitizers. Theor Chem Acc. 2012 Mar;131(3):1199-6.

220. Al-Sehemi AG, Irfan A, Al-Melfi MAM. Highly efficient donor–acceptor hydrazone dyes-inorganic Si/TiO 2 hybrid solar cells. Spectrochimica Acta Part A: Molecular and Biomolecular Spectroscopy. 2015 Jun;145:40–6.

221. Al-Sehemi AG, Irfan A, Asiri AM, Ammar YA. Synthesis, characterization and DFT study of methoxybenzylidene containing chromophores for DSSC materials. Spectrochimica Acta Part A: Molecular and Biomolecular Spectroscopy. 2012 Jun;91:239–43.

222. Al-Sehemi AG, Irfan A, Asiri AM, Ammar YA. Molecular design of new hydrazone dyes for dye-sensitized

solar cells: Synthesis, characterization and DFT study. Journal of Molecular Structure. 2012 Jul;1019:130–4.

223. Shen P, Liu X, Jiang S, Wang L, Yi L, Ye D, et al. Synthesis of new N, N-diphenylhydrazone dyes for solar cells: Effects of thiophene-derived π-conjugated bridge. Dyes and Pigments. 2012 Mar;92(3):1042–51.

224. Urnikaite S, Daskeviciene M, Send R, Wonneberger H, Sackus A, Bruder I, et al. Organic dyes containing a hydrazone moiety as auxiliary donor for solid-state DSSC applications. Dyes and Pigments. 2015 Mar;114:175–83.

225. Urnikaite S, Malinauskas T, Gaidelis V, Bruder I, Send R, Sens R, et al. Simple and Inexpensive Organic Dyes with Hydrazone Moiety as π-Conjugation Bridge for Solid-State Dye-Sensitized Solar Cells. Chem Asian J. 2013 Mar;8(3):538–41.

226. Urnikaite S, Malinauskas T, Bruder I, Send R, Gaidelis V, Sens R, et al. Organic Dyes with Hydrazone Moieties: A Study of Correlation between Structure and Performance in the Solid-State Dye-Sensitized Solar Cells. J Phys Chem C. 2014 Apr 17;118(15):7832–43.

227. Al-Sehemi AG, Allami SAS, Kalam A. Design and synthesis of organic dyes with various donor groups:

promising dyes for dye-sensitized solar cells. Bull Mater Sci. 2020 Dec;43(1):224.

228. Vasileva MYu, Ershov AYu, Baigildin VA, Lagoda IV, Kuleshova LYu, Shtro AA, et al. Synthesis of Silver Glyconanoparticles Based on 3-Thiopropionylhydrazones of Mono- and Disaccharides. Russ J Gen Chem. 2018 Jan;88(1):109–13.

229. Wong MS, Meier U, Pan F, Gramlich V, Bosshard C, Günter P. Five-membered heteroaromatic hydrazone derivatives for second-order nonlinear optics. Adv Mater. 1996 May;8(5):416–20.

230. Xu W, Shao Z, Han Y, Wang W, Song Y, Hou H. Light-adjustable third-order nonlinear absorption properties based on a series of hydrazone compounds. Dyes and Pigments. 2018 May;152:171–9.

231. Follonier S, Bosshard Ch, Meier U, Knöpfle G, Serbutoviez C, Pan F, et al. New nonlinear-optical organic crystal: 4-dimethyl-aminobenzaldehyde- 4-nitrophenyl-hydrazone. J Opt Soc Am B. 1997 Mar 1;14(3):593-601.

232. Chung PJ, Chang HJ. Synthesis of 6-Alkyl-3-Chromonealdehyde (2, 2-dialkyl) hydrazone Derivatives for Green Light Emitting Materials. Applied Chemistry for Engineering. 2010;21(4):424–9.

Characterization of Paper-Like Material Prepared from Chitosan/Graphene Oxide Composite

Thi Sinh Vo[1]* iD **, Tran Thi Bich Chau Vo[2]** iD

[1]Sungkyunkwan University, School of Mechanical Engineering, Suwon, 16419, Korea

[2]Can Tho University, Department of Industrial Management, Can Tho, Vietnam

Abstract: Chitosan (CTS) is considered to be a common biomacromolecule/poly-cationic compound containing the potential functional groups that can be utilized as a feedstock for novel materials. In this study, CTS/graphene oxide (CTS/GO, CG) mixtures were prepared at different conditions to confirm a suitable hydrogel formation, then applied to produce paper-like materials with various thickness via a simple casting method. As a result, the morphological structure finally yielded the paper-like materials (CG2 papers with varying numbers of casting times) with the layer-by-layer structures instead of the tightly-sticky paper-like structure (GO paper). Based on the possible interactions between the CTS molecules and GO nanosheets, the CG mixtures could also be determined by FTIR and Raman analysis; concomitantly, their thermal properties reach higher than that of the pure GO. Notably, the strong interactions and compatibility of the CTS molecules and GO nanosheets revealed good dispersion and interfacial adhesion, leading to significantly enhancing the mechanical properties of the CG2 paper-like materials with increasing number of casting times or compared to GO paper. Therefore, the CG2 paper-like materials with the various numbers of casting times fabricated in the present study can expose new approaches for the design and application of future foil/paper-like materials, as well as the desired thickness of these foil/paper-like materials can be controlled easily.

INTRODUCTION

Polymeric systems, as is well known, have been widely used in various research fields and practical applications (1-5). At same time, the most remarkable factors of a polymeric material were almost entirely physical, chemical, and interface properties. Thus, it is necessary to conduct considerable modification methods that can obtain better desired results corresponding to multiple research studies. Especially, foil/paper-like materials are concerned as integral parts of the current technological development owing to potential characteristic features (i.e.: protective layers,

super-capacitors/electrical batteries, chemical /physical filters, molecular storage, adhesive layers, etc.) (5-10). Chitosan (CTS) is considered to be a typical biomacromolecule/poly-cationic compound with excellent properties (i.e.: low toxicity, antimicrobial activity, biocompatibility, appreciable biodegradability, admirable low immunogenicity, etc.) that has been utilized widely in various applications (i.e., biomedical, environmental, and food fields, etc.) (11). Basically, CTS is an extensively classified linear copolymer in natural material sources, especially in de-acetylation of chitin, which has become a potential candidate to be applied in lots of different research fields (3, 12-14).

Concomitantly, graphene oxide (GO) with potential functional groups has originated from a chemically modified graphene material, which can be incorporated with various organic macromolecules (15-17). Moreover, the GO material can be encouraged to fabricate the large-area paper-like materials for applications of thin-films/membranes with controlled permeability, super-capacitors, anisotropic ionic conductors, and molecular storage, etc. Besides, owing to the available hydrophilic nature of GO nanosheets, their paper-like structure can be used as a carrier substance to probably produce paper-like hybrid materials containing ceramics, polymers, or metals (11). More obviously, Singh et al. (18) reported a facile design and synthesis of magnetic iron oxide incorporated CTS/GO hydrogel nanocomposites by employing in situ mineralization of iron ions in a hydrogel matrix, which resulted in this material being able to enable dye removal in a wide variety of solution conditions and offering a promising platform for sustainable development of water purification technology. Whereas, Lyn et al. (19) investigated the application of active packaging from CTS incorporated with GO to maintain the quality and extend the storage life of palm-oil-based margarine. More notably, Menazea et al. (20) studied well the possible interactions between some divalent heavy metals and CTS/GO, which was based on the density functional theory (DFT) at B3LYP level with LANL2DZ basis set. Nonetheless, a foil/paper-like materials from GO-like structure is not commonly reported. In fact, the outstanding chemical and mechanical properties can yield a promising GO-based paper, as well as a paper-like material system that can be applied effectively in various practical applications.

In this study, the possible interaction mechanism of the CTS/GO (CG) mixtures without any cross-linker regarding CG hydrogel formation and damage was conducted on investigations of different parameters and conditions based on visual observations of different CG mixtures, and the mechanism involving thermo-induced hydrogel formation was explained in detail as well. Then, a suitable CG mixture was applied to produce paper-like materials with various thickness via a simple casting method. In particular, the chemical characterization, thermal properties and morphological structure of finally yielded paper-like materials were confirmed through several analysis instruments and compared with those of GO paper. Interestingly, the mechanical properties of the produced paper-like materials with increasing number of casting times were investigated as well, which revealed a dispersion and interfacial adhesion between CTS molecules and GO nanosheets inside the prepared CG mixtures. Hence, these paper-like materials with various numbers of casting times can expose new approaches for the design and desired thickness control of future foil/paper-like materials, as well as this paper-like material can be applied directly in various practical applications, i.e., heavy metals or organic dye removal, adsorption or filtration membranes, cell culture, super-capacitors, sensors, etc.

MATERIALS AND METHODS

Materials
Aqueous acetic acid solution and CTS powder (DD = ~85%) were obtained from Sigma–Aldrich. Aqueous GO dispersion was purchased from a Korean company.

Preparation of CG papers
CG mixtures at different conditions were prepared by blending CTS solution (1.00 g of CTS in 100 mL of 2.5% acetic acid solution) and aqueous GO dispersion (volume ratio of CTS/GO = 1/5, 1/10, and 1/15, v/v) (Table 1). The CG mixtures were stirred overnight for 2 – 3 days and sonicated for 10 min. The gelation/hydrogel formation of vials containing CG mixtures at room temperature (~80 °C) was confirmed via visual observation with a tube inversion. Next, the CG mixtures (~2.00 g) were cast on one substrate once, which was dried at room temperature. After that, an amount of CG mixtures (~2.00 g) was continued to be cast on the above CG paper and dried at room temperature, which was conducted until 2 – 5 times. The synthetic route of CG utilizing paper-like materials is shown in Fig. 1.
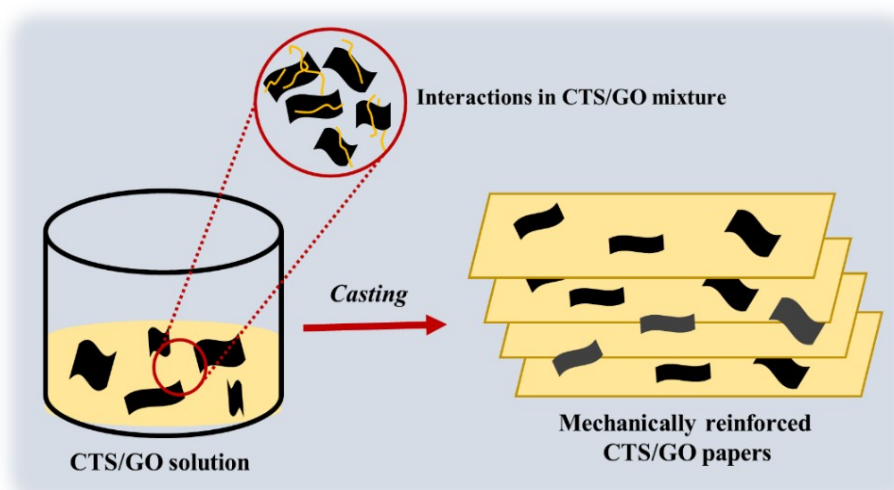
Figure 1: Synthetic route of CG utilizing as paper-like materials.

Table 1. Information of CGs.

Sample	CG1	CG2	CG3
Volume ratio of CTS/GO	1/5	1/10	1/15

Analysis instruments
SEM analysis
Morphological structures of the paper-like materials (top-surface and cross-section) were measured by a field-emission scanning electron microscope (FESEM) (JSM-7600F, JEOL) at different magnifications.

FT-IR and Raman analysis
The chemical characterization of the paper-like materials was analyzed by a Fourier-transform infrared (FT-IR) and Raman spectroscopies. FT-IR spectra was recorded on an Nicolet 380 system (Ietled Co.) using pellet – KBr method with a scanned 4000–400 cm^{-1} wavenumber. Raman spectra was scanned by an XperRam200 instrument with a laser wavelength of 405 nm.

Thermal gravimetric analysis
Thermal gravimetric analysis (TGA) was obtained on a Seiko Exstar6000 instrument with an applied 30–500 °C temperature range / 10 °C min^{-1} heating rate.

Tensile analysis
Typical stress–strain curves of the paper-like materials (1 cm x 5 cm original size) were measured by a universal tensile machine (UTM model 5565, UK) with 250 N of load cell at the pulling rate of 10 mm﹤min^{-1}. Prior to the tensile test, the paper-like materials were stored for more than one day at room temperature. All reported results for the tensile tests were averages of three measured values.

RESULTS AND DISCUSSION

General observation
As known, CTS molecules and GO nanosheets contain several potential functional groups to be favorable in noncovalent interactions, which could operate a complex network formation between the CTS molecules and GO nanosheets to create a hydrogel state for a suitable CTS/GO (CG) mixture (11). In fact, these were also similarly presented in several previous lectures (21-24), especially in Zeta (ζ) potential of the CTS/GO composite (24). Basing on visual observation of the prepared CG mixtures under different conditions (Fig. 2), the CG2 mixture (volume ratio of CTS/GO = 1/10, Table 1) has formed a stable hydrogel state at both room temperature and ~80 °C (Fig. 2 B, E), as well as that hydrogel formation was still stable until be cooled to room temperature (Fig. 2H). The CG1 mixture (volume ratio of CTS/GO = 1/5, Table 1) was in a sol state at both room temperature (Fig. 2A) and ~80 °C (Fig. 2D) regarding deficient interactions between the CTS molecules and GO nanosheets, while the sol state of CG3 mixture (volume ratio of CTS/GO = 1/15, Table 1) only occurred at room temperature (Fig. 2C) and its gel state was at ~80 °C (Fig. 2F). Especially, a thermo-reversible gelation behavior has appeared in the CG3 mixture at ~80 °C (Fig. 2F), which could return to the sol state until cooled to room temperature

(Fig. 2I). Therefore, a damaged hydrogel state was negotiated through a gel−sol−gel transition, and the hydrogel formation could be renewed to its origin state in the CG3 mixture (11). As such, the CG2 mixture is seen as a CG mixture that has obtained optimal parameters and conditions to be applied to the next experiments.
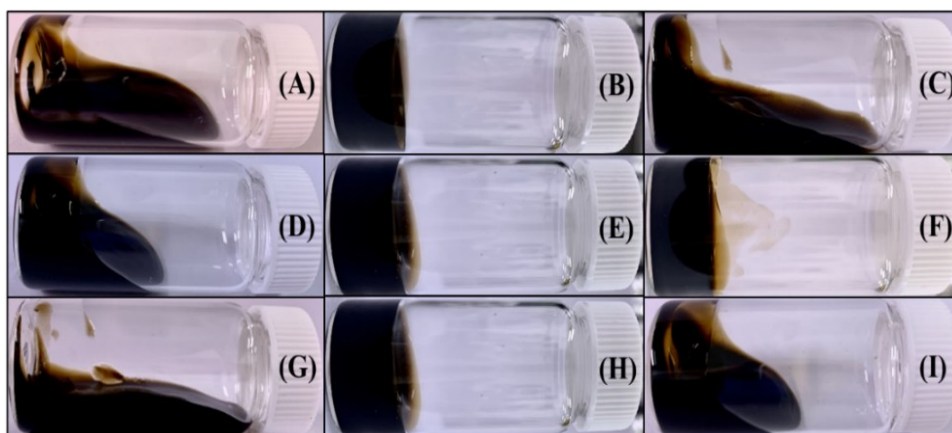
Figure 2: CTS/GO mixtures at room temperature [CG1 – (A), CG2 – (B), CG3 – (C)] and at ~80 °C [CG1 – (D), CG2 – (E), CG3 – (F)]. The CTS/GO mixtures [CG1 – (D), CG2 – (E), CG3 – (F)] are cooled to room temperature [CG1 – (G), CG2 – (H), CG3 – (I)].

To understand further the hydrogel state of various prepared CG mixtures, Fig. 3 shows the possible interaction mechanism of the CG mixtures at different conditions involving the CG hydrogel formation and damage. Basically, both CTS molecules and GO nanosheets contained lots of potential functional groups for the noncovalent interactions that have occurred in the CG hydrogel formation. Specifically, the noncovalent interactions could operate a complex network formation between the CTS molecules and GO nanosheets. Nonetheless, the mechanism regarding the thermo-induced hydrogel formation is still unclearl. Herein, the possible interactions in the CG mixtures could be encouraged with H_2O, CTS and GO (i.e.: $F_{H2O–H2O}$, $F_{CTS–CTS}$, $F_{GO–GO}$, $F_{H2O–CTS}$, $F_{CTS–GO}$, $F_{H2O–GO}$); concomitantly, the hydrogel formation has limited the interactions between CTS molecules and GO nanosheets with H_2O, especially at high temperatures. Specifically, the CG mixtures would contain electrostatic attraction interactions between the CTS molecules and GO nanosheets at room temperature, as well as the CTS chains being clustered because of a complexation in inter-/intra-molecular hydrogen bonds. As the weak hydrogen bonds among CTS chains increased, the interactions between the CTS chain and GO nanosheets became stronger with regard to the increase in their free motion at high temperature. As such, the stretched chains had lots of chances to interact with other GO nanosheets, as well as the entanglement possibility of CTS chains increased to form a complex network formation of them at the end. Herein, the CG2 mixture is chosen to be a representative mixture for the next analysis.
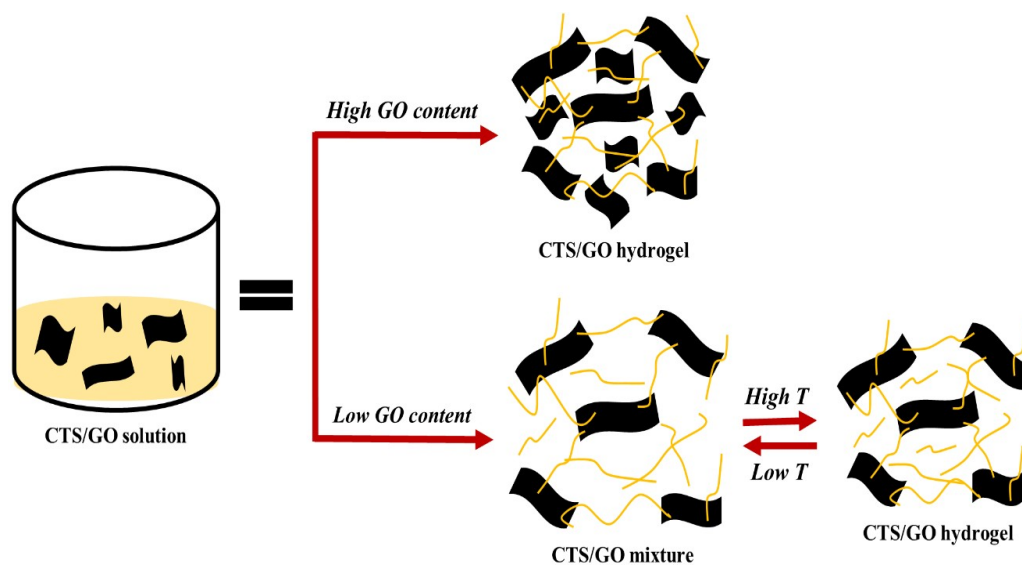
Figure 3: Possible interaction of CTS/GO mixtures at different conditions.

Chemical and thermal characterization of CTS/GO papers

CTS/GO mixture

-COO⁻ --- NH₃⁺: Electrostatic ion pairing
>C=O --- HN-: Hydrogen bonding
Aromatic rings: π-stacking
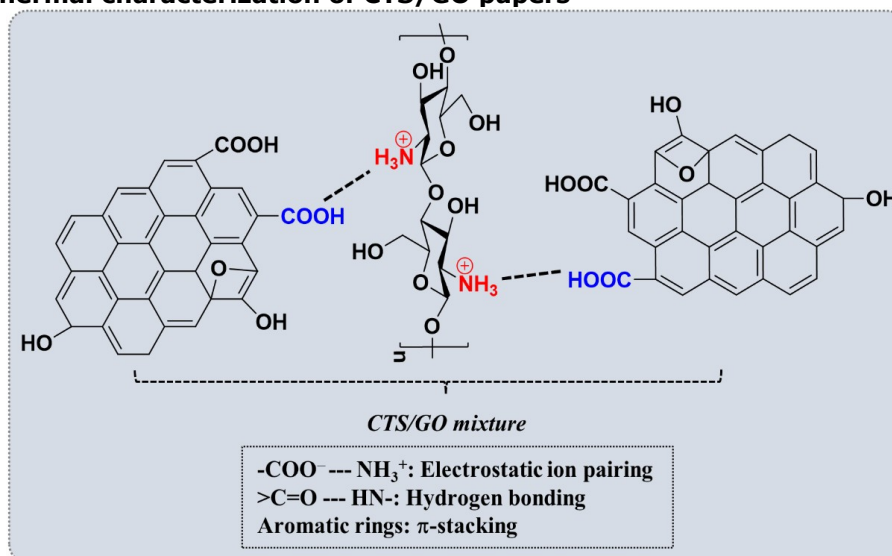
Figure 4: Mechanism of chemical reaction between CTS and GO.

Fig. 4 shows that in the CTS/GO spectrum, the −COOH groups of GO interacted with the −NH$_3^+$ groups of CTS, resulting in strong hydrogen bonds and leading to a far more miscible CTS/GO mixture (11). The interfacial interactions among them can be very important to the corresponding properties of the CTS/GO, especially for a stable hybrid network structure (25, 26). More specifically, for chemical characterization of the prepared paper-like materials, FI-TR spectra were employed to investigate, as shown in Fig. 5 (A, B). In the pure CTS spectra (Fig. 5A), the characteristic peaks of symmetric/asymmetric −CH deformation, symmetric/asymmetric C−C−O stretching and C−C bending are observed at 1421.90 – 1383.03 cm^{-1}, 1081.92 – 1029.02 cm^{-1} and 663.42 – 516.85 cm^{-1}, respectively (5, 27, 28). Besides, the various peaks

have also appeared at 1159.87 cm^{-1} (C−O−C) and 897.04 cm^{-1} regarding the available saccharide structure of CTS (5, 28-30). In particular, the remaining characteristic peaks at 1652.32 – 1598.32 cm^{-1} have corresponded to −NH stretching/bending vibrations in −NH$_2$ groups (5, 27). While the pure GO spectra has revealed the peaks at 1734.25, 1632.36, 1400.01, 1229.96 and 1053.03 cm^{-1} corresponding to C=O carboxylic group, C=C alkenyl group, −OH deformation, C−O alkoxy group, and epoxy C−O−C stretching, respectively (31-33) (Fig. 5A). Especially, a broad peak was observed at 3700 – 3000 cm^{-1} regarding to −OH/−NH groups for all samples (Fig. 5B). In the CG2 paper's spectra, the peaks at 522.64 – 665.35 cm^{-1} and 1076.13 – 1019.96 cm^{-1} correspond to C−C bending and symmetric/asymmetric C−C−O

stretching vibrations, respectively. Interestingly, it also revealed that the characteristic peaks of saccharide structure of CTS and −OH deformation of GO have been moved to higher wavenumber regions such as at 1176.37 cm^{-1} (C−O−C), 899.70 cm^{-1} (C−O−C bridge) and 1412.05 cm^{-1} (−OH), indicating possible hydrogen bond formations between CTS and GO contained inside the CG mixtures. Furthermore, the peaks at 1753.05 cm^{-1} (C=O group) and 1669.76 – 1561.24 cm^{-1} (−NH/C=C groups) of CG2 paper were induced from the pure GO (C=O group, 1734.25 cm^{-1}) and CTS (−NH group, 1652.32 – 1598.32 cm^{-1}), respectively. However, these characteristic peaks have been not only moved to the higher wavenumber regions but also lower intensities compared with the pure materials, mainly due to the amide linkage formation (1669.76 cm^{-1}, −CONH$_2$) between carboxyl group (GO) and amino group (CTS), as reported in detail by Zhang et al. (25).

Concomitantly, two characteristic peaks of GO nanosheets were observed at 1348 cm^{-1} (D band) and 1605 cm^{-1} (G band) in both the pure GO and CG2 paper without a movement (Fig. 5C). Nonetheless, I_D/I_G ratio of the CG2 paper (0.997) was higher than that of the pure GO (0.957) leading to a rising defect density of the CG2 paper. In other words, this increased defect could contribute significantly to the possible interactions in the CTS/GO mixtures. Moreover, thermal properties of the prepared paper-like materials were investigated by TGA instrument (Fig. 5D). The first loss weight occurred at ~50 °C regarding to the moisture loss for all samples, while the second loss weight of the CG2 paper was decomposed at 212.39 °C, as well as its thermal stability was better than that of pure GO (188.93 °C). Therefore, it was concluded that there were possible interactions (hydrogen bond, electrostatic attraction, and amide linkage formation) between the CTS molecules and GO nanosheets inside the CTS/GO mixtures (Fig. 3 and Fig. 4) through the above-analyzed FT-IR, Raman, and TGA results.
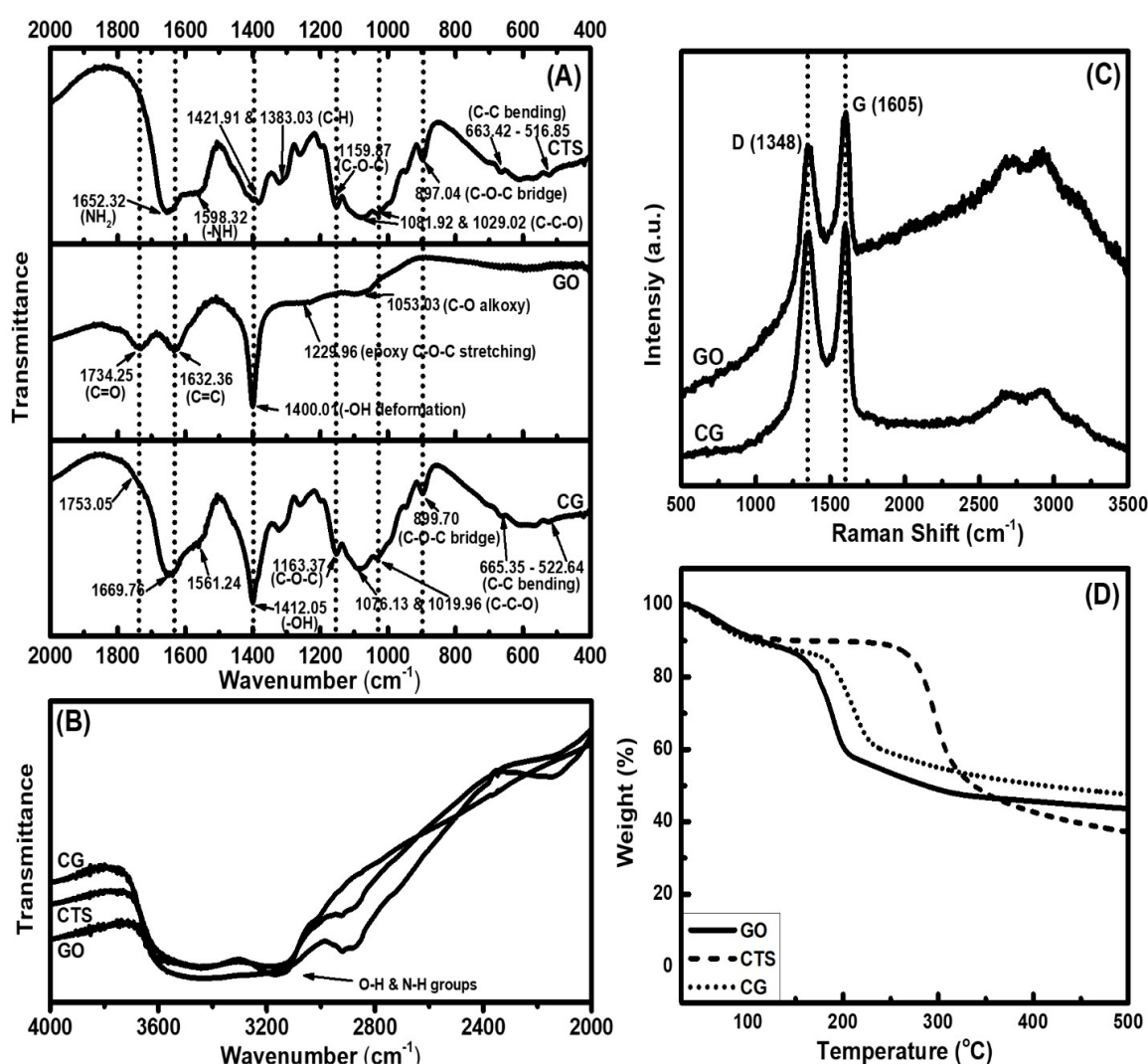
Figure 5: FTIR (A, B), Raman (C) and TGA curve of CTS, GO and CG2 paper.

Morphological properties of CTS/GO papers

For morphological properties of the prepared paper-like materials, SEM analysis was conducted (Fig. 6). The top-surface image of GO was considered to have a sheet-like structure (Fig. 6A), while its cross-sectional image was observed to be tightly-sticky paper-like structure owing to the available hydrophilic nature of GO nanosheets (Fig. 6B). For the prepared CG2 paper-like materials with the various numbers of casting times (Fig. 6 C – H), it was revealed that there was a strong network structure contained inside the CG2 mixture through the top-surface images of CG2 papers (Fig. 6 C – E). Specifically, the surface structure of CG2 papers (CG21 paper – CG2 paper with 1 casting time, CG23 paper – CG2 paper with 3 casting times, and CG25 paper – CG2 paper with 5 casting times) became wrinkled more instead of the sheet-like structure with the increasing number of casting times, probably due to the contraction of CTS chains in dry conditions. Concomitantly, the CTS particles were not observed in these top-surface images, suggesting that the CTS chains were well distributed inside the CG2 mixture as well as on the GO nanosheets. Moreover, the cross-sectional images of CG2 papers (Fig. 6 F – H) showed that the amount of CG2 mixture was supplemented further with the increasing number of casting times, leading to being deposited and stackedly-arranged like a layer-by-layer structure instead of the tightly-sticky paper-like structure, mainly due to the polymer backbone length of CTS on the GO nanosheets. Thereby, the strong electrostatic interactions between carboxyl group (GO) and amino group (CTS), as well as amide linkage formation ($-CONH_2$) have effectively occurred in the CG2 mixture (Fig. 3 and Fig. 4). Overall, the simple casting method could be considered as one of efficient methods to fabricate various foil/paper-like materials, as the desired thickness of foil/paper-like materials can also be controlled easily. Herein, the final thickness of paper-like materials reached about 4.750 ± 0.132 µm; 5.125 ± 0.441 µm; 6.625 ± 0.205 µm and 11.625 ± 0.383 µm for the GO, CG21, CG23, and CG25 papers, respectively.
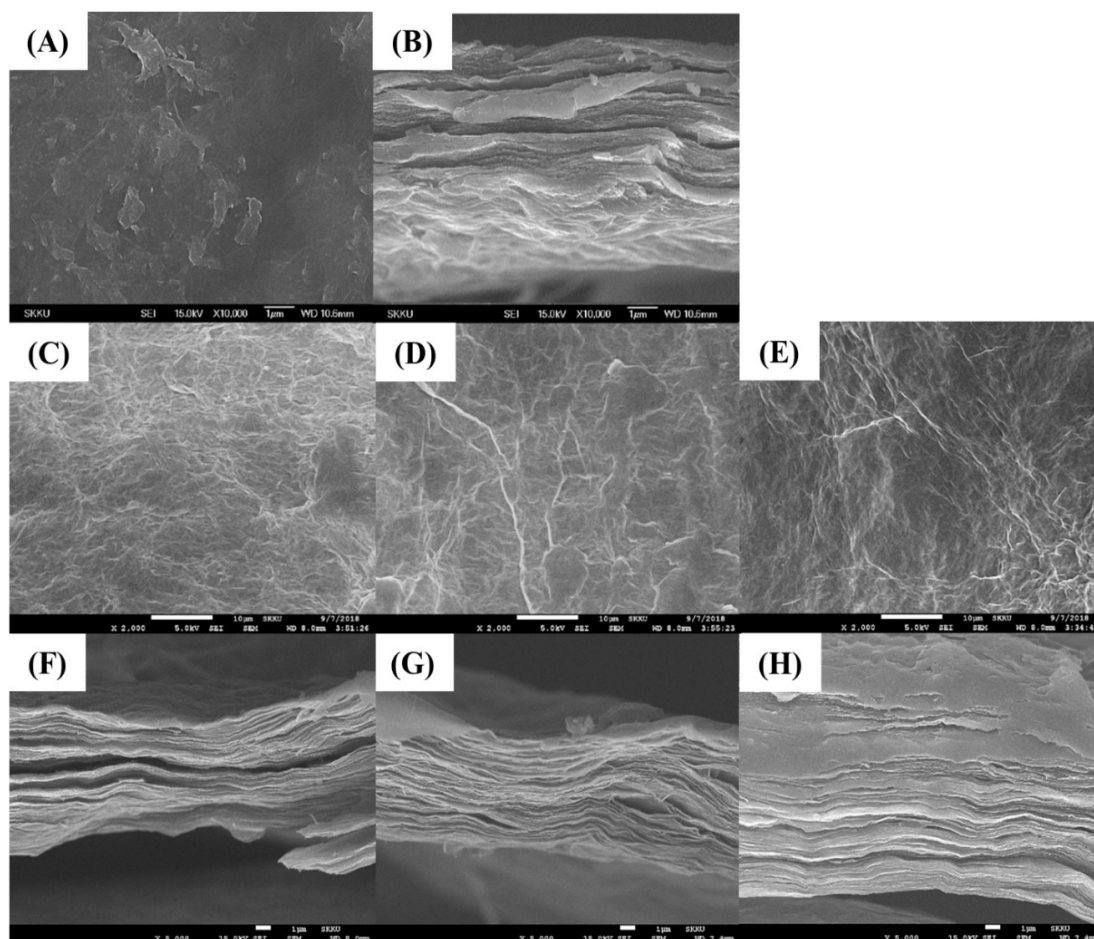
Figure 6: SEM images of GO [top-surface – (A) and cross-section – (B)]; various CG2 papers [top-surface: (C – E), and cross-section – (F – H)]: CG21 (C, E), CG23 (D, G) and CG25 (E, H).

Mechanical properties of CTS/GO papers
In addition to the above-mentioned characterization and morphological properties, the mechanical properties are also considered to be one of the important features for the paper-like materials (GO, CG2 papers with various numbers of casting times) based on the tensile tests at room temperature. Typical stress–strain curves for GO paper and CG2 papers with various numbers of casting times are shown in Fig. 7 [Digital camera images of CG2 paper − (A) and from tensile loading − (B)]. For the GO paper, its tensile strength, elongation at break, and modulus ($\varepsilon = {\sim}0.5\%$) were lower than those of CG papers (GO paper: δ= 5.19 MPa, $\varepsilon = 2.36\%$, and E = 1.83 MPa) relating to the hydrogen bond and van der Waals forces within the GO nanosheets of the produced GO paper (34). While the tensile strength and modulus ($\varepsilon = {\sim}0.5\%$) of CG papers increased significantly with increasing number of casting times (19.21 MPa & 1.95 MPa / CG21 paper, 22.77 MPa & 2.55 MPa / CG23 paper, and 26.81 MPa & 2.64 MPa / CG25 paper), there

was only a small decrease in the elongation at break of CG23 paper (5.46% / CG21 paper, 4.94% / CG23 paper, and 5.74% / CG25 paper). Thereby, the enhancement of tensile strength and modulus of the CG papers manifests good dispersion of both CTS molecule and GO nanosheets, as well as their strong interactions (hydrogen bond, electrostatic attraction, and amide linkage formation) inside the CTS/GO mixtures. Concomitantly, the increase in tensile strength and modulus of CG papers exhibited stiffer behavior, implying a transition in their intermolecular interactions with increasing CG2 loading. In other words, the resultant hydrogen bond, electrostatic attraction, and amide linkage formation between the CTS molecules and GO nanosheets have supported rearrangements in the CG2 paper-like structures (layer-by-layer structure), leading to increased steric hindrance and lowering the torsion of the polymer backbone, as well as strong interlayer interactions in the CG2 papers (35-38).
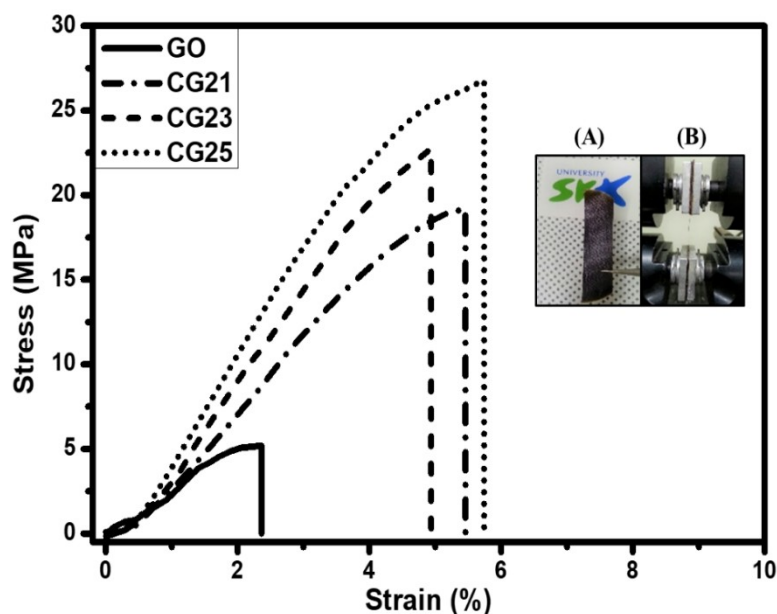
Figure 7: Typical stress–strain curves of the paper-like materials (GO, CG2 papers with various number of casting times). Digital camera images of CG2 paper (A) and paper from tensile loading (B).

Overall, good dispersion and interfacial stress transfer are considered significant factors in preparing the mechanically reinforced paper-like materials. It causes a more uniform stress distribution as well as minimizes the presence of the stress concentration center (39). As mentioned above, the GO nanosheets with oxygen-containing groups and negative charges can interact well with the CTS molecules – poly-cationic compounds through hydrogen bond, electrostatic attraction and amide linkage formation (Fig. 3 and Fig. 4). Furthermore, the contraction and backbone length of the CTS chains on the GO nanosheets promote stress transfer under dry conditions. Additionally,

the strong interactions and compatibility between the CTS molecules and GO nanosheets significantly increase the unidirectional dispersion of GO nanosheets in the CTS molecules as well as the interfacial adhesion, leading to significantly enhanced mechanical properties of the CG2 paper-like materials.

CONCLUSIONS

A simple casting method has yielded the paper-like materials (CG2 papers the various casting times) possessing layer-by layer structures instead of the tightly-sticky paper-like structures (GO paper)

based on the morphological properties (top-surface and cross-sectional SEM images). Besides, the strong interactions (hydrogen bond, electrostatic attraction, and amide linkage formation) between the CTS molecules and GO nanosheets have been determined through the FTIR and Raman results, as well as the thermal property has also become more stable in the prepared mixture with the CTS molecules and GO nanosheets. Moreover, the strong interactions and compatibility of them indicated good dispersion and interfacial adhesion, leading to significantly enhancing the mechanical properties of the CG2 paper-like materials with an increasing number of casting times or compared to GO paper. Therefore, the CG2 paper-like materials with the various numbers of casting times prepared in the present study can open up new avenues for the design and application of future foil/paper-like materials, as well as the desired thickness of these foil/paper-like materials can be controlled easily.

REFERENCES

1. Vo TS, Vo TTBC. Preparation and Characterization of Bis-Propargyl-Succinate, and its Application in Preliminary Healing Ability of Crosslinked Polyurethane using" Azide-Alkyne" Click. Journal of Engineering Science & Technology Review. 2020;13(4).

2. Vo TS, Vo TTBC, TiEn TT, SiNh NT. Enhancement of mechanical property of modified polyurethane with bis-butyl succinate. JOTCSA. 2021 Mar 30;8(2):519–26. <DOI>.

3. Vo TS, Vo TTBC. A Self-Healing Material Based on Microcapsules of Poly(Urea-Formaldehyde)/Bis-Propargyl-Succinate Containing in Polyurethane Matrix. JOTCSA. 2021 Jul 26;8(3):787–802. <DOI>.

4. Vo TS, Vo TTTN, Chau TTB. Preparation and Characterization of Microcapsules Containing Canola Oil with Poly (urea-formaldehyde) Shell and its Stability. Journal of Engineering Science & Technology Review. 2021;14(4):21–36.

5. Vo TS, Vo TTBC, Nguyen TS, TiEn TT. Fabrication and Characterization of Gelatin/Chitosan Hydrogel Utilizing as Membranes. Journal of the Turkish Chemical Society Section A: Chemistry. 2021 Oct 1;8(4): 1045–56. <DOI>.

6. Pitkethly MJ. Nanomaterials – the driving force. Materials Today. 2004 Dec;7(12):20–9. <DOI>.

7. Reynolds R, Greinke R. Influence of expansion volume of intercalated graphite on tensile properties of flexible graphite. Carbon. 2001;3(39):479–81.

8. Hennrich F, Lebedkin S, Malik S, Tracy J, Barczewski M, Rösner H, et al. Preparation, characterization and applications of free-standing single walled carbon nanotube thin films. Phys Chem Chem Phys. 2002 May 20;4(11):2273–7. <DOI>.

9. Coleman JN, Blau WJ, Dalton AB, Muñoz E, Collins S, Kim BG, et al. Improving the mechanical properties of single-walled carbon nanotube sheets by intercalation of polymeric adhesives. Appl Phys Lett. 2003 Mar 17;82(11):1682–4. <DOI>.

10. Berhan L, Yi YB, Sastry AM, Munoz E, Selvidge M, Baughman R. Mechanical properties of nanotube sheets: Alterations in joint morphology and achievable moduli in manufacturable materials. Journal of Applied Physics. 2004 Apr 15;95(8):4335–45. <DOI>.

11. Vo TS. Progresses and expansions of chitosan-graphene oxide hybrid networks utilizing as adsorbents and their organic dye removal performances: A short review. Journal of the Turkish Chemical Society Section A: Chemistry. 2021 Oct 18;8(4):1121–36. <DOI>.

12. Velmurugan N, Kumar GG, Han SS, Nahm KS, Lee YS. Synthesis and characterization of potential fungicidal silver nano-sized particles and chitosan membrane containing silver particles. Iranian Polymer Journal. 2009;18(5(107)):383–92.

13. Jiao TF, Zhou J, Zhou J, Gao L, Xing Y, Li X. Synthesis and characterization of chitosan-based Schiff base compounds with aromatic substituent groups. Iranian Polymer Journal. 2011;20(2):123–36.

14. Rao KK, Rao KM, Kumar PN, Chung ID. Novel chitosan-based pH sensitive micro-networks for the controlled release of 5-fluorouracil. Iranian Polymer Journal. 2010;19(4):265–76.

15. Xu Y, Wu Q, Sun Y, Bai H, Shi G. Three-Dimensional Self-Assembly of Graphene Oxide and DNA into Multifunctional Hydrogels. ACS Nano. 2010 Dec 28;4(12):7358–62. <DOI>.

16. Tung VC, Kim J, Cote LJ, Huang J. Sticky Interconnect for Solution-Processed Tandem Solar Cells. J Am Chem Soc. 2011 Jun 22;133(24):9262–5. <DOI>.

17. Bai H, Li C, Wang X, Shi G. On the Gelation of Graphene Oxide. J Phys Chem C. 2011 Apr 7;115(13):5545–51. <DOI>.

18. Singh N, Riyajuddin S, Ghosh K, Mehta SK, Dan A. Chitosan-Graphene Oxide Hydrogels with Embedded Magnetic Iron Oxide Nanoparticles for Dye Removal. ACS Appl Nano Mater. 2019 Nov 22;2(11):7379–92. <DOI>.

19. Han Lyn F, Tan CP, Zawawi RM, Nur Hanani ZA. Physicochemical properties of chitosan/ graphene oxide composite films and their effects on storage stability of palm-oil based margarine. Food Hydrocolloids. 2021 Aug;117:106707. <DOI>.

20. Menazea AA, Ezzat HA, Omara W, Basyouni OH, Ibrahim SA, Mohamed AA, et al. Chitosan/graphene oxide composite as an effective removal of Ni, Cu, As, Cd and Pb from wastewater. Computational and Theoretical Chemistry. 2020 Nov;1189:112980. <DOI>.

21. Januário EFD, Vidovix TB, Beluci N de CL, Paixão RM, Silva LHBR da, Homem NC, et al. Advanced graphene oxide-based membranes as a potential alternative for dyes removal: A review. Science of The Total Environment. 2021 Oct;789:147957. <DOI>.

22. Sharma P, Das MR. Removal of a Cationic Dye from Aqueous Solution Using Graphene Oxide Nanosheets:

Investigation of Adsorption Parameters. J Chem Eng Data. 2013 Jan 10;58(1):151–8. <DOI>.

23. Kahya N, Erim FB. Graphene oxide/chitosan-based composite materials as adsorbents in dye removal. Chemical Engineering Communications. 2021 Oct 6;1–16. <DOI>.

24. Sabzevari M, Cree DE, Wilson LD. Graphene Oxide–Chitosan Composite Material for Treatment of a Model Dye Effluent. ACS Omega. 2018 Oct 31;3(10):13045–54. <DOI>.

25. Zhang H ping, Yang B, Wang ZM, Xie C, Tang P, Bian L, et al. Porous graphene oxide/chitosan nanocomposites based on interfacial chemical interactions. European Polymer Journal. 2019 Oct;119:114–9. <DOI>.

26. Yang X, Tu Y, Li L, Shang S, Tao X ming. Well-Dispersed Chitosan/Graphene Oxide Nanocomposites. ACS Appl Mater Interfaces. 2010 Jun 23;2(6):1707–13. <DOI>.

27. Mansur HS, Mansur AAP, Curti E, De Almeida MV. Functionalized-chitosan/quantum dot nano-hybrids for nanomedicine applications: towards biolabeling and biosorbing phosphate metabolites. J Mater Chem B. 2013;1(12):1696. <DOI>.

28. El Ichi S, Zebda A, Alcaraz JP, Laaroussi A, Boucher F, Boutonnat J, et al. Bioelectrodes modified with chitosan for long-term energy supply from the body. Energy Environ Sci. 2015;8(3):1017–26. <DOI>.

29. Vo TS, Vo TTBC, Nguyen TS, Pham ND. Incorporation of hydroxyapatite in crosslinked gelatin/chitosan/poly(vinyl alcohol) hybrids utilizing as reinforced composite sponges, and their water absorption ability. Progress in Natural Science: Materials International. 2021 Oct;31(5):664–71. <DOI>.

30. Vo TS, Vo TTBC, Tran TT, Pham ND. Enhancement of water absorption capacity and compressibility of hydrogel sponges prepared from gelatin/chitosan matrix with different polyols. Progress in Natural Science: Materials International. 2022 Feb;32(1):54–62. <DOI>.

31. Bano S, Mahmood A, Kim SJ, Lee KH. Graphene oxide modified polyamide nanofiltration membrane with improved flux and antifouling properties. J Mater Chem A. 2015;3(5):2065–71. <DOI>.

32. Shen L, Xiong S, Wang Y. Graphene oxide incorporated thin-film composite membranes for forward osmosis applications. Chemical Engineering Science. 2016 Apr;143:194–205. <DOI>.

33. He D, Peng Z, Gong W, Luo Y, Zhao P, Kong L. Mechanism of a green graphene oxide reduction with reusable potassium carbonate. RSC Adv. 2015;5(16):11966–72. <DOI>.

34. Dikin DA, Stankovich S, Zimney EJ, Piner RD, Dommett GHB, Evmenenko G, et al. Preparation and characterization of graphene oxide paper. Nature. 2007 Jul;448(7152):457–60. <DOI>.

35. Wool RP, Statton WO. Dynamic polarized infrared studies of stress relaxation and creep in polypropylene. J Polym Sci Polym Phys Ed. 1974 Aug;12(8):1575–86. <DOI>.

36. Wool RP. Mechanisms of frequency shifting in the infrared spectrum of stressed polymer. J Polym Sci Polym Phys Ed. 1975 Sep;13(9):1795–808. <DOI>.

37. Wool RP. Infrared studies of deformation in semicrystalline polymers. Polym Eng Sci. 1980 Aug;20(12):805–15. <DOI>.

38. Ward IM, Hadley DW. An introduction to the mechanical properties of solid polymers. 1993. ISBN: 0-471-93874-2.

39. Coleman JN, Khan U, Gun'ko YK. Mechanical Reinforcement of Polymers Using Carbon Nanotubes. Adv Mater. 2006 Mar 17;18(6):689–706. <DOI>.

QSER Modeling of Half-Wave Oxidation Potential of Indolizines by Theoretical Descriptors

Nabil Bouarra[1,2]* (iD), **Nawel Nadji[1,2]** (iD), **Soumaya Kherouf[3]** (iD), **Loubna Nouri[1,4]** (iD), **Amel Boudjemaa[1]** (iD), **Khaldoun Bachari[1]** (iD), **Djelloul Messadi[3]** (iD)

[1]Scientific and Technical Research Center in Physico-Chemical Analysis, Industrial Zone, Tipaza, 42004, Algeria.

[2]Badji Mokhtar University, Laboratory of Environmental Engineering, Annaba, 23000, Algeria.

[3]Badji Mokhtar University, Department of Chemistry, Annaba, 23000, Algeria.

[4]University of Sciences and Technology Houari – Boumediene, Laboratory of Reaction Engineering, Algiers, 16111, Algeria.

Abstract: Indolizine derivatives hold essential biological functions and have been researched for hypoglycemic, antibacterial, anti-inflammatory, analgesic, and anti-tumor actions. Indolizine scaffold has intrigued conjecture and continuous attention and has become an effective parent system for generating powerful novel medication candidates. This research focused on applying the quantitative structure-electrochemistry relationship (QSER) approach to the half-wave potential ($E_{1/2}$) for Indolizine derivatives using theoretical molecular descriptors. After calculating the descriptors and splitting the data into both sets, training and prediction. The QSER model was constructed using the Genetic Algorithm/Multiple Linear Regression (GA/MLR) technique, which was used to choose the optimal descriptors for the model. A four-parameter model has been established. Many assessment procedures, including cross-validation, external validation, and Y-scrambling testing, were used to assess the model's performance. Furthermore, the applicability domain (AD) was investigated using the Williams and Insubria graphs to assess the correctness of the established model's predictions. The constructed model exhibits great goodness-of-fit to experimental data, as well as high stability (R^2=0.893, Q^2_{LOO}= 0.851, Q^2_{LMO}=0.843 $RMSE_{tr}$= 0.052, s= 0.056). Prediction results show a good agreement with the experimental data of $E_{1/2}$ (R^2ext= 0.912, Q^2_{F1}= 0.883, Q^2_{F2}= 0.883, Q^2_{F3}= 0.919, CCC_{ext}= 0.942, $RMSE_{ext}$=0.045).

INTRODUCTION

Indolizine is a heteroaromatic molecule composed of two condensed rings (five and six members) and a bridging nitrogen atom (1). Indolizine has been referred to by various names in the literature, including pyrindole, pyrrodine, pyrrolo[1,2-a]pyridine, and pyrrocoline (2). Indolizines (indolizine derivatives) are heterocyclic compounds comprised of indolizine heterocyclic nuclei. Indolizidines are widely dispersed in nature, particularly in plants, but aromatic indolizines are uncommon (2). Heterocycles possessing indolizine cores play an essential role in pharmaceutical and

materials chemistry. Several high-performance materials, dyes, and medicines are intrinsically heterocyclic (3). Numerous pharmacological activities have been reported for indolizines, like anti-inflammatory activity (4), antiviral activity (5), aromatase inhibitory activity (6), analgesic activity (7), and anticancer activity (8,9). Indolizine scaffold has intrigued conjecture and continuous attention and has become a significant parent system for the generation of novel medication candidates (9).

Electrochemical techniques are helpful tools for studying electron-transfer processes and may also provide important information that can contribute to understanding various biological phenomena (10). The oxidation reaction is the most commonly seen route during the beginning phase of drug biotransformation. Because of this, electrochemistry is often used as a simulation technique in drug metabolism investigations (11). Organic compounds' half-wave oxidation potential ($E_{1/2}$) is a significant electrochemical feature, which is a constant that defines an oxidation-reduction system according to the definition. The $E_{1/2}$ may be used to predict the electrochemical properties of other organic molecules as well (12). A typical electrochemical technique used in studies of electro-oxidation systems is voltammetry (13). Since the synthesis and the evaluation of novel drugs based on indolizines and their investigation by voltammetric methods are restricted in time and cost (14), the construction of theoretical models to predict the features of these compounds is essential and required.

The quantitative structure-property relationship (QSPR) approach, referred to as the quantitative structure-electrochemistry relationship (QSER), allows for the prediction and interpretation of $E_{1/2}$ of drugs and organic compounds, based on the relationship between both their $E_{1/2}$ and structural molecular descriptors. These descriptors contain chemical information related to the molecule's physicochemical features (15). QSER models are suitable because they minimize the number of experiments by saving time and money while measuring physicochemical or bio-activities. Several studies on the use of QSPR in electrochemistry have been conducted (16-20). Hemmateenejad and Shamsipur used PCR and PC-ANN to determine the

$E_{1/2}$ of 69 organic compounds. They developed an ideal PC-ANN model that can explain 96% of the $E_{1/2}$ data variances (16). Nesmerak *et al.* relate Hammet substituent constants and HOMO orbital energy to $E_{1/2}$ of 40 benzoxazines. They discovered a significant relationship between HOMO and E1/2 oxidation. (17). Fatemi et al. constructed a QSPR model based on multiple linear regression to predict $E_{1/2}$ values of 15 substituted nitrobenzenes (18). Hemmateenejad and Yazdani used MLR and PCR to investigate the half-wave reduction potential ($E_{1/2}$) of 40 steroids (19). Goudarzi *et al.* (20) used a genetic algorithm-partial least squares (GA-PLS) and stepwise regression-partial least squares (SR-PLS) approach to estimate the half-wave reduction potentials of 21 chlorinated organic compounds.

In this work, we have attempted to develop a new QSER model by predicting the half-wave oxidation potential of different sets of indolizines. Our purposes are:

1) To investigate the relationship between the half-wave oxidation potentials of indolizines and their molecular structures;

2) To build a precise and stable model with great predictive potential using a rapid and straightforward method of regression;

3) To predict $E_{1/2}$ values for different indolizines without experimental data using the established model.

MATERIAL AND METHODS

Dataset
Fifty-two structurally diverse indolizines were selected for data; their molecular structures are described in Table S1 in supplementary materials. Experimental $E_{1/2}$ values were obtained from the literature (21). Recorded values vary from 0.362 to 0.966 Volts. Table 1 summarizes the data obtained for indolizine derivatives by cyclic voltammetry (CV). The cyclic voltammograms were recorded according to these experimental conditions: A platinum disk electrode (d=1.0 mm). acetonitrile solutions (1mM) of the substrate containing 0.1 M TBATFB as the supporting electrolyte, and all measurements were performed at 20 °C and at 1 V/s scan rate (21).

Table 1: Cyclic voltammetry data and descriptors values for the studied compounds.

Nº.	$E_{1/2}$ (V) b	T(O..O)	SIC4	R8m	TPSA(NO)
1	0.386	0	0.869	0.223	37.12
2	0.429	0	0.869	0.378	37.12
3	0.461	0	0.869	0.503	37.12
4	0.385	0	0.83	0.251	37.12
5	0.362	26	0.802	0.274	55.58
6	0.435	0	0.873	0.379	37.12
7	0.446	6	0.878	0.399	46.35

Bouarra N et al. JOTCSA. 2022; 9(3): 709-720.

RESEARCH ARTICLE

Nº.	$E_{1/2}$ (V) b	T(O..O)	SIC4	R8m	TPSA(NO)
8	0.647	5	0.903	0.383	46.35
9	0.671	4	0.903	0.418	46.35
10	0.443	0	0.882	0.458	37.12
11	0.522	0	0.882	0.442	37.12
12	0.45	0	0.91	0.474	37.12
13	0.436	0	0.875	0.346	37.12
14	0.391	0	0.856	0.421	37.12
15	0.492	0	0.878	0.403	46.35
16	0.443	20	0.819	0.343	64.81
17	0.676	8	0.896	0.462	63.42
18	0.688	10	0.907	0.394	63.42
19	0.679	12	0.882	0.386	63.42
20	0.692	0	0.877	0.347	54.19
21	0.77	0	0.875	0.473	71.26
22	0.807	0	0.875	0.594	71.26
23	0.825	0	0.875	0.758	71.26
24	0.74	0	0.816	0.475	71.26
25	0.68	64	0.848	0.486	89.72
26	0.792	0	0.872	0.423	71.26
27	0.773	0	0.879	0.393	71.26
28	0.966	0	0.872	0.729	71.26
29	0.743	0	0.842	0.49	74.5
30	0.776	0	0.875	0.486	71.26
31	0.815	0	0.882	0.525	71.26
32	0.804	18	0.878	0.473	80.49
33	0.477	0	0.872	0.35	47.47
34	0.688	22	0.872	0.485	64.54
35	0.711	22	0.878	0.5	64.54
36	0.411	0	0.816	0.464	47.47
37	0.686	0	0.889	0.248	71.26
38	0.683	0	0.858	0.356	71.26
39	0.791	36	0.875	0.454	89.72
40	0.772	32	0.88	0.485	89.72
41	0.754	34	0.88	0.481	89.72
42	0.782	0	0.901	0.514	71.26
43	0.788	0	0.879	0.457	71.26
44	0.78	0	0.847	0.491	71.26
45	0.809	0	0.903	0.623	71.26
46	0.79	0	0.903	0.615	71.26
47	0.722	0	0.869	0.391	60.36
48	0.669	0	0.869	0.38	60.36
49	0.606	0	0.88	0.429	48.12
50	0.671	0	0.889	0.566	48.12

Nº.	$E_{1/2}$ (V) b	T(O..O)	SIC4	R8m	TPSA(NO)
51	0.698	0	0.889	0.691	48.12
52	0.601	0	0.857	0.419	48.12

Generation of Descriptors

ChemDraw 7.0 software (22) was used to sketch the chemical structures of all molecules.

The three-dimensional geometries were optimized using the semi-empirical PM7 method (23) and the MOPAC software (24) to reach the low-energy conformation for each chemical compound. After the geometric optimization, the Dragon software (V.5.5) was used to generate more than 3000 descriptors (25) from different families, including topological descriptors, molecular counts, connection indices, information indices, 2D autocorrelations, edge adjacency indices, topological charge indices, and eigenvalues-based indices, among the molecular descriptors generated. Constant or almost constant descriptor values and descriptors that were found highly correlated (r >0.95) (26) were omitted to minimize repetitive and unnecessary information.

GA-MLR procedure

The obtained descriptors and experimental $E_{1/2}$ values were analyzed using a genetic algorithm-multivariate linear regression (GA-MLR). GA (27,28) is done to explore the feature space and choose the main descriptors related to the compounds' activities or properties ($E_{1/2}$ in this study). Briefly, the GA is built up of the following fundamental phases: 1) a vector (chromosome) comprising zeros and ones (genes) is produced with the size corresponding to the number of factors; 2) a population of chromosomes is randomly generated; 3) the value of fitness function is examined for every new created chromosomes(The fitness function here is the cross-validation coefficient (Q^2_{LOO})); 4) the chromosomes with the better predictions (according to their fitness function value) are then used to generate new populations by operations including selection, crossover and mutation. These phases of evolution continue until the halting criteria are fulfilled. After that, the MLR is used to associate the descriptors chosen by GA with the values of $E_{1/2}$. The MLR provides an equation relating the structural descriptors to the $E_{1/2}$:

$$E_{1/2} = b_0 + b_1y_1 + ... + b_ny_n \qquad (1)$$

Where the intercept (b_0) and the regression coefficients of the descriptors (b_i) are calculated using the least-squares method. y_i is the independent variable or descriptor.

Validation of QSER model

Following the Organization for Economic Cooperation and Development (OECD) guidelines, a quantitative structure-activity relationship (QSAR) model should give acceptable metrics of quality, robustness, and reliability. Whereas a training set provides the model's internal performance, reliability is evaluated using a suitable test set (29).

The following statistical metrics (R^2 and Q^2_{LOO}) were calculated to verify the model's accuracy. R^2 evaluates the model's fit to the observed data in the training set. In other words, R^2 governs the fit of the build model. The cross-validation coefficient (Q^2_{LOO}), one of the most frequent internal validation procedures, was calculated for the quantitative assessment of model robustness. This procedure was repeated for the full training set by eliminating one molecule and developing and verifying each molecule's model (29, 30).

$$\qquad (2)$$
$$R^2 = 1 - \frac{\sum_{i=1}^{n}(\hat{y}_i - y_i)^2}{\sum_{i=1}^{n}(y_i - \bar{y})^2}$$

$$\qquad (3)$$
$$Q^2_{LOO} = 1 - \frac{\sum_{i=1}^{n}(y_i - \hat{y}_{i/i})^2}{\sum_{i=1}^{n}(y_i - \bar{y}_i)^2}$$

Where y_i is the experimental $E_{1/2}$, $\hat{y}_i$ is the value of $E_{1/2}$ calculated by the model equation, $\bar{y}$ is the average value of $E_{1/2}$ for the whole set, n is the total compounds in the training set, and $\hat{y}_{i/i}$ is the value of $E_{1/2}$ predicted by the generated model according to the LOO method.

Internal validation using leave-many-out (LMO) is an effective method. In theory, LMO model validation employs fewer training sets than the LOO procedure. The LOO (leave-one-out) procedure employs n training sets of n-1 objects in and predicts each excluded object in the test set, which may be performed several times owing to the possibility of more combinations leaving several compounds out of the training set. It can reasonably be inferred that the model obtained is stable if there is an excellent average QSPR model in Q^2_{LOO} validation (31). In this work, 30% of the compounds were separated from the training set randomly.

External validation was used to assess the developed model's prediction performance based on a series of coefficients: R^2_{ext} (which describes the correlation inside the validation set between both predicted and experimental values), Q^2_{F1}(32), Q^2_{F2}(33), Q^2_{F3} (34,35) and the Concordance Correlation Coefficient (CCC) (36-38). This last one verifies the tiniest variation in predictions between experimental and external data. Moreover, the root means squared error (RMSE), which recapitulates the total error of the developed model, measures and compares the reliability of predictions in both the training ($RMSE_{tr}$) and the prediction set ($RMSE_{ext}$), defined as follows:

$$RMSE = \sqrt{\frac{1}{n}\Sigma_{i=1}^{n}(y_i-\hat{y}_i)^2} \tag{4}$$

One of the most commonly used strategies for ensuring the accuracy and robustness of the created model is Y-scrambling. It is not unusual for a model with good statistical results for training to have fortuitous correlations but descriptors that do not necessarily relate to the modeled property. The Y-scrambling procedure detects these random models. The experimental property of the training set is randomly mixed, and the learning algorithm is retrained to obtain a model using the same descriptors. Typically, the resulting models should have poor efficiency (30).

RESULTS AND DISCUSSION

Development of the Model

The experimental data of the $E_{1/2}$ were randomly split into two subsets, namely training set (70%) and prediction set (30%). The QSARINS software used the hybrid Genetic Algorithm-multiple linear regression (GA-MLR) approach on the training set to build numerous linear models (39). The set of parameters were used in QSARINS, including the population size of 1000, the generation per size of 1000, the number of models per size of 100, the mutation rate of 80, the crossover rate of 0.6, and the QUIK rule of 0.05. As a result, different models of many sizes have been generated based on the statistics on the cross-validation (Q^2_{LOO}), multiple correlation coefficients (R^2), and standard error (s). However, some of them may be over-fitted.

Figure 1 depicts the effects of the number of descriptors on R^2 and Q^2_{LOO} statistics. As seen in fig.1, models containing 5 and 6 descriptors do not significantly improve model statistics.
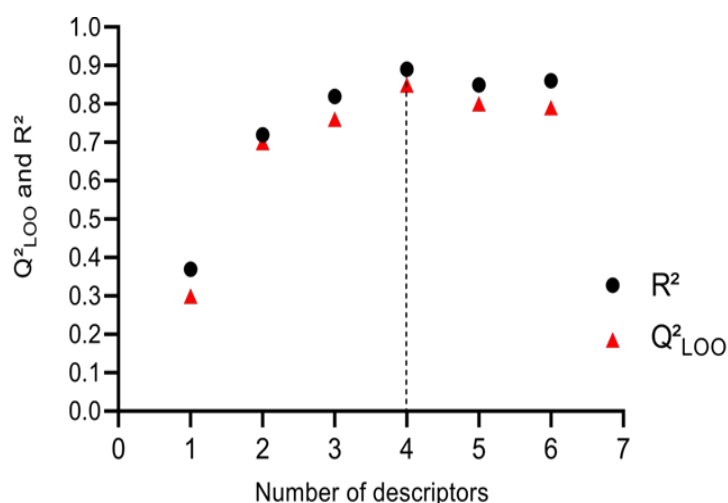
Figure 1: The plot of Q^2_{LOO} and R^2 for the obtained models *versus* the number of descriptors.

Based on figure 1, the model of 4-parameters should be chosen as the best model defined by the following equation:

$$E_{1/2} \text{ (V)} = -1.28 - 0.003 \, T \, (O..O) + 1.46 \, SIC4 + 0.327 \, R8m + 0.008 \, TPSA \, (NO) \tag{5}$$

R^2= 0.893, Q^2_{LOO}= 0.851, Q^2_{LMO}= 0.847, $RMSE_{cv}$= 0.061, $RMSE_{tr}$= 0.052, CCC_{tr}= 0.943, $RMSE_{ext}$= 0.045, R^2_{ext}= 0.912, Q^2_{F1}= 0.883, Q^2_{F2}= 0.883, Q^2_{F3}= 0.919, CCC_{ext}= 0.942, s = 0.0581, F= 66.727.

The statistics prove the constructed model's stability, robustness, and predictive ability (Equation 5). Therefore, the model was accepted with values of R^2 and CCC_{tr} above 0.7 and 0.85, respectively. Moreover, this model has the smallest values for $RMSE_{tr}$ and the highest values for CCC_{tr}, indicating that this model has the lowest error, i.e., the minor differences from the predicted data. In addition, the model's Q^2_{LOO} and Q^2_{LMO} values are more significant

than 0.6 and close to R^2. Furthermore, the established model has the lowest RMSEcv values, proving its efficiency. The built model's external validation results showed a high predictive ability because the R^2_{ext} and the CCC_{ext} values are more significant than 0.7 and 0.85, respectively. Other external validation metrics (Q^2_{F1}, Q^2_{F2}, and Q^2_{F3}) show that they accepted the model based on the literature-recommended criteria (38).

The correlation matrix presented in table 2 was examined to ensure that these descriptors are independent. It is clear from table 2 that none of the descriptor pairs has a significant correlation. In addition, to check the multicollinearity of the descriptors concerned, the Variance Inflation Factor (*VIF*) was calculated (40). From table 2, the *VIF* values are less than 5.0, indicating that the selected descriptors are not collinear. As a result, the model that has been established is reliable.

Table 2: The Correlation matrix.

Descriptors	Definition	T(O..O)	SIC4	R8m	TPSA(NO)	VIF
T(O..O)	Sum of topological distances between O..O	1				**1.653**
SIC4	Structural Information Content index (neighborhood symmetry of 4-order)	-0.101	1			**1.065**
R8m	R autocorrelation of lag 8 / weighted by mass	0.051	0.217	1		**1.310**
TPSA(NO)	Topological polar surface area using N, O, S and P polar contributions	0.589	0.05	0.389	1	**1.936**

Predicted data versus experimental ones and radar plots for training and prediction sets are given in figure 2. The experimental and predicted values are fairly similar, as illustrated in Fig.2 (left). This model matches the experimental data well (R^2 = 0.883, $RMSE_{tr}$ = 0.052, for the training set and R^2_{ext} = 0.912, $RMSE_{ext}$ = 0.045, for the prediction set). The difference between the experimental and predicted $E_{1/2}$ in training and prediction sets may be explained by the degree of overlap between the experimental and predicted $E_{1/2}$ lines in the radar plot (Fig. 2. Right). The radar plot shows a good overlap between experimental and predicted data.
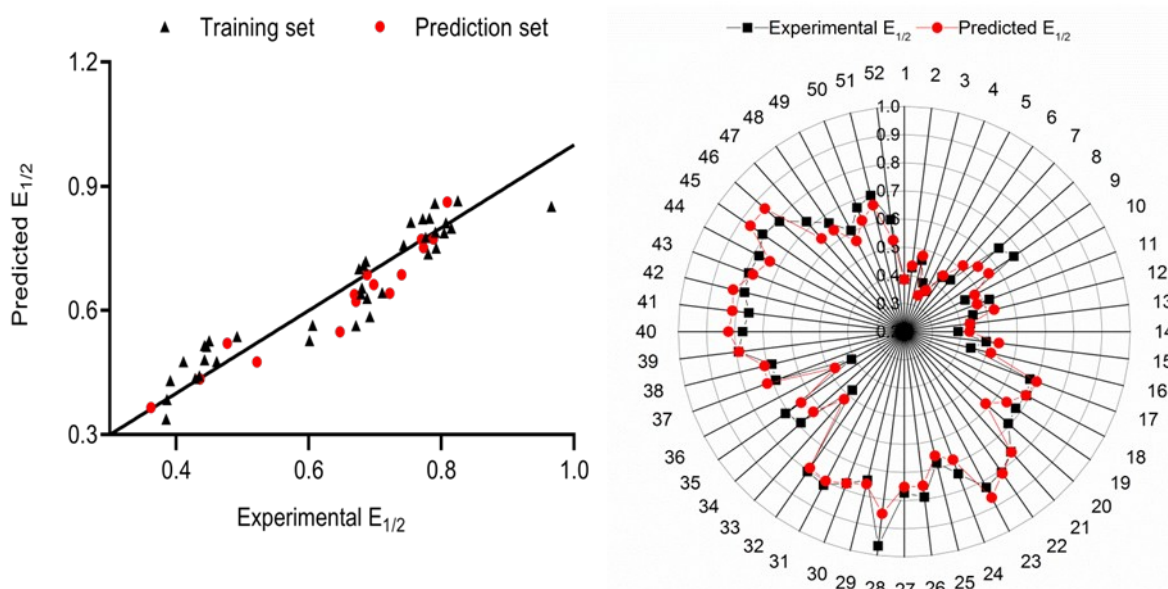
Figure 2: Predicted versus experimental values of E1/2 **(Left)**. The radar plot of QSER model **(Right)**.

The residuals of the training and prediction data sets are represented in Figure 3. As seen in Figure 3, all residuals are scattered consistently and randomly on both sides of the zero line. Consequently, the developed model has no systematic errors.
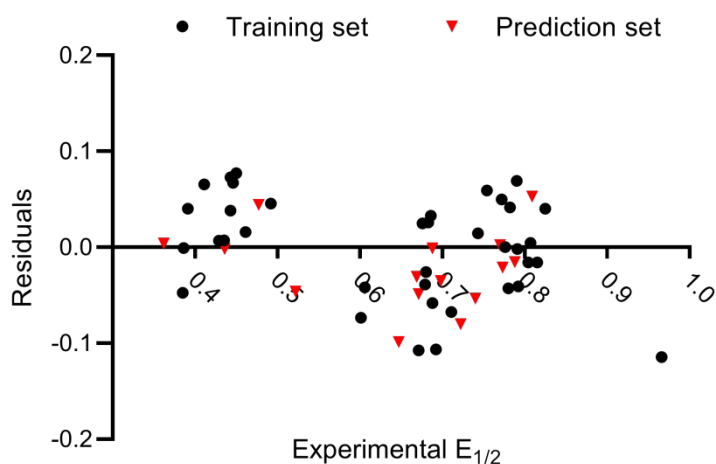
Figure 3: The residuals *vs.* training and prediction values.

The randomization test was applied to avoid correlations by chance and to validate the developed model. By generating two hundred models, the results (R^2Ysc and Q^2Ysc as a function of Kxy) are reproduced in Figure 4, where K_{xy} is the overall correlation in the model descriptors (including $E_{1/2}$). The low R^2Ysc and Q^2Ysc (0.4) values indicate that the favorable results of the created model were not related to random correlations.
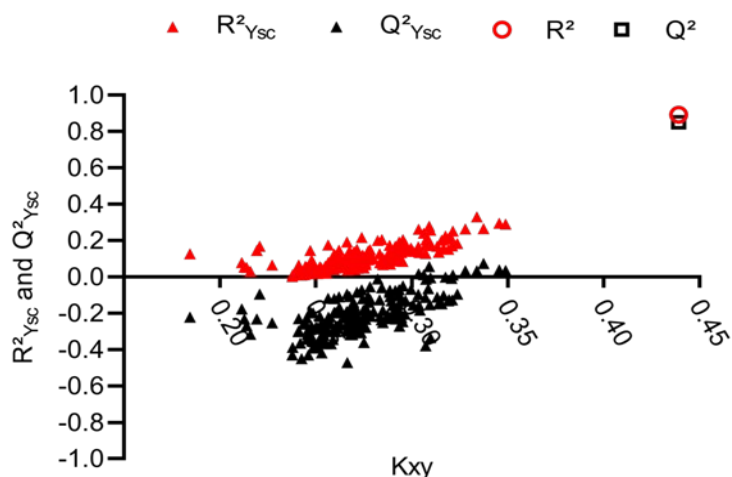
Figure 4: Randomization test.

The applicability domain (AD) belongs to the model validation technique, also known as the model prediction space. The AD was checked to: 1) determine the correct zone for model predictions such that predictions in this zone are reliable and 2) use this AD for making predictions of new compounds. The Williams plot is a standard graphic representation of the standardized residuals vs. leverages values (h_i). The details of this concept are defined in the literature (30,41). Suppose a compound has high leverage (> h^*), this compound will be out of AD. In general, h^* equals 3(p+1)/n, where p is the model's size and n is the number of training compounds. The high standardized residuals (>|3SD| units) (26) are another criterion that places a chemical out of AD.

Figure 5 presents the standardized prediction errors as a function of the values of the leverages (h_i). As shown in figure 4, the presence of an influential point (Compound #25) of the training set, h^* equal 0.405. Thus, this compound can have a positive leverage effect on the stability of the model and make it more accurate. We also note that all residuals are in the range (± 3 SD) (horizontal lines); this denotes that the developed model has an excellent predictive capacity.
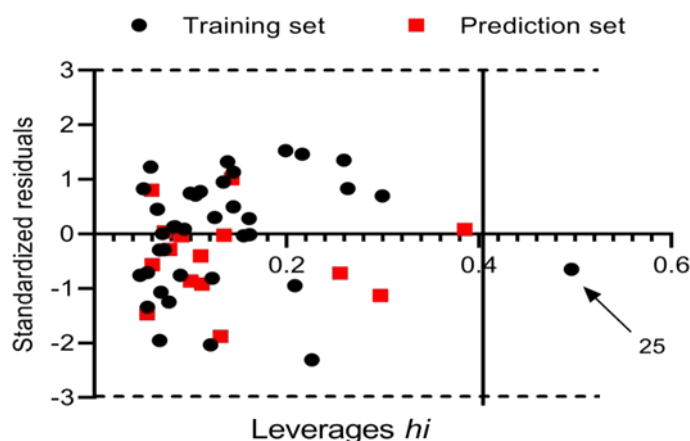
Figure 5: Williams plot of the developed model.

Furthermore, the applicability domain was checked using the Insubria graph (40), which plots leverage values vs. predicted values for compounds with no experimental data. This is useful for visualizing the proposed model's interpolated and extrapolated predictions for novel chemicals without experimental data (51 compounds with no data in this work). The minimum and maximum values of the experimental $E_{1/2}$ of the training set are always presented in the graph, a zone of higher reliability, where predictive ability is good, for both structures less than h^* and $E_{1/2}$ predictions placed within Y_{min} and Y_{max}. In addition, chemical predictions are extrapolated and may be less accurate if their leverages are $h_i > h^*$ (outside the structural domain of the training set).
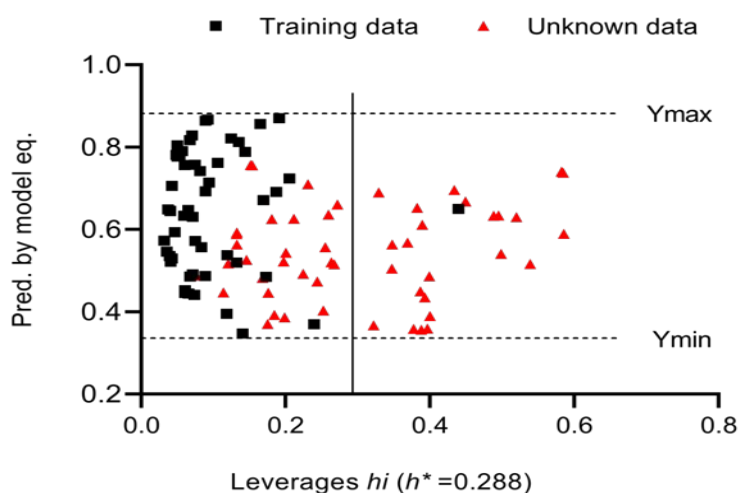
Figure 6: Insubria graph for the developed model: Leverages h_i vs. predicted $E_{1/2}$.

The Insubria graph of the developed model is reported in Figure 6. As can be seen in this figure, the predictions for 53% of indolizines from the prediction set were located within the model's AD, suggesting that this model reliably interpolated the $E_{1/2}$ predictions. Otherwise, 47% of these compounds are outside the AD ($h_i > h^*$), meaning that the predictions obtained are less reliable since they are extrapolations from the structural domain of the model. It demonstrates that, with a few exceptions, the model developed in this study can make reliable predictions for structurally similar indolizines.

Interpretation of descriptors
The following is an order of decreasing descriptor significance in the model:
TPSA(NO) (39.7013%) >T(O..O) (22.9569%) > R8m (19.6070%) > SIC4 (17.7348%).

TPS(NO) (Topological Polar Surface Area defined by nitrogen and oxygen contributions) is the most crucial descriptor in the constructed model. It belongs to the molecular properties descriptor family, expressed as a polar part of the molecule linked to oxygen, nitrogen, sulfur atoms, and hydrogen connected to these heteroatoms and specific charge interactions (15,43). Based on the summation of the tabular polar fragment surface contributions, the topological polar surface area may

be calculated directly (i.e., atoms regarding their bonding pattern). TPSA(NO) has demonstrated a strong correlation (0.826) with half-wave potential in the developed model. The positive TPSA(NO) coefficient suggests that as the topological polar surface area increases, the $E_{1/2}$ increases as well.

The second important descriptor is T(O..O) (Sum of the topological distance between (O..O), which belongs to the topological descriptors (15,43). The topological distance is the length (i.e., the number of involved bonds) of the shortest route between two atoms. The equivalent row sum of the distance matrix, which is the sum of the topological distance between the atom and every other atom, is the atom's distance degree. The sum of topological distances between (O..O) is obtained by the sum of topological distances between all pairs of (O..O) (15,43). The negative coefficient of T(O..O) in equation 5 demonstrates an inverse relationship with $E_{1/2}$, implying that decreasing the descriptor value increases $E_{1/2}$.

The third important descriptor was R8m (the R autocorrelation of lag 8 ∕weighted by atomic masses) (15,43), which belongs to GETAWAY descriptors. The GETAWAY descriptors are built on the leverage matrix, the most widely used for regression diagnostics and the same one determined in statistics (42). Via the use of the molecular influence matrix, atomic connections by molecular topology, and chemical information, these molecular descriptors attempt to match 3D Molecular Geometry through the use of distinct atomic weights and the use of the molecular influence matrix (atomic mass, polarizability, van der Waals volume and electronegativity, etc.) (15,43). The SIC4 descriptor has a positive sign, indicating that the $E_{1/2}$ is associated with this descriptor.

The structural information content (neighborhood of symmetry of 4-order) (SIC4) (15,43) was the last important descriptor. This descriptor is among the information indices determined based on neighbor degrees and edge multiplicity for the H-included molecular graph (15,43). The information indices can be used as a quantitative indicator of structural homogeneity or graph diversity. Therefore, it is related to the symmetry associated with the structure. The positive coefficient of SIC4 implies that the $E_{1/2}$ may grow as SIC4 increases.

According to our findings, $E_{1/2}$ of indolizines is mainly determined by combining the descriptors mentioned above: molecular properties, topological properties, GETAWAY property descriptors, and information index descriptors.

CONCLUSION

The available evidence in the literature suggests that indolizines comprise a substantial class of heterocycles that possess various intriguing biological actions, including hypoglycemic,

antibacterial, analgesic, and anti-inflammatory activities. The half-wave potential ($E_{1/2}$) is an essential electrochemical characteristic. It is a valuable metric for determining the antioxidant activity of organic compounds. The primary goal of this work is to build a quantitative structure-electrochemistry relationship model that could be used to predict the oxidation half-wave potential ($E_{1/2}$) of a series of indolizines using the GA-MLR approach. The developed model has four descriptors derived from the structures of the chemical compounds. The proposed model has a high statistical significance. The $E_{1/2}$ predictions have a good match with the experimental values. Furthermore, the leverage approach assessed the model's applicability domain. The developed model can correctly predict the $E_{1/2}$ for novel compounds that are structurally similar to indolizines, as well as other existing indolizines with undefined $E_{1/2}$ experimental values.

CONFLICT OF INTEREST

The authors declare that they have no known competing financial interests or personal relationships that could have appeared to influence the work reported in this paper.

REFERENCES

1.   Georgescu E, Dumitrascu F, Georgescu F, Draghici C, Barbu L. A Novel Approach for the Synthesis of 5-Pyridylindolizine Derivatives via 2-(2-Pyridyl) pyridinium Ylides. Journal of Heterocyclic Chemistry. 2013;50(1):78-82. <DOI>.

2.   Borrows E, Holland D. The Chemistry of the Pyrrocolines and the Octahydropyrrocolines. Chemical reviews. 1948;42(3):611-43. <DOI>.

3.   Katritzky A R, Rees C W, Scriven E F V, Lohray B B, Bhushan V., Comprehensive Heterocyclic Chemistry II. Pergamon Press;1996 .11628 p. ISBN: 0-08-042072-9.

4.   Kitadokoro K, Hagishita S, Sato T, Ohtani M, Miki K. Crystal structure of human secretory phospholipase A2-IIA complex with the potent indolizine inhibitor 120–1032. The Journal of Biochemistry. 1998;123(4):619-23. <DOI>.

5.   De Bolle L, Andrei G, Snoeck R, Zhang Y, Van Lommel A, Otto M, et al. Potent, selective and cell-mediated inhibition of human herpesvirus 6 at an

early stage of viral replication by the non-nucleoside compound CMV423. Biochemical pharmacology. 2004;67(2):325-36. <DOI>.

6.   Sonnet P, Dallemagne P, Guillon J, Engueard C, Stiebing S, Tangue J, Bureau B, Rault S, Auvray P, Moslemi S, Sourdaine P, Séralini G E, New aromatase inhibitors. Synthesis and biological activity of aryl-substituted pyrrolizine and indolizine derivatives, Bioorg Med Chem. 2000;8 (5):945-955. <DOI>.

7.   Campagna F, Carotti A, Casini G, Macripo M. Synthesis of new heterocyclic ring systems: indeno [2, 1-b]-benzo [g] indolizine and indeno [1', 2': 5, 4] pyrrolo [2, 1-a] phthalazine. Heterocycles (Sendai). 1990;31(1):97-107. <DOI>.

8.   Lillelund VH, Jensen HH, Liang X, Bols M. Recent developments of transition-state analogue glycosidase inhibitors of non-natural product origin. Chemical reviews. 2002;102(2):515-54. <DOI>.

9.   Das A, Banik BK. Chapter 5 - Microwave-assisted synthesis of N-heterocycles. In: Das A, Banik B, editors. Microwaves in Chemistry Applications: Elsevier; 2021. p. 143-98. <DOI >.

10.   Keyzer H, Eckert GM, Gutmann F. Electropharmacology. CRC Press; 1990. 432 p. ISBN:978-0-8493-5409-0.

11.   Eberson L. Electron-Transfer Reactions in Organic Chemistry. In: Gold V, Bethell D, éditeurs. Advances in Physical Organic Chemistry [Internet]. Academic Press; 1982. p. 79-185. <DOI>.

12.   Guengerich FP, Willard RJ, Shea JP, Richards LE, Macdonald TL. Mechanism-based inactivation of cytochrome P-450 by heteroatom-substituted cyclopropanes and formation of ring-opened products. Journal of the American Chemical Society. 1984;106(21):6446-7. <DOI>.

13.   Scholz F. Electroanalytical Methods: Guide to Experiments and Applications. Springer Science & Business Media; 2009. 366 p. ISBN:978-3-642-02915-8.

14.   Macchiarulo A, Costantino G, Fringuelli D, Vecchiarelli A, Schiaffella F, Fringuelli R. 1, 4-Benzothiazine and 1, 4-benzoxazine imidazole derivatives with antifungal activity: a docking study. Bioorganic & medicinal chemistry. 2002;10(11):3415-23. <DOI>.

15.   Todeschini R, Consonni V. Handbook of Molecular Descriptors. John Wiley & Sons; 2000. 692 p. <DOI>. ISBN: 9783527613106.

16.   Hemmateenejad B, Shamsipur M. Quantitative structure-electrochemistry relationship

study of some organic compounds using PC-ANN and PCR. Internet Electronic Journal of Molecular Design. 2004;3(6):316-34. <URL>.

17.   Nesmerak K, Nemec I, Sticha M, Waisser K, Palat K. Quantitative structure–property relationships of new benzoxazines and their electrooxidation as a model of metabolic degradation. Electrochimica acta. 2005;50(6):1431-7. <DOI>.

18.   Fatemi MH, Hadjmohammadi MR, Kamel K, Biparva P. Quantitative structure–property relationship prediction of the half-wave potential for substituted nitrobenzenes in five nonaqueous solvents. Bulletin of the Chemical Society of Japan. 2007;80(2):303-6. <DOI>.

19.   Hemmateenejad B, Yazdani M. QSPR models for half-wave reduction potential of steroids: A comparative study between feature selection and feature extraction from subsets of or entire set of descriptors. Analytica Chimica Acta. 2009;634(1):27-35. <DOI>.

20.   Goudarzi N, Goodarzi M, Hosseini MM, Nekooei M. QSPR models for prediction of half wave potentials of some chlorinated organic compounds using SR-PLS and GA-PLS methods. Molecular Physics. 2009;107(17):1739-44. <DOI>.

21.   Teklu S, Gundersen L-L, Rise F, Tilset M. Electrochemical studies of biologically active indolizines. Tetrahedron. 2005;61(19):4643-56. <DOI>.

22.   ChemDraw Utra "Ultra-chemical structure drawing standard". Version 7. 2002. Copyright Cambridge Soft Corporation.

23.   Stewart JJ. Optimization of parameters for semiempirical methods VI: more modifications to the NDDO approximations and re-optimization of parameters. Journal of molecular modeling. 2013;19(1):1-32. <DOI>.

24.   MOPAC2016, Stewart James J P, Stewart Computational Chemistry, Colorado Springs, CO, USA, <URL> (2016).

25.   Todeschini R, Consonni V, Mauri A, Pavan M, DRAGON Software – version 5.4-TALETE srl, (2005).

26.   Liu H, Gramatica P. QSAR study of selective ligands for the thyroid hormone receptor β. Bioorganic & medicinal chemistry. 2007;15(15):5251-61. <DOI>.

27.   Karakaplan M, Avcu FM. A parallel and non-parallel genetic algorithm for deconvolution of NMR

spectra peaks. Chemometrics and Intelligent Laboratory Systems. 2013;125:147-52. <DOI>.

28. Avcu FM, Karakaplan M. Finding exact number of peaks in broadband UV-Vis spectra using curve fitting method based on evolutionary computing. Journal of the Turkish Chemical Society Section A: Chemistry. 2020;7(1):117-24. <DOI>.

29. Organisation for Economic Co-operation and Development, Guidance Document on the Validation of (Quantitative) Structure-Activity Relationships [(Q)SAR] Models,ENV/JM/MONO (2007) 2, OECD Publishing, Paris. <URL>.

30. Tropsha A, Gramatica P, Gombar VK. The importance of being earnest: validation is the absolute essential for successful application and interpretation of QSPR models. QSAR & Combinatorial Science. 2003;22(1):69-77. <DOI>.

31. De Lima Ribeiro FA, Ferreira MMC. QSPR models of boiling point, octanol–water partition coefficient and retention time index of polycyclic aromatic hydrocarbons. Journal of Molecular Structure: THEOCHEM. 2003;663(1-3):109-26. <DOI>.

32. Gramatica P. External evaluation of QSAR models, in addition to cross-validation: verification of predictive capability on totally new chemicals. Molecular informatics. 2014;33(4):311-4. <DOI>.

33. Schüürmann G, Ebert R-U, Chen J, Wang B, Kühne R. External validation and prediction employing the predictive squared correlation coefficient-Test set activity mean vs training set activity mean. Journal of Chemical Information and Modeling. 2008;48(11):2140-5. <DOI>.

34. Consonni V, Ballabio D, Todeschini R. Comments on the definition of the Q^2 parameter for QSAR validation. Journal of chemical information and modeling. 2009;49(7):1669-78. <DOI>.

35. Consonni V, Ballabio D, Todeschini R. Evaluation of model predictive ability by external validation techniques. Journal of chemometrics. 2010;24(3-4):194-201. <DOI>.

36. Chirico N, Gramatica P. Real external predictivity of QSAR models: how to evaluate it? Comparison of different validation criteria and proposal of using the concordance correlation coefficient. Journal of chemical information and modeling. 2011;51(9):2320-35. <DOI>.

37. Lawrence I, Lin K. A concordance correlation coefficient to evaluate reproducibility. Biometrics. 1989:255-68. <DOI>.

38. Chirico N, Gramatica P. Real external predictivity of QSAR models. Part 2. New intercomparable thresholds for different validation criteria and the need for scatter plot inspection. Journal of Chemical Information and Modeling. 2012;52(8):2044-58. <DOI>.

39. Gramatica P, Chirico N, Papa E, Cassani S, Kovarich S, QSARINS, Software for the Development and validation of QSAR MLR Models, available on request in <URL>.

40. Kherouf S, Bouarra N, Bouakkadia A, Messadi D. Modeling of linear and nonlinear quantitative structure property relationships of the aqueous solubility of phenol derivatives. Journal of the Serbian Chemical Society. 2019;84(6):575-90. <DOI>.

41. Bouarra N, Nadji N, Nouri L, Boudjemaa A, Bachari K, Messadi D. Predicting retention indices of PAHs in reversed-phase liquid chromatography: A quantitative structure retention relationship approach. Journal of the Serbian Chemical Society. 2021;86(1):63-75. <DOI>.

42. Gramatica P, Cassani S, Roy PP, Kovarich S, Yap CW, Papa E. QSAR modeling is not "push a button and find a correlation": a case study of toxicity of (benzo-) triazoles on algae. Molecular Informatics. 2012;31(11-12):817-35. <DOI>.

43. Todeschini R, Consonni V. Molecular descriptors for chemoinformatics: volume I: alphabetical listing/volume II: appendices, references: John Wiley & Sons; 2009. ISBN: 3527628770.

44. Consonni V, Todeschini R, Pavan M. Structure/response correlations and similarity/diversity analysis by GETAWAY descriptors. 1. Theory of the novel 3D molecular descriptors. Journal of chemical information and computer sciences. 2002;42(3):682-92. <DOI>.

RESEARCH ARTICLE

Ameliorative Effects of Vanadyl Sulfate on Some Biochemical Parameters of Experimental Diabetic Rat Kidneys

Nurdagul Orhan[1] iD **, Sevim Tunali[2]** iD **, Refiye Yanardag[2]** iD

[1]Yildiz Technical University, Department of Chemistry, Istanbul, 34220, Turkey.
[2]Istanbul University-Cerrahpasa, Department of Chemistry, Istanbul, 34320, Turkey.

Abstract: Diabetes mellitus (DM), closely related to diabetic nephropathy, is one of the major public health problems worldwide. Today, with the increasing understanding of the underlying pathophysiology of DM, new oral anti-diabetic treatment strategies are being developed. Vanadium is a transition element that is widely distributed in nature, and its oral administration has been reported to improve DM in humans and a variety of diabetic animal models. The purpose of the research is to explore the effect of vanadyl sulfate (VS) administration on the different enzyme activities associated with kidney injury in streptozotocin-(STZ) induced diabetic rats. Male rats were assigned into groups as follows: untreated control, control animals given VS (100 mg/kg), diabetic (a single dose of intraperitoneal STZ, 65 mg/kg), and diabetic + VS (same dose) group. VS was administered orally for 60 days after the induction of diabetes. On the 60th day of experiment, kidney samples were taken for analysis. According to the data obtained from the biochemical analysis, the activities of transaminases, alkaline phosphatase, carbonic anhydrase, and γ-glutamyl transpeptidase decreased, whereas superoxide dismutase activity elevated in the kidney tissue of VS treated hyperglycemic animals. The results suggested that VS improved the diabetic renal injury, probably by VS insulin-mimic and antioxidant behavior through decreased oxidative stress and increased antioxidant capacity. Therefore, vanadyl sulfate might be used as a potential oral anti-diabetic compound in the treatment of the diabetic nephropathy, and as an important control for elevated blood glucose levels in the diabetic state.

INTRODUCTION

Diabetes mellitus (DM) is a metabolic disease defined by unusual insulin secretion disorder, insulin deficiency, and hyperglycemia. Dysfunction in various tissues such as the kidney and liver can be counted among the secondary complications caused by DM (1). Renal failure, the important long-term complications of DM worldwide, is the result of kidney disease caused by hyperglycemia. Most of patients with both type 1 and 2 DM develop chronic kidney disease characterized by clinically damaged renal functions or increased albumin excretion with urine (2).

Oxidative stress plays a pivotal role in the pathogenesis and progression of diabetes (3). Increased oxidative stress, inflammation, and abnormal growth factors all qualify as mediators of tissue damage. High intracellular glucose levels are closely associated with the formation of advanced glycation end products (AGEs), which cause dysfunction and stimulation of expression of some transcription factors that are the major contributors to the development of diabetic kidney disease (2,4).

In the last three decades, streptozotocin (STZ) has been widely applied to many animal species in the

inducement of experimental diabetic models and, accordingly, in the screening and development of various anti-diabetic compounds. STZ causes necrosis of pancreatic beta cells, reducing insulin secretion and inducing clinical features of diabetes similar to those in humans. For this reason, STZ-induced diabetic models are used both to examine the mechanisms of various anti-diabetic agents and to understand their effects on hyperglycemia (5).

Since 1980s, vanadium and its different compounds have been evaluated as potential anti-diabetic compounds in type 1 and type 2 DM (6). Some compounds of vanadium have demonstrated interesting effects in lowering blood glucose levels and improving many biochemical parameters in various diabetic tissues (7-10).

Vanadium, either in its vanadate $[VO_4]^{3-}$ or vanadyl $[VO]^{2+}$ forms, has received great interest because of its possible therapeutic value as an insulin-mimic agent, as insulin is not orally active against diabetes (11). It is known that different vanadyl compounds or their synthesized new complexes exhibit insulin-mimic properties, which means they are involved in the regulation of glucose homeostasis (12).

Previous studies of our research team have demonstrated that both VS and its new synthesized oxovanadyl complex have potential effects on the treatment of DM and recovery in the different tissues on the biochemical and histopathological levels (7,8,13-15). On the other hand, the fact that we obtained remarkable data in kidney tissue in our previous research forced us to examine the effect of VS on different biochemical parameters of the same tissue (16).

EXPERIMENTAL SECTION

Animals, Induction of Diabetes, and Administration of Vanadyl Sulfate
All care and handling of animals were performed with the approval of Animal Care and Use Institute's Committee of Istanbul University. Male, 6-6.5-month-old, Swiss albino rats weighing between 230 g and 250 g were used. The animals were completely healthy and fed with commercial standard pellets. The rats were randomly divided as follows: Group I: untreated control (n=13); group II: control animals given VS (100 mg/kg; n=5); group III: STZ-diabetic (a single dose of intraperitoneal STZ, 65 mg/kg; n=8); group IV: (STZ)-diabetic animals given VS (same dose; n=9). Diabetes was induced in the two diabetic groups with only one dose of 65 mg STZ in citric acid buffer (pH=4.5; 0.01 M) solution per 1 kg of body mass (17). At 24 hours subsequent to the injections, the weight and level of glucose were measured and the animals with glucose levels above 200 mg/dL were accepted as diabetic and used for the study. Briefly, after assessment of 1st day fasting blood glucose, the rats were administered with VS in a dose of 100

mg/kg/day *via* intragastric gavage for 60 days. Throughout the experimental period, body weights and blood glucose levels were monitored at 0th, 1st, 30th, and 60th days (13). In all samples, blood was collected through the tail vein of the rats, and the 18-h-fasting blood glucose levels were determined by o-toluidine method (18). At the end of experiment day, animals were sacrificed and kidney tissues were directly inserted into plastic tubes containing ice-cold physiological saline and kept frozen at −80 °C until the time of analysis.

Biochemical Assays of Kidney Tissue
Cold saline solution (0.9%) was used for preparation of 10% (w/v) kidney homogenates, which were centrifuged before determination of the activities of kidney enzymes and protein analysis.

Transaminase activities (AST and ALT) were determined by Reitman-Frankel method (19). For the clear kidney homogenates, AST and ALT activities were performed using buffered solutions. The quantities of formed oxaloacetate and pyruvate were measured spectrophotometrically at 490 nm.

Alkaline phosphatase (ALP) activity was estimated by Walter and Schüt's two-points method (20). The dense yellow color obtained under alkaline conditions was measured at 405 nm.

Kidney γ-glutamyl transpeptidase (GGT) activity was determined by Szasz (21). The absorbance of formed nitroaniline as a result of the reaction was measured at 405 nm.

Carbonic anhydrase (CA) activity was assayed according to the method described by Verpoorte et al (22). The absorbance changes obtained of 3 min period at 25 °C were monitored at 348 nm.

The activity of superoxide dismutase (SOD) was estimated according to Mylroie et al., and measurements of kidney total protein levels were performed according to the method of Lowry (23,24).

Statistical Analysis
Results were evaluated using an unpaired t test and analysis of variance (ANOVA) using the NCSS statistical computer package. The values were expressed as mean ± SD. $p < 0.05$ was considered as significant.

RESULTS

This part of the results regarding body weight and fasting blood glucose levels in the current animal study has already been published previously (13,16). The loss seen in the body weight of the diabetic animals was prevented by VS administration in the days of 1st, 30th and 60th days ($P_{ANOVA} = 0.011$, $P_{ANOVA} = 0.0001$, $P_{ANOVA} = 0.0001$, respectively) (Table 1). Blood glucose levels that

were increased by STZ administration were diminished by VS treatment. Accordingly, significance was also observed between groups in the blood glucose levels for 1st, 30th, and 60th days (P_{ANOVA}=0.0001, P_{ANOVA}=0.0001, P_{ANOVA}=0.0001, respectively) (Table 2) (13).

Table 1: Mean levels of weight parameters (g) for all groups (13).

Groups	0 Day*	1 Day*	30 Day*	60 Day*	P_{t-test}
Control	246.64±44.43	243.35±39.50	275.51±34.40	283.48±30.35	0.016
Control + VS	224.14±16.13	221.03±12.58	253.14±14.06	251.91±20.41	0.007
Diabetic	231.67±37.71	197.02±37.47	175.74±38.48	171.70±34.67	0.002
Diabetic + VS	229.65±32.14	203.93±30.57	197.46±34.40	199.16±36.2	0.101

*Mean± SD
SD: standard deviation; P_{ANOVA}: analysis of variance; P_{t-test}: unpaired t test; VS: vanadyl sulfate.

Table 2: Mean levels of blood glucose for all groups (mg%) (13).

Groups	0 Day*	1 Day*	30 Day*	60 Day*	P_{t-test}
Control	74.52±14.69	78.19±12.74	80.92±13.31	69.05±9.15	0.107
Control + VS	72.92±9.40	85.05±19.30	76.06±16.19	86.40±11.03	0.401
Diabetic	65.52±5.76	211.75±43.12	216.71±36.61	323.39±131.29	0.0001
Diabetic + VS	71.88±13.78	253.93±38.62	135.76±46.16	131.68±72.30	0.0001
P_{ANOVA}	0.324	0.0001	0.0001	0.0001	

*Mean± SD
SD: standard deviation; P_{ANOVA}: analysis of variance; P_{t-test}: unpaired t test; VS: vanadyl sulfate.

Significant increases in kidney tissue transaminase (AST and ALT) activities were observed in STZ-diabetic rats as compared to control animals (p<0.005). VS application caused a remarkable decrease in the activities of both transaminases (p<0.005) in comparison to diabetic rats (Table 3). Similar results were observed in the ALP activities.

There was a significant increment in the diabetic group ALP activity as compared to non treated healthy animals (p<0.005). In fact, VS administration significantly reversed this increase compared to kidney tissue of hyperglycemic animals (p<0.005) (Table 3).

Table 3: Effect of VS on the kidney tissue AST, ALT and ALP activities in control and experimental groups.

Groups	AST(mU/mg protein)*	ALT(mU/mg protein)*	ALP(mU/mg protein)*
Control	15.68 ± 1.75	18.24 ± 4.19	122.43 ± 32.70
Control + VS	12.00 ± 5.20	14.30 ± 1.92	100.76 ± 28.45
Diabetic	22.91± 4.49[a]	28.28 ± 13.33[a]	237.82 ± 56.47[a]
Diabetic + VS	12.50 ± 5.20[b]	15.83 ± 5.47[b]	118.09 ± 46.46[b]
P_{ANOVA}	0.002	0.0001	0.001

*Mean ± SD
[a] p<0.005 versus to control group
[b] p<0.005 versus to diabetic group
SD: standard deviation; P_{ANOVA}: analysis of variance; VS: vanadyl sulfate;
AST: aspartate aminotransferase; ALT: alanine aminotransferase; ALP: alkaline phosphatase.

Table 4 presents the GGT, CA, and SOD activities for all groups. The activity of GGT, the marker enzyme of enhanced oxidative stress, was significantly elevated in STZ diabetic renal tissue as compared to untreated control group (p<0.05). VS application lowered this activity in a significant manner in comparison to diabetic rats (p<0.0001). Consistent with these data, elevated CA activity in the diabetic kidneys when compared to controls

(p<0.005) was also seen. In addition, vanadium significantly reduced the kidney CA activities in the diabetic animals in comparison to non treated hyperglycemic animals (p<0.0001). On the contrary, it was observed that the activity of SOD was decreased meaningfully in the renal tissue of hyperglycemic animals (p<0.05) whereas this value was insignificantly increased in the hyperglycemic group treated with VS (Table 4).

Table 4: Effect of VS on the kidney GGT, CA and SOD activities in control and experimental groups.

Groups	GGT(mU/mg protein)*	CA(U/mg protein) *	SOD(U/mg protein) *
Control	48.63±11.67	6.63±0.32	24.26±3.91
Control + VS	52.66±28.09	4.96±0.44	16.53±2.63
Diabetic	76.90±10.73[a]	10.23±1.30[c]	15.87±1.57[a]
Diabetic + VS	40.60±6.23[b]	5.94±0.80[b]	18.29±1.87
P$_{ANOVA}$	0.020	0.0001	0.021

*Mean ± SD
[a]$p<0.05$ versus to control group
[b]$p<0.0001$ versus to diabetic group
[c]$p<0.005$ versus to control group
SD: standard deviation; P$_{ANOVA}$:analysis of variance; VS: vanadyl
sulfate; GGT: γ-glutamyl transpeptidase; CA: carbonic anhydrase; SOD:
superoxide dismutase.

DISCUSSION

Kidney diseases, one of the most notable problems in DM, are also the main cause of renal failure (2). Loss of function in the kidneys, changes the body's homeostasis excessively, which can result in death from kidney failure (25). Although the liver is the main organ where gluconeogenesis takes place, the studies demonstrated that the production of glucose under diabetic conditions in the renal tissue is ranged about 25% and increased to 50% during prolonged starvation or DM (26). This suggests that renal gluconeogenesis is of physiological importance for maintaining blood glucose concentration at a certain level (27).

Vanadium is involved in many mechanisms with its insulin-enhancing activity on diabetes, and the most widely accepted of them is the inhibition of tyrosine phosphatase, an enzyme acting on insulin receptors (28). According to the studies, the anti-diabetic effect of vanadium is verified by the diversity of vanadyl compounds and its different oxidation states (29,30). Kiertszan et al. reported that vanadium inhibits gluconeogenesis more strongly in kidney tissue than in the liver (27). In the same work, it was demonstrated that vanadyl acetylacetonate - an organically chelated vanadyl compound - reduced gluconeogenesis in renal cortex tubules by inhibition of pyruvate carboxylase (PC), phosphoenol-pyruvate carboxykinase (PEPCK), and also decreased the activity of fructose-1,6-bisphosphatase (FBP) (27). The first reason for the differences in the effects of the same compound on glucose synthesis metabolism in the liver and kidney, may be caused by the differences between isosymes of regulatory enzymes in the gluconeogenic pathway, such as FBP, a main enzyme in this process, which is unaffected by ribose-1,5-bisphosphate in rabbit liver but is inhibited in rat kidney cortex (31, 32). The second point of inhibition of FBP activity in isolated hepatocytes could also be clarified by the vanadyl-induced elevated level of fructose-2,6-bisphosphate

(33). In general, the reason why vanadium is more effective on the kidney gluconeogenesis than the hepatic one is may be due to the high accumulation of vanadium in the kidney cortex in comparison to hepatic tissue (27).

In our previous research, we observed that hyperglycemia caused loss of renal function in diabetic rats, which was closely related to the decreased GSH level, the formation of non enzymatic glycolization (NEG), and increased serum creatinine and urea concentrations. Treatment with VS resulted in an increase in body weight, a decrease in blood glucose concentration, and both biochemical and histological improvement in diabetic damaged kidney tissue (16). These effects may be associated with insulin-mimic behavior of vanadyl compounds. Obtaining remarkable data in this sense, made us wonder about the influence of VS on other biochemical parameters such as transaminases, ALP, GGT, CA, and SOD in diabetic kidney tissue.

AST and ALT are the transferases that are involved in the transport of amino groups from one specific amino acid to another alpha keto acid (34). Instead of AST and ALT being the markers of hepatic injury, both transaminases are also mainly expressed in a variety of tissues, including kidney, skeletal and cardiac muscles (8,10,35). Feilleux-Duche et al. demonstrated in their research that AST is expressed too much in the renal cortex, and is regulated by glucocorticoids in an extremely cell-specific manner (36). Under stress conditions (both somatic and psychological), the glucocorticoid hormone synthesis is increased significantly in the adrenal cortex. According to the same research, the reason for the high AST activity in the kidneys is an indication of the high physiological stress exposure of the animals. This suggests that the renal AST levels might serve as a sensitive marker for evaluating the induced stress (35). In our previous research, based on the effect of VS on the liver tissue, we observed increased serum AST and ALT

activities as well as degenerative changes in diabetic liver detected by light and electron microscopes (10). In support of this findings, in the current research, we also observed the elevation of both transaminases activities that significantly increased in diabetic rats in comparison to non treated animals kidney tissues. Administration of VS lowered the activities of AST and ALT meaningfully in comparison to the diabetic animals.

ALP is a membrane-bound glycoprotein hydrolase capable of transferring phosphate groups from molecules such as nucleotides and proteins. Most effectively operating in an alkaline environment, ALP stimulates mineralization mainly by balancing the levels of inorganic phosphate and inorganic pyrophosphate. In patients with chronic kidney disease, ALP is a well-recognized biomarker of renal osteodystrophy and a risk factor for increased mortality (37). Therefore, ALPs are important for bone mineralization, but increment of their levels can also be deleterious for other processes, such as vascular calcification. In our research administration with vanadyl, the evident decrement of ALP activity in diabetic rats' renal tissue in comparison to non treated diabetic animals was observed. Another enzyme widely found in tissues with secretory activity, such as the proximal tubular cells in kidneys is GGT (38). This enzyme plays the essential role in the glutathione metabolism (GSH) by catalyzing its degradation into glutamyl and glutamate amino acids (39). It has been previously reported that the highest GGT activity in kidneys is detected on the outer surface of the microvillus membrane in the renal proximal tubule (40). The activation of GGT in the proximal tubule may enhance oxidative stress, leading to kidney damage (38). In this study, we examined the higher GGT activity in diabetic kidney tissue in comparison to non treated animals' renal tissue. In our previous research, we detected a decreased GSH level in the renal tissue of non treated diabetic animals (16). Since GGT is an enzyme responsible for the breakdown of GSH after glomerular infiltration, an increment in its activity in the kidney tissue of diabetic animals is expected (41). Application of oral vanadyl decreased the level of kidney's GGT activity in the hyperglycemic rats via vanadyls' antioxidant behavior during the oxidant and pro-oxidant diabetic conditions in the kidney tissue.

CA is a cytosolic enzyme that is responsible for the inter-conversion of CO_2 to HCO_3^- in many tissues of higher vertebrates. It is related to some processes such as gas swapping, ion carriage, and pH control (42). In metabolic diseases like DM and hypertension, the activity of CA is variable (43). It was reported that changed activity in erythrocyte CA can count as early evidence of altered DM metabolism (43). Similarly, in another study, it was noted that CA activity elevated twofold in the hyperglycemic liver due to its important function in providing substrate for hepatic gluconeogenesis and

ureagenesis (44). Consistent with previous research on different tissues, we also found a higher activity in diabetic kidney CA (9,10,15). The oral administration of vanadyl supplement reduced the activity of the enzyme in diabetic animals.

SOD is one of the most essential endogenous enzymes in the living organisms' antioxidant system, which scavenges the superoxide radicals by converting them into H_2O_2 and molecular oxygen. Overproduction of free radicals in damaged tissues may be a response to decreased or inhibited SOD activity (45). According to our results shown in Table 4, the hyperglycemic animals' kidney SOD activities demonstrated a significant decrease as compared to non treated rats. The treatment with VS enhanced the activity of SOD and that may assist in controlling diabetic rats' free radical levels (45).

Looking at the literature in general, the effect of vanadyl compounds on the kidney is a contentious issue. Some vanadyl compounds are nephrotoxic, even in therapeutic doses, but some articles support that some vanadyl compounds may improve diabetic kidney function because of its hypoglycemic potential (46-50). In our current and previous studies, we observed death in normal rats administered only VS. On the contrary, there was no such loss in diabetic animals given VS, and also, a healing effect on diabetic kidney tissue was observed. These findings show that VS may be a suitable oral anti-diabetic for the improvement of hyperglycemia if it is used in appropriate doses only in diabetic rats.

CONCLUSION

The present study showed that VS exerted insulin-mimic behavior and antioxidant properties that prevent kidney damage caused by diabetes. It has been observed previously that orally given vanadyl (IV) supplemention dramatically reduced STZ-induced blood glucose, improved AGEs formation, lipid peroxidation levels, some renal biomarkers, and renal histopathological damage. In the current research, we demonstrate that vanadyl treatment also alleviated activities of transaminases and ALP in diabetic rats' kidney tissue. Also, VS reduced the activities of GGT and CA, and increased antioxidant capability by inducing the activity of SOD in diabetic rats. Therefore, based on previous and current studies, we can say that the applicability of VS as a new anti-diabetic agent in the treatment of renal tissue damage with diabetic nephropathy would be appropriate. Further research into the functions of vanadyl and its different complexes will aid in the development of new substances to improve the treatment of diabetic nephropathy.

CONFLICT OF INTEREST

Authors declared no conflict of interest.

REFERENCES

1. Hu R, He C, Liu J, Wu Y, Li J, Feng Z, et al. Effects of insulin-mimetic vanadyl-poly(γ-glutamic acid) complex on diabetic rat model. Journal of Pharmaceutical Sciences. 2010 Jul;99(7):3041–7. <DOI>.

2. Akhtar M, Taha NM, Nauman A, Mujeeb IB, Al-Nabet ADMH. Diabetic kidney disease: Past and present. Advances in Anatomic Pathology. 2020 Mar;27(2):87–97. <DOI>.

3. Zhang P, Li T, Wu X, Nice EC, Huang C, Zhang Y. Oxidative stress and diabetes: antioxidative strategies. Frontiers of Medicine. 2020 Oct;14(5):583–600. <DOI>.

4. Tunali S, Yanardag R. Effect of vanadyl sulfate on the status of lipid parameters and on stomach and spleen tissues of streptozotocin-induced diabetic rats. Pharmacological Research. 2006 Mar;53(3):271–7. <DOI>.

5. Zafar M, Naqvi SN ul H. Effects of STZ-Induced diabetes on the relative weights of kidney, liver and pancreas in albino rats: a comparative study. International Journal of Morphology. 2010;28(1):135–42.

6. Heyliger CE, Tahiliani AG, McNeill JH. Effect of Vanadate on Elevated Blood Glucose and Depressed Cardiac Performance of Diabetic Rats. Science. 1985 Mar 22;227(4693):1474–7. <DOI>.

7. Tunali S, Gezginci-Oktayoglu S, Bolkent S, Coskun E, Bal-Demirci T, Ulkuseven B, et al. Protective effects of an oxovanadium(IV) complex with N2O2 chelating thiosemicarbazone on small intestine injury of STZ-Diabetic Rats. Biological Trace Element Research. 2021 Apr;199(4):1515–23. <DOI>.

8. Yanardag R, Demirci TB, Ülküseven B, Bolkent S, Tunali S, Bolkent S. Synthesis, characterization and antidiabetic properties of N1-2,4-dihydroxybenzylidene-N4-2-hydroxybenzylidene-S-methyl-thiosemicarbazidato-oxovanadium(IV). European Journal of Medicinal Chemistry. 2009 Feb;44(2):818–26. <DOI>.

9. Yilmaz-Ozden T, Kurt-Sirin O, Tunali S, Akev N, Can A, Yanardag R. Ameliorative effect of vanadium on oxidative stress in stomach tissue of diabetic rats. Bosnian Journal of Basic Medical Sciences. 2014 May;14(2):105–9. <DOI>.

10. Koyuturk M, Tunali S, Bolkent S, Yanardag R. Effects of Vanadyl Sulfate on Liver of Streptozotocin-Induced Diabetic Rats. Biological Trace Element Research. 2005;104(3):233–48. <DOI>.

11. Yuen VG, Caravan P, Gelmini L, Glover N, McNeill JH, Setyawati IA, et al. Glucose-lowering properties of vanadium compounds: Comparison of coordination complexes with maltol or kojic acid as ligands. Journal of Inorganic Biochemistry. 1997 Nov;68(2):109–16. <DOI>.

12. Ścibior A, Pietrzyk Ł, Plewa Z, Skiba A. Vanadium: Risks and possible benefits in the light of a comprehensive overview of its pharmacotoxicological mechanisms and multi-applications with a summary of further research trends. Journal of Trace Elements in Medicine and Biology. 2020 Sep;61:126508. <DOI>.

13. Bolkent S, Bolkent S, Yanardag R, Tunali S. Protective effect of vanadyl sulfate on the pancreas of streptozotocin-induced diabetic rats. Diabetes Research and Clinical Practice. 2005 Nov;70(2):103–9. <DOI>.

14. Tunali S, Yanardag R. The effects of vanadyl sulfate on glutathione, lipid peroxidation and nonenzymatic glycosylation levels in various tissues in experimental diabetes. Journal of the Faculty of Pharmacy of Istanbul University. 2021 Apr;51(1):73+. <URL>.

15. Tunali S, Peksel A, Arisan I, Yanardag R. Study of the beneficial effect of vanadium sulfate on the liver of experimental diabetic rats. Journal of the Faculty of Pharmacy of Istanbul University. 2020 Dec;50(3):211+. <URL>.

16. Yanardag R, Bolkent S, Karabulut-Bulan O, Tunali S. Effects of vanadyl sulfate on kidney in experimental diabetes. Biological Trace Element Research. 2003;95(1):73–86. <DOI>.

17. Junod A, Lambert AE, Stauffacher W, Renold AE. Diabetogenic action of streptozotocin: relationship of dose to metabolic response. The Journal of Clinical Investigation. 1969 Nov 1;48(11):2129–39. <DOI>.

18. Relander A, Räihä CE. Differences between the enzymatic and o-toluidine methods of blood glucose determination. Scandinavian Journal of Clinical and Laboratory Investigation. 1963 Jan;15(3):221–4. <DOI>.

19. Reitman S, Frankel S. A colorimetric method for the determination of serum glutamic oxalacetic and glutamic pyruvic transaminases. American Journal of Clinical Pathology. 1957;28(1):56–63.

20. Bergmeyer HU, Gawehn K, Walter K, Schütt C, editors. Acid and alkaline phosphatase in serum (two-point method). In: Methods of enzymatic analysis Volume 2 [Internet]. Weinheim; New York:

Verlag Chemie ; Academic Press; 1974 [cited 2022 May 3]. Available from: <URL>.

21. Szasz G. A kinetic photometric method for serum γ-glutamyl transpeptidase. Clinical Chemistry. 1969 Feb 1;15(2):124–36. <DOI>.

22. Verpoorte JA, Mehta S, Edsall JT. Esterase activities of human carbonic anhydrases B and C. Journal of Biological Chemistry. 1967 Sep;242(18):4221–9. <DOI>.

23. Mylroie AA, Collins H, Umbles C, Kyle J. Erythrocyte superoxide dismutase activity and other parameters of copper status in rats ingesting lead acetate. Toxicology and Applied Pharmacology. 1986 Mar;82(3):512–20. <DOI>.

24. Lowry OliverH, Rosebrough NiraJ, Farr AL, Randall RoseJ. Protein measurement with the folin phenol reagent. Journal of Biological Chemistry. 1951 Nov;193(1):265–75. <DOI>.

25. Krośniak M, Kowalska J, Francik R, Gryboś R, Blusz M, Kwiatek WM. Influence of vanadium–organic ligands treatment on selected metal levels in kidneys of STZ rats. Biological Trace Element Research. 2013 Jun;153(1–3):319–28. <DOI>.

26. Stumvoll M, Meyer C, Mitrakou A, Nadkarni V, Gerich JE. Renal glucose production and utilization: New aspects in humans. Diabetologia. 1997 Jun 24;40(7):749–57. <DOI>.

27. Kiersztan A, Modzelewska A, Jarzyna R, Jagielska E, Bryła J. Inhibition of gluconeogenesis by vanadium and metformin in kidney-cortex tubules isolated from control and diabetic rabbits. Biochemical Pharmacology. 2002 Apr;63(7):1371–82. <DOI>.

28. Fantus IG, Tsiani E. Multifunctional actions of vanadium compounds on insulin signaling pathways: Evidence for preferential enhancement of metabolic versus mitogenic effects. In: Srivastava AK, Posner BI, editors. Insulin Action [Internet]. Boston, MA: Springer US; 1998 [cited 2022 May 3]. p. 109–19. Available from: <URL>.

29. Li M, Ding W, Smee JJ, Baruah B, Willsky GR, Crans DC. Anti-diabetic effects of vanadium(III, IV, V)–chlorodipicolinate complexes in streptozotocin-induced diabetic rats. Biometals. 2009 Dec;22(6):895–905. <DOI>.

30. Crans DC. Chemistry and insulin-like properties of vanadium(IV) and vanadium(V) compounds. Journal of Inorganic Biochemistry. 2000 May;80(1–2):123–31. <DOI>.

31. Ishikawa E, Ogushi S, Ishikawa T, Uyeda K. Activation of mammalian phosphofructokinases by ribose 1,5-bisphosphate. Journal of Biological Chemistry. 1990 Nov;265(31):18875–8. <DOI>.

32. Ozaki I, Mitsui Y, Sugiya H, Furuyama S. Ribose 1,5-bisphosphate inhibits fructose-1,6-bisphosphatase in rat kidney cortex. Comparative Biochemistry and Physiology Part B: Biochemistry and Molecular Biology. 2000 Jan;125(1):97–102. <DOI>.

33. Rider MH, Bartrons R, Hue L. Vanadate inhibits liver fructose-2,6-bisphosphatase. European Journal of Biochemistry. 1990 May;190(1):53–6. <DOI>.

34. Rajesh MG, Latha MS. Preliminary evaluation of the antihepatotoxic activity of Kamilari, a polyherbal formulation. Journal of Ethnopharmacology. 2004 Mar;91(1):99–104. <DOI>.

35. Guo K, Zhang Y, Fang X, Fan P, Shang S, Fan F, et al. Effects of acute exposure to ultra-wideband pulsed electromagnetic fields on the liver and kidneys of mice. Electromagnetic Biology and Medicine. 2020 Apr 2;39(2):109–22. <DOI>.

36. Feilleux-Duche S, Garlatti M, Aggerbeck M, Poyard M, Bouguet J, Hanoune J, et al. Cell-specific regulation of cytosolic aspartate aminotransferase by glucocorticoids in the rat kidney. American Journal of Physiology-Cell Physiology. 1993 Nov 1;265(5):C1298–305. <DOI>.

37. Bover J, Ureña P, Aguilar A, Mazzaferro S, Benito S, López-Báez V, et al. Alkaline phosphatases in the complex chronic kidney disease-mineral and bone disorders. Calcified Tissue International. 2018 Aug;103(2):111–24. <DOI>.

38. Kwiatkowska E, Domański L, Bober J, Safranow K, Pawlik A, Kwiatkowski S, et al. Gamma-glutamyl transpeptidase as the marker of kidney graft function. Advances in Clinical and Experimental Medicine. 2014 Dec;23(6):947–52. <DOI>.

39. Wickham S, Regan N, West MB, Thai J, Cook PF, Terzyan SS, et al. Inhibition of human γ-glutamyl transpeptidase: development of more potent, physiologically relevant, uncompetitive inhibitors. Biochemical Journal. 2013 Mar 15;450(3):547–57. <DOI>.

40. Tate S, Meister A. Gamma-glutamyl transpeptidase from kidney. Methods in Enzymology. 1985;113:400–19.

41. Kobayashi S, Ikeda Y, Shigeno Y, Konno H, Fujii J. γ-Glutamylcysteine synthetase and γ-glutamyl transferase as differential enzymatic sources of γ-glutamylpeptides in mice. Amino Acids. 2020 Apr;52(4):555–66. <DOI>.

42. Gambhir KK, Ornasir J, Headings V, Bonar A. Decreased total carbonic anhydrase esterase activity

and decreased levels of carbonic anhydrase 1 isozyme in erythrocytes of type II diabetic patients. Biochemical Genetics. 2007 Jun 18;45(5–6):431–9. <DOI>.

43. Gambhir K, Oates P, Verma M, Temam S, Cheatham W. High fructose feeding enhances erythrocyte carbonic anhydrase 1 mRNA levels in rat. Annals of the New York Academy of Sciences. 1997;827(1):163–9.

44. Dodgson SJ, Watford M. Differential regulation of hepatic carbonic anhydrase isozymes in the streptozotocin-diabetic rat. Archives of Biochemistry and Biophysics. 1990 Mar;277(2):410–4. <DOI>.

45. M. Naglah A, Al-Omar MA, Almehizia AA, Obaidullah AJ, Bhat MA, Kalmouch A, et al. Synthesis, characterization, and anti-diabetic Aactivity of some novel vanadium-folate-amino acid materials. Biomolecules. 2020 May 18;10(5):781. <DOI>.

46. Espinosa-Zurutuza M, González-Villalva A, Albarrán-Alonso JC, Colín-Barenque L, Bizarro-Nevares P, Rojas-Lemus M, et al. Oxidative stress as a mechanism involved in kidney damage after subchronic exposure to vanadium inhalation and oral sweetened beverages in a mouse model. International Journal of Toxicology. 2018 Jan;37(1):45–52. <DOI>.

47. Liu J, Cui H, Liu X, Peng X, Deng J, Zuo Z, et al. Dietary high vanadium causes oxidative damage-induced renal and hepatic toxicity in broilers. Biological Trace Element Research. 2012 Feb;145(2):189–200. <DOI>.

48. Ávila-Casado M, Soto-Abraham V, López-Krauletz S, Fortoul T. Capítulo 7: The kidney and vanadium effects. Vanadium its impact on health; Fortoul, TI, Ávila-Acosta, MR, Eds. 2007;57–62.

49. Ścibior A, Gołębiowska D, Adamczyk A, Niedźwiecka I, Fornal E. The renal effects of vanadate exposure: potential biomarkers and oxidative stress as a mechanism of functional renal disorders—preliminary studies. BioMed Research International. 2014;2014:1–15. <DOI>.

50. Karalius VP, Shoham DA. Dietary sugar and artificial sweetener intake and chronic kidney disease: a review. Advances in Chronic Kidney Disease. 2013 Mar;20(2):157–64. <DOI>.

Ozkok F et al. JOTCSA. 2022; 9(3): 729-740.

RESEARCH ARTICLE

Evaluation of Acetyl- and Butyrylcholinesterase Enzyme Inhibitory Activities and Cytotoxic Activities of Anthraquinone Derivatives

Funda Ozkok[1] (ID) **, Mehmet Boga[2]** (ID) **, Muhammed Tuneg[2] , Vildan Enisoglu Atalay[3,4]** (ID) **,**
Nihal Onul[1]* (ID) **, Kamala Asgarova[1]** (ID) **, Rabia Tigli[4] , Sıla Arslan[4] , Dilan Akagunduz[4] ,**
Rumeysa Cebecioglu[4] , Tunc Çatal[3,4] (ID)

[1]Organic Chemistry Division, Department of Chemistry, Faculty of Engineering, Istanbul University-Cerrahpaşa, Avcılar, 34320, Istanbul, Turkey.
[2]Dicle University, Faculty of Pharmacy, Department of Analytical Chemistry, 21280, Diyarbakir, Turkey.
[3]Uskudar University, Faculty of Engineering and Natural Sciences, Department of Molecular Biology and Genetics, 34662, Uskudar, Istanbul, Turkey.
[4]Istanbul Protein Research-Application and Inovation Center (PROMER), Uskudar University 34662 Uskudar, Istanbul, Turkey.

Abstract: In this study, the enzyme activity of anthraquinone compounds which were synthesized beforehand by our research group was investigated. Molecular docking studies were performed for compounds 1-(4-aminophenylthio)anthracene-9,10-dione **(3)** and 1-(4-chlorophenylthio)anthracene-9,10-dione **(5).** Compound **3** was synthesized from the reaction of 1-chloroanthraquinone **(1)** and 4-aminothiophenol **(2).** Compound **5** was synthesized (1) from the reaction of 1-chloroanthraquinone **(1)** and 4-chlorothiophenol **(4).** Anthraquinone analogs **(3, 5)** were synthesized with a new reaction method made by our research group (2). Inhibitory effects of compounds **3** and **5** were investigated against acetylcholinesterase (AChE) and butyrylcholinesterase (BuChE) enzymes which are related to Alzheimer's Disease (AD). Compounds **3** and **5** exhibited strong anti-acetyl- and butyryl-cholinesterase inhibition activities than galanthamine used as standard compound (92.11±1.08 and 80.95±1.77 %, respectively). The E_{HOMO}-E_{LUMO} values, molecular descriptors, and the calculated UV-Vis spectra of anthraquinone derivatives were computed by B3LYP/6-31+G(d,p) levels in the $CHCl_3$ phase. Based on the fluorescence property of the anthraquinone skeleton, the fluorescence activity of the bioactive anthraquinone analogue (**5**) was investigated. MTT test was performed to determine the cytotoxic effects of thioanthraquinone molecules **3** and **5**. In MTT analyses, 3 compounds showed the highest effect against Ishikawa cells at a dose of 10 μg/mL, while compound **5** showed the highest effect at a dose of 50 μg/mL. The cell viability for compound **3** was 84.18% for 10 μg/mL and the cell viability for compound **5** was 75.02% for 50 μg/mL.

Ozkok F et al. JOTCSA. 2022; 9(3): 729-740.

RESEARCH ARTICLE

INTRODUCTION

Anthraquinones are cyclic compounds that have a class of conjugated cyclic diketones and play an active role due to electrochemical activity of main skeleton in biological and organic reactions. Anthraquinones and their analogs have applications in many areas such as medicine, pharmacy, chemistry, and material engineering (3-10). Anthraquinones can have estrogenic activity. In a study (11) with hydroxyl anthraquinones, Emodin compound having hydroxyl groups showed estrogenic activity. The discovery of important anti-cancer drugs such as Daunomycin, Adriamycin, and Mitoxantrone has led scientists to investigate anthraquinone and its derivatives that have an anti-cancer effect, especially biological activity (12-15). Damnacanthal, which is a natural bioactive compound isolated from phenolic phase of noni roots, may be found in Rubiaceae plants, too (16-17). Damnacanthal is defined as the most powerful selector inhibitor of p56Ick tyrosine kinase which is a protein activity that plays key role in chemotactic reaction of T cells to CXCL12 (18-19). Additionally, an active anthraquinone analogue, Damnacanthal, may also inhibit other tyrosine kinases (PDGFR, erbB2, EGFR and insulin receptor) in their IC50 values in micromolar concentration aperture (18). It was established in studies that Damnacanthal is also a powerful inhibitor of c-Met and acts as an antitumoral agent against hepatocellular carcinoma (20). Anthraquinone compounds, especially daunoribicin, doxorubicin, epirubicin and mitoxantrone, are the most effective clinical anticancer medications (21). Mitoxantrone, with its planar anthraquinone structure, is a clinically useful antineoplastic agent (22-28) SZ-685C, one of sea anthraquinone metabolites, represses human breast cancer and human nasopharyngeal carcinoma cells (29). Anthraquinones have high antitumor effect. They are responsible for conjunction of DNA double-helix to DNA, interactions via interpolation and decomposition, direct membrane effects, DNA damage, topoisomerase II inhibition, production of free radicals such as reactive oxygen species (ROS), apoptosis induction through topoisomerase inhibition and production of functional p53 and ROS. Additionally, anthraquinones trigger (c-Jun N terminal kinase) Akt / PKB (Protein Kinase B) through JNK and apoptosis through mitochondrial paths (29-35). Cholinesterase enzymes (acetyl and butyryl) in the central nervous system are responsible for the termination of cholinergic signaling by hydrolyzing the neurotransmitter acetylcholine (ACh). In the brain, decreased levels of ACh with the loss of cholinergic neurons leads to memory loss and progressive cognitive decline, which are common symptoms of Alzheimer's disease (AD) (36). Although the reason of AD is unknown, many studies have reported that ACh levels have been exhausted in patients suffering from AD. AChE and BuChE inhibition is an effective mechanism for the treatment of AD (37-38). According to the results of our literature review, there are several cholinesterase inhibitors namely galanthamine, rivastigmine, donepezil, and tacrine used for the treatment of AD. Therefore, the above mentioned drugs possess constricted efficacy, toxicity, and have unfavorable side effects such as diarrhea, vomiting, dizziness, hepatotoxicity, and nausea (39), so there is a need for more potent and highly efficient cholinesterase inhibitors for the treatment of AD. According to literature surveying, there are a few studies about anticholinesterase activity studies on anthraquinone compounds (40-43) but there is not any study about thioanthraquinone compounds except for the study of Tonelli et al. (44), in which only one thioanthraquinone compound was investigated for anticholinesterase activity. This study is important to examine the properties of anti-acetyl and butyrylcholinesterase inhibitory activities for thioanthraquinone compounds. In this study, synthesis was done via a method (2) that had been discovered by our team prior to this study, enzyme activities of anthraquinone analogs were examined and molecular docking studies of analogs were performed. Moreover, cytotoxicity studies of thioanthraquinone molecules were also conducted in the study.

MATERIALS AND METHODS

Chemistry

General
All chemicals were purchased from either Sigma-Aldrich or Merck. Solvents, unless otherwise specified, were of reagent grade and distilled once prior to use. Thin layer chromatography was performed on Merck (60 F 254) TLC-plates (aluminum-based). Melting points were measured on a Buchi B-540 apparatus and were uncorrected. Mass spectra were recorded on Shimadzu LCMS-8030 triple quadrupole spectrometer in ESI (+) polarity.

Synthesis

In this study, compounds **3** and **5** were synthesized in a previous study (1). Various bioactive amino- and thioanthraquinone analogues were synthesized in our previous studies (45-46). In this work, enzyme, *in silico* and *in vitro* study of these compounds were performed. Our target molecule 1-(4-chlorothiophenyl)-anthracene-9,10-dione (**3**) was obtained from reaction of starting material 1-aminoanthraquinone (**1**) and 1-(4-aminothio)phenol (**2**) according to a patent method (2). A yellowish reaction mixture was obtained at the end. 10 mL of aquous potassium hydroxide solution was added to this mixture, and the reaction temperature was raised to 120–130

°C. After reflux (48 h), an orange crystal thio-anthraquinone compound (**3**) was obtained. The new product (**3**) was extracted with chloroform (30 mL). The organic layer was washed with water and dried with calcium sulfate. The synthesized novel analogue (**3**) was purified by column chromatography. Another target molecule 1-(4-chlorophenylthio)anthracene-9,10-dione (**5**) was obtained from reaction of starting material 1-aminoanthraquinone (**1**) and 1-(4-chlorothio)phenol (**4**) according to a patent method (2). A yellowish reaction mixture was obtained at the end. 10 mL of aquous potassium hydroxide solution was added to this mixture, and

the reaction temperature was raised to 120–130 °C. After reflux (48 h), an orange crystal thio-anthraquinone compound (**3**) was obtained. The new product (**5**) was extracted with chloroform (30 mL). The organic layer was washed with water and dried with calcium sulfate. The synthesized novel analogues (**3**, **5**) were purified by column chromatography. The chemical structure of novel thio-anthraquinone compounds (**3, 5**) were characterized by spectroscopic methods such as FT-IR, NMR, MS, and (UV)–visible spectrophotometry. Synthesized analogs **3** and **5** were shown in Figure 1.
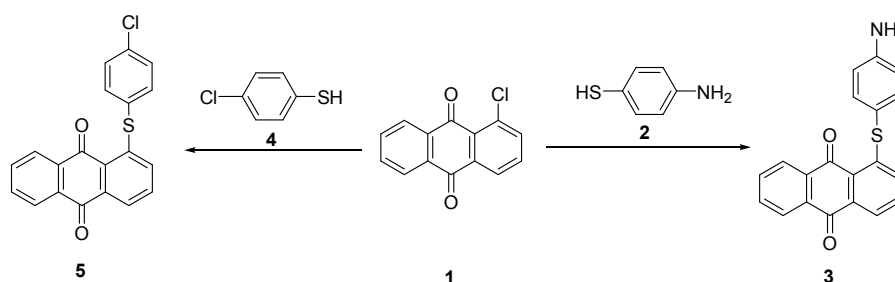
Figure 1: Illustrations of thioanthraquinone analogs in this study.

(**3**): Orange crystal, mp: 227-228 °C. Yield: 0.76 g (52%). Rf [Petroleum ether/chloroform (1:1)]: 0.43. IR (KBr, cm^{-1}): υ= 3021, 2913 (C-Harom), 1594 (C=C), 1647 (C=O). UV-vis(CHCl$_3$): λmax (logε)= 3.79 (427 nm), 4 (302 nm), 4.63 (247 nm). ^{1}H NMR (499.74 MHz, CDCl$_3$): δ= 7.29-8.17 (m, 4H, Harom). ^{13}C NMR (125.66 MHz, CDCl$_3$): δ= 123.27, 125.95, 126.47, 127.21, 129.33, 129.53, 130.69, 131.64, 131.92, 132.87, 133.38, 134.14, 135.30, 136.10, 136.34, 144.69 (C$_{arom}$ and CH$_{arom}$), 181.93 (C=O). C$_{20}$H$_{11}$O$_2$SCl, (M, 350.82 g/mol).

(**5**): Red solid, mp: 208-209 °C. Yield: 0.78 g (57%). Rf [Petroleum ether/chloroform (1:1)]: 0.48. IR (KBr, cm^{-1}): υ= 2923, 2852 (C-Harom), (C=C), (C=O). UV-Vis (CHCl$_3$): λmax (logε)= 3.77 (430 nm), 4.04 (303 nm), 4.71 (249 nm). ^{1}H NMR (499.74 MHz, CDCl$_3$): δ= 6.69-6.71 (m, 4H, Harom), 7.09-8.30 (m, 7H, Harom). ^{13}C NMR (125.66 MHz, CDCl$_3$): δ= 125.83, 126.46, 127.79,

130.76, 131.62, 131.67, 132.64, 133.07, 133.27, 134.09, 136.11, 136.59, 147.10, 147.32 (C$_{arom}$ and CH$_{arom}$), 182.23 (C=O). C$_{20}$H$_{13}$NO$_2$S, (M, 331.39 g/mol).

Fluorescence Analysis

In this study, fluorescent spectra for **5** have been investigated. Anthraquinone skeleton as a rigid structure is very effective in fluorescent behavior of compound **5**. There is a π-bond delocalization in aromatic thiosubstituted anthraquinone structure. Additionally, carbonyl groups in the structure of molecules are strong withdrawing groups. Aromatic thiosubstituted group in compound **5** amplifies fluorescence aspect of anthraquinone. In the fluorescence spectrum of **5**, excitation and emission wavelengths were observed at 435 nm (λ$_{exc.}$) and 683 nm (λ$_{em.}$), respectively. Fluorescence spectrum of thiosubstituted anthraquinone compound **5** is shown in Figure 2.

Figure 2: Excitation (left) and emission spectrum (right) of **5** (2.0×10^{-3} M) in $CHCl_3$ solution.

Anticholinesterase activity

The acetyl-cholinesterase and butyryl-cholinesterase inhibitory activities of the compounds **3** and **5** were tested by using a slightly modified Ellman method (47). Acetylthiocholine iodide (or butyrylthiocholine iodide) was used as substrate of the reaction and DTNB (5,5'dithiobis nitrobenzoic acid) was used for the measurement of the anticholinesterase activity. Galanthamine was used as the standard drug. 130 µL of sodium phosphate buffer (pH 8.0), 10 µL of 4 mM sample solution and 20 µL of AChE (or BChE) solution were mixed in each well and incubated for 15 min at 25 °C. The reaction was then initiated by the addition of 10 µL of DTNB and 10 µL of acetylthiocholine iodide (or butyrylthiocholine iodide). Final concentration of the tested solutions was 200 µg/mL. The hydrolysis of these substrates was monitored using microplate ELISA reader XS by the formation of yellow 5-thio-2-nitrobenzoate anion as the result of the reaction of DTNB with thiocholine, released by the enzymatic hydrolysis of acetylthiocholine iodide or butyrylthiocholine iodide, at a wavelength of 412 nm.

$$\%\text{Inhibition} = (A_{Cont} - A_{Sample})/A_{Cont} \times 100,$$

where A_{Cont} is the absorbance of the control and A_{Sample} is the absorbance in the presence of the sample

Cell Culture

Preparation of the extracts of compounds 3 and 5

To prepare 10 mg/mL concentration of compound **3** and **5**, 10 mg of the compounds were weighed and transferred into a sterile Eppendorf and 1 mL of 100% methanol (CH_3OH) was added into the tube. This mixture was dissolved by an ultrasonicator at 65 °C for 15 minutes and vortexed for 2 minutes and this process was repeated 3 times. The stock solutions of compounds **3** and **5** were prepared in this way. After the stock solutions, doses were prepared for MTT Assay by serial dilution methods such as 500 µg /mL, 100 µg /mL, 50 µg /mL, 10 µg /mL, 5 µg /mL and 1 µg /mL with serum-free medium.

Human endometrial adenocarcinoma cell line (Ishikawa) and human endothelial cell line (ECV304) were used in the study. The cells were cultured in DMEM medium (Gibco, 11960044, UK) supplemented with 10% of fetal bovine serum (Gibco), 1% penicillin/streptomycin, and L-glutamate at 37 °C in a humidified atmosphere of 5% CO_2. Ishikawa cells and ECV 304 were grown in 35-mm culture dishes for 24 h before the experiments. Cells were diluted to 10^5 cells /mL with Gibco DMEM (1x) medium.
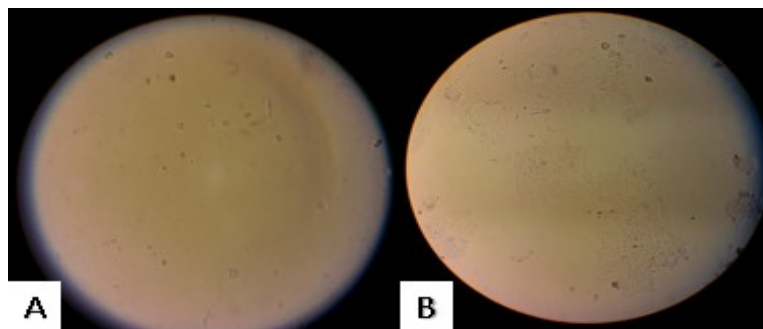
Figure 3 (A): Microscopic view of Ishikawa (x10*).*   **Figure 3 (B):** Microscopic view of ECV 304 (x10).

Cytotoxicity Assay

To determine the cytotoxic effect of **3** and **5** extracts on the cells' MTT assay ((3- (4,5-dimethyl thiazole-2-yl)-2,5-diphenyl tetrazolium bromide), 90 μL of cell- medium with serum mixture was added to have 9000 cells in each well within Nest 96 Well Plate. The 96 Well Plate is incubated at 37 °C and 5% CO_2 for 24 hours. After this period, 10 μL of **3** and **5** solutions in different concentrations that were suitable for each well were added. The 96 Well Plate is incubated at 37 °C and 5% CO_2 for 24 hours. After 24 hours, 10 μL of MTT (Invitrogen, Cat No: M6494). Solution with stock concentration 5 mg/mL and prepared in sterile PBS was added to each well. The 96 Well Plate is incubated at 37 °C and 5% CO_2 for 3 hours, after which 90 μL was discarded from the wells without touching the cells and 100 μL 50% DMSO (VWR, Cat No: 23500.322)- 50% Isopropanol (VWR, Cat No: 20842.323) was added on each well. The surface of the 96 Well Plate was covered with aluminum foil. The 96 Well Plate was left at room temperature for 45 minutes. Then, 96 Well Plate was measured at 570 nm with a spectrophotometer. Cytotoxicity index (CI) was calculated to following formula;

CI %(Cytotoxicity index) = 1- OD treated wells / OD control wells X 100

Computational Methods

The conformer analysis of synthesized compounds were performed to find the stable structures with a semi-empirical PM6 method (48-49) using the program Spartan'16 v1.1.4 (Spartan'16 Wavefunction, Inc. Irvine, CA.). The calculated most stable structures were optimized with a semi-empirical PM6 method, for the better geometries optimized structures made *re*-optimize and were obtained UV-Vis Spectra with the Density Functional Theory (DFT) B3LYP (Becke's Three

Parameter Hybrid Functional using the Lee, Yang and Parr Correlation Functional) (50) with the 6-31+G(d,p) method in the gas and $CHCl_3$ phases with the IEF-PCM approach (51).

The E_{HOMO}-E_{LUMO} were calculated using time-dependent density functional theory (TD-DFT) at the B3LYP/6-31+G(d,p) levels in $CHCl_3$ phase, which was done by using the Self-Consistent Reaction Field (SCRF) method. At the same time molecular descriptors such as electronegativity (χ), electron affinity (*A*), hardness (η), softness (*S*), electrophilicity index (ω) must be defined by the same computational methods. There is a practical calculation method to calculate for chemical hardness (η) and electronegativity (χ) (Eq. 1), as given by Parr and Pearson (52-53).

$$\eta \approx (I-A)/2 \qquad x \approx (I+A)/2 \quad \text{(Eq. 1)}$$

where *I* is the ionization potential and *A* is the electron affinity. The Koopman's theorem was used for the calculation of *I* and *A* values derived from the frontier orbital energies of optimized neutral molecules, according to this theorem $I = -E_{HOMO}$ and $A = -E_{LUMO}$. Using Koopman's theorem, the chemical hardness and electronegativity are defined in terms of orbital energies (Eq. 2):

$$\eta \approx (E_{LUMO} - E_{HOMO})/2$$
$$x = -\mu \approx -(E_{LUMO} - E_{HOMO})/2 \quad \text{(Eq. 2)}$$

The ω and *S* values are calculated by the following Eq. 3:

$$\omega \approx \mu^2/2\eta, \qquad S \approx 1/(2\eta) \quad \text{(Eq. 3)}$$

All visualizations and calculations were carried out with the methods implemented in GaussView5.0 (54) and Gaussian 09 package (55)
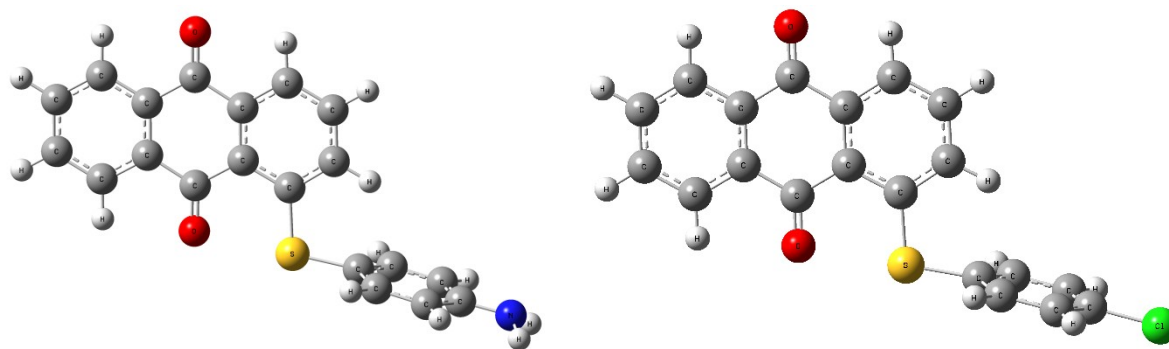
Figure 4: Optimized structures of the synthesized anthraquinone derivatives: **3** (left), **5** (right).

RESULTS

Chemistry
Characterization of synthesized compounds
1-(4-Aminothiophenyl)-anthracene-9,10-dione (3): M.p: 187-188 °C
1-(4-Chlorothiophenyl)-anthracene-9,10-dione (5): M.p: 192-193 °C

Biochemical results
Enzyme Activity
The acetylcholinesterase (AChE) and butyrylcholinesterase (BChE) enzyme inhibitory activities were evaluated for the determination of the therapeutic potential of the compounds **3** and **5** for the treatment of Alzheimer's disease (AD). The inhibition of AChE and BChE were given as percentage at 200 μg/mL concentration in Table 1 and compared with the galanthamine which is used as a standard drug. Compounds **3** and **5** demonstrated strong anti-acetyl and anti-butyrylcholinesterase activities better than galanthamine. While the galanthamine showed 80.03±1.04 and 84.54±0.39%, acetyl and butyrylcholinesterase inhibition, respectively, compound **5** exhibited 80.95±1.77 and 93.67±1.01% inhibition. Compound **3** is stronger than compound **5** and galanthamine with 92.11±1.04 inhibition against acetylcholinesterase enzyme. Also compound **3** showed weak butyrylcholinesterase inhibitory activity.

Table 1. Enzyme inhibition activities of samples and standard compound.

| Samples | Inhibition %[a] | |
	AChE	BChE
3	92.11±1.08	35.25±0.36
5	80.95±1.77	93.67±1.01
Galantamine[b]	80.03±1.04	84.54±0.39

[a] 200 μg/mL
[b] Standard compound
NA: Not Active

In the study of Tonelli et al. (44), only one thioanthraquinone compound named 1-{[(1R,9aR)-(octahydro-2H-quinolizin-1-yl)methyl]thio}-9,10-anthraquinone, was synthesized and investigated for its anticholinesterase activities. This compound showed moderate inhibitory activity against acetyl and butyrylcholinesterase enzymes with IC$_{50}$:3.6 μM and 3.4 μM values, respectively. Therefore, there is no literature about anticholinesterase activity of thioanthraquinone compounds except for the study of Tonelli et al. (44) presented study is very important in this respect.

In vitro
MTT Assay was applied to the cells with methanol (CH$_3$OH) extract prepared from compound **3** and compound **5** with a stock concentration of 10 mg/mL. As cell lines, Vessel Endothelial Cell Line ECV304 and Human Endometrial Adenocarcinoma Cell Line Ishikawa were used.
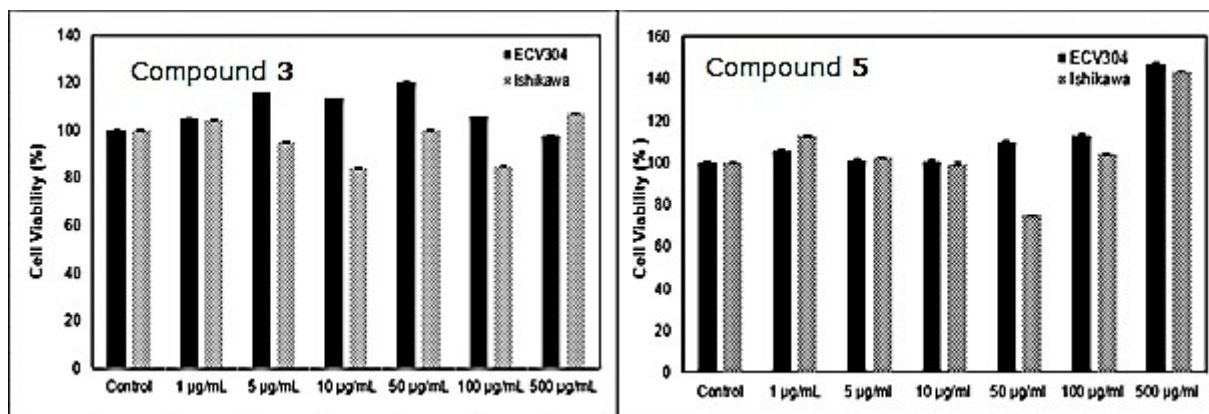
Figure 5: MTT Assay Results of **3** and **5**.

According to these results, the cell viability of **3** on ECV304, the healthy cell line of Methanol (CH_3OH) extract was calculated as 105.02% at 1 µg /mL dose and 97.69% at 500 µg /mL dose. On the cancer cell line Ishikawa, it was calculated as 104.43% at 1 µg /mL dose and 106.92% at 500 µg /mL dose. According to MTT Assay results, **3** was determined as at 10 µg/mL dose was the most effective on Ishikawa and cell viability at this dose was measured as 84.18%. Also, at 50 µg/mL dose was the most effective on ECV304 and cell viability at this dose was measured as 120.20%. The cell viability of compound **5** on ECV304, the healthy cell line of Methanol (CH_3OH) extract was calculated as 105.45% at 1 µg /mL dose and 147.14% at 500 µg /mL dose. On the cancer cell line Ishikawa, It was calculated as 112.79% at 1 µg /mL dose and 143.52% at 500 µg /mL dose. According to MTT Assay results, **3** was determined as at 10 µg/mL dose and **5** was determined as at 50 µg/mL was the most effective on Ishikawa. Cell viability at 10 µg/mL dose was measured as 84.18% and cell viability at 50 µg/mL dose was measured as 75.02%. Compound **3** was determined as at 50 µg/mL dose and compound **5** was determined as at 500 µg/mL was the most effective on ECV304. Cell viability at 50 µg/mL dose was measured as 120.20% and cell viability at 500 µg/mL dose was measured as 147.14%.

DISCUSSION

In this study, which aims to determine and analyze the synthesized compounds by quantum chemical methods. The HOMO-LUMO distribution and bandgap values for synthesized compounds were calculated by theoretical methods gathered in gas and $CHCl_3$ phases (Figure 6). The E_{HOMO}-E_{LUMO} are responsible to ionization potential and electron affinity. The energy values, E_{HOMO}-E_{LUMO} bandgap, and distribution of the HOMO-LUMO are a crucial point of stability for the molecules. The small band gap points to the compound called polarized and soft molecule. For the studied molecules, the HOMO's are mainly localized on the sulfur and surrounding atoms, whereas the LUMO's are distributed within the cyclic structures of the molecule. This means that the aromatic group in the molecule would be more easily attacked. The other important result is solvent effect, the E_{HOMO}-E_{LUMO} bandgaps for the studied **3** and **5** molecules in the $CHCl_3$ phase are 0.10512 and 0.11962 eV, respectively, are smaller than in the gas phase. The results depicts that the molecules in the solvent have a stronger electron donating ability.
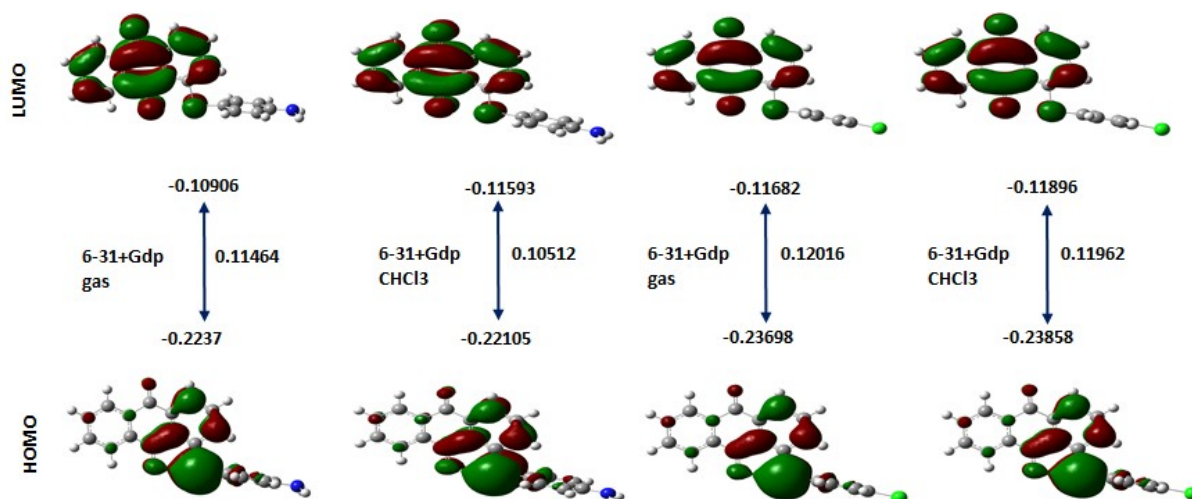
Figure 6: E_{HOMO} and E_{LUMO} levels along with bandgap values (eV) in the gas and CHCl$_3$ phases obtained by TD-DFT//B3LYP/6-31+G(d, p) method of the studied compounds.

Molecular identifier values obtained from the total energy for the **3** and **5** molecules in gas and CHCl$_3$ solvents are listed in Figure 6. The η is one-half the HOMO–LUMO gap of the molecules, the meaning is the larger gap the greater hardness and stability. This property is therefore a powerful identifier that hard molecules are less reactive than softer molecules. Table 2 shows that hardness is affected by solvent, the molecules **3** and **5** have larger hardness value in when dissolved in CHCl$_3$, as hard molecules are less reactive than softer molecules (56); the stability order is therefore CHCl$_3$>gas phase. Low chemical potentials for the molecules are causing a good electrophile, while an extremely hard molecules have feeble electron acceptability. Electrophilicity depends on both the chemical potential and hardness (57) The obtained χ and ω values show that the polar solvent contributes to accentuate the parametric representation of activity. We observed in this study and our previous studies (58-59) that solvent phase and selection have a considerable effect on electrophile/nucleophile interactions.

Table 2: Calculated Molecular identifier, E_{HOMO} and E_{LUMO} as well as band gap energy (eV) values of the studied compounds by TD-DFT//B3LYP/6-31+G (d, p) method in gas and CHCl$_3$ phases.

Compound	Solvent	Molecular Descriptors								
		E_{HOMO}	E_{LUMO}	ΔE	A	I	η	χ	ω	S
3	Gas	-0.2237	-0.1091	0.1146	0.2237	0.1091	-0.0573	0.1664	-0.2415	-8.7229
	CHCl$_3$	-0.2211	-0.1159	0.1051	0.2211	0.1159	-0.0526	0.1685	-0.2701	-9.5129
5	Gas	-0.2369	-0.1168	0.1202	0.2369	0.1168	-0.0601	0.1769	-0.2604	-8.3222
	CHCl$_3$	-0.2386	-0.1189	0.1196	0.2386	0.1189	-0.0598	0.1787	-0.2672	-8.3598

The calculated UV-Vis spectra for **3** and **5** molecules with the DFT//B3LYP/6-31+G(d,p) method in the gas and CHCl$_3$ phases are given in Figure 7 below. The Figure 7 depicted that the excitation energies are effected by solvent phase, an average energy shifts were calculated for each molecule.

Ozkok F et al. JOTCSA. 2022; 9(3): 729-740.

RESEARCH ARTICLE

Compounds

Phase	3	5
Gas	Excitation Energy(nm): 470.44 Oscillatory Strength: 0.0001	Excitation Energy(nm): 417.37 Oscillatory Strength: 0
CHCl$_3$	Excitation Energy(nm):514.18 Oscillatory Strength: 0	Excitation Energy(nm): 456.39 Oscillatory Strength: 0.1664
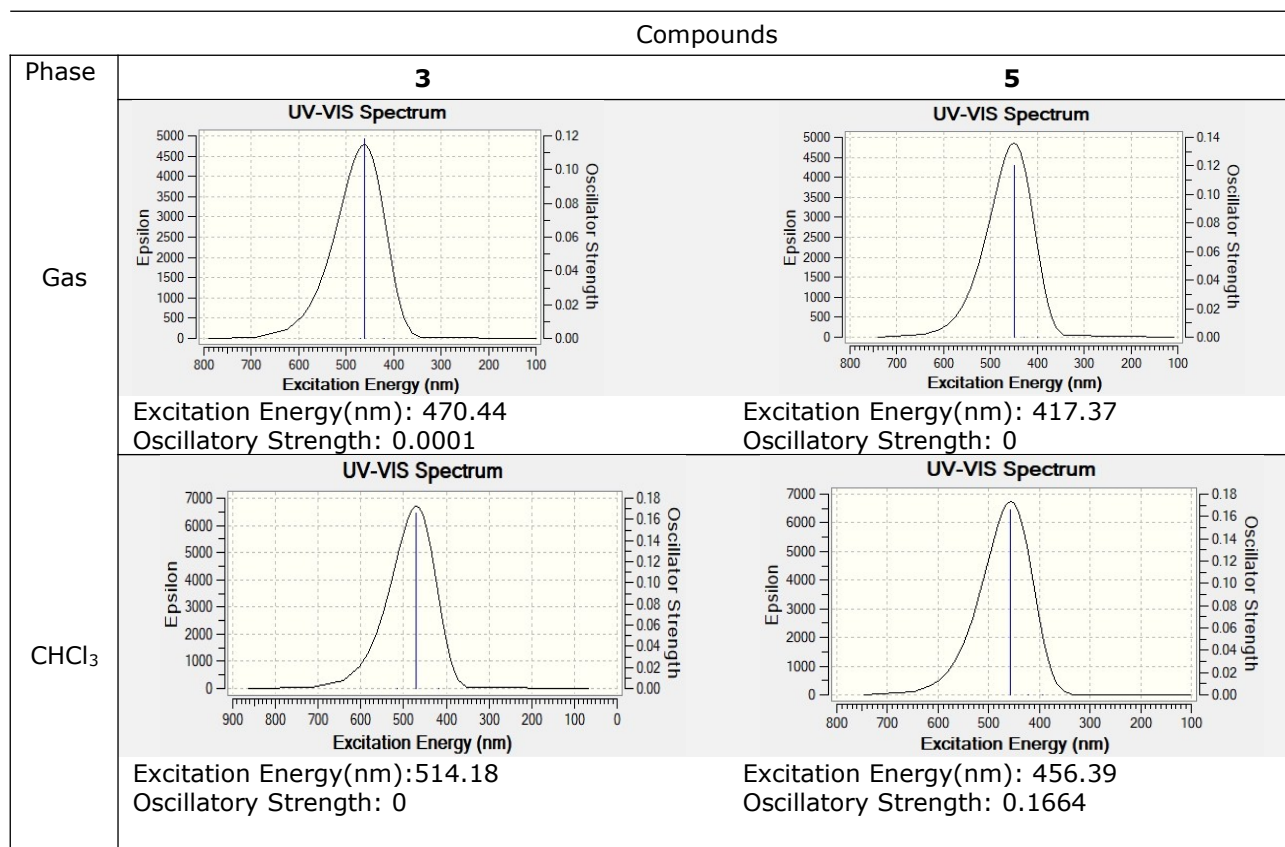
Figure 7: Calculated UV-VIS spectra for **3** and **5** molecules.

CONCLUSIONS

The investigated compounds having anthracene-9,10-dione skeletal structure showed very good anti-Alzheimer's activity, the potential of being drug candidates for anti-Alzheimer's treatment of compounds **3** and **5** and the same skeletal structures should be explored in more detail. Although compounds **3** and **5** did not show any significant results on Ishikawa, the dose of compound **3** at a concentration of 10 µg/ mL increased the cytotoxic level. Also, the dose of compound **5** at a concentration of 50 µg/ mL increased the cytotoxic level. The dose of compound **3** at a concentration of 50 µg/mL and the dose of compound **5** at a concentration of 500 µg/mL on ECV304 increased proliferation. The value of the E$_{HOMO}$, E$_{LUMO}$ and band gap energies produce a crucial information about investigated compounds in the gas and CHCl$_3$ phases. **3** compound is determined more stable molecule than **5** according to the E$_{HOMO}$-E$_{LUMO}$ bandgap (0.1051 eV) in the CHCl$_3$, indicating that the molecule in CHCl$_3$ solvent has stronger electron donating ability. Thioanthraquinone analogs compound **3** and **5** showed remarkable biological activity results. Thioanthraquinone derivatives formed via reaction of anthraquinones and thiols are very limited in the literature. Within this scope, when both the specificity of and the biological activity potential of thioanthraquinone compounds are taken into consideration, these may be expected to be a good medication molecule candidate.

ACKNOWLEDGMENTS

CONFLICT OF INTERESTS

The authors declare that there are no conflict of interests.

REFERENCES

1. Haciosmanoglu E, Ozkok F, Onsu AK, Bektas M, Varol B, Pehlivan S. Synthesis of New Anthraquinone Derivatives and Anticancer Effects on Breast Cancer Cell Lines. Eurasia Proc Sci Technol Eng Math. 2018 Dec 4; (4):271–6.

2. Ozkok F, Sahin YM. BİYOAKTİF ANTRAKİNON ANALOGLARI VE BUNLARIN SENTEZİNE YÖNELİK METOT. 2016/19610. p. https://portal.turkpatent.gov.tr/anonim/arastirma/patent/dosya-takibi.

Ozkok F et al. JOTCSA. 2022; 9(3): 729-740.

RESEARCH ARTICLE

3. Kshirsagar AD, Panchal PV, Harle UN, Nanda RK, Shaikh HM. Anti-Inflammatory and Antiarthritic Activity of Anthraquinone Derivatives in Rodents. Int J Inflamm. 2014;2014:1–12.

4. DemiRezer LO, Uzun M, Ozenver N, Guvenalp Z. Determination of Phytoestrogenic Potential of Anthranoids by Molecular Docking Studies. :1.

5. Aulenta F, Ferri T, Nicastro D, Majone M, Papini MP. Improved electrical wiring of microbes: anthraquinone-modified electrodes for biosensing of chlorinated hydrocarbons. New Biotechnol. 2011 Dec;29(1):126–31.

6. Kang D, White RJ, Xia F, Zuo X, Vallée-Bélisle A, Plaxco KW. DNA biomolecular-electronic encoder and decoder devices constructed by multiplex biosensors. NPG Asia Mater. 2012 Jan;4(1):e1–e1.

7. Mariappan K, Basa PN. Coordination polymers of 1,8-bis(2-methylthioethoxy)anthraquinone and 1,5-bis(2-methylthioethoxy)anthraquinone with Ag(I): Synthesis and X-ray crystallography. Inorganica Chim Acta. 2011 Jan;366(1):344–9.

8. Chang M-Y, Tai H-Y. Synthesis of 2-substituted 9,10-anthraquinones. Synth Commun. 2013 Dec 17;43(24):3363–72.

9. Jarrahpour A, Ebrahimi E, Khalifeh R, Sharghi H, Sahraei M, Sinou V, et al. Synthesis of novel β-lactams bearing an anthraquinone moiety, and evaluation of their antimalarial activities. Tetrahedron. 2012 Jun;68(24):4740–4.

10. Liang D, Su Z, Tian W, Li J, Li Z, Wang C, et al. Synthesis and screening of novel anthraquinone–quinazoline multitarget hybrids as promising anticancer candidates. Future Med Chem. 2020 Jan;12(2):111–26.

11. Li F, Li X, Shao J, Chi P, Chen J, Wang Z. Estrogenic Activity of Anthraquinone Derivatives: In Vitro and In Silico Studies. Chem Res Toxicol. 2010 Aug 16;23(8):1349–55.

12. Dimarco A, Gaetani M, Orezzi P, Scarpinato BM, Silvestrini R, Soldati M, et al. "DAUNOMYCIN", A NEW ANTIBIOTIC OF THE RHODOMYCIN GROUP. Nature. 1964 Feb 15;201:706–7.

13. White RichardJ, Durr FrederickE. Development of mitoxantrone. Invest New Drugs [Internet]. 1985 [cited 2021 Jul 11];3(2). Available from: http://link.springer.com/10.1007/BF00174154

14. Hua DH, Lou K, Havens J, Perchellet EM, Wang Y, Perchellet J-P, et al. Synthesis and in vitro antitumor activity of substituted anthracene-1,4-diones. Tetrahedron. 2004 Nov;60(45):10155–63.

15. Cairns D, Michalitsi E, Jenkins TC, Mackay SP. Molecular Modelling and Cytotoxicity of Substituted Anthraquinones as Inhibitors of Human Telomerase. Bioorg Med Chem. 2002 Mar;10(3):803–7.

16. Kanokmedhakul K, Kanokmedhakul S, Phatchana R. Biological activity of Anthraquinones and

Triterpenoids from Prismatomeris fragrans. J Ethnopharmacol. 2005 Sep;100(3):284–8.

17. Singh DN, Verma N, Raghuwanshi S, Shukla PK, Kulshreshtha DK. Antifungal anthraquinones from Saprosma fragrans. Bioorg Med Chem Lett. 2006 Sep;16(17):4512–4.

18. Faltynek CR, Schroeder J, Mauvais P, Miller D, Wang S, Murphy D, et al. Damnacanthal Is a Highly Potent, Selective Inhibitor of p56lck Tyrosine Kinase Activity. Biochemistry. 1995 Sep 26;34(38):12404–10.

19. Inngjerdingen M, Torgersen KM, Maghazachi AA. Lck is required for stromal cell–derived factor 1₋ (CXCL12)–induced lymphoid cell chemotaxis. 2002;99(12):8.

20. García-Vilas JA, Quesada AR, Medina MA. Damnacanthal, a noni anthraquinone, inhibits c-Met and is a potent antitumor compound against Hep G2 human hepatocellular carcinoma cells. Sci Rep. 2015 Jul;5(1):8021.

21. Weiss RB. The anthracyclines: will we ever find a better doxorubicin? Semin Oncol. 1992 Dec;19(6):670–86.

22. Randall K.Johnson. Experimental Antitumor Activity of Aminoanthraquinones.

23. Cheng CC, Zee-Cheng RKY, Narayanan VL, Ing RB, Pauli KD. The collaborative development of a new family of antineoplastic drugs. Trends Pharmacol Sci. 1981;2:223–4.

24. Cotter FE. Therapeutic milestones. Novantrone (mitozantrone). Br J Clin Pract. 1988 May;42(5):207–9.

25. Amadori S, Meloni G, Petti MC, Papa G, Miniero R, Mandelli F. Phase II trial of intermediate dose ARA-C (IDAC) with sequential mitoxantrone (MITOX) in acute myelogenous leukemia. Leukemia. 1989 Feb;3(2):112–4.

26. Satyamoorthy K, Chitnis MP, Pradhan SG, Advani SH. Modulation of Mitoxantrone Cytotoxicity by Verapamil in Human Chronic Myeloid Leukemia Cells. Oncology. 1989;46(2):128–31.

27. Durr FE, Wallace RE, Citarella RV. Molecular and biochemical pharmacology of mitoxantrone. Cancer Treat Rev. 1983 Dec;10:3–11.

28. Hoff DDV, Coltman CA, Forseth B. Activity of Mitoxantrone in a Human Tumor Cloning System. 1981;4.

29. Xie G, Zhu X, Li Q, Gu M, He Z, Wu J, et al. SZ-685C, a marine anthraquinone, is a potent inducer of apoptosis with anticancer activity by suppression of the Akt/FOXO pathway: SZ-685C induces apoptosis and inhibits tumour growth. Br J Pharmacol. 2010 Feb;159(3):689–97.

30. Zhu X, He Z, Wu J, Yuan J, Wen W, Hu Y, et al. A Marine Anthraquinone SZ-685C Overrides Adriamycin-Resistance in Breast Cancer Cells through Suppressing Akt Signaling. Mar Drugs. 2012 Mar 23;10(12):694–711.

31.   Huang H-S, Chiou J-F, Fong Y, Hou C-C, Lu Y-C, Wang J-Y, et al. Activation of Human Telomerase Reverse Transcriptase Expression by Some New Symmetrical Bis-Substituted Derivatives of the Anthraquinone. J Med Chem. 2003 Jul 1;46(15):3300–7.

32.   Gewirtz D. A critical evaluation of the mechanisms of action proposed for the antitumor effects of the anthracycline antibiotics adriamycin and daunorubicin. Biochem Pharmacol. 1999 Apr;57(7):727–41.

33.   Minotti G, Menna P, Salvatorelli E, Cairo G, Gianni L. Anthracyclines: Molecular Advances and Pharmacologic Developments in Antitumor Activity and Cardiotoxicity. Pharmacol Rev. 2004 Jun;56(2):185–229.

34.   Laurent G, Jaffrézou J-P. Signaling pathways activated by daunorubicin. Blood. 2001 Aug 15;98(4):913–24.

35.   Wang J, Duncan D, Shi Z, Zhang B. WEB-based GEne SeT AnaLysis Toolkit (WebGestalt): update 2013. Nucleic Acids Res. 2013 Jul 1;41(W1):W77–83.

36.   Scarpini E, Cogiamanian F. Alzheimer's disease: from molecular pathogenesis to innovative therapies. Expert Rev Neurother. 2003 Sep;3(5):619–30.

37.   Stellenboom N. Comparison of the inhibitory potential towards carbonic anhydrase, acetylcholinesterase and butyrylcholinesterase of chalcone and chalcone epoxide: STELLENBOOM. J Biochem Mol Toxicol. 2019 Feb;33(2):e22240.

38.   Ali TB, Schleret TR, Reilly BM, Chen WY, Abagyan R. Adverse Effects of Cholinesterase Inhibitors in Dementia, According to the Pharmacovigilance Databases of the United-States and Canada. Cavalli A, editor. PLOS ONE. 2015 Dec 7;10(12):e0144337.

39.   Lolak N, Akocak S, Türkeş C, Taslimi P, Işık M, Beydemir Ş, et al. Synthesis, characterization, inhibition effects, and molecular docking studies as acetylcholinesterase, α-glycosidase, and carbonic anhydrase inhibitors of novel benzenesulfonamides incorporating 1,3,5-triazine structural motifs. Bioorganic Chem. 2020 Jul;100:103897.

40.   Augustin N, Nuthakki VK, Abdullaha Mohd, Hassan QP, Gandhi SG, Bharate SB. Discovery of Helminthosporin, an Anthraquinone Isolated from Rumex abyssinicus Jacq as a Dual Cholinesterase Inhibitor. ACS Omega. 2020 Jan 28;5(3):1616–24.

41.   Zengin G, Degirmenci N, Alpsoy L, Aktumsek A. Evaluation of antioxidant, enzyme inhibition, and cytotoxic activity of three anthraquinones (alizarin, purpurin, and quinizarin). Hum Exp Toxicol. 2016 May;35(5):544–53.

42.   Hong C, Luo W, Yao D, Su Y-B, Zhang X, Tian R-G, et al. Novel aromatic–polyamine conjugates as cholinesterase inhibitors with notable selectivity toward butyrylcholinesterase. Bioorg Med Chem. 2014 Jun;22(12):3213–9.

43.   Lee Y, Bang H, Oh J, Whang W. Bioassay-Guided Isolated Compounds from Morinda officinalis Inhibit Alzheimer's Disease Pathologies. Molecules. 2017 Sep 29;22(10):1638.

44.   Tonelli M, Catto M, Tasso B, Novelli F, Canu C, Iusco G, et al. Multitarget Therapeutic Leads for Alzheimer's Disease: Quinolizidinyl Derivatives of Bi- and Tricyclic Systems as Dual Inhibitors of Cholinesterases and β-Amyloid (Aβ) Aggregation. ChemMedChem. 2015 Jun;10(6):1040–53.

45.   Celik S, Ozkok F, Ozel AE, Müge Sahin Y, Akyuz S, Sigirci BD, et al. Synthesis, FT-IR and NMR characterization, antimicrobial activity, cytotoxicity and DNA docking analysis of a new anthraquinone derivate compound. J Biomol Struct Dyn. 2020 Feb 11;38(3):756–70.

46.   Ozkok F, Sahin YM, Enisoglu Atalay V, Asgarova K, Onul N, Catal T. Sensitive detection of iron (II) sulfate with a novel reagent using spectrophotometry. Spectrochim Acta A Mol Biomol Spectrosc. 2020 Oct;240:118631.

47.   Bingul M, Şenkuytu E, Saglam MF, Boga M, Kandemir H, Sengul IF. Synthesis, photophysical and antioxidant properties of carbazole-based bis-thiosemicarbazones. Res Chem Intermed. 2019 Sep;45(9):4487–99.

48.   Stewart JJP. Application of the PM6 method to modeling the solid state. J Mol Model. 2008 Jun;14(6):499–535.

49.   Stewart JJP. Application of the PM6 method to modeling proteins. J Mol Model. 2009 Jul;15(7):765–805.

50.   Lee C, Yang W, Parr RG. Development of the Colle-Salvetti correlation-energy formula into a functional of the electron density. Phys Rev B. 1988 Jan 15;37(2):785–9.

51.   Scalmani G, Frisch MJ. Continuous surface charge polarizable continuum models of solvation. I. General formalism. J Chem Phys. 2010 Mar 21;132(11):114110.

52.   Parr RG, Pearson RG. Absolute hardness: companion parameter to absolute electronegativity. J Am Chem Soc. 1983 Dec;105(26):7512–6.

53.   Pearson J, Havill DC. The Effect of Hypoxia and Sulphide on Culture-Grown Wetland and Non-Wetland Plants: II. METABOLIC AND PHYSIOLOGICAL CHANGES. J Exp Bot. 1988;39(4):431–9.

54.   Gaussview 5.0.9 [Internet]. Available from: https://www.strath.ac.uk/is/software/gaussview509/

55.   Gaussian 09 [Internet]. Available from: https://gaussian.com/glossary/g09/

56.   Fierro C, Anderson AB, Scherson DA. Electron donor-acceptor properties of porphyrins, phthalocyanines, and related ring chelates: a molecular orbital approach. J Phys Chem. 1988 Dec;92(24):6902–7.

57.   Islam N, Ghosh DC. On the Electrophilic Character of Molecules Through Its Relation with

Electronegativity and Chemical Hardness. Int J Mol Sci. 2012 Feb 17;13(2):2160–75.

58. Sen P, Yıldız SZ, Atalay VE, Kanmazalp SD, Dege N. Synthesis, molecular structure, spectroscopic and computational studies on 4-(2-(2-(2-formylphenoxy)ethoxy)ethoxy)phthalonitrile as Functionalized Phthalonitrile. Maced J Chem Chem Eng. 2019 May 24;38(1):63.

59. Enisoglu-Atalay V, Atasever-Arslan B, Yaman B, Cebecioglu R, Kul A, Ozilhan S, et al. Chemical and molecular characterization of metabolites from Flavobacterium sp. Agbor G, editor. PLOS ONE. 2018 Oct 17;13(10):e0205817.

Novel lanthanide metallophthalocyanines bearing iodine group and their singlet oxygen generation ability

Baybars Köksoy iD

Bursa Technical University, Department of Chemistry, 16310 Yıldırım-Bursa, Turkey

Abstract: In this study, five novel mono rare earth metallo phthalocyanine derivatives (**1a-e**) were synthesized by cyclotetramerization of 4-iodophthalonitrile and corresponding metal salts. These novel compounds were characterized by FT-IR, elemental analyses, UV–Vis, and MALDI-TOF spectral data. Moreover, the ability of singlet oxygen generation and aggregation behavior of these phthalocyanines were investigated in dimethyl sulfoxide using UV-Vis spectroscopy. Gadolinium metallo phthalocyanine has the best singlet oxygen quantum yield and it can be a potential candidate for the photodynamic therapy (PDT) of cancer.

INTRODUCTION

Phthalocyanine compounds (Pcs) and their derivatives are a family of aromatic molecules which are delocalized with an 18-π electron system and they have been comprehensively studied in many areas as chemical sensors (1, 2), liquid crystals (3), solar cell applications (4, 5), photodynamic therapy (PDT) (6-8) and catalysts (9). In recent years, they have been used as a photosensitizer in photodynamic therapy (PDT) because of their high singlet oxygen generation ability and good photostability (10, 11). The main problem of phthalocyanines is poor solubility in common organic solvents. To overcome this problem, it can be decorated with some non-polar/polar groups on the Pc core (12, 13). Another disadvantage of these compounds is called "aggregation" which means they stack on each other in the solvent and affect the photochemical properties. Also, Pc aggregation

is another limitation in their applications which drastically decreases their fluorescence quantum yields, shortens their triplet state lifetime, and reduces their photosensitizing efficiency, especially in aqueous media.

Peripheral substitution of the macrocyclic ring with halogen groups leads to phthalocyanine products which are soluble in common organic solvents (14). Moreover, it is anticipated that the introduction of halogen/ester groups into a moiety of phthalocyanine compound will induce high solubility in organic solvents and improved photosensitizer activity of Pcs for PDT (15-19).

For phthalocyanine photosensitizers, the metal atom is very important to singlet oxygen generation and PDT applications, incorporating zinc(II), indium(III), aluminum(III), gallium(III), and silicon(IV) (20, 21). On the other hand, the number of phthalocyanines

including lanthanide metals in the literature is rare for PDT applications.

Phthalocyanines containing lanthanide series metal atoms have been studied by scientists for a long time. Double-decker and triple-decker phthalocyanines containing lutetium or europium metals were synthesized and various applications were studied (22-23). Additionally, the synthesis of homoleptic and heteroleptic complexes containing rare earth elements is also available in the literature (24-25). It has been reported that rare earth element phthalocyanine complexes are used in electrochromic materials (22) liquid crystal (26), nonlinear optics (25) and optoelectronic materials applications.

According to this information, the aim of this study is to synthesize and characterize novel phthalocyanines containing lanthanide metal atoms (Eu, Sm, Gd, Tb, Dy) and bearing iodine groups that may have high production of singlet oxygen.

EXPERIMENTAL

General Information
1,3-diphenylisobenzofuran (DPBF), 4-iodophthalonitrile, Ln(OAc)$_3$ metal salts, and other chemicals/reagents were purchased from Aldrich. All reagents and solvents were of reagent grade quality and were obtained from commercial suppliers.

FT-IR spectra were recorded on a Perkin Elmer Spectrum 100 FT-IR spectrometer. Positive ion and linear mode MALDI-TOF-MS of Pcs were obtained in 1,8,9-anthracenetriol (DIT) as a MALDI matrix using nitrogen laser accumulating 50 laser shots using Bruker Microflex LT MALDI-TOF mass spectrometer. Absorption spectra in the UV-visible region were recorded with a Shimadzu 2101 UV-Vis spectrophotometer. Fluorescence excitation and emission spectra were recorded on a Varian Eclipse spectrofluorometer using 1 cm path length cuvettes at room temperature.

Photo-irradiations were done using a General Electric quartz line lamp (300 W). A 600 nm glass cut-off filter (Schott) was used to filter off ultraviolet and low wavelength visible parts of the spectrum. A water filter was also used to filter off infrared radiations. An interference filter (Intor, 670 nm with a bandwidth of 40 nm) was additionally placed in the light path before the sample. Light intensities were

measured with a POWER MAX5100 (Molelectron detector incorporated) power meter

Synthesis
All lanthanide series metallo-phthalocyanines were synthesized from 4-iodophthalonitrile and Ln(OAc)$_3$ metal salts in n-pentanol/DBU solvent-base system at reflux. Phthalocyanine compounds (**1a-e**) including iodine groups were recovered in pure form with column chromatography using dichloromethane-ethanol as eluent. All these phthalocyanine derivatives were fully characterized by spectroscopic methods such as FT-IR, UV-Vis, fluorescence, MALDI-TOF, and elemental analyses as well.

General synthesis of mono-phthalocyanine derivatives (**1a-e**)
4-Iodophthalonitrile (0.1 g, 0.393 mmol) and lanthanide metal salt (50 mg, 0.075 mmol samarium(III) acetate monohydrate for SmPc; 50 mg 0.076 mmol europium (III) acetate monohydrate for EuPc; 50 mg, 0.074 mmol gadolinium(III) acetate monohydrate for GdPc: 50 mg, 0.074 mmol terbium (III) acetate monohydrate for TbPc; and 50 mg, 0.073 mmol dysprosium(III) acetate monohydrate for DyPc) were stirred and heated in sealed tubes at reflux temperature in 24 h. After one day, the greenish solutions were poured into 50 mL of hot methanol. The greenish precipitates were centrifuged and washed several times with hot water, ethyl acetate, and diethyl ether, and then all mono-Pcs were separated by column chromatography on silica gel using dichloromethane-ethanol as eluent, and final products were dried in the vacuum.

2(3),9(10),16(17),23(24)-Tetra(iodo)phthalocyaninatosamarium (III) acetate (**1a**)
Yield: 35 mg (29%), Chemical Formula: C$_{34}$H$_{15}$N$_8$O$_2$I$_4$Sm, FT-IR(ATR), v_{max}/cm^{-1}: 3090-3059 (Aromatic-CH), 2949-2854 (Aliphatic-CH), 1716 (C=O, acetate), 1583-1491 (C=C), 818 (Ar-I), UV-Vis (DMSO): λ_{max} nm (log ε): 356 (4.93), 616 (4.36), 684 (5.08), Anal. Calc. for C$_{34}$H$_{15}$N$_8$O$_2$I$_4$Sm, C: 33.32, H: 1.23, N: 9.14%, Found: C: 33.28; H: 1.19, N: 9.11%; MS(MALDI-TOF) (DHB): 1166.13 (M-OAc)$^+$, 1320.61 (M-OAc+DHB)$^+$.

*2(3),9(10),16(17),23(24)-Tetra(iodo)phthalocyaninatoeuropium (III) acetate* (**1b**)
Yield: 30 mg (24.8%), Chemical Formula: C$_{34}$H$_{15}$N$_8$O$_2$I$_4$Eu, FT-IR(ATR), v_{max}/cm^{-1}: 3088-3057 (Aromatic-CH), 2949-2851 (Aliphatic-CH), 1718 (C=O, acetate), 1585-1490 (C=C), 819

(Ar-I), UV-Vis (DMSO): λ_{max} nm (log ε): 346 (4.86), 617 (4.35), 684 (5.11) Anal. Calc. for $C_{34}H_{15}N_8O_2I_4Eu$, C: 33.28, H: 1.23, N: 9.13%, Found: C: 33.22; H: 1.21, N: 9.12%, MS(MALDI-TOF) (DHB): 1168.23 (M-OAc)[+], 1322.55 (M-OAc+DHB)[+].

2(3),9(10),16(17),23(24)-Tetra(iodo)phthalocyaninatogadolinium (III) acetate (1c)
Yield: 42 mg (34.6%), Chemical Formula: $C_{34}H_{15}N_8O_2I_4Gd$, FT-IR(ATR), v_{max}/cm[-1]: 3089-3058 (Aromatic-CH), 2948-2854 (Aliphatic-CH), 1719 (C=O, acetate), 1581-1488 (C=C), 820 (Ar-I), UV-vis (DMSO): λ_{max} nm (log ε): 356 (4.80), 617 (4.36), 685 (5.11), Anal. Calc. for $C_{34}H_{15}N_8O_2I_4Gd$, C: 33.14, H: 1.23, N: 9.09%, Found: C: 33.12; H: 1.20, N: 9.05%, MS(MALDI-TOF) (DHB): 1173.44 (M-OAc)[+], 1327.33 (M-OAc+DHB)[+].

2(3),9(10),16(17),23(24)-Tetra(iodo)phthalocyaninatoterbium (III) acetate (1d)
Yield: 39 mg (32.1%), Chemical Formula: $C_{34}H_{15}N_8O_2I_4Tb$, FT-IR(ATR), v_{max}/cm[-1]: 3088-3059 (Aromatic-CH), 2947-2852 (Aliphatic-CH), 1719 (C=O, acetate), 1580-1491 (C=C), 821 (Ar-I), UV-Vis (DMSO): λ_{max} nm (log ε): 352 (4.95), 619 (4.42), 686 (5.11), Anal. Calc. for $C_{34}H_{15}N_8O_2I_4Tb$, C: 33.09, H: 1.23, N: 9.08%, Found: C: 33.01; H: 1.17, N: 9.04%, MS(MALDI-TOF) (DHB): 1175.22 (M+H-OAc)[+], 1329.19 (M+H-OAc+DHB)[+].

2(3),9(10),16(17),23(24)-Tetra(iodo)phthalocyaninatodysprosium (III) acetate (1e)
Yield: 33 mg (27.1%), Chemical Formula: $C_{34}H_{15}N_8O_2I_4Dy$, FT-IR(ATR), v_{max}/cm[-1]: 3089-3061 (Aromatic-CH), 2949-2853 (Aliphatic-CH), 1720 (C=O, acetate), 1584-1488 (C=C), 820 (Ar-I), UV-Vis (DMSO): λ_{max} nm (log ε): 356 (4.79), 617 (4.38), 686 (5.10). Anal. Calc. for $C_{34}H_{15}N_8O_2I_4Dy$, C: 33.00, H: 1.22, N: 9.05%, Found: C: 32.98; H: 1.18, N: 9.03%, MS(MALDI-TOF) (DHB): 1178.45 (M-OAc)[+], 1332.67 (M-OAc+DHB)[+].

RESULT AND DISCUSSION

The synthetic pathway of novel lanthanide series phthalocyanines was figured out in Scheme 1. The final products were obtained by 4-iodophthalonitrile and corresponding Ln(OAc)$_3$ metal salts with catalytic amount DBU in the solvent of n-pentanol. All synthesized phthalocyanines were characterized by using various spectroscopic characterization techniques such as ground state electronic spectra, FT-IR, MALDI-TOF, and elemental analysis. The obtained results from these techniques are compatible with the proposed structures for all the newly prepared compounds.

CHARACTERIZATION

The vibrational peak appeared at 2230 cm^{-1} for 4-iodophthalonitrile was disappeared in the FT-IR spectra of metallophthalocyanines **1a-e** as expected. This is an important clue concerning the formation of the phthalocyanine macrocycle from the corresponding phthalonitriles. The typical carbonyl (acetate group) vibration was observed in the range of 1720-1716 cm^{-1} for all metallophthalocyanines (**1a-e**). The aromatic-CH and aliphatic-CH stretching peaks for all synthesized phthalocyanines were appeared between 3090-3057 cm^{-1} and 2949-2852 cm^{-1} regions, respectively. Also, other typical bands Ar-C=C and Ar-I were monitored at 1585-1488 cm^{-1}, 821-818 for novel lanthanide(III) phthalocyanines. The MALDI-TOF spectra of **1a-e** were recorded using a 2,5-dihydroxybenzoic acid matrix and given in Figure-1. All the lanthanide(III) phthalocyanine compounds showed (M[+]-OAc) and (M[+]-OAc+DHB) peaks. The values of molecular ion peaks (*m/z*) were monitored at 1166.13 and 1320.61 Da for **1a**, 1168.23, and 1322.55 Da for **1b**, 1173.44 and 1327.33 Da for **1c**, 1175.22 and 1329.19 Da for **1d,** 1178.45 and 1332.67 Da for **1e.**
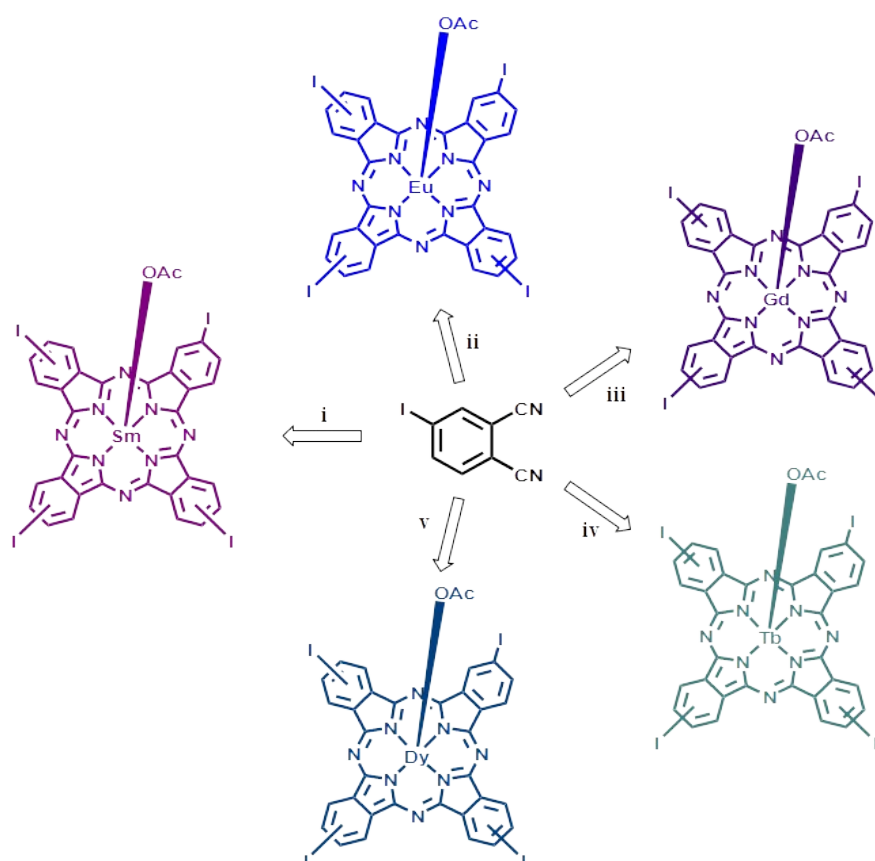
i) Sm(OAc)$_3$, 1-pentanol, DBU, reflux, 12 h ii) Eu(OAc)$_3$, 1-pentanol, DBU, reflux, 14 h, iii) Gd(OAc)$_3$, 1-pentanol, DBU, reflux, 10 h, iv) Tb(OAc)$_3$, 1-pentanol, DBU, reflux, 12 h, v) Dy(OAc)$_3$, 1-pentanol, DBU, reflux, 14 h.

Scheme 1: Synthetic route of mono lanthanide metallophthalocyanines (**1a-e**).

UV-Vis and Aggregation

For the phthalocyanine macrocycles, there are two main transitions known as π-π* in the UV-Vis spectrum. These transitions named as Q and B band are generally found at 300-450 nm and 650-850 nm, respectively. In this work, synthesized metallo-phthalocyanine derivatives exhibited a sharp-single Q band at the range of 684-686 nm in the DMSO solvent. Also, B bands of these phthalocyanines were observed within the range of 346-356 nm. Aggregation is a phenomenon that occurs when two or more compounds stack on top of each other, encountered in macrocyclic structures or planar compounds with π electrons. Whereas this phenomenon is an advantage in applications such as energy transfer, it is a disadvantage in healthcare applications such as PDT. For this reason, it is important data that the photosensitizer to be used in PDT applications does not show aggregation.

In this study, the aggregation attitudes of all lanthanide phthalocyanines including iodine atom (1a-e) were examined at 2-12 μM in DMSO (Figure-2). The Beer-Lambert law was fitted for studied phthalocyanines (**1a-e**) at 12 to 2 μM concentration range and there was no aggregation behavior of these lanthanide metallophthalocyanines in DMSO.
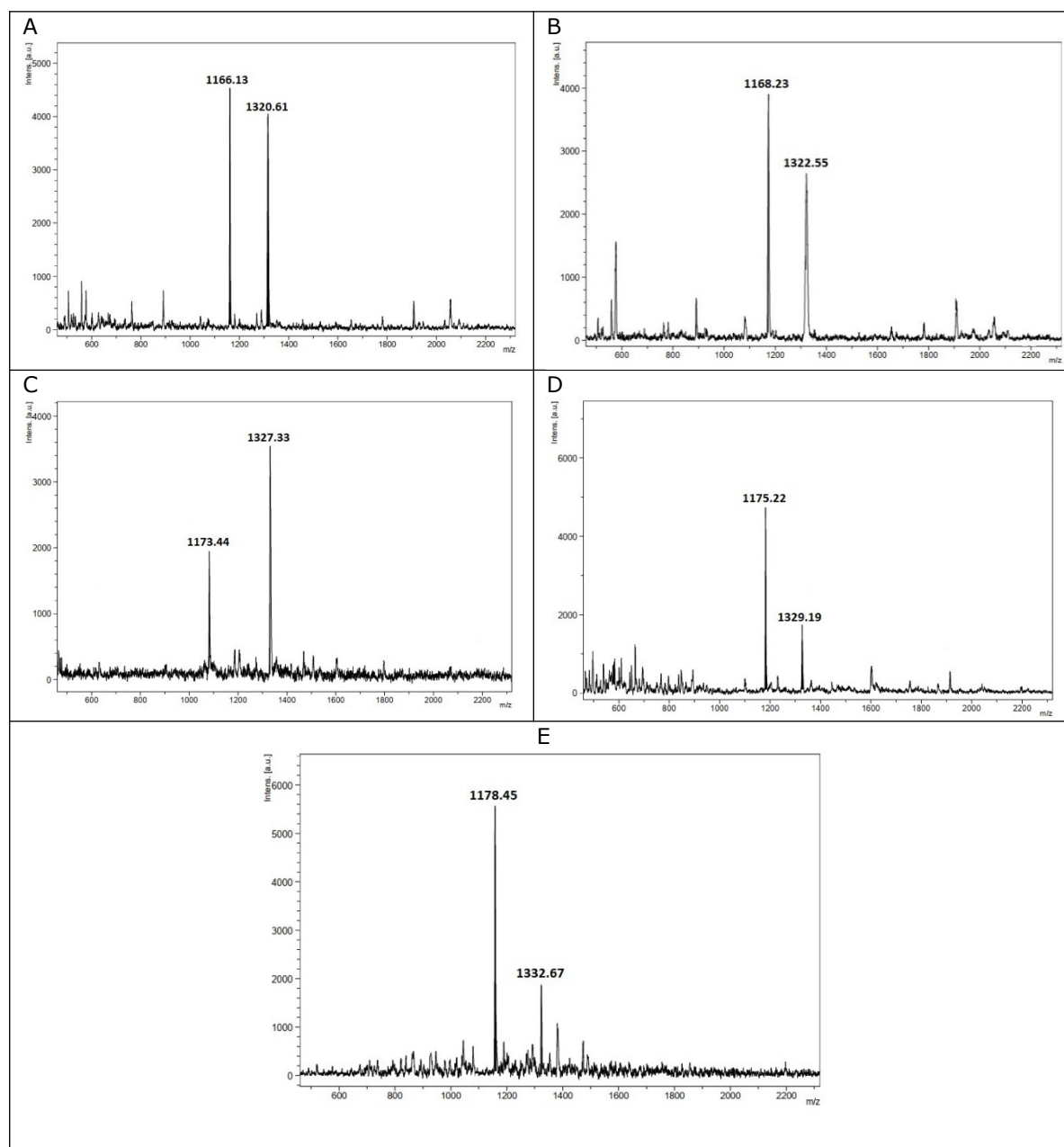
Figure 1: Maldi-TOF mass spectra of synthesized lanthanide metallophthalocyanines using DHB as a matrix (A: compound **1a**, B: compound **1b**, C: compound **1c**, D: compound **1d**, E: compound **1e**).
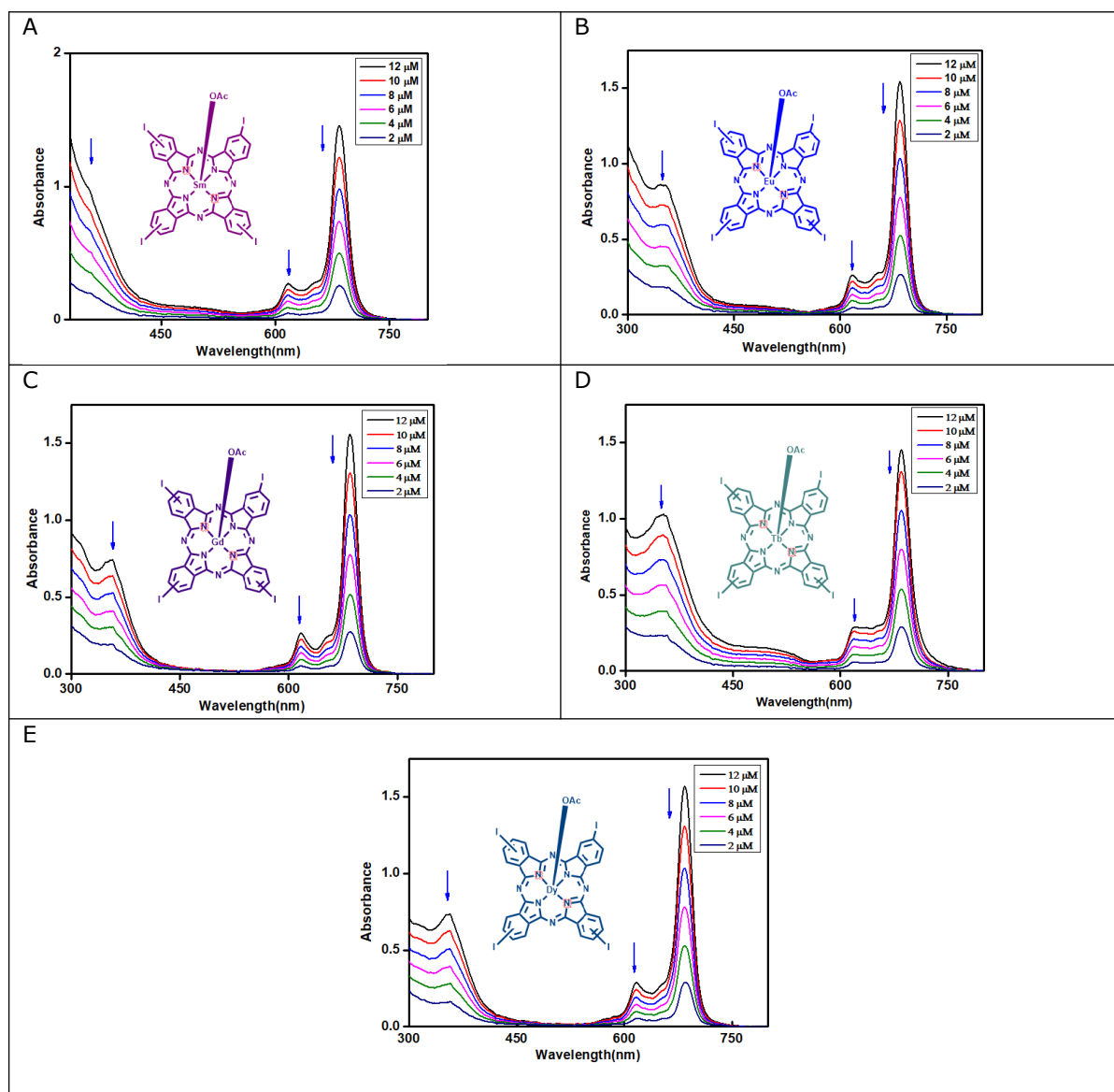
Figure 2: UV–Vis spectra of lanthanide metallophthalocyanines (**1a-e**) in DMSO at different concentration (2-12 ppm) (A: compound **1a**, B: compound **1b**, C: compound **1c**, D: compound **1d**, E: compound **1e**).

Singlet Oxygen Generation

Photodynamic therapy (PDT) which is based on the destruction of cancer cells by singlet oxygen, is a new treatment for cancer disease. This process consists of three important basic stones, "light, oxygen, and photosensitizer". It is believed that during photosensitization, the electrons of the photosensitizer are excited by the light and pass to the triplet state (inter-crossing systems) and transfer their energy to molecular oxygen for occurring the singlet oxygen. These reactive types of oxygen which are called "singlet oxygen" kill the cancer cells.

The Φ_Δ for compound (**1a-e**) were studied and calculated in DMSO by a chemical method using 1,3-diphenylisobenzofuran (DPBF) as a quencher. The decreasing of DPBF at 417 nm was observed using a UV-Vis spectrophotometer. The Φ_Δ value of compound **1a-e** was found lower than standard zinc (II) (StdZnPc) except compound **1c** in DMSO as given in Figure 3.
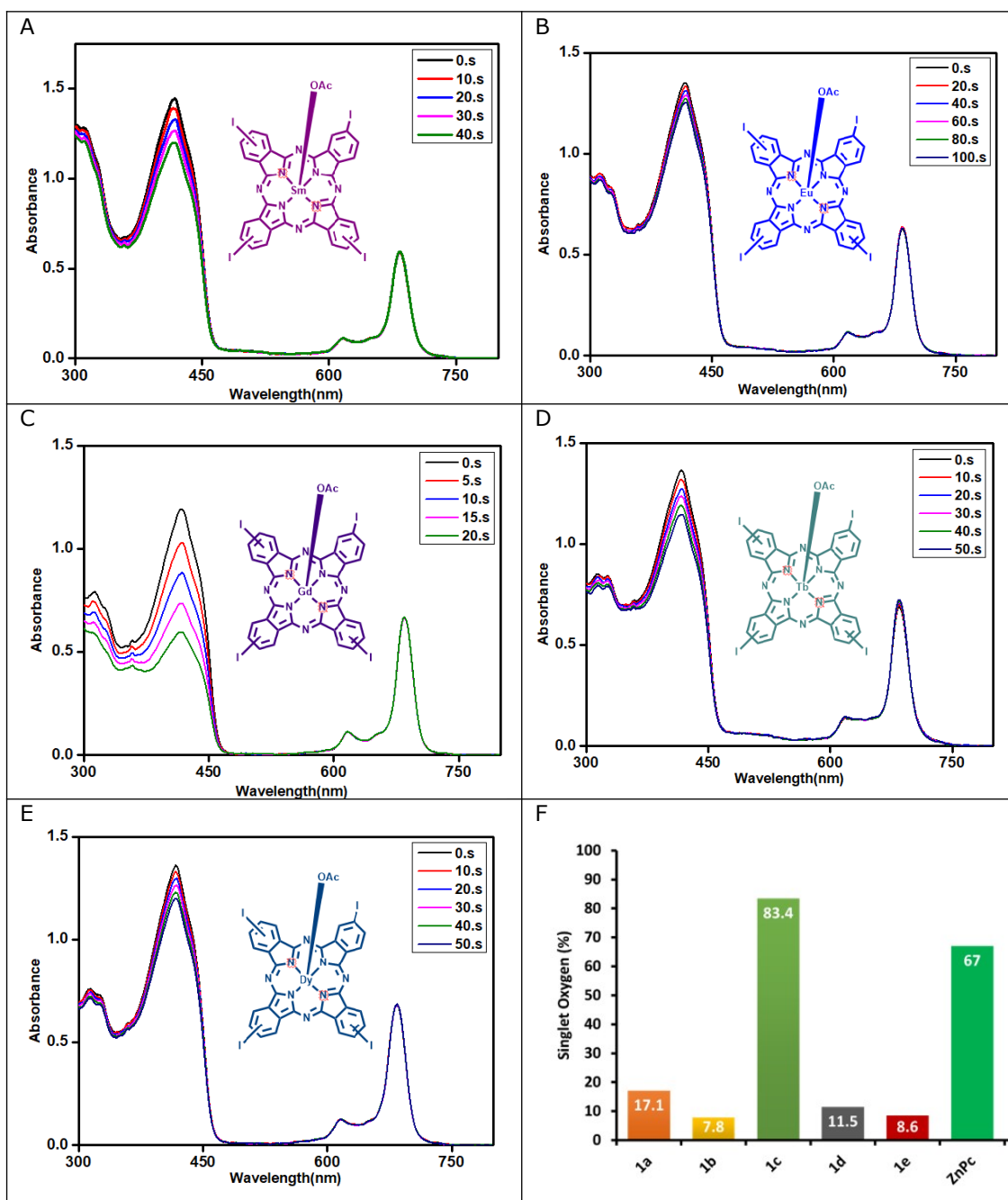
Figure 3: The absorption spectral changes during the determination of singlet oxygen quantum yields. This determination was for all compounds (**1a-e**) in DMSO at a concentration of 1×10^{-5} M (A: compound **1a**, B: compound **1b**, C: compound **1c**, D: compound **1d**, E: compound **1e**) and bar graphic of singlet oxygen quantum yields of synthesized mono lanthanide metallophthalocyanines (F).

Normally, singlet oxygen quantum yields of photosensitizers containing heavy atoms such as bromine or iodine are higher than other types. However, the metal atom in the center of the phthalocyanine nucleus has a great effect on the electrons that pass into the triplet level. As seen in this study, the singlet oxygen values of compounds **1a**, **1b**, **1d**, and **1e**, which contain metals from the lanthanide series in their center, were measured low despite the

presence of iodine in their structure. The tetraiodophthalocyanine derivative containing only gadolinium metal in its center produced singlet oxygen much better than both its own species and the standard zinc(II) phthalocyanine derivative. The reason for this can be related to the spherically symmetrical property of gadolinium metal, which has similar examples in the literature (27, 28).

ACKNOWLEDGMENT

CONCLUSION

As a result, the singlet oxygen generation properties of five phthalocyanine building block compounds with lanthanide series metal atom in its center and iodine as heavy atom in its peripheral position were investigated in this study. It was determined that the gadolinium phthalocyanine derivative produced the highest singlet oxygen obtained from the macrocyclic phthalocyanine compounds. The singlet oxygen quantum yields of the other four phthalocyanine derivatives were quite low. It has also been observed that these compounds did not produce fluorescence due to both the heavy atom effect and the effect of the metal atoms in the center.

The important part of the study in terms of literature is that these compounds can easily be modified with important reactions using different catalysts. Important and useful reactions such as Sonogashira, Suzuki, and Heck cross-coupling reactions can be performed over the iodine atom in the peripheral position, and the physical and chemical properties of these phthalocyanines can be changed as desired. In addition, gadolinium phthalocyanine compound, which has the highest singlet oxygen quantum yield, can be made a more effective photosensitizer candidate by attaching it with water-soluble groups, which is especially important for PDT, and a potential PDT agent.

REFERENCES

1. Hosseini H, Mahyari M, Bagheri A, Shaabani A. A novel bioelectrochemical sensing platform based on covalently attachment of cobalt phthalocyanine to graphene oxide. Biosensors and Bioelectronics. 2014 Feb;52:136–42. <DOI>.

2. Fogel R, Mashazi P, Nyokong T, Limson J. Critical assessment of the Quartz Crystal Microbalance with Dissipation as an analytical tool for biosensor development and fundamental studies: Metallophthalocyanine–glucose oxidase biocomposite sensors. Biosensors and Bioelectronics. 2007 Aug;23(1):95–101. <DOI>.

3. Basova T, Hassan A, Durmuſ M, Gürek AG, Ahsen V. Liquid crystalline metal phthalocyanines: Structural organization on the substrate surface. Coordination Chemistry Reviews. 2016 Mar;310:131–53. <DOI>.

4. Urbani M, de la Torre G, Nazeeruddin MK, Torres T. Phthalocyanines and porphyrinoid analogues as hole- and electron-transporting materials for perovskite solar cells. Chem Soc Rev. 2019;48(10):2738–66. <DOI>.

5. Güzel E. Dual-purpose zinc and silicon complexes of 1,2,3-triazole group substituted phthalocyanine photosensitizers: synthesis and evaluation of photophysical, singlet oxygen generation, electrochemical and photovoltaic properties. RSC Adv. 2019;9(19):10854–64. <DOI>.

6. Singh S, Aggarwal A, Bhupathiraju NVSDK, Arianna G, Tiwari K, Drain CM. Glycosylated Porphyrins, Phthalocyanines, and Other Porphyrinoids for Diagnostics and Therapeutics. Chem Rev. 2015 Sep 23;115(18):10261–306. <DOI>.

7. Jia X, Jia L. Nanoparticles Improve Biological Functions of Phthalocyanine Photosensitizers Used for Photodynamic Therapy. CDM. 2012 Sep 1;13(8):1119–22. <DOI>.

8. Wong RCH, Lo PC, Ng DKP. Stimuli responsive phthalocyanine-based fluorescent probes and photosensitizers. Coordination Chemistry Reviews. 2019 Jan;379:30–46. <DOI>.

9. Sorokin AB. Phthalocyanine Metal Complexes in Catalysis. Chem Rev. 2013 Oct 9;113(10):8152–91. <DOI>.

10. Köksoy B, Durmuş M, Bulut M. Tetra- and octa-[4-(2-hydroxyethyl)phenoxy bearing novel metal-free and zinc(II) phthalocyanines: Synthesis, characterization and investigation of photophysicochemical properties. Journal of Luminescence. 2015 May;161:95–102. <DOI>.

11. Ghazal B, Husain A, Ganesan A, Durmuş M, Zhang XF, Makhseed S. Exceptionally effective generation of singlet oxygen in aqueous media via iodinated zinc-phthalocyanine. Dyes and Pigments. 2019 May;164:296–304. <DOI>.

12. Bıyıklıoğlu Z, Acar I. Peripheral and non-peripheral long-chain tetrasubstituted phthalocyanines: Synthesis, spectroscopic characterization and aggregation properties. Synthetic Metals. 2012 Aug;162(13–14):1156–63. <DOI>.

13. Gao Z, Tao X, Cui Y, Satoh T, Kakuchi T, Duan Q. Synthesis of end-functionalized poly(N-isopropylacrylamide) with group of asymmetrical phthalocyanine via atom transfer radical

polymerization and its photocatalytic oxidation of Rhodamine B. Polym Chem. 2011;2(11):2590. <DOI>.

14. Bakboord JV, Cook MJ, Hamuryudan E. Non-uniformly substituted phthalocyanines and related compounds: alkylated tribenzo-imidazolo[4,5]-porphyrazines. J Porphyrins Phthalocyanines. 2000 Aug;04(05):510–7. <DOI>.

15. George RD, Snow AW. Synthesis of 3-nitrophthalonitrile and tetra-α-substituted phthalocyanines. Journal of Heterocyclic Chemistry. 1995 Mar;32(2):495–8. <DOI>.

16. Cook MJ, McMurdo J, Miles DA, Poynter RH, Simmons JM, Haslam SD, et al. Monolayer behaviour and Langmuir–Blodgett film properties of some amphiphilic phthalocyanines: factors influencing molecular organisation within the film assembly. J Mater Chem. 1994;4(8):1205–13. <DOI>.

17. George RD, Snow AW, Shirk JS, Barger WR. The Alpha Substitution Effect on Phthalocyanine Aggregation. J Porphyrins Phthalocyanines. 1998 Jan;02(01):1–7. <DOI>.

18. Esenpınar AA, Durmuş M, Bulut M. Photophysical, photochemical and BSA binding/BQ quenching properties of quaternizable coumarin containing water soluble zinc phthalocyanine complexes. Spectrochimica Acta Part A: Molecular and Biomolecular Spectroscopy. 2011 Aug;79(3):608–17. <DOI>.

19. Taştemel A, Karaca BY, Durmuş M, Bulut M. Photophysical and photochemical properties of novel metallophthalocyanines bearing 7-oxy-3-(m-methoxyphenyl)coumarin groups. Journal of Luminescence. 2015 Dec;168:163–71. <DOI>.

20. Güzel E, Günsel A, Bilgiçli AT, Atmaca GY, Erdoğmuş A, Yarasir MN. Synthesis and photophysicochemical properties of novel thiadiazole-substituted zinc (II), gallium (III) and silicon (IV) phthalocyanines for photodynamic therapy. Inorganica Chimica Acta. 2017 Oct;467:169–76. <DOI>.

21. Yanık H, Aydın D, Durmuş M, Ahsen V. Peripheral and non-peripheral tetrasubstituted aluminium, gallium and indium phthalocyanines: Synthesis, photophysics and photochemistry. Journal of Photochemistry and Photobiology A: Chemistry. 2009 Jul;206(1):18–26. <DOI>.

22. Ceyhan T, Altındal A, Özkaya AR, Erbil MK, Bekaroğlu Ö. Synthesis, characterization, and electrochemical, electrical and gas sensing properties of a novel tert-butylcalix[4]arene bridged bis double-decker lutetium(III) phthalocyanine. Polyhedron. 2007 Jan;26(1):73–84. <DOI>.

23. Pushkarev VE, Shulishov EV, Tomilov YV, Tomilova LG. The development of highly selective approaches to sandwich-type heteroleptic double- and triple-decker lutetium(III) and europium(III) phthalocyanine complexes. Tetrahedron Letters. 2007 Jul;48(30):5269–73. <DOI>.

24. Pushkarev VE, Tolbin AYu, Borisova NE, Trashin SA, Tomilova LG. A 3 B-Type Phthalocyanine-Based Homoleptic Lanthanide(III) Double-Decker π-Radical Complexes Bearing Functional Hydroxy Groups: Synthetic Approach, Spectral Properties and Electrochemical Study. Eur J Inorg Chem. 2010 Nov;2010(33):5254–62. <DOI>.

25. Ren B, Sheng N, Gu B, Wan Y, Rui G, Lv C, et al. Changing optical nonlinearities of homoleptic bis(phthalocyaninato) rare earth praseodymium double-decker complexes by the redox reaction. Dyes and Pigments. 2017 Apr;139:788–94. <DOI>.

26. Nekelson F, Monobe H, Shiro M, Shimizu Y. Liquid crystalline and charge transport properties of double-decker cerium phthalocyanine complexes. J Mater Chem. 2007;17(25):2607. <DOI>.

27. Ke XS, Ning Y, Tang J, Hu JY, Yin HY, Wang GX, et al. Gadolinium(III) Porpholactones as Efficient and Robust Singlet Oxygen Photosensitizers. Chem Eur J. 2016 Jul 4;22(28):9676–86. <DOI>.

28. Galindev O, Dalantai M, Ahn WS, Shim YK. Gadolinium complexes of chlorin derivatives applicable for MRI contrast agents and PDT. J Porphyrins Phthalocyanines. 2009 Jul;13(07):823–31. <DOI>.

Voltammetric Determination of Antipsychotic Drug Flupentixol HCl in Human Serum at a Boron-Doped Diamond Electrode

Burcin Bozal-Palabiyik[1]*

[1] Ankara University, Faculty of Pharmacy, Department of Analytical Chemistry, Ankara, 06560, Turkey

Abstract: This study aims to offer a voltammetric method for determining the antipsychotic drug flupentixol from serum samples. According to pH and scan rate studies, the oxidation behavior of flupentixol at boron-doped diamond electrode was found as irreversible and diffusion-controlled. To determine flupentixol from bulk form and serum samples, differential pulse voltammetry was preferred as the working method because of the repeatability. Linear responses were obtained in the range of $6.0 \times 10^{-7} - 8.0 \times 10^{-6}$ M and $8.0 \times 10^{-7} - 1.0 \times 10^{-5}$ M for bulk form and serum samples in pH 2.0 Britton-Robinson buffer solution, with detection limit values of 1.09×10^{-7} M and 1.08×10^{-7} M, respectively. Required validation parameters were also studied and according to recovery from serum samples (99.91%) and precision studies, it can be inferred that the developed method was accurate and precise.

INTRODUCTION

Depression is one of the most common and schizophrenia is one of the most serious psychiatric illnesses worldwide. According to the World Health Organization (WHO), around 280 million people have been diagnosed with depression (1) and nearly 20 million people with schizophrenia (2). Because of the severity and breadth of these two diseases, the pharmaceutical industry is encouraged to develop new and more effective medications. One of such drugs is flupentixol dihydrochloride (FLP, Scheme 1), which is a thioxanthene derivative antipsychotic drug used for the relief of psychotic symptoms such as schizophrenia and depression. Its oral bioavailability is approximately 55%, and the peak serum concentration occurs between 3 and 8 hours (3).
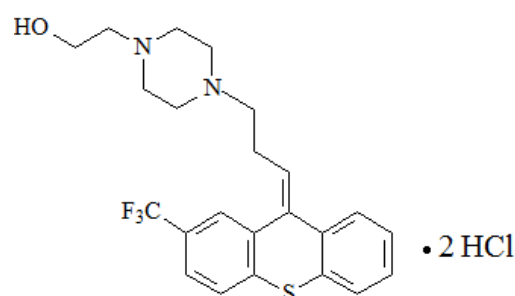
Scheme 1: Chemical structure of FLP.

Electrochemical methods, particularly voltammetry, are frequently preferred because they are simple, cheap, sensitive and reliable; also, their short analysis time makes them more popular (4). Carbon-based materials are commonly used as electrode materials in voltammetric studies because they match the specifications of an ideal electrode material, which is expected to be stable over time, have low residual current and a wide potential range (5). Even though all allotropes of carbon have diverse chemical, electrical, and physical properties, diamond stands out for its exceptional thermal conductivity and mechanical strength. However, diamond has very low conductivity that

can be overcome by doping it with boron (6). Diamond behaves like an insulator, a metal-like conductor, or even a low-temperature superconductor, depending on the level of doping. A relatively high boron doped diamond (10^3 - 10^4 ppm) can be used as an electrode material and it demonstrates metal-like conductivity. Highly conductive boron-doped diamond (BDD) electrodes are quite popular in various electrochemical assays (7).

When compared to traditional electrodes, BDD working electrode offers numerous benefits. In both alkaline and acidic conditions, these electrodes are exceptionally robust, corrosion resistant, chemically inert, and electrochemically stable. Moreover, they have high thermal conductivity and resist passivation of the electrode surface. In addition, they are less sensitive to dissolved oxygen and have a very low and stable background, allowing them to operate over a wide range of potentials (7,8).

Antipsychotics are typically given at oral doses of only a few milligrams per day and are extensively metabolized in the body and plasma concentrations of these medications are quite low. Furthermore, therapeutic drug monitoring (TDM) of antipsychotic medicines has proven to be useful in identifying patients' poor compliance and resolving the problems associated with significant genetic variability in their metabolism. Highly sensitive, selective, and accurate bioanalytical methods are required to undertake pharmacological and toxicological investigations and clinical TDM of antipsychotics, as well as to address the problems associated with polypharmacy and drug metabolism (9). When the literature studies are examined, it has been seen that there are voltammetric (10), potentiometric (11), spectrofluorimetric (12), second-order spectrophotometric (13), reversed-phase high performance liquid chromatographic (HPLC) (14), LC-MS/MS (3) and LC-ESI-MS (15) methods designed to determine FLP from the pharmaceutical preparations and biological samples in an individual manner.

In this study, voltammetric behavior of FLP was investigated utilizing a boron-doped diamond electrode and employing DP voltammetric method for its determination from the serum. The absence of a voltammetric study for FLP with BDDE in the literature shows the originality of the study.

EXPERIMENTAL SECTION

Chemicals and Reagents
1×10^{-3} M FLP (kindly supplied from Lundbeck, Istanbul) stock solution was prepared in methanol and kept in a refrigerator. Analytical grade reagents were used for preparing required solutions. Measurement solutions were prepared before use by adding 20% methanol and supporting electrolyte onto the required amount of FLP solutions. H_2SO_4 solutions (0.1 and 0.5 M) and Britton-Robinson (BR) buffer solutions (0.04 M, pH 2.0 – 10.0) were preferred as supporting electrolytes and prepared in distilled water. Sigma-Aldrich provided the synthetic serum samples.

Apparatus and Measurements
AUTOLAB 204 PGSTAT device and NOVA 2.1 software were used for electrochemical measurements. A conventional three-electrode cell was used, BDDE (Windsor Scientific Ltd.; 3 mm diameter) working electrode, Ag/AgCl (BAS, 3 M NaCl) reference electrode and platinum wire auxiliary electrodes were employed. Baseline correction was applied (except cyclic voltammograms) to the measured voltammograms using moving average. Alumina powder and a polishing cloth were used to clean the electrode surface before each measurement. Cyclic voltammetry (CV), DPV and square wave voltammetry (SWV) were employed for investigating the oxidation behavior of FLP. DPV was selected for the determination of FLP with the following parameters: step potential: 10 mV; modulation amplitude: 50 mV; modulation time: 50 ms; interval time: 500 ms. The pH of the buffer solutions was measured using a SevenCompact™ pH/Ion S220 model pH meter (Mettler Toledo, Switzerland).

Preparation of Serum Samples
Serum stock solution containing 1×10^{-3} M FLP was prepared by mixing required volume of 1×10^{-2} M FLP, methanol and acetonitrile that was used to precipitate serum proteins. The mixture was ultrasonicated for 15 minutes and centrifuged at 5000 rpm for 15 minutes to collect the precipitate at the bottom of the tube. Supernatant was carefully transferred to a clean tube and measurement solutions were prepared from this supernatant with the addition of 20% methanol and pH 2.0 BR buffer solution. Recovery studies were carried out by adding standard solution onto the known amount of serum solution. Results were analyzed using calibration curve obtained from serum studies.

RESULTS AND DISCUSSION

pH and Scan Rate Effect on FLP Signal at BDDE
To examine the voltammetric behavior of FLP at BDDE, pH scanning was first performed. For this purpose, the response of FLP in BR buffer solutions with pH values between 2.0 and 10.0 and 0.5 M and 0.1 M H_2SO_4 solutions were studied by using CV, DPV and SWV methods.

Figure 1 shows repetitive cyclic voltammograms of 8×10^{-5} M FLP in 0.5 M H_2SO_4 solution (A), pH 2.0 BR buffer (B), and pH 6.0 BR (C) buffer solution at a scan rate of 100 mV/s. FLP showed two well-defined oxidation peaks and a very weak wave in 0.5 M H_2SO_4 solution; a well-defined oxidation peak and a wave in pH 2.0 BR buffer (optimum pH value) and one well-defined oxidation peak in pH 6.0 BR buffer solutions. As can be observed from the figure, in the first scan, the intensity of peaks was higher compared to the second and third scans. The decrease in the peak intensity could be explained via electrode surface fouling. In the cathodic direction, no peak was observed which showed the irreversible electrode reaction.
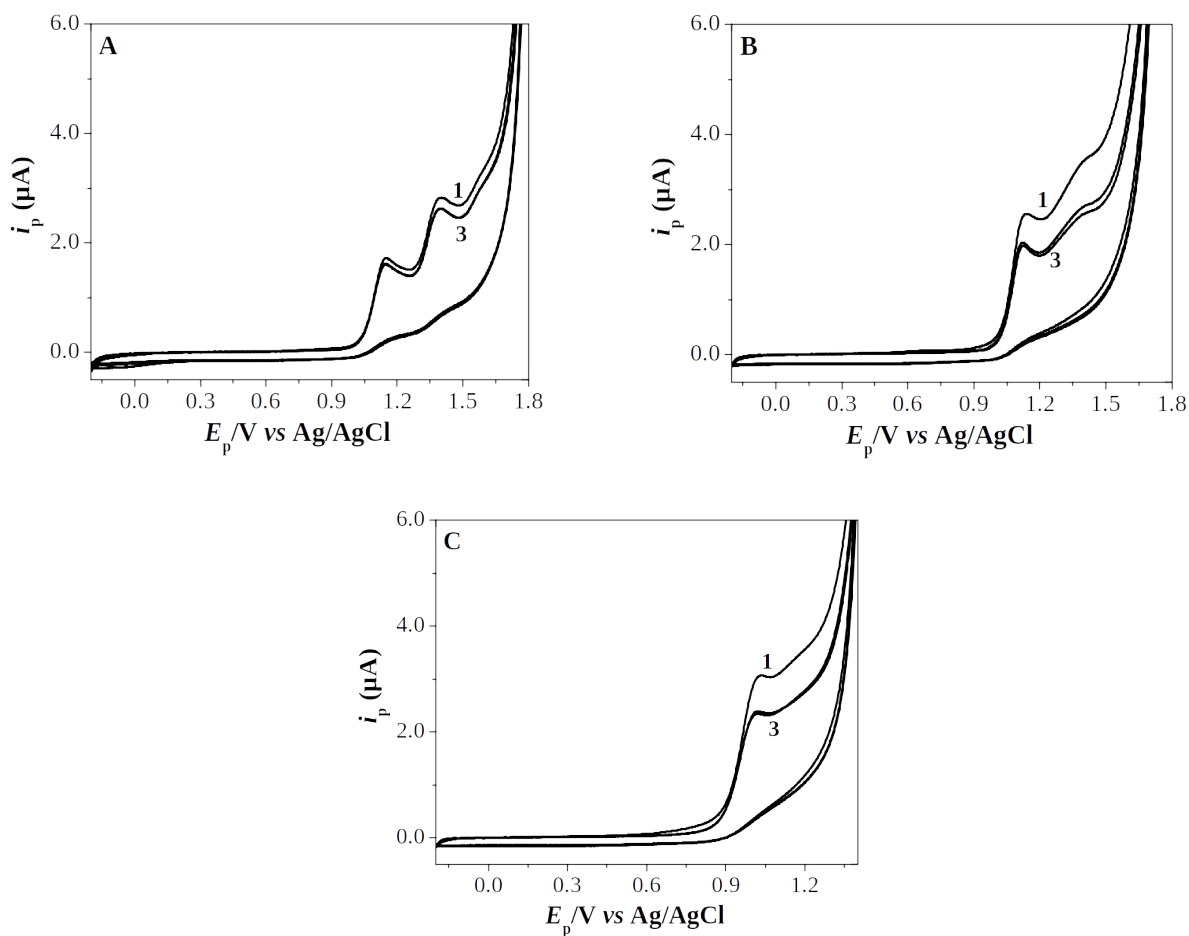
Figure 1: Repetitive cyclic voltammograms of 8×10^{-5} M FLP in 0.5 M H$_2$SO$_4$ (A), pH 2.0 BR buffer (B), pH 6.0 BR buffer (C) solutions. Scan rate: 100 mV/s. "1" means first scan and "3" means third scan of voltammograms.

The increase in the pH value resulted in a slight shift towards less positive potential values in the peak potential until pH 8.0 (using CV, DPV, SWV). The reason for this shift may probably be stemmed from the changes in protonation of the acid-base functions in the FLP. After this pH (pH 8.0), peak potential was nearly constant meaning that there were no proton transfer steps before the electron transfer rate-determining step at these pH values (Figure 2). The breakup at about pH 4.0 (for SWV pH 3.0) and pH 8.0 may be attributed to the pK$_a$ values of FLP which are 4.64 (pK$_{a1}$) and 8.16 (pK$_{a2}$) (10). The shift in the Ep values is given by the following equations:

E_p (mV) = –34.5 pH + 1192.5; r = 0.966 (pH 1.0 – 4.0 with CV)

E_p (mV) = –15.0 pH + 1119.4; r = 0.983 (pH 4.0 – 8.0 with CV)

E_p (mV) = –34.5 pH + 1115.9; r = 0.988 (pH 0.3 – 4.0 with DPV)

E_p (mV) = –18.0 pH + 1054.0; r = 0.976 (pH 4.0 – 8.0 with DPV)

E_p (mV) = –30.8 pH + 1131.1; r = 0.970 (pH 0.3 – 3.0 with SWV)

E_p (mV) = –20.1 pH + 1104.8; r = 0.976 (pH 4.0 – 8.0 with SWV)
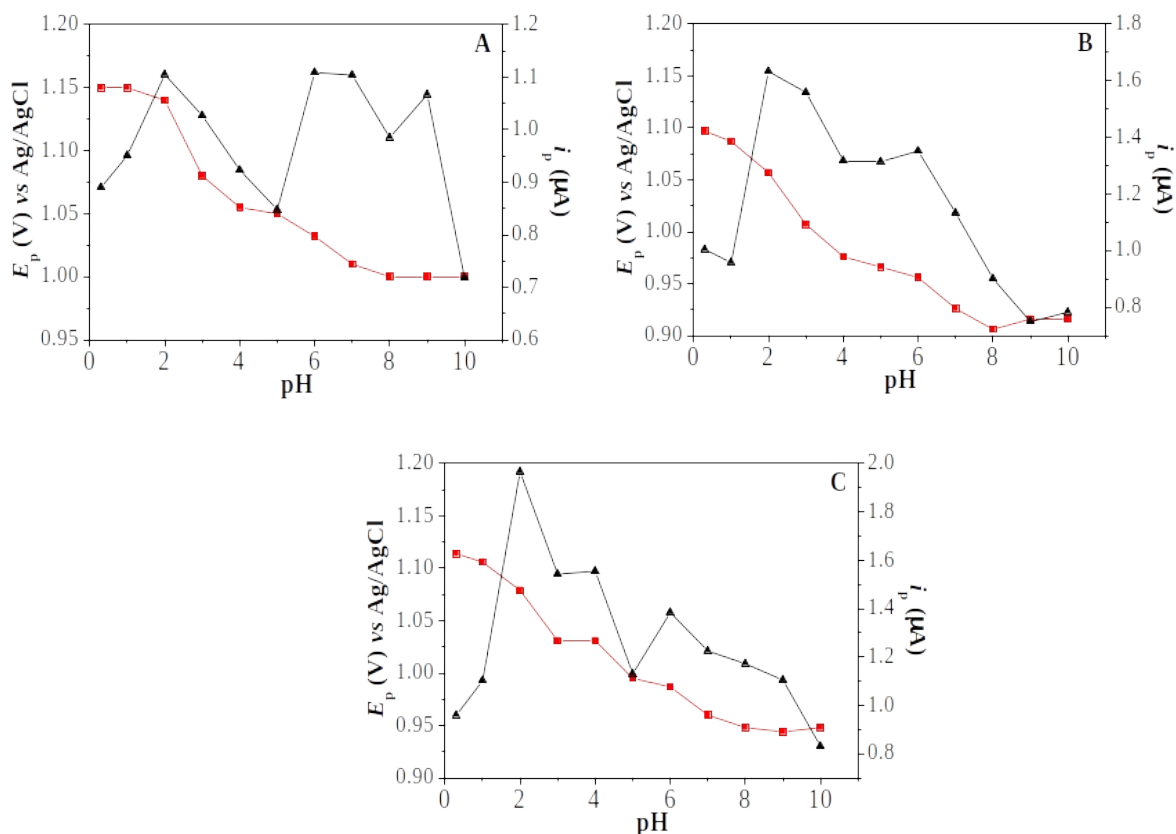
Figure 2: E_p – pH (red) and i_p – pH (black) graphs of $8.0×10^{-5}$ M FLP using CV (A), DPV (B) and SWV (C).

The graph of the pH values against the measured current values in this working pH range was shown in Figure 2. As can be seen from the graph, pH 2.0 BR buffer solution with the highest peak current and the best peak shape was selected as the most suitable medium for further studies.

The scanning rate studies were performed via CV by using $1.0×10^{-4}$ M FLP in pH 2.0 BR buffer solution at the range of 5 – 1000 mV/s. The result of the linear Randles-Sevcik plot (i_p vs $v^{1/2}$) with a correlation coefficient of 0.9944 showed that the mass transport to the electrode surface was diffusion controlled. This result was also confirmed by plotting log i_p against log v; a straight line with a slope of 0.5207 was obtained (r = 0.9981) (Figure 3). Related equations were given below:

$\log i_p = 0.5207 \log v – 0.9973$, n = 10, r = 0.9981
$i_p = 0.1189\, v^{1/2} – 0.0696$, n = 10, r = 0.9944

Increase in the scan rate values from 5 mV/s to 1000 mV/s resulted in 66 mV shift towards the positive potential values which was related to the electrode reaction irreversibility (16).

Calibration and Validation
Quantitative assessment is based on the linear relationship between current and concentration. Therefore, DPV was selected because of the repeatability. The studies were performed in pH 2.0 BR buffer solution (the methanol ratio was kept constant at 20%) where the best peak shape and the highest peak current were found. Linearity was obtained at the concentration range of $6.0×10^{-7}$ – $8.0×10^{-6}$ M (Figure 4). The related equation between peak current and concentration was as follows:

i_p (μA) = 25525.44 C (M) – 0.00969 (r = 0.999)

The regression data of the calibration is shown in Table 1. The precision of the method is demonstrated by repeated measurements of the peak potential and peak current of the FLP, within and between days. LOD and limit of quantification (LOQ) values were calculated with the formulas of 3 s/m and 10 s/m, respectively; where "s" represents the standard deviation of the response and "m" represents the slope of the calibration curve. LOD and LOQ values showing the sensitivity of the proposed method were presented in Table 1.
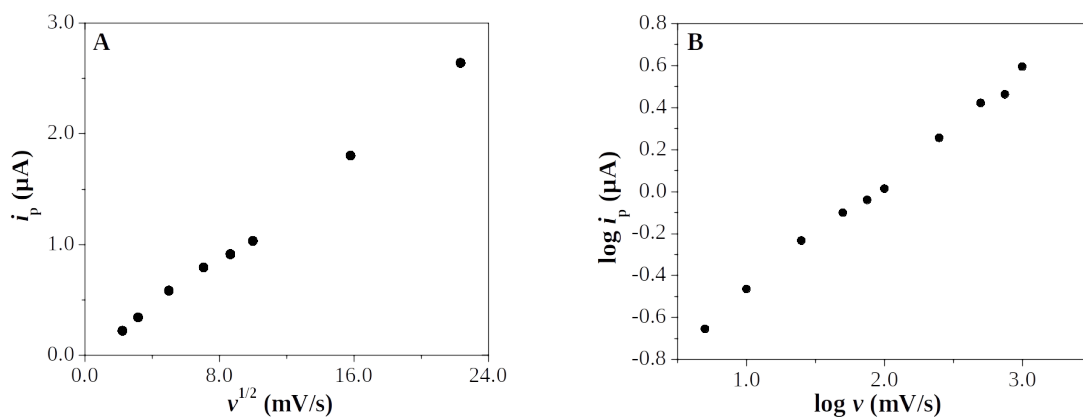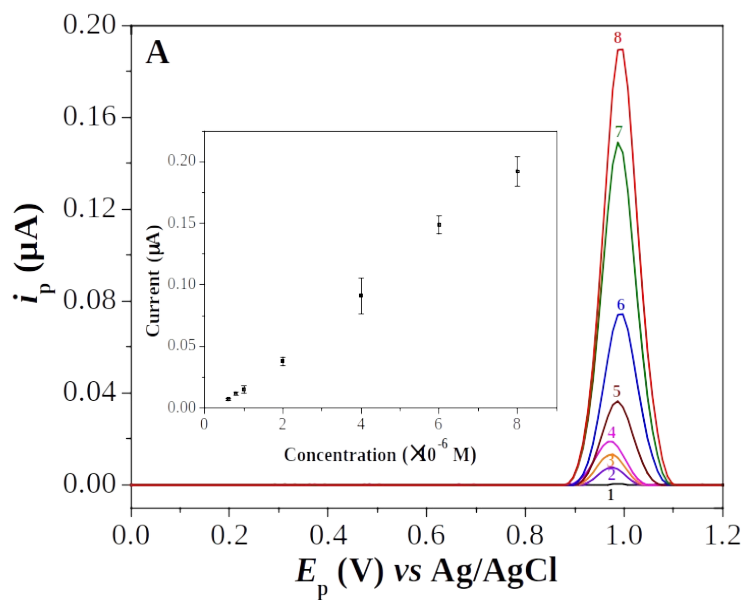
Figure 3: i_p *vs* $v^{1/2}$ (A) and log i_p *vs* log v (B) graphs of $1.0×10^{-4}$ M FLP in pH 2.0 BR buffer solution obtained in the range of 5 – 1000 mV/s.
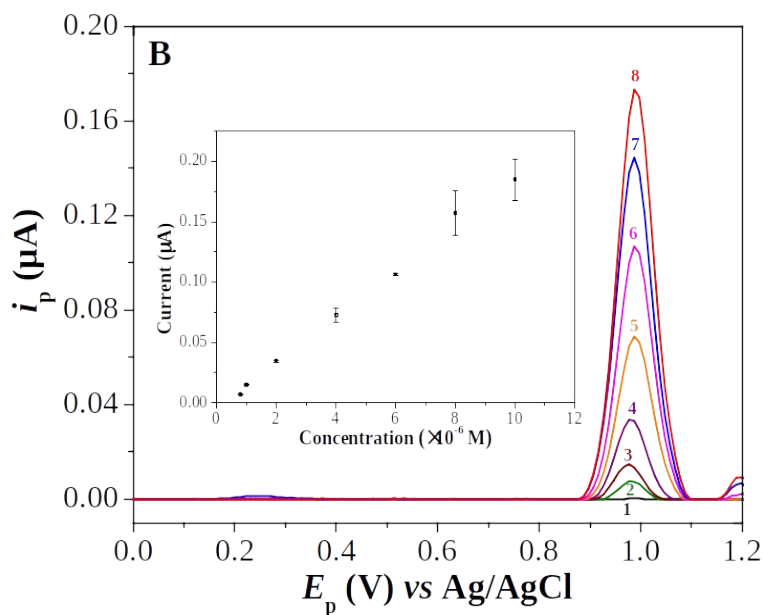
Figure 4: DP voltammograms for FLP (bulk solution) in different concentrations between 6.0×10^{-7} – 8.0×10^{-6} M (A) and DP voltammograms of serum samples in different concentrations between 8.0×10^{-7} – 1.0×10^{-5} M (B) in pH 2.0 BR buffer solution. Inset: Calibration curves.

Table 1: Regression data for calibration of FLP obtained from bulk solution and serum samples using DPV at BDDE.

	Bulk form	Serum
Measured potential (mV)	986	986
Linearity range (M)	6.0×10^{-7}–8.0×10^{-6}	8.0×10^{-7}–1.0×10^{-5}
Slope ($\mu A\ M^{-1}$)	25525.44	19435.34
Intercept (μA)	–0.00969	–0.00571
Correlation coefficient (*r*)	0.999	0.998
LOD (M)	1.09×10^{-7}	1.08×10^{-7}
LOQ (M)	3.64×10^{-7}	3.61×10^{-7}
Intra-day precision of peak current (RSD %)*	1.98	1.86
Inter-day precision of peak current (RSD %)*	2.42	2.83

*Obtained from five measurements.

Serum Sample Analysis

Quantitative determination of FLP from synthetic serum samples was realized in pH 2.0 BR buffer solutions and linear relationship between concentration and peak current was obtained as 8.0×10^{-7} – 1.0×10^{-5} M (Figure 4) with the equation below:

i_p (μA) = 19435.34 *C* (M) – 0.00571 (*r* = 0.998)

LOD and LOQ values obtained from spiked serum samples were calculated as 1.08×10^{-7} M and 3.61×10^{-7} M, respectively. Recovery studies were also made, and the average recovered % result was obtained as 99.91% using five repeatable measurements. Regression results for the calibration of serum samples were summarized in Table 1 and recovery results were shown in Table 2.

Table 2: Recovery studies obtained from serum samples using DPV at BDDE.

	DPV
Added concentration (M)	2.00×10^{-6}
Found concentration (M)	1.99×10^{-6}
Average recovered %	99.91
Number of experiments	5
RSD % of recovery	3.34
Bias %	0.09

Comparison of Published Analysis Methods

Table 3 showed the comparison of literature methods for FLP determination according to linearity range, LOD and LOQ values. Potentiometry (11), LC-MS/MS (3) and LC-ESI-MS (15) studies gave lower LOD or LOQ values when compared to this study. When comparing LC-MS/MS and LC-ESI-MS, it can be said that in the voltammetric method the requirement for organic solvent and the cost of instrumentation were minimum, also there was no need for separation and pre-treatment steps. In the potentiometric method, multi-walled carbon nanotube and copper nanoparticles modified carbon paste electrode was used for the determination of FLP which was time-consuming and costly. The method developed in this study was compared to the previously offered voltammetric methods (10), in which a glassy carbon electrode (GCE) was used. The parameters of comparison were linearity range and limit of detection (LOD) values. In this study linearity range and LOD value were obtained as $6.0\times10^{-7} - 8.0\times10^{-6}$ M and 1.09×10^{-7} M, respectively which were comparable to the literature study ($8.0\times10^{-7} - 1.0\times10^{-4}$ M and 1.17×10^{-7} M using differential pulse voltammetry-DPV). The serum analysis results via DPV revealed that the LOD value (1.08×10^{-7} M) obtained by using BDDE was lower than that obtained by using GCE (5.06×10^{-7} M). These results demonstrate that BDDE can be preferred as an alternative electrode to GCE for better detection and determination of FLP from bulk form and especially from serum.

Table 3: Comparison of developed method with literature studies about FLP.

Method	Linearity range (M)	LOD (M)	LOQ (M)	Reference
DPV	$8.0\times10^{-7} - 1.0\times10^{-4}$	1.17×10^{-7}	3.89×10^{-7}	(10)
SWV	$1.0\times10^{-6} - 1.0\times10^{-4}$	2.86×10^{-7}	4.29×10^{-7}	
Potentiometry	$1.0\times10^{-10} - 1.0\times10^{-2}$	2.5×10^{-11}	-	(11)
Spectrofluorimetry	$9.85\times10^{-7} - 4.92\times10^{-6}$	1.77×10^{-7}	5.71×10^{-7}	(12)
Second-order spectrophotometry	$5.91\times10^{-6} - 2.95\times10^{-5}$	7.09×10^{-7}	2.18×10^{-6}	(13)
LC-MS/MS	$1.97\times10^{-11} - 3.94\times10^{-9}$	-	1.97×10^{-11}	(3)
LC-ESI-MS	$7.68\times10^{-11} - 4.92\times10^{-9}$	-	7.68×10^{-11}	(15)
DPV	$6.0\times10^{-7} - 8.0\times10^{-6}$	1.09×10^{-7}	3.64×10^{-7}	This study

CONCLUSION

The voltammetric oxidation behavior of FLP was investigated by using H_2SO_4 supporting electrolytes and BR buffer solutions with pH values of 0.3 – 10.00 at BDDE. In all pH media, FLP was irreversibly oxidized, and the electrode transfer process onto the electrode surface was found to be diffusion-controlled. DPV method was used for the determination of FLP from bulk form and synthetic serum samples combined with BDDE. When the developed method was compared to DP voltammetric method in the literature (10) it was shown that the LOD values were lower in the present study. It can be said that simple, low cost, relatively fast, environmentally friendly, accurate and precise electrochemical method was developed for FLP detection and determination.

CONFLICT OF INTEREST

There is no conflict of interest.

REFERENCES

1. World Health Organization. Depression [Internet]. 2021. <URL>.

2. World Health Organization. Schizophrenia [Internet]. 2019. <URL>.

3. Abdelbary A, Bendas ER, Ramadan AA, Mostafa DA. Pharmaceutical and Pharmacokinetic Evaluation of a Novel Fast Dissolving Film Formulation of Flupentixol Dihydrochloride. AAPS PharmSciTech. 2014 Aug;15(6):1603–10. <DOI>.

4. Bozal-Palabiyik B, Uslu B. A novel electroanalytical nanosensor based on MWCNT/Fe2O3 nanoparticles for the determination of antiparkinson drug ropinirole. Ionics 2015 221. 2015 Aug;22(1):115–23. <DOI>.

5. Uslu B, Ozkan SA. Electroanalytical application of carbon based electrodes to the pharmaceuticals. Anal Lett. 2007 Apr;40(5):817–53. <DOI>.

6. Yence M, Cetinkaya A, Ozcelikay G, Kaya SI, Ozkan SA. Boron-Doped Diamond Electrodes: Recent Developments and Advances in View of Electrochemical Drug Sensors. Crit Rev Anal Chem. 2021; <DOI>.

7. Einaga Y. Development of Electrochemical Applications of Boron-Doped Diamond Electrodes. Bull Chem Soc Jpn. 2018 Oct;91(12):1752–62. <DOI>.

8.   Šelešovská R, Hlobeňová F, Skopalová J, Cankař P, Janíková L, Chýlková J. Electrochemical oxidation of anti-inflammatory drug meloxicam and its determination using boron doped diamond electrode. J Electroanal Chem. 2020 Feb;858:113758. <DOI>.

9.   Zhang G, Terry A V., Bartlett MG. Bioanalytical methods for the determination of antipsychotic drugs. Biomed Chromatogr. 2008 Jul;22(7):671–87.

10.   Dogan B, Özkan SA, Uslu B. Electrochemical characterization of flupenthixol and rapid determination of the drug in human serum and pharmaceuticals by voltammetry. Anal Lett. 2005;38(4):641–56. <DOI>.

11.   Abdallah NA. Nanoparticles based carbon paste electrodes for the determination of flupentixol dihydrochloride: Application to pharmaceutical analysis and pharmacokinetic study. Int J Electrochem Sci. 2016;11(12):10715–31. <DOI>.

12.   Mostafa IM, Derayea SM, Nagy DM, Omar MA. Benzofurazan-based fluorophore for the selective determination of flupentixol dihydrochloride: Application to content uniformity testing. Luminescence. 2018 Apr;33(6):1026–32. <DOI>.

13.   Lakshminarayana B, Jose Gnana Babu G, Menaka T, Yogesh DB. Development and Validation of Second Order Spectrophotometric Method for Quantitative estimation of Flupentixol dihydrochloride in Bulk and Pharmaceutical dosage form. Int J ChemTech Res. 2011;3(2):580–3.

14.   Sheikh IA, Charde MS, Kasture AV. Estimation of Flupenthixol HCl in single dosage form by RP-HPLC method. Int J Pharm Anal. 2009;1(2):11–9.

15.   Zuo XC, Zhang BK, Chen BM, Liu SG, Yang GP, Liu SK, et al. LC-ESI-MS determination of flupentixol in human plasma. Chromatographia. 2009 Nov;69(3–4):301–5. <DOI>.

16.   Pinar PT, Saadi Ali H, Abdullah AA, Yardim Y, Şentürk Z. Electroanalytical determination of salbutamol in pharmaceutical formulations using cathodically pretreated boron-doped diamond electrode. Marmara Pharm J. 2018;22(3):460–8. <DOI>.

Application of *Pistacia atlantica* Leaves Powder as Natural Material To Remove Nitrate and Phosphate Ions From Domestic Wastewater by Characterization, Bio-removal, and Phytotoxicity Studies

Obaida Alhajali¹* (iD)**, Adnan Ali-Nizam¹** (iD)**, Rasha Almostafa²** (iD)

¹Damascus University, Department of Plant Biology, Damascus, Syria.
²International University for Science and Technology, Department of General and Analytical Chemistry, Syria.

Abstract: Description of *Pistacia* leaves powder using scanning electron microscopy (SEM), Fourier transform infrared spectroscopy (FT-IR), Energy-dispersive X-ray spectroscopy (EDX), specific surface area according to nitrogen adsorption (S_{BET}) and methylene Blue (MB), and point of zero charge determination (pHpzc). A series of batch adsorption tests were conducted to study effect of various factors (plant powders dose, contact time, temperature, pH) on the percentage of nitrate and phosphate removal from domestic wastewater. The adsorption kinetics, regeneration ability test of plant powder, and phytotoxicity tests for treated water and spent powder on germination were studied. Results of S_{BET} analysis showed that *Pistacia* leaves powders have a low surface area and microscopic pores, SEM images revealed rough surfaces with uneven cavities, EDX analysis showed that there are high percentages of carbon and oxygen, good percentages for nitrogen, and few percentages of potassium, calcium, magnesium, phosphorous, sulfur and chlorine, and FTIR analysis showed that there are more than five distinct absorption peaks. The maximum value of nitrate and phosphate removal was 76.47% and 52.20%, respectively, at powder dose of 2 g/L, temperature 25 °C, and pH 5, and the percentage of nitrate and phosphate removal increased with increasing contact time until equilibrium was reached after 120 min for nitrate and 180 min for phosphate, and It was found that adsorption of ions follows kinetics of reaction from pseudo-second-order model, and powders can be Regeneration and used for two successive cycles with a slight decrease in removal efficiency. Germination tests on *Lepidium sativum* indicate no phytotoxicity. That is, *Pistacia* leaves powder is one of the natural products that are effective in removing nitrate and phosphate from domestic wastewater.

Keywords: Domestic Wastewater, *Pistacia* Leaves, Nitrate, Phosphate, Adsorption Kinetics, Regeneration Study, Phytotoxicity.

INTRODUCTION

Unquantifiable quantities of domestic, agricultural and industrial wastewater are discharged untreated into natural water systems; Which causes serious environmental problems in many countries of the world. These wastes contain heavy metals, dyes, inorganic anions and harmful chemicals, some of which are stable and indissoluble, in addition to environmental movement and bioaccumulation in the food chain, beside their toxicity and health risks to humans and animals at very low concentrations (1). Nitrate and phosphate concentrations above 0.5-1 mg/L in water bodies lead to the emergence of

eutrophication phenomenon, excessive growth of algae and consumption of dissolved oxygen, which leads to damage in water systems and deterioration of water quality (2), and leaching of nitrate and phosphate lead to pollution of groundwater and water bodies. Increased nitrate cause miscarriages and reduced milk production, and a high concentrations (> 300 mg/L) in water or plants irrigated with wastewater lead to an acute toxicity to livestock and the occurrence of diseases, and cause Methemoglobinemia syndrome and cancer.

Several chemical, physical and biological techniques have been used to remove nitrate and phosphate, such as biological de-nitrification, electrocoagulation, reverse osmosis, electro-dialysis, ion exchange, and chemical precipitation by aluminium sulfate and iron sulfate, and membrane technology (7), but these technologies are expensive, requires additional operation and maintenance costs, and produces large amounts of toxic sludge. Therefore, use of plant waste as an adsorbent in wastewater treatment is an effective and inexpensive alternative, as it is highly efficient, environmentally friendly and renewable (3), such as removing heavy metals (4), and chemical ions (5, 6) from water. More than 90% of phosphate was removed from aqueous solutions using *Phoenix dactylifera* powder at 120 min, 18 °C, pH 5, a shaking rate of 200 rpm, and an initial phosphate concentration of 50 mg/L (8), 80% removal of nitrate using Banana peels powder during 30 minutes, and an initial concentration of nitrate 200 mg/L (9), and removing nitrate between 96-100% and phosphates between 56-77% using leaves powders of three plant species (10).

Biosorption mechanisms include by plant waste powders different mechanisms such as Electrostatic Attraction, Van der Waals Attraction, Ion Exchange, Complexation, and Covalent Binding (11). The effectiveness of biosorption depends on the physical and chemical properties of plant waste, in addition to the initial concentration of the contaminated, plant powder dose, contact time, pH, and temperature (12).

The aim of this study was to characterize *Pistacia atlantica* leaves powder using different techniques (SEM, EDX, FT-IR, SBET, and pHpzc), and to evaluate its efficiency as low-cost, available and environmentally friendly materials in removing nitrate and phosphate from domestic wastewater by studying the effect of various factors (plant powders dose, contact time, temperature, and pH), and test its regeneration ability, and to test the reusability of this water through phytotoxicity studies in order to reduce negative impacts on the environment and achieve sustainable development and economic feasibility.

MATERIALS AND METHODS

Preparation of Plant Powder
Leaves of *Pistacia atlantica* were collected from Sweida city in Syria, and washed with distilled water 2-3 times, and dried in shade for two weeks until the weight was stable, then they were ground and sieved with 250 µm mesh, and stored in sterilized glassware in the refrigerator at 4°C until use without any treatment. The symbol *Pa*-LP is used to indicate *Pistacia atlantica* leaves powder.

Collection of Domestic Wastewater Samples
Samples were collected from the end point in Jaramana city (east of Damascus) in polyethylene glass bottles with a capacity of 1000 mL. The glassware was washed with hydrochloric acid and then distilled water 3 times to remove acid residues (13). The values of some physical, chemical and microbiological characteristics of domestic wastewater samples used in the experiments are shown in Table 1.

Table 1: Minimum and maximum values for the characteristics of domestic wastewater samples used in experiments.

Tests	Untreated domestic wastewater	Units
Temperature	21.32 – 23.43	°C
pH	7.20 – 7.62	-
Total Dissolved Solids	571 - 606	mg/L
Electrical Conductivity	823 – 949.66	µS/cm
Turbidity	169 – 189	NTU
Nitrate	30.5 – 40	mg/L
Phosphate	42 - 50	mg/L
Biochemical Oxygen Demand	195 – 250	mg/L
Viable Count Bacteria	276×10^5 - 322×10^5	CFU/mL
Total Coliform	224×10^4 – 295×10^4	CFU/mL

Characterization of Prepared Plant Powder
Point of zero charge determination (pHpzc)
Mass titrations method was adopted by taking 0.02-6 g of powder and adding 20 mL of 0.03 M KNO_3 solution to it for 24 hours at a temperature of 25 °C and a shaking speed of 250 rpm (14). The pHpzc value is the balanced pH versus amount of plant powder.

Determination of specific surface area (S_{BET}) of plant powders by nitrogen adsorption
The specific surface area and porosity of the plant powders used in experiments were measured by Micromeritics Gemini 3 device according to Brunauer, Emmett and Teller (BET) for adsorption of nitrogen (N2).

Determination of surface area of plant powders by methylene blue adsorption
Methylene blue dye adsorption was studied by preparing a series of concentrations from its aqueous solution 0 to 5.82 mg/L (Figure 1), 0.05 g of powder was taken and 10 mL of dye solution was added at a concentration of 93.75 mg/L at room temperature for 150 minutes at a shaking speed of 160 cycle/min and pH 8, then the solutions were centrifuged at 4500 rpm for 15 minutes. The absorbance was measured by a UV/VIS spectrophotometry device (Model: Optizen 2120UV PLUS) at the maximum wavelength λmax = 665 nm. The concentration of each solution at equilibrium C_e

(mg/L) was calculated from the calibration curve, adsorbate amount of the dye was calculated according to the following relationship (15):

$$a = V(C_0-C_e)/W \quad \ldots\ldots\ldots \quad (1)$$

Where C_0 is the initial concentration of the dye (mg/L), C_e is the equilibrium concentration of the solution (mg/L), V is the total volume of solution (L), W is the weight of *Pa*-LP (g).

The percentage removal R (%) was calculated from the following relationship (15):
$$R = C_0-C_e/ C_0 \times 100 \quad \ldots\ldots\ldots \quad (2)$$

The surface area of the powders was calculated by applying the relationship:
$$S= q_e \times N_a \times 130 \times 10^{-20} \quad \ldots\ldots\ldots \quad (3)$$

Note that the cross-sectional area of methylene blue is 130×10^{-20}, $N_a = 6.022 \times 10^{23}$.
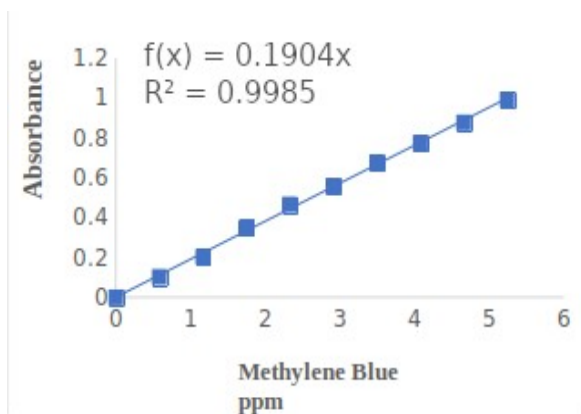
Figure 1: Absorbance of a methylene blue solution as a function of concentration.
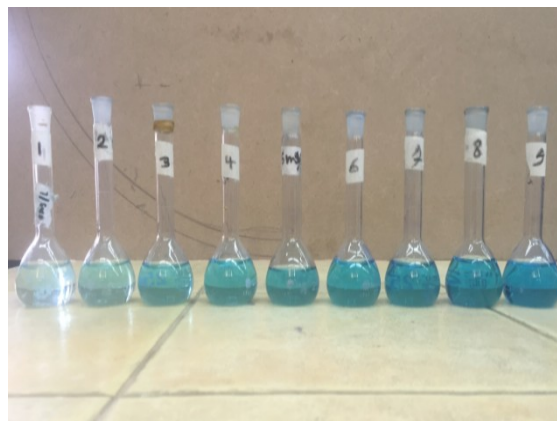
Characterization of the prepared plant powder using a scanning electron microscopy (SEM)
A VEGA_{XMU} electron microscope was used, which is connected to an X-ray analysis unit (EDAX-AMETEX), the sample was dried and then placed on a piece of special carbon adhesive, and attached to an aluminum holder, then inserted into the sample chamber of the microscope, and a high vacuum system was applied to it 10^{-3} mbar and 30 KV high voltage for chemical composition analysis of samples and determining pore dimensions (8).

Fourier transform infrared (FT-IR) analysis
The FT-IR spectrum was recorded with a Nicolet 6700 device to determine the effective functional groups of plant powders by taking 1 ± 0.1 mg of the sample with 100 ± 0.1 mg of dry potassium bromide (KBr) by placing the mixture between two metal discs and by pressing the material turned into a coherent transparent disc within a special holder, which was placed in FT-IR spectroscopy device disk (16). The conditions used were: Number of sample scans: 32, Number of scan points: 8480, spectral

range: 400 - 4000 cm^{-1}, and Laser frequency: 15798.3 cm^{-1}.

Experiments of Domestic Wastewater Treatment by *Pistacia atlantica* Leaves Powder
A series of experiments were conducted to study the effect of plant powders dose, contact time, temperature, and pH to removing nitrate and phosphate from domestic wastewater (Table 2) by batch adsorption method with some modification (6, 17)**.** 250 mL Erlenmeyer flasks each with 100 mL of domestic wastewater with a laboratory shaker at 150 rpm, the water was filtered after treatment with Whatman (No.45). The concentrations of nitrate and phosphate were measured after treatment according to standard methods using HACH DR 5000 spectrophotometer (13). The wastewater pH values were adjusted using HCl (0.1 M) and NaOH (0.1 M), and all experiments were performed with triplicates, and the removal efficiency was calculated by the following equation (17):

$$\% \text{ Removal} = C_i–C_f/C_i \times 100 \quad \ldots\ldots\ldots \quad (4)$$

Where C_i, C_f are the initial and final concentration of nitrate and phosphate in domestic wastewater.

Regeneration Ability Test of Plants Powder
This experiment was conducted to evaluate the efficiency of plant powder prepared for reuse three successive cycles after the first cycle for removing nitrate and phosphate from domestic wastewater**.** It was placed according to the optimal conditions (Table 2) in 100 mL of domestic wastewater, then the efficiency of removing nitrate and phosphate

from the water was determined (Cycle 0), the samples were dried in shade at room temperature and placed in 100 mL of NaOH solution (0.5 M) for 180 minutes at a temperature of 25 °C depending on the ion exchange mechanism, then washed with distilled water, the dried samples were applied in the next treatment process and the removal efficiency was calculated from the water (cycle 1), the treatment process was repeated through three successive cycles, and all experiments were performed with three replications (17, 18).

Table 2: A series of experiments for removing nitrate and phosphate from domestic wastewater by using *Pa*-LP.

Series of Experiments	Powder Dose (g/L)	Contact Time (min)	Temperature (°C)	pH	Nitrate concentration in wastewater (mg/L)	Phosphate concentration in wastewater (mg/L)
Effect of Powder Dose	0.5-4	300	27	6.5	32.56	42
Effect of Contact Time	2	30-240	27	6.5	31.53	44
Effect of Temperature	2	120 (NO_3) 180 (PO_4^{-3})	15-35	6.5	30.5	42.5
Effect of pH	2	120 (NO_3) 180 (PO_4^{-3})	25	5-9	36.56	49.8
Powder Regeneration	2	120 (NO_3) 180 (PO_4^{-3})	25	6	40	50

Phytotoxicity Tests For Treated Domestic Wastewater and Spent Plant Powders
The germination percentage of *Lepidium sativum* seeds was studied to determine the phytotoxicity of the treated domestic wastewater and spent plant powders after the treatment process as follows (19):

(1) Determination of the phytotoxicity of treated water: 40 g of sterile soil moistened with treated domestic wastewater (30 mL) was placed in 50 g plastic plates and 30 seeds of *Lepidium sativum* were planted in each plate. Drinking water was used as a positive control and untreated domestic wastewater as a negative control, then the plates were placed at 25°C and alternated between dark and light (10 h dark vs 14 h light) for 10 days.

(2) Determination of the phytotoxicity of spent plant powders after the treatment process: the plant powders were dried in the shade for 14 days until the weight was relatively stable. 20 g of the dried powders were placed in 50 g plastic plates, 30 seeds of *Lepidium sativum* were planted in them and irrigated with distilled water (30 mL), and soil was used as a positive control, then the plastic plates were placed for 3 days at a temperature of 25°C alternated between dark and light (10 h dark vs 14 h light). All experiments were performed with three replications and the percentages of germination for all experiments were calculated using the following equation (19):

Germination percentage of *Lepidium sativum* seeds (%) = number of germinated seeds / total number of seeds x 100 .... (5).

Study of Adsorption Kinetics
The adsorption kinetics of nitrate and phosphate ions were studied according to the pseudo-first order and pseudo-second-order model, which are known in batch systems.

The pseudo-first-order model is expressed by the following equation (20):

$$\ln (a_e - a) = \ln a_{1e} - k_1 t \text{ .... (6)}$$

Where a_1: the reaction rate constant of pseudo-first-order (min^{-1}), a_{1e}: the adsorbate amount (mg/g); [calculated by graph from the slope and secant value when plotting $\ln (a_e - a)$ versus t], a_e and a (mg/g) are the amount of nitrate and phosphate sorbed at equilibrium and time, respectively.

The pseudo-second-order model is expressed by the following equation (20):

$$t/a = 1/k_2(a_{2e})2 + (1/a_{2e}) t \text{ .... (7)}$$

Where k_2: the reaction rate constant of pseudo-second-order (g/mg min), a_{2e}: the adsorbate amount (mg/g); [calculated by graph from the slope and secant value when plotting t/a versus t], a: the amount of nitrate and phosphate sorbed during time.

The adsorbate amount of nitrate and phosphate was calculated according to the following relationship (20):

$$a = V(C_0 - C_e)/W \text{ .... (8)}$$

Where C_0 is the initial concentration of the dye (mg/L), Ce is the equilibrium concentration of the solution (mg/L), V is the total volume of solution (L), W is the weight of the *Pa*-LP (g).

Statistical Study

Correlation relationships were studied based on Pearson's correlation coefficients using Correlation Matrix (SPSS[22] software), and one-way analysis of variance (ANOVA) was adopted to test the presence of significant differences. Data was considered statistically significant at minimum level of $P < 0.05$.

RESULTS AND DISCUSSION

Point of zero charge determination (pHpzc) of *Pa*-LP

The pHpzc of the used powder was set at 6.97 (Figure. 2); which indicates that the charge is negative on the surface of the powder at pH higher than 6.97 and positive at pH less than 6.97. The pHpzc value of the used powder corresponded to that of *Salix babylonica* and *Platanus* leaves powder 6.98 and 7.00, respectively (21, 22), and was less than that of coconut pulp fiber 8.2 (23), and higher than olive stones and Grape Stalks residues 4.2 and 5.2, respectively (14). The pHpzc is an essential property in determining the electrical neutrality of materials used in treatment at a certain pH value, in addition to its effect on the ionization of surface functional groups and understanding the mechanism of the effect of pH of solution.
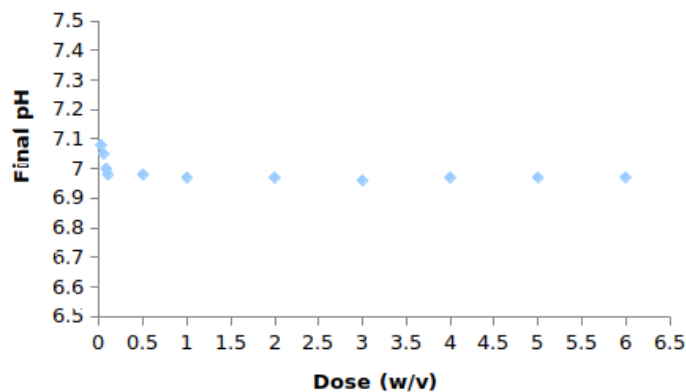
Figure 2: The pHpzc of *Pa*-LP.

Determination of the surface area of plant powder according to nitrogen adsorption (S_{BET}) and methylene blue (MB)

The specific surface area of *Pa*-LP was 1.1 ± 0.05 m²/g according to BET, and total pore volume was $0.030 \times 10^{-2} \pm 0.02$ cm³/g, and the average pore radius was 0.543 ± 0.27 nm; That is, the plant powder has micropores (24). This is consistent with several studies that indicated a decrease in the specific surface area and pore size of plant powder that was not treated physically or chemically. The specific surface area ranged between 0.48-10.9 m²/g (25, 26, 27, 28, 29), and the total pore size ranged between 0.0002-0.11 cm³/g (30, 31, 32, 33, 34), and the average pore diameter of *Pistacia vera* shell powder was 0.77 nm (30) and *Prunus dulcis*

leaves 3.713 nm (33) and *Arundo donaxn* plant 4.320 nm (18).

The surface area of the studied powders according to adsorption of methylene blue was 40.283 ± 0.09 m²/g, which confirms the adsorption efficiency (Figure. 3); The percentage removal of methylene blue was $97.695\% \pm 0.23$ and the adsorption capacity (qe) was 18.317 ± 0.04 mg/g; this may be attributed to the electrostatic attraction forces between dye (+) and sites (-) on the surface of the powder because the specific surface area of the leave powder is low and the ability of the surface functional groups is greater in removing contaminants (35).
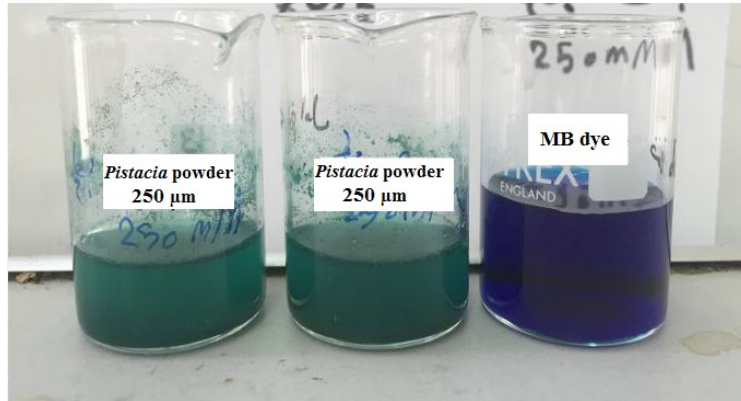
Figure 3: Efficiency of *Pa*-LP in removing methylene blue dye.

The adsorption capacity of methylene blue for oak leaves powder was 33.5 mg/g (15), and for orange and banana peels 18.6 and 20.8 mg/g, respectively (36). The surface area according to adsorption of methylene blue to chemically modified tea leaves was 174.8 m^2/g, and *Aegle marmelos* trees leaves powder 110.21 m^2/g (37). It is noticed that the recorded surface area of the powders prepared according to the adsorption of methylene blue is higher than the surface area according to nitrogen adsorption.

Characterization of samples prepared using scanning electron microscopy (SEM)

The results showed that studied samples contain irregularly shaped structure with uneven cavities, heterogeneous rough surfaces and pores of different dimensions (Figure. 4). Researches has indicated that the irregular surface structure of the plant powder is effective in removing anions, cations and heavy metals from domestic wastewater (10, 38, 39).
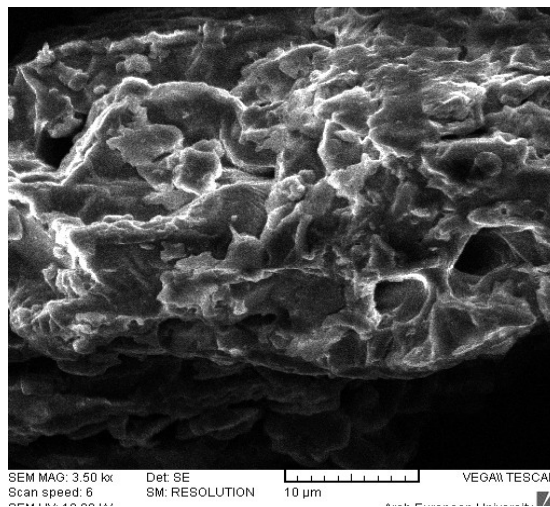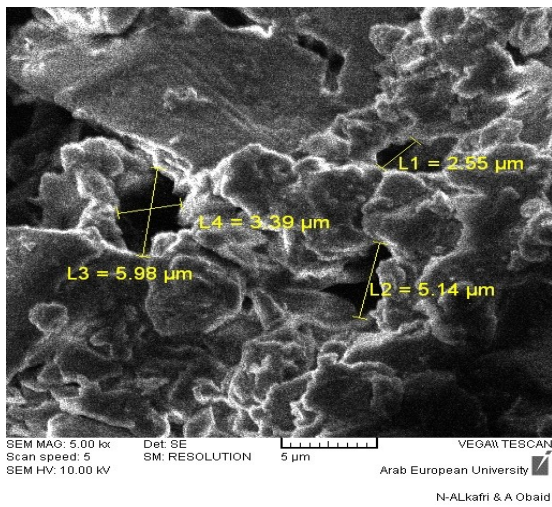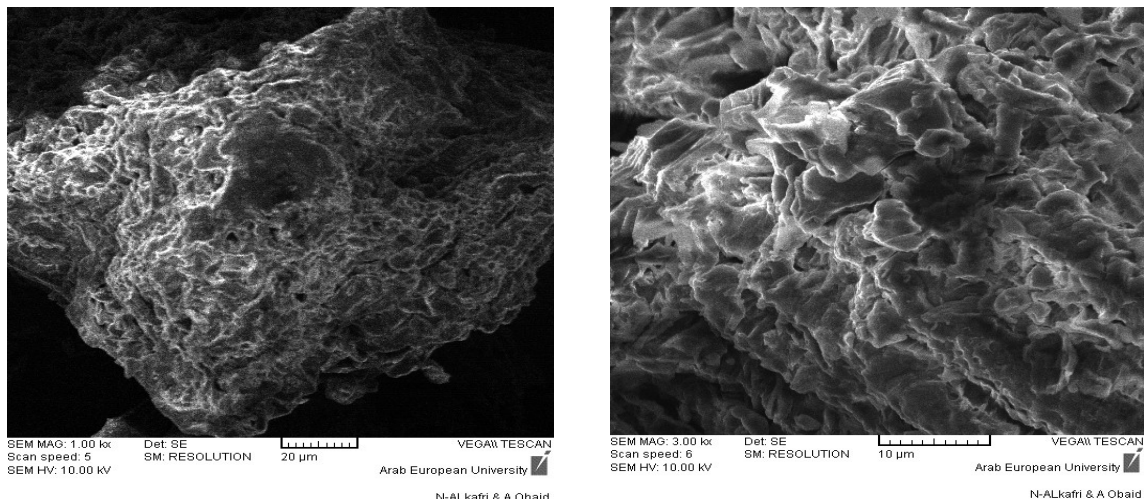
Figure 4: The surface structure of *Pa*-LP using SEM.

Characterization of samples prepared by Energy-dispersive X-ray spectroscopy (EDX)

EDX analysis showed the presence of high percentages of carbon and oxygen and good percentages for nitrogen. In addition to the presence of few percentages of potassium, calcium, magnesium, phosphorous, sulfur and chlorine (Figure 5), as all the previous elements are essential in *Pistacia atlantica*, and the appearance of silicon is due to the sample holder made of aluminum and dotted with silicon. It is noted that the weight percentages of same elements differ in several areas of the surface of samples (Table. 3). This indicates that the surfaces of samples are heterogeneous. These results are consistent with the researches that confirmed that plant powders contain high percentages of carbon and oxygen between 29.10-38.52% and 52.25-59.51%, respectively, and low rates between 0.22-3.72% for the rest of the elements such as potassium, calcium, magnesium, sodium, chlorine, sulfur and iron (10). Plant leaves powders contain high percentages of carbon and oxygen between 31-51% and 31.4-64.1%, respectively, and nitrogen between 0.34-3.61%, this varies according to characteristics and composition of leaves for each plant species (40).

Table 3: The weight percentages % of elements analyzed by EDX in the studied areas on the surface of *Pa*-LP.

Elements (K)	Area 1	Area 2	Area 3	Area 4	Average Percentages%
C (K)	59.09	59.14	61.4	61.13	60.19
O (K)	30.64	34.88	27.7	27.55	30.1925
N (K)	5.77	3.88	10.62	6.77	6.76
K (K)	2.24	0.39	-	1.0	0.9075
Ca (K)	1.85	-	0.03	1.05	0.7325
P (K)	0.41	0.35	-	0.48	0.31
Mg (K)	-	0.84	0.08	0.56	0.37
S (K)	-	0.15	-	0.45	0.15
Cl (K)	-	0.15	-	0.4	0.1375
Si (K)	-	0.22	0.01	0.62	0.2125
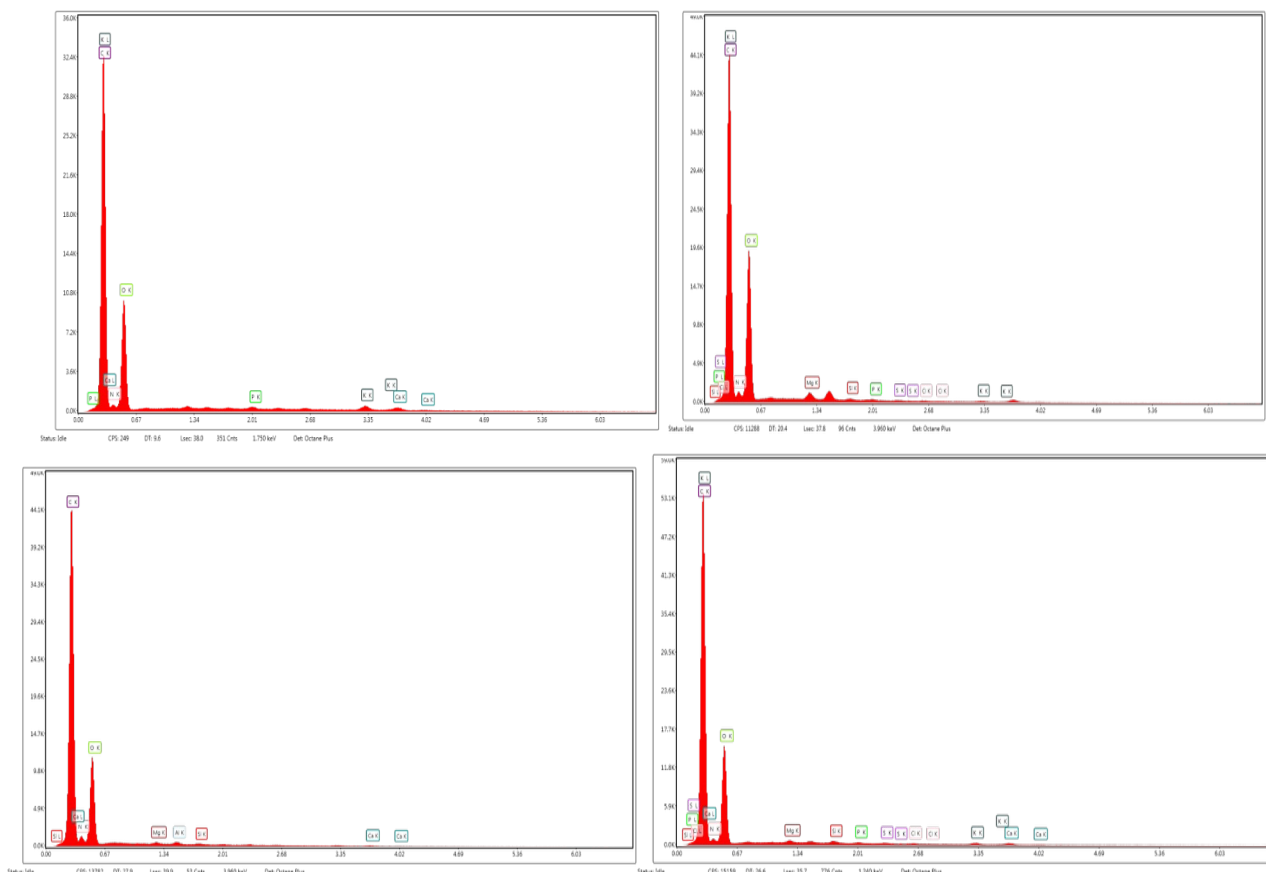
Figure 5: EDX spectra of studied areas on the surface of *Pa*-LP.

Fourier transform infrared (FT-IR) Spectroscopy of *Pa*-LP

More than five distinct absorption peaks are observed (Figure. 6); This confirms the complex nature of the studied samples (41). The broad and strong peak observed between 3000-3700 cm^{-1} is du to the stretching vibration of the hydroxyl (-OH) group of of alcoholic and phenolic compounds, and stretching vibration of the amine (-NH) group (42, 43). The peaks at 2920 and 2842 cm^{-1} are attributed to the asymmetric and symmetric stretching of the methylene (CH$_2$) and methyl (CH$_3$) groups (44, 45), and the peak corresponding to stretching vibrations –NH$_2^+$, –NH$^+$, and –NH groups appears in the range 2300-2800 cm^{-1} usually (46). The observed peak at 1700-1725 cm^{-1} is attributed to stretching of carbonyl (C=O) group of carboxylic acid or ketones (43, 47), and the peak at 1620 cm^{-1} appears for C=O bond stretch of the amide group, or N-H bond bend, or carbonyl group stretch of -COOH (41, 44, 48). The peak 1536 cm^{-1} belongs to carboxyl groups (44), and the peak 1454 cm^{-1} corresponds to the bending of C-H group that appears in the range 1445-1485 cm^{-1} (41), and the peak 1370 cm^{-1} is attributed to the bending of CH3 group or C–N stretching vibration, which corresponds to the amine groups (8, 47, 49). The peak corresponding to the stretching of P-O-C group appears in the range between 1190-1240 cm^{-1} (41), and the peak 1070 cm^{-1} is attributed to the

stretching of C-O or C-N group of the primary amine group (41, 42, 48), while the peaks at 763 and 831 cm^{-1} are due to the bending of C-H group in the aromatic ring (47).

Some changes were observed on *Pistacia atlantica* powdered leaves after removal of nitrate and phosphate, such as a decrease in the intensity of the broad peak between 3000-3700 cm^{-1}, This is consistent with the research that indicated that changes in the intensity of the peak between 3400-3600 cm^{-1} after adsorption may be attributed to the complexation of ions with hydroxyl groups -OH, which confirms the important role of acidic groups (hydroxyl and carboxyl ions) in the complexation of ions and ion exchange process (44). The changes observed at the peak 2920 cm^{-1} indicate ion exchange between symmetric or asymmetric C-H protons of aliphatic acids (44), and the peak disappears at 2355 cm^{-1} indicating the possibility of adsorption of nitrate and phosphate onto the surface of the powder by the electrostatic attraction between NO$_3^-$, PO$_4^{-3}$ and positively charged amine sites (50). It was observed that the intensity of the peak 1620 cm^{-1} became less extreme, and this agrees with many studies that confirmed the changes at the peak of 1620 cm^{-1} after adsorption of phosphate, lead (Pb^{+2}) and cadmium (Cd^{+2}) on

766

lemon peel powders and mistletoe leaves from polluted water (48).

Changes in the range between 1500-1660 cm^{-1} may be due to electrostatic attraction forces between adsorption sites and adsorbate ions (44), it was observed that the peak intensity of 1225 cm^{-1} decreased, which may be attributed to an important role in the stretch of P-O-C group in adsorption of

phosphate; The P-O-C group has a major role in adsorption of phosphate from aqueous solutions on *Phoenix dactylifera* fiber powders (8). FTIR spectroscopy analysis shows that the former surface functional groups present in *Pa*-LP are involved in adsorption and removal of contaminants from domestic wastewater by various mechanisms (eg. ion exchange, electrostatic attraction, surface complexity).
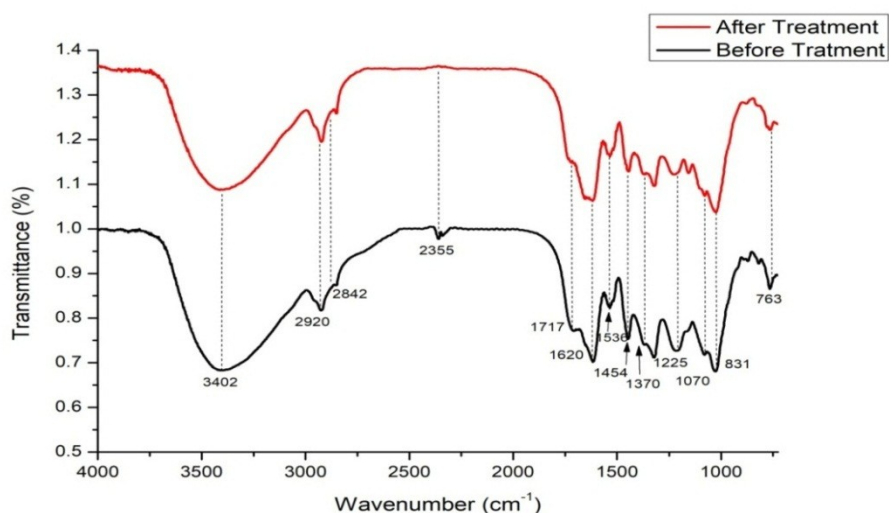
Figure 6: FT-IR spectroscopy of *Pa*-LP before and after domestic wastewater treatment.

Removing nitrate and phosphate from domestic wastewater using *Pa*-LP
Effect of Plant Powder Dose
Figure 7 shows that increasing *Pa*-LP dose from 0.5 to 3 g/L led to an increase in removal efficiency of nitrate from 26.28 to 64.37% and phosphate from 17.85 to 47.61%; This confirms the existence of a direct correlation between powder dose and efficiency of removal to a certain extent, and the adsorption capacity at 2 g/L was 10.28 mg/g for nitrate and 9.55 mg/g for phosphate which decreased to 6.98 mg/g for nitrate and 6.66 mg/g

for phosphate when using 3 g/L, so 2 g/L of powder was used to complete the experiments. This is due to the fact that increase in powder dose leads to an increase in the surface area and available adsorption sites (50, 51), but the increase in powder dose over the optimum value leads to a decrease in removal efficiency due to the accumulation and agglomeration of powder particles (52). This is consistent with the results of researches on *Phoenix dactylifera* fibers and stones (8, 53), rice husk and citrus limetta residues (2), and tea leaves treated with N,N-dimethylformamide (50).
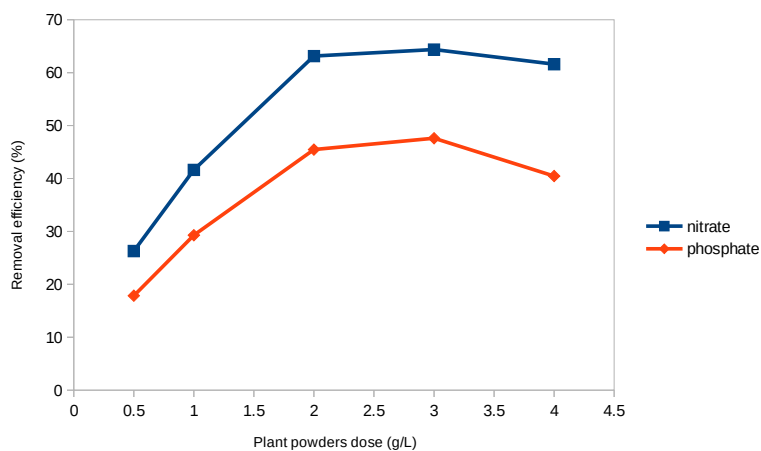

Figure 7: Effect of *Pa*-LP dose in removing nitrate and phosphate from domestic wastewater (Contact Time: 300 minutes, Temperature: 27 °C, pH 6.5, and Shaking Speed: 150 rpm.

Effect of Contact Time
Figure 8 shows the increase in the efficiency of removing nitrate and phosphate with an increase in contact time to a certain extent until stability. The process of removing ions from water is carried out in two stages. The first is fast during 60 min at a rate of 60.67% for nitrate and 120 min at a rate of 42.72% for phosphate, then followed by a gradual increase in removal, but became slow until 120 min at a rate of 63.52% for nitrate and 180 min at a rate of 44.54% for phosphate and after that the removal is relatively constant, so the equilibrium time was adopted at 120 min for nitrate and 180 min for phosphate to complete the experiments, and the rapid removal is initially attributed to the abundance of active sites on the surface of powder, and the result of their gradual occupancy due to presence of repulsive forces between adsorbate ions on the surface of powder and other ions in the water, thus the adsorption becomes less efficient and slower until it reaches equilibrium (10). It has been observed that the removal efficiency of prepared powders depends on the type of ions because the removal of nitrate is higher than that of phosphate; This may be attributed to the specificity of the interactions between the ions and the active sites on the surface of the powder (39), in addition to the presence of many ions in domestic wastewater that may compete with phosphate ions for adsorption sites (54).

The equilibrium time required to remove nitrate and phosphate from water varied with the species of plant powder; As it was 120 min for plant powders with a removal efficiency of 96, 98, 100% when using 1 g/L (10), 25-30 min for wheat straw powder modified with amino groups (55), and the percentage of phosphate removal from wastewater was 89.1% after 120 min using 2 g/L of chemically modified rice husk powder (56). It was possible to remove about 80% of phosphate after 60 min of treatment using 1.5 g/L of lemon peel powder and pH 5.5 (48), and it was 94.68% after 120 min of treatment using 6 g/L of *Phoenix dactylifera* fiber powders, temperature of 18 °C, shaking speed of 200 rpm, and pH 5 (8), and this differs from the results of this research due to the difference in the species of plant powder and the conditions of the experiment.
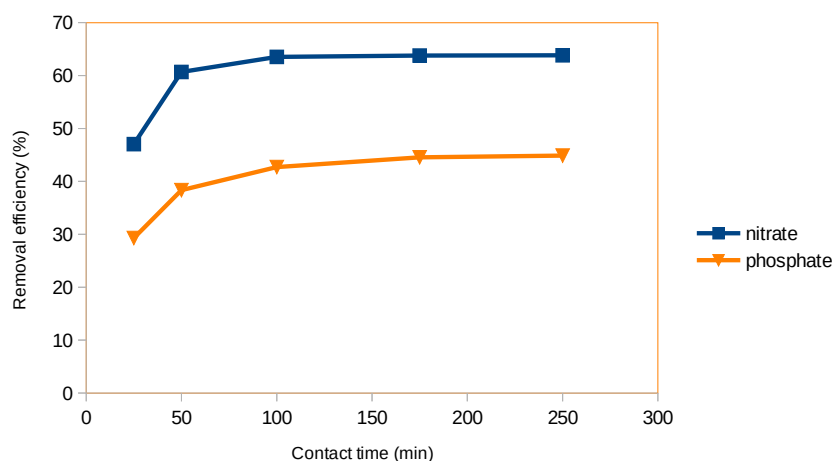

Figure 8: Effect of contact time in removing nitrate and phosphate from domestic wastewater (Powder Dose: 2 g/L, Temperature: 27 °C, pH 6.5, and Shaking Speed: 150 rpm).

Effect of Temperature
Figure 9 shows a gradual increase in the efficiency of removing nitrate from 54.75 to 63.50% and phosphate from 36.47 to 44.47% with increasing temperature from 15 to 25 °C. Several studies have indicated an increase in the removal efficiency of nitrate and phosphate with increasing temperature (16, 48, 57). Decreased removal efficiency is observed when the temperature is increased above 25°C; The efficiency of removing nitrate and phosphate decreased to 57.86% and 34.58%, respectively, when the temperature was increased to 35 °C, and this is in agreement with one of the studies that indicated a decrease in the phosphate removal efficiency from 75.5% to 55.2% when the temperature was increased from 30 to 40 °C (56).

This is attributed to the exothermic adsorption process or to the weak adsorption forces between the active sites of the plant powders and the adsorbate ions. The adsorption capacity of various pollutants such as dyes, heavy metals, anions and cations increases with the increase in temperature, due to the rapid increase in the mobility of ions; This facilitates its diffusion from the solution to the active surface adsorption sites, in addition to a decrease in the viscosity of the solution, an increase in the number of active sites for the sample, and a decrease in the thickness of the boundary layer surrounding to the adsorbent material (sample); Which leads to a decrease in the mass transfer resistance of the adsorbates (ions) in the boundary layer at high temperatures and increases the

adsorption efficiency, and this indicates that the adsorption process is endothermic (6, 58, 59). Other studies have indicated a decrease in the adsorption efficiency when the temperature is increased, due to the weak bonds between the adsorbate molecules and the active binding sites of the adsorbent, which indicates that the adsorption process is exothermic (60, 61). The adsorption capacity increases with an increase in temperature to a certain extent and then decreases with any additional increase in temperature (35), and a slight increase in the adsorption capacity was observed with increasing temperature and the removal was independent of temperature (62, 63).
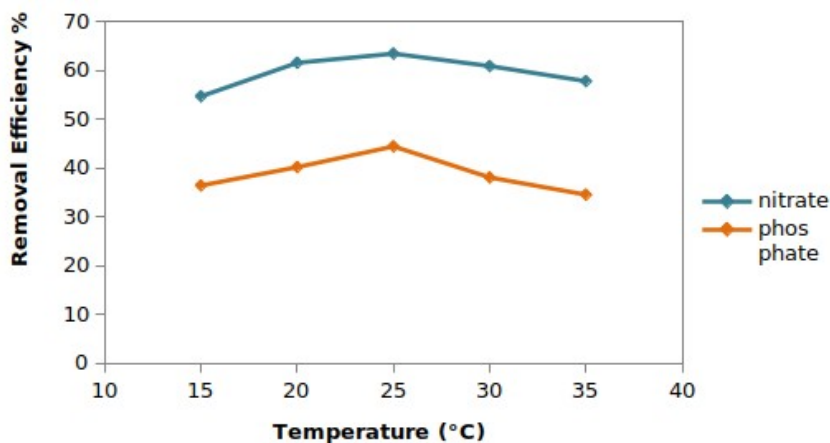
Figure 9: Effect of temperature in removing nitrate and phosphate from domestic wastewater (Powder Dose: 2 g/L, Contact Time: 120 minutes For Nitrate, 180 minutes For Phosphate, pH 6.5, and Shaking Speed: 150 rpm).

Effect of pH
Figure 10 shows that the removal efficiency of nitrate gradually increases from 20.67 to 76.47% and phosphate from 13.05 to 52.20% with decreasing pH values from 9 to 5. This is consistent with several studies that indicated the best removal of nitrate and phosphate at low pH values (acidic medium); This is due to the fact that in the range of high pH values, the surfaces of the powders acquire more negative charges due to the increase of OH⁻, which leads to a decrease in the removal efficiency due to the increase in the repulsive force between the nitrate and phosphate ions and the negatively charged OH⁻ ions, in addition to the possibility of competing OH⁻ ions with nitrate and phosphate for active adsorption sites, while at lower pH values, the surfaces of the powders acquire more positive charges due to the increase in H⁺ ions leads to the increase in the removal efficiency due to the electrostatic attraction between the nitrate and phosphate ions and the active surface sites of the powder (19, 23, 52, 53, 56). It has been observed that adsorption of anionic pollutants often occurs at low pH values of the solution due to the large contribution of electrostatic attraction forces (40).

Studying of regeneration of *Pa*-LP
The results showed that the percentage of nitrate and phosphate removal decreased by about 11% after two successive cycles of treatment compared to the initial value (cycle 0). While the percentage of removal was observed to decrease more than 30% after the third cycle of treatment (Table 4) compared to the initial value (cycle 0), so it is possible to use the powder of the spent leaves for two successive cycles in removing nitrate and phosphates from domestic wastewater with a slight decrease in removal efficiency. The results of this research did not agree with other research; The efficiency of removing phosphate from aqueous solutions decreased by 13.63% and 14.25%, respectively, after the third cycle using NaOH (0.2 M) as a regeneration solution for *Brassica pekinensis* and *Brassia campestris* L powders modified with layered double Mg-Al oxides (17). Amine cross-linked reed powders can be used for at least three successive cycles with a slight decrease in the efficiency of removing nitrate and phosphate (18).
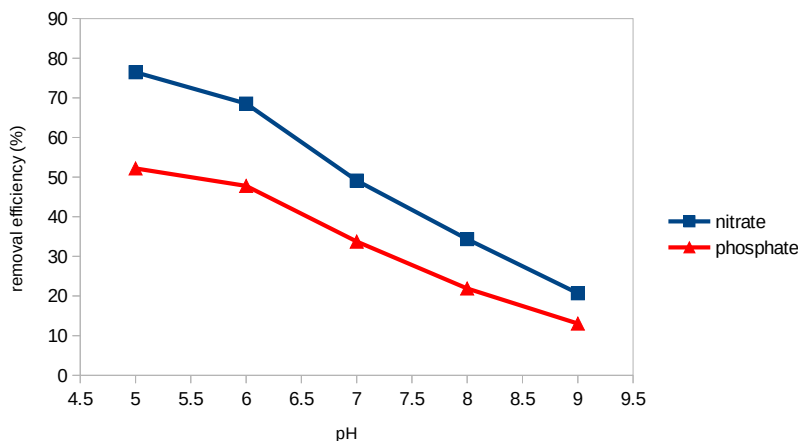
Figure 10: Effect of pH in removing nitrate and phosphate from domestic wastewater (Powder Dose: 2 g/L, Contact Time: 120 minutes For Nitrate, 180 minutes For Phosphate, Temperature: 25 °C, and Shaking Speed: 150 rpm).

The decrease efficiency of removing nitrate and phosphate after several successive cycles of treatment may be attributed to the following reasons: Loss of plant powder weight each cycle, partially due to the destruction of cellulose and hemicellulose at acidic or alkaline conditions (1), and Loss of some surface functional groups or active adsorption sites (18, 64), or due to the accumulation of ions in the adsorption sites (65) and the difficulty of their desorption at regeneration, in addition to the rupture and damage to the plant powder structure as a result of its regeneration by NaOH solution that was used In this research.

Several studies indicated a gradual decrease in the adsorption efficiency of various pollutants such as dyes and heavy metals with an increase in the number of regeneration cycles (22, 66), and other studies indicated increase in the adsorption efficiency after the first cycle (67) as a result of using HNO_3 solution in regeneration, it is an activator of adsorption sites.

Table 4: Average percentage of removal of nitrate and phosphate from domestic wastewater after three successive cycles using *Pa*-LP.

Tests	Treatment Cycles (Adsorption Cycles)			
	0	1	2	3
Nitrate	68.57%	66.50%	57.50%	38%
Phosphate	47.80%	43.74%	39%	15.4%

Study of adsorption kinetics
Table 5 and Figure 11 shows the adsorption kinetics parameters for the nitrate and phosphate ions according to the pseudo-first-order and pseudo-second-order equations. It was observed that a good agreement of the experimental data with the pseudo-second-order equation model, due to the convergence of the value of a_{2e} = 10.53 mg/g calculated graphically from its experimental value of a_e = 10.06 mg/g for nitrate, and the convergence of the value of a_{2e} = 10.75 mg/g calculated graphically from its experimental value of a_e = 9.87 mg/g for phosphate. In addition to that R^2 of pseudo-second-order equation (R^2 = 0.9989) for nitrate and (R^2 = 0.9995) for phosphate is higher than its value for the pseudo-first-order equation (R^2 = 0.9811) for nitrate and (R^2 = 0.9878) for phosphate. Therefore, the adsorption process of nitrate and phosphate on the *Pa*-LP follows a pseudo-second-order equation, this is in agreement with several studies that confirmed that adsorption of nitrate and phosphate on raw or modified plant powders follows a pseudo-second-order equation (17, 19, 50, 55, 68).

Table 5: Adsorption kinetics parameters for nitrate and phosphate ions.

Tests	a_e (experimental)	Pseudo-first-order			Pseudo-second-order		
		a_{1e} (calculated)	K_1 1/min	R^2	a_{2e} (calculated)	K_2 g/(mg·min)	R^2
Nitrate	10.06	5.737	0.036	0.9811	10.53	0.0111	0.9989
Phosphate	9.87	7.323	0.025	0.9878	10.75	0.00535	0.9995
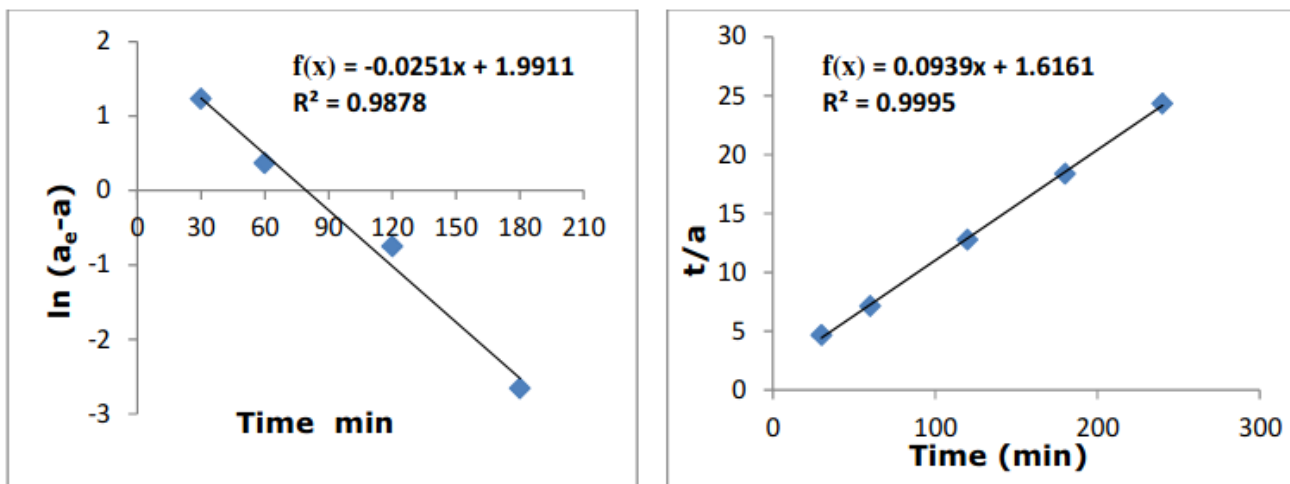
Phosphate adsorption kinetics: (left) Pseudo-first-order model (right) Pseudo-second-order model.
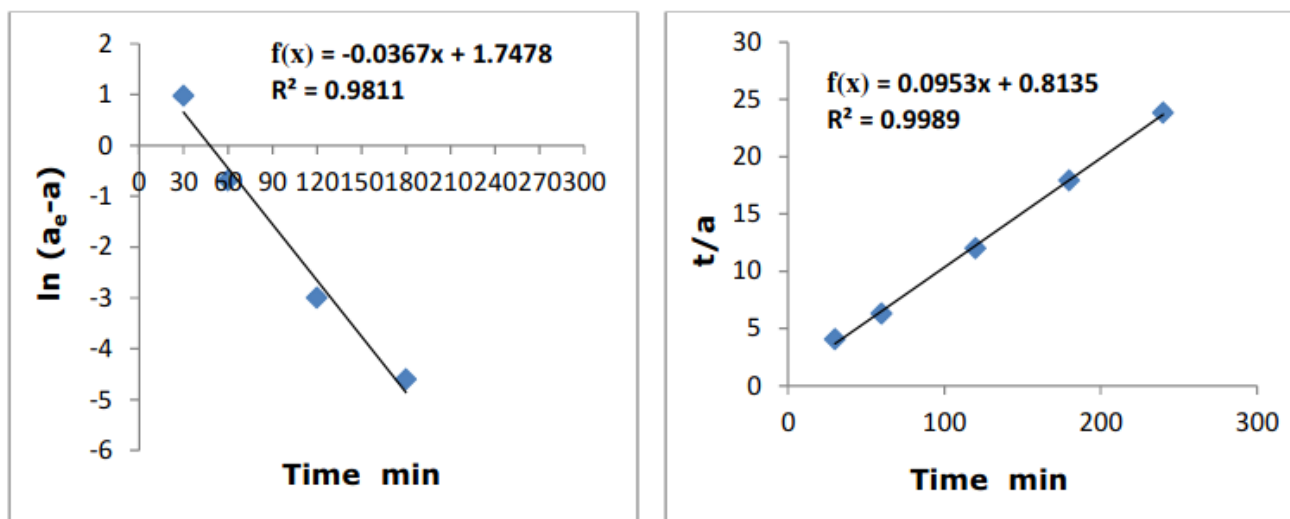
Nitrate adsorption kinetics: (left) Pseudo-first-order model (right) Pseudo-second-order model.

Figure 11: Adsorption kinetics of nitrate and phosphate according to Pseudo-first-order model and Pseudo-second-order model.
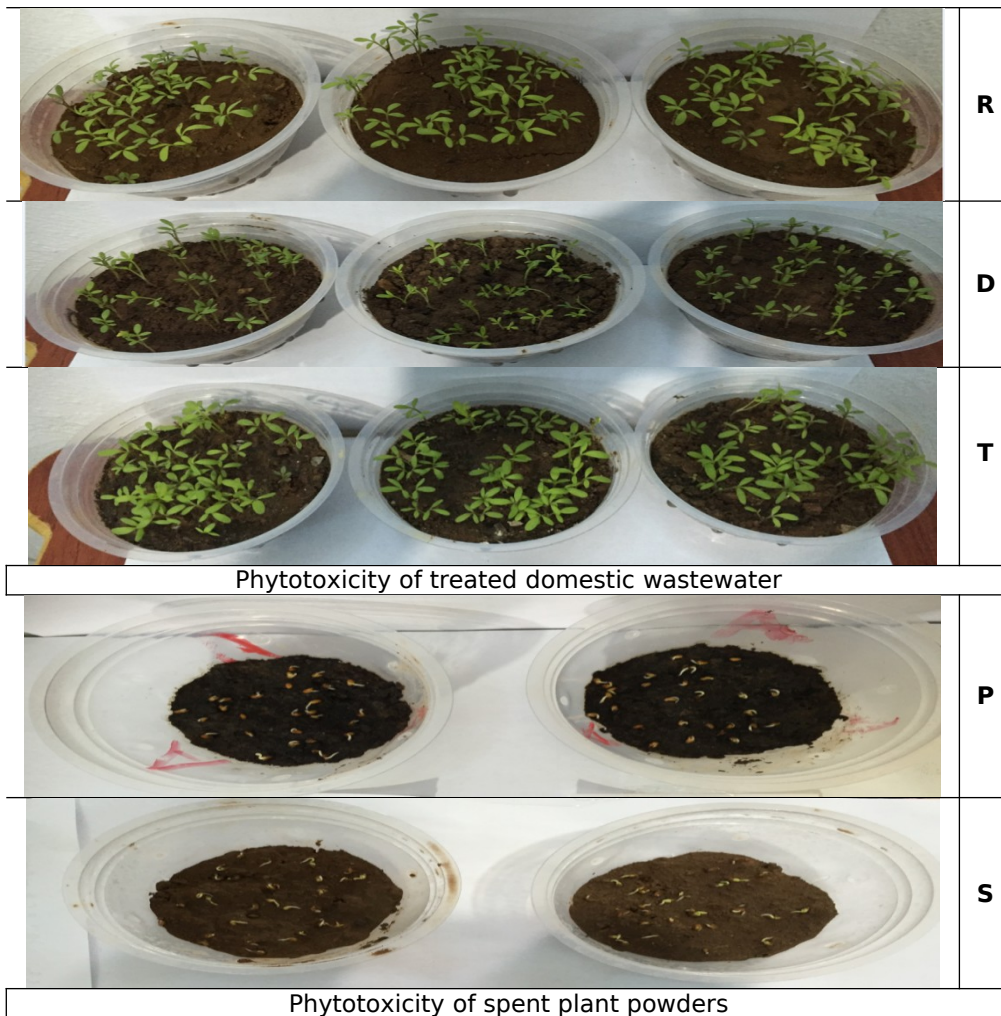
Phytotoxicity tests for treated domestic wastewater and spent plant powders

The test for the germination of *Lepidium sativum* seeds is an indicator for the rapid assessment of phytotoxicity. The percentage of germination of *Lepidium sativum* irrigated with treated domestic wastewater by Pistacia leaves powder after 10 days was 93.33%, higher than the percentage of germination of *Lepidium sativum* irrigated with untreated domestic wastewater, which was 88.86%, and reached 97.76% when irrigating seeds with drinking water. It was observed that the germination of seeds irrigated with untreated domestic wastewater and drinking water began to germinate after 3 days to reach stability after 7 days, but the germination percentage increased from 90% for seeds irrigated with treated wastewater after 7 days to 93.33% after 10 days (Figure 12). The delay in seed growth in treated water may be due to the presence of polyphenols released from *Pistacia* leaves; High concentrations lead to inhibition or delay of seed germination, unlike low concentrations (69). The temperature between 20-30 °C is one of the most important external factors affecting germination; As the percentage of *Lepidium sativum* germination irrigated with water from different sources (dams, wells, distilled, sewage) exceeded 90% (70), this is consistent with the results of the experiments of this research conducted at 25 °C, and the best percentage was when irrigated with drinking water; This may be due to the fact that it contains mineral elements and salts in moderate

concentrations that can be easily absorbed by the seeds (71). The effect of raw domestic wastewater was bad due to the high concentration of salts, harmful substances and heavy metal ions such as chromium and cadmium, which have an inhibitory effect on seed germination (71, 72). These results confirm the possibility of reusing treated domestic wastewater for irrigation.

The spent *Pistacia* powders were non-toxic to *Lepidium sativum* plant due to their biodegradable nature and the germination percentage was 82.2% after three days. Spent plant powders can be added as a soil quality enhancer as it increases permeability, water holding capacity, organic matter content and is a source of soil nitrate and phosphate supply (19, 73, 74).

R: untreated Domestic Wastewater (Negative Control), D: Drinking Water (Positive Control), T: Treated Domestic Wastewater, P: Spent *Pistacia* Powders, S: Soil (Control).

Figure 12. Phytotoxicity tests of treated domestic wastewater and spent plant powders.

Statistical Study
The statistical study confirmed the presence of a strong positive correlation between nitrate and phosphate $R^2= 0.984$ for the effect of plant powder dose, $R^2= 0.989$ for the effect of contact time, $R^2= 0.995$ for the effect of temperature, and $R^2= 0.998$ for the effect of pH value. The one-way analysis (ANOVA) test showed that there were significant differences between all the average values recorded for the tests after wastewater treatment at a significant $P < 0.05$.

CONCLUSION

This study indicated the possibility of using *Pa*-LP without prior treatment or modification as an environmentally friendly, low cost and good effective in removing nitrate and phosphate ions from domestic wastewater. The results of the SEM analysis which is connected to EDAX-AMETEX unit showed a heterogeneous, irregular, and rough surface structure with pores of different dimensions, in addition to containing a group of elements such as carbon, oxygen and nitrogen, potassium, calcium, magnesium, phosphorous, sulfur and chlorine. FTIR analysis showed the presence of hydroxyl,

carboxylate, carbonyl, amine, and methylene groups.

The maximum removal of nitrate and phosphate was at powder dose of 2 g/L and temperature 25 °C. The equilibrium time was reached within 120 min for nitrate and 180 min for phosphate from exposure time, and the removal efficiency decreased significantly with increasing pH values from 5 to 9. The nitrate and phosphate adsorption kinetics follows the pseudo-second-order equation model. The regeneration studies showed the possibility of using *Pa*-LP in two successive cycles to remove nitrate and phosphate with a slight decrease in the removal efficiency compared to the initial value.

The results of the phytotoxicity study showed the possibility of using wastewater treated by *Pa*-LP in irrigating crops without any toxic effects on germination rates. The spent *Pa*-LP were non-toxic to plants and due to their biodegradable nature they could be added as soil enhancer in agricultural land.

The results of the present study show that the low cost and good removal efficiency of non-modified, non-toxic, and reusable *Pa*-LP make them potentially attractive natural materials for removing nitrate and phosphate from domestic wastewater. Further experiments should be conducted in future studies to test the adsorption dynamics of nitrate and phosphate onto *Pa*-LP in fixed-bed column experiments, and determining isotherms and thermodynamics of adsorption. In addition to expanding the scope of research and studying the possibility of removing heavy metals from wastewater using *Pa*-LP.

REFERENCES

1. Xu X, Gao B, Jin B, Yue Q. Removal of anionic pollutants from liquids by biomass materials: A review. Journal of Molecular Liquids. 2016 Mar;215:565–95. <DOI>.

2. Yadav D, Kapur M, Kumar P, Mondal MK. Adsorptive removal of phosphate from aqueous solution using rice husk and fruit juice residue. Process Safety and Environmental Protection. 2015 Mar;94:402–9. <DOI>.

3. Abdolali A, Guo WS, Ngo HH, Chen SS, Nguyen NC, Tung KL. Typical lignocellulosic wastes and by-products for biosorption process in water and wastewater treatment: A critical review. Bioresource Technology. 2014 May;160:57–66. <DOI>.

4. Rashed MK, Tayh W. Removal of Heavy Metals from Wastewater Using Pomegranate Peel. IOP Conf Ser: Mater Sci Eng. 2020 Jul 1;881(1):012187. <DOI>.

5. Diriba D, Hussen A, Rao VM. Removal of Nitrite from Aqueous Solution Using Sugarcane Bagasse and Wheat Straw. Bull Environ Contam Toxicol. 2014 Jul;93(1):126–31. <DOI>.

6. Hodúr C, Bellahsen N, Mikó E, Nagypál V, Šereš Z, Kertész S. The Adsorption of Ammonium Nitrogen from Milking Parlor Wastewater Using Pomegranate Peel Powder

for Sustainable Water, Resources, and Waste Management. Sustainability. 2020 Jun 15;12(12):4880. <DOI>.

7. Velusamy K, Periyasamy S, Kumar PS, Vo DVN, Sindhu J, Sneka D, et al. Advanced techniques to remove phosphates and nitrates from waters: a review. Environ Chem Lett. 2021 Aug;19(4):3165–80. <DOI>.

8. Riahi K, Thayer BB, Mammou AB, Ammar AB, Jaafoura MH. Biosorption characteristics of phosphates from aqueous solution onto Phoenix dactylifera L. date palm fibers. Journal of Hazardous Materials. 2009 Oct 30;170(2–3):511–9. <DOI>.

9. Reddy ChA, N P, P HB, S JM. Banana Peel as a Biosorbent in Removal of Nitrate from Water. International Advanced Research Journal in Science, Engineering and Technology. 2015 Oct 20;2(10):94–8. <DOI>.

10. Chiban M, Soudani A, Sinan F, Tahrouch S, Persin M. Characterization and Application of Dried Plants to Remove Heavy Metals, Nitrate, and Phosphate Ions from Industrial Wastewaters. Clean Soil Air Water. 2011 Apr;39(4):376–83. <DOI>.

11. Michalak I, Chojnacka K, Witek-Krowiak A. State of the Art for the Biosorption Process—a Review. Appl Biochem Biotechnol. 2013 Jul;170(6):1389–416. <DOI>.

12. Crini G, Lichtfouse E, Wilson LD, Morin-Crini N. Adsorption-Oriented Processes Using Conventional and Non-conventional Adsorbents for Wastewater Treatment. In: Crini G, Lichtfouse E, editors. Green Adsorbents for Pollutant Removal [Internet]. Cham: Springer International Publishing; 2018 [cited 2022 May 19]. p. 23–71. (Environmental Chemistry for a Sustainable World; vol. 18). <URL>.

13. Bridgewater LL, Baird RB, Eaton AD, Rice EW, American Public Health Association, American Water Works Association, et al., editors. Standard methods for the examination of water and wastewater. 23rd edition. Washington, DC: American Public Health Association; 2017. 1 p. ISBN: 978-0-87553-287-5.

14. Fiol N, Villaescusa I. Determination of sorbent point zero charge: usefulness in sorption studies. Environ Chem Lett. 2009 Feb;7(1):79–84. <DOI>.

15. Sulyman M, Gierak A. Green environmental approach for adsorption of hazardous dye from water using tree and sea plant leaves (Dead L.). Acta Scientific Agriculture. 2020;4(2):1–10.

16. Benyoucef S, Amrani M. Removal of phosphorus from aqueous solutions using chemically modified sawdust of Aleppo pine (Pinus halepensis Miller): kinetics and isotherm studies. Environmentalist. 2011 Sep;31(3):200–7. <DOI>.

17. Zhang Z, Yan L, Yu H, Yan T, Li X. Adsorption of phosphate from aqueous solution by vegetable biochar/layered double oxides: Fast removal and mechanistic studies. Bioresource Technology. 2019 Jul;284:65–71. <DOI>.

18. Ren Z, Xu X, Wang X, Gao B, Yue Q, Song W, et al. FTIR, Raman, and XPS analysis during phosphate, nitrate and Cr(VI) removal by amine cross-linking biosorbent. Journal of Colloid and Interface Science. 2016 Apr;468:313–23. <DOI>.

19. Robalds A, Dreijalte L, Bikovens O, Klavins M. A novel peat-based biosorbent for the removal of phosphate from synthetic and real wastewater and possible utilization of spent sorbent in land application. Desalination and Water Treatment. 2016 Jun 14;57(28):13285–94. <DOI>.

20. Wang X, Liu Z, Liu J, Huo M, Huo H, Yang W. Removing Phosphorus from Aqueous Solutions Using Lanthanum Modified Pine Needles. Joles JA, editor. PLoS ONE. 2015 Dec 2;10(12):e0142700. <DOI>.

21. Khodabandehloo A, Rahbar-Kelishami A, Shayesteh H. Methylene blue removal using Salix babylonica (Weeping willow) leaves powder as a low-cost biosorbent in batch mode: Kinetic, equilibrium, and thermodynamic studies. Journal of Molecular Liquids. 2017 Oct;244:540–8. <DOI>.

22. Kong L, Gong L, Wang J. Removal of methylene blue from wastewater using fallen leaves as an adsorbent. Desalination and Water Treatment. 2015 Feb 27;53(9):2489–500. <DOI>.

23. Krishnan KA, Haridas A. Removal of phosphate from aqueous solutions and sewage using natural and surface modified coir pith. Journal of Hazardous Materials. 2008 Apr;152(2):527–35. <DOI>.

24. Zdravkov B, Čermák J, Šefara M, Janků J. Pore classification in the characterization of porous materials: A perspective. Open Chemistry. 2007 Jun 1;5(2):385–95. <DOI>.

25. Hanafiah MAKM, Ngah WSW. Preparation, Characterization and Adsorption Mechanism of Cu(II) onto Protonated Rubber Leaf Powder. Clean Soil Air Water. 2009 Sep;37(9):696–703. <DOI>.

26. Vilvanathan S, Shanthakumar S. Removal of Ni(II) and Co(II) ions from aqueous solution using teak (Tectona grandis) leaves powder: adsorption kinetics, equilibrium and thermodynamics study. Desalination and Water Treatment. 2016 Feb 19;57(9):3995–4007. <DOI>.

27. Hossain MA, Ngo HH, Guo WS, Nguyen TV, Vigneswaran S. Performance of cabbage and cauliflower wastes for heavy metals removal. Desalination and Water Treatment. 2014 Jan 28;52(4–6):844–60. <DOI>.

28. Haghighizadeh M, Zare K, Aghaie H, Monajjemi M. Preparation and characterization of Chicory leaf powder and its application as a nano-native plant sorbent for removal of Acid Blue 25 from aqueous media: isotherm, kinetic and thermodynamic study of the adsorption phenomenon. J Nanostruct Chem. 2020 Mar;10(1):75–86. <DOI>.

29. Hossain MA, Ngo HH, Guo W, Zhang J, Liang S. A laboratory study using maple leaves as a biosorbent for lead removal from aqueous solutions. Water Quality Research Journal. 2014 Aug 1;49(3):195–209. <DOI>.

30. Moussavi G, Khosravi R. Removal of cyanide from wastewater by adsorption onto pistachio hull wastes: Parametric experiments, kinetics and equilibrium analysis. Journal of Hazardous Materials. 2010 Nov;183(1–3):724–30. <DOI>.

31. Ahmad A, Ghazi ZA, Saeed M, Ilyas M, Ahmad R, Muqsit Khattak A, et al. A comparative study of the removal of Cr(vi) from synthetic solution using natural biosorbents. New J Chem. 2017;41(19):10799–807. <DOI>.

32. Khan Rao RA, Khatoon A. Aluminate treated Casuarina equisetifolia leaves as potential adsorbent for sequestering Cu(II), Pb(II) and Ni(II) from aqueous solution. Journal of Cleaner Production. 2017 Nov;165:1280–95. <DOI>.

33. Jain SN, Gogate PR. Acid Blue 113 removal from aqueous solution using novel biosorbent based on NaOH treated and surfactant modified fallen leaves of Prunus Dulcis. Journal of Environmental Chemical Engineering. 2017 Aug;5(4):3384–94. <DOI>.

34. Lafi R, Hamdi N, Hafiane A. Study of the performance of Esparto grass fibers as adsorbent of dyes from aqueous solutions. Desalination and Water Treatment. 2015 Oct 16;56(3):722–35. <DOI>.

35. Ponnusami V, Vikram S, Srivastava SN. Guava (Psidium guajava) leaf powder: Novel adsorbent for removal of methylene blue from aqueous solutions. Journal of Hazardous Materials. 2008 Mar 21;152(1):276–86. <DOI>.

36. Annadurai G, Juang R, Lee D. Use of cellulose-based wastes for adsorption of dyes from aqueous solutions. Journal of Hazardous Materials. 2002 Jun 10;92(3):263–74. <DOI>.

37. Baruah S, Devi A, Bhattacharyya KG, Sarma A. Developing a biosorbent from Aegle Marmelos leaves for removal of methylene blue from water. Int J Environ Sci Technol. 2017 Feb;14(2):341–52. <DOI>.

38. O. I, O. E, K. Audu TO. Application of Luffa Cylindrica in Natural form as Biosorbent to Removal of Divalent Metals from Aqueous Solutions - Kinetic and Equilibrium Study. In: Garca Einschlag FS, editor. Waste Water - Treatment and Reutilization [Internet]. InTech; 2011 [cited 2022 May 19]. ISBN: 978-953-307-249-4.

39. Chiban M, Soudani A, Sinan F, Persin M. Wastewater treatment by batch adsorption method onto micro-particles of dried Withania frutescens plant as a new adsorbent. Journal of Environmental Management. 2012 Mar;95:S61–5. <DOI>.

40. Tran HN, Nguyen HC, Woo SH, Nguyen TV, Vigneswaran S, Hosseini-Bandegharaei A, et al. Removal of various contaminants from water by renewable lignocellulose-derived biosorbents: a comprehensive and critical review. Critical Reviews in Environmental Science and Technology. 2019 Dec 2;49(23):2155–219. <DOI>.

41. Nandiyanto ABD, Oktiani R, Ragadhita R. How to Read and Interpret FTIR Spectroscope of Organic Material. Indonesian J Sci Technol. 2019 Mar 7;4(1):97. <DOI>.

42. Giannakoudakis DA, Hosseini-Bandegharaei A, Tsafrakidou P, Triantafyllidis KS, Kornaros M, Anastopoulos I. Aloe vera waste biomass-based adsorbents for the removal of aquatic pollutants: A review. Journal of Environmental Management. 2018 Dec;227:354–64. <DOI>.

43. Mirahmadi F, Mizani M, Sadeghi R, Givianrad MH. Chemical composition and thermal properties of Pistacia atlantica subsp. Kurdica gum. Appl Biol Chem. 2019 Dec;62(1):4. <DOI>.

44. Wahab MA, Jellali S, Jedidi N. Ammonium biosorption onto sawdust: FTIR analysis, kinetics and adsorption isotherms modeling. Bioresource Technology. 2010 Jul;101(14):5070–5. <DOI>.

45. Poletto M, Zattera AJ, Santana RMC. Structural differences between wood species: Evidence from chemical composition, FTIR spectroscopy, and thermogravimetric analysis. J Appl Polym Sci. 2012 Oct 25;126(S1):E337–44. <DOI>.

46. Aslam M, Rais S, Alam M, Pugazhendi A. Adsorption of Hg(II) from Aqueous Solution Using Adulsa (Justicia adhatoda) Leaves Powder: Kinetic and Equilibrium Studies. Journal of Chemistry. 2013;2013:1–11. <DOI>.

47. Coates J. Interpretation of Infrared Spectra, A Practical Approach. In: Meyers RA, editor. Encyclopedia of Analytical Chemistry [Internet]. Chichester, UK: John Wiley & Sons, Ltd; 2006 [cited 2022 May 19]. p. a5606. <URL>.

48. Muhaisen LF. Lemon peel as natural biosorbent to remove phosphate from simulated wastewater. Journal of Engineering and Sustainable Development. 2016;20(2):163–73.

49. Pholosi A, Ofomaja AE, Naidoo EB. Effect of chemical extractants on the biosorptive properties of pine cone powder: Influence on lead(II) removal mechanism. Journal of Saudi Chemical Society. 2013 Jan;17(1):77–86. <DOI>.

50. Qiao H, Mei L, Chen G, Liu H, Peng C, Ke F, et al. Adsorption of nitrate and phosphate from aqueous solution using amine cross-linked tea wastes. Applied Surface Science. 2019 Jul;483:114–22. <DOI>.

51. Yang L, Yang M, Xu P, Zhao X, Bai H, Li H. Characteristics of Nitrate Removal from Aqueous Solution by Modified Steel Slag. Water. 2017 Oct 1;9(10):757. <DOI>.

52. Ahmadparia H, Hashemi Garmdareh SE, Afarinandeh A. Preliminary study of the process of nitrate removal optimization from aqueous solutions using Taguchi method. Revista Ingeniera UC. 2019;26(2):154–62. <URL>.

53. Ismail ZZ. Kinetic study for phosphate removal from water by recycled date-palm wastes as agricultural by-products. International Journal of Environmental Studies. 2012 Feb;69(1):135–49. <DOI>.

54. Namasivayam C, Höll WH. Quaternized biomass as an anion exchanger for the removal of nitrate and other anions from water: Removal of nitrate and other anions from water. J Chem Technol Biotechnol. 2005 Feb;80(2):164–8. <DOI>.

55. Xu X, Gao Y, Gao B, Yue Q, Zhong Q. Adsorption studies of the removal of anions from aqueous solutions onto an adsorbent prepared from wheat straw. Sci China Chem. 2010 Jun;53(6):1414–9. <DOI>.

56. Mor S, Chhoden K, Ravindra K. Application of agro-waste rice husk ash for the removal of phosphate from the wastewater. Journal of Cleaner Production. 2016 Aug;129:673–80. <DOI>.

57. Sadeghi Afjeh M, Bagheri Marandi G, Zohuriaan-Mehr MJ. Nitrate removal from aqueous solutions by adsorption onto hydrogel-rice husk biochar composite. Water Environment Research. 2020 Jun;92(6):934–47. <DOI>.

58. Sharma R, Kaith BS, Kalia S, Pathania D, Kumar A, Sharma N, et al. Biodegradable and conducting hydrogels based on Guar gum polysaccharide for antibacterial and dye removal applications. Journal of Environmental Management. 2015 Oct;162:37–45. <DOI>.

59. Bello OS, Alabi EO, Adegoke KA, Adegboyega SA, Inyinbor AA, Dada AO. Rhodamine B dye sequestration using Gmelina aborea leaf powder. Heliyon. 2020 Jan;6(1):e02872. <DOI>.

60. Abdelwahab O, Fouad YO, Amin NK, Mandor H. Kinetic and thermodynamic aspects of cadmium adsorption onto raw and activated guava (Psidium guajava) leaves. Environ Prog Sustainable Energy. 2015 Mar 4;34(2):351–8. <DOI>.

61. Pathak U, Das P, Banerjee P, Datta S. Treatment of Wastewater from a Dairy Industry Using Rice Husk as Adsorbent: Treatment Efficiency, Isotherm, Thermodynamics, and Kinetics Modelling. Journal of Thermodynamics. 2016 Jan 20;2016:1–7. <DOI>.

62. Mondal DK, Nandi BK, Purkait MK. Removal of mercury (II) from aqueous solution using bamboo leaf powder: Equilibrium, thermodynamic and kinetic studies. Journal of Environmental Chemical Engineering. 2013 Dec;1(4):891–8. <DOI>.

63. Kuppusamy S, Thavamani P, Megharaj M, Venkateswarlu K, Lee YB, Naidu R. Potential of Melaleuca diosmifolia leaf as a low-cost adsorbent for hexavalent chromium removal from contaminated water bodies. Process Safety and Environmental Protection. 2016 Mar;100:173–82. <DOI>.

64. Assila O, Tanji K, Zouheir M, Arrahli A, Nahali L, Zerrouq F, et al. Adsorption Studies on the Removal of Textile Effluent over Two Natural Eco-Friendly Adsorbents. Pérez PA, editor. Journal of Chemistry. 2020 Aug 13;2020:1–13. <DOI>.

65. Mohan S, Sumitha K. Removal of Cu (II) by Adsorption Using Casuarina Equisetifolia Bark. Environmental Engineering Science. 2008 May;25(4):497–506. <DOI>.

66. Nag S, Mondal A, Mishra U, Bar N, Das SK. Removal of chromium(VI) from aqueous solutions using rubber leaf powder: batch and column studies. Desalination and Water Treatment. 2015 Sep;1–16. <DOI>.

67. Saha GC, Hoque MdIU, Miah MAM, Holze R, Chowdhury DA, Khandaker S, et al. Biosorptive removal of lead from aqueous solutions onto Taro (Colocasiaesculenta(L.) Schott) as a low cost bioadsorbent: Characterization, equilibria, kinetics and biosorption-mechanism studies. Journal of Environmental Chemical Engineering. 2017 Jun;5(3):2151–62. <DOI>.

68. Wang Y, Gao BY, Yue WW, Yue QY. Adsorption kinetics of nitrate from aqueous solutions onto modified wheat residue. Colloids and Surfaces A: Physicochemical and Engineering Aspects. 2007 Oct;308(1–3):1–5. <DOI>.

69. Ignat I, Radu DG, Volf I, Pag AI, Popa VI. Antioxidant and antibacterial activities of some natural polyphenols. Cytokines. 2013;4:387–99.

70. Bansal R. Effect of temperature on seed germination behaviour in Asalio (Lepidium sativum Linn.) and Safed Musli (Chlorophytum borivilianum). New Agriculturist. 2015;26(1,2):1–7.

71. Nana R, Maïga Y, Ouédraogo RF, Kaboré WGB, Badiel B, Tamini Z. Effect of Water Quality on the Germination of Okra (Abelmoschus esculentus) Seeds. International Journal of Agronomy. 2019 Oct 31;2019:1–7. <DOI>.

72. Pavel VL, Sobariu DL, Diaconu M, Statescu F, Gavrilescu M. Effects of Heavy Metals on Lepidium Sativum Germination and Growth. Environ Eng Manag J. 2013;12(4):727–33. <DOI>.

73. Feria JJ, Polo Corrales L, Hernández Ramos E. Evaluación de lodos de coagulación de agua cruda tratada con Moringa oleífera para uso agrícola. Ing.Inv. 2016 Aug 24;36(2):14. <DOI>.

74. Aldás Sandoval MB, Buenaño Bautista BB, Vera Calle ER. Study of coagulating/flocculating characteristics of organic polymers extracted from biowaste for water treatment. Ing Inv [Internet]. 2019 Jan 1 [cited 2022 May 19];39(1). <DOI>.

RESEARCH ARTICLE

Pollution Removal Performance of Chemically Functionalized Textile Waste Biochar Anchored Poly(vinylidene fluoride) Adsorbent

Huseyin Gumus¹* iD **, Bulent Buyukkidan²** iD

¹Bilecik Seyh Edebali University, Osmaneli Vocational School, Bilecik, 11500, Turkey
²Kutahya Dumlupinar University, Department of Chemistry, Kutahya, Turkey

Abstract: Preparation of adsorbent materials in powder and polymeric composite form was achieved by controlled carbonization of $ZnCl_2$ pretreated textile waste at low temperatures. Structural and surface properties of carbonized textile waste samples (CTW) and polymeric composites were prepared by the addition of CTW to PVDF-DMF solution at 0, 5, 10, 15, 20, and 30 mass% ratios analyzed by FT-IR, XRD, SEM, and BET analysis. Adsorption performances of powder and composite adsorbents were investigated for MO dye removal from an aqueous solution. Zn-CTW obtained with carbonization of $ZnCl_2$ treated textile waste at 350 °C presented 117.5 mg/g MO removal. Those were higher than CTW-350 and CTW-400. The presence of 1545 cm^{-1} band at the IR spectrum of Zn-CTW proved the formation of functional groups that increase dye adsorption performance with honeycomb-like pores on the surface. Zn-CTW reflected its properties onto the PVDF matrix. Improved porosity percentage, BET surface, and dye adsorption of Pz20 were recorded as 105.3, 15.22 m²/g, and 41 mg/g, respectively, compared with bare PVDF. Disposal of textile waste and preparation of functional activated carbon were achieved in a low-cost and easy way. Zn-CTW loaded PVDF composites are promising materials to use as a dye removal adsorbent from water or filtration membranes.

INTRODUCTION

Carbon materials have been preferred as an adsorbent for centuries because of their stability in hard aqueous environments, large surface area, sufficient surface properties for modification as a catalyst, and other applications such as cation exchange capacity and functional groups with low-cost production (1). It is possible to classify the source of carbon materials simply as mineral and biobased according to its obtaining methods. The emerging trend in using carbon sources was through biobased stock materials such as wood and fiber types because of their low cost, high yield, and lower ash content compared with sources of mineral-based (2–4). However, the main preferential reasons for increasing usage of biomaterials for biochar production may be explained by their renewable properties (5,6). Fe_2O_3 modified biochar obtained from the carbonization of maple wood and corn stover, used

for H_2S adsorption from biogas, showed 23.9 mg/g H_2S adsorption performance. Thanks to the Fe_2O_3 structure placed into pores, biochar presented good interaction with H_2S (7). Large kinds of biomass are classified basically as woody and nonwoody materials such as bamboo, pecan, peanut nutshell, rice husk, post-harvest residue, and chitosan, which are used to obtain biochar by carbonization techniques called pyrolysis (300-700 °C), hydrothermally (180-300 °C and wetted biomass), torrefaction (<300 °C), gasification (8). Biochar prepared by carbonization of poplar wood and tea by heating at 450 and 750 °C were used for remediation of trichloroethylene (TCE)-contaminated water (9). The best TCE removal was obtained in biochar prepared from poplar wood with 50-100 μm pores, and the highest vinyl chloride removal was obtained from poplar wood carbonized at 750 °C. Modified biochar prepared by castor seed cake for methylene blue (MB) removal (10), activated wakame biochar for MB, rhodamine

blue (RB), malachite green (11), and palm petioles biochar for crystal violet (12) were used as dye adsorbents from aqueous solution with high amounts. Ethylene-co-vinyl alcohol-supported 1.5% rice straw biochar electrospinning membranes showed the highest recovery performance (13). However, the high carbonization temperatures ranging from 450-700 °C, the applied activation methods, and raw biomass usage may be considered as disadvantages of the method. Disposal of carbon-rich waste materials by reducing them to obtain activated carbon can be defined as a further level of environmentalist approach compared with natural biomass usage. Natural biomass can be disposable in the environment, whereas most industrial waste requires extra hard conditions to decompose, and even so, chemical residues can reach soil or water resources. A huge amount of waste material emerges from the textile industry around the world, and disposal problems also threaten the environment. It was reported that 75 percent of textile waste are disposed of in Europe every year due to a lack of efficient recycling and only a small amount of waste textile could be reused as a textile industry due to the necessity of complex separation and purification steps of fibers (14). Textile waste was mainly classified into three groups: specific process waste, secondary waste, and out-of-process waste (15). Carbon-rich textile waste materials consist of synthetic and natural fibers and their residues, such as cotton, polyester yarn, fabric, garments, and fibers, which are included in specific process waste groups, and recycling them has great potential to provide a source of carbon-rich material. Also, that provides environmental protection instead of polluting by stocking or other air polluting methods. The studies dealing with converting textile waste to biogas, ethanol, bio-oil, biofuel, and glycolysis in the presence of single and double oxide catalysts such as Mg-Al were conducted on a lab-scale (16–22). These strategies require a high amount of chemicals such as organic solvents and ionic liquids with the enzymatic reaction, which increases cost and makes applications complicated. Additionally, new waste and chemicals arising from the new system cause a new conflict with the disposal activities of textile waste aimed at environmental protection. A more beneficial strategy may be provided by converting these wastes into valuable bioproducts with low-cost ash and residues. Hanoğlu et al. investigated the effects of fiber type and temperature on the torrefaction of textile fiber at 300-400 °C (23). A significant effect of temperature was reported on the torrefaction process and the energy densification effect of fiber type. Biochar from effluent treatment waste of the textile industry, which has a 91 m^2/g surface area, was prepared for ofloxacin removal from aqueous solutions. Biochar prepared from denim fabric with H_3PO_4 activation presented 19.74 mg/g adsorption capacity as an efficient adsorbent for removing a textile dye from an aqueous solution, and it was separated magnetically from the solution due to magnetic ferrous content (24,25). However, they used a large amount of acid and energy. In another study, the heavy metal content of biochar obtained by carbonization of textile dye sludge at 400-700 °C for disposing of waste sludge was investigated, and the optimum temperature for biochar, which has a minimal toxic effect, was reported as 400 °C with lower heavy metal risk (26). Well-known active carbon preparation methods depend on the heating of natural carbon sources. However, waste materials that are chemical or physical pollutants in case of spreading or staking on the environment may provide a high amount of carbon source. Reusing waste materials has been an important issue for the last three decades, especially due to climate change on a global scale, voiced with agreements (27). Even so, waste recycling is not being applied sufficiently for reasons such as complex structure and specific requirements of waste recycling systems, lack of technology or knowledge, and the easier obtaining of equivalent raw materials. According to our literature survey, we could not come across any studies about the conversion of textile waste that emerged from the Uşak region of Turkey to activated carbon that functional groups decorated at low cost and easy conditions. Also, the preparation and pollution removal studies of chemically functionalized active carbon-polymer composites as a practical adsorbent were first planned and applied in this study.

Conversion of carbon-rich textile waste materials to biochar is applied as an environment protective method for both disposal and new products. The addition of these molecules in a polymer matrix could improve the efficiency of biochar. Thus, easy separation of featured materials such as composite adsorbents or filtration membranes could be achieved. Usable poly(vinylidene fluoride) (PVDF) composites, including carbonized textile waste additives were prepared for dye removal from water. Converting waste materials to biochar with a simple process was investigated with the aim of disposal and environmental protection. The surface, structural properties, and dye removal performance of carbonized textile waste and composites obtained with carbonized samples were investigated. Effects of chemical treatment before carbonization were investigated to obtain well-structured biochar at a lower temperature. Methyl orange removal performance of carbonized samples and composites was investigated at batch experiments, and behaviors of adsorbent in powder form and loaded to PVDF were compared. Although a large amount of research has been conducted to obtain biochar from woody and fiber biomass for different purposes, we aimed to show: (i) the possibility of obtaining fine materials (adsorbent powder and composites) from textile waste with waste specific treatments and conditions, (ii) how important is waste recycling is for the environment, both for disposal and raw material potential. Chemically carbonized textile waste was added to PVDF, and it was used for dye removal in this study. The study includes outcomes focusing on environmental preservation strategies thanks to

biochar preparation steps with moderate conditions. The prepared Zn-CTW added PVDF composites are also promising candidates for filtration and purification systems.

MATERIALS AND METHODS

Materials
Waste textile samples were obtained from UŞAK organized industrial zone, Turkey. C_2H_5OH and $ZnCl_2$ were purchased from Sigma Aldrich and used without any purification. The polymer matrix and solvent were PVDF (Solef 6010, MINGER) and N, N-dimethylformamide, DMF (73.09 g/mol, 0.944 g/mL Sigma Aldrich). During the dye removal experiments, double distilled water, methyl orange (MO, Sigma Aldrich), NaOH, and HCl (Sigma Aldrich) was used for pH adjustments.

Preparation of Carbonized Textile Waste (CTW) Samples and Composites
Waste textile samples were first washed with ethanol and water to remove particles and dye remnants until a clear eluent was obtained. Waste materials were washed and dried at 60°C for 24 h. Five grams of washed sample were wetted by 25 mL $ZnCl_2$ solutions at a mass ratio of activating species: textile waste 0.14-1.4:50 for 1 h. Samples were kept for 24 h at 60 °C in an oven. Dried samples were put into a porcelain cup and carbonized in a muffle furnace (with a heating rate of 15 °C/min) at temperature ranges of 350-400 °C for 1-1.5 h. The air conditions were adjusted with static N_2 inert gas. Control samples were prepared by carbonization of samples at 350 and 400 °C without exposure to any chemicals. After cooling to room temperature, carbonized textile waste (CTW) samples were weighed and ground with a manual grinder. Samples were passed through a 150 μm sieve. Obtained samples were called following modification procedures such as 05-Zn-1-350. Where 05 stands for concentration of chemicals (mol/L) used before carbonization, Zn, 1, and 350 for $ZnCl_2$, treatment time, and carbonization temperature, respectively.

Zn-CTW added PVDF composites were prepared as 1,6 g polymer added to 10 mL DMF and stirred for 2 h at 60 °C. Powder 05-Zn-1-350 was added to polymer solution to obtain 0, 5, 10, 15, 20, and 30% Zn-CTW:PVDF mass ratio. The mixture was stirred at 250 rpm at 65 °C for 3 hours to provide homogeneous dispersion. Zn-CTW-PVDF solution was held for a while to avoid air bubbles and cast onto a glass plate (20 cm x 20 cm) with a casting knife with 300 μm at 25 °C. The mixture was spread onto the glass surface, and it was quickly immersed into the distilled water bath for 24 h. Prepared composites were stored in a storage cup filled with pH 9 distilled water to prevent drying and bacterial contamination until adsorption experiments. Samples were dried and cut into appropriate pieces before structural analysis for optimum results. Composites containing carbonized additives activated by $ZnCl_2$ (Zn-CTW) were called P, Pz5, Pz10, Pz15, Pz20, and Pz30

according to the mass ratio content of Zn-CTW (05-Zn-1-350).

Characterization of carbonized textile waste and composites
Diffraction patterns and organic groups of samples were analyzed by XRD (Rigaku 2000) at 2θ:2°-80° with 2°/min scanning speed and Perkin Elmer FTIR over a range of 4000–400 cm^{-1}. The morphologies of composites were examined by scanning electron microscopy at 10 kV (Carl Zeiss ULTRA Plus). Surface areas of samples were analyzed by the TriStar II 3020 Version 3.02 BET device. After pH adjusting with 0.1 mol/L NaOH/HCl solutions, a 100 ppm methyl orange solution (MO) was prepared and used. The amount of dye content in the solution was determined by a UV-visible spectrometer (Shimadzu, 2550).

Water uptake capacity (WU) of composites was investigated to get knowledge about interactions between virgin PVDF, Zn-CTW added composites, and water. That was useful to estimate their behaviors in the aqueous area during the adsorption. WU calculations were conducted as described: composites in water were mopped slightly with blotting paper and weighted (W_w). Wet samples were dried in a 40 °C vacuum oven for two hours. Dried composites were weighted (W_d) again. Water uptake capacities were calculated by using wet and dry values of composites according to eq. (1).

$$WU(\%) = \frac{W_w - W_d}{W_w} \times 100 \qquad \text{(Eq. 1)}$$

Porosities of composite surfaces (PO%) were calculated by the weight of wet and dry composites. The following equation (2) was used for porosity calculation.

$$PO(\%) = \frac{W_w - W_d}{dA\delta} \times 100 \qquad \text{(Eq. 2)}$$

Where d is the density of water used at 25 °C, A is the composite area in a wet state (cm^2), and δ is the thickness of composite in wet form (cm) determined by using a thickness gauge (Syntek, ±0.01).

Adsorption Experiments
Adsorption experiments were conducted in a flask by the batch technique. 50 mL aqueous solutions of MO (prepared at 50-150 ppm initial concentrations) were put into a conical glass flask with the adsorbent (0.01-0.1 g adsorbent dosage) and stirred at 150 rpm for 1-3 h. The effects of different temperatures (298-328 K) and pH values (pH 3.00-9.00 of solutions was adjusted by 0.05 mol/L HCl and NaOH solutions) were investigated. After the adsorption equilibrium, adsorbents were filtered, and the filtrate was analyzed with a UV-vis spectrometer at 660 for MO. Adsorption capacity Q_e (mg/g), efficiency E_{AD} (%) of composites, and

CTW adsorbents were calculated by equations 3 and 4 (28).

$$Q_e = \left(\frac{C_0 - C_e}{M}\right) \times V \quad \text{(Eq. 3)}$$

$$E_{AD}(\%) = \left(\frac{C_0 - C_e}{C_0}\right) \times 100 \quad \text{(Eq. 4)}$$

Where C_0 and C_e represent initial and equilibrium dye concentrations, M (g) represents the amount of adsorbent, and V (L) is the volume of dye solution. Recycling studies of samples were conducted. Filtrated adsorbents were washed with an acid solution (0.5 mol/L HCl, 25 mL) and rinsed with distilled water until a neutral eluent was obtained. Adsorbents were dried and used for other cycles. This procedure was repeated 5 times. Langmuir and Freundlich isotherm models were applied to evaluate the obtained adsorption data of Zn-CTW by using equations 5 and 6.

$$Q_e = \frac{K_L C_e Q_{max}}{1 + K_L C_e} \quad \text{(Eq. 5)}$$

$$Q_e = K_f C_e^{\frac{1}{n}} \quad \text{(Eq. 6)}$$

The maximum adsorption capacities (Q_{max}) and Langmuir constants (K_L) were calculated by using the slope and cutting point of the line of the graph obtained by C_e versus $1/Q_e$. Plotting the graph by $\log_{Q_e}$ versus $\log_{C_e}$ Freundlich constant and max adsorption capacity of adsorbents were calculated (29).

RESULT AND DISCUSSION

Characterization of Zn-CTW and Composites
The X-ray diffraction patterns of Zn-CTW and Pz composites are shown in Figure 1. The Zn-CTW showed a single broad peak at around 2θ=8.08, pointing out the semi-crystalline structure of the carbonized sample. Shifting a peak position to a low angle indicates disordered cages and microporosity, whereas an increase in peak strength means an increase in interplanar crystal spacing, which contributes to adsorption (30). Only the small peak at around 2θ=30 may be attributed to the ZnO crystal formed because of using a chemical modification (31). Peaks at around 2θ=18.58, 20.21, and 27.2 indicated characteristic α-phase, and the broad peak, which can be seen clearly at 39.3, corresponds γ-phase of PVDF. The evidence for the β-phase structure of PVDF was determined by broad 2θ=36.46 with a clearly visible 2θ=20.06 peak (32). From the diffraction patterns of composites, the peak strength of the Zn-CTW loaded PVDF matrix has decreased a little bit. The reason for broad peaks was decreasing crystallinity of PVDF with additives. Reduced or lack of crystal structure resulted in a broad peak, which means low strength and nonclear or lower inorganic content (33). From the peak strength of the composites, mixture behaviors of PVDF with Zn-CTW can interfere as Pz-5 has a more homogenous structure than Pz-30. Because of increased Zn-CTW, the characteristic peak of PVDF at around 2θ=18.58 became more visible like it is at virgin PVDF. A combination of Zn-CTW with PVDF at the ratio of Pz5-Pz20 was decided that those have moderate constituents as Zn-CTW-PVDF composites.
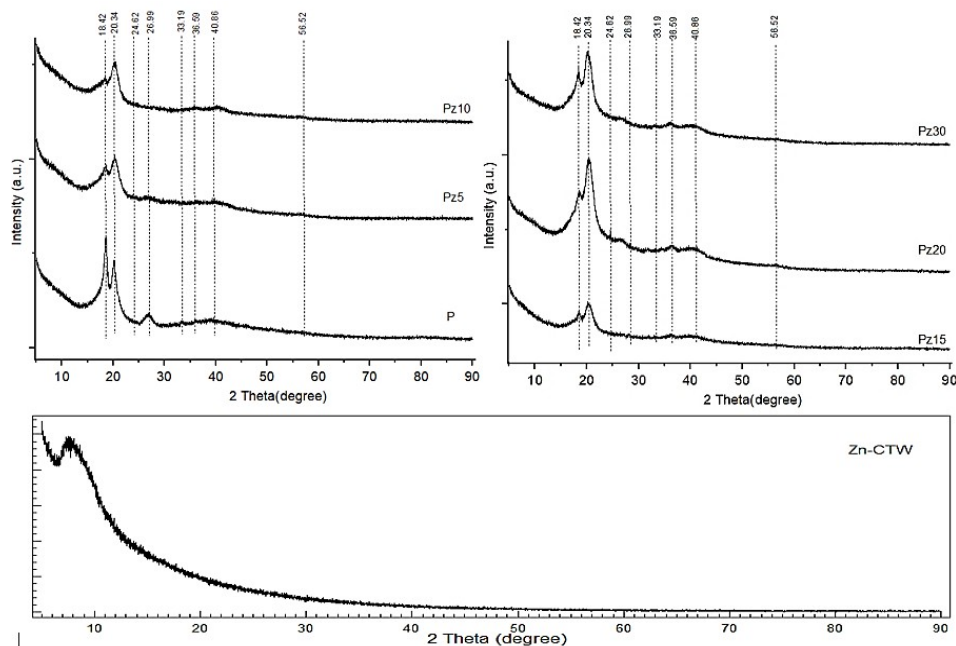

Figure 1: XRD patterns of Zn-CTW and composites.

FT-IR spectra of composites and Zn-CTW are presented in Fig. 2. Typical PVDF bands indicating the CH, CF$_2$, and CF band stretching vibrations were observed at around 1401, between 875-1180 and 1066 cm^{-1}, respectively. There was no change or disappearance observed at those, except for a shift to a lower wavenumber on a small scale (34). Changes in the IR band positions of PVDF are highly compatible with literature, and those are evidence of phase changes in the structure due to additive interaction. The bands at around 1383, 975, 796, 762, 613, and 531 cm^{-1}, which pointed out α-phases of PVDF, disappeared, or their intensity was reduced prominently with increased addition of Zn-CTW. However, new crystal formations classified as electroactive phases for PVDF appeared interestingly. The band at around 1274 cm^{-1} represents β-phases, with the band at 1234 cm^{-1} (γ-phase of PVDF) emerged and became clear at the FT-IR spectrum of Pz20. (35,36). These findings are important key constituents as they provide knowledge for suitability and loading ratios of Zn-CTW additives to obtain electroactive PVDF products. Successful incorporation of Zn-CTW onto the PVDF chain can be understood by FT-IR bands, which point out the change in PVDF crystal structure. The broad bands of Zn-CTW at around 3059 cm^{-1} may be attributed to OH stretching of physically sorbet water or polysaccharides from cellulosic textile waste.

The presence of carbonyl and alkene groups (C=O and C=C) was understood by stretching bands at 1716 and 1545 cm^{-1}, respectively, due to waste materials' polyester and cellulose structure (23). The intense band at 1094 cm^{-1} corresponds to the C-O-C vibration of organic groups and aromatic stretching and metal oxide bands between 528 and 857 cm^{-1}. (37–39). Morphological analysis of composites and Zn-CTW was done through SEM of the samples' surfaces. Pores of Zn-CTW obtained by carbonization of waste polyester/cotton samples after ZnCl$_2$ treatment can be seen in complex disorganized order in Figure 3a.
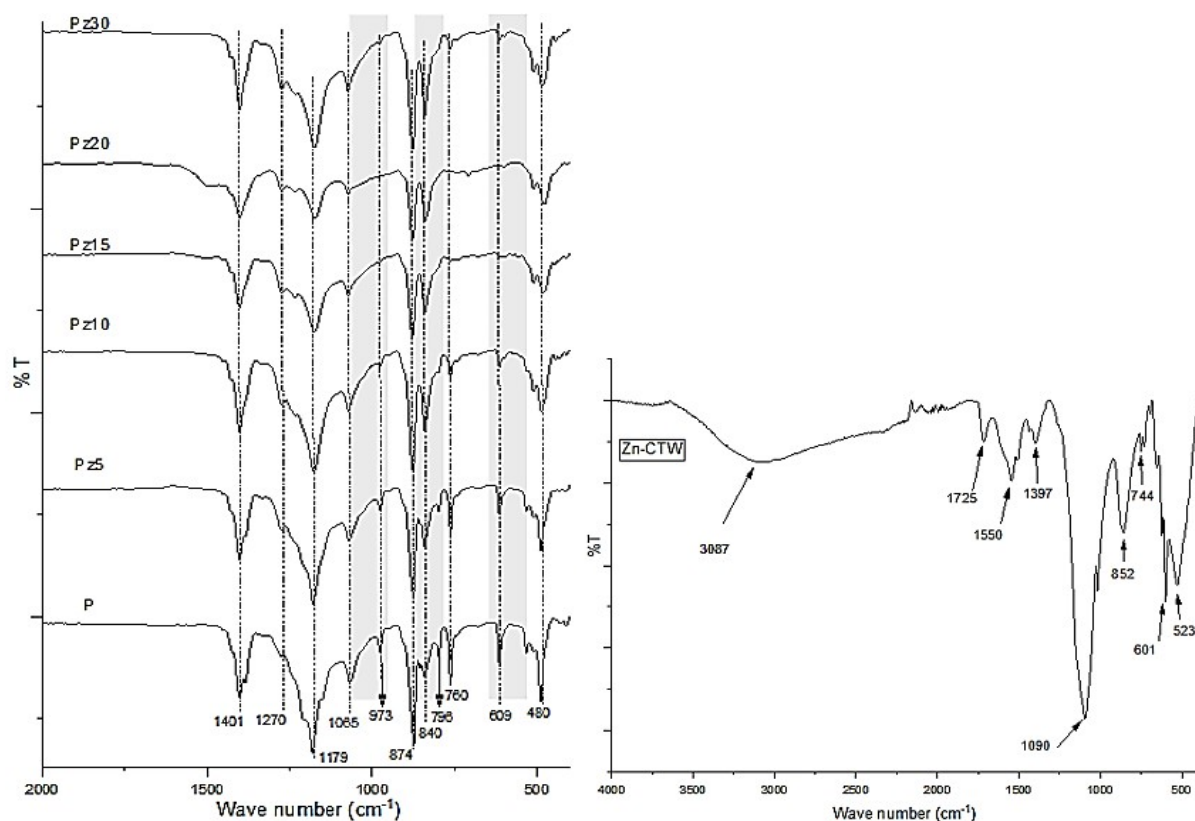

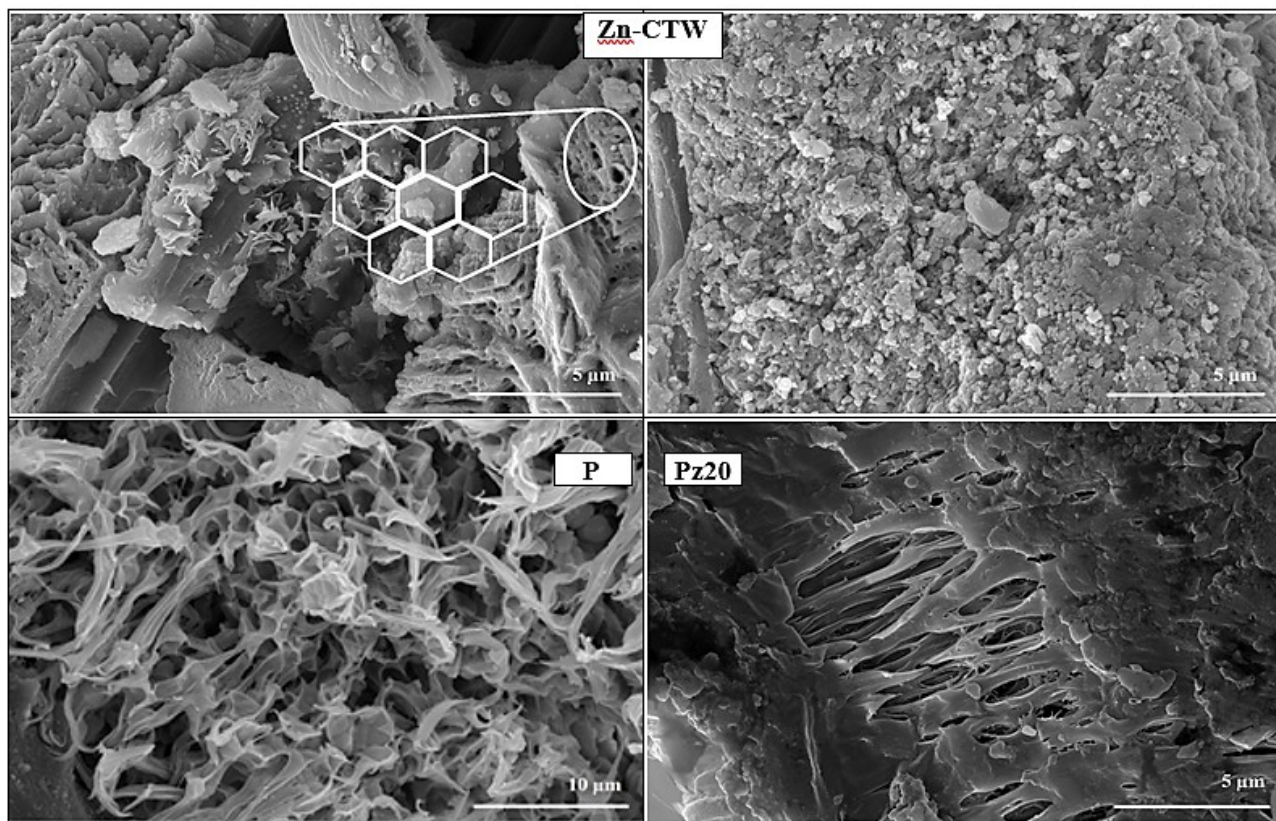**Figure 2:** FT-IR spectra of PVDF composites and Zn-CTW.

Figure 3a: SEM images of Zn-CTW with the inner section of P and Pz20.

Formations of unburned chemicals and their oxides, such as ZnO, around the channels and surface of the structure could be seen in the images. Also, melted polyesters and cotton remnants that have not burned completely took place inherently in the carbonized samples. Nevertheless, the presence of honeycomb structure was satisfactory evidence of the success of the textile waste carbonization because it provides moderate performance as an adsorbent relatively with its cost-effective and straightforward procedures. Morphological changes in the Zn-CTW loaded PVDF structure were investigated. With increasing additive, the structure became more pressed, and pores turned to narrowed shape inevitably. The amount of Zn-CTW was increased by aiming for the higher performance, but the limit of the performance-additive amount was determined as Pz20. After that, structure heterogeneity increased, and polymer-solid incorporation weakened due to an excess amount of additive. These determinations are compatible and proved with the disappearance of peaks in XRD and FT-IR of Pz30. The inner section of the structure turned into a pressed finger-like compared with the cage-like structure with large space (Fig. 3b).
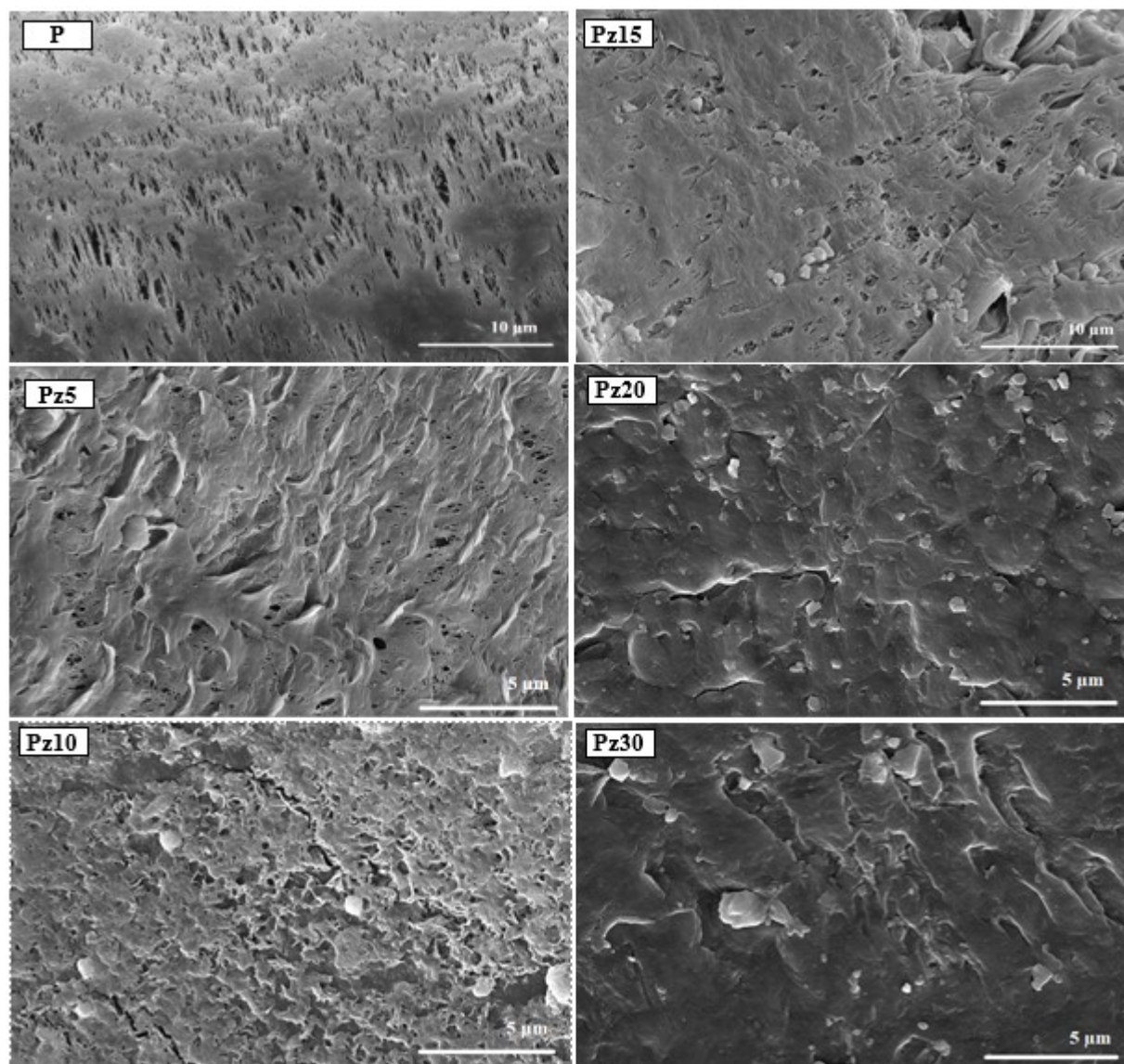
Figure 3b: SEM images of composites.

BET analysis results of samples supported by wettability and porosity data can explain visible shrinkage on the composite structure. Analysis results of Zn-CTW and composites were presented in Table 1. with PO% and WU%.

Table 1: BET area, water uptake (WU%), and porosity percentages of Zn-CTW and composites.

Sample	S_{BET} (m²/g)	V_{total}(cm³/g)	Pore width (nm)	WU%	PO%
Zn-CTW	79.5	0.07	3.7	-	-
P	4.11	0.042	6.3	57.2	65.5
Pz5	8.23	0.036	5.8	58.6	65.0
Pz10	8.62	0.017	5.6	56.2	69.2
Pz15	10.42	0.046	5.4	95.7	130.5
Pz20	15.22	0.044	5.7	73.0	105.3
Pz30	7.4	0.036	6.2	45.5	53.3

*S_{BET} :BET surface area
*V_{total} : total pore volume

The effect of the Zn-CTW additive on the surface of composites could be understood from the BET surface of Pz5-Pz30. Remarkable improvement on the surface of PVDF was achieved with Zn-CTW addition from 4.11 to 15.22 m²/g for P and Pz20, respectively. This was critical for functional polymeric composites, which have tunable properties depending on their application. The satisfactory surface area of Zn-CTW obtained by heating at a low temperature was obtained at 79.5 m²/g. Compared with the literature, large pores recorded at 3.7 nm resulted in large holes instead

of a high number of small pores, which also provided a higher surface area (40). Total pore volume increased with additive amounts except for Pz5 and Pz10 and reached 0.046 cm^3/g with Pz15. On the other hand, the surface area of composites regularly increased until Pz20 and then decreased until Pz30. The results I: pore volumes changed with the additive amount and structural adjustment, II: the porosity percentage provides information about pore number (PO%) and water uptake (WU%), which are as crucial as pore width and pore volume for composites. It was seen that when the pore volume decreased, it was tolerated by increased PO%. In another sense, Zn-CTW addition pressed pores but increased pore numbers. The changes in WU% are going together with composites' pore volumes, indicating that pore volume is proportional to water penetrating inside the structure. The highest surface area, however, decreasing WU and PO%, was provided by Pz20. The different behavior of surface area and WU-PO% of Pz20 attributes to well-interacted polymer powder that enables reflection of Zn-CTW surface properties even in the polymer matrix. Because of the pressed and blocked structure, the Pz30 composition had the lowest surface area and WU-PO%.

Dye Adsorption Studies Onto Zn-CTW and Composites
Dye adsorption studies were conducted with MO model chemicals on Zn-CTW and composites. The optimal pH, time, adsorbent dosage, and temperature of MO adsorption on the Zn-CTW were determined. The adsorption performance of Zn-CTW was investigated to compare when it was loaded on to PVDF matrix in terms of MO adsorption. To understand the effect of temperature on the adsorption performance, studies were conducted at 308, 318, and 328 K, but any remarkable increase was not observed. So, 298 K was decided as the adsorption temperature for this study.

Effect of solution pH
Adsorption percentages of Zn-CTW at different pH values are presented in Fig. 4. No remarkable changes were observed at pH ranges between 6-9 for MO adsorption. According to reports, one of the predominant reasons for adsorption is the charge of particles in an aqueous solution and surface (41). The functional groups discussed in section 3.1 in this study, predominantly consisting of organic structures, acted as suitable MO adsorbers. The best conditions for attraction of MO and surface were formed at pH values of 7-8. According to the literature, an adsorbent's electrical repulsion and attraction forces can be estimated using its isoelectric points; however, activated carbons and dyes can be amphoteric, and their surface charge varies with acidity (42). The surface became favorable for adsorption when cationic particles were negatively charged at higher pH values from the isoelectric point. MO behaviors in aqueous solution pH 7.44 were determined as favorable, but free electrons of dye with delocalized π-electrons of surface effectively changed the surface charge, and optimum pH of adsorption may shift to different values. The 7.44 pH value was adjusted for aqueous solutions.

Effect of adsorbent dosage
The effect of adsorbent dosage was investigated using a 100 mg/L MO solution and is presented in Fig. 5 in the units of both percentage and mg/g. 43% adsorption performance increased to 71% (142 mg/g) with an increased amount of adsorbent from 10 to 50 mg. That was explained simply by the high number of adsorption sites of Zn-CTW. However, with increased adsorbent amounts, the adsorption percentage reached saturation, and it was recorded at 149, 153, and 158 mg/g for 75, 100, and 150 mg adsorbents, respectively. By considering the Zn-CTW amounts in composites, 50 mg was preferred as a favorable dosage for this study.
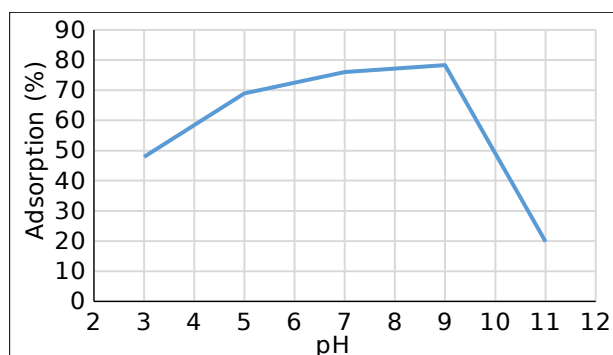

Figure 4: Effect of solution pH on the MO adsorption of 50 mg Zn-CTW with 100 mg/L dye concentration for 1 h contact time at 298 K.
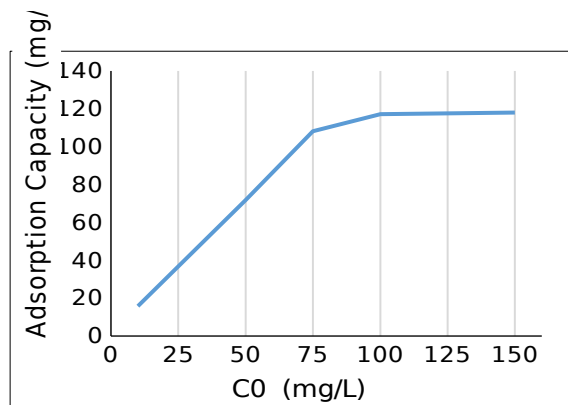
Figure 4: Effect of solution pH on the MO adsorption of 50 mg Zn-CTW with 100 mg/L dye concentration for 1 h contact time at 298 K.
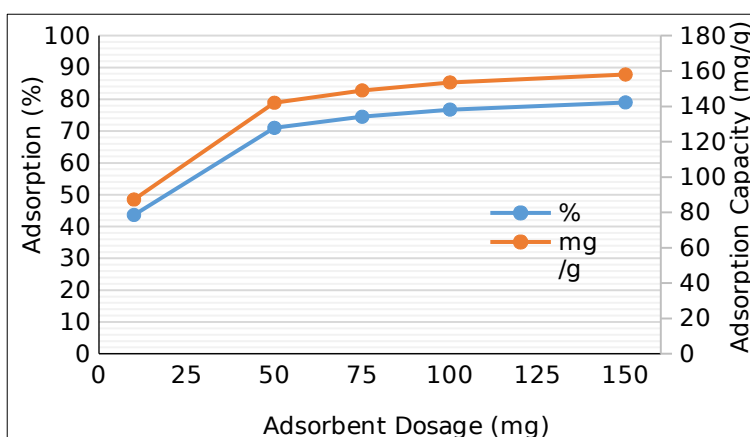

Figure 5: Effect of adsorbent dosage (in terms of removal% and mg/g) on the MO adsorption of Zn-CTW with 100 mg/L dye concentration for 1 h contact time at 298 K..

Effect of contact time and dye concentration
The effects of dye concentration and contact time were given separately in Figures 6a and 6b. From the results, the highest adsorption was obtained when the initial concentration was 100 mg/L with 50 mg of adsorbent. The presence of a large number of adsorption sites resulted in high adsorption. With increased MO, adsorption decreased due to saturation compiled with an explanation of increased adsorbent dosage. The difference between the usual trend of increased adsorption with increased initial concentration may be attributed to the low interaction of vacancies and occupied sites on the surface. Thus, MO particles are adsorbed without affecting the repulsive forces of adsorbed molecules.
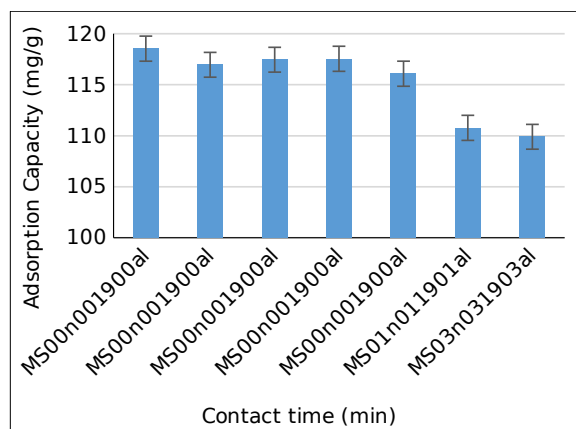

Figure 6: Effect of initial dye concentration for 1 h (a) and contact time (b, dye concentration:100 mg/L) on the MO adsorption of 50 mg Zn-CTW at 298 K.

When the concentration increased, a small increase was recorded after 100 mg/L. Another reason for the low motion of particles that could not adhere to the surface, although the high concentration may be the pH of the studied aqueous. The pH of the studied aqueous may also be a factor in the low motion of particles that could not adhere to the surface. As explained in "effect of pH" (section 3.2.1), MO can be assumed to be charged with neutral or very low anionic and cationic forms at the studied pH. Contact time and adsorption capacity values are presented in Fig 6b, and 120 min was considered the optimum time for adsorption studies for Zn-CTW.

Adsorption performance of Zn-CTW and composites
MO dye adsorption capacities of composites from aqueous solutions were investigated, and the results are presented in Fig. 7. MO adsorption capacity of composites generally increased from Pz5-Pz20. MO adsorption of Pz5 was 59 mg/g while it was 24 mg/g for P. The Zn-CTW additive increased MO adsorption by inducing the formation of new pores and channels and in addition to the adsorption capability of the additive. The importance of regular pores and structure has priority compared with the additive rate in terms of adsorption capacity.
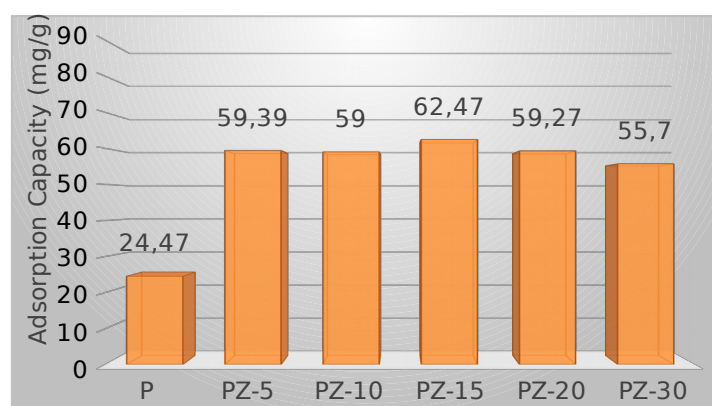

Figure 7: MO dye adsorption performance of composites (adsorbent dosage:50 mg, dye concentration: 100 mg/L, contact time: 2 hours, temperature: 298 K).

As can be seen, the MO adsorption capacity of composites decreased with increased amounts (after PZ-15). It reached the lowest with Pz30 due to its impressed structure. Adsorption decreased as the trapped structure prevented the aqueous solution from entering the composite surface. On the other hand, the MO model dye solution only consisted of basic MO molecules. Therefore, it is estimated that the dye removal performance of composites from industrial wastewater may be different as they contain particles of different sizes in addition to dye.

The bare additive amount loaded onto the PVDF matrix should be considered in addition to the formation of polymer structure induced by the additive. Even if the entire mass of Zn-CTW is loaded into PVDF, there are lots of parameters that affect adsorption performance inside the polymer matrix. It can be inferred that the dye adsorption mechanism onto polymeric composite includes significant differences from traditional solid adsorbents, which was the aim of this study. The composite pore, structure, and interaction with the aqueous solution are highly important for the adsorption performance of the composite. Pz15-Pz20 combinations were decided to be the best Zn-CTW and PVDF compositions for this study.

Adsorption isotherms
Isotherm models that are useful for estimating the interaction between particles and surface were applied to adsorption data. Equilibrium dye concentration and adsorption capacity of only powder form Zn-CTW adsorbent were used for Langmuir and Freundlich isotherm models according to equations 7 and 8 (43). Thus, it is aimed to learn whether the MO adsorption on the powder surface conforms to the adsorption isotherms. The structural differences inherent in the composite surface require investigation of which isotherm the composite adsorption fits the best. This should be discussed in detail in a different study.

$$\frac{C_e}{Q_e} = \frac{1}{K_L Q_{max}} + \frac{C_e}{Q_{max}} \qquad \text{(Eq. 7)}$$

$$\log_{Q_e} = \log_{K_f} + \frac{1}{n} \log_{C_e} \qquad \text{(Eq. 8)}$$

Where C_e (mg/L), the concentration of dye in the eluent after adsorption, Q_{max}: max adsorption capacity of sorbent, K_f, n and K_L are the constants of isotherm of Freundlich and Langmuir models respectively at equilibrium. From the R^2 values presented in Table 2.

Table 2: Isotherm parameters of Zn-CTW for MO adsorption.

	Langmuir Isotherm				Freundlich Isotherm		
	Q_{max} (mg/g)	K_L (L/mg)	R_L	R^2	K_f (mg^{1-n}/g L^n)	n	R^2
Zn-CTW	135.13	0.0992	0.1969	0.9829	0.33	0,6486	0.8717

It was understood that the adsorption mechanism matched the Langmuir model determined by monolayer adsorption on a homogeneous surface. According to the Langmuir model, Q_{max}, the max adsorption capacity of the adsorbent was found to be 135.13 mg/g. That could be seen as reasonable in terms of mechanism and experimental results. Although it is a low-cost process, Zn-CTW performed over moderate adsorption capacity than other adsorbents obtained from biomass and textile waste. The value of the dimensionless constant separation factor called R_L is a constant to explain the feasibility of the Langmuir isotherm and was also calculated by Eq. 9 (44).

$$R_L = \frac{1}{1 + b C_0} \qquad \text{(Eq. 9)}$$

In a sense, R_L is an indicator of the shape of the isotherm. If $R_L=1$, that means the isotherm is linear; if $R_L>1$, it is unfavorable, and when $R_L=0$ or $0<R_L<1$, that means the isotherm is irreversible and favorable, respectively. R_L value of 0.1969 for Zn-CTW is evidence of the feasibility of adsorption as favorable.

When considering the amount of Zn-CTW loaded onto PVDF and composite performance, it can be understood that Zn-CTW provided high adsorption capacity to the polymer matrix. The adsorbent dosage was adjusted as 0.05 g for Zn-CTW and composites, although composite contains a small amount of Zn-CTW (approximately 15% of total mass). The well interaction of the polymer and additive was responsible for the improvement effect of Zn-CTW loading onto PVDF. That gives rise to proper pores, channels, and surfaces rather than simply attaching additives to the polymer. Obtained composite is a promising agent as a pollution removal agent for filtration material for ultrafiltration or other applications.

Advantages of Chemical Activation on Carbonization and Adsorption

Biomass usage to prepare adsorbent materials is a preferred method to get low-cost raw materials. Converting carbon-rich materials to activated carbon has the potential of a couple of benefits: disposal of waste and preparation of activated carbon. Converting the textile waste to valuable products economically requires investigation of the

yielded procedures according to their structure. Textile wastes consisting of polyester and cotton mixture were handled and carbonized. It was concluded that carbonized samples with chemical activation showed high adsorption of MO. These can be explained by high surface area, crystallinity, porous structure, and functional surface groups observed in the analysis spectra. Chemical activation induced the formation of C=O and OH, NH groups, which are highly effective in adsorption on the surface of the carbonized sample. Zn^{2+} and a small amount of ZnO acted as catalysts, and functional groups increased. The higher catalytic activity of Zn^{2+} than ZnO was reported for n-butane to n-butene transformation even at lower temperatures (45). The transformation mechanism advanced on the Zn^{2+}....-O^{2-} acid-base pair may be proposed for polyester-cellulose textile waste. That continued with the adsorption of substrates on the Lewis acid-base pair, the formation of zinc-substrate intermediates, electron transfer, and the formation of yield (46).

The presence of Zn accelerated the carbonization, and more organic structures decomposed at 350 °C. Compared with Zn activated and nonactivated samples, the ash remnant of Zn activated samples is less than others with higher adsorption performance (Table 3).

Additionally, the absence of functional groups was understood at CTW-350 and CTW-400 surfaces from the IR bands attributed to C=C and C-O-C vibrations at 1545 and 1094 cm^{-1}, as shown in Figure 8. Concerned with all findings such as functional groups, porous honeycomb structure, and adsorption capacity, chemical activation is necessary to decrease temperature and obtain activated carbon with a modified structure.

Table 3: Remnant (after carbonization) and MO adsorption performances of CTW.

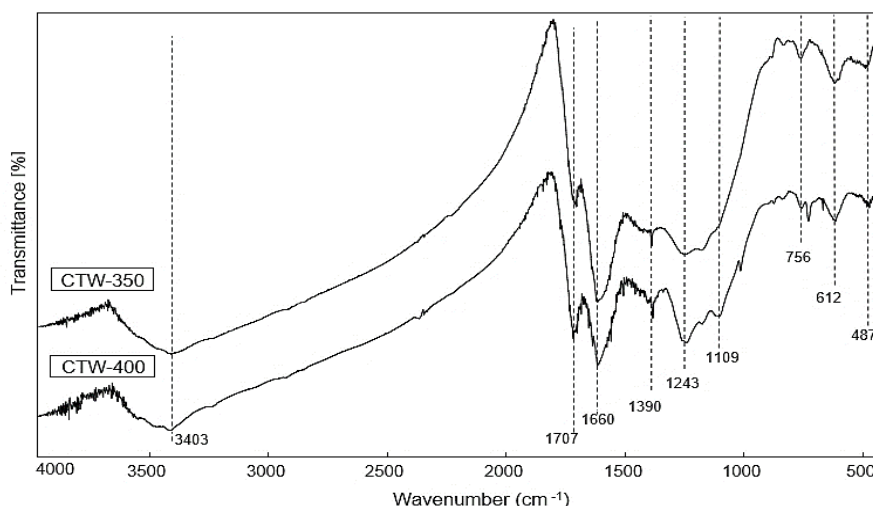| Sample	Mass%	MO%
Zn-CTW	67.1	74.8
CTW-350	28	27.6
CTW-400	13.8	52.5

Figure 8: FT-IR spectra of activated carbons obtained at 350 (CTW-350) and 400 °C (CTW-400) without chemical pretreatment.

Regeneration

The reusability of adsorbents was tested after washing as described in section 2.4. After 4 cycles of MO adsorption and desorption, there was no observed decrease in the adsorption capacity of samples (Figure 9). Even a small amount of increase was observed for regenerated Zn-CTW after acid treatment. Washing with an acidic solution may break off some species locked in the pores with adsorbed dye molecules and result in a well transporting structure.
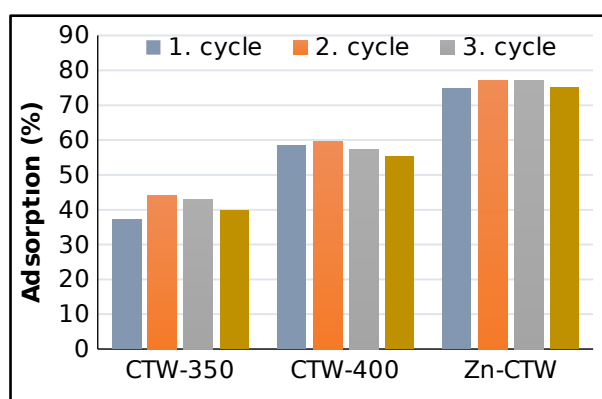
Figure 9: Reusing performance of 350 (CTW-350),400 °C (CTW-400), and Zn-CTW.

CONCLUSION

Carbonization of $ZnCl_2$ pretreated textile waste samples was conducted. Their structure, surface, and dye adsorption properties were investigated. The obtained sample was loaded into the PVDF matrix to understand the usability of its adsorption properties inside composites for different applications. Chemical activated samples showed better porosity, water uptake, and noticeable structural adjustment for high adsorption of MO. 05-Zn-1-350 (Zn-CTW) has 117 mg/g MO dye adsorption performance. Composites obtained by adding 0, 5, 10, 15, 20, 25, and 30% Zn-CTW were investigated for an additive effect on the structure and dye adsorption performance. Interaction of additive with PVDF chain was determined by decreasing XRD peak strength that showed α-phase PVDF at around 2°=18.58, 20.21, and 27.2 with IR bands of 1383, 975, 796, 762, 613, and 531 cm^{-1}. The optimum additive amount was decided as 15-20% due to increased structural strain and adsorption capacity until that ratio. Polymeric composites consist of two or more kinds of different combinations of materials to improve the properties of polymeric structure and gain easy usage as powder. Zn-CTW added PVDF provided increased adsorption performance compared with raw PVDF. That made it preferable for different applications, such as filtration or pollution removal from water. Biochar prepared by simple chemical activation could show triple effects. Upon disposal of textile waste, obtaining moderately featured activated carbon acted as an additive material for composite preparation.

CONFLICT OF INTEREST

The authors have no conflicts of interest to declare relevant to this article's content, and all authors agree that the study should be published.

ACKNOWLEDGMENTS

REFERENCES

1.   Vieira O, Ribeiro RS, Pedrosa M, Lado Ribeiro AR, Silva AMT. Nitrogen-doped reduced graphene oxide – PVDF nanocomposite membrane for persulfate activation and degradation of water organic micropollutants. Chem Eng J [Internet]. Elsevier; 2020;402(March):126117. Available from: <DOI>.

2.   Pala M, Kantarli IC, Buyukisik HB, Yanik J. Hydrothermal carbonization and torrefaction of grape pomace: A comparative evaluation. Bioresour Technol. 2014;161:255–62. <DOI>.

3.   Arteaga-Pérez LE, Segura C, Bustamante-García V, Cápiro OG, Jiménez R. Torrefaction of wood and bark from Eucalyptus globulus and Eucalyptus nitens: Focus on volatile evolution vs feasible temperatures. Energy. 2015;93:1731–41. <DOI>.

4.   Tag AT, Duman G, Ucar S, Yanik J. Effects of feedstock type and pyrolysis temperature on potential applications of biochar. J Anal Appl Pyrolysis. 2016;120:200–6. <DOI>.

5.   Ambaye TG, Vaccari M, van Hullebusch ED, Amrane A, Rtimi S. Mechanisms and adsorption capacities of biochar for the removal of organic and inorganic pollutants from industrial wastewater. Int J Environ Sci Technol [Internet]. Springer Berlin Heidelberg; 2020; Available from: <DOI>.

6.   De Oliveira GF, De Andrade RC, Trindade MAG, Andrade HMC, De Carvalho CT. Thermogravimetric and spectroscopic study (Tg-DTA/FT-IR) of activated carbon from the renewable biomass source babassu. Quim Nova. 2017;40(3):284–92. <DOI>.

7.   Choudhury A, Lansing S. Adsorption of hydrogen sulfide in biogas using a novel iron-impregnated biochar scrubbing system. J Environ Chem Eng [Internet]. Elsevier Ltd; 2020;9(1):104837. Available from: <DOI>.

8.   Yaashikaa PR, Kumar PS, Varjani S, Saravanan A. A critical review on the biochar production techniques, characterization, stability and applications for circular bioeconomy. Biotechnol Reports [Internet]. Elsevier B.V.; 2020;28:e00570. Available from: <DOI>.

9.   Della L, Ducousso M, Batisse N, Dubois M, Verney V, Xavier V, et al. Poplar wood and tea biochars for trichloroethylene remediation in pure water and contaminated groundwater. Environ Challenges [Internet]. Elsevier B.V.; 2020;1(August):100003. Available from: <DOI>.

10.   Silva RVS, Gonçalves AD, Vinhal JO, Cassella RJ, Santos RC, Sasso MAD, et al. Bioproducts from the pyrolysis of castor seed cake: basic dye adsorption capacity of biochar and antifungal activity of the aqueous phase. J Environ Chem Eng. 2020;9(August 2020):104825. <DOI>.

11.   Yao X, Ji L, Guo J, Ge S, Lu W, Chen Y, et al. An abundant porous biochar material derived from wakame (Undaria pinnatifida) with high adsorption performance for three organic dyes. Bioresour Technol [Internet]. Elsevier; 2020;318(September):124082. Available from: <DOI>.

12.   Chahinez HO, Abdelkader O, Leila Y, Tran HN. One-stage preparation of palm petiole-derived biochar: Characterization and application for adsorption of crystal violet dye in water. Environ Technol Innov [Internet]. Elsevier B.V.; 2020;19:100872. Available from: <DOI>.

13.   Ali NA, Hussein EA. Characterization of functional electrospun polymeric nanofiber membranes. Int J Environ Sci Technol [Internet]. Springer Berlin Heidelberg; 2019;16(12):8411–22. Available from: <DOI>.

14.   Haslinger S, Hummel M, Anghelescu-Hakala A, Määttänen M, Sixta H. Upcycling of cotton polyester blended textile waste to new man-made cellulose fibers. Waste Manag [Internet]. The Author(s); 2019;97:88–96. Available from: <DOI>.

15.   Anonim. Sektörel Atık Kılavuzları. 2016;146.

16.   Nautiyal P, Subramanian KA, Dastidar MG. Experimental investigation on adsorption properties of biochar derived from algae biomass residue of biodiesel production. Environ Process. 2017;4:S179–93. <DOI>.

17.   Jeihanipour A, Aslanzadeh S, Rajendran K, Balasubramanian G, Taherzadeh MJ. High-rate biogas production from waste textiles using a two-stage process. Renew Energy [Internet]. Elsevier Ltd; 2013;52:128–35. Available from: <DOI>.

18.   Jeihanipour A, Karimi K, Niklasson C, Taherzadeh MJ. A novel process for ethanol or biogas production from cellulose in blended-fibers waste textiles. Waste Manag [Internet]. Elsevier Ltd; 2010;30(12):2504–9. Available from: <DOI>.

19.   Xu Z, Qi R, Xiong M, Zhang D, Gu H, Chen W. Conversion of cotton textile waste to clean solid fuel via surfactant-assisted hydrothermal carbonization: Mechanisms and combustion behaviors. Bioresour Technol. 2021;321(November 2020). <DOI>.

20.   Kwon D, Yi S, Jung S, Kwon EE. Valorization of synthetic textile waste using CO2 as a raw

material in the catalytic pyrolysis process. Environ Pollut [Internet]. Elsevier Ltd; 2021;268:115916. Available from: <DOI>.

21.   Subramanian K, Chopra SS, Cakin E, Li X, Lin CSK. Environmental life cycle assessment of textile bio-recycling – valorizing cotton-polyester textile waste to pet fiber and glucose syrup. Resour Conserv Recycl [Internet]. Elsevier; 2020;161(May):104989. Available from: <DOI>.

22.   Guo Z, Eriksson M, Motte H de la, Adolfsson E. Circular recycling of polyester textile waste using a sustainable catalyst. J Clean Prod [Internet]. Elsevier Ltd; 2020;283:124579. Available from: <DOI>.

23.   Hanoğlu A, Çay A, Yanık J. Production of biochars from textile fibres through torrefaction and their characterisation. Energy. 2019;166:664–73. <DOI>.

24.   Singh V, Srivastava VC. Self-engineered iron oxide nanoparticle incorporated on mesoporous biochar derived from textile mill sludge for the removal of an emerging pharmaceutical pollutant. Environ Pollut [Internet]. Elsevier Ltd; 2020;259:113822. Available from: <DOI>.

25.   Silva TL, Cazetta AL, Souza PSC, Zhang T, Asefa T, Almeida VC. Mesoporous activated carbon fibers synthesized from denim fabric waste: Efficient adsorbents for removal of textile dye from aqueous solutions. J Clean Prod. 2018;171:482–90. <DOI>.

26.   Wang X, Li C, Li Z, Yu G, Wang Y. Effect of pyrolysis temperature on characteristics, chemical speciation and risk evaluation of heavy metals in biochar derived from textile dyeing sludge. Ecotoxicol Environ Saf [Internet]. Elsevier Inc.; 2019;168(August 2018):45–52. Available from: <DOI>.

27.   Hein J, Guarin A, Frommé E, Pauw P. Deforestation and the Paris climate agreement: An assessment of REDD + in the national climate action plans. For Policy Econ [Internet]. Elsevier; 2018;90(November 2017):7–11. Available from: <DOI>.

28.   Li Z, Hanafy H, Zhang L, Sellaoui L, Schadeck Netto M, Oliveira MLS, et al. Adsorption of congo red and methylene blue dyes on an ashitaba waste and a walnut shell-based activated carbon from aqueous solutions: Experiments, characterization and physical interpretations. Chem Eng J. 2020;388(December 2019). <DOI>.

29.   Patra C, Gupta R, Bedadeep D, Narayanasamy S. Surface treated acid-activated carbon for adsorption of anionic azo dyes from single and binary adsorptive systems: A detail insight. Environ Pollut. 2020;266. <DOI>.

30.   Li L, Fan C, Zeng B, Tan M. Effect of pyrolysis temperature on lithium storage performance of pyrolitic-PVDF coated hard carbon derived from cellulose. Mater Chem Phys. 2020;242. <DOI>.

31.   Arularasu M V., Harb M, Vignesh R, Rajendran T V., Sundaram R. PVDF/ZnO hybrid nanocomposite applied as a resistive humidity sensor. Surfaces and Interfaces. 2020;21(September). <DOI>.

32.   Saha P, Debnath T, Das S, Chatterjee S, Sutradhar S. β-Phase improved Mn-Zn-Cu-ferrite-PVDF nanocomposite film: A metamaterial for enhanced microwave absorption. Mater Sci Eng B Solid-State Mater Adv Technol [Internet]. Elsevier; 2019;245(April 2018):17–29. Available from: <DOI>.

33.   Abdulsalam J, Mulopo J, Oboirien B, Bada S, Falcon R. Experimental evaluation of activated carbon derived from South Africa discard coal for natural gas storage. Int J Coal Sci Technol [Internet]. Springer Singapore; 2019;6(3):459–77. Available from: <DOI>.

34.   Gumus H. Performance investigation of Fe 3 O 4 blended poly (vinylidene fluoride) membrane on filtration and benzyl alcohol oxidation: Evaluation of sufficiency for catalytic reactors. Chinese J Chem Eng. Elsevier B.V.; 2019;27(2):314–21. <DOI>.

35.   Medeiros KAR, Rangel EQ, Sant'Anna AR, Louzada DR, Barbosa CRH, D'Almeida JRM. Evaluation of the electromechanical behavior of polyvinylidene fluoride used as a component of risers in the offshore oil industry. Oil Gas Sci Technol. 2018;73(2). <DOI>.

36.   Cai X, Lei T, Sun D, Lin L. A critical analysis of the α, β and γ phases in poly(vinylidene fluoride) using FTIR. RSC Adv. Royal Society of Chemistry; 2017;7(25):15382–9. <DOI>.

37.   Sartova K, Omurzak E, Kambarova G, Dzhumaev I, Borkoev B, Abdullaeva Z. Activated carbon obtained from the cotton processing wastes. Diam Relat Mater. 2019;91(June 2018):90–7. <DOI>.

38.   Yedurkar S, Maurya C, Mahanwar P. Biosynthesis of Zinc Oxide Nanoparticles Using Ixora Coccinea Leaf Extract—A Green Approach. Open J Synth Theory Appl. 2016;5(1):1–14. <DOI>.

39.   Ahmad F, Daud WMAW, Ahmad MA, Radzi R. Cocoa (Theobroma cacao) shell-based activated carbon by CO 2 activation in removing of Cationic dye from aqueous solution: Kinetics and equilibrium studies. Chem Eng Res Des. 2012;90(10):1480–90. <DOI>.

40.   Choi GG, Jung SH, Oh SJ, Kim JS. Total utilization of waste tire rubber through pyrolysis to obtain oils and CO2 activation of pyrolysis char. Fuel Process Technol. 2014;123:57–64. <DOI>.

41.   Chiang CH, Chen J, Lin JH. Preparation of pore-size tunable activated carbon derived from waste coffee grounds for high adsorption capacities of organic dyes. J Environ Chem Eng. 2020;8(4). <DOI>.

42.   Xiao W, Garba ZN, Sun S, Lawan I, Wang L, Lin M, et al. Preparation and evaluation of an effective activated carbon from white sugar for the adsorption of rhodamine B dye. J Clean Prod. 2020;253. <DOI>.

43.   León O, Muñoz-Bonilla A, Soto D, Pérez D, Rangel M, Colina M, et al. Removal of anionic and cationic dyes with bioadsorbent oxidized chitosans. Carbohydr Polym. 2018;194:375–83. <DOI>.

44.   Gabrienko AA, Arzumanov SS, Lashchinskaya ZN, Toktarev A V., Freude D, Haase J, et al. n-Butane transformation on Zn/H-BEA. The effect of different Zn species (Zn2+ and ZnO) on the reaction performance. J Catal [Internet]. Elsevier Inc.; 2020;391:69–79. Available from: <DOI>.

45.   Gumus H. Catalytic performance of polyvinylidene fluoride (Pvdf) supported TiO2 additive at microwave conditions. J Turkish Chem Soc Sect A Chem. 2020;7(2):361–74. <DOI>.

Proximate, Phytochemicals, Minerals, and Antinutritional Contents of *Ficus Thonningii* Seed

Hamza Ibrahim Muhammad[1]* iD **, Omolara Olusola Oluwaniyi[2]** iD

[1]Federal University of Lafia, Department of Chemistry, Lafia, Nigeria.
[2]University of Ilorin, Department of Industrial Chemistry, Ilorin, Nigeria.

Abstract: The proximate, phytochemicals, minerals, and anti-nutritional content of *Ficus thonningii* seed obtained from Nasarawa, Nasarawa State, Nigeria were investigated. The proximate analysis revealed that the seed is abundant in ash (8.36 ± 0.77 %), protein (27.52 ± 0.17 %) and carbohydrate (40.02%) but contains low moisture (8.76 ± 0.06 %) and fiber (2.81 ± 0.09 %). The minerals analysis showed very high quantities of Ca (2067.50 mg/100 g), P (1985.40 mg/100 g), Mg (1184.10 mg/100 g), K (918.30 mg/100 g) S (192.50 mg/100 g), Fe (434.10 mg/100 g), Mn (39.30 mg/100 g), Cu (57.40 mg/100 g), and Zn (63.60 mg/100 g), Co (1.2 mg/100 g) and Mo (1.10 mg/100 g). Phytochemicals analysis revealed that it contains more flavonoids (6.13 ± 0.02 g/100 g) and phenolics (8.77 ± 0.01 g/100 g) than saponins (1.73 ± 0.02 g/100 g), tannins (4.37 ± 0.06 g/100 g) and alkaloids (0.62 ± 0.01 g/100 g). The study has shown that *Ficus thonningii* seed is highly nutritive with very high mineral content and low quantities of anti-nutrients which make it a good source of food for humans and animals. It also contains biologically active phytochemicals which could have medicinal uses.

INTRODUCTION

Global food security and economic growth now depends on a declining number of plant species (1). Nigeria, and Africa at large, is bestowed with seed-bearing plants, which over the years have served various purposes, and yet many of them remain unused (2). The lack of information on the characteristics and usefulness of these many and varied plants is more of a problem than their shortage (3). Underutilized plants can also meet nutritional requirements due to their better nutritional value compared to some optimally utilized plants (1, 4). The seed bearing plants within our environments drop their fruits and large amounts of fruit seeds are being discarded yearly at processing plants. This is not only a waste of potentially valuable resources but also worsens an already serious waste disposal problem (5). In addition, the medicinal values of plants lie in their phytochemical components, which produce definite physiological results on the human body. Polyphenolics for example appear to play a significant role as antioxidants in the protective effect of plant-derived foods and medicines and have become the focus of nutritional and therapeutic interest in recent years (6).

Ficus thonningii (Moracceae) is a member of the pan tropical genus *Ficus* which contains more than 700 species (7). It is a wild evergreen plant about 30 m in length, with a dense crown that spreads around. It also grows sometimes as a climber by growing on and wrapping itself around other trees. *Ficus thonningii* is characterised by simple, dark green, smooth, slightly elongated leaves and small,

globose, slightly rough-surfaced fruit which is green, greenish-yellow or yellow, depending on maturity and usually in season around October in Africa (8). The seed is simple, spherical, smooth-surfaced, yellow, and about 1-3 mm in diameter.

Ficus thonningii is a neglected and underutilized plant. There is limited information on the chemical composition of its different parts despite the fact that it is a traditionally valuable plant with both nutritional and therapeutic benefits. It is drought resistant, easy to propagate, has high growth rate and has no allelopathy (9). Work has been carried out on its leaf (7, 10-15), bark and twig (9) and its root, leaf, and stem bark (14, 17, 18). This study aims to evaluate the proximate, mineral, phytochemical and antinutritional composition of its seed in order to assess its potential as food, fodder, medicine, and energy source.

MATERIALS AND METHODS

Sample Source and Preparation
Fully mature *Ficus thonningii* fruits were collected fresh from some trees beside Pilot Central Primary School Nasarawa, Nasarawa Local Government Area, Nasarawa State, Nigeria and the fruits where identified at the Herbarium Unit, Department of Plant Biology, University of Ilorin, Ilorin, Nigeria. The fruits were dried partially before the seeds were manually removed, dried completely under the shed, milled, and stored properly in a polyethylene bag for further analysis.

Proximate Analysis
The proximate composition was determined as described by Ijaritimi *et al.* (19).

Moisture Content
2 g of the defatted seed in pre-weighed crucible was placed in an oven at 105 °C for 24 h, cooled, and reweighed. The percentage moisture was calculated as follows:

$$\text{Moisture \%} = \frac{W_2 - W_3}{W_2 - W_1} x\,100$$

where W_1 is the weight of the crucible, W_2 is the weight of the crucible and sample before drying at 105 °C, and W_3 is the weight of the crucible and the sample after drying and cooling in airtight desiccators.

Ash Content
2 g of the defatted seed was added into a pre-weighed crucible incinerated in muffle furnace at 550 °C for 5-6 h.

$$\text{Ash (\%)} = \frac{W_2 - W_3}{W_2 - W_1} x\,100$$

Where W_1 is the weight of cleaned, dried, ignited, and cooled crucible, W_2 the weight of the crucible and sample before incinerating at 550 °C, and W_3 the weight of the crucible and sample after cooling in the oven.

Crude Protein Content
Crude protein was determined using semi micro Kjeldahl method. 5 g of sample was separately and accurately weighed and placed into Kjeldahl digestion flask. To the flask, 25 ml conc. H_2SO_4, 5 g of copper sulfate and 2.5 g of sodium sulfate salt and 0.5 g of selenium dioxide was added. The solution was then digested in a fume hood slowly to avoid undue frothing for at least forty-five minutes until sample became clearer. The obtained sample was allowed to cool and made up to 250 mL with distilled water. About 10 mL of the digest was collected for distillation; 10 mL of 40% NaOH was added to the digest in the distillation flask. The distillate was collected into 2% boric acid solution to absorb the liberated ammonia. This was titrated against 0.01 M HCl using drops of methyl red and bromocresol green indicators and titer value after color change from green to pink was observed and recorded. A blank (without sample) was likewise prepared, distilled, and titrated. The protein content was calculated as:

$$\% \text{ Crude protein} = \frac{14\,x\,10^{-5} \times (\text{sample titer} - \text{blank titer}) \times 250 \times 6.25}{\text{weight of sample used}\,x\,10} \times 100$$

Where 14 is the molecular weight of nitrogen and 6.25 is the nitrogen factor.

Determination of Crude Fiber Content
2 g of sample was weighed into a digestion flask and 200 mL of 1.25% sulfuric acid was added. The sample was connected to a condenser and heated for 30 minutes. The flask was removed and content filtered through linen in a fluted Büchner funnel and washed with hot water until washing was no longer acidic. The residue obtained was further placed in a flask and 200 mL of 1.25% NaOH was added. The resulting solution was boiled for 30 minutes after which it was removed, filtered, and washed as above. The digested sample was then washed with 25 mL of 1% HCl solution and 25 mL of industrial spirit. The residue collected was put into a pre weighed crucible and dried for about 2 hours at 100 °C in an air oven, cooled in a desiccator, and weighed. The cooled sample was ignited in a muffle furnace at 600 °C for 3 hours, cooled, and weighed. The loss in weight of residue was recorded as the crude fiber content.

$$\% \text{ Crude fiber} = \frac{\text{Loss in wt (g)}}{\text{weight of original sample (g)}} \times 100$$

Carbohydrate Content
The carbohydrate content was determined by difference, that is, addition of all the percentages of moisture, fat, crude protein, ash, and crude fiber was subtracted from 100%. This gave the amount of nitrogen-free extract otherwise known as carbohydrate.

Carbohydrate% = 100 - (Moisture% + Fat% + Ash% + Crude fiber% + Crude protein%)

Calorific Value
The energy content of the seed was calculated from the formula:

Total Energy (kcal/kg) = (4 x Carbohydrate%) + (9 x Fat%) + (4 x Crude protein%)

Minerals Analysis
The minerals content of the seed cake was analyzed using the Skyray Instrument EDX3600B X-ray fluorescence spectrometer.

Quantification of Phytochemicals and Anti-Nutrients
The phytochemical and antinutritional analysis was carried out according to the methods described by Oluwaniyi *et al.;* and Oluwaniyi and Bazambo (20, 21).

Quantitative Determination of Saponins
5 g of the defatted seed was dispersed in 100 mL of 20% ethanol. The suspension was heated over a hot water bath for 4 hours with continuous stirring at about 55 °C and filtered using Whatman No 1 filter paper. The residue was re-extracted with another 100 mL of 20% ethanol. The combined extract was reduced to 40 mL over a water bath at about 90 °C. The concentrate was transferred into 250 mL separating funnel and extracted using diethyl ether by adding 20 mL of diethyl ether, shaken vigorously and then allowed to settle and then discard the ether layer. The purification process was repeated. The aqueous layer was extracted twice with n-butanol and washed twice with 10 mL of 5% aqueous sodium chloride. The solution was then evaporated over a water bath and dried to a constant weight. (20)

Quantitative Determination of Tannins
5 g of the defatted seed was weighed into a conical flask and 100 mL of 2 M HCl was added. The content was boiled on a water bath for 30 minutes. The extract was cooled and filtered using Whatman No.1 filter paper. The filtrate was taken twice in diethyl ether with two 40 mL portions. The ether extract was heated to dryness and weighed (20).

Quantitative Determination of Alkaloids
5 g of defatted seed was weighed into a 250 mL beaker, 200 mL of 20% acetic acid in ethanol was added and allowed to stand for 4 hours. This was then filtered and the extract was concentrated using a water bath to evaporate about a quarter of the original volume. Concentrated ammonia was added drop-wise to the extract until precipitation was completed. The entire solution was allowed to settle and the precipitate collected by filtration and weighed. (20)

Quantitative Determination of Total Phenolics
2 g of the defatted seed was soaked in 100 mL of n-hexane for 4 hours to remove all fats. The residue was extracted with 50 mL of diethyl ether, and the ether extract was extracted into 50 mL of 10% NaOH solution. The aqueous layer was acidified to pH 4.0 with 10% HCl solution and then extracted into 5 mL of dichloromethane (DCM). The organic layer was finally collected, dried, and weighed (21).

Quantitative Determination of Flavonoids
10 g of the defatted seed was extracted with 100 mL of 80% aqueous methanol repeatedly at room temperature. The whole solution was filtered through Whatman filter paper No 42 (125 mm) and the filtrate evaporated to dryness over a water bath, dried and weighed (21).

Quantitative Determination of Cyanide
4 g of the defatted seed was soaked in a mixture containing 40 mL of distilled water and 2 mL of orthophosphoric acid, mixed stoppered and left overnight at room temperature to free bound hydrocyanic acid. 5 mL of the resulting mixture was distilled into 40 mL of distilled water containing 0.1 g of NaOH pellets. The distillate was made up to 50 mL with distilled water and 20 mL of this was titrated against 0.01 M silver nitrate solution using 1.0 mL of 5% potassium iodide solution to an end point indicated by a faint but permanent turbidity (21).

Quantitative Determination of Oxalates
75 mL of 0.3 M H_2SO_4 was added to 1 g of the defatted seed stirred and filtered. 25 mL of the filtrates (extract) was titrated still hot (80-90 °C) against 0.05 M $KMnO_4$ solution to the point when pink color appeared that persisted for at least 30 seconds. (21)

$$\% \text{ oxalate}\,(mg/100\,g) = \frac{T\,x\,[Vme]\,[DF]\,x\,2.4\,x\,100}{ME\,x\,Mf}$$

Where T = titer of $KMnO_4$
V_m = Volume-mass equivalent (i.e 1 mL of 0.05 M $KMnO_4$ solution is equivalent to 0.00225 g of anhydrous oxalic acid)
DF = Dilution factor, VT/A
VT = Total volume of filtrate (75 mL), A = Aliquot used (25 mL)
ME = Molar equivalent of $KMnO_4$
Mf = Mass of sample used.

Quantitative Determination of Phytates
4.0 g of the defatted seed was soaked in 100 mL of 2% HCl for 3 hours and 25 mL of the filtrate was titrated with a standard iron(III) chloride solution using 0.3% ammonium thiocyanate as indicator until a brownish yellow color appeared which persisted for 5 mins. (21)

RESULTS AND DISCUSSION

Proximate Analysis

Table 1: Proximate content of the seed.

Parameter	Mean ± SD
Fats (%)	12.53 ± 0.85
Protein (%)	27.52 ± 0.17
Ash (%)	8.36 ± 0.77
Fibre (%)	2.81 ± 0.09
Moisture (%)	8.76 ± 0.06
Carbohydrate (%)	40.02
Calorific Value (kcal/kg)	382.93

Values are means ± s.d of triplicate determinations.

The seed has low fats content (12.53 ± 0.85 %). This is much lower than 31.52 % reported for *Ficus sycomorus* seed (22), 34% found in sweet orange seed (23) and 44% reported for pumpkin seeds (24). This implies that *Ficus thonningii* seed is not suitable as a source of fats for applications that require large quantity of fats. The protein content (27.52 ± 0.17 %) is higher than the 23.4% and 21.8% reported for watermelon seeds (25,26), 9.23% found in *Ficus sycomorus* seed (22), and 13.5% found in *Dendrocalamus strictus* (27) but lower than 31.44% for *Mucuna pruriens* (28). This indicates that the seed can be used as protein supplement in animal feeds. The seed has high percent ash content (8.36 ± 0.77 %) which is close to 7.24% reported for *Ficus sycomorus* seed (22) but higher than 4.11% for *Mucuna pruriens* (28). Hence, it can be an excellent source of minerals. The percent fiber content (2.81 ± 0.09 %) is lower than 3.02% in *Ficus sycomorus* seed (22), 5.35% found in bambara groundnut (28), 10.89% reported

for okra (30) and 4.61% found in mung bean (31). The moisture content of a seed determines its susceptibility to microbial activity and its shelf life. The moisture content (8.76 ± 0.06 %) is lower than 9.65% reported for *Ficus sycomorus* seed (22), 10.39% reported for cowpea and 8.30% found in mung bean (31) but higher than 6.45% for bambara groundnut (29), 6.43% found in sweets orange seed (23) and 7.731% for pumpkin seed (24). The percent carbohydrate content (40.02%) is high. It is however close to 39.34% reported for *Ficus sycomorus* seed (22). The energy content of the seed is 382.93 kcal/kg.

Minerals Composition
The minerals present in the seed cake are shown in Table 2 below. The seeds cake contains 2067.50 mg/100 g of Ca. This is much higher than the reported 390.77 mg/100 g for *Ficus sycamore* seed, 309 mg/100 g for *Icacina senegalensis* seed and 128.33 mg/100 g for *Moringa oleifera* seed (22, 19). The phosphorus content is 1985.40 mg/100 g. This is also much higher than 119.14 mg/100 g for *Ficus sycamore* seed, 380.24 mg/100 g for *Icacina senegalensis* seed and 103.33 mg/100 g for *Moringa oleifera* seed (22, 19). Especially for children, high intake of calcium and phosphorus are required for bone and teeth formation (32). The seed contains 1184.10 mg/100 g of Mg. This is higher than 300.67 mg/100 g reported for *Ficus sycamore* seed and 268 mg/100 g for *Tamarindus indica* seed (22, 33). Mg is important in protein synthesis, membrane integrity, nervous tissue conduction, muscle contraction and hormone secretion in animals (34) while potassium contributes to the bioelectrical potential of the body (35). The potassium content (918.30 mg/100 g) is also higher than 398.41 mg/100 g and 2.84 mg/100 g reported for lima beans seed coat (6, 22). The seed contains 192.50 mg/100 g of S and 236.60 mg/100 g of Al. Sulfur is a part of cysteine and methionine, both of which are key metabolic intermediates in biosynthesis of glutathione and other sulfur metabolites (36). The microelements: Fe (434.10 mg/100 g), Mn (39.30 mg/100 g), Cu (57.40 mg/100 g), and Zn (63.60 mg/100 g) are so much higher than those reported for *Ficus sycamore* (11.64 mg/100 g Fe, 1.52 mg/100 g Cu and 9.56 mg/100 g Zn) (22) as well as those reported for African locust bean seed (0.60 mg/100 g Mn, 0.08 mg/100 g Cu, and 0.10 mg/100 g Fe) (37). Other micronutrients in this seed include Co (1.2 mg/100 g) and Mo (1.10 mg/100 g). Fe is important in cellular oxygen transport and use, Mn activates enzymes transfer ATP to ADP, Zn promotes DNA and RNA replication and foetal growth, Cu helps melanin pigment formation, and Mo catalyzes reduction of nitrogen to ammonia (38).

Table 2: Minerals Content of the seed.

Minerals	Quantity (mg/100 g)
Mg	1184.10
P	1985.40
S	192.50
K	918.30
Ca	2067.50
Mn	39.30
Co	1.20
Fe	434.10
Cu	57.40
Zn	63.60
Mo	1.10

Table 3: Phytochemical and antinutritional content of *Ficus thonningii* seed.

Phytochemicals	Mean ± sd
Saponins (g/100 g)	1.73 ± 0.02
Tannins (g/100 g)	4.37 ± 0.06
Alkaloids (g/100 g)	0.62 ± 0.01
Flavonoids (g/100 g)	6.13 ± 0.02
Total phenolics (g/100 g)	8.77 ± 0.01
Phytates (mg/100 g)	0.97 ± 0.05
Oxalates (mg/100 g)	0.13 ± 0.01
Cyanides (mg/100 g)	0.04 ± 0.01

Values are means ± s.d of triplicate determinations.

Phytochemicals and Anti-Nutrients

The phytochemical contents of *Fucus thonningii* seeds are shown in Table 3. Saponins produce foams when in aqueous solutions precipitate, coagulate red blood cells and bind cholesterol (39). The saponin content (1.73 ± 0.02 g/100 g) is similar to 1.75% reported for *Ficus sycomorus* seed (22). The tannin content (4.37 ± 0.06 g/100 g) is close to 4.03% found in *Ficus sycomorus* seed (22). The alkaloid content (0.62 ± 0.01 g/100 g) is lower than 5.65% reported for *Ficus sycomorus* seed (22). The Flavonoid content (6.13 ± 0.02 g/100 g) is higher than 3.63% reported for *Ficus sycomorus* seed (22). Flavonoids have health-promoting properties which include the prevention of allergies and ulcers and their antioxidant effects (40). Their powerful antioxidant property is the reason for the recent interest in flavonoids as health-promoting compounds. The total phenolics content (8.77 ± 0.01 g/100 g) is high. Phenolics have antioxidant properties and have been found to prevent the formation of oxidized low-density lipoprotein by inhibiting the autoxidation of unsaturated fats which causes cardiovascular disease (41). The phytate content (0.97 ± 0.05 mg/100 g) is lower than 1.98% reported for *Ficus sycomorus* seed (22). Phytates have been known to possess anticancer and antioxidant properties beside their ability to chelate divalent minerals which results in precipitation of such minerals, making them unavailable for absorption in the intestines (42). Oxalate content (0.13 ± 0.01 mg/100 g) is lower than 2.85% found in *Ficus sycomorus* seed (22). The cyanide content (0.04 ± 0.01 mg/100 g) is below the recommended limit of 10 mg HCN Eq/Kg (43) thus making it safe for consumption.

CONCLUSION

The search, identification, and study of new plant resources is a vital and unending endeavor with the alarming increase in human population and depletion of natural resources. The *Ficus thonningii* seed is a very good source of dietary nutrients. The high proportions of carbohydrate and protein give it a good nutritional value. The high ash content as proved by the incredible quantities of dietary minerals present make it a great minerals supplement and suitable component in feed formulation where high minerals source is required. The flavonoid and phenolic contents make the seed an excellent and natural antioxidant with health-promoting properties. The seed contains very little quantities of anti-nutrients. Plant materials are exploited for their nutritional, therapeutic and antimicrobial properties. *Ficus thonningii* is an underutilized plant whose seed have the potential for food, fodder, energy, and industrial uses.

REFERENCES

1. Salvi J, Katewa S. A review: underutilized wild edible plants as a potential source of alternative nutrition. Int J Bot Stud. 2016;1(4):32–6.

2. Ugoeze KC, Ehianeta, T, Alaribe, C, Anyakora, C. Analysis and identification of oils from seed extract of Anthonotha macrophylla using gas chromatography-mass spectrometry (GC-MS). Afr J Biotechnol. 2014 May 28;13(22):2260–4. <DOI>.

3. Ikhuoria EU, Aiwonegbe AE, Okoli P, Idu M. Characteristics and Composition of African Oil Bean Seed (Pentaclethra macrophylla Benth). J of Applied Sciences. 2008 Mar 15;8(7):1337–9. <DOI>.

4. Feyssa DH, Njoka JT, Asfaw Z, Nyangito MM. Wild Edible Fruits of Importance for Human Nutrition in Semiarid Parts of East Shewa Zone, Ethiopia: Associated Indigenous Knowledge and Implications to Food Security. Pakistan J of Nutrition. 2010 Dec 15;10(1):40–50. <DOI>.

5. Ajayi IA. Physicochemical attributes of oils from seeds of different plants in Nigeria. Bull Chem Soc Eth. 2010 Mar 17;24(1):145–9. <DOI>.

6. Seidu KT, Osundahunsi O, Olaleye M, Oluwalana I. Chemical composition, phytochemical constituents and antioxidant potentials of lima bean seeds coat. Annals of Food Science and Technology. 2014;15(2):288–98.

7. Tegegne D. Importance of Ficus thonningii Blume in Soil Fertility Improvement and Animal Nutrition in Gondar Zuria, Ethiopia [Internet] [Master of Science Thesis]. [Vienna, Austria]: University of Natural Resources and Applied Life Science; 2008. Available from: <URL>.

8. Orwa C, Mutua A, Kindt R, Jamnadass R, Anthony S. Agroforestree Database: a tree reference and selection guide [Internet]. Agroforestree Database. 2009. Available from: <URL>.

9. Balehegn M, Hintsa K. Effect of maturity on chemical composition of edible parts of Ficus thonningii Blume (Moraceae): an indigenous multipurpose fodder tree in Ethiopia. Livestock Research for Rural Development. 2015;27(12):1–8.

10. Jokthan GE, Afikwu EV, Olugbemi TS. The Utilization of Fig (Ficus thonningii) and Mango (Mangifera indica) Leaves by Rabbits. Pakistan J of Nutrition. 2003 Jun 15;2(4):264–6. <DOI>.

11. Adungbe Bamikole M, Julius Ikhatua U. Nutritional evaluation of Ficus thonningii-Panicum maximum mixtures in West African dwarf goats. Nutrition & Food Science. 2010 May 25;40(3):280–8. <DOI>.

12. Ogunwande IA, Sonibare MA, Thang TD, Dung NX, Soladoye MO, Morohunfolu OO. Comparative Analysis of the Oils of Three Ficus Species from Nigeria. Journal of Essential Oil Research. 2008 Sep;20(5):386–9. <DOI>.

13. Tegbe TSB, Adeyinka IA, Baye KD, Alawa JP. Evaluation of Feeding Graded Levels of Dried and Milled Ficus thonningii Leaves on Growth Performance, Carcass Characteristics and Organs of Weaner Rabbits. Pakistan J of Nutrition. 2006 Oct 15;5(6):548–50. <DOI>.

14. Olisakwe H, Ikpambese K, Ipilakyaa T, Ekengwu I. The Inhibitive Effect of Ficus Thonningii Leaves Extract in 1m HCL Solution as Corrosion Inhibitors on Mild Steel. Int J Innov Sci Res Tech. 2022;7(1):769–76.

15. Nawaz H, Waheed R, Nawaz M. Phytochemical Composition, Antioxidant Potential, and Medicinal Significance of Ficus. In: Kahramanoglu I, Ebru Kafkas N, Küden A, Çömlekçioğlu S, editors. Modern Fruit Industry [Internet]. IntechOpen; 2020 [cited 2022 May 12]. ISBN: 978-1-78984-730.

16. Ndukwe, I G, Bello, A I, Habila, J D, et al. Phytochemical and antimicrobial screening of the crude petroleum spirit and methanol extracts of the stem bark, leaves and roots of Ficus thoningii (blume). Afr J Biotechnol. 2007 Dec 31;6(23):2645–9. <DOI>.

17. Oyelere SF, Tunwagun DA, Bamikunle MV, Ayoade TE, Adebayo TA, Oluwatola BS, et al. Phytochemical analysis of Ficus thonningii: A qualitative study. JMHE. 2021 Jul 17;47–51. <DOI>.

18. Adane H, Atnafie SA, Kifle ZD, Ambikar D. Evaluation of In Vivo Antiulcer Activity of Hydro-Methanol Extract and Solvent Fractions of the Stem Bark of Ficus thonningii (Moraceae) on Rodent Models. Hernandez LR, editor. BioMed Research International. 2021 Apr 9;2021:1–10. <DOI>.

19. Ijarotimi OS, Adeoti OA, Ariyo O. Comparative study on nutrient composition, phytochemical, and functional characteristics of raw, germinated, and fermented Moringa oleifera seed flour. Food Sci Nutr. 2013 Nov;1(6):452–63. <DOI>.

20. Oluwaniyi O, Odebunmi E, Owolabi C. Qualitative and quantitative evaluation of the phytochemicals of Raphia hookeri and Raphia farinifera fruits. Science Focus. 2014;19(1):28–33.

21. Oluwaniyi O, Bazambo I. Anti-nutritional and phytochemical evaluation of raw and fermented African locust bean (Parkia biglobosa) seeds. Glo Jnl Pure Appl Sci. 2014 Dec 8;20(2):105–9. <DOI>.

22. Okoronkwo C, Ogwo P, Udensi E, Agu R. Nutritional and phytochemical composition of utu (Icacina senegalensis) and sycamore (Ficus sycomorus). seeds. Journal of Environmental Science, Toxicology and Food Technology. 2014;8(7):49–53.

23. Okoye C, Ibeto C, Ihedioha J. Preliminary studies on the characterization of orange seed and pawpaw seed oils. American Journal of Food Technology. 2011;6(5):422–6.

24. Abd El-Aziz A, Abd El-Kalek H. Antimicrobial proteins and oil seeds from pumpkin (Cucurbita moschata). Nature and Science. 2011;9(3):105–19.

25. Ojieh G, Ogunlowo Y. Compositional Studies of Citrullus lanatus (watermelon) seeds. The internet journal of Nutrition and wellness. 2008;6:25–31. <URL>.

26. Mirjana M, Ksenija P. Characteristics and Composition of Melon Seed Oil. Journal of Agricultural Sciences. 2005;50:41–7.

27. Bhargava A, Kumbhare V, Srivastava A, Sahai A. Bamboo parts and seeds for additional source of nutrition. Journal of Food Science and Technology. 1996;33(2):145–6.

28. Siddhuraju P, Vijayakumari K, Janardhanan K. Chemical Composition and Protein Quality of the Little-Known Legume, Velvet Bean (Mucuna pruriens (L.) DC.). J Agric Food Chem. 1996 Jan 1;44(9):2636–41. <DOI>.

29. Mune Mune MA, Rene Minka S, Lape Mbome I, Etoa FX. Nutritional Potential of Bambara Bean Protein Concentrate. Pakistan J of Nutrition. 2011 Jan 15;10(2):112–9. <DOI>.

30. Adetuyi F, Osagie A. Nutrient, antinutrient, mineral and zinc bioavailability of okra Abelmoschus esculentus (L) Moench Variety. AJFN. 2011 Apr;1(2):49–54. <DOI>.

31. Butt MS, Batool R. Nutritional and Functional Properties of Some Promising Legumes Protein Isolates. Pakistan J of Nutrition. 2010 Mar 15;9(4):373–9. <DOI>.

32. Niemann D, Butterworth D, Niemann C. Nutrition-Winc. Brown Publication Dubuque USA. 1992;237–312.

33. Akajiaku L, Nwosu J, Onuegbu N, Njoku N, Egbeneke C. Proximate, Mineral and An ti-nutrient Composition of Processed (Soaked and Roasted) Tamarind (Tamarindus indica) Seed nut. Curr Res Nutr Food Sci. 2014 Dec 31;2(3):136–45. <DOI>.

34. Laires MJ. Role of cellular magnesium in health and human disease. Front Biosci. 2004;9(1–3):262. <DOI>.

35. Lukaski HC, Johnson PE, Bolonchuk WW, Lykken GI. Assessment of fat-free mass using bioelectrical impedance measurements of the human body. The American Journal of Clinical Nutrition. 1985 Apr 1;41(4):810–7. <DOI>.

36. Nimni ME, Han B, Cordoba F. Are we getting enough sulfur in our diet? Nutr Metab (Lond). 2007;4(1):24. <DOI>.

37. Aremu M, Awala E, Opaluwa O, Odoh R, Bamidele T. Effect of Processing on Nutritional Composition of African Locust Bean (Parkia biglobosa) and Mesquite Bean (Prosopis africana) Seeds. Commun Appl Sci. 2015;3(1):22–41. <URL>.

38. Khursid SJ, Qureshi IH. The role of inorganic elements in the human body. Nucleus. 1984;21(4):3–23.

39. Kim D, Bae E, Han M, Choo M, Park E, Park J. Novel use of the extract of processed panax genus plant and saponin compound isolated there from. US Patent Application.2003/0190377 A1. Available from: <URL>.

40. Hooper L, Kroon PA, Rimm EB, Cohn JS, Harvey I, Le Cornu KA, et al. Flavonoids, flavonoid-rich foods, and cardiovascular risk: a meta-analysis of randomized controlled trials. The American Journal of Clinical Nutrition. 2008 Jul 1;88(1):38–50. <DOI>.

41. Amić D, Davidović-Amić D, Bešlo D, Trinajstić N. Structure-Radical Scavenging Activity Relationships of Flavonoids. Croatica Chemica Acta. 2003;76(1):55-61.

42. Oboh G, Akindahunsi AA, Oshodi AA. Dynamics of phytate-zinc balance of fungi fermented cassava products (gari and flour). Plant Foods Hum Nutr. 2003;58(3):1–7. <DOI>.

43. FAO/WHO. Codex standard for Edible cassava flour-African Regional standard. West Africa [Internet]. FAO/WHO Food Standards Programme. 2017. Available from: <URL>.

Comparison of Polyacrylonitrile-and Polypyrrole-based Electrochemical Sensors for Detection of Propamocarb in Food Samples

Selcan Karakuş[1]* (iD)**, Cihat Taşaltın[2]** (iD)**, İlke Gürol[2]** (iD)**, Barbaros Akkurt[3]** (iD)**,
Gülsen Baytemir[4]** (iD)**, Nevin Taşaltın[4,5]*** (iD)

[1]Istanbul University-Cerrahpasa, Department of Chemistry, Istanbul, Turkey.
[2]TUBITAK Marmara Research Center, Institute of Materials, Gebze, Kocaeli, Turkey.
[3]Istanbul Technical University, Department of Chemistry, 34469 Istanbul, Turkey
[4]Maltepe University, Department of Electrical & Electronics Engineering, Istanbul, Turkey.
[5]Maltepe University, Department of Basic Sciences, Istanbul, Turkey.

Abstract: Food safety is a crucial issue; all countries have struggled against pesticides for years. In this study, Polypyrrole (PPy)- and Polyacrylonitrile (PAN)-based non-enzymatic electrochemical sensors were investigated to detect the pesticide propamocarb (PM) in food samples. Under the experimental conditions, the proposed strategy exhibited a high selectivity of the disposable PPy-based and PAN-based sensors for the determination of propamocarb pesticide in the concentration of 1 µM with a rapid detection within 1 min at pH 7.4 and 25 °C. We demonstrated the detection of PM residues on cucumber and tomato samples with good electrochemical performances towards the real-time usability on real food samples. PAN-based non-enzymatic electrochemical sensor has good sensitivity, higher selectivity, and stability than PPy-based non-enzymatic electrochemical sensor. The prepared PAN-based non-enzymatic electrochemical sensor is a potential candidate to be used in devices which perform food safety in agricultural products.

INTRODUCTION

Food safety is one of the significant issues for human beings and environment due to constant population growth and industrial development (1,2). The use of pesticides and fungicides have toxic effects, which are extensively common to kill or control insects, mollusks, weeds, fungi, and bacteria in agriculture (3,4). Due to the use of these chemicals at global scale, their residues become a vital issue to protect the natural environment (5). From this perspective, rapid, sensitive, and portable detection of these

chemicals in food products, soil and water in low concentrations has gained momentum in research (6–8).

Sensitive, portable, and low-cost biosensors have started to be preferred with nanotechnological approach instead of expensive and not-easy-to-apply methods such as gas chromatography (GC), mass spectrometry (MS), and high-performance liquid chromatography (HPLC) (9,10). In previous studies, ultra-highly sensitive nanostructure-based biosensors with different shapes, structures, and sizes were produced and their effectiveness in

sensor applications was investigated for environmental pollutants (11,12). In this regard, the performances of these sensors have been developed using different structures such as Ag_2O-ZnO composite nanocone (13), Pr_2O_3-ZnO nanocomposites (14), V_2O_5-doped ZnO nanocomposites (15), CuO nanocomposites (11), TiO_2 nanoparticles/ molybdenum disulfide (MoS_2) nanosheets (16), iron oxide (Fe_3O_4) nanoparticles (17), reduced graphene oxide nanosheets - gold nanoparticles (18), reduced graphene oxide-wrapped silver nanoparticles (19), and polypyrrole (PPy) nanotubes (20). However, there are numerous studies in literature that reported novel non-enzymatic electrochemical biosensors to give some information in development of the sensitive pesticide sensors. For instance, Zhai et al. developed a highly selective and recyclable sensor for the electroanalysis of phosphothioate pesticides using silver - doped arrays of ZnO nanorods (21). Cesana et al. reported the synthesis and application as electrochemical sensor of the pesticide fenitrothion with fluorescent Cdots(N)-Silica composites (22). Chen et al. investigated the fluorometric determination of pesticide ferbam using the organic-inorganic manganese(II) halide hybrids-based paper sensor (23). Dissanayake et al. developed a highly sensitive plasmonic metal nanoparticle-based sensors for the detection of organophosphorus pesticides (24). Recently, PPy and PANI are commonly used as the preferred conductive polymers due to their unique electrical, electrochemical, and optical properties in diagnostics, food, and environmental applications (25–31). PPy, which is known to be a conductive organic polymer, has superior properties such as the mobility of charge carriers and fast electron transfer rate, can be used in electronics, optical, biological, and biomedical applications (32,33). Also, polyaniline (PANI) is another kind of conductive polymer which is prepared using the electrochemical oxidation of aniline in acidic medium (34). To the best of our knowledge, polyacrylonitrile (PAN) and PPy-based non-enzymatic electrochemical sensors have not been reported for the ultra-sensitive detection of the pesticide propamocarb in food samples. Furthermore, a clear proof of the existence of conductive polymers and their non-enzymatic-sensing mechanism for propamocarb pesticide needs to be experimentally clarified in food samples. Therefore, the highlight of this study was to use the electrochemical activities of PPy and PAN towards PM detection in tomato and cucumber samples. The goal of this study was to demonstrate a sensing platform based on non-enzymatic electrochemical polymers for low-cost, selective, and rapid detection of PM in real samples.

MATERIALS AND METHODS

Materials
Turkish tomatoes (Solanum lycopersicum) and cucumbers (Cucumis sativus L.) were purchased from a local supermarket (İstanbul, Turkey). All samples were harvested from Antalya (Turkey) on July and were stored at 15 °C until use. PPy (average Mw ~12,000 g/mol) and PAN (average Mw~150,000 g/mol) were purchased from Sigma Aldrich Company (Germany). N-N-Dimetylformamide (DMF) (purity (GC), ≥ 99.8 %) and ethanol (purity (GC), ≥ 99.9 %) were purchased from Merck Company (Germany). Propamocarb (PESTANAL®, analytical standard, formula:$C_9H_{20}N_2O_2$, molecular weight: 188.27 g/mol), a carbamate pesticide, was obtained from Sigma Aldrich Company (Germany). Electrochemical transducers were purchased from Ebtro Electronics. All chemicals and reagents were used without further purification.

Fabrication of PPy and PAN-based electrodes
2 mg of PPy powder was dissolved in 5 mL of ethanol, 2 mg of PAN powder was dissolved in 5 mL of DMF for 30 min via high stirring at 25 °C. The gold (Au) electrochemical transducers were rinsed with ethanol, distilled water, and dried with nitrogen. The electrochemical transducers were coated with PPy solution and PAN solution by drop casting, and then the sensing films were dried at 40 °C. All electrochemical sensor measurements were performed using Ebtro Electronics voltammetric electrochemical workstation. 1 μM of PM analyte was prepared. All sensor measurements were carried out at room temperature.

RESULTS AND DISCUSSION

There is a growing concern about extremely hazardous chemical pesticides and their influence on human health and the environment (35–37). For this purpose, in this study, it was aimed to selectively detect different pesticides such as malathion, deltamethrin, cypermethrin, and propamocarb (PM) by comparing them with different PPy and PAN-based sensors in food samples (tomato and cucumber). Measurements of PPy- and PAN-based non-enzymatic electrochemical sensors were performed at [−1, +1] V with a scanning rate of 50 mV/s. Comparative current density-voltage graphs of PPy and PAN-based non-enzymatic electrochemical sensors against pesticides were presented (see Figure 1). Figure 1 showed the non-enzymatic electrochemical responses of the PPy- and PAN-based non-enzymatic electrochemical sensors for the presence of 1μM pesticides (malathion, deltamethrin, cypermethrin, and PM) at a scanning rate of 50 mV/s.

The peaks seen in Figure 1a-b are attributed to redox reactions resulting from interactions between the polymers and PM. According to experimental results, the PPy and PAN-based non-enzymatic electrochemical sensors did not show a noticeable response in the presence of malathion, deltamethrin, and cypermethrin; however, the prepared sensors were only selective against PM. The results were statistically significant when compared with the experimental results. Both PPy- and PAN-based non-enzymatic electrochemical sensors have high selectivity against 1 μM PM within 1-minute cyclic voltammetry measurement. Additionally, the experimental results were confirmed by the selective pesticide detection-based assessment of the vegetable, and therefore proving the sensor's application potential for the rapid detection for the vegetable quality.
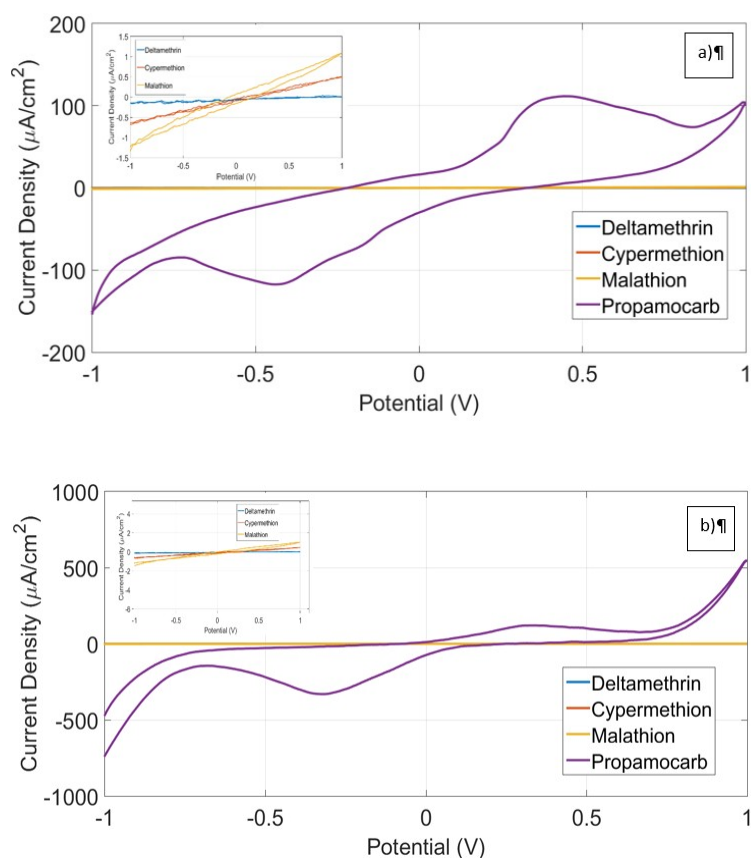
Figure 1: **(a)** Current density-voltage graphs of PPy-based non-enzymatic electrochemical sensor, and **(b)** Current density-voltage graphs of PAN-based non-enzymatic electrochemical sensor against pesticides.

PPy and PAN polymer--based PM sensors have not been previously reported in the literature. This is the first report presenting the preparation and PM tests of PPy and PAN-based non-enzymatic electrochemical sensors. The sensors are facile, selective, low-cost, and repeatable for agricultural usage. For food safety in agriculture this study highlighted the application of the sensor in detection of the pesticide PM on real cucumber and tomato samples. Current density-voltage graphs of repeated 2 tests of PPy- and PAN-based non-enzymatic electrochemical sensors against 1 μM PM applied real cucumber and tomato samples are presented (see Figure 2).

Various studies in literature have proven that biosensors had an excellent electrochemical performance against pesticides. We compared these experimental results with previous studies reported based on non-enzymatic/ enzymatic electrochemical sensors for pesticide determination in Table 1. The experimental results showed that the fabricated PAN-based electrodes had unique electrochemical properties and these results were appreciable from the comparison with the results of previous reports in the literature (Table 1). The proposed PAN-based sensor showed good sensitivity for rapid detection of PM. Moreover, the proposed sensor has different advantages such as easy to prepare, disposable, and portable.
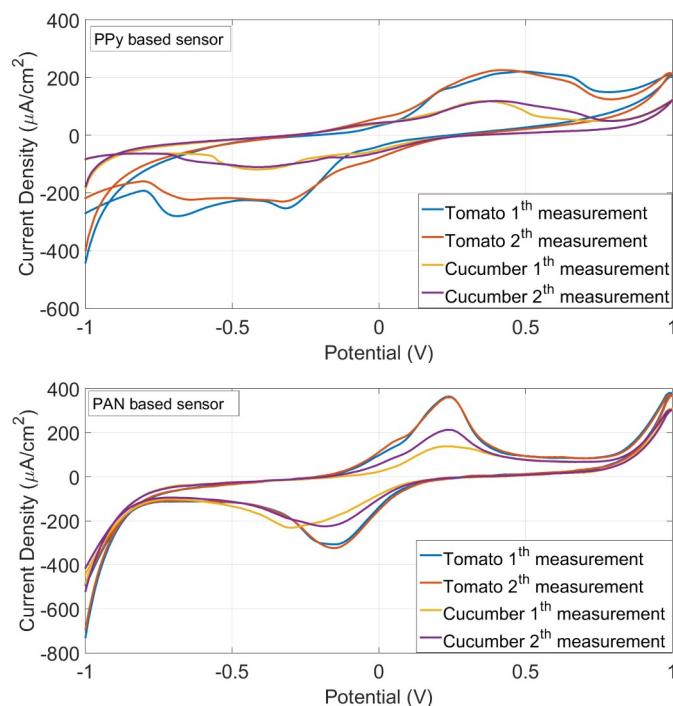
Figure 2: **(Top)** Current density-voltage graphs of PPy-based non-enzymatic electrochemical sensor, and **(bottom)** PAN-based non-enzymatic electrochemical sensor against 1 μM PM applied cucumber and tomato.
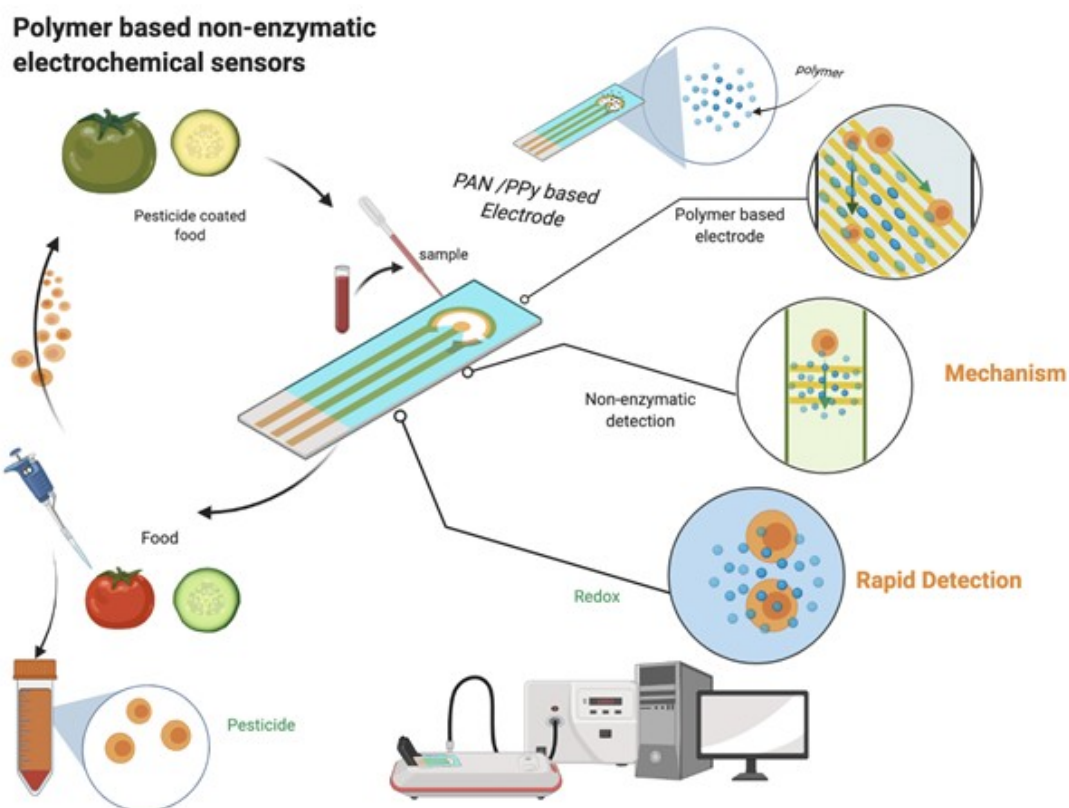

Figure 3: The schematic diagram of polymer-based non-enzymatic electrochemical sensors for the detection of pesticides from foods.

Karakuş S et al. JOTCSA. 2022; 9(3): 801-808.

RESEARCH ARTICLE

In Figure 3, the schematic diagram of polymer-based non-enzymatic electrochemical sensors for the detection of pesticides from foods was presented.

Table 1: The comparison of electrochemical experimental results of various biosensors for the detection of pesticide.

Sample	Analyte	Platform	References
Tyrosinase/poly(2-hydroxybenzamide)-modified graphite electrode	Fenitrothion	Enzymatic, electrochemical	(38)
PPy nanocomposite	Carbaryl Pesticide	Enzymatic, electrochemical	(39)
Boron dipyrromethene-phthalocyanine-single walled carbon nanotube hybrid	Methyl Parathion, Deltamethrin, Chlorpyrifos and Spinosad	Non-enzymatic, electrochemical	(40)
CuO microspheres	Endosulfan	Non-enzymatic, electrochemical	(41)
Reduced graphene oxide decorated on Cu/CuO-Ag nanocomposite	Carbaryl And Fenamiphos Pesticides	Non-enzymatic, electrochemical	(42)
Boronic acid functionalized nanocomposites	Glycoside Toxins	Non-enzymatic, electrochemical	(43)
Nickel oxide modified screen-printed electrodes	Parathion Pesticide	Non-enzymatic, electrochemical	(44)
Cu nanoparticles	Phorate	Non-enzymatic, electrochemical	(45)
PPy and PAN-based electrodes	Malathion, Deltamethrin, Cypermethrin, And Propamocarb	Non-enzymatic, electrochemical	This study

PPy- and PAN-based non-enzymatic electrochemical sensors detected 1 µM PM residue on real cucumber and tomato samples. Figure 2a-b shows the result of the sensor tests, the sensors detected 1 µM PM residue on food (cucumber and tomato) samples within a 1-minute cycle. PAN-based non-enzymatic electrochemical sensor has higher stability. PAN-based non-enzymatic electrochemical sensor has a significant potential in the field of the PM pesticide detection. According to the experimental results, we can provide the basis study for the selective and efficient processing of the polymer--based sensor with excellent electrochemical performances with food analytical methods for the monitoring of food safety and quality. Future studies will focus on integrating advanced sensor applications using the latest analytical methods to design and optimize the conductive polymer--based sensors for the monitoring of pesticide residues in food samples.

CONCLUSION

In this study, PPy and PAN-based non-enzymatic electrochemical sensors were investigated to detect the pesticide propamocarb (PM) in food samples. The PPy-based sensor and PAN-based sensor detected 1 µM propamocarb pesticide on cucumber and tomato with high selectivity within 1 min. We demonstrated the detection of PM residues on cucumber and tomato samples with good electrochemical performances towards the real-time usability on real agricultural samples. PAN-based non-enzymatic electrochemical sensor has good sensitivity, and higher selectivity and stability than PPy-based non-enzymatic electrochemical sensor. The prepared PAN-based non-enzymatic electrochemical PM sensor may be used in a portable detector kit for detection of PM type pesticide in food samples.

CONFLICT OF INTEREST

All authors declare that they have no conflict of interest.

REFERENCES

1. Popp J, Pető K, Nagy J. Pesticide productivity and food security. A review. Agron Sustain Dev. 2013 Jan;33(1):243–55. <DOI>.

2. Rastogi S, Kumari V, Sharma V, Ahmad FJ. Gold Nanoparticle-based Sensors in Food Safety Applications. Food Anal Methods. 2022 Feb;15(2):468–84. <DOI>.

3. Tang FHM, Lenzen M, McBratney A, Maggi F. Risk of pesticide pollution at the global scale. Nat Geosci. 2021 Apr;14(4):206–10. <DOI>.

4. Wei X, Anfeng Z, Ali T, Zhang Z, Davis KF, Wu F. China's Food Security and Water, Fertilizer, Pesticide, and GHG Saving through Crop Redistribution [Internet]. Department of Agricultural Economics, Purdue University, West Lafayette, IN: Global Trade Analysis Project (GTAP); 2020. Available from: <URL>.

5. Sharma A, Shukla A, Attri K, Kumar M, Kumar P, Suttee A, et al. Global trends in pesticides: A looming threat and viable alternatives. Ecotoxicology and Environmental Safety. 2020 Sep;201:110812. <DOI>.

6. Dong J, Yang H, Li Y, Liu A, Wei W, Liu S. Fluorescence sensor for organophosphorus pesticide detection based on the alkaline phosphatase-triggered reaction. Analytica Chimica Acta. 2020 Sep;1131:102–8. <DOI>.

7. Fan L, Wang F, Zhao D, Peng Y, Deng Y, Luo Y, et al. A self-penetrating and chemically stable zinc (ii)-organic framework as multi-responsive chemo-sensor to detect pesticide and antibiotics in water. Appl Organomet Chem [Internet]. 2020 Dec [cited 2022 May 21];34(12). <DOI>.

8. Rasheed Z, Vikraman AE, Thomas D, Jagan JS, Kumar KG. Carbon-Nanotube-Based Sensor for the Determination of Butylated Hydroxyanisole in Food Samples. Food Anal Methods. 2015 Jan;8(1):213–21. <DOI>.

9. Lu Y, Tan Y, Xiao Y, Li Z, Sheng E, Dai Z. A silver@gold nanoparticle tetrahedron biosensor for multiple pesticides detection based on surface-enhanced Raman scattering. Talanta. 2021 Nov;234:122585. <DOI>.

10. Ge X, Zhou P, Zhang Q, Xia Z, Chen S, Gao P, et al. Palladium Single Atoms on TiO2 as a Photocatalytic Sensing Platform for Analyzing the Organophosphorus Pesticide Chlorpyrifos. Angew Chem. 2020 Jan 2;132(1):238–42. <DOI>.

11. Liu X, Sakthivel R, Liu WC, Huang CW, Li J, Xu C, et al. Ultra-highly sensitive organophosphorus biosensor based on chitosan/tin disulfide and British housefly acetylcholinesterase. Food Chemistry. 2020 Sep;324:126889. <DOI>.

12. Cheng Y, Ma B, Tan CP, Lai OM, Panpipat W, Cheong LZ, et al. Hierarchical macro-microporous ZIF-8 nanostructures as efficient nano-lipase carriers for rapid and direct electrochemical detection of nitrogenous diphenyl ether pesticides. Sensors and Actuators B: Chemical. 2020 Oct;321:128477. <DOI>.

13. Chakraborty U, Bhanjana G, Kannu, Kaur N, Sharma R, Kaur G, et al. Microwave-assisted assembly of Ag2O-ZnO composite nanocones for electrochemical detection of 4-Nitrophenol and assessment of their photocatalytic activity towards degradation of 4-Nitrophenol and Methylene blue dye. Journal of Hazardous Materials. 2021 Aug;416:125771. <DOI>.

14. AlAbdulaal TH, AlShadidi M, Hussien MSA, Vanga G, Bouzidi A, Rafique S, et al. Enhancing the electrical, optical, and structure morphology using Pr2O3-ZnO nanocomposites: Towards electronic varistors and environmental photocatalytic activity. Journal of Photochemistry and Photobiology A: Chemistry. 2021 Sep;418:113399. <DOI>.

15. Alam MM, Asiri AM, Rahman MM. Fabrication of phenylhydrazine sensor with V2O5 doped ZnO nanocomposites. Materials Chemistry and Physics. 2020 Mar;243:122658. <DOI>.

16. Singh AP, Balayan S, Gupta S, Jain U, Sarin RK, Chauhan N. Detection of pesticide residues utilizing enzyme-electrode interface via nano-patterning of TiO2 nanoparticles and molybdenum disulfide (MoS2) nanosheets. Process Biochemistry. 2021 Sep;108:185–93. <DOI>.

17. Wang L, Huang X, Wang C, Tian X, Chang X, Ren Y, et al. Applications of surface functionalized Fe3O4 NPs-based detection methods in food safety. Food Chemistry. 2021 Apr;342:128343. <DOI>.

18. Yan L, Yan X, Li H, Zhang X, Wang M, Fu S, et al. Reduced graphene oxide nanosheets and gold nanoparticles covalently linked to ferrocene-terminated dendrimer to construct electrochemical sensor with dual signal amplification strategy for ultra-sensitive detection of pesticide in vegetable. Microchemical Journal. 2020 Sep;157:105016. <DOI>.

19. Minh PN, Hoang VT, Dinh NX, Van Hoang O, Van Cuong N, Thi Bich Hop D, et al. Reduced graphene oxide-wrapped silver nanoparticles for applications in ultrasensitive colorimetric detection of Cr(vi) ions and the carbaryl pesticide. New J Chem. 2020;44(18):7611–20. <DOI>.

20. Ding S, Lyu Z, Li S, Ruan X, Fei M, Zhou Y, et al. Molecularly imprinted polypyrrole nanotubes based electrochemical sensor for glyphosate detection. Biosensors and Bioelectronics. 2021 Nov;191:113434. <DOI>.

21. Zhai X, Xu F, Li Y, Jun F, Li S, Zhang C, et al. A highly selective and recyclable sensor for the electroanalysis of phosphothioate pesticides using silver-doped ZnO nanorods arrays. Analytica Chimica Acta. 2021 Apr;1152:338285. <DOI>.

22. Cesana R, Ferreira JHA, Gonçalves JM, Gomes D, Nakamura M, Peres RM, et al. Fluorescent Cdots(N)-Silica composites: Direct synthesis and application as electrochemical sensor of fenitrothion pesticide. Materials Science and Engineering: B. 2021 May;267:115084. <DOI>.

23. Chen S, Gao J, Chang J, Zhang Y, Feng L. Organic-inorganic manganese (II) halide hybrids based paper sensor for the fluorometric determination of pesticide ferbam. Sensors and Actuators B: Chemical. 2019 Oct;297:126701. <DOI>.

24. Dissanayake NM, Arachchilage JS, Samuels TA, Obare SO. Highly sensitive plasmonic metal nanoparticle-based sensors for the detection of organophosphorus pesticides. Talanta. 2019 Aug;200:218–27. <DOI>.

Karakuş S et al. JOTCSA. 2022; 9(3): 801-808.

RESEARCH ARTICLE

25. Ragazzini I, Gualandi I, Selli S, Polizzi C, Cassani MC, Nanni D, et al. A simple and industrially scalable method for making a PANI-modified cellulose touch sensor. Carbohydrate Polymers. 2021 Feb;254:117304. <DOI>.

26. Lv D, Shen W, Chen W, Tan R, Xu L, Song W. PSS-PANI/PVDF composite based flexible NH3 sensors with sub-ppm detection at room temperature. Sensors and Actuators B: Chemical. 2021 Feb;328:129085. <DOI>.

27. Matindoust S, Farzi G, Nejad MB, Shahrokhabadi MH. Polymer-based gas sensors to detect meat spoilage: A review. Reactive and Functional Polymers. 2021 Aug;165:104962. <DOI>.

28. Kumar V, Mirzaei A, Bonyani M, Kim KH, Kim HW, Kim SS. Advances in electrospun nanofiber fabrication for polyaniline (PANI)-based chemoresistive sensors for gaseous ammonia. TrAC Trends in Analytical Chemistry. 2020 Aug;129:115938. <DOI>.

29. Oh WC, Fatema KN, Cho KY, Biswas MRUD. Microwave-assisted synthesis of conducting polymer matrix based thin film NaLa (MoO4)2-G-PPy composites for high-performance gas sensing. Surfaces and Interfaces. 2020 Dec;21:100713. <DOI>.

30. Hien HT, Van Tuan C, Anh Thu DT, Ngan PQ, Thai GH, Doanh SC, et al. Influence of surface morphology and doping of PPy film simultaneously polymerized by vapour phase oxidation on gas sensing. Synthetic Metals. 2019 Apr;250:35–41. <DOI>.

31. Dai H, Cao P, Chen D, Li Y, Wang N, Ma H, et al. Ni-Co-S/PPy core-shell nanohybrid on nickel foam as a non-enzymatic electrochemical glucose sensor. Synthetic Metals. 2018 Jan;235:97–102. <DOI>.

32. Ding A, Wang J, Ni A, Li S. Ageing of sandwich composites with E-glass fibre/vinylester skins and PVC foam core in synergistic environmental agents. Composite Structures. 2018 Oct;202:253–60. <DOI>.

33. Kannan A, Radhakrishnan S. Fabrication of an electrochemical sensor based on gold nanoparticles functionalized polypyrrole nanotubes for the highly sensitive detection of l-dopa. Materials Today Communications. 2020 Dec;25:101330. <DOI>.

34. Shen Y, Qin Z, Li T, Zeng F, Chen Y, Liu N. Boosting the supercapacitor performance of polyaniline nanofibers through sulfonic acid assisted oligomer assembly during seeding polymerization process. Electrochimica Acta. 2020 Oct;356:136841. <DOI>.

35. Delińska K, Yavir K, Kloskowski A. Ionic liquids in extraction techniques: Determination of pesticides in food and environmental samples. TrAC Trends in Analytical Chemistry. 2021 Oct;143:116396. <DOI>.

36. Kumar M, Yadav AN, Saxena R, Paul D, Tomar RS. Biodiversity of pesticides degrading microbial communities and their environmental impact. Biocatalysis and Agricultural Biotechnology. 2021 Jan;31:101883. <DOI>.

37. Zaynab M, Fatima M, Sharif Y, Sughra K, Sajid M, Khan KA, et al. Health and environmental effects of silent killers Organochlorine pesticides and polychlorinated biphenyl. Journal of King Saud University - Science. 2021 Sep;33(6):101511. <DOI>.

38. Alves M de F, Corrêa RAM de S, da Cruz FS, Franco DL, Ferreira LF. Electrochemical enzymatic fenitrothion sensor based on a tyrosinase/poly(2-hydroxybenzamide)-modified graphite electrode. Analytical Biochemistry. 2018 Jul;553:15–23. <DOI>.

39. Loguercio LF, Thesing A, Demingos P, de Albuquerque CDL, Rodrigues RSB, Brolo AG, et al. Efficient acetylcholinesterase immobilization for improved electrochemical performance in polypyrrole nanocomposite-based biosensors for carbaryl pesticide. Sensors and Actuators B: Chemical. 2021 Jul;339:129875. <DOI>.

40. Köksoy B, Akyüz D, Şenocak A, Durmuş M, Demirbas E. Sensitive, simple and fast voltammetric determination of pesticides in juice samples by novel BODIPY-phthalocyanine-SWCNT hybrid platform. Food and Chemical Toxicology. 2021 Jan;147:111886. <DOI>.

41. Rathnakumar SS, Noluthando K, Kulandaiswamy AJ, Rayappan JBB, Kasinathan K, Kennedy J, et al. Stalling behaviour of chloride ions: A non-enzymatic electrochemical detection of α-Endosulfan using CuO interface. Sensors and Actuators B: Chemical. 2019 Aug;293:100–6. <DOI>.

42. Hashemi P, Karimian N, Khoshsafar H, Arduini F, Mesri M, Afkhami A, et al. Reduced graphene oxide decorated on Cu/CuO-Ag nanocomposite as a high-performance material for the construction of a non-enzymatic sensor: Application to the determination of carbaryl and fenamiphos pesticides. Materials Science and Engineering: C. 2019 Sep;102:764–72. <DOI>.

43. Shi Z, Lu Y, Chen Z, Cheng C, Xu J, Zhang Q, et al. Electrochemical non-enzymatic sensing of glycoside toxins by boronic acid functionalized nano-composites on screen-printed electrode. Sensors and Actuators B: Chemical. 2021 Feb;329:129197. <DOI>.

44. Khairy M, Ayoub HA, Banks CE. Non-enzymatic electrochemical platform for parathion pesticide sensing based on nanometer-sized nickel oxide modified screen-printed electrodes. Food Chemistry. 2018 Jul;255:104–11. <DOI>.

45. Fu J, An X, Yao Y, Guo Y, Sun X. Electrochemical aptasensor based on one step co-electrodeposition of aptamer and GO-CuNPs nanocomposite for organophosphorus pesticide detection. Sensors and Actuators B: Chemical. 2019 May;287:503–9. <DOI>.

RESEARCH ARTICLE

Poly(MMA-co-MI) Nanocomposite with Modified Nano ZRP with KH570 Linker: Preparation, Characterization and Transparency Properties

Fariborz Atabaki*[1] [iD], **Gholam Ali Koohmareh[2]** [iD] and **Samira Sarikhani[1]** [iD]

[1]Department of Chemistry, College of Science, Malek-ashtar University of Technology, Isfahan, Iran.
[2]Department of Chemistry, University of Isfahan, Isfahan, 81746-73441, Iran.

Abstract: In this study, zirconium phosphate was synthesized and modified with KH570 linker. It was then used to prepare several nanocomposites with different percent with poly (methyl methacrylate-co-N-2-methyl-4-nitro-phenylmaleimide) (Poly (MMA-co-MI)). The synthesized compounds were characterized by Fourier transform infrared spectroscopy (FTIR), X-ray diffraction (XRD), and field-emission scanning electron microscopy (FE-SEM). The particles size and structure determining showed nanoparticle are sheet and about 9-20 nm. Thermal stability of these compounds were evaluated by thermogravimetric analysis (TGA). The results showed adding nanoparticles to copolymer increased starting weight lost about 20 $^{\circ}$C and finishing weight lost about 90 $^{\circ}$C. The results of differential scanning calorimetry (DSC), showed that adding nanoparticles decreased the glass transition temperatures (T_g) of the copolymer. The transparency of these nanocomposites were examined by ultraviolet–visible (UV–Vis) spectroscopy. The results showed the best transparency refer to nanocomposites 0.5 to 1% of nanoparticles.

INTRODUCTION

The use of polymer nanocomposites has been recently paid much attention to applied and industrial researches. The polymeric matrices and nano fillers in nanocomposite structure have a special importance in determining their features and applications. Since the nanotechnology has been utilized to create materials with improving mechanical and physical properties, nanoparticles were added into the base of materials to form composite materials with unique physical and mechanical properties (1,2), such as the properties of polymers such as flexibility, optical clarity, and excellent dimensional stability of poly methyl methacrylate (PMMA), whereas inorganic materials show mechanical strength, thermal stability, and a high modulus (3-5).

PMMA is one of the common medical polymers employed widely in manufacturing various implants, especially in the fabrication of an ophthalmic intraocular lenses due to its mechanical properties, mould ability, and optical rehabilitation (6,7). Methyl methacrylate (MMA) has been used as a comonomer in several reports such as block copolymer with styrene (6,8,9), copolymerization with tricyclodecyl methacrylate (10), and copolymerization reaction with maleimide (11,12). In addition, the use of PMMA in the preparation of various nanocomposites with several additives such as SiO_2 (13), Clay (14), TiO_2 (15), ZrO_2 (16), MWCNT (17), and Al_2O_3 (18) has been reported.

The use of TiO_2 thin-films with high transmittance in the visible region as antibacterial coating could be effective for PMMA in ophthalmic applications (19,20). It was used with ZrO_2 nano particle for denture base applications, too (7,21).

Inorganic hybrid nanoparticles are highly attractive in both academic and industrial researches. They are able not only to combine the properties of both components, polymers and inorganic matter, but also provide unique and tuneable properties (22,23). One of the major issues in these materials is dispersing degree of particles into the polymer matrix and the interfacial property between the organic and inorganic components (24,25).

In order to enhance the stability of nanoparticles in the polymer matrix, surface modification of the nanoparticles is needed. It could be improved by introducing coupling agents or reactive functional groups onto the surface of nanoparticles (26).

Zirconium phosphate (ZrP) serves as nano filler in the polymeric interface, where their presence affects profoundly the chemical, mechanical, and thermal properties of the nanocomposite. It is acidic, inorganic cation exchange materials which usually presents a layered structure. There are various phases of ZrP that differ in their interlamellar spaces and their crystalline structure. Among all the ZrP phases, the most widely used are the α-phase and the γ-phase, whose crystal structures were elucidated by Clearfield and co-workers (27). Yamanaka and Hattori reported a mixed ɣ-zirconium phosphate (ɣ-ZrP) benzene phosphonate can be obtained by contacting ɣ-ZrP with benzene phosphoric acid. However, at that time ɣ-ZrP was formulated as $Zr(HPO_4)_2.2H_2O$ and its structure was believed erroneously to be similar to that of α-ZrP but with a different packing of the layers, so it was not possible to give a correct interpretation in order to experimental data (28). While layered ZrP micro-crystals might not be as ideal as porous materials, because of small hydroxyl accessibility, single-layer ZrP nano sheets from the exfoliation of its micro-crystals serve as an ideal candidate for post-grafting since after exfoliation, the hydroxyl groups are fully exposed and readily react with silane. The hydroxyl groups exist on both sides of nano sheets. After surface grafting, the obtained compounds are expected to possess a high density of functional groups, which are critical for high catalytic performance. Furthermore, the lateral dimension of ZrP nano sheets can be altered by tuning the synthetic conditions. Another major advantage of using ZrP nano sheets as the solid substrate is nano sheets can be uniformly dispersed in a wide range of polar solvents, leading to high catalytic efficiency, but meanwhile they can be easily separated from the dispersion system using centrifugation (29).

Modified silica nano particles -3-methacryloxypropyltrimethoxysilane- (KH-570 linker) can be attached to metallic surface by a condensation reaction resulting in a covalent bond and also cause a good interaction with PMMA to preparing nanocomposite (5). As N-2-methyl-4-nitro-phenylmaleimide (MI) was added in PMMA matrix to improve its thermal stability in previews work (30), in this research our goal is to modify nano ZrP with KH570 linker and make a nanocomposite based on this modified nanoparticles with poly(MMA-co-MI).

EXPERIMENTAL SECTION

Materials
Zirconium(IV) chloride (ZrCl$_4$, Aldrich), orthophosphoric acid (H$_3$PO$_4$, 85%, Aldrich), tetra-n-butylammonium

hydroxide (TBA, Aldrich), nitric acid (Aldrich), KH-570 linker (γ-methacryloyloxypropyl trimethoxy silane, Aldrich), methyl methacrylate (Merck). Benzoyl peroxide (BPO, Merck), 2-methyl-4-nitroaniline (Merck), maleic anhydride (MA, Merck), ethyl acetate, and methanol were distilled over potassium hydroxide under vacuum.

Preparation of N-2-methyl-4-nitro-phenylmaleimide
MI was prepared according to our previous research (30). First, maleic anhydride (4.9 g, 0.05 mol) was dissolved in 15 mL of acetone. Then, a solution of 2-methyl-4-nitroaniline (7.6 g, 0.05 mol) in 15 mL of acetone was added dropwise under vigorous stirring. After complete addition, the mixture is stirred for 1 h. The solid (maleamic acid) which precipitated was filtered off (11.1 g, 89%, mp: 169-171 °C). Maleamic acid (10.0 g, 0.04 mol) was then dissolved in 15 mL of acetic anhydride with added 0.3 g of sodium acetate. The mixture was heated for 6 h under reflux. A cream solid is recovered (8.64 g, 93%. mp: 251–253 °C).

Preparation of Nanoparticle
In order to modify ZrP with KH-570 linker, first ZrP was synthesized and exfoliated with TBA according to reported procedures. It was then modified with KH-570 linker (Scheme 1).

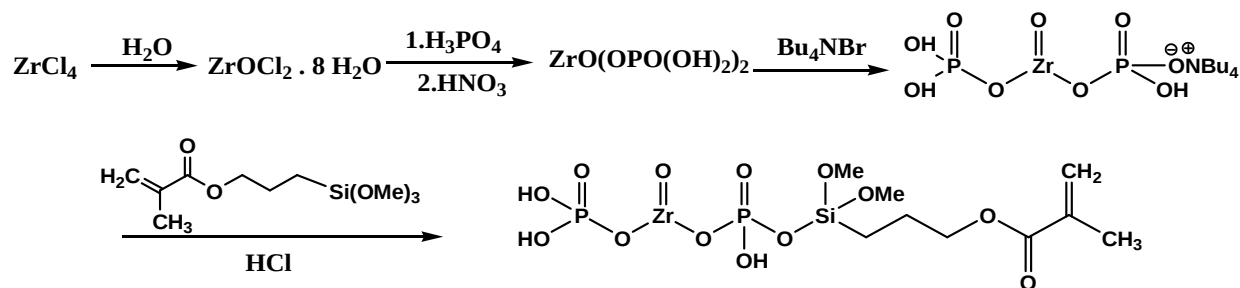*Preparation of zirconium phosphate (31,32)*
Zirconium tetrachloride (4.66 g, 20 mmol) was dissolved in water (25 mL) and heated 100 °C, to make a saturated 2 M zirconium solution. Upon cooling, Zirconium oxychloride crystals (5.51 g, yield: 85.3%, mp: 149-152 °C) were formed. Zirconium oxychloride (5 g) was mixed with 50 mL of 6.0 M orthophosphoric acid solution in demineralized water (DMW) at 25 °C for 1 h and at 80 °C for 24 h. The precipitate was collected, followed by washing with DMW, and drying for 24 h in oven at 80 °C. This product was then treated with 20 mL (0.1 M) nitric acid solution for complete replacement of counter ions with H$^+$ ions at 25 °C for 1 h and was washed with DMW (7.12 g, yield:71.4%)

Reaction of ZrP with TBA (29)
The prepared ZrP (2.2 g in 10 mL of water) was reacted and exfoliated with TBA (10 mL of 0.5 M aqueous solution) in an ice bath for 6 h and at 25 °C for 18 h. The precipitate was smoothed and dried at 25 °C (1.8 g, yield: 81.8%, decomposed at 311 °C)

Modification of exfoliated ZrP with KH-570 linker
A solution of KH-570 linker (1 mL in 10 ml HCl 0.1 M) was added to a solution of exfoliated ZrP (1 g, in 5 mL of water) and spired at 65 °C for 1 h. The precipitate was collected (0.94 g, yield: 95.9%, mp>293 °C, XRF data acquired from the analyzer is (P, 18.2; Zr, 21.4; other 57.7), other is for elements smaller than Na such as C, O, H, Si; and calculated elemental analysis for (ZrOPO(OH)OSi(OMe)$_2$(CH$_2$)$_3$OCOCCH$_3$CH$_2$)OPO(OH)$_2$) is (C, 20.89; H, 3.90; O, 40.19; P, 11.97; Si, 5.43; Zr, 17.63).
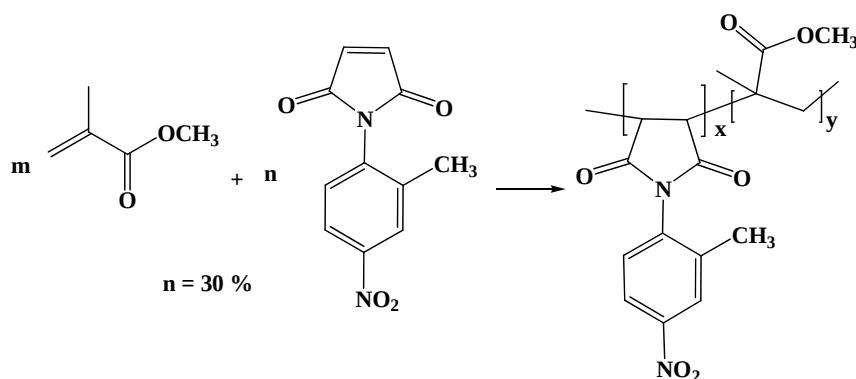
Scheme 1.

Synthesis of poly (MMA-co-MI)

In a 250 mL round bottomed flask, equipped with reflux condenser and nitrogen inlet tube, a solution of MMA (1.1 mL, 10 mmol), and MI (1 gr, 0.4 mmol) in ethyl acetate (6 mL) was prepared. BPO (0.02 g) was added and the reaction mixture was heated for 8h at 77 °C (reflux). The solution was then poured in methanol and the precipitate was washed with methanol and dried. (1.8 gr, yield: 85.7%, CHNS data acquired from the analyzer is (C, 58.49; H, 6.04; N, 5.58), and calculated elemental analysis for predicted copolymer is (C, 58.36; H, 5.91; N, 6.01; O, 29.73). Percentage of MI in copolymer is 27.8% (Scheme 2).

Scheme 2.

Preparation of Nanocomposite

A solution of synthesized copolymer (1 g) in ethyl acetate (10 mL) was prepared. A dispersion of modified nanoparticles (0.01 g) in ethyl acetate (5 mL) was sonicated for 20 min and was added to a prepared polymer solution and sonicated again for 20 min. The solution was then precipitated in methanol to afford 1% nanocomposite powder. Four other percentages were prepared according to the same procedure. In other reaction experiments, an in-situ nanocomposites were prepared by adding the appropriate nanoparticle amounts into monomers mixtures during polymerization reaction.

Characterization

FT-IR spectral data were recorded with a Bruker spectrometer in the range of 4000–400 cm^{-1} using KBr disks. SEM image of the electrospinning nanofibers was obtained through the scanning electron microscopy (SEM). The morphology of the pristine α-ZrP powder was also observed at an accelerating voltage of 5 kV. The chemical state of the surface was characterized by X-ray photoelectron spectroscopy Bruker model D8ADVANCE. TEM micrographs were obtained with an H-7500 transmission electron microscope (Philips 208 S 100 kW) at an accelerating voltage of 75 kV. Ultrathin sections were microtome at room temperature. Thermal stabilities were measured via thermogravimetric analysis in nitrogen with a TA Instruments model Q2000 at a heating rate of 20 °C min^{-1}. DSC was used to measure glass transition temperature using a TA Q2000 instrument in nitrogen atmosphere at the heating rate of 20 °C/min from 80 to 150 C and a cooling rate of 10 °C/min. The adsorption ability of Poly (MMA-co-MI)/nano (ZrP-KH570) was investigated by solution adsorption technique. For measuring transmittance in UV and visible area, 50 mg of nanocomposite was dissolved in 10 mL ethyl acetate, Ultraviolet-visible spectrophotometer model Photonix Ar 2015 was used. X-Ray Fluorescence analysis (XRF) was determined with XRF device model Niton from Thermo Company. Elemental analyses (CHNS) was determined by device model Vario EL Ш from Elementar Company.

RESULTS AND DISCUSSION

Characterization

Modified ZrP with KH-570 was prepared according to Scheme 1. FTIR spectra of these compounds are illustrated in Figure 1. For ZrP, the peaks locating at 3594, 3510 are due to the water molecules in the interlayer space of ZrP, 3164, and 1620 cm^{-1} are assigned as symmetric and bending vibrations of –

OH groups, respectively (29). The peaks at 3384, 1251 968 cm^{-1} are attributed to P–OH stretching vibrations or deformation vibrations. The strong bands in the range of 1000–1200 cm^{-1} are characteristic of PO$_4$ stretching vibrations and 597 cm^{-1} is ascribed to the vibration of Zr−O (33). After reaction of ZrP with TBA, no significant change was occurred and just the P-OH at 1200 cm^{-1} become broader, which was due to the presence of ammonium salt. After modification with KH-570 linker, a peak at 1745 cm^{-1} was appeared and confirmed presence of carbonyl group in the particles and 2957 cm^{-1} is ascribed to the asymmetric C–H stretching of SiOMe and The peaks at 980 cm^{-1} is attributed to C=C bending (34).
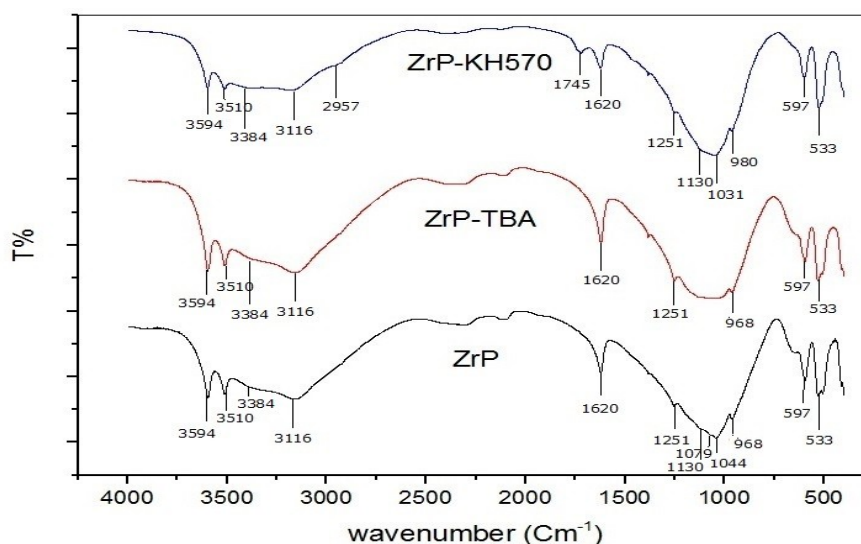

Figure 1: FTIR spectra of ZrP nano particles, ZrP modified by TBA and ZrP modified by KH-570 linker.

Solution polymerization of MMA with synthesized MI was led to poly (MMA-co-MI) due to Scheme 2. It was then sonicated with modified ZrP with KH-570 to prepare the related nanocomposites. Evaluation of the best technique for preparation of nanocomposite an in situ preparation during polymerization was also investigated. All of the polymers and composites were investigated using FTIR spectroscopy. (Figure 2).

The peaks of C=O (1727 cm^{-1}), CH3–O (1148, 1194 cm^{-1}), and C–O (1242, 1270 cm^{-1}) are consistent with those of PMMA as reported in the literature (35,36). And also the bands at 1782 cm^{-1} (C=O imide stretching), 1589 cm^{-1} (C=C aromatic stretching), 1530 and 1348 cm^{-1} (N=O stretching) show the maleimide units as mentioned in the literature and also peaks of nano particle that is discussed in Figure 1 (30,37,38).
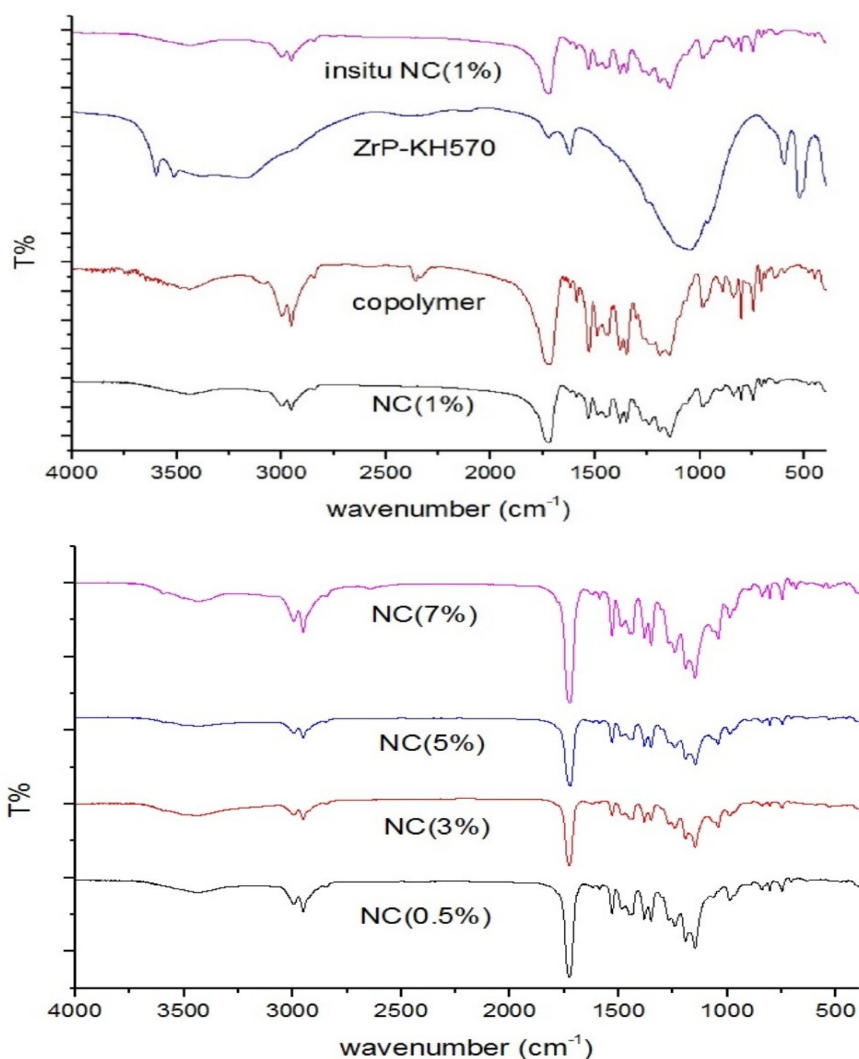
Figure 2: FTIR spectra of poly (MMA-co-MI)–ZrP nanocomposites, poly (MMA-co-MI).

XRD analysis: It is known that ZrP has a clay-like layered structure, which can be characterized using XRD, with interlayer separation calculated from the Bragg equation. Figure 3(a–d) presents the XRD results. Sharpening the peaks of Figure 3b confirms the preparation of ammonium salts of nanoparticles compared to the peaks of Figure 3a. As shown in Figure 3d nanocomposite have both nanoparticles and PMMA background peak (39). The diffractogram of ZrP sample shows peaks at 2θ values: 7, 14, 23, 29, 40, 44, and 56. Reacted ZrP with TBA's spectrum shows same peaks, with a large difference in peak wide at 2θ: 7. Modified ZrP by KH-570's spectrum shows all peaks above except 44. According to Scherrer equation ($D = (0.9 \lambda)/ (\beta \cos \theta)$) the size of

crystals of nano particles can be determined. D is the mean size of the ordered (crystalline) domains, which may be smaller or equal to the particle size. λ is the X-ray wavelength (1.789 A$^\circ$). β is the line broadening at half the maximum intensity (FWHM) in radian and θ is the Bragg angle. The results are summarized in Table 1 (40).

Table 1: Size of nano particles.

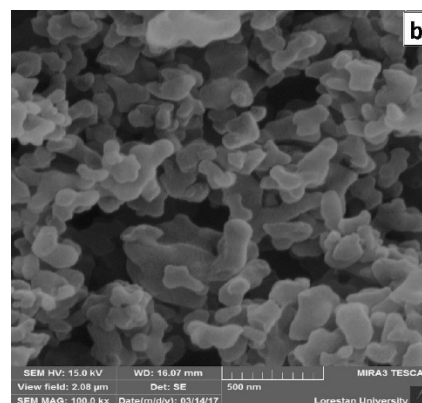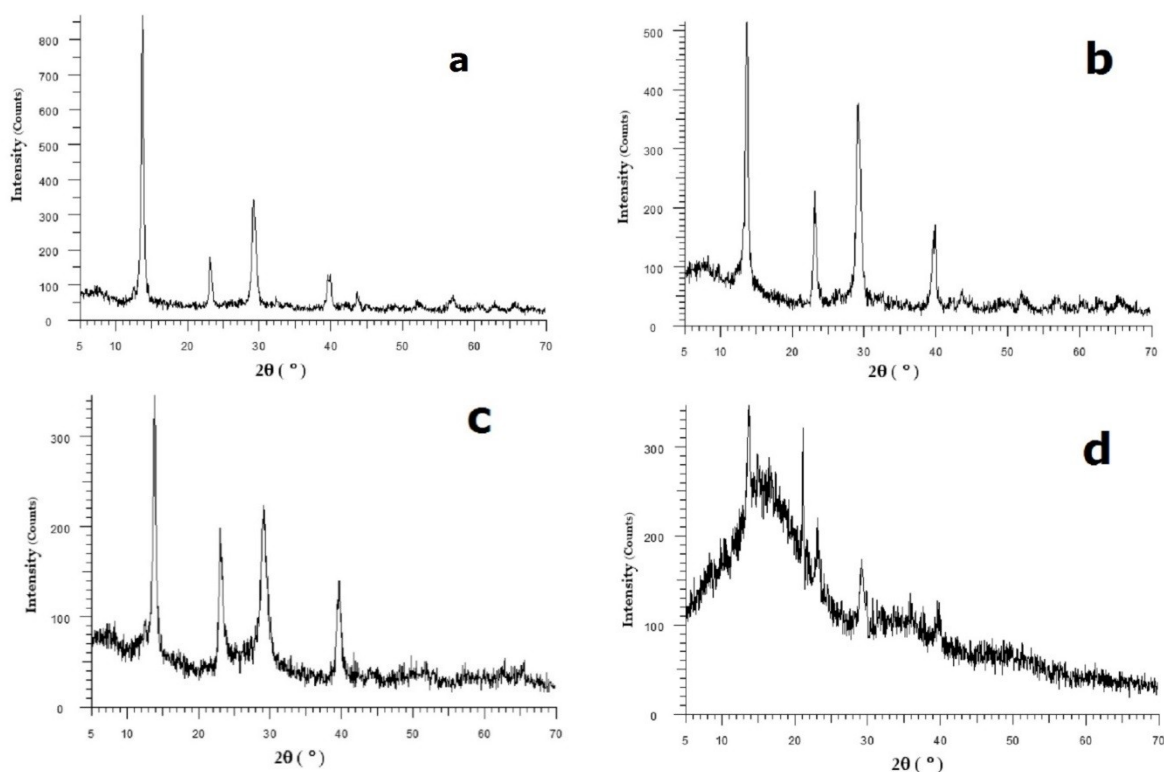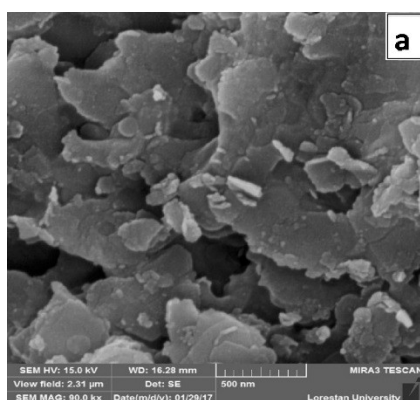| Nanoparticles	ZrP	ZrP-TBA	ZrP-KH
D(nm)	19.13	10.359	9.347
Used 2θ ($^\circ$)	14	14	14

Figure 3: XRD results: (a) ZrP, (b) ZrP modified by TBA, (c) ZrP modified by KH-570 linker, (d) MMA-co-MI/ZrP 1% nanocomposite.

SEM micrographs: Figure 4 shows SEM micrographs of the ZrP modified by KH-570 linker and nanocomposites. Figure 4a confirms modified ZrP crystals sheet structure clearly. Figure 4b-d shows the good dispersion of nanoparticle in polymer layers. Figure 4e shows the undesirable accumulation of nanoparticle in nanocomposite 5%. It can make this composite unsuitable in some properties.
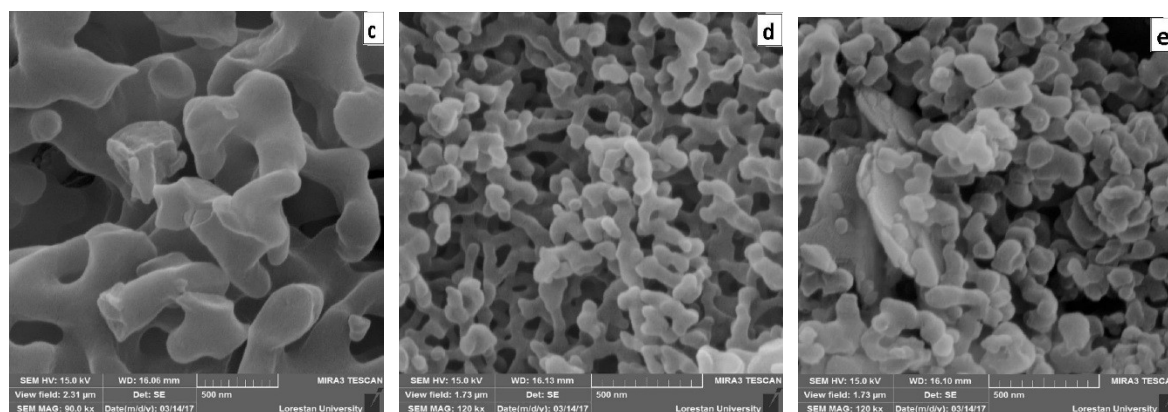
Figure 4: SEM micrographs of pristine ZrP nano particle (a) and poly (MMA-co-MI)/ZrP nanocomposite (b: 0.5%; c; 1%; d: 3%; e: 5%)

TEM micrographs: TEM micrographs of modified nano ZrP and nanocomposite are shown in Figure 5. As seen clearly, nanoparticles are evenly distributed in the polymer matrix.
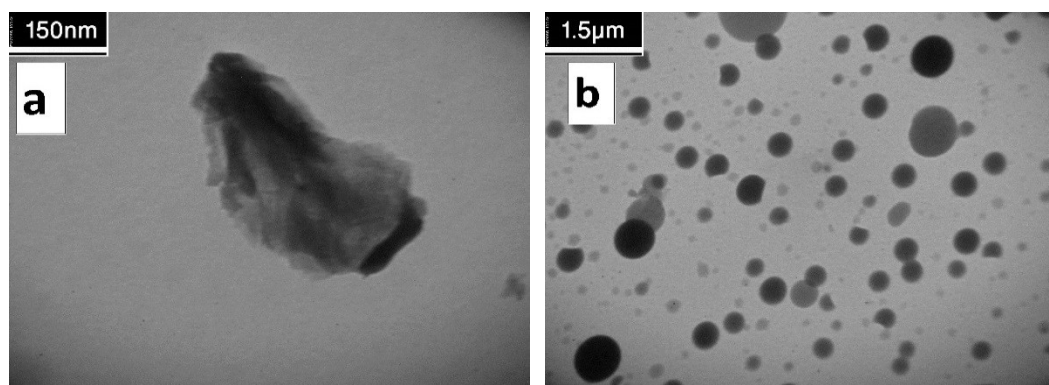

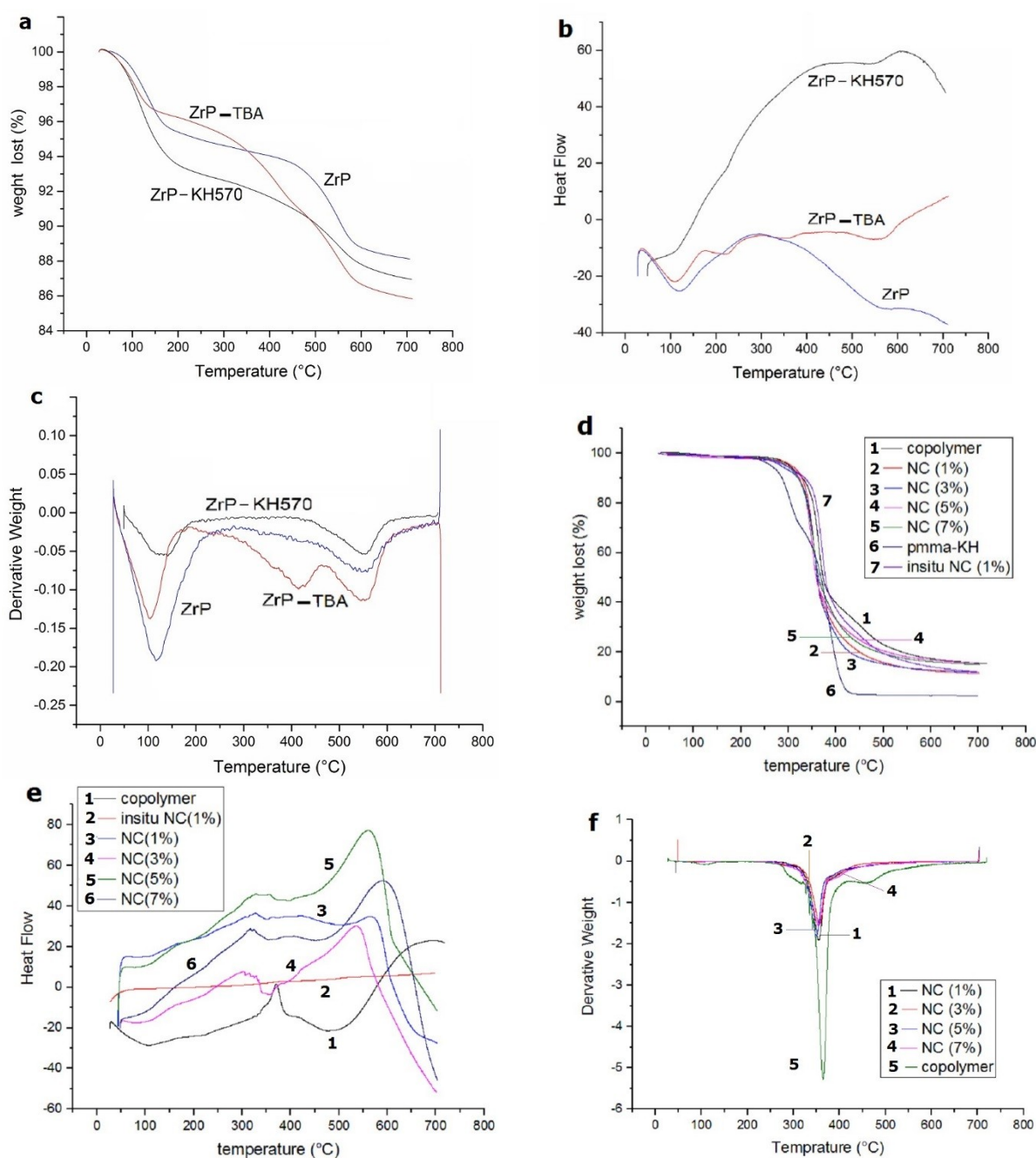**Figure 5:** TEM micrographs of (a) modified nano ZrP and (b) poly (MMA-co-MI)/ZrP nanocomposite.

The thermal decomposition of the pristine ZrP and modified ZrP nanoparticle were studied by TGA, DSC, DTG (Figure 6a-c). The range of two major weight losses of the pristine ZrP crystals are 95−170 and 430−590 °C. They refer to the loss of hydration water and condensation water in ZrP, respectively. Three major weight losses in 70−140, 320-440 and 490−600 °C range were observed in the modified ZrP by TBA. They correspond to the loss of hydration water, elimination of TBA and condensation water in ZrP-TBA. Two weight loss steps were observed in 85-185 and 470-620 °C in the modified ZrP by KH-570. First, it refers to the losing water and methoxy group, then losing methacrylate (29,41,42). Nanocomposites thermal properties and behaviour were investigated by TGA and DSC. The results are summarized in Table 2. The T_{10}, T_{50} and T_{max} were highlighted; T_{10} is the onset temperature, at which 10% degradation occurs, while T_{50} is the midpoint temperature, corresponding to 50% degradation.

T_{max} is the weight lost finishing temperature. The copolymer start losing weight at around 265 °C and when nanoparticles were added into its matrix, the temperature increase around 20 °C for starting weight loss of nanocomposites. The copolymer weight lost finishing around 576 °C while nanocomposites around 667 °C. It means improving the thermal stability. Nanocomposite's T_{10}, T_{50}, T_{max} and initiation weight lost temperature are more than PMMA nanocomposite. It shows good improvement of thermal stability nanocomposite than PMMA nanocomposite (43,44).

The eighth column shows time of using in-situ nanoparticles. As seen, adding ZrP nanoparticles to copolymer decrease amount of T_g, but the nanocomposite T_g are higher than PMMA nanocomposite. Also adding nanoparticle during polymerization have more effects on decrease of T_g.

Table 2: Sample designations; T_{max} and T_g of poly (MMA-co-MI)/ZrP-nanocomposite films measured from TGA and DSC curves.

Sample designation	PMMA-ZrP	Copolymer	CP/ZrP-1	CP/ZrP-3	CP/ZrP-5	CP/ZrP-7	In-situ nanocomposite
α-ZrP (w%)	1	0	1	3	5	7	1
$T_{10\%}$	284.5	327.52	328.1	318.02	321.51	318.79	334.7
$T_{50\%}$	367.6	369.96	360.07	360.46	359.11	361.82	378.5
T_{max} (°C)	488.2	576.18	667.6	679.06	669.0	674.22	691.5
T_g (°C)	96.1	133.7	113.85	114.11	115.2	115.35	106.6
Coal Productivity	2.87	15.30	11.51	12.04	15.74	15.09	12.25

Figure 6: a, b, c are TGA, DSC and DTG of the nanoparticle, respectively. d, e, f are TGA, DSC and DTG of the nanocomposite, respectively.

Atabaki F et al. JOTCSA. 2022; 9(3): 809-820.

RESEARCH ARTICLE

The transparency of the polymer and prepared nanocomposites were examined by UV-Vis spectroscopy. Figure 7 shows UV-Vis spectra of copolymer and nanocomposite solutions in EtOAc. The transparency of nanocomposite solutions 5 and 7% in 400 nm was about 11% which was not suitable. It reached to 73% that is near the copolymer transparency in nanocomposite solutions (3%). The best transparencies were observed in nanocomposites solutions 0.5, 1%, and in-situ, was 95% in 400 nm. All of the nanocomposites have more transmittance than PMMA nanocomposite except 5, 7%. Since nanocomposites 0.5 and 1% transmit the visible light as well as PMMA, they can be used whenever PMMA is used as a substitute for glass. Furthermore, nanocomposites do not transmit UV light so they can be used in sunglasses.
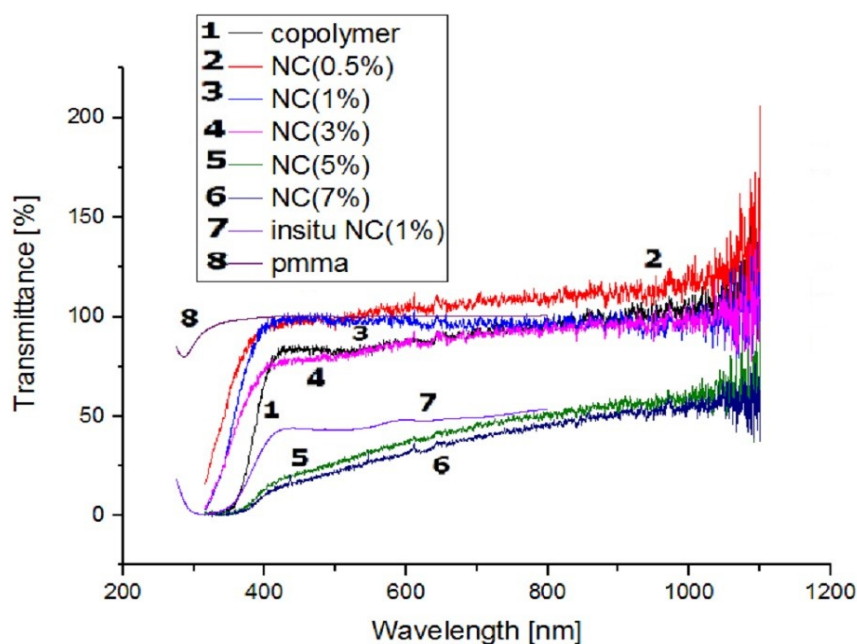

Figure 7: UV-Vis spectra of nanocomposite solutions.

CONCLUSION

A series of nanocomposites based on poly (MMA-co-MI) as a matrix and modified ZrP-KH570 was prepared and characterized by FTIR spectroscopy. The crystalline structure and the size of nanoparticles were confirmed by XRD. The surface morphology of these compounds, evaluated by SEM, were observed as sheet for nanoparticles. It was successfully dispersed in polymer matrix after sonication. The dispersion of nanoparticles into polymer matrix was also confirmed by TEM. Thermal analysis of nanoparticle was investigated.

The thermal stability of nanocomposites was examined by TGA and the results show that adding nanoparticle improve copolymer's thermal stability. Also, thermal behavior of these compounds, evaluated by DSC, shows a decrease in T_g after adding of nanoparticles into polymer matrix. It was probably due to location of nanoparticles between the polymer layers and so decrease interaction between polymer layers.

The results of transparency by UV-Vis spectroscopy showed that the best percent refer to nanocomposite 0.5 and 1% of nanoparticles. Nanocomposites absorb UV light well.

REFERENCES

1. Shafiee Hasani S, Ghazi Tabatabaei Z. Synthesis of Nanocomposites of Single-Wall Carbon Nanotubes Coated with ZnO Nanoparticles in a Matrix of Poly Methyl Methacrylate and Study of Its Optical Properties. Nashrieh Shimi va Mohandesi Shimi Iran. 2019;38(3):23–32.

2. Fatalla AA, Tukmachi MS, Jani GH. Assessment of some mechanical properties of PMMA/silica/zirconia nanocomposite as a denture base material. IOP Conference Series: Materials Science and Engineering. 2020 Nov;987(1):012031. <DOI>.

3. Tucureanu V, Matei A, Mihalache I, Danila M, Popescu M, Bita B. Synthesis and characterization of YAG:Ce,Gd and YAG:Ce,Gd/PMMA nanocomposites for optoelectronic applications. J Mater Sci. 2015 Feb;50(4):1883–90. <DOI>.

4. Singh AK, Prakash R, Pandey D. A comparative thermal, optical, morphological and mechanical properties studies of pristine and C15A nanoclay-modified PC/PMMA blends: a critical evaluation of the role of nanoclay particles as compatibilizers. RSC Adv. 2013;3(35):15411-20. <DOI>.

5. Schoth A, Wagner C, Hecht LL, Winzen S, Muñoz-Espí R, Schuchmann HP, et al. Structure control in PMMA/silica

hybrid nanoparticles by surface functionalization. Colloid Polym Sci. 2014 Oct;292(10):2427–37. <DOI>.

6. Gianotti V, Antonioli D, Sparnacci K, Laus M, Giammaria TJ, Ferrarese Lupi F, et al. On the Thermal Stability of PS- b -PMMA Block and P(S- r -MMA) Random Copolymers for Nanopatterning Applications. Macromolecules. 2013 Oct 22;46(20):8224–34. <DOI>.

7. Ali Sabri B, Satgunam M, Abreeza N, N. Abed A. A review on enhancements of PMMA Denture Base Material with Different Nano-Fillers. Jones IP, editor. Cogent Engineering. 2021 Jan 1;8(1):1875968. <DOI>.

8. Azimi HR, Rezaei M, Majidi F. The non-isothermal degradation kinetics of St–MMA copolymers. Polymer Degradation and Stability. 2014 Jan;99:240–8. <DOI>.

9. Teodorescu M. Free-radical copolymerization of methyl methacrylate with styrene in the presence of 2-mercaptoethanol II. Influence of methyl methacrylate/styrene ratio. European Polymer Journal. 2002 May;38(5):841–6. <DOI>.

10. Lin CT, Kuo SW, Huang CF, Chang FC. Glass transition temperature enhancement of PMMA through copolymerization with PMAAM and PTCM mediated by hydrogen bonding. Polymer. 2010 Feb;51(4):883–9. <DOI>.

11. Gevrek TN, Bilgic T, Klok HA, Sanyal A. Maleimide-Functionalized Thiol Reactive Copolymer Brushes: Fabrication and Post-Polymerization Modification. Macromolecules. 2014 Nov 25;47(22):7842–51. <DOI>.

12. Konsulov V, Grozeva Z, Tacheva J, Tachev K. Study of the copolymerization of n-(dichlorophenyl) maleimides with methyl methacrylate. Bulgarian chemical communications. 2009;41(1):31–8.

13. Sanchez FA, Redondo M, Olmos D, Kuzmanovic M, González-Benito J. A Near-Infrared Spectroscopy Study on Thermal Transitions of PMMA and PMMA/SiO 2 Nanocomposites. Macromol Symp. 2014 May;339(1):48–59. <DOI>.

14. Lerari D, Peeterbroeck S, Benali S, Benaboura A, Dubois Ph. Combining atom transfer radical polymerization and melt compounding for producing PMMA/clay nanocomposites. J Appl Polym Sci. 2011 Aug 5;121(3):1355–64. <DOI>.

15. Hosoda T, Yamada T. Effect of TiO 2 on morphology and mechanical properties of PVDF/PMMA blend films prepared by melt casting process. J Appl Polym Sci. 2014 Jul 5;131(13):1-10. <DOI>.

16. Akinci A, Sen S, Sen U. Friction and wear behavior of zirconium oxide reinforced PMMA composites. Composites Part B: Engineering. 2014 Jan;56:42–7. <DOI>.

17. Zanotto A, Luyt AS, Spinella A, Caponetti E. Improvement of interaction in and properties of PMMA-MWNT nanocomposites through microwave assisted acid treatment of MWNT. European Polymer Journal. 2013 Jan;49(1):61–9. <DOI>.

18. Hazim A, Abduljalil HM, Hashim A. Structural, Spectroscopic, Electronic and Optical Properties of Novel Platinum Doped (PMMA/ZrO2) and (PMMA/Al2O3) Nanocomposites for Electronics Devices. Trans Electr Electron Mater. 2020 Dec;21(6):550–63. <DOI>.

19. Su W, Wang S, Wang X, Fu X, Weng J. Plasma pre-treatment and TiO2 coating of PMMA for the improvement of antibacterial properties. Surface and Coatings Technology. 2010 Oct;205(2):465–9. <DOI>.

20. Yıldırım A, Acay H, Baran A. Synthesis and characterization of the molecularly imprinted composite as a novel adsorbent and its competition with non-imprinting composite for removal of dye. JOTCSA. 2021;8(2):609–22. <DOI>.

21. Zidan S, Silikas N, Alhotan A, Haider J, Yates J. Investigating the Mechanical Properties of ZrO2-Impregnated PMMA Nanocomposite for Denture-Based Applications. Materials. 2019 Apr 25;12(8):1344. <DOI>.

22. Yi C, Yang Y, Liu B, He J, Nie Z. Polymer-guided assembly of inorganic nanoparticles. Chem Soc Rev. 2020;49(2):465–508. <DOI>.

23. Adnan M, Dalod A, Balci M, Glaum J, Einarsrud MA. In Situ Synthesis of Hybrid Inorganic–Polymer Nanocomposites. Polymers. 2018 Oct 11;10(10):1129. <DOI>.

24. Hassanzadeh-Aghdam MK, Ansari R, Mahmoodi MJ, Darvizeh A. Effect of nanoparticle aggregation on the creep behavior of polymer nanocomposites. Composites Science and Technology. 2018 Jul;162:93–100. <DOI>.

25. Hamming LM, Qiao R, Messersmith PB, Catherine Brinson L. Effects of dispersion and interfacial modification on the macroscale properties of TiO2 polymer–matrix nanocomposites. Composites Science and Technology. 2009 Sep;69(11–12):1880–6. <DOI>.

26. Chau JLH, Hsieh CC, Lin YM, Li AK. Preparation of transparent silica–PMMA nanocomposite hard coatings. Progress in Organic Coatings. 2008 Jun;62(4):436–9. <DOI>.

27. Díaz A, Mosby BM, Bakhmutov VI, Martí AA, Batteas JD, Clearfield A. Self-Assembled Monolayers Based Upon a Zirconium Phosphate Platform. Chem Mater. 2013 Mar 12;25(5):723–8. <DOI>.

28. Alberti G, Vivani R, Biswas RK, Murcia-Mascarós S. Preparation and some properties of γ-zirconium phosphate benzenephosphonate. Reactive Polymers. 1993 May;19(1–2):1–12. <DOI>.

29. Zhou Y, Huang R, Ding F, Brittain AD, Liu J, Zhang M, et al. Sulfonic Acid-Functionalized α-Zirconium Phosphate Single-Layer Nanosheets as a Strong Solid Acid for Heterogeneous Catalysis Applications. ACS Appl Mater Interfaces. 2014 May 28;6(10):7417–25. <DOI>.

30. Atabaki F, Abdolmaleki A, Barati A. Free radical copolymerization of methyl methacrylate and N-2-methyl-4-nitro-phenylmaleimide: Improvement in the Tg of PMMA. Colloid Polym Sci. 2016 Feb;294(2):455–62. <DOI>.

31. Carter DP. Preparation of zirconium oxychloride [Internet]. US4256463A.1981 Available from: <URL> .

32. Baig U, Wani WA, Ting Hun L. Facile synthesis of an electrically conductive polycarbazole–zirconium(iv)phosphate cation exchange nanocomposite and its room temperature ammonia sensing performance. New J Chem. 2015;39(9):6882–91. <DOI>.

33. Barraclough C, Bradley D, Lewis J, Thomas I. 510. The infrared spectra of some metal alkoxides,

trialkylsilyloxides, and related silanols. Journal of the Chemical Society (Resumed). 1961;2601–5.

34. Matinlinna JP, Özcan M, Lassila LVJ, Vallittu PK. The effect of a 3-methacryloxypropyltrimethoxysilane and vinyltriisopropoxysilane blend and tris(3-trimethoxysilylpropyl)isocyanurate on the shear bond strength of composite resin to titanium metal. Dental Materials. 2004 Nov;20(9):804–13. <DOI>.

35. Zhang FA, Song C, Yu CL. Effects of preparation methods on the property of PMMA/SBA-15 mesoporous silica composites. J Polym Res. 2011 Nov;18(6):1757–64. <DOI>.

36. Licoccia S, Trombetta M, Capitani D, Proietti N, Romagnoli P, Di Vona ML. ATR–FTIR and NMR spectroscopic studies on the structure of polymeric gel electrolytes for biomedical applications. Polymer. 2005 Jun;46(13):4670–5. <DOI>.

37. Choudhary V, Mishra A. Studies on the copolymerization of methyl methacrylate and N-aryl maleimides. J Appl Polym Sci. 1996 Oct 24;62(4):707–12. <DOI>.

38. Lee SS, Ahn TO. Direct polymer reaction of poly(styrene-co-maleic anhydride): Polymeric imidization. J Appl Polym Sci. 1999 Feb 14;71(7):1187–96. <DOI>.

39. Shobhana E. X-Ray diffraction and UV-visible studies of PMMA thin films. International Journal of Modern Engineering Research. 2012;2(3):1092–5.
40. Patterson AL. The Scherrer Formula for X-Ray Particle Size Determination. Phys Rev. 1939 Nov 15;56(10):978–82. <DOI>.

41. Li X, Wang Z, Wu L, Tsai T. One-step in situ synthesis of a novel α-zirconium phosphate/graphene oxide hybrid and its application in phenolic foam with enhanced mechanical strength, flame retardancy and thermal stability. RSC Adv. 2016;6(78):74903–12. <DOI>.

42. Kozawa Y, Suzuki S, Miyayama M, Okumiya T, Traversa E. Proton conducting membranes composed of sulfonated poly(etheretherketone) and zirconium phosphate nanosheets for fuel cell applications. Solid State Ionics. 2010 Mar 11;181(5–7):348–53. <DOI>.

43. Carvalho HWP, Suzana AF, Santilli CV, Pulcinelli SH. Structure and thermal behavior of PMMA–polysilsesquioxane organic–inorganic hybrids. Polymer Degradation and Stability. 2014 Jun;104:112–9. <DOI>.

44. Hatanaka LC, Diaz A, Wang Q, Cheng Z, Mannan MS. Thermal Stability of Optically Transparent Alpha-Zirconium Phosphate/Poly(methyl methacrylate) Nanocomposites with High Particle Loading. Polymers and Polymer Composites. 2017 May;25(4):267–72. <DOI>.

Photodynamic Therapy: An Overview and Insights into a Prospective Mainstream Anticancer Therapy

Vidujith A.V.A.[1] (iD)**, Jayasinghe C.D.[2]** (iD)**, Costa M.D.P. De.[3]** (iD)**, and Senthilnithy R.[1]*** (iD)

[1]Department of Chemistry, The Open University of Sri Lanka, Nugegoda, Sri Lanka
[2]Department of Zoology, The Open University of Sri Lanka, Nugegoda, Sri Lanka
[3]Department of Chemistry, University of Colombo, Sri Lanka
*Corresponding author (email: rsent@ou.ac.lk)

Abstract: Photodynamic therapy (PDT) procedure has minimum invasiveness in contrast to conventional anticancer surgical procedures. Although clinically approved a few decades ago, it is not commonly used due to its poor efficacy, mainly due to poor light penetration into deeper tissues. PDT uses a photosensitizer (PS), which is photoactivated on illumination by light of appropriate wavelength and oxygen in the tissue, leading to a series of photochemical reactions producing reactive oxygen species (ROS) triggering various mechanisms resulting in lethal effects on tumor cells. This review looks into the fundamental aspects of PDT, such as photochemistry, photobiological effects, and the current clinical applications in the light of improving PDT to become a mainstream therapeutic procedure against a broad spectrum of cancers and malignant lesions. The side effects of PDT, both early and late-onset, are elaborated on in detail to highlight the available options to minimize side effects without compromising therapeutic efficacy. This paper summarizes the benefits, drawbacks, and limitations of photodynamic therapy along with the recent attempts to achieve improved therapeutic efficacy via monitoring various cellular and molecular processes through fluorescent imagery aided by suitable biomarkers, prospective nanotechnology-based targeted delivery methods, the use of scintillating nanoparticles to deliver light to remote locations and also combining PDT with conventional anticancer therapies have opened up new dimensions for PDT in treating cancers. This review inquires and critically analyses prospective avenues in which a breakthrough would finally enable PDT to be integrated into mainstream anticancer therapy.

INTRODUCTION TO PHOTODYNAMIC THERAPY

PDT involves the use of electromagnetic radiation (emr) of a specific wavelength (light) and photosensitizer (PS) molecules to form in-situ singlet oxygen or other ROS (Reactive Oxygen Species) to eliminate malignant cells ((1). It is a clinically approved, but poorly utilized technique in treating cancers due to its poor efficacy and inability to reach deeper tissues. Compared to other oncology techniques, PDT is less invasive, and the known adverse effects are limited to prolonged residual photosensitivity (1).

Individual components of PDT, i.e., emr, photosensitizer, and molecular oxygen, are non-toxic. In PDT, topical or systemic administration of PS is followed by light activation through careful irradiation of the location by emr of appropriate wavelength, triggering a photochemical reaction generating other Reactive Oxygen Species (ROS) labeled as type I reaction or a photochemical reaction causing highly reactive singlet oxygen which is labeled as type II reaction (1). The accumulation of other ROS or singlet oxygen in cells results in direct cell killing by an intense oxidative burst or cell death via apoptosis or necrosis (1). In ideal conditions, it kills off the tumor cells while sparing the healthy ones.

Vidujith AVA et al. JOTCSA. 2022; 9(3): 821-848.

REVIEW ARTICLE

The Photochemical Aspect of PDT

In PDT, the PS administered is expected to concentrate on the cancer tissue selectively. The tissue is then exposed to suitable light in which photons' absorption causes the excitation and subsequent de-excitation of photosensitizer molecules. De-excitation emits photons that are to be absorbed by the surrounding substrate molecules. Notably, a certain fraction of the excited singlet state molecules is transformed into an excited triplet state, relatively long-lived. The transformation occurs via intersystem crossing (1). The molecules that have attained the excited triplet state can either form free radicals or radical ions by electron transfer or hydrogen atom extraction to biochemical substrate molecules such as membrane lipids, oxygen, solvent molecules, etc.

These free radicals and the radical ions interact with ground-state molecular oxygen to produce ROS, such as superoxide anion radicals, hydrogen peroxides, and hydroxyl radicals through type I reaction (1). Highly reactive singlet oxygen is made from a type II reaction where energy from the excited triplet state molecule is directly transferred to ground state molecular oxygen. The above responses of types I and II coincide; the substrate's specific nature and the PS determine the ratio between the two reaction rates (2). ROS are usually considered toxicants that induce deleterious effects such as cell dysfunction, death, or malignant transformation (3). Under normal conditions, ROS are generated in the cells through enzymatic and non-enzymatic reactions (3). ROS may cause opposite cellular effects, such as promoting cell proliferation and tumor progression or cell death and tumor regression, which can be utilized in therapeutic techniques against cancer (1). In PDT, since the light activation of the PS triggers ROS generation, the selective accumulation of the PS in malignant tissue leads to improved therapeutic efficacy (3).

Photosensitizers Used in PDT

A photosensitizer suitable for PDT should display a strong absorption peak in the far visible region (650 - 800 nm) (4), in which the absorption by the body should be minimal (For example, haemoglobin absorbs radiation between 478 and 672 nm). Illumination by light having wavelengths longer than 800 nm does not provide sufficient energy to excite oxygen to its singlet state. It seems an ideal PS ought to have a strong absorption peak lower than 478 nm and a fluorescence peak within 478 nm to 672 nm. Most of the PSs used in PDT have a tetrapyrrole backbone and are relatively hydrophobic compounds. They rapidly diffuse through the plasma membrane into tumor cells and localize in organelles such as mitochondria and endoplasmic reticulum (ER) (4). An ideal PS's chemical nature facilitates its entry into the tumor cells without precipitation in aqueous environments and selectivity to target cells instead of healthy cells. It also enables appropriate extinction coefficients and accumulation rates in target tissues (5). It has been noted that many of the effective PSs are preferentially low-density lipoproteins (LDL) among various serum proteins. Hamblin *et al.* suggested that over-expressed LDL receptors found on tumor cells could be playing a role in tumor localization (4).

PS Used in PDT

Photosensitizers are generally categorized into porphyrins and non-porphyrins. Porphyrin-derived PSs are further classified into 1st, 2nd, or 3rd generation PSs (1). Hematoporphyrin (Hp), its derivatives (HpDs), and Photofrin (Porfimer Sodium) are classified as 1st generation PSs.

Photofrin is a commercially available PS, employed mainly in PDT (1). At 500 nm, it absorbs light with maximum excitation along with two other peaks at 540 and 560 nm, while the maximum emission occurs at 615 nm, associated with a second peak at ~680 nm (5). The research work by Bechet (5) also sheds light upon the influence of electric pulses (EP) delivery on the Photofrin uptake and its localization in human breast cancer cell line (MCF-7) and Chinese Hamster Ovary (CHO) cells. With the aid of fluorescence image analysis, it was observed that epithelial cells (EP) of CHO cells significantly improved Photofrin uptake. Due to electropermeabilization, Photofrin entered the cell and accumulated in the entire cell (5). Photofrin is commonly employed as a PS in PDT to treat advanced-stage lung cancer, early-stage esophageal, gastric, and cervical cancer. Absences of intrinsic toxicity, the possibility of using in small doses, sufficient clearance from healthy tissue, and the possibility of repeated administrations without serious repercussions except for prolonged photosensitivity to the neoplastic patient are among the many benefits of using Photofrin as PS in PDT (1).

Benzoporphyrin derivatives, chlorins, phthalocyanines, texaphrins, naturally occurring hypericin and 5-aminolevulinic acid (5-ALA), and other related esters that promote the production of endogenous protoporphyrin IX (PpIX) are classified as 2nd generation PS(1). 5-aminolevulinic acid (5-ALA) is metabolically converted into photosensitizable protoporphyrin IX, and hence it acts as a pro-drug. During the biosynthesis of heme, both 5-ALA and PpIX are generated as intermediates, where heme inhibits the endogenous generation of excess 5-ALA. The presence of exogenous 5-ALA allows bypassing the abovementioned regulatory mechanism, resulting in the accumulation of PpIX in cells (1). 5-ALA induced PpIX is known to have good tumor selectivity, limited systemic toxicity, and low skin photosensitization (1).

Nyman *et al.* reported that PpIX displays a Soret peak (intense absorption peak in the blue wavelength region of the visible spectrum) at about 405 nm and additional absorption at 510, 545, 580, and 630 nm, which are referred to as Q bands. Its

fluorescence peaks are observed at 635 nm and 705 nm (8).

Hypericin is a naturally occurring compound that can be a promising alternative to chemically synthesized photosensitizers (1), but it has a few unfavourable characteristics that limit its usage in PDT. Its absorption peaks are around 595 nm and it does not absorb light above 630 nm. This specific spectral region of light has limited penetration. The potential application of hypericin in PDT lies in treating superficial lesions. Recent clinical work has addressed its use as a PS in treating bladder cancer due to its specific accumulation in urothelial carcinoma lesions (8). Low selectivity, weak absorption in the red wavelength region, resulting in difficulty in treating deep tumors, and residual skin photosensitivity being the significant side effect are the drawbacks of 1st generation PS.

Meta-tetra(hydroxyphenyl)chlorine (m-THPC), commercially known as Foscan or Temoporfin, is a 2nd generation PS with a very high potential to be used in PDT for the treatment of neck and head cancers. The molecule has a hydrophobic nature and a short plasma half-life in humans. M-THPC can be photoactivated at about 652 nm, and the photosensitization results in a very high yield of singlet oxygen accumulating in tumor cells. In addition to the direct damage to tumor cells by oxidants, m-THPC also causes intense and sustained vascular damage owing to its pharmacokinetic behaviour (1). It has been observed that m-THPC has two major absorption peaks at 420 nm and 652 nm. In clinical use, light activation of m-THPC is done at 652 nm as light in the spectral region of 420 nm has limited penetration. Studies have been conducted to improve the efficacy of m-THPC in the treatment of neck and head cancers (1).

Mono-l-aspartyl chlorin e6 (Talaporfin sodium) is a 2nd generation PS with a core chlorin structure and a highly aromatic system, characterized by excellent solubility in aqueous media and short half-life. Preclinical studies involving Talaporfin sodium have revealed that on light activation, in addition to cytotoxicity, the simultaneous induction of systemic, tumor-specific immuno-modulation mediated by CD8+T cells aids in overcoming tumor resistance through micro-vessels closure and upregulation of both cytolysis and memory cells (1,2,9).

Attempts have been made to develop 3rd generation PSs by utilizing the Warburg effect, which relates to cancer cells' ability to absorb glucose in large quantities compared to healthy cells (9). 3rd generation PS ought to have higher tumor cell selectivity and specificity. G-chlorin is a probable candidate for such a PS displaying strong anti-tumor effects against gastric cancer and colon cancer. It was also recorded to be 20–50 times more cytotoxic than Talaporfin sodium (10). M-chlorin, which is mannose conjugate chlorin designed to target tumor-associated-macrophages, Katoaka *et al.* recorded similar cytotoxic effects as G-chlorin *in*

vitro studies, but *in vivo* allograft model study, M-chlorin PDT showed the most substantial antitumor effects (10). Although results are inconclusive for G-chlorin and M-chlorin, this opens up a route to another line of work to develop PS conjugated with biological molecules to enhance their selectivity and specificity to become 3rd generation PS.

Optimizing PDT Outcome
To achieve a better therapeutic outcome, the three main pillars of PDT, namely light, PS, and tissue oxygen, are present in optimum proportions throughout treatment procedures. During clinical applications, light and PS dose is administered empirically without any inter or intra-treatment variations. A crude practice ignores fluctuations in the pharmacokinetics of PS, tissue optics, and tissue oxygenation, thus leading to poor efficacy. A strong, reliable, and more personalized dosimetric system has been suggested. The practical execution requires a system to measure PDT dose explicitly by extrapolating from measured PS and light amount or implicitly by measuring the photobleaching or directly measuring the concentration of singlet oxygen in the tissue under treatment. All the proposed dosimetric approaches to PDT aim at directly or indirectly quantifying the primary effector of PDT (singlet oxygen) (12).

Monitoring tissue oxygenation and a delivered dose of light in real-time is crucial so that the treatment plan can be manipulated to enhance the therapeutic efficacy. It is also beneficial to look into the cellular level mechanisms that affect PDT outcome to understand the possibilities available to influence overall tumor cell death for better therapeutic development.

Accurate measurement of PDT dose
In photobleaching, a dye or a fluorophore of a PS molecule in PDT undergoes a photochemical change resulting in its permanent inability to fluoresce, caused either by cleaving covalent bonds or non-specific reactions between the fluorophore and surrounding chemical species. Photo modification, where the loss of absorbance or fluorescence occurs at a particular wavelength, yet the chromophore is retained at an altered state, is also considered a photobleaching form (15).

As shown by Dysart *et al.,* the rate of change in the ground-state (S_0) photosensitizer concentration $\dfrac{d(S_0)}{dt}$ due to $^1O_2$-mediated photobleaching can be expressed by the differential equation given below (10). (Concentration of the PS is (S_0), and the concentration of the oxygen in the tissue is $(^1O_2)$).

$$\frac{d(S_0)}{dt} = -k_{os}[S_0] + \delta \times (^1O_2) \qquad (1)$$

Thus, the reaction between $^1O_2$ and ground-state photosensitizer molecules is governed by the bimolecular reaction rate constant k_{OS}. The reaction

leads to irreversible degradation of the photosensitizer and also oxygen consumption (11). The term δ accounts for the reaction of a $^1O_2$ molecule with the same photosensitizer molecule involved in its generation. The reactions of ground state photosensitizer molecules with $^1O_2$ are considered to be dominant reactions at the low concentrations usually found in cells and tissues (less than micromolar) since singlet oxygen has a higher probability of reacting with other targets before diffusing into another sensitizer molecule. δ is given by:

$$\delta = \frac{1}{d^3 N_A} \qquad (2)$$

Where N_A is the Avogadro's number and d is the mean $^1O_2$ diffusion distance, defined as $d = \sqrt{6 D\tau_D}$ where D is the diffusion coefficient of $^1O_2$ and τ_D is the $^1O_2$ lifetime. The instantaneous $^1O_2$ concentration can be determined by rearranging equation (1) to

$$\left(^1O_2\right) = \frac{d[S_0]}{k_{os}\left([S_0]+\delta\right) dt} \qquad (3)$$

As $^1O_2$ is the primary cytotoxic in PDT, the PDT dose is the cumulative of $^1O_2$ generated, thought to be equal to the amount of $^1O_2$ reacted, other deactivation pathways being less probable to occur. Hence, the PDT dose over a time T is (10)

$$Dose = \int_0^T [^1O_2](t)\frac{dt}{\tau_D}$$

$$Dose = \frac{1}{\tau D \times k_{os}\ln[S_0]_0 + \delta/[S_0](T)+\delta} \qquad (4)$$

The PDT dose is calculated from photobleaching of photosensitizer (decrease in (S0)) if $1/(\tau_{D \times k_{OS}})$ and δ are determined experimentally. In clinical practice, practitioners continue to face difficulties in determining the exact dose required to achieve complete healing from the condition. Such challenges often lead to inaccuracies that might result in under-treatment of the targeted lesions. Jarvi *et al.* report their findings employing SOL (singlet oxygen luminescence) to directly measure singlet oxygen dose compared to estimate made via measured photobleaching, displaying an excellent correlation between the two methods. The study also highlighted that photobleaching-based PDT dose analysis was unreliable at tissue oxygen concentrations below 5ℳ M due to rapid changes in fluorescence intensity, which weren't observed by Dysart *et al*. However, these results cannot be generalized to all PS as this study deployed m-Tetra(hydroxyphenyl)chlorin (m-THPC) (13).

Jarvi *et al.* further reported comparative polts between fluence rate, triplet state oxygen ($^3O_2$), and

photobleaching, consistent with the findings of Dysart *et al.,* indicating a discontinuous and poorly correlated variation of light fluence and $^3O_2$ with singlet oxygen. Thus, it can be proposed that explicit measurement of PDT dose is a crude and unreliable method. The work done by Jarvi *et al.* provides additional evidence for singlet oxygen being the primary cytotoxin of PDT as proposed by photochemistry (13). SOL (singlet oxygen luminescence) based dosimetry analyses the luminescence signals emitted by singlet oxygen generated at the tissue under treatment, thus a direct measurement method was utilized by Jarvi et al. their investigation. Though SOL provides accurate dose measurements where difficulties in translating it to clinical use were encoutered due to cost, complexity, and weak signal strength, which constitutes an invaluable tool in evaluating alternative dosimetric techniques. Photobleaching-based dosimetry is an option to be used clinically, given that at tissue oxygen concentrations above 5 M (13). Sharwani *et al.* report a positive correlation between loss of fluorescence (photobleaching) and PDT outcome in a clinical study conducted using a fluorescence imaging system to estimate the photobleaching of PpIX (14). However, the findings of Sharwani *et al.* are yet to be validated with a more extensive range of test data.

Effective delivery of light
PDT requires a single dose of PS administered to the patient, followed by the photoactivation of the PS after a specific time interval by a single illumination using light of appropriate wavelength. Illumination is conventionally done by using broad-spectrum light sources such as arc lamps and filament lamps. Difficulty in coupling them with light delivery fibers without reducing the power output, difficulty in calculating the effectively delivered dose, limited maximum power output (1W), and the presence of UV and IR radiation are the limitations to their use over advantages of being cheap and easy to use. Modern lasers, being inexpensive, compact, and mobile compared to first-generation lasers, are widely used in PDT, and can be equipped with units capable of carrying out dosimetric calculations and programmed treatment plans (15). Diode lasers emit only one wavelength of light, limiting their versatility in contrast to light-emitting diodes (LEDs). Both varieties are used clinically. Fiber optic media is used to deliver the light dose locally. A successful PDT procedure requires providing an adequate amount of light from the source to the target and ensuring homogeneous distribution of light (15). A light delivery system must be used in conjunction with advanced dosimetric software for its efficient utilization, in which measured diagnostic signals are fed into a dose distribution calculation program (40-43). In the illumination, the accepted approach is to deliver a threshold dose, which is a minimum dose adequate to cause direct cell death, delivered to a target tissue volume (15).

$$D_{PDT} = \int_0^T \epsilon \, [PS] \, \phi \, dt \qquad (5)$$

$$D_{fluence} = \int_0^T \phi \, dt \qquad (6)$$

Equation (5) refers to PDT dose, which is determined by the extinction coefficient of the PS (ϵ), the concentration of the PS [PS], fluence (number of photons arriving per unit cross-sectional area) rate (Φ), and the time interval of illumination (dt). Assuming a homogeneous distribution of PS in the target tissue volume, equation (6) relates the fluence dose to a simplified dose calculation. Fluence rate is estimated via calibrated optical probes; these point measurements are utilized to obtain representative readings of the light dose delivered to a location. The photon propagation is required to be theoretically calculated to spatially map the fluence rate throughout the entire target tissue volume (15). In addition to that, the optical properties of the target tissue are estimated.

$$\phi_{(r)} = \frac{P}{4\pi \, D \, r \exp(-\mu_{eff} \, r)} \qquad (7)$$

The above equation, which illustrates a theoretical model for photon propagation, is obtained as an analytical solution for the diffusion equation, where P:source power in watts, D:diffusion coefficient (in cm), μ_{eff} :effective attenuation coefficient of light in the target tissue, r:radial distance from the point source (in cm) (15).

Davidson *et al.* devised a treatment-planning software package utilized in Phase II clinical trial of Tookad™-mediated I-PDT of persistent prostate carcinoma following radiation therapy (24). This software uses a patient-specific I-PDT treatment plan based on predicted light distributions in the prostate and surrounding tissue. The model used the diffusion equation and the finite elements method (FEM) numerical analysis, with the volume of interest discretized into a 4-noded tetrahedral mesh. Treatment plans were designed according to the pre-treatment MRI images. In tumors treated with a light dose greater than 23 J/cm^2, a complete pathological response was observed. No patient with a D(90) less than 23 J cm^{-2} was reported to have a complete biopsy response, while 8/13 (62%) of patients with a D(90) greater than 23 J cm(-2) had negative biopsies six months post-treatment (23). Swartling *et al.* developed a treatment planning software utilizing Interactive Dosimetry by Sequential Evaluation (iDOSE) (23). The software enabled dose plans with optical fiber positions according to 3-D tissue models developed via ultrasound, calculated the best fiber positions, and provided an optimal treatment plan. The clinical study used Temoporfin-mediated photodynamic therapy (PDT) for low-grade (T1c) primary prostate cancer. Residual viable cancer cells were present in the prostrate tissue from a histopathological analysis of tissue biopsies taken six months post-PDT. The authors proposed that the low threshold dose of light, which was set to 5 J/cm^2 could be the possible cause of the incomplete treatment (23).

Savenberg et al. at Lund University reported a clinical trial using an 18-fiber interstitial PDT system on recurrent prostate cancer, yielding satisfactory results (15). The 18-fiber interstitial PDT system developed by the Lund University research group could carry out pre-treatment planning and dosimetric calculations during treatment. It is noteworthy to mention that the rationale of the research group at Lund University is to adopt bare-end optical fibers, which allow well-defined positions when used as sources or detectors, resulting in a well-defined source-detector distance in all measurements taken with the use of fibers (15). The Lund group has used the data from researchers and clinical practitioners over the past two decades, but the PDT system they developed was clinically tested with four prostate cancer patients, downplaying the reliability. The treatment planning software package from Davidson *et al.* comparatively has better footing in positive clinical test results and a larger sample size of 13 test subjects (24). Treatment planning software regimes should be tested clinically with larger samples to validate the findings and improve overall therapeutic outcomes. Better software can be developed to aid more complex mathematical models integrating variables such as PS concentration, tissue oxygen, distribution patterns of tumor cell death, etc. Another major limitation in treatment planning software is the assumption of light homogeneity and PS dispersion and the tissue structure when software and models are developed.

It was observed that collimated laser beams scatter forward when encountered by tissues. As a result, they have increased tissue penetration depth compared to non-coherent LED or arc lamps. In contrast, non-collimated light sources bear more divergent beam properties, leading to reduced forward scattering of light, making them unfit to treat deeper lesions (16). Lasers are a common source of illumination used in PDT nowadays. The first lasers ever used in PDT were gold (Au) vapor or copper (Cu) vapor lasers and argon-ion-pumped dye lasers, which emit light in the red wavelength region of the visible spectrum. Solid-state diode lasers came into clinical use in the late 1990s. The benefit of using lasers in therapeutic PDT is the possibility of transmitting the light through optical fibers to reach remote destinations. This procedure created an opportunity to treat tumors in hollow organs, such as the urinary bladder, the bronchus, the intestines, and the esophagus (15). In a clinical study, Jeries et al. reported image-guided optical fibers' placement in treating deep tumors in the head and neck. During the procedure, multiple fibers were positioned under ultrasound guidance into various deep-seated tumors, including head and neck tumors and vascular anomalies in the limbs. Over a

hundred patients were treated with mTHPC-PDT, more than 50% of patients had a good response, while five patients became disease-free, and 80% reported improvements in breathing, swallowing, and speech (17). Pulsed PDT regimes are proposed to increase the depth of necrotic cell death. Thus, it is thought to enhance PDT efficacy primarily on the hypothesis that the downtime between light irradiation will permit tissue re-oxygenation and re-accumulation of photosensitizer at the lesion, subsequently leading to a better therapeutic outcome (18).

The investigation conducted by Pogue *et al.* on the depth of necrosis of a 48 hrs post PDT resulting from continuous wave (CW), and pulsed irradiation displayed no significant difference statistically under the same average incident irradiance (19). A study by Grecco *et al.* yielded a contradictory result: a femtosecond laser irradiation produced a necrotic zone twice as deep in comparison to a CW laser at an equivalent dose (150 J/cm^2) using hematoporphyrin derivative (HpD) as PS (20). Pogue et al., by simulating the deposited amount, reported that the pulsed laser irradiation would help treat deep tissue tumors with PDT. These outcomes are modest and strongly dependent on the PS, the laser pulse width, the pulse energy, and the repetition rate (21). In a study conducted by Sterenborg et al., the simulations concluded that pulsed excitation in PDT was identical to continuous wave (CW) excitation for fluence rates below 4×10^8 Wm^{-2}. It was noted that at higher fluence rates, pulse PDT's effectiveness drops significantly (22). The available evidence is contradictory, so pulsed irradiation cannot be favoured against the use of CW irradiation to achieve an increased depth of tumor necrosis.

Despite the advancements in light sources, delivery, and dosimetric approaches, delivering therapeutic light to deep tumors is still a hurdle to be overcome as it vastly limits the use of PDT. The use of self-luminescent chemical or biological probes has been investigated. While Philip *et al.* were the first to report the use of chemiluminescent probes, Carpenter *et al.* reported the use of bioluminescent probes. The light dose produced by chemical or bio-luminescent probes is lower than that usually expected for PDT, but efficient induction of cytotoxicity is noteworthy. Due to the complexity and limited understanding of the processes involved, further investigations are required to validate their efficiency (either as free probes or in nanoparticle form) before clinical translations. NIR (Near Infra-Red) radiation is proposed as an ideal candidate to achieve increased tissue penetration in PDT. Although better than visible radiation, NIR radiation has a limited penetration depth of approximately 1 cm. Treatment of large superficial tumors may be possible with NIR light, but tumors residing in deeper tissues remain unreachable without a secondary light delivery strategy.To improve the penetration depth of photons, X-rays can be potentially employed in conjunction with PS and radiosensitizers (RS) with minimum tissue penetration limitations, even though ionizing radiation is known to cause intrinsic toxicities (27). Luksiene *et al.* investigated the RS *in vivo* properties of three different PS (HPde, Photofrin II (PII), and hematoporphyrin derivative (HPD)), and revealed RS effect of these PSs was cell line dependent (28). The low efficiency of PS that acts as RS under direct excitation and cell line dependence has contributed to diminishing the interest in any advancements in this area. Attention was given to approaches that can locally generate visible light using X-ray irradiation, such as Cerenkov radiation and nanoscintillators.

Cerenkov emission occurs when charged particles, such as electrons or positrons, travel faster than the phase velocity of light in a given medium. The works of Alexsson *et al.* and Kotagiri *et al.* have given solid proof of the concept and usability of Cerenkov radiation for deep tissue illumination in PDT. The number of studies conducted in this area is few until a wide range of investigations bears favorable conclusive evidence, clinical implementations will be afar (29,30). Implementation of Cerenkov radiation in PDT as per the investigations conducted so far was dependent on clinical linear accelerators or PET scanners, creating a barrier to the use of PDT as a low-cost alternative treatment approach to cancer. Chen and Zhang suggested the use of nanoscintillators in combination with PS. Scintillating nanoparticles are nanoparticles (NP) that convert ionizing radiation into visible light (31). With the advent of nanoscience, this area of research has been very dynamic in recent decades. Morgan *et al.* developed a model to predict the maximum amount of $^1O_2$ generated under X-ray irradiation via quantifying the amount of energy stored in nanoscintillators during the irradiation; this led to the conclusion that only X-rays with energy below 300 keV could cause sufficient cytotoxicity. These predictions were further refined using Monte Carlo simulations. A more accurate estimation of energy deposited in a nanoscintillator was found by Bulin *et al.* (32,33). Investigations have been conducted using nanoscintillators such as terbium oxide ($Tb_2O_3@SiO_2$ NPs), ($SrAl_2O_4:Eu^{2+}$), and ($LiYF_4:Ce^{3+}$) in conjunction with PS respectively, by Bulin *et al.*, Chen *et al.* and Zhang *et al.* providing insights into different mechanisms and successful tumor elimination (34-36). Their work is conclusive and reliable in terms of outcomes and sample size. We believe nanoscintillators hold the key to unlocking the reach of PDT into deeper tumors. We are hopeful that with more thorough *in vitro* and *in vivo* studies in the future, this technique's full clinical translation potential can be realized.

Monitoring tissue oxygenation
The current techniques available for monitoring tissue oxygenation during PDT are as follows. Point measurements are obtained via oxygen electrodes or luminescence-based optodes for direct tissue oxygen measurements or by employing optical spectroscopy for measuring the oxygen saturation of haemoglobin (123). Imaging is considerably more

complicated but feasible with techniques like Blood Oxygen Level Dependent Magnetic Resonance Imaging (BOLD MRI), a functional MRI with a low signal-to-noise ratio. Preclinical research has demonstrated dramatic changes in tissue oxygenation during PDT, which vary depending on the photosensitizer and light delivery methods. Better oxygenation throughout treatment can be achieved by keeping the light fluence rate low to maintain the rate of oxygen consumption at a low level. Real-time monitoring to ensure adequate oxygenation at strategic points in the targeted tissues during PDT is crucial for increased efficacy, particularly in the image-guided treatment of tumors in solid organs (123). In our evaluation, an image-based tissue oxygen monitoring mechanism coupled with an image-based dose measurement system would be a more feasible approach in clinical transformation.

PHOTOBIOLOGICAL AND CYTOLOGICAL EFFECTS OF PDT

PDT-induced cytotoxicity, causing tumor cell death, is the primary biochemical phenomenon in anticancer PDT. In principle, it is believed that only the cells directly affected by the treatment undergo cell death due to the different toxic agents, and neighboring cells that are not affected by the treatment will live on (6). Recent evidence supports the idea called 'By Stander Effect', which states that cells die in clusters when treated with a photosensitizer and light, not as individuals (6). Dahle *et al.* reported that 'the propagated inactivation' model best describes the spread of dead cells mathematically by a study executed using Madin-Darby Canine Kidney (MDCK) II cells and some other cells (47-50). The available literature proposes no single pathway through which cell death occurs in photodynamic therapy (PDT). Instead, multiple cell death routes are activated due to PDT (1). The primary molecular targets of PDT should be located within a few nanometers from the intercellular site of photosensitizer localization since the singlet oxygen produced has a short-life span and spatially limited diffusion (1). PDT causes tumor cell death via direct pathways such as apoptosis, necrosis, and autophagy and indirectly through vascular shutdown and immune response. The balance between apoptosis and necrosis is considered as a major factor that determines the fate of tumor cells after PDT and also intracellular localization of PS, which is solely determined by the chemical nature of PS and the light fluence of delivered light (4).

Apoptosis
PDT is capable of causing either apoptosis or necrosis, or a combination of both. In the majority of cases, PDT is highly effective in inducing apoptosis (6). Apoptosis, commonly addressed as programmed cell death, is a complex enzyme governed cell death program genetically inherited by all living cells (1). Apoptotic cells stand out due to their characteristic morphological appearance as shrunken cells with condensed nuclear chromatin retracted from surrounding cells (6). The apoptosis process eventually activates a specific protease family known as caspases (cysteine-dependent aspartate specific proteases) (1,6). In PDT, mainly oxidative stress leads to the initiation of apoptosis. Apoptosis is triggered either by the mitochondrial release of cytochrome c or by the activation of cell death receptors, triggering the activation of executioner caspases such as caspase 3, 6, and 7 (6). In cells, caspase activation occurs either by extrinsic or intrinsic apoptotic pathways, which refers to the location of origination of stimuli (1). The extrinsic pathway is activated upon the stimulation of death receptors of the TNFR (tumor necrosis factor receptor) family. The stimuli, such as DNA damage, cytotoxic insults, etc., activate the intrinsic apoptotic pathway, which acts through the mitochondria controlled by proteins in the Bcl-2 family (1). The Bcl-2 family is a set of proteins that has the potential to promote or inhibit apoptosis by adjusting the outer mitochondrial membrane (51).

The convergence of signals from death receptors at the cell surface or damaged sites on mitochondria results in the following changes: a) permeabilization of both inner and outer mitochondrial membranes; b) dissipation of the transmembrane potential of the inner mitochondrial membrane; c) release of cytochrome c and other apoptotic proteins, apoptosis-inducing factor (AIF), the second-mitochondria-derived activator of caspases (SMAC) and specific proteases from the mitochondrial intermembrane space. Although the above-stated mitochondrial changes have implications on apoptotic pathways, their respective order of execution remains in dispute, as reported by Kessel *et al.* and others (6, 52, 53). There are multiple viewpoints about how the discharge of apoptosis-related mitochondrial factors and the collapse of mitochondrial transmembrane potential occur. Permeability transition pore complex (PTPC) is one such model, which ascribes the loss of transmembrane potential and other changes that follows to an opening of a large conducting channel known as permeability transition pore complex (PTPC) formed at the contact sites of the outer and inner mitochondrial membranes (6), which is believed to be consisting of transmembrane proteins such as (a) 30kDa inner membrane adenine nucleotide translocator (ANT), (b) 32kDa outer membrane voltage-dependent anion channel(VDAC) or mitochondrial porin (c) 18kDa outer membrane peripheral benzo-diazepine receptor (PBR), etc. (6). Localization of the photosensitizer in mitochondria has been more efficient in inducing cell killing than PS localization at other cellular sites (6).

Bcl-2 family of proteins controls apoptosis induced by a variety of apoptotic stimuli. The pro-survival Bcl-2 family includes Bcl-2, BclXL, Bcl-w, A1, and Mc11 groups of proteins. It is believed that photodamage caused to pro-survival members of the Bcl-2 family triggers the activation of pro-apoptotic family members. Several *in-vivo* studies

supported this idea, e.g., in cervical cancer cells during the apoptosis induced by 5-ALA mediated PDT, there was significant suppression of Bcl-2 mRNA level and an increase in Bax mRNA level. Similar results were observed with the oesophageal cancer cell line (62) and in hypericin mediated PDT with breast adenocarcinoma cell line where a down-regulation of Bcl-xl and up-regulation of Bax was observed (1,6,62). The Bax: Bcl-2 is known to play a pivotal role in PDT-induced apoptosis. A higher percentage is found to promote cell death via apoptosis, and researchers have recorded evidence to support this (63,64). He *et al.* reported this phenomenon in a study conducted using Chinese hamster ovary cell lines transfected with a Bcl-2 gene. The study results exhibited that in the presence of Bcl-2, the incidence of apoptosis following PDT was significantly lower, and Bcl-2 was capable of inhibiting overall cell killing (62). Genes that code for Bcl-2 family proteins differ between species, putting the validity of *in vivo* studies conducted using non-human cell lines into question. He *et al have* transfected the human Bcl-2 gene into Chinese hamster ovary cells to eliminate inter-specific variability.

Nuclear factor-kappa B (NF-κB) is a transcription factor that promotes gene expression of several proteins related to immune-regulatory and pro-inflammatory processes. NF-κB dimers are found in the cytoplasm in association with an inhibitory subunit; specific inhibitors are IκB factors (6,62). NF-κB is known as an inhibitor of programmed cell death "apoptosis." Granville *et al.* confirmed the idea that NF-κB generates an anti-apoptotic signal following PDT (65,66). Mitogen-activated protein kinases (MAPK) are a critical component of a complex signaling network in cells that regulate gene expression for various external stimuli. The MAPK signaling pathways modulate numerous cellular activities such as mitogen-induced cell cycle progression through the G1 phase, cell movement, and apoptosis (1,62). Apoptosis can be rightly called the most extensively studied form of cell death. Available literature provides a wholesome overview of the factors contributing to and pathways leading to apoptotic cell death, but the sequence of events remains in dispute. PDT-related apoptosis investigations are conclusive and sound, many of them have converged on the same primary factors, yet stimuli triggering apoptosis are poorly understood. Currently accepted mechanisms and signaling pathways have been integrated into computational models to simulate apoptotic cell death based on Monte Carlo stochastic simulations to explore further fluctuations in apoptosis signaling to predict outcomes (34). Mathematical modeling can be used as a tool to investigate the sequence and probability of events following certain intrinsic or extrinsic stimuli. It is fair to propose by designing PS to localize mitochondria using mitochondrial markers; apoptotic cell death can be optimized (28). Another possible approach to promote apoptosis is developing photoactivated chemical factors that bind to cell death receptors triggering apoptotic cell

death pathway. This is already been attempted with the aid of photoCORMs (Carbon Monoxide Releasing Molecules) (26).

Necrosis
Necrosis is considered as accidental and uncontrolled in the manner in which cell death proceeds. It is believed to be operating without the underlying signaling events, but the accumulating evidence suggests the existence of caspase-independent pathways. The occurrence of cellular necrosis proceeds through cytoplasmic and organelle swelling, followed by loss of membrane integrity followed by cellular content discharge, which characterizes necrotic cell death (1,62,68).

Apoptosis operates as the default cell death mechanism, while necrosis will only occur when the activation of caspases fails. Necroptosis is the programmed form of necrotic cell death that proceeds either through FasLigand (FasL), a member of the tumor Necrosis Factor (TNF) family of proteins and tumor necrosis factor-related Apoptosis-Inducing Ligand-Receptor-1 (TRAIL-R) or other members of tumor Necrosis Factor (TNF) family. Fas-Associated protein with Death Domain (FADD) plays an essential role as an adaptor protein in Fas and TRAIL-R-induced necrosis. Still, its part in TNF-induced necrosis remains controversial (62,65,69,70). The basic format of cell death caused by PDT switches to necrosis with PS localized in the plasma membrane and lysosomes. The biochemical pathway leading to necrosis after PDT has yet to be identified. Factors such as intracellular Ca^{2+} and specific ROS have been recognized as necessary in promoting necrotic cell death following PDT (1). Studies conducted so far have not provided sound evidence on the factors at play during necrosis, so it cannot be adapted successfully into a mathematical model to develop simulations for further examination; the molecular biological approach remains the only option available.

Autophagy
Autophagy is a catabolic pathway that allows the degradation of eukaryotic cells and recycles cellular contents. In a basic sense, autophagy contributes to maintaining intracellular and cellular homeostasis. The role of autophagy in causing cell death has raised controversy since its discovery; autophagy is known to accompany cell death, while its pro-survival role is well established (71,99). Autophagy acts as a defense mechanism against ROS-induced damage following PDT by clearing the cells of all the damaged organelles, but its effect on the overall outcome of PDT is yet to be revealed (1,96). Studies on PDT-induced autophagy with different cancer cell lines and PS led to the following conclusions: PDT is capable of direct induction of autophagy independent of PS target. Apoptosis frequently occurs in cells that are already undergoing autophagy following PDT. In cells that can undergo apoptosis, autophagy performs a pro-survival function. In contrast, cells less likely to experience apoptotic cell death promote cell death via

necrosis(62,65). In our view, autophagy needs to be studied in the light of increasing overall cell death; existing literature vaguely indicates the possibilities of autophagy with little evidence to support the claims, the mechanism, and the factors leading to autophagy are yet to be understood.

Vascular Damage
Cytotoxicity and tumor regression have effectively resulted from microvascular stasis and consequential hypoxia. Blood flow stasis following PDT occurs due to combined damage to sensitive microvasculature locations and the consequent physiological responses. It is generally hypothesized that vessel stasis mechanisms begin with perturbation and damage to endothelial cells during light activation of photosensitizers in tissues. The physiological cascade of responses, including platelet aggregation, the release of vasoactive molecules, leukocyte adhesion, an increment of vascular permeability, and vessel constriction, combine to produce blood flow stasis, and the formation of thrombogenic sites within the vessel lumen is a result of endothelial cell damage (72). Studies have revealed that second-generation PS, MV6401 evokes a biphasic vascular response in experimental animals after PDT. The late formation of a thrombus and necrosis following vasoconstriction was the most rapid response observed (73). A delay in tumor growth usually accompanies the vascular effects; similar vascular effects were observed with Photofrin–PDT (1,73). It was noted that angiogenic factors such as vascular endothelial growth factor (VEGF) and cyclooxygenase (COX-2) were upregulated during PDT (74). The action by which blood vessels are formed from the existing ones is termed angiogenesis. Angiogenic factors promote it. The use of specific inhibitors for these angiogenic factors can influence the overall outcome of PDT positively. An investigation conducted utilizing benzoporphyrin derivative monoacid ring A (BPD–MA, Verteporfin) as the PS led to the unveiling of a correlation between the timing of vascular damage and cure, which implies the significant role played by blood flow stasis in tumor destruction following PDT (1,70,73).

Standish *et al*. used interstitial Doppler optical coherence tomography (IS-DOCT) to investigate the microvascular changes during PDT. The study results indicated a dependence of microvascular closure on irradiance rate and total irradiance during PDT. While faster vascular shutdown rates were associated with increasing PDT irradiance rate and total irradiance, a threshold effect at irradiance rates above 66 mW/cm^2 was recorded. No further increase in vascular shutdown rate was reported. Use of irradiance or total irradiance value that causes an abrupt vasculature shut down during PDT limits the supply of molecular oxygen to the region of interest, leading to ineffective treatment, as will a shallow irradiance rate. It is understood that microvascular closure takes place at different rates, and a correlation was found between PDT total irradiance and irradiance rates. These dependencies

can be put into effective use in PDT treatment planning, feedback control for treatment optimization, and post-treatment assessment.

PDT is a complex and dynamic process that requires accurate, real-time assessments of treatment delivery and therapeutic response. IS-DOCT may be a suitable option for real-time monitoring. Still, the difficulty remains in deriving the optimal IS-DOCT/PDT monitoring metrics and predicting treatment response and outcome based on them (37). Only a few biochemical factors leading to blood flow stasis following PDT haven't been revealed experimentally, but available evidence has established a positive correlation between blood flow stasis and tumor cell killing. More *in vivo and in vitro* investigations need to be carried out to identify specific factors and their specific contributions to tumor microvascular closure so that they can be manipulated in favour of increased overall tumor cell death.

Immune Response
One of the first events after PDT at the tumor site is the generation of damage-associated molecular patterns (DAMPs) or so-called 'danger' signals, which contribute as warning signals for innate immune response. Studies on the release of DAMPs following PDT indicated that DAMP associated with PDT could differ in the same cancer cells between in vivo and in vitro settings (73). It was observed that DAMPs released after PDT correlated well with the sub-cellular localization of PS since it's the origin of ROS-induced stress (75). A good correlation between DAMPs and PDT can be established only following further research into the molecular and cellular mechanisms (73). DAMPs released following PDT will be detected by the innate immune cells such as monocytes or macrophages, neutrophils, and dendritic cells (DCs) recruited to the tumor site treated with PDT. Then these innate immune cells infiltrate in massive numbers to attack the damaged tumor cells (75). The innate immune cells' primary function is to neutralize the DAMPs by engulfing and eliminating the cellular debris and compromised tissue components, promoting local healing by restoring normal tissue function.

Investigations have been conducted to identify the factors mediating the crosstalk between the immune system's innate and adaptive sections following PDT. It has been revealed that the enhancement of adaptive anti-tumor immunity by PDT involves the activation of dendritic cells (DCs), which are stimulated by the recognition of DAMPs/Cell Death Associated Molecular Patterns (CDAMPs) discharged by dying tumor cells (75). 70 Kilodalton heat shock proteins(Hsp70) are among the best-characterized DAMPs released following PDT, form stable chaperone complexes with cytoplasmic tumor antigens by HSP-antigen complexes binding to the danger signal receptors, Toll-like receptors 2 and 4on the surface of dendritic cells (73, 75). DCs remain in an immature state in the absence of inflammation. Following tissue inflammation and

release of DAMPs, the dendritic cells (DCs) mature and rush to the draining lymph nodes in massive numbers. The transition to the mature state of DC is correlated with the elevation in the numbers of surface major histocompatibility class I and II molecules (MHC I and MHC II) and the costimulatory molecules CD80 and CD86. Costimulatory molecules are a heterogeneous group of cell surface molecules capable of amplifying or counteracting the initial activating signals given to T cells by the T cell receptor (TCR) following interaction with an antigen/major histocompatibility complex (MHC). These changes permit the DCs to express peptide-MHC complexes at the cell surface and CD4$^+$T helper cells and CD8$^+$cytotoxic T lymphocytes (CTLs) to trigger an adaptive immune response (75). It is not only antigen-specific T cells that can provide post-PDT adaptive immunity but also B cells that produce antigen-specific immunoglobulins, thus mounting the so called humoral immune response. So far, there is only one study conducted by Preise *et al.* displaying the activation of humoral immunity as an implication of PDT-induced systemic antitumor protection (77).

The first clinical case of systemic PDT-immune response was observed and published in 2007, recording PDT of multifocal angiosarcoma of the head and neck located on the right upper limb of a patient, causing spontaneous regression of the untreated distant tumors on the contralateral left upper limb, accompanied by increased immune cell infiltration (78). Kabingu *et al.* (2009) reported that PDT treatment of BCC lesions enhanced the reactivity of patients' lymphocytes against Hip1, a known BCC-associated TA (tumor Antigen) (79). Post PDT adaptive immune response and increased immune cell infiltration are required to be studied extensively in clinical studies before any valid conclusion can be made.

The immunology of tumor cells has been extensively studied with a broad scope of molecular biological approaches as it is crucial to all forms of anticancer therapies. The existing theoretical basis provides a sound background for any future research on post-PDT tumor immune response. Grace *et al.* developed a mathematical model to understand and explore tumor immune cell interactions (38). Our belief is such models integrating PDT will give more insights into how immune response can be regulated to optimize PDT outcome. Although important insights can be gained from mathematical modeling, the development of such models incorporating patient-specific data remains a vital goal yet to be realized for potential clinical benefit.

Effects on Cells Surviving PDT
There is strong evidence suggesting that PDT can cause considerable damage and inhibit the growth rate of tumor cells that survive the PDT procedure. Cancer cells are highly invasive and display a rapid growth rate. A study conducted using ALA\PDT has been able to provide evidence for a deceased cellular invasion in surviving cancer cells (1). In addition to that, reduced mitochondrial function and suppressed cellular invasiveness were the notable phenotypic changes in the surviving tumor cell lines. A correlation was found between the surviving cells' reduced invasive ability and the downregulation of the Epidermal Growth Factor Receptor (EGFR). Researchers confirm that there is a considerable probability that these effects pass on to the progeny (1). Surviving tumor tissue demonstrates a lower growth rate, which may require a cell cycle arrest in the surviving tumor cells. A study conducted with the non-small lung cancer cell line H1299, which used Photofrin /PDT, targeted the G0/G1 phase of the cell cycle, resulting in a notable reduction of Bcl-2 expression (76).

In addition to this, early proteasome malfunction induced G2/M phase arrest, which was time-limited (1). Only lung cancer cell lines A549 and H1299 delivered consistent results concerning the G0/G1 phase arrest hypothesis. An upregulation of p-21 and expression of p-53 and a temporary reduction in Bcl-2 were noted simultaneously with this arrest (80). Ahmad et al. reported similar results with human epidermoid carcinoma cells A431 treated with Pc4/PDT, in addition to cell cycle arrest through G0/G1 phase arrest. It was observed that the expression and activity of cyclin-dependent kinases CDK2, CDK6, and the inhibition of regulatory counterparts cyclin E and cyclin disassociated with G0/G1 phase arrest (1,74,81). Research data provides strong evidence for reduced expression and activity of CDKs in cells following PDT, explaining the observed decreased Rb phosphorylation (1,75).

The role of MAPKs in the survival or death of cells following PDT remains controversial. Research data from time to time reports either promotion or protection from apoptosis caused by MAPK involvement (82,83). NF-κB plays a role in modulating anti-apoptotic gene expression, which may negatively impact tumor destruction (1). NF-κB is also suspected to be involved with tumor recurrence since it may upregulate the expression of specific factors promoting proliferation and angiogenesis. The apparent dichotomy in NF-κB activity has not yet been completely understood (84). The proteasomes' act on substrates as tumor suppressors, signaling molecules, cell cycle regulators, transcription factors, and anti-apoptotic proteins. Thus Synthesis of NF-κB precursor or the degradation of NF-κB suppressor can be controlled by the proteasome (85,86). Arrest or retardation of tumor cell progression may inhibit the proteasome since it would interrupt the systematic degradation of cell cycle proteins and factors such as NF-κB (1,74). Chiaviello *et al.* extensively studied the proteasome activity of lung adenocarcinoma cells with sub-lethal Photofrin/PDT and recorded a reversible inhibition of proteasome activity shortly after photosensitization (87). The effects that are expected to have on the cells surviving PDT are mainly based on the understanding of the cell cycle and cytology. Still, there is a complex network of

parameters at interplay at the cellular level. The available evidence is too few, inconclusive, and contradictory to establish the factors determining the effects on cells surviving PDT. Multiple *in vitro* studies have been done to investigate the effects of cells surviving PDT. It has been found that under the influence of PDT, cellular migration and attachment were suppressed in many cell lines (89,90). It has also been proven that PDT decreases cellular invasion in lung adenocarcinomas, melanoma, breast carcinoma, and head and neck cancer cell lines (91,92). Malignant lesions are treated repeatedly with PDT to achieve a reasonable efficacy; a sound understanding of the effects on the surviving cells and the causative factors might open up possible avenues to induce post-treatment cell death, leading to enhanced overall efficacy.

CLINICAL APPLICATIONS of PDT

Even though the first use of PDT in treating skin cancer was attempted in the 1980s, it helped spread slowly as an alternative treatment technique for other cancer types. The PS used for PDT has come to their third generation, and the search is underway for better and more effective PS with minimum side effects. PDT has been attempted for different types of cancer, and studies have been carried out via clinical trials. PDT is ideally suited to treat skin cancer. The first large clinical trial using hematoporphyrin derivative (HpD) illuminated by red light resulted in more than 85% of complete recovery (CR) rates. Numerous studies have shown that PDT has been able to achieve response rates equivalent to those achieved by conventional anticancer treatment methods for superficial skin cancers (58). Patients with a few localized lesions are treated with a procedure that follows a topical application of ALA a few hours before the illumination. This procedure has reportedly generated excellent CR rates of 86% to 100% for basal cell carcinoma (BCC) (93). One significant drawback of ALA PDT is that the illumination is very painful during the first few minutes. Cold air and local anesthesia can be used to alleviate the pain (88).

Multiple skin-cancer lesions are treated with PDT using a systemic application of PSs such as porfimer sodium or mTHPC, with a recorded CR of 91% for BCC. Treatment periods are found to be shorter for BCC treated with mTHPC PDT (88). The only primary skin neoplastic condition that is not treatable with PDT is malignant melanoma. This type must be surgically uprooted for extensive histopathological examination, prognostic evaluation, and continued management. One treatment session is adequate for neoplastic lesions with a thickness of up to 3 mm. Thicker lesions are usually retreated after follow-up, or pretreated, e.g., with curettage, which means that a layer of the tumor is removed surgically, and PDT is performed on the tumor bed (15).

Clinical trials have proved HpD/PDT and porfimer sodium/PDT to be effective for superficial and recurrent bladder cancer. Response rates were initially high, about 70 to 100%, and the long-term response rates were about 30%-60%. PDT has not become an established treatment method for bladder carcinoma due to the high incidence of side effects such as urinary frequency, pain, and persistent reduction in bladder capacity. But these side effects were caused mainly by the excessive and non-uniform light doses delivered during early clinical studies (88). A standardized procedure with lower drug and light doses or less penetrating light of 514nm for illumination resulted in reasonable CR rates with side effects such as transmural bladder injury and treatment-related morbidity (88). More recent efforts of using ALA/PDT for recurrent superficial bladder cancer produced CR rates of 40%-52% at 18-24 months without a persistent reduction in bladder capacity. In this attempt, ALA /PDT was given as a single treatment and in combination with mitomycin C (94-96). PDT done using green light for illumination coupled with appropriate dosimetry has proven to be a promising in situ treatment option for superficial bladder carcinoma.

Conventional treatment for early-stage head and neck carcinoma is surgery or radiotherapy, while chemoradiation is the standardized treatment for advanced stages. These traditional treatment procedures have their limitations and drawbacks. The surgical treatment procedure for head and neck cancer requires a wide margin, leading to functional damage to adjacent tissue resulting in difficulties in swallowing and speech. Also, radiotherapy has a risk of xerostomia, trismus, and osteonecrosis. At the same time, chemoradiation is related to high morbidity.

In contrast, trials have proved PDT to be equally effective as conventional treatment methods for small superficial tumors, but PDT spared the healthy tissue beneath the tumor. PDT generated excellent long-term functional and cosmetic results in clinical trials, and it could also be utilized in the palliative treatment of recurrent head and neck carcinoma (97). CR rates have been recorded as 85% at year 1 and 77% at two years for early-stage primary tumors in the oral cavity and oropharynx. For lip carcinoma, it was recorded as 96% (97-99). Patients with head and neck cancers have a lifetime risk of 20%-30% of developing second or multiple cancers after the treatment for the primary. In such cases, PDT can be used following radiotherapy or surgery since there is no cumulative tissue toxicity after PDT (97-99). When conventional therapy fails, PDT can also be used as a salvage treatment for recurrent head and neck cancers (63-65). In treating large tumors PDT was used interstitially (97).

Numerous studies have established the therapeutic use of PDT in endobronchial cancer of different stages. Palliative treatment of obstructive endobronchial cancer using HpD or porfimer sodium PDT has been recorded to relieve symptoms in the vast majority of patients (100-103). Side effects

included cough, expectoration of necrotic debris, and dyspnea, in addition to skin photosensitivity, which lasted a few days following the treatment. PDT was recorded to be employed as a curative treatment for early-stage lung cancers, where survival rates were 56%-70% for five years, and for carcinoma-in-situ (CIS), the 5-year survival rate was about 90% (101,104,105). Sometimes, after endobronchial cancers are treated via resection and irradiation, field cancerization or recurrence of tumors may occur. Due to limited pulmonary reserve, these patients cannot undergo irradiation or resection once more, and such patients can be conveniently treated with PDT.

The standard treatment procedure for esophageal cancer is esophagectomy (88), a surgical technique of complete or partial removal of the esophagus via an incision made in the chest or abdomen. Esophagectomy is associated with high morbidity and mortality, leading to the development and application of less invasive techniques to treat esophageal cancer. Endoscopic mucosal resection, coagulation, and PDT were notable among these less invasive methods. Initial studies of PDT were conducted on obstructive esophageal tumors as palliative treatment, and subsequent studies confirmed the efficacy of PDT as a treatment for such tumors (106-108). PDT has an observed CR rate of 87% at six months for treating small superficial tumors in the esophagus. This was achieved by using porfimer sodium as PS, and even mTHPC gave comparable results (109,110). Despite the high efficacy, PDT caused severe side effects in most clinical trials since the esophagus is a thin-walled structure. These side effects ranged from transient skin photosensitivity to stenosis, fistulas, and perforations and were reported in 57% of the patients treated with PDT using red light. It was noticed that when PDT was carried out using less penetrable green light and m-THPC as the PS, fistulas, and perforations were not observed as side effects, and the procedure did not compromise the efficacy (108-110).

Barrett's esophagus is considered a serious complication of GERD (Gastroesophageal reflux disease). In this condition, the normal tissue lining of the esophagus changes to a form that resembles the tissue lining of the intestine. Patients with this condition have a higher risk of developing esophageal cancers, specifically esophageal adenocarcinoma. Researchers have attempted to treat Barrett's esophagus via PDT; the studied document shows a notable reduction in the risk of developing esophageal cancer when patients are treated with porfimer sodium-PDT. In clinical practice, endoscopic mucosal resection is widely used to treat severe conditions of Barrett's esophagus over highly invasive esophagectomy. A combination of endoscopic mucosal resection and PDT has proved to be as effective as esophagectomy in producing CR rates of 83 to 100% in 1 year (111,112). It is fair to conclude PDT as a potential candidate for an alternative anticancer

treatment procedure as it demonstrates average CR rates exceeding 60% for superficial cancers on the skin, head, neck, and in hollow organs, given these rates are highly variable and dependent on parameters such as PS, illumination, tumor size, and tissue oxygenation.

In a systematic review and meta-analysis, Patel *et al.* reported that PDT had a 14% better chance of complete lesion clearance at three months post-treatment than cryotherapy for thin AKs (Actinic keratoses) on the face and scalp (114). A clinical study conducted by Chhatre *et al.* on the survival outcomes of stage III and stage IV Non-Small Cell Lung Cancer (NSCLC) patients observed a lower risk of mortality in the PDT group and radiation with chemotherapy group compared to the radiation alone group (50% and 53% lower, respectively). Among NSCLC (Non-Small Cell Lung Cancer) patients with stage III or stage IV disease not eligible for surgery, the addition of PDT to chemotherapy and radiation therapy offered survival benefits over radiation therapy alone (115). The results of this clinical study provide evidence for the potential use of PDT in later-stage lung cancer to improve survival rates. Due to the large sample size of 147 participants, it is a relatively effective outcome in terms of reliability. Li Bo Li *et al.,* in a retrospective study comparing PDT and chemotherapy on advanced esophageal cancer, concluded; PDT combined with chemotherapy for advanced esophageal cancer is superior to PDT alone and chemotherapy alone (116). It is not about which therapeutic technique triumphs over cancer. It is about ensuring the defeat of cancer. The future of anticancer therapy appears to be complex combination treatments, and PDT has already approved itself as a viable and potent candidate for the blend.

LIMITATIONS, ADVANTAGES, AND DISADVANTAGES OF PDT

PDT has many advantages, potentially promoting its use as an anticancer treatment. In comparison with other treatment modalities used for anticancer therapy, PDT is characterized by the following:
- Selective action on the sensitized tumor
- Minimally invasive technique
- Possibility of being repeated
- No accumulation of toxicity
- The meager mutagenic potential
- Healing is fast with sound cosmetic effects
- Organ functionality is retained
- Short treatment time
- Compared to conventional anticancer treatments, fewer adverse effects
- Cost-effectiveness

Light is delivered selectively to the tumor, which initiates the photodynamic action, so the overall activity of PDT is selective and localized. Due to fewer adverse effects and the absence of accumulated toxicity, the procedure can be repeated in the case of recurrent tumors. The

treatment duration of PDT is shorter compared to conventional treatment methods, and it is also cost-effective. PDT causes minimum damage to the healthy tissue in the vicinity, so the organ functionality remains undisturbed, and the cosmetic effect is also high (113,117).

One of the significant limitations of PDT is that light used to photoactivate the PS cannot penetrate a tissue thicker than 1 cm, which limits the use of PDT in treating tumors on or just below the skin or on the lining of internal organs or cavities (113). PDT is less effective in treating large tumors due to the inability of light penetration deep into large tumors (113,117). PDT is a localized treatment and generally cannot be employed to treat metastasized cancers (113). In clinical practice, PDT is faced with many challenges, including accurate identification of cancer within a respective tissue, precise prediction of the behavior of that cancer, and definitive treatment of the identified target volume. Furthermore, the hurdles included assessing the tissue after treatment to determine whether the planned treatment volume received the intended treatment and providing appropriate follow-up for the untreated part of the tumor, which may lead to the recurrence.

PDT results in residual photosensitivity in patients, which may last for several days after treatment. The therapeutic efficacy of the PDT procedure depends heavily on the accuracy of light delivery to the target site. Tissue oxygenation acts as a limiting factor for the therapeutic efficacy of PDT. Among the adverse effects of PDT, pain is the most prominent one, apart from photosensitivity (117).

SIDE EFFECTS OF PDT

Early-Onset Side Effects
Pain has been an issue of general concern since it is the most common and limiting side effect of conventional PDT. During the clinical trials, it is recorded that about 58% of the patients who have undergone PDT procedures complain about severe pain (93). A painful burning sensation starts almost immediately during the illumination process, which rapidly becomes intense and reaches a peak during the first few minutes. The pain usually decreases with time and subsides towards the end of the treatment procedure (2). Pain can be severe in some instances, stopping light exposure prematurely, leading to inadequate therapeutic results. Thus patients experiencing severe pain are hardly satisfied with the effectiveness and the convenience of PDT, eventually negatively influencing them to discontinue further treatments (93).

PDT-induced pain results from an interplay between intrinsic and extrinsic factors, yet the exact mechanism of PDT-induced pain is unknown. Reactive Oxygen Species (ROS) have been identified as the primary mediators of pain during PDT. The intensity of the pain will depend primarily on the depth of skin at which singlet oxygen is produced,

which is, in turn, dependent on the wavelength of light used for illumination and on the PS. Studies have not reported any correlation between PDT-related pain and age or gender. Some studies vaguely reported a higher intensity of pain in fair-skinned patients, although in general, skin phototype seems not to have any effect on the pain experience (93). Regarding PS, many studies investigated the intensity of pain while using ALA or MAL, but the results are hard to interpret since these drugs are used differently in clinical practice (93).

Other factors that are notable in influencing pain during PDT are lesion type, location, and size of the treatment area. Studies have identified actinic keratosis (AK) as the most painful lesion to treat using PDT. In contrast, the head and neck as the location have the most significant impact on pain perception due to the high nerve density. Researchers also noticed that the lesions on the limbs caused a greater degree of pain during treatment than the lesions in the trunk (117). As a result of many studies conducted, researchers were able to derive a positive correlation between the intensity of the PDT-induced pain and the size of the treatment area (117).

Among Local Skin Reactions (LSRs) developed on the local skin area exposed to light during PDT, erythema and edema are the main phototoxic effects. Erythema is the appearance of redness in the skin, and edema is characterized by swelling of tissue or inflammation. These are the typical inflammatory responses to phototoxicity. A clinical study carried out to investigate the adverse effects using a large sample group of patients undergoing topical PDT over five years recorded 89% of erythema and edema occurrence, 80% of scaling and itching, 9% of crusting, 6% of pustules, 1.2% of erosions and 0.4% of infections (93). Research involving ALA-PDT demonstrated that acute inflammatory response causes immediate stinging, followed by prolonged erythema. The study also revealed the role of histamine as a mediator in bringing about an acute inflammatory response to PDT. It was observed that post-treatment dermal histamine level peaks about 30 minutes after the illumination, remains stable till about 4 hours, then gradually returns to baseline level within about 24 hours following treatment (93).

Clinical research carried out to study the effect of oral H1 antihistamine therapy on reducing LSR didn't find any reduction in the inflammatory response or the therapeutic efficacy of ALA-PDT. So the role of histamine as the key mediator of the post-PDT inflammatory response is still under dispute (93). PDT is also capable of causing local and systemic immunosuppression and reducing delayed-type hypersensitivity (DTH) responses to recall antigens. It was observed that ALA-PDT and MAL-PDT are both immunosuppressive locally, even after one treatment procedure (93). Urticaria, also commonly called hives, is an upsurge of swollen,

pale red bumps or plaques (wheals) on the skin. Literature has described urticarial reactions in response to ALA and MAL PDT, where 0.9% of patients suffered from prevailing severe itching and wheal within the first minute of light exposure (93). Clinicians have recorded the early-onset side effects eagerly. A more systematic and integrated approach can be proposed for studying side effects, as they are mainly outcomes of the innate immune response. In light of such investigations, more insight can be gained on ways and means of minimizing and managing side effects.

Late-Onset Side Effects

PDT has only a few late-onset side effects, which appear to be rare in most cases. These can appear, ranging from a few weeks to months. In rare cases, PDT can induce hyperpigmentation and a sense of fear. Hyperpigmentation is usually a transient condition, displaying a slow resolution in the months following the treatment. The reason for hyperpigmentation is not recorded in the literature, though it is assumed to be a result of phototoxic damage caused to the melanocytes (93). Bullous pemphigoid is a rare skin condition marked by the formation of large, fluid-filled blisters. They are known to develop on areas of skin that often flex — such as the lower abdomen, upper thighs, or armpits. Literature available describes the appearance of BP at sites treated with PDT for Bowen's disease. Yet, the causative mechanism for this condition remains unknown (93).

PDT has the potential to induce or stimulate skin carcinogenesis in patients treated with the procedure. Several literature sources recorded the post-PDT onset of basal cell carcinoma (BCC), invasive squamous cell carcinoma (SCC), and keratoacanthoma (93). Various pathogenic mechanisms, including immunosuppression, mutagenesis, and isotopic response, may lead to carcinogenic risk. The mutagenic effect of PDT remains in dispute. Simultaneously, some researchers claimed that there is no direct effect of PDT on mutagenic DNA; others proposed that ROS generated during photosensitization can cause DNA mutations and oncogene activation (93). The occurrence of skin cancer at the sites exposed to PDT is explained by a concept known as an immunocompromised district (ICD). The idea suggests that a damaged skin area with an immune response imbalance is prone to distinct secondary disease. The role played by PDT as a promoter of skin malignancies is not fully understood, and further studies are required in that regard. Since late on-set side effects less frequently reported are given poor attention in the literature. Immunosuppression and mutagenic effects need to be further explored via in vivo and in vitro models to fully comprehend the causative factors and mechanisms before integrating PDT into mainstream anticancer therapies.

Alleviation of Side Effects

Managing pain is a major challenge in PDT. Different techniques are employed to manage pain during PDT treatment procedures, such as cold air analgesia, topical anesthesia, infiltration anesthesia, and nerve block hypnosis. But none of them has proved to be completely effective. Daylight photodynamic therapy (DL PDT), wherein the exposure to average daylight causes photoactivation of PS without using a directed beam, can be considered a painless alternative to conventional PDT (93,119). In a randomized clinical study conducted to investigate the effect of cold water and pauses in illumination to reduce pain during PDT, one area was cooled during the first half of the illumination. The other area was cooled during the second half of illumination. A three-minute pause was carried out between the two halves of illumination. An immediate fall in pain intensity has been recorded when illumination is stopped (120). A light delivery platform that supports programmable paused illumination equipped with a mechanism to cool the PDT site would be advantageous to promote the application of PDT.

Urticarial reactions are explained by the release of histamine from the mast cells of the dermis. These reactions can be controlled by administering an antihistamine before the treatment (93). Thanos *et al.* showed that the immune suppressive effects of PDT could be reduced by the administration of oral or topical nicotinamide (Vitamin B3) (93). More investigations are needed to verify the effect of antihistamine administration in suppressing urticarial reactions before it becomes a norm in clinical practice.

FUTURE PROSPECTS OF PDT

PDT has excellent potential to be developed into a mainstream anticancer treatment procedure. In recent years, researchers have attempted to utilize modern imaging techniques coupled with molecular biology to monitor and guide PDT procedures. Simultaneously, focus has been given to improving the targeted and selective delivery of PS to the tumor cells. A combination of ground-breaking research and developments in cancer biomarkers, nanotechnology, and targeted molecular medicine has opened a new realm of possibility for anticancer PDT, which is more personalized and predictive than ever before. Combining PDT with conventional anticancer treatments has opened up new opportunities for improved therapeutic efficacy.

Detection of Tumor Biomarkers

Developing a technique to detect the overexpression of several tumor marker genes simultaneously, being aware that a single cell generally expresses more than one altered gene must have a high predictive value in identifying cancer cells amidst the typical cellular background. Fluorescent probes have been designed to detect the levels of expression of different biomarkers in tumor cells and tissues. The expression of

Vidujith AVA et al. JOTCSA. 2022; 9(3): 821-848.

REVIEW ARTICLE

biomarkers such as messenger RNAs (mRNAs) or the presence of a specific mutation in an oncogene in tumor cells can be detected via molecular beacons (MBs) capable of emitting fluorescent signals only after binding to their specific target mRNAs. These biomarkers may work as indicators for a well-defined clinical outcome (118,121). A biomarker is defined as an objectively measured characteristic that describes a normal or abnormal biological state in an organism by analyzing biomolecules such as DNA, RNA, protein, peptide, and biomolecular chemical modifications (122).

A cancer biomarker provides a measurement of the risk of developing cancer in a specific tissue or the risk of cancer progression or possible response to anticancer therapy (122). Identification of these biomarkers using molecular beacon (MB) and fluorescence imaging will enable monitoring tumor growth, progression, and location, thus efficiently guiding PDT treatment. With the advent of molecular biology, cancer biomarkers have been studied at length, even to the extent of developing a new generation of PS that can selectively bind to tumor cells. However, there is a possibility of the variability of tumor marker expression depending on the type and stage of cancer, so the findings of a specific study cannot be generalized without broadly investigating the variability factors.

Targeted and Effective Delivery of PS
Many PS drugs in use are hydrophobic with poor solubility in water (124). As a result, they easily aggregate under physiological conditions, significantly reducing the quantum yields of ROS production (124). The development of effective delivery systems that include customized PS drugs and a mechanism to transfer them into target tissues/cells and addressing critical biological barriers for conventional PS delivery are crucial. In recent days, PS drugs conjugated with nanomaterials have gained attention in the field of PDT due to their ability to circumvent the critical limitations of conventional PS drugs as follows (124). Through hydrophilic properties, nanomaterials can significantly improve the solubility of PS drugs in water by increasing their cellular uptake. Once formed into nanoparticles with nanomaterials, PS drugs can achieve passive targeting of a tumor by the enhanced permeability and retention effect (EPR) (124), which is often attributed to the leaky tumor vasculature and poor lymphatic drainage of tumor tissues. Furthermore, the cell-specificity of PS drugs can be noticeably improved by surface modification of the nanoparticles to bind active targeting moieties such as antibodies, peptides, and aptamers (124).

Incorporating PSs in nanostructured drug delivery units, such as polymeric nanoparticles (PNPs), solid lipid nanoparticles (SLNs), nanostructured lipid carriers (NLCs), gold nanoparticles (AuNPs), hydrogels, liposomes, liquid crystals, dendrimers, and cyclodextrins, is considered as a way of surpassing the limitations of conventional PS. In addition, nanotechnology-based drug delivery systems may improve the transcytosis of a PS through epithelial and endothelial barriers and permit the simultaneous co-delivery of multiple drugs (125).

The novel smart drug delivery and phototoxicity on/off nano-system proposed by Yanchun *et al*. are based on graphene oxide (NGO) as the carrier and modified to implement subcellular targeting and attacking (126). In designing the nano-drug (PPa-NGO-mAb), NGO is modified with the integrin αvβ3 monoclonal antibody (mAb) for tumor targeting. Pyropheophorbide-a (PPa) conjugated with polyethylene-glycol is used to coat the surface of the NGO to induce phototoxicity (126). The polyethylene-glycol phospholipid is loaded to improve water solubility. The results verify that the phototoxicity of PPa on NGO can be switched on and off in organic and aqueous environments, respectively. This smart system also offers a potential alternative to drug delivery systems in anticancer therapy (126). Recent advances in light-activated drug release by various techniques such as photocage, photo-induced isomerization, optical upconversion, and photothermal releases by which different wavelength ranges can be successfully implemented in the effective delivery of PS to the tumor tissues. Light-activated drug release also contributes to controlling undesired photobleaching during the PDT procedure. Joanna *et al*. evaluated the influence of electroporation on the Photofrin uptake and distribution in breast adenocarcinoma cells (MCF-7) and healthy Chinese hamster ovary cells (CHO) lacking voltage-dependent channels in vitro (67). The uptake of Photofrin was measured using flow cytometry and fluorescence microscopy methods. Observations indicated that electropermeabilization of cells in the presence of Photofrin increased the uptake of the photosensitizer (128). Targeted delivery will significantly reduce the PS dose that needs to be administered, thus reducing post-treatment photosensitivity. The metabolism of nanoparticles intended to be used in PS drugs has been studied carefully before any clinical translations. We are optimistic about nano-particle-assisted drug delivery approaches to eventually breakthrough effective and efficient PS delivery during PDT.

Combination Therapy
Combining PDT with conventional anticancer therapies such as chemotherapy, radiotherapy, and novel approaches like immunostimulant and antioxidant agents have been explored in recent years. The studies aimed to find a combined outcome to be additive, synergetic, or antagonistic (131). Though the efficacy of combined therapy is empirical, systematic methods were also employed to analyze its effectiveness. Graphic isobologram and finding combination index are two such methods used (132). Varriale *et al.* and Crescenzi *et al.* mentioned the specific applications of combination index and isobolographic analysis in developing PDT as a combined modality (133).

PDT has a good potential of triggering an anti-tumor immune response by specified mechanisms described early in this review. Combining this anti-tumor immune response with immunostimulants to generate a combined effect has been attempted. These studies have been carried out across various cancer models, including lung cancer, colon cancer, squamous cell carcinoma, melanoma, and breast cancer, and have displayed promising in vivo results with increased survival and reduced tumor volumes (134). To generate combined effects, immunostimulants were administered during PDT intratumorally, intravenously, or topically depending on the type and location of the tumor (135). Although studies did provide substantial evidence that the therapeutic effect of the combination therapy was independent of the type of PS used, many studies used Photofrin as the PS (136,137). Brodin *et al.* summarized the results of recent studies on the applications of PDT as a combined modality with immunostimulants, ionizing radiation, and chemotherapy (134).

PDT combined with ionizing radiation (IR) has shown synergetic effects, but early reports were limited to purely additive results (149,150). Investigations related to Bowmen's Disease (BD) highlighted the synergetic impact of PDT with IR (151). The IR and ALA- PDT combination therapy proved to have improved the therapeutic efficacy of the IR treatment for BD while reducing the irradiation dose with no recorded side effects on the skin (152). It was noted in many studies that the irradiation dose and the time elapsed between the administration of PS and the irradiation played a key role in PDT –IR interaction (153). The possible mechanisms for the high toxicity of the combined therapy may be due to the loss of a critical number of tumor cells and altered biochemical microenvironment, leading to late tissue changes and additive toxicity (154). It is noteworthy that the combination of PDT with IR also utilizes the potential of sure PSs to function as radiosensitizers (149). The results yielded by research to some degree are ambiguous, and it is reasonable to conclude that the interaction between PDT and IR are dependent on numerous parameters such as type of pathology, dose and dose rate of both ionizing radiation and light, and the sequence and time of the treatments (118). Luksiene et al. (149) and Allman et al. (159) reported additive effects, while Sazgarnia et al. (162) found the outcomes to be exceeding that of an additive effect in contrast to Sharma et al. (160), reporting effects less than additive, in their respective *in vitro* tumor models tested with IR – PDT combined therapy.

Another promising emerging approach that uses nanoparticles to enable interaction of PDT with radiotherapy (RT) in treating cancers located in deep tissues was proposed by Chen and Zhang in 2006 (156). This proposed technique uses luminescent nanoparticles to deliver the PS to the target tissue. When irradiation with an appropriate dose of X rays, the nanoparticles scintillate, activating the PS. Thus, the method eliminates the need for an external light source to activate the PS. As the high-energy radiation beams can penetrate deep tissues, this approach might be a feasible way to treat deep tumors (157). The enhanced performance of the combination was established by the investigations executed using Lanthanide doped nanoparticles. Yet, some concerns contribute to the disturbingly reduced efficacy. Out of which most notable, Lanthanide doped nanoparticles exhibit a strong emission between 450 nm and 600 nm while most of the PSs used are porphyrins or their derivatives, which have a maximum absorption at about 400 nm. As a result, lanthanide-based nanoparticles are unable to activate the PS efficiently through scintillation (155). Utilization of the afterglow luminescence combined with scintillation luminescence in photoactivation has yielded positive results in improved PDT- RT combined outcome (157). The metabolic activity-based PET (Positron Emission Tomography) probe, 2-deoxy-2(^{18}F) Fluoro-D-glucose (^{18}FDG) has been attempted to be employed as a substitute for a light source for photoactivation, has proved to be a promising new approach to treat deep tumors (158).

In combining PDT with chemotherapy, many possible options are available in achieving a combined or synergetic outcome (134). Evidence suggests that PDT affects cell membrane permeability, causing better delivery of cytotoxic drugs, leading to a mixed result. Some chemotherapy drugs act as cytotoxic agents and a PS, enabling illumination following the chemotherapy drug administration, giving room to synergetic products (162). Additive and synergetic effects of PDT-chemotherapy combination reduce the required chemotherapy dose, minimizing the possibility of severe side effects. Recent research carried out in the PDT-Chemotherapy combination suggests vastly improved therapeutic efficacy. Table 1 summarizes all the recent studies carried out in that regard (134).

Table 1: Studies conducted on PDT and chemotherapy combination.

Implemented therapy Combination	PS used	Outcome	Reference
Cisplatin (6.25 mg/mL in vitro and 2mg/kg in vivo) along with the photosensitizer prior to PDT was evaluated	In vitro: cells were incubated with 5-aminolevulinic acid(5-ALA) at 25 or 50 mg/mL for 24 h In vivo: 375 mg/kg 5-ALAwas administered 6 h before PDT	(1) Combined 5-ALA PDT and cisplatin increased cytotoxicity (2) greater efficiency against tumor recurrence	Ahn et al. (163)
treatment with 24 h incubation with low-dose cisplatin followed by PDT, evaluated through cell viability and cell death mechanisms	After incubation with cisplatin, cells were incubated with 5-aminolevulinic acid (5-ALA) for 4 hr prior to PDT	(1 with cisplatin doses >1mg/L synergistically enhanced cytotoxicity(2) Increased apoptosis rate, related to upregulation ofp53 and changes in p21, Bcl-2, and Bax expression	Wei et al. (164)
doxorubicin of varying concentration (4-16 mmol/L) on a multidrug-resistant cell line was evaluated in vitro	Cells were incubated with pheophorbide a (Pa) photosensitizer 2 h before PDT	(1) Synergistic effect on cytotoxicity from combined doxorubicin þ PDT mediated by intracellular ROS generation (2) A synergistic effect is observed only in the multidrug-resistant line	Cheung et al. (165)
Gefitinib, which can inhibit ABCG2 protein-mediated efflux of porphyrin out from neoplastic cells, was assessed at different concentrations in vitro in combination with PDT	Following gefitinib incubation, cells were incubated with 1 mmol/L 5-aminolevulinic acid (5- ALA) for 6 h prior to PDT	(1) outcome was a dose-dependent reduction of the surviving glioma fraction(2) Effect due to decreased ABCG2 expression and subsequent increase in intracellular porphyrin levels	Sun et al. (166)
The apoptosis-inducing protein apoptin experimented in combination with PDT via PVP3 plasmid administration	Cells were incubated with 5-aminolevulinic acid (5-ALA) at 1 mmol/L for 6h before PDT, and the mice were administered 5-ALAat 100 mg/kg 3 h prior to PDT	Notably, stronger antitumor effects in vitro and in vivo compared to monotherapies	Fang et al. (167)
5-FU, gemcitabine, oxaliplatin and cis-diammine dichloroplatinum chemotherapy in combination with PDT in vitro and gemcitabine and oxaliplatin in combined with PDT in vivo	Cells were incubated for 24 h with 20 mg/mL talaporfin sodium (TPS) photosensitizer. The mice were injected with 5 mg/kg TPS at 2 h before PDT	(1) Significant increase in tumor necrotic area and apoptosis-positive cells (2) Synergistic cytotoxicity increase from oxaliplatin and gemcitabine þ PDT	Nonaka et al. (168)

Implemented therapy Combination	PS used	Outcome	Reference
PDT was combined with 5 mg/kg Adriamycin to investigate increased antitumor effects through potentially enhanced apoptosis and inhibited tumor angiogenesis	The photosensitizer benzoporphyrin derivative monoacid ring (BPD-MA) was intravenously injected 24 h before PDT at 1 mg/kg	(1) Adriamycin PDT resulted in significantly reduced tumor volumes (2) Also, a considerable increase in survival compared to separate Adriamycin or PDT	Tong et al. (169)
Combining doxorubicin or vincristine with PDT in the treatment of sensitive or resistant murine leukemia cells was experimented	Cells were incubated for 4 h prior to PDT with 1 mmol/ L 5-aminolevulinic acid (5-ALA)	(1)Chemotherapy-resistant LBR-D160 and LBR- V160 cell lines were sensitive to 5-ALA PDT (2) No increase in treatment efficacy	Diez et al. (170)
The polytherapy combination of Navelbine or cisplatin chemotherapy followed by PDT, and by adoptive immunotherapy with splenic lymphocytes from PDT-treated mice was investigated	mTHPC (Foscan) was administered post-chemotherapy and 24 h prior to PDT at 0.3 mg/kg	(1) Chemotherapy, PDT and adoptive immunotherapy was successful against this aggressive metastatic tumor (2) PDT or chemotherapy alone showed no survival advantage over control	Canti et al. (171)

Other than studies conducted by Diez et al. and Canti et al., all further investigations reported positive outcomes in terms of increased cytotoxicity and tumor control. Cheung et al. and Nonaka et al. observed synergetic effects between PDT and chemotherapy in their respective *in vivo* and *in vitro* studies. Chemotherapy is widely used as an anticancer therapy; the combined use of PDT can be promoted as a way forward to familiarize PDT. Since the synergetic effects are highly dependent on the PS used, the outcomes of these investigations cannot be generalized. An acceptable range of *in vivo* and *in vitro* studies to unveil the variables that determine synergetic and increased cytotoxic effects, followed by clinical investigations, will be a feasible way forward for this combined modality.

The use of antioxidant agents or radical scavengers ought to nullify or counteract the effects caused by PDT, but several studies propose otherwise (132). Buettner e*t al.* reported having metal traces (in their case, iron). Ascorbate combined with Photofrin/PDT caused a heightened production of radicals and decreased cell survival of various cell lines (132). A cooperative therapeutic outcome was observed when ascorbate was associated with other photosensitizers in other systems under different conditions (132). Many studies have proposed various interpretations and explanations. Finally, it was concluded that the enhanced toxicity of the photodynamic action results from the augmented formation of highly diffusible hydrogen peroxide and other toxic radicals on the addition of ascorbate to cells expressing high myeloperoxidase levels followed by photosensitization (172). Melnikova *et al.* recorded the efficacy of m-tetrahydroxyphenylchlorinmTHPC/PDT could be synergistically improved in the presence of alpha-tocopherol, but only at the elevated concentrations of vitamin in a study with HT29 adenocarcinoma cells and MRC-25 normal fibroblasts (173). While the final therapeutic outcome of incorporating antioxidants with PDT may depend on many variables, including antioxidant concentration, the presence or absence of catalytic trace metals, the order and the time interval between the administration of the drug and the light exposure, the light fluence, the oxygen accessibility and more (132). Since variables are too many use of antioxidants for enhanced PDT is not a promising area for future explorations.

CONCLUSIONS

Over the past several decades, many researchers have committed to making PDT a viable alternative treatment procedure for cancer. Still, PDT has not become a mainstream anticancer therapeutic procedure, owing to its poor efficacy and inability to treat deeper lesions; despite the past, we can be hopeful for the near future. New approaches are being looked into to increase the therapeutic efficacy of PDT and the reach of PDT to deep tumors. Most of the studies conducted on the novel approaches have yielded promising results consistently. In our view, combining PDT with conventional anticancer therapies, enhanced light delivery, and dosimetric systems, 3rd generation PS coupled with nanotechnology based targeted drug delivery, and effective and systematic management of side effects are the key areas where a breakthrough can be expected. The use of mathematical modeling as a tool, where possible, will contribute immensely to quickening the pace of broader investigations conducted to validate previous findings. It is crucial that adequate *in vivo* and *in vitro* testing should be performed prior to any clinical interpretation.

ACKNOWLEDGMENTS

REFERENCES

1. Chiaviello A, Postiglione I, Palumbo G. Targets and Mechanisms of Photodynamic Therapy in Lung Cancer Cells: A Brief Overview. Cancers. 2011 Mar 3;3(1):1014–41. <DOI>.

2. Dougherty TJ, Gomer CJ, Henderson BW, Jori G, Kessel D, Korbelik M, et al. Photodynamic Therapy. JNCI Journal of the National Cancer Institute. 1998 Jun 17;90(12):889–905. <DOI>.

3. Abrahamse H, Hamblin MR. New photosensitizers for photodynamic therapy. Biochemical Journal. 2016 Feb 15;473(4):347–64. <DOI>.

4. Bechet D, Couleaud P, Frochot C, Viriot ML, Guillemin F, Barberi-Heyob M. Nanoparticles as vehicles for delivery of photodynamic therapy agents. Trends in Biotechnology. 2008 Nov;26(11):612–21. <DOI>.

5. Oleinick N, Morris R, Belichenko I. The role of apoptosis in response to photodynamic therapy: what, where, why, and how. Photochem Photobiol Sci. 2002 Jan 7;1(1):1–21. <DOI>.

6. Nyman ES, Hynninen PH. Research advances in the use of tetrapyrrolic photosensitizers for photodynamic therapy. Journal of Photochemistry and Photobiology B: Biology. 2004 Jan;73(1–2):1–28. <DOI>.

7. D'Hallewin MA, De Witte PA, Waelkens E, Merlevede W, Baert L. Fluorescence detection of flat bladder carcinoma in situ after intravesical instillation of hypericin. Journal of Urology. 2000 Aug;164(2):349–51. <DOI>.

8. Wang S, Bromley E, Xu L, Chen JC, Keltner L. Talaporfin sodium. Expert Opinion on Pharmacotherapy. 2010 Jan;11(1):133–40. <DOI>.

9. Kataoka H, Nishie H, Hayashi N, Tanaka M, Nomoto A, Yano S, et al. New photodynamic therapy with next-generation photosensitizers. Ann Transl Med. 2017 Apr;5(8):183. <DOI>.

10. Bonnett R, Djelal BD, Hamilton PA, Martinez G, Wierrani F. Photobleaching of 5,10,15,20-tetrakis(m-hydroxyphenyl)porphyrin (m-THPP) and the corresponding chlorin (m-THPC) and bacteriochlorin(m-THPBC). A comparative study. Journal of Photochemistry and Photobiology B: Biology. 1999 Nov;53(1–3):136–43. <DOI>.

11. Dysart JS, Singh G, Patterson MS. Calculation of Singlet Oxygen Dose from Photosensitizer Fluorescence and Photobleaching During mTHPC Photodynamic Therapy of MLL Cells¶. Photochemistry and Photobiology. 2007 May 23;81(1):196–205. <DOI>.

12. Jarvi MT, Patterson MS, Wilson BC. Insights into Photodynamic Therapy Dosimetry: Simultaneous Singlet Oxygen Luminescence and Photosensitizer Photobleaching Measurements. Biophysical Journal. 2012 Feb;102(3):661–71. <DOI>.

13. Sharwani A, Alharbi FA. Monitoring of photobleaching in photodynamic therapy using fluorescence spectroscopy. Gulf J Oncolog. 2014 Jul;1(16):79–83. PMID: 25316396.

14. Svanberg K, Bendsoe N, Axelesson J, Engles S, Svanberg S. Photodynamic therapy: superficial and interstitial illumination. J Biomed Opt. 2010 Jul 1;15(4):485–505. <DOI>.

15. Weersink R, Lilge L. Fluorescence in photodynamic therapy dosimetry. In: Hamblin MR, Mróz P, editors. Advances in photodynamic therapy: basic, translational, and clinical. Boston, Mass: Artech House; 2008. p. 91–110. (Artech House engineering in medicine & biology series). ISBN: 978-1-59693-277-7.

16. Jerjes W, Upile T, Alexander Mosse C, Hamdoon Z, Morcos M, Morley S, et al. Prospective evaluation of 110 patients following ultrasound-guided photodynamic therapy for deep seated pathologies. Photodiagnosis and Photodynamic Therapy. 2011 Dec;8(4):297–306. <DOI>.

Vidujith AVA et al. JOTCSA. 2022; 9(3): 821-848.

REVIEW ARTICLE

17. de Bruijn HS, Kruijt B, van der Ploeg – van den Heuvel A, Sterenborg HJCM, Robinson DJ. Increase in protoporphyrin IX after 5-aminolevulinic acid based photodynamic therapy is due to local re-synthesis. Photochem Photobiol Sci. 2007;6(8):857. <DOI>.

18. Pogue BW, Momma T, Wu HC, Hasan T. Transient absorption changes in vivo during photodynamic therapy with pulsed-laser light. Br J Cancer. 1999 May;80(3–4):344–51. <DOI>.

19. Grecco C, Moriyama LT, Cosci A, Pratavieira S, Bagnato VS, Kurachi C. Necrosis response to photodynamic therapy using light pulses in the femtosecond regime. Lasers in medical science. 2013;28(4):1177–82.

20. Pogue BW, Lilge L, Patterson MS, Wilson BC, Hasan T. Absorbed photodynamic dose from pulsed versus continuous wave light examined with tissue-simulating dosimeters. Appl Opt. 1997 Oct 1;36(28):7257. <DOI>.

21. Sterenborg HJCM, Gemert MJC van. Photodynamic therapy with pulsed light sources: a theoretical analysis. Phys Med Biol. 1996 May 1;41(5):835–49. <DOI>.

22. Swartling J, Höglund OV, Hansson K, Södersten F, Axelsson J, Lagerstedt AS. Online dosimetry for temoporfin-mediated interstitial photodynamic therapy using the canine prostate as model. J Biomed Opt. 2016 Feb 17;21(2):028002. <DOI>.

23. Davidson SRH, Weersink RA, Haider MA, Gertner MR, Bogaards A, Giewercer D, et al. Treatment planning and dose analysis for interstitial photodynamic therapy of prostate cancer. Phys Med Biol. 2009 Apr 21;54(8):2293–313. <DOI>.

24. Peng TI, Chang CJ, Guo MJ, Wang YH, Yu JS, Wu HY, et al. Mitochondrion-Targeted Photosensitizer Enhances the Photodynamic Effect-Induced Mitochondrial Dysfunction and Apoptosis. Annals of the New York Academy of Sciences. 2005 May;1042(1):419–28. <DOI>.

25. Vidhyapriya P, Divya D, Manimaran B, Sakthivel N. Photoactivated [Mn(CO)3Br(μ-bpcpd)]2 induces apoptosis in cancer cells via intrinsic pathway. Journal of Photochemistry and Photobiology B: Biology. 2018 Nov;188:28–41. <DOI>.

26. Morgan WF. Non-targeted and Delayed Effects of Exposure to Ionizing Radiation: II. Radiation-Induced Genomic Instability and Bystander Effects In Vivo, Clastogenic Factors and Transgenerational Effects. Radiation Research. 2003 May;159(5):581–96. <DOI>.

27. Luksiene Z, Juzenas P, Moan J. Radiosensitization of tumours by porphyrins. Cancer Letters. 2006 Apr;235(1):40–7. <DOI>.

28. Axelsson J, Davis SC, Gladstone DJ, Pogue BW. Cerenkov emission induced by external beam radiation stimulates molecular fluorescence: Cerenkov emission stimulates molecular fluorescence. Med Phys. 2011 Jun 23;38(7):4127–32. <DOI>.

29. Kotagiri N, Sudlow GP, Akers WJ, Achilefu S. Breaking the depth dependency of phototherapy with Cerenkov radiation and low-radiance-responsive nanophotosensitizers. Nature Nanotech. 2015 Apr;10(4):370–9. <DOI>.

30. Chen W, Zhang J. Using Nanoparticles to Enable Simultaneous Radiation and Photodynamic Therapies for Cancer Treatment. J Nanosci Nanotech. 2006 Apr 1;6(4):1159–66. <DOI>.

31. Morgan NY, Kramer-Marek G, Smith PD, Camphausen K, Capala J. Nanoscintillator Conjugates as Photodynamic Therapy-Based Radiosensitizers: Calculation of Required Physical Parameters. Radiation Research. 2009 Feb;171(2):236–44. <DOI>.

32. Bulin AL, Vasil'ev A, Belsky A, Amans D, Ledoux G, Dujardin C. Modelling energy deposition in nanoscintillators to predict the efficiency of the X-ray-induced photodynamic effect. Nanoscale. 2015;7(13):5744–51. <DOI>.

33. Bulin AL, Truillet C, Chouikrat R, Lux F, Frochot C, Amans D, et al. X-ray-Induced Singlet Oxygen Activation with Nanoscintillator-Coupled Porphyrins. J Phys Chem C. 2013 Oct 17;117(41):21583–9. <DOI>.

34. Chen H, Wang GD, Chuang YJ, Zhen Z, Chen X, Biddinger P, et al. Nanoscintillator-Mediated X-ray Inducible Photodynamic Therapy for In Vivo Cancer Treatment. Nano Lett. 2015 Apr 8;15(4):2249–56. <DOI>.

35. Zhang C, Zhao K, Bu W, Ni D, Liu Y, Feng J, et al. Marriage of Scintillator and Semiconductor for Synchronous Radiotherapy and Deep Photodynamic Therapy with Diminished Oxygen Dependence. Angew Chem Int Ed. 2015 Feb 2;54(6):1770–4. <DOI>.

36. Raychaudhuri S, Willgohs E, Nguyen TN, Khan EM, Goldkorn T. Monte Carlo Simulation of Cell Death Signaling Predicts Large Cell-to-Cell Stochastic Fluctuations through the Type 2 Pathway of Apoptosis. Biophysical Journal. 2008 Oct;95(8):3559–62. <DOI>.

37. Mahlbacher GE, Reihmer KC, Frieboes HB. Mathematical modeling of tumor-immune cell interactions. Journal of Theoretical Biology. 2019 May;469:47–60. <DOI>.

38. Standish BA, Jin X, Smolen J, Mariampillai A, Munce NR, Wilson BC, et al. Interstitial Doppler optical coherence tomography monitors

microvascular changes during photodynamic therapy in a Dunning prostate model under varying treatment conditions. J Biomed Opt. 2007;12(3):034022. <DOI>.

39. Johansson A, Johansson T, Thompson MS, Bendsoe N, Svanberg K, Svanberg S, et al. In vivo measurement of parameters of dosimetric importance during interstitial photodynamic therapy of thick skin tumors. J Biomed Opt. 2006;11(3):034029. <DOI>.

40. Johansson A, Soto Thompson M, Johansson T, Bendsoe N, Svanberg K, Svanberg S, et al. System for integrated interstitial photodynamic therapy and dosimetric monitoring. In: Kessel D, editor. San Jose, CA; 2005 [cited 2022 May 7]. p. 130. <DOI>.

41. Johansson A, Hjelm J, Eriksson A, Andersson-Engels S. Pre-Treatment Dosimetry for Interstitial Photodynamic Therapy. In: Therapeutic Laser Applications and Laser-Tissue Interactions II [Internet]. Munich, Germany: OSA; 2005 [cited 2022 May 7]. p. TuA1. <DOI>.

42. Johansson A, Axelsson J, Andersson-Engels S, Swartling J. Realtime light dosimetry software tools for interstitial photodynamic therapy of the human prostate: Realtime prostate-PDT dosimetry. Med Phys. 2007 Oct 19;34(11):4309–21. <DOI>.

43. Stenberg M, Thompson MS, Johansson T, Palsson S, af Klinteberg C, Andersson-Engels S, et al. Interstitial photodynamic therapy: diagnostic measurements and treatment in experimental malignant rat tumors. In: Bigio IJ, Mueller GJ, Puppels GJ, Steiner RW, Svanberg K, editors. Amsterdam, Netherlands; 2000 [cited 2022 May 7]. p. 151. <DOI>.

44. Johansson T, Soto Thompson M, Stenberg M, Klinteberg C af, Andersson-Engels S, Svanberg S, et al. Feasibility study of a system for combined light dosimetry and interstitial photodynamic treatment of massive tumors. Appl Opt. 2002 Mar 1;41(7):1462. <DOI>.

45. Soto Thompson M, Johansson A, Johansson T, Andersson-Engels S, Svanberg S, Bendsoe N, et al. Clinical system for interstitial photodynamic therapy with combined on-line dosimetry measurements. Appl Opt. 2005 Jul 1;44(19):4023. <DOI>.

46. Johansson A, Johansson T, Thompson MS, Bendsoe N, Svanberg K, Svanberg S, et al. In vivo measurement of parameters of dosimetric importance during interstitial photodynamic therapy of thick skin tumors. J Biomed Opt. 2006;11(3):034029. <DOI>.

47. Dahle J, Kaalhus O, Moan J, Steen HB. Cooperative effects of photodynamic treatment of cells in microcolonies. Proc Natl Acad Sci USA. 1997 Mar 4;94(5):1773–8. <DOI>.

48. Dahle J, Steen HB, Moan J. The Mode of Cell Death Induced by Photodynamic Treatment Depends on Cell Density. Photochem Photobiol. 1999 Sep;70(3):363–7. <DOI>.

49. Dahle J. The bystander effect in photodynamic inactivation of cells. Biochimica et Biophysica Acta (BBA) - General Subjects. 2000 Jul 26;1475(3):273–80. <DOI>.

50. Dahle J, Mikalsen SO, Rivedal E, Steen HB. Gap Junctional Intercellular Communication is not a Major Mediator in the Bystander Effect in Photodynamic Treatment of MDCK II Cells. Radiation Research. 2000 Sep;154(3):331–41. <DOI>.

51. Shamas-Din A, Kale J, Leber B, Andrews DW. Mechanisms of Action of Bcl-2 Family Proteins. Cold Spring Harbor Perspectives in Biology. 2013 Apr 1;5(4):a008714–a008714. <DOI>.

52. Kroemer G, Reed JC. Mitochondrial control of cell death. Nat Med. 2000 May;6(5):513–9. <DOI>.

53. Reed JC. Mechanisms of Apoptosis. The American Journal of Pathology. 2000 Nov;157(5):1415–30. <DOI>.

54. Oseroff AR, Ohuoha D, Ara G, McAuliffe D, Foley J, Cincotta L. Intramitochondrial dyes allow selective in vitro photolysis of carcinoma cells. Proc Natl Acad Sci USA. 1986 Dec;83(24):9729–33. <DOI>.

55. Ball DJ, Luo Y, Kessel D, Griffiths J, Brown SB, Vernon DI. The induction of apoptosis by a positively charged methylene blue derivative. Journal of Photochemistry and Photobiology B: Biology. 1998 Feb;42(2):159–63. <DOI>.

56. Pluskalová M, Pešlová G, Grebeňová D, Halada P, Hrkal Z. Photodynamic treatment (ALA-PDT) suppresses the expression of the oncogenic Bcr-Abl kinase and affects the cytoskeleton organization in K562 cells. Journal of Photochemistry and Photobiology B: Biology. 2006 Jun;83(3):205–12. <DOI>.

57. Tedesco AC, Sousa G, Zângaro RA, Silva NS, Pacheco MTT, Pacheco-Soares C, et al. Analysis of mitochondria, endoplasmic reticulum and actin filaments after PDT with AlPcS 4. Lasers in Medical Science. 2004 Mar 1;18(4):207–12. <DOI>.

58. Tsai JC, Wu CL, Chien HF, Chen CT. Reorganization of cytoskeleton induced by 5-aminolevulinic acid-mediated photodynamic therapy and its correlation with mitochondrial dysfunction. Lasers Surg Med. 2005 Jun;36(5):398–408. <DOI>.

59. Kvam E, Stokke T, Moan J. The lengths of DNA fragments light-induced in the presence of a photosensitizer localized at the nuclear membrane of human cells. Biochimica et Biophysica Acta (BBA) - Gene Structure and Expression. 1990 May;1049(1):33–7. <DOI>.

60. Akhlynina TV, Jans DA, Rosenkranz AA, Statsyuk NV, Balashova IY, Toth G, et al. Nuclear Targeting of Chlorin e6 Enhances Its Photosensitizing Activity. Journal of Biological Chemistry. 1997 Aug;272(33):20328–31. <DOI>.

61. Xue L yan, Chiu S mao, Oleinick NL. Photodynamic Therapy-Induced Death of MCF-7 Human Breast Cancer Cells: A Role for Caspase-3 in the Late Steps of Apoptosis but Not for the Critical Lethal Event. Experimental Cell Research. 2001 Feb;263(1):145–55. <DOI>.

62. Mroz P, Yaroslavsky A, Kharkwal GB, Hamblin MR. Cell Death Pathways in Photodynamic Therapy of Cancer. Cancers. 2011 Jun 3;3(2):2516–39. <DOI>.

63. Kim H, Luo Y, Li G, Kessel D. Enhanced Apoptotic Response to Photodynamic Therapy after bcl-2 Transfection. Cancer Res. 1999;59(14):3429–32. <URL>.

64. Srivastava M, Ahmad N, Gupta S, Mukhtar H. Involvement of Bcl-2 and Bax in Photodynamic Therapy-mediated Apoptosis. Journal of Biological Chemistry. 2001 Jan;276(18):15481–8. <DOI>.

65. Duprez L, Wirawan E, Berghe TV, Vandenabeele P. Major cell death pathways at a glance. Microbes and Infection. 2009 Nov;11(13):1050–62. <DOI>.

66. Granville DJ, Carthy CM, Jiang H, Levy JG, McManus BM, Matroule JY, et al. Nuclear factor-κB activation by the photochemotherapeutic agent verteporfin. Blood. 2000 Jan 1;95(1):256–62. <DOI>.

67. Assefa Z, Vantieghem A, Declercq W, Vandenabeele P, Vandenheede JR, Merlevede W, et al. The Activation of the c-Jun N-terminal Kinase and p38 Mitogen-activated Protein Kinase Signaling Pathways Protects HeLa Cells from Apoptosis Following Photodynamic Therapy with Hypericin. Journal of Biological Chemistry. 1999 Mar;274(13):8788–96. <DOI>.

68. Danial NN, Korsmeyer SJ. Cell Death. Cell. 2004 Jan;116(2):205–19. <DOI>.

69. Lin Y, Choksi S, Shen HM, Yang QF, Hur GM, Kim YS, et al. Tumor Necrosis Factor-induced Nonapoptotic Cell Death Requires Receptor-interacting Protein-mediated Cellular Reactive Oxygen Species Accumulation. Journal of Biological Chemistry. 2004 Mar;279(11):10822–8. <DOI>.

70. Holler N, Zaru R, Micheau O, Thome M, Attinger A, Valitutti S, et al. Fas triggers an alternative, caspase-8–independent cell death pathway using the kinase RIP as effector molecule. Nat Immunol. 2000 Dec;1(6):489–95. <DOI>.

71. Maiuri MC, Zalckvar E, Kimchi A, Kroemer G. Self-eating and self-killing: crosstalk between autophagy and apoptosis. Nat Rev Mol Cell Biol. 2007 Sep;8(9):741–52. <DOI>.

72. Fingar VH. Vascular Effects of Photodynamic Therapy. Journal of Clinical Laser Medicine & Surgery. 1996 Oct;14(5):323–8. <DOI>.

73. Agostinis P, Berg K, Cengel KA, Foster TH, Girotti AW, Gollnick SO, et al. Photodynamic therapy of cancer: An update. CA: A Cancer Journal for Clinicians. 2011 Jul;61(4):250–81. <DOI>.

74. Crescenzi E, Chiaviello A, Canti G, Reddi E, Veneziani BM, Palumbo G. Low doses of cisplatin or gemcitabine plus Photofrin/photodynamic therapy: Disjointed cell cycle phase-related activity accounts for synergistic outcome in metastatic non–small cell lung cancer cells (H1299). Mol Cancer Ther. 2006 Mar;5(3):776–85. <DOI>.

75. Reginato E. Immune response after photodynamic therapy increases anti-cancer and anti-bacterial effects. WJI. 2014;4(1):1. <DOI>.

76. Preise D, Oren R, Glinert I, Kalchenko V, Jung S, Scherz A, et al. Systemic antitumor protection by vascular-targeted photodynamic therapy involves cellular and humoral immunity. Cancer Immunol Immunother. 2009 Jan;58(1):71–84. <DOI>.

77. Thong PSP, Ong KW, Goh NSG, Kho KW, Manivasager V, Bhuvaneswari R, et al. Photodynamic-therapy-activated immune response against distant untreated tumours in recurrent angiosarcoma. The Lancet Oncology. 2007 Oct;8(10):950–2. <DOI>.

78. Kabingu E, Oseroff AR, Wilding GE, Gollnick SO. Enhanced Systemic Immune Reactivity to a Basal Cell Carcinoma Associated Antigen Following Photodynamic Therapy. Clin Cancer Res. 2009 Jul 1;15(13):4460–6. <DOI>.

79. Crescenzi E, Chiaviello A, Canti G, Reddi E, Veneziani BM, Palumbo G. Low doses of cisplatin or gemcitabine plus Photofrin/photodynamic therapy: Disjointed cell cycle phase-related activity accounts for synergistic outcome in metastatic non–small cell lung cancer cells (H1299). Mol Cancer Ther. 2006 Mar;5(3):776–85. <DOI>.

80. Crescenzi E, Varriale L, Iovino M, Chiaviello A, Veneziani BM, Palumbo G. Photodynamic therapy with indocyanine green complements and enhances low-dose cisplatin cytotoxicity in MCF-7 breast cancer cells. Molecular cancer therapeutics. 2004;3(5):537–44.

81. Ahmad N, Feyes DK, Agarwal R, Mukhtar H. Photodynamic therapy results in induction of WAF1/CIP1/P21 leading to cell cycle arrest and apoptosis. Proc Natl Acad Sci USA. 1998 Jun 9;95(12):6977–82. <DOI>.

Vidujith AVA et al. JOTCSA. 2022; 9(3): 821-848.

REVIEW ARTICLE

82. Xue L yan, He J, Oleinick NL. Promotion of photodynamic therapy-induced apoptosis by stress kinases. Cell Death Differ. 1999 Sep;6(9):855–64. <DOI>.

83. Assefa Z, Vantieghem A, Declercq W, Vandenabeele P, Vandenheede JR, Merlevede W, et al. The Activation of the c-Jun N-terminal Kinase and p38 Mitogen-activated Protein Kinase Signaling Pathways Protects HeLa Cells from Apoptosis Following Photodynamic Therapy with Hypericin. Journal of Biological Chemistry. 1999 Mar;274(13):8788–96. <DOI>.

84. Coupienne I, Piette J, Bontems S. How to Monitor NF-κB Activation After Photodynamic Therapy. In: Gomer CJ, editor. Photodynamic Therapy [Internet]. Totowa, NJ: Humana Press; 2010 [cited 2022 May 7]. p. 79–95. (Methods in Molecular Biology; vol. 635). <URL>.

85. Karin M, Cao Y, Greten FR, Li ZW. NF-κB in cancer: from innocent bystander to major culprit. Nat Rev Cancer. 2002 Apr;2(4):301–10. <DOI>.

86. Palombella V, Rando O, Goldberg A, Maniatis T. The Ubiquitin-Proteasome Pathway is required for processing the NF-kappa B1 Precursor Protein and the Activation of NF-kappa B. Cell. 1994;78:773–85.

87. Chiaviello A, Paciello I, Postiglione I, Crescenzi E, Palumbo G. Combination of photodynamic therapy with aspirin in human-derived lung adenocarcinoma cells affects proteasome activity and induces apoptosis: PDT and aspirin. Cell Proliferation. 2010 Aug 30;43(5):480–93. <DOI>.

88. Uzdensky A, Kolpakova E, Juzeniene A, Juzenas P, Moan J. The effect of sub-lethal ALA-PDT on the cytoskeleton and adhesion of cultured human cancer cells. Biochimica et Biophysica Acta (BBA) - General Subjects. 2005 Feb;1722(1):43–50. <DOI>.

89. Schreiber S, Gross S, Brandis A, Harmelin A, Rosenbach-Belkin V, Scherz A, et al. Local photodynamic therapy (PDT) of rat C6 glioma xenografts with Pd-bacteriopheophorbide leads to decreased metastases and increase of animal cure compared with surgery. Int J Cancer. 2002 May 10;99(2):279–85. <DOI>.

90. Tsai T, Ji HT, Chiang PC, Chou RH, Chang WSW, Chen CT. ALA-PDT results in phenotypic changes and decreased cellular invasion in surviving cancer cells: sustained ala-pdt reduced cellular invasion. Lasers Surg Med. 2009 Apr;41(4):305–15. <DOI>.

91. Yang TH, Chen CT, Wang CP, Lou PJ. Photodynamic therapy suppresses the migration and invasion of head and neck cancer cells in vitro. Oral Oncology. 2007 Apr;43(4):358–65. <DOI>.

92. Triesscheijn M, Baas P, Schellens JHM, Stewart FA. Photodynamic Therapy in Oncology. The Oncologist. 2006 Oct 1;11(9):1034–44. <DOI>.

93. Borgia F, Giuffrida R, Caradonna E, Vaccaro M, Guarneri F, Cannavò S. Early and Late Onset Side Effects of Photodynamic Therapy. Biomedicines. 2018 Jan 29;6(1):12. <DOI>.

94. Waidelich R, Beyer W, Knchel R, Stepp H, Baumgartner R, Schrder J, et al. Whole bladder photodynamic therapy with 5-aminolevulinic acid using a white light source. Urology. 2003 Feb;61(2):332–7. <DOI>.

95. Kriegmair M, Baumgartner R, Lumper W, Waidelich R, Hofstetter A. Early clinical experience with 5-aminolevulinic acid for the photodynamic therapy of superficial bladder cancer. BJU Int. 1996 May;77(5):667–71. <DOI>.

96. Skyrme RJ, French AJ, Datta SN, Allman R, Mason MD, Matthews PN. A phase-1 study of sequential mitomycin C and 5-aminolaevulinic acid-mediated photodynamic therapy in recurrent superficial bladder carcinoma. BJU Int. 2005 Jun;95(9):1206–10. <DOI>.

97. Copper MP, Tan IB, Oppelaar H, Ruevekamp MC, Stewart FA. Meta-tetra(hydroxyphenyl)chlorin Photodynamic Therapy in Early-Stage Squamous Cell Carcinoma of the Head and Neck. Arch Otolaryngol Head Neck Surg. 2003 Jul 1;129(7):709. <DOI>.

98. Hopper C, Kübler A, Lewis H, Tan IB, Putnam G, the Foscan 01 Study Group. mTHPC-mediated photodynamic therapy for early oral squamous cell carcinoma: mTHPC in Early Oral Cancer. Int J Cancer. 2004 Aug 10;111(1):138–46. <DOI>.

99. Kübler AC, de Carpentier J, Hopper C, Leonard AG, Putnam G. Treatment of squamous cell carcinoma of the lip using Foscan-mediated Photodynamic Therapy. International Journal of Oral and Maxillofacial Surgery. 2001 Dec;30(6):504–9. <DOI>.

100. McCaughan JS, Williams TE. Photodynamic therapy for endobronchial malignant disease: A prospective fourteen-year study. The Journal of Thoracic and Cardiovascular Surgery. 1997 Dec;114(6):940–7. <DOI>.

101. Kato H. Photodynamic therapy for lung cancer — A review of 19 years' experience. Journal of Photochemistry and Photobiology B: Biology. 1998 Feb;42(2):96–9. <DOI>.

102. Diaz-Jimenez J, Martinez-Ballarin J, Llunell A, Farrero E, Rodriguez A, Castro M. Efficacy and safety of photodynamic therapy versus Nd-YAG laser resection in NSCLC with airway obstruction. Eur Respir J. 1999 Oct 1;14(4):800. <URL>.

103. Moghissi K, Dixon K, Stringer M, Freeman T, Thorpe A, Brown S. The place of bronchoscopic photodynamic therapy in advanced unresectable

Vidujith AVA et al. JOTCSA. 2022; 9(3): 821-848.

REVIEW ARTICLE

lung cancer: experience of 100 cases. European Journal of Cardio-Thoracic Surgery. 1999 Jan;15(1):1–6. <DOI>.

104. Furuse K, Fukuoka M, Kato H, Horai T, Kubota K, Kodama N, et al. A prospective phase II study on photodynamic therapy with photofrin II for centrally located early-stage lung cancer. The Japan Lung Cancer Photodynamic Therapy Study Group. JCO. 1993 Oct;11(10):1852–7. <DOI>.

105. Imamura S, Kusunoki Y, Takifuji N, Kudo S, Matsui K, Masuda N, et al. Photodynamic therapy and/or external beam radiation therapy for roentgenologically occult lung cancer. Cancer. 1994 Mar 15;73(6):1608–14. <DOI>.

106. McCaughan JS, Hicks W, Laufman L, May E, Roach R. Palliation of esophageal malignancy with photoradiation therapy. Cancer. 1984 Dec 15;54(12):2905–10. <DOI>.

107. Moghissi K, Dixon K, Thorpe JAC, Stringer M, Moore PJ. The role of photodynamic therapy (PDT) in inoperable oesophageal cancer. European Journal of Cardio-Thoracic Surgery. 2000 Feb;17(2):95–100. <DOI>.

108. Schweitzer VG, Bologna S, Batra SK. Photodynamic therapy for treatment of esophageal cancer: a preliminary report. The Laryngoscope. 1993;103(6):699–703.

109. Sibille A, Lambert R, Souquet JC, Sabben G, Descos F. Long-term survival after photodynamic therapy for esophageal cancer. Gastroenterology. 1995 Feb;108(2):337–44. <DOI>.

110. Grosjean P, Savary JF, Mizeret J, Wagnieres G, Woodtli A, Theumann JF, et al. Photodynamic Therapy for Cancer of the Upper Aerodigestive Tract Using Tetra(m -hydroxyphenyl)chlorin. Journal of Clinical Laser Medicine & Surgery. 1996 Oct;14(5):281–7. <DOI>.

111. Wolfsen HC. Carpe luz—seize the light: endoprevention of esophageal adenocarcinoma when using photodynamic therapy with porfimer sodium. Gastrointestinal Endoscopy. 2005 Oct;62(4):499–503. <DOI>.

112. Pacifico RJ, Wang KK, Wongkeesong L Michel, Buttar NS, Lutzke LS. Combined endoscopic mucosal resection and photodynamic therapy versus esophagectomy for management of early adenocarcinoma in Barrett's esophagus. Clinical Gastroenterology and Hepatology. 2003 Jul;1(4):252–7. <DOI>.

113. Patel G, Armstrong AW, Eisen DB. Efficacy of Photodynamic Therapy vs Other Interventions in Randomized Clinical Trials for the Treatment of Actinic Keratoses: A Systematic Review and Meta-analysis. JAMA Dermatol. 2014 Dec 1;150(12):1281. <DOI>.

114. Chhatre S, Vachani A, Allison RR, Jayadevappa R. Survival Outcomes with Photodynamic Therapy, Chemotherapy and Radiation in Patients with Stage III or Stage IV Non-Small Cell Lung Cancer. Cancers. 2021 Feb 15;13(4):803. <DOI>.

115. Li L bo, Xie J ming, Zhang X na, Chen J zhang, Luo Y ling, Zhang L ying, et al. Retrospective study of photodynamic therapy vs photodynamic therapy combined with chemotherapy and chemotherapy alone on advanced esophageal cancer. Photodiagnosis and Photodynamic Therapy. 2010 Sep;7(3):139–43. <DOI>.

116. Rigual N, Shafirstein G, Cooper MT, Baumann H, Bellnier DA, Sunar U, et al. Photodynamic Therapy with 3-(1′-Hexyloxyethyl) Pyropheophorbide a for Cancer of the Oral Cavity. Clin Cancer Res. 2013 Dec 1;19(23):6605–13. <DOI>.

117. Wilson BC. Photodynamic Therapy for Cancer: Principles. Canadian Journal of Gastroenterology. 2002;16(6):393–6. <DOI>.

118. Gonzalgo M, Pavlovich C, Lee S, Nelson W. Prostate Cancer Detection by GSTP1 Methylation Analysis of Postbiopsy Urine Specimens. Clinical Cancer Research. 2003;9(7):2673–7.

119. Lane KLS, Hovenic W, Ball K, Zachary CB. Daylight photodynamic therapy: The Southern California experience: Daylight photodynamic therapy. Lasers Surg Med. 2015 Feb;47(2):168–72. <DOI>.

120. Wiegell SR, HæDERSDAL M, Christian Wulf H. Cold water and pauses in illumination reduces pain during photodynamic therapy: a randomized clinical study. Acta dermato-venereologica. 2009;89(2):145–9.

121. Golub TR, Slonim DK, Tamayo P, Huard C, Gaasenbeek M, Mesirov JP, et al. Molecular Classification of Cancer: Class Discovery and Class Prediction by Gene Expression Monitoring. Science. 1999 Oct 15;286(5439):531–7. <DOI>.

122. Tyagi S, Kramer FR. Molecular Beacons: Probes that Fluoresce upon Hybridization. Nat Biotechnol. 1996 Mar;14(3):303–8. <DOI>.

123. Woodhams JH, MacRobert AJ, Bown SG. The role of oxygen monitoring during photodynamic therapy and its potential for treatment dosimetry. Photochem Photobiol Sci. 2007;6(12):1246. <DOI>.

124. Hong EJ, Choi DG, Shim MS. Targeted and effective photodynamic therapy for cancer using functionalized nanomaterials. Acta Pharmaceutica Sinica B. 2016 Jul;6(4):297–307. <DOI>.

125. Calixto G, Bernegossi J, de Freitas L, Fontana C, Chorilli M. Nanotechnology-Based Drug Delivery

Systems for Photodynamic Therapy of Cancer: A Review. Molecules. 2016 Mar 11;21(3):342. <DOI>.

126. Wei Y, Zhou F, Zhang D, Chen Q, Xing D. A graphene oxide based smart drug delivery system for tumor mitochondria-targeting photodynamic therapy. Nanoscale. 2016;8(6):3530–8. <DOI>.

127. James N, Cheruku R, Missert J, Sunar U, Pandey R. Measurement of Cyanine Dye Photobleaching in Photosensitizer Cyanine Dye Conjugates Could Help in Optimizing Light Dosimetry for Improved Photodynamic Therapy of Cancer. Molecules. 2018 Jul 24;23(8):1842. <DOI>.

128. Wezgowiec J, Derylo MB, Teissie J, Orio J, Rols MP, Kulbacka J, et al. Electric Field-Assisted Delivery of Photofrin to Human Breast Carcinoma Cells. J Membrane Biol. 2013 Oct;246(10):725–35. <DOI>.

129. Sahu NK, Shilakari G, Nayak A, Kohli DV. Antisense Technology: A Selective Tool for Gene Expression Regulation and Gene Targeting. Current Pharmaceutical Biotechnology. 2007;8(5):291–304. <URL>.

130. Brown PK, Qureshi AT, Moll AN, Hayes DJ, Monroe WT. Silver Nanoscale Antisense Drug Delivery System for Photoactivated Gene Silencing. ACS Nano. 2013 Apr 23;7(4):2948–59. <DOI>.

131. Chou TC, Talalay P. Quantitative analysis of dose-effect relationships: the combined effects of multiple drugs or enzyme inhibitors. Advances in Enzyme Regulation. 1984 Jan;22:27–55. <DOI>.

132. Postiglione I, Chiaviello A, Palumbo G. Enhancing Photodynamyc Therapy Efficacy by Combination Therapy: Dated, Current and Oncoming Strategies. Cancers. 2011 Jun 9;3(2):2597–629. <DOI>.

133. Crescenzi E, Varriale L, Iovino M, Chiaviello A, Veneziani BM, Palumbo G. Photodynamic therapy with indocyanine green complements and enhances low-dose cisplatin cytotoxicity in MCF-7 breast cancer cells. Molecular Cancer Therapeutics. 2004 May 12;3(5):537–44. <DOI>.

134. Brodin NP, Guha C, Tomé WA. Photodynamic Therapy and Its Role in Combined Modality Anticancer Treatment. Technol Cancer Res Treat. 2015 Aug;14(4):355–68. <DOI>.

135. St. Denis TG, Aziz K, Waheed AA, Huang YY, Sharma SK, Mroz P, et al. Combination approaches to potentiate immune response after photodynamic therapy for cancer. Photochem Photobiol Sci. 2011;10(5):792. <DOI>.

136. Korbelik M, Sun J, Posakony JJ. Interaction Between Photodynamic Therapy and BCG Immunotherapy Responsible for the Reduced Recurrence of Treated Mouse Tumors¶.

Photochemistry and Photobiology. 2007 May 1;73(4):403–9. <DOI>.

137. Korbelik M, Cecic I. Enhancement of tumour response to photodynamic therapy by adjuvant mycobacterium cell-wall treatment. Journal of Photochemistry and Photobiology B: Biology. 1998 Jul;44(2):151–8. <DOI>.

138. Chen WR, Korbelik M, Battels KE, Liu H, Sun J, Nordquist RE. Enhancement of Laser Cancer Treatment by a Chitosan-derived Immunoadjuvant. Photochemistry and Photobiology. 2007 May 23;81(1):190–5. <DOI>.

139. Korbelik M, Sun J, Cecic I, Serrano K. Adjuvant treatment for complement activation increases the effectiveness of photodynamic therapy of solid tumors. Photochem Photobiol Sci. 2004;3(8):812. <DOI>.

140. Winters U, Daayana S, Lear JT, Tomlinson AE, Elkord E, Stern PL, et al. Clinical and Immunologic Results of a Phase II Trial of Sequential Imiquimod and Photodynamic Therapy for Vulval Intraepithelial Neoplasia. Clin Cancer Res. 2008 Aug 15;14(16):5292–9. <DOI>.

141. Uehara M, Sano K, Wang ZL, Sekine J, Ikeda H, Inokuchi T. Enhancement of the photodynamic antitumor effect by streptococcal preparation OK-432 in the mouse carcinoma. Cancer Immunology, Immunotherapy. 2000 Oct 22;49(8):401–9. <DOI>.

142. Korbelik M, Sun J, Posakony JJ. Interaction Between Photodynamic Therapy and BCG Immunotherapy Responsible for the Reduced Recurrence of Treated Mouse Tumors¶. Photochemistry and Photobiology. 2007 May 1;73(4):403–9. <DOI>.

143. Korbelik M, Cecic I. Enhancement of tumour response to photodynamic therapy by adjuvant mycobacterium cell-wall treatment. Journal of Photochemistry and Photobiology B: Biology. 1998 Jul;44(2):151–8. <DOI>.

144. Korbelik M, Naraparaju V, Yamamoto N. Macrophage-directed immunotherapy as adjuvant to photodynamic therapy of cancer. Br J Cancer. 1997 Jan;75(2):202–7. <DOI>.

145. Reginato E, Mroz P, Chung H, Kawakubo M, Wolf P, Hamblin MR. Photodynamic therapy plus regulatory T-cell depletion produces immunity against a mouse tumour that expresses a self-antigen. Br J Cancer. 2013 Oct;109(8):2167–74. <DOI>.

146. Goląb J, Wilczyński G, Zagożdżon R, Stoklosa T, Dąbrowska A, Rybczyńska J, et al. Potentiation of the anti-tumour effects of Photofrin®-based photodynamic therapy by localized treatment with G-CSF. Br J Cancer. 2000 Apr;82(8):1485–91. <DOI>.

147. Jalili A, Makowski M, Świtaj T, Nowis D, Wilczyński GM, Wilczek E, et al. Effective Photoimmunotherapy of Murine Colon Carcinoma Induced by the Combination of Photodynamic Therapy and Dendritic Cells. Clin Cancer Res. 2004 Jul 1;10(13):4498–508. <DOI>.

148. Saji H, Song W, Furumoto K, Kato H, Engleman EG. Systemic Antitumor Effect of Intratumoral Injection of Dendritic Cells in Combination with Local Photodynamic Therapy. Clin Cancer Res. 2006 Apr 15;12(8):2568–74. <DOI>.

149. Luksiene Z, Kalvelyte A, Supino R. On the combination of photodynamic therapy with ionizing radiation. Journal of Photochemistry and Photobiology B: Biology. 1999 Oct;52(1–3):35–42. <DOI>.

150. Allman R, Cowburn P, Mason M. Effect of photodynamic therapy in combination with ionizing radiation on human squamous cell carcinoma cell lines of the head and neck. Br J Cancer. 2000 Sep;83(5):655–61. <DOI>.

151. Lehmann P. Methyl aminolaevulinate? photodynamic therapy: a review of clinical trials in the treatment of actinic keratoses and nonmelanoma skin cancer. Br J Dermatol. 2007 May;156(5):793–801. <DOI>.

152. Nakano A, Watanabe D, Akita Y, Kawamura T, Tamada Y, Matsumoto Y. Treatment efficiency of combining photodynamic therapy and ionizing radiation for Bowen's disease: Combination of PDT and radiation for Bowen's disease. Journal of the European Academy of Dermatology and Venereology. 2011 Apr;25(4):475–8. <DOI>.

153. Wang J, Hyun W, Lamborn K, Deen D. Measurement of Radiation-induced Damage in Human Glioma Cells with Flow Cytometry. Cancer Research. 1996;56(1):154–7. <URL>.

154. Sanfilippo NJ, Hsi A, DeNittis AS, Ginsberg GG, Kochman ML, Friedberg JS, et al. Toxicity of photodynamic therapy after combined external beam radiotherapy and intraluminal brachytherapy for carcinoma of the upper aerodigestive tract. Lasers Surg Med. 2001;28(3):278–81. <DOI>.

155. Xu J, Gao J, Wei Q. Combination of Photodynamic Therapy with Radiotherapy for Cancer Treatment. Journal of Nanomaterials. 2016;2016:1–7. <DOI>.

156. Chen W, Zhang J. Using Nanoparticles to Enable Simultaneous Radiation and Photodynamic Therapies for Cancer Treatment. J Nanosci Nanotech. 2006 Apr 1;6(4):1159–66. <DOI>.

157. Juzenas P, Chen W, Sun YP, Coelho MAN, Generalov R, Generalova N, et al. Quantum dots and nanoparticles for photodynamic and radiation therapies of cancer. Advanced Drug Delivery Reviews. 2008 Dec;60(15):1600–14. <DOI>.

158. Ran C, Zhang Z, Hooker J, Moore A. In Vivo Photoactivation Without "Light": Use of Cherenkov Radiation to Overcome the Penetration Limit of Light. Mol Imaging Biol. 2012 Apr;14(2):156–62. <DOI>.

159. Allman R, Cowburn P, Mason M. Effect of photodynamic therapy in combination with ionizing radiation on human squamous cell carcinoma cell lines of the head and neck. Br J Cancer. 2000 Sep;83(5):655–61. <DOI>.

160. Sharma P, Farrell T, Patterson MS, Singh G, Wright JR, Sur R, et al. In Vitro Survival of Nonsmall Cell Lung Cancer Cells Following Combined Treatment with Ionizing Radiation and Photofrin-mediated Photodynamic Therapy. Photochemistry and Photobiology. 2009 Jan;85(1):99–106. <DOI>.

161. Nakano A, Watanabe D, Akita Y, Kawamura T, Tamada Y, Matsumoto Y. Treatment efficiency of combining photodynamic therapy and ionizing radiation for Bowen's disease: Combination of PDT and radiation for Bowen's disease. Journal of the European Academy of Dermatology and Venereology. 2011 Apr;25(4):475–8. <DOI>.

162. Sazgarnia A, Montazerabadi AR, Bahreyni-Toosi MH, Ahmadi A, Aledavood A. In vitro survival of MCF-7 breast cancer cells following combined treatment with ionizing radiation and mitoxantrone-mediated photodynamic therapy. Photodiagnosis and Photodynamic Therapy. 2013 Feb;10(1):72–8. <DOI>.

163. Ahn JC, Biswas R, Mondal A, Lee YK, Chung PS. Cisplatin enhances the efficacy of 5-Aminolevulinic acid mediated photodynamic therapy in human head and neck squamous cell carcinoma. gpb. 2014;33(01):53–62. <DOI>.

164. Wei XQ, Ma HQ, Liu AH, Zhang YZ. Synergistic Anticancer Activity of 5-Aminolevulinic Acid Photodynamic Therapy in Combination with Low-dose Cisplatin on Hela Cells. Asian Pacific Journal of Cancer Prevention. 2013 May 30;14(5):3023–8. <DOI>.

165. Cheung KKY, Chan JYW, Fung KP. Antiproliferative effect of pheophorbide a–mediated photodynamic therapy and its synergistic effect with doxorubicin on multiple drug-resistant uterine sarcoma cell MES-SA/Dx5. Drug and Chemical Toxicology. 2013 Oct;36(4):474–83. <DOI>.

166. Sun W, Kajimoto Y, Inoue H, Miyatake SI, Ishikawa T, Kuroiwa T. Gefitinib enhances the efficacy of photodynamic therapy using 5-aminolevulinic acid in malignant brain tumor cells. Photodiagnosis and Photodynamic Therapy. 2013 Feb;10(1):42–50. <DOI>.

167. Fang X, Wu P, Li J, Qi L, Tang Y, Jiang W, et al. Combination of apoptin with photodynamic therapy induces nasopharyngeal carcinoma cell death in vitro and in vivo. Oncology Reports. 2012 Dec;28(6):2077–82. <DOI>.

168. Nonaka Y, Nanashima A, Nonaka T, Uehara M, Isomoto H, Abo T, et al. Synergic effect of photodynamic therapy using talaporfin sodium with conventional anticancer chemotherapy for the treatment of bile duct carcinoma. Journal of Surgical Research. 2013 May;181(2):234–41. <DOI>.

169. Tong Z Sheng, Miao P Tian, Liu T Ting, Jia Y Sheng, Liu X Dong. Enhanced antitumor effects of BPD-MA-mediated photodynamic therapy combined with adriamycin on breast cancer in mice. Acta Pharmacol Sin. 2012 Oct;33(10):1319–24. <DOI>.

170. Diez B, Ernst G, Teijo MJ, Batlle A, Hajos S, Fukuda H. Combined chemotherapy and ALA-based photodynamic therapy in leukemic murine cells. Leukemia Research. 2012 Sep;36(9):1179–84. <DOI>.

171. Canti G, Calastretti A, Bevilacqua A, Reddi E, Palumbo G, Nicolin A. Combination of photodynamic therapy + immunotherapy + chemotherapy in murine leukiemia. neo. 2010 Jan;57(2):184–8. <DOI>.

172. Kramarenko GG, Wilke WW, Dayal D, Buettner GR, Schafer FQ. Ascorbate enhances the toxicity of the photodynamic action of Verteporfin in HL-60 cells. Free Radical Biology and Medicine. 2006 May;40(9):1615–27. <DOI>.

173. Melnikova V, Bezdetnaya L, Belitchenko I, Potapenko A, Merlin JL, Guillemin F. Meta-tetra(hydroxyphenyl)chlorin-sensitized photodynamic damage of cultured tumor and normal cells in the presence of high concentrations of α-tocopherol. Cancer Letters. 1999 May;139(1):89–95. <DOI>.

Chemical Composition, Pharmacological Activities, and Biofuel Production of *Eichhornia crassipes* (Water Hyacinth): A Review

Hadush Gebrehiwot[1] iD **, Aman Dekebo[1]** iD **and Milkyas Endale[1*]** iD

[1]Adama Science and Technology University, School of Applied Natural Sciences, Department of Applied Chemistry, P.O. Box: 1888, Adama, Ethiopia.

Abstract: *Eichhornia crassipes* (Mart.) Solms, commonly known as water hyacinth, is one of the free-floating macrophytes with substantial damaging effects on aquatic environment, but it has significant industrial and medicinal applications. Several metabolites such as vitamins, tannins, saponins, terpenoids, phenolic compounds, lignins, flavonoids, alkaloids, and sterols have been reported from the plant. The presence of such secondary metabolites made it possess a wide array of therapeutic properties, of which alkaloids, phenolic compounds, triterpenoids, flavonoids, tannins, and saponins reported from the plant were found to show promising pharmacological effects. This review endeavors to provide a comprehensive and up-to-date compilation of documented chemical constituents, pharmacological activities, and renewable energy profiles of water hyacinth. The literature encountered showed that potassium, chlorine, calcium, and aluminum were among the nutritionally important elements reported in large amounts from the plant. In this review, the findings of different extracts (methanol, aqueous, chloroform, and hexane extracts) of the plant have been reviewed for their pharmacological and biological effects and results were promising. The plant's anti-inflammatory, antioxidant, antifungal, antiaging, anticancer, hepatoprotective, and antibacterial properties, as well as other biological activities like insecticidal, allelopathic, and larvicidal effects, are extensively documented. The plant also demonstrated a wide spectrum of uses, including biofuel production, compost production, and bioremediation. On the other hand, clogging of waterways, breeding grounds for pests and disease, reduction of water quality, loss of biodiversity, and economic recession in invaded areas are negative aspects associated with it. So, the present review summarizes the potential of *Eichhornia crassipes* as a valuable source of natural compounds with desirable pharmacological effectiveness, predicting that the compilation will benefit future studies. The renewable energy profiles of the weed are also well presented.

INTRODUCTION

Natural resources, especially plants, have long been used as the basis of traditional and modern medicine systems. Such widespread dependence of human beings on natural resources has raised marvelous attention in the scientific world (1), which eventually led to the isolation of an enormous number of phytochemicals with significant multipurpose advantages (2). Marine plants have a large number of social, traditional, economic, and environmental benefits. Some aquatic plants are used in human diet, whereas others have medicinal values and are sources of vitamins, minerals, and renewable energy (3). Aquatic herbs and weeds are known to differ widely in their physico-chemical constituents as a result of the genotype of the plant species, seasonal variation, and location. Hence, an insight into their phytochemistry is important if utilization prospects are to be considered (4).

Eichhornia crassipes, also known as water hyacinth (Figure 1), is an aquatic plant belonging to the family *Pontideraceae* native to South America (5, 6).

The plant is considered as one of the most invasive weeds due to its rapid spread, ecological adaptability, and negative impacts on the environment (7-11), economic development, and human health (12, 13). It can rapidly grow to very high densities (over 60 kg/m^2), completely clogging water bodies, which in turn may have negative effects. The plant thrives in tropical deserts, subtropical or warm temperate deserts, and rainforest zones (14). It tolerates annual temperatures ranging from 21.1°C to 27.2°C and its pH tolerance is estimated at 5.0 to 7.5. Water hyacinth is also called "the beautiful blue devil", known by its lavender flowers, short stems and shining bright leaves which spreads at an alarming rate in aquatic grounds. The plant is able to tolerate both fresh and seawater and thus its spread has no boundaries (15).

E. crassipes has harmful side effects on human health, aquatic environment, and economic aspects of water bodies (16, 17). The extensive impacts of the plant falls to its quick growth in large areas of aquatic environment and is able to destroy the quality and quantity of waterbodies (18-20). Thus, it can create higher sedimentation rates within the plant's complex root structure and increase evapotranspiration rates from water hyacinth leaves when compared to open water, even by a factor of 10 and cause scarcity of water in some areas. Dense mats of the weed also decrease the dissolved oxygen concentrations, thus creating good breeding

conditions for mosquito vectors of malaria, encephalitis, and filariasis beneath these mats (21).

The plant reduces the yield of phytoplankton and submerged vegetation under dense mats. It also destroys the native vegetation and associated flora, thus causing a disproportion in marine environment (22). The large mass of the plant in water bodies also affects the lives of fish and other aquatic communities. Recent reports of huge invasions and their environmental problems have been revealed from different parts of the world, like Lake Tana of Ethiopia, Lake Victoria of Uganda, other regions of East Africa, Lake Chapala of Mexico, Lake Navishka of Kafue river, Zambia, and Florida (12, 21).

A number of traditional and mechanical weed management approaches are applied to control the fast spread of the weed (23). Chemical and biological control methods are being used to control it but such methods may lead to water pollution and other aquatic life problems (5). Recently, much emphasis has been placed on harvesting this aquatic plant for practical purposes in order to partially offset the cost of removing plants from waterways and using them as an economical source in many parts of the world (21). Thus, the present review endeavors to provide a comprehensive and up-to-date compilation of documented chemical constituents, pharmacological activities, and renewable energy profile of water hyacinth and discusses future potentials and threats of the weed.

Figure 1: *Eichhornia crassipes* (24).

CHEMICAL COMPOSITION, PHARMACOLOGICAL ACTIVITY AND BIOFUEL POTENTIAL OF *Eichhornia crassipes*

Chemical Composition of *Eichhornia crassipes*
The plant is rich in several secondary metabolites, including alkaloids, terpenoids, phenolic compounds, flavonoids, and tannins (25-27) (Table 3). Reports from different parts of the plant revealed that it is

composed of many nutritionally important elements, of which silicon, potassium, and aluminum were reported to be in large amounts in the roots, whereas stems and leaves of the plant are rich sources of potassium, chlorine, and calcium (Table 1). Heavy metals were not found in the studied samples, and the high concentration of inorganic substances makes this plant attractive for use as compost (28).

Table 1: Elemental analysis of *E. crassipes* using energy dispersive X-ray spectroscopy (EDS), where, (mg/gdw=milligram/gram dry weight) (28).

No.	Elements (mg/gdw)	Plant part		
		Roots	**Stems**	**Leaves**
1	Sodium	0.67 ± 0.06	4.43 ± 0.60	1.51 ± 0.33
2	Magnesium	0.46 ± 0.05	5.33 ± 0.02	3.76 ± 0.59
3	Aluminum	8.84 ± 0.53	0.82 ± 0.07	0.03 ± 0.01
4	Silicon	62.80 ± 0.06	8.06 ± 0.03	2.21 ± 0.03
5	Phosphorus	1.81 ± 0.01	5.12 ± 0.06	8.61 ± 0.04
6	Sulfur	1.07 ± 0.09	2.44 ± 0.03	2.76 ± 0.02
7	Chlorine	0.71 ± 0.01	19.43 ± 0.33	17.44 ± 0.12
8	Potassium	10.92 ± 0.03	38.36 ± 0.03	47.29 ± 0.30
9	Calcium	5.30 ± 0.00	15.05 ± 0.05	16.11 ± 0.08
10	Manganese	1.96 ± 0.03	0.70 ± 0.06	0.28 ± 0.02
11	Iron	5.45 ± 0.07	0.26 ± 0.01	Not detected

The energy dispersive X-ray spectroscopy method displayed that silicon showed maximum content in the roots and potassium concentration was found to be high in the leaves and stems of the plant (Table 1) (28).

Alkali solution extracts have low molecular weight carbohydrates consisting mainly of hemicellulose and degraded cellulose, and this treatment can influence the natural durability of lignocellulosic materials (23). Moreover, the alkali solubility values of the plant are larger than the other parameters in the three sections, so the plant could be easily attacked by microorganisms (Table 2) (28).

Table 2: Physicochemical characterization of *E. crassipes* (23, 28).

No.	Parameter	Plant part		
		Roots	**Stems**	**Leaves**
1	pH	4.6 ± 0.01	4.7 ± 0.04	4.7 ± 0.14
2	Ash (wt %)	26.0 ± 0.22	26.8 ± 0.39	19.9 ± 0.25
3	Alkali solubility (wt %)	54.4 ± 0.21	52.4 ± 0.34	51.8 ± 0.27
4	Total extractives (wt %)	35.9 ± 0.82	58.0 ± 0.78	47.5 ± 0.12
5	Holocellulose (wt %)	23.7 ± 0.45	11.4 ± 0.50	17.1 ± 0.06
6	Cellulose (wt %)	16.0 ± 0.77	8.4 ± 0.21	8.7 ± 0.76
7	Hemicellulose (wt %)	7.7	3.0	8.4

The physicochemical analysis of the plant showed highest extractive values (58%) in the stem parts of *E. crassipes*. Whereas, highest alkali solubility values (54, 52, and 51%) were presented from the root, stem, and leaf parts of the plant respectively (28) (Table 2).

Phenolic compounds were identified from the various parts of the plant using different solvent systems (29, 30). 2-methylresorcinol **(1)**, catechol **(2)**, 4-methylresorcinol **(3)**, p-hydroxybenzoic acid **(4)**, vanillic acid **(5)** and salicylic acid have been detected in the ethanolic root extract (26, 31), whereas 4-methylresorcinol **(3)**, 2-methylresorcinol **(1)**, resorcinol and catechol **(2)**, were present in rhizomes. In a related study, an antifungal 2,5-dimethoxy-4-phenyl-benzoindenone **(6)**, a red oily metabolite, was also reported from the plant (32) (Figure 2).

Flavonoids such as Apigenin **(7)**, gossypetin **(8)**, and chrysoeiol **(9)** were also reported in petroleum and aqueous extracts (26), whereas kaempferol **(10)**, quercetin **(11)**, and isovitexin **(12)** were reported in the shoot and rhizome (15). In a related study, anthocyanins **(13)** were present in the aqueous extract of the plant (15, 26, 33, 34) (Figure 5). Moreover, gallic acid **(14)**, 3,4-dihydro-2-phenyl-2H-chromen-3-ol **(15)**, catechin **(16)**, and epicatechin **(17)** were the reported tannins in methanol and aqueous extracts (15, 35) (Figure 2).

Qualitative investigation of alkaloids by TLC showed that cytosine **(18)**, codeine **(19)**, nicotine **(20)** and quinine **(21)** are some noticeable alkaloids reported from various parts of thep lant (15, 26). A related study revealed that, β-carotene **(22)** and phytol **(23)** were also some of the terpenoids isolated from the ethanolic extracts of the plant by GC-MS. The phytochemical analysis of the methanolic extract of the plant also showed the presence of alkaloid derivatives (16). According to the report (18, 19-secoyohimban-19-oic acid, 16, 17, 20, 21-tetradehydro-16-(hydroxymethyl)-, methyl ester (15 beta, 16 E) **(24)**, di amino-di nitro-Methyl dioctyl phthalate **(25)** and 9-(2,2-Dimethyl propanoilhydrazono)-2,7-bis-[2-{diethylamino)-ethoxy] dichloride **(26)** were present in the plant extracts (16, 36-38) (Figure 2).

Jayanthi *et al.*, (2011) (26) and Lalitha *et al.*, (2012) (31) reported the presence of phenalenone and sterols in various extracts of *E. crassipes* (39-43), including 4α-methyl-5α-ergosta-7,24(28)-diene-3β,4β-diol (**27**), 4α-methyl-5α-ergosta-8,24(28)-diene-3β,4β-diol (**28**), 4α-methyl-5α-ergosta-8,14,24(28)-triene-3β,4β-diol (**29**), 6α-hydroxystigmata-4,22-diene-3-one (**30**), and phenalenone derivatives (**31-35)** (31)**.**

Terpene derivatives were also presented from the methanolic extract of *E. crassipes (39, 44-46). 1,2-*Benzene dicarboxylic acid, mono-(2-ethylhexyl ester) (**36**), 1, 2-benzenedicarboxylic acid, diisooctyl ester (**37**), 1, 2-Benzenedicarboxylic acid, dioctyl ester (**38**) and Isooctyl phthalate (**39**) were among the reported terpenoid derivatives in the plant (16) (Figure 2).

20

21

22

23

24

25

26

27

28

29

30

31

32

33
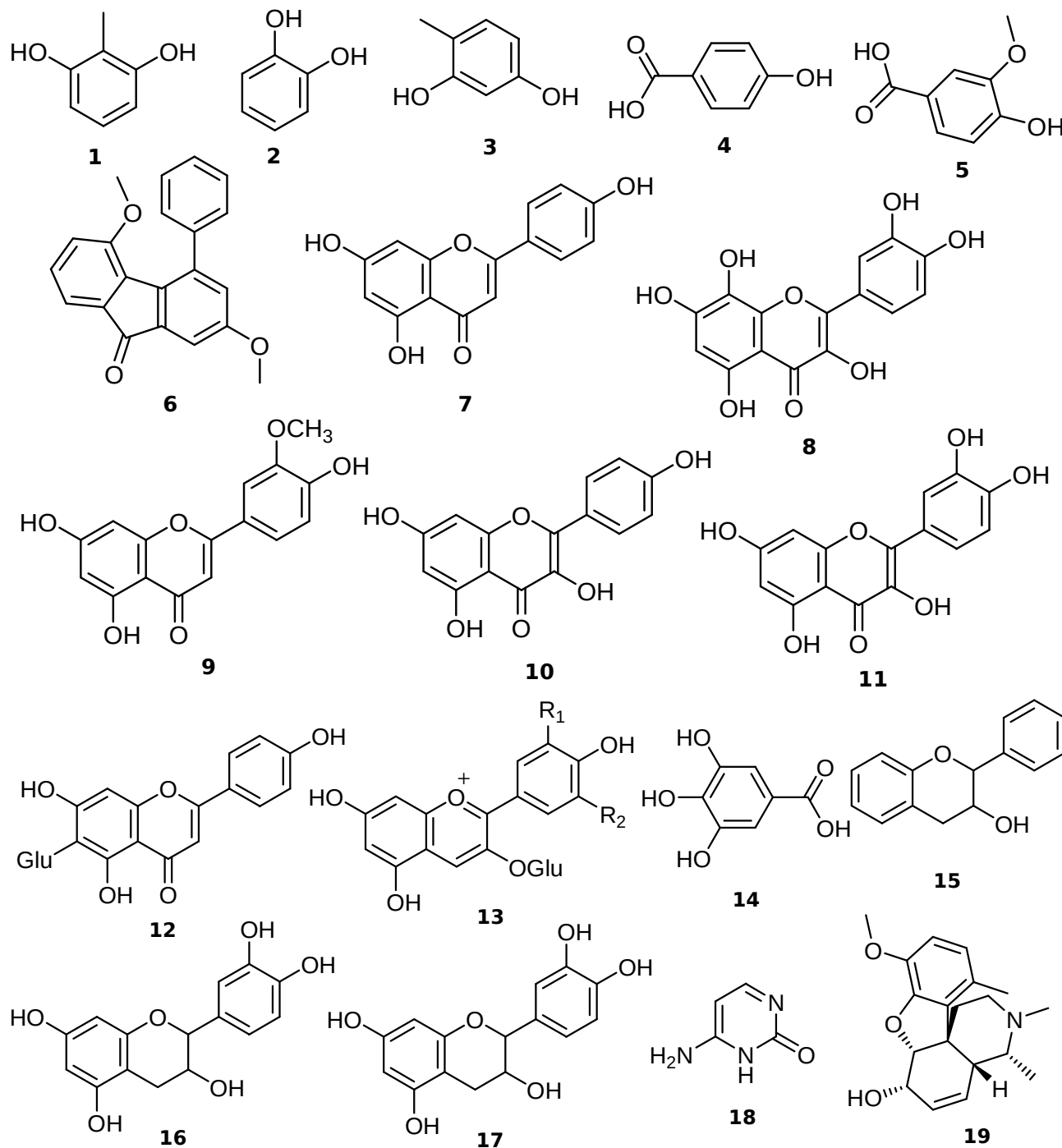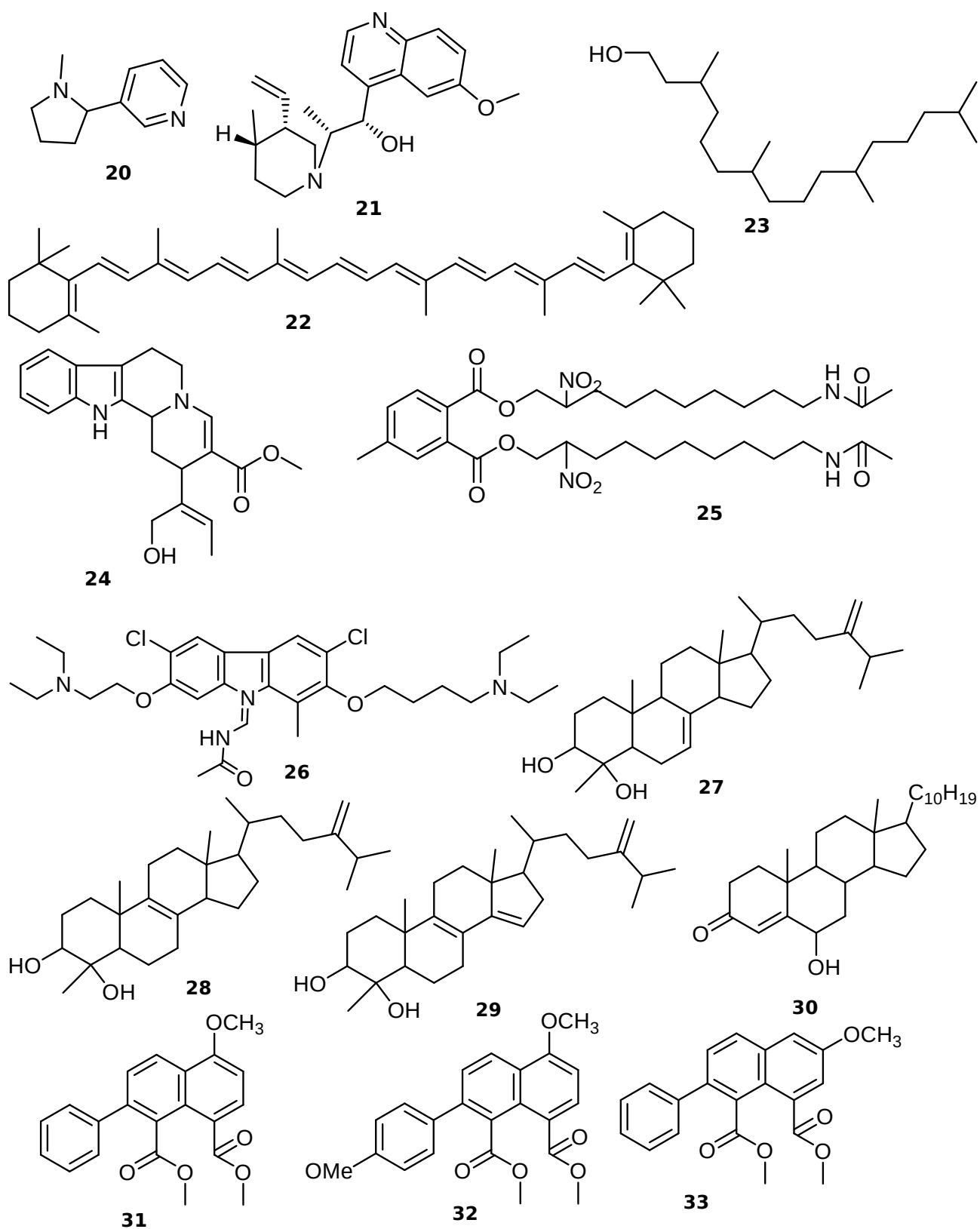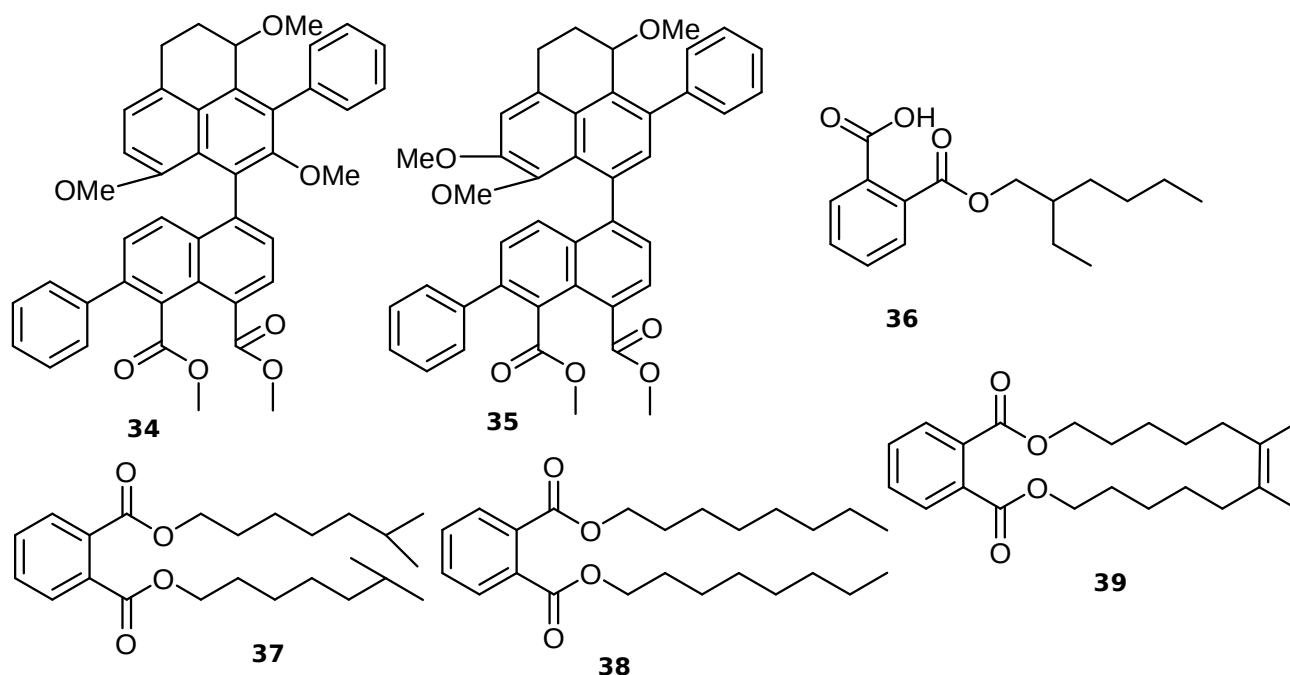
Figure 2: Suggested structures of natural products reported from *E. crassipes.*

Resins, anthraquinones, saponins, fatty acids, phenalenes, organic acids, phlobatannins, carbohydrates, proteins, and lipids were also important metabolites that have been identified in the different parts of *E. crassipes* by different analytical methods (26, 47-50) (Table 3).

Table 3: Phytochemical study of leaf extracts of *E. crassipes* (26).

No.	Phytochemicals	Plant extract			
		Water	**Acetone**	**Ethanol**	**Methanol**
1	Terpenoids	+	+	+	+
2	Tannins	-	+	-	+
3	Amino acids	-	-	+	-
4	Proteins	-	-	+	-
5	Carbohydrates	+	-	+	-
6	Phenolics	-	-	+	+
7	Flavonoids	-	-	-	+
8	Alkaloids	+	+	-	+
9	Saponins	-	-	+	+

+=indicates being present and - = indicates being absent.

GC-MS results of the extracts of the plant displayed twenty organic acids, three steroids, and one terpenoid (39). Carboxylic acids were reported in the leaf and stem extracts. Levulinic acid, oxalic acid, caprilic acid, malonic acid, nonanoic acid, succinic acid, myristic acid, lauric acid, linolenic acid, palmitic acid, oleic acid, pentadecanoic acid, vaccenic acid, linoleic acid, arachidonic acid, squalene, cholestane, β-stigmasterol, and spirostane were among the reported compounds in the extracts of the plant using different solvent systems (30, 39, 44, 45, 51).

Another report, Verma *et al.*, (2021) (52), showed that GC-MS analysis of the extracts of *E. crassipes* displayed the presence of various components in the methanol leaf extracts of the plant. Palmitic acid (24.18%), 9-hexadecenal (10.29%), neophytediene (8.42%), 3-undecanone (7.36%), stearic acid (6.35%), and vitamin E (5.85%) were among the major compounds reported in the study.

Pharmacological Activities of *Eichhornia crassipes*
Antibacterial, antifungal, antioxidant, anti-inflammatory, immunomodulatory, and cytotoxicity effects of *E. crassipes* were broadly studied and results showed that the plant possess promising pharmacological activities (53-56) (Table 4).

Table 4: Selected pharmacological activities of *E. crassipes.*

Plant part studied	Extract type	Type of study/ Tested cell/ Animal used	Results	Refs
Antioxidant activities				
Leaf	Ethanol	*In vitro* (DPPH)	A good antioxidant activity was observed	(57)
The whole parts	n-hexane, methanol, chloroform	DPPH	The IC50 values were 0.387, 0.018 and 1.03 µg/mL respectively	(58)
Leaf	Chloroform, ethanol	Lab assay	The extracts showed good activity at all concentrations (25-100 µg/mL)	(59)
The whole parts	Methanol	DPPH	Showed high activity between 97.0 ± 5.4 and 97.4 ± 2.7 µg/mL	(60)
Anticancer activities				
Leaf	Ethanol	Breast cancer cell lines	80% inhibition of the cell growth at 100 µg/mL	(44)
The whole parts	Methanol	HeLa cell lines	Showed acceptable efficiency with IC_{50} of 1.6	(61)
Leaf	50% methanol	B16F1 mouse melanoma	Showed antitumor effect towards radiotherapy	(44)
Anti-inflammatory activities				
The whole parts	Methanol	Lab assay	Showed strong activity with maximum inhibition of albumin denaturation protein (80%) at 500 µg/mL	(58)
Antimicrobial activities				
Flowers	Methanol	*S. aureus* (disc diffusion method)	Showed significant antibacterial activity at 20 µg/mL	(62)
The whole parts	n-hexane	*P. aeruginosa, S. aureus, E.coli, Salmonella typhi* (disc diffusion method)	Tested active against all pathogens except *S.typhi*	(44)
Leaf	Hydro-methanolic extract	Human and aquatic pathogens (disc diffusion method)	Showed good antimicrobial activity against *S. iniae* and *E. coli* with MIC of 128-512 mg/mL and 64-256 mg/mL respectively	(63)
Leaf	Ethanol	Sub-gingival plaque bacteria colony (serial tube dilution method)	No growth at 12.5, 25, 50, and 100%. Growth was observed at 3.125%	(64)

Antimicrobial Activity
The plant displayed good antibacterial activity (40, 65-73) against certain Gram-positive bacteria (*Staphylococcus aureus, Streptococcus faecalis* and *Bacillus subtilis*) and Gram-negative bacteria (*Escherichia coli*). Of the results studied by Vadlapudi *et al.* (2010) (74) towards six extracts, n-butyl alcohol extract displayed promising antibacterial activity against *S. pyogenes, S. aureus,* and *E. coli* compared to streptomycin (Table 5) (74). Verma *et al.* (2021) (52) reported the antibacterial activity of ethanol and methanol extracts which showed promising inhibition against *V. harveyi* at different concentrations (5, 10, 20 mg/mL) compared to ciprofloxacin.

Various extracts of the plant failed to show antifungal activity towards *Aspergillus niger* and *Aspergillus flavus*, whereas all fractions were active against *Trichophyton megnini* (74) (Table 6). The most promising observation was the ethanol and water extracts of the plant, with good activity against *A. flavus* compared to Fluconazole (31). Substantial studies have reported that compounds isolated from the plant exhibit antibacterial properties against many gram positive and gram negative bacteria (53, 55). The reported antimicrobial activities of the weed were due to the alkaloids, saponins, and tannins screened in the plant (Table 3).

Anti-oxidant Activity
E. crassipes showed good antioxidant activity (30, 33, 58) and the glutathione content of the plant was found to be 32 ± 1.6 nmol/gram of dry water hyacinth leaves (75). The methanol extract revealed

promising activity at 250 µg/mL with 80% inhibition compared to ascorbic acid at the same concentration (90% inhibition). The antioxidant potential of the extracts using different solvent systems by both DPPH and ABTS methods displayed a dose-dependent activity (60, 76).

The methanol and ethanol leaf extracts studied by Verma *et al.*, (2021) (52) showed that both extracts possess good antioxidant properties in reference to the standards, with higher activity observed for the methanol extract (52, 57) (Table 7). The antioxidant properties of the plant may be due to the presence of flavonoids and phenolic compounds in their extracts, which have excellent radical scavenging activities (Table 3).

Table 5: Antibacterial activities of *E. crassipes* (74).

No.	Bacterial pathogens	Zone of inhibition in different solvent systems (diameter in mm)						
		n-butyl alcohol	Methanol	Ethyl acetate	Ethanol	Distilled water	Acetone	Standard (Streptomycin)
1	*S. pyogenes*	12±0.23	8±0.16	10±0.35	9±0.18	-	9±0.42	19±0.50
2	*S. aureus*	10±0.14	10±0.33	-	10±0.31	-	-	12±0.20
3	*S. pullorum*	10±0.31	8±0.11	-	-	-	8±0.10	13±0.15
4	*P. vulgaris*	-	-	-	10±0.28	9±0.21	11±0.27	14±0.16
5	*E. coli*	10±0.20	9±0.22	-	9±0.32	8±0.30	10±0.16	12±0.44

Table 6: Antifungal activities of *E. crassipes* (74).

No.	Fungal pathogens	Zone of inhibition in different solvent systems (diameter in mm)						
		n-butyl alcohol	Methanol	Ethyl acetate	Ethanol	Distilled water	Acetone	Standard (Fluconazole)
1	*T.megnini*	10±0.30	-	9±0.33	8±0.22	9±0.14	10±0.22	19±0.40
2	*C. albicans*	11±0.16	-	-	8±0.24	9±0.37	10±0.23	20±0.42
3	*A. ochraceus*	10±0.26	-	-	12±0.10	9±0.28	15±0.41	18±0.10
4	*A. fumigates*	10±0.38	-	8±0.46	13±0.12	10±0.30	14±0.10	19±0.22
5	*A. flavus*	-	-	-	10±0.15	9±0.20	10±0.12	13±0.25

Table 7: Antioxidant activity of methanol extract of *E. crassipes* (52).

Treatments	Concentrations (µg/mL)	% inhibition of DPPH
Ascorbic acid	50	52
	100	69
	150	74
	200	82
	250	90
Methanol extract	50	44
	100	59
	150	65
	200	72
	250	80

According to the results presented by Aboul-Enein *et al.* (2014) (16), nine fractions (alkaloid and terpenoid derivatives) were isolated from the methanol extract of the plant and showed anticancer and antioxidant activities. The crude methanolic extract showed the highest antioxidant activity with an IC_{50} of 74.80 ± 4.5 µg/mL. Three of the nine compounds recorded comparable activities (92.40 ± 6.5, 95.4 ± 3.1, and 96.5 ± 2.7 µg/mL).

Anti-inflammatory Activity
The anti-inflammatory effects of the aqueous extract, ethyl acetate, and petroleum ether extracts of the plant were presented and results were promising (77-79). The results of the study showed a substantial reduction in the growth of oedema in the hind paws of the mice when treated with the extracts. The three solvent systems displayed variable anti-inflammatory effects. The report also revealed that the petroleum ether and ethyl acetate extracts showed maximum inhibition of the oedema (64.8% and 67.5%, respectively). The presence of phenolic compounds, flavonoids, alkaloids, and anthraquinones in the extracts of the plant plays a significant role in the anti-inflammatory activities of the plant (80) (Table 3).

A related study by Tulika *et al.* (2017) (81) on the methanol extract of the plant showed promising results. The activity was examined by the inhibition of albumin denaturation protein. The evaluation of the anti-inflammatory potential of the plant extract, the inhibition of protein denaturation was studied, and results were encouraging. According to the study, the methanol extract of the plant displayed promising inhibition of albumin denaturation at the concentration of 500 µg/mL with 79% of inhibition compared to ibuprofen (96% of inhibition) (82)(Table 8).

Table 8: Anti-inflammatory activity of methanolic extract of *E. crassipes* (83).

Treatments	Concentrations (µg/mL)	% inhibition of protein denaturation
Ibuprofen	100	42
	200	54
	300	74
	400	80
	500	96
Methanol extract	100	20
	200	42
	300	60
	400	72
	500	79

Anti-cancer Activity
Results of anticancer activities showed that methanol extracts of the plant have moderate anticancer effects (36, 80). This phenomenon has been supported by various solvent extracts tested on mice embryonic fibroblast cell lines. The methanol extracts of the various parts of the plant at different concentrations showed anti-cancer activities against HeLa cell lines with 17% growth inhibition at 200 µg/mL using MTT assay method. The growth inhibition zones and concentrations of the extracts showed smooth relationships (Table 9) (80). The major classes of phytochemicals responsible for the anticancer effects of the plant were alkaloids, saponins, polyphenols, flavonoids, tannins, triterpenes, and quinones (84) (Table 3).

Table 9: IC_{50} analysis value of *E. crassipes* extract against HeLa cells (80).

S/No	Number of subjects	Concentration (µg/mL)	Observed responses	Expected responses	Probability
1	100	0	0	37.14	0.37
2	100	50	98	57.12	0.57
3	100	100	89	75.40	0.75
4	100	200	83	95.57	0.96

Wound healing activity
Three solvent extracts of the plant (methanol, ethyl acetate, and aqueous extracts) were investigated for their wound healing potential in an excision experimental model of wounds in rats. The experiments showed a better wound contraction effect, which was considerably greater than the control (79, 81).

Larvicidal activity
Eggs and larvae of C*hironomus ramosus chaudhuri* were subjected to various concentrations of the root extracts of the plant and showed 100% efficiency

(82). According to the reports of Lalitha *et al.* (2012) (31), putative cytokinin glucoside-like activity was detected only in leaves and flowers of the plant. The cytokinin complements of the leaves and the roots were qualitatively different. Certain cytokinins supplied by the roots are metabolized in the leaves, and certain cytokinins are synthesized in the leaves themselves. Larvicidal, pupicidal, and repellent activity carried out on petroleum ether, ethyl acetate, aqueous extracts, methanol, and ethanol fractions against *Culex quinquefasciatus* also showed good activity (82, 85).

Antitumor activity

The methanolic leaf extract of *E. crassipes* (50%) at different doses (200 mg/kg body weight to 500 mg/kg body weight) showed good response against B16F10 *in vivo* melanoma tumor bearing hybrid mice models (31). In comparison to the isolated compounds, the crude extract, displayed better activity against several tumor cells. Some fractions exhibited selective anticancer activity against a liver cancer cell line, while other fractions exhibited high anticancer activity against hormone-dependent tumor types (cervix and breast cancers). The potency of the crude extract compared to its fractions has been attributed to the auto-synergistic effect of these fractions within the same extract (60).

Source of Renewable Energy

Bote *et al.* (2020) (83) presented their work on the use of *E. crassipes* compost on other green plants such as vegetables and flowering plants and its side effects. In this report, nine morphological yield parameters were studied on saplings grown with *E. crassipes* compost and compared with the untreated ones. The experiments were carried out in kitchen gardens to demonstrate how *E. crassipes* compost can be used instead of regular compost. Based on the findings, they concluded that the green plants grown with *E. crassipes* compost showed good results in terms of all the studied parameters, suggesting that the plant can be applied effectively through the vermin composting process. A fermentative system using *E. crassipes* has been reported to produce ethanol and found to be promising (Figure 3) (83).
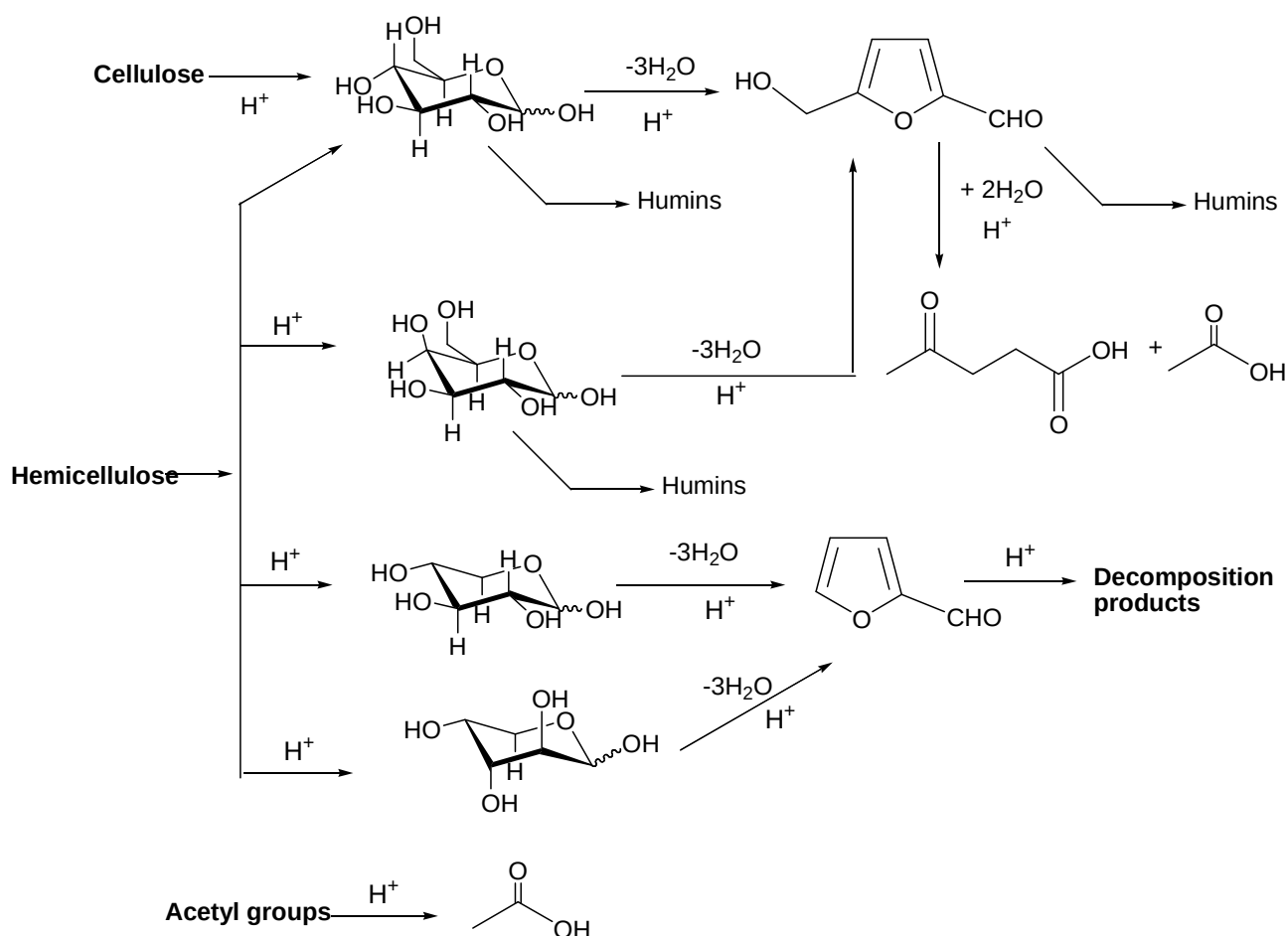
Figure 3: Hydrolysis reaction of *E. crassipes* (83).

The plant also has large amounts of lignin, cellulose, and hemicellulose, which are prominent for processing useful products such as biofuels (86-92).

Recent reports revealed that *one* hectare of standing *E. crassipes* produces more than 70.000 m^3 of biogas. The bacterial fermentation of one ton of

the plant produces about 26500 cubic foot of gas with 25.4% hydrogen, 51.6% methane, 1.2% oxygen, and 22.1% carbon dioxide (93).

Significant research has been conducted in various parts of the world to produce bio-fuel from *E. crassipes*, and the results show that the plant can be used as a future alternative source of renewable energy (94-99) (Figure 4). The plant produced biodiesel (6.36% m/m) primarily composed of saturated fatty acids. The biodiesels produced from the plant have good suitability and stability to be used in diesel engines. The by-products which are made up of glycerol and other pigments, were recorded 1.05 mmol/L and 4.69 mg/g, respectively (100).

The potential and threat of *E. crassipes* studied by Mitan (2019) (101) indicated that proper management and treatment of the plant are strongly recommended in order to utilize it as a source of energy, agriculture, water treatment, chemical and biological sources. Moreover, the proliferation of the plant needs to be more focused on maintaining the sustainability of the environment (101).

Alagu *et al.* (2019) (102) focused on *E. crassipes* biodiesel as a potential alternative fuel for existing unmodified diesel engine. The work examined the feasibility of biodiesel derived from the plant in a compression ignition engine and showed that the plant is also a potential source of renewable energy as it is available in fresh water and aquatic ecosystems in many parts of the world (102).
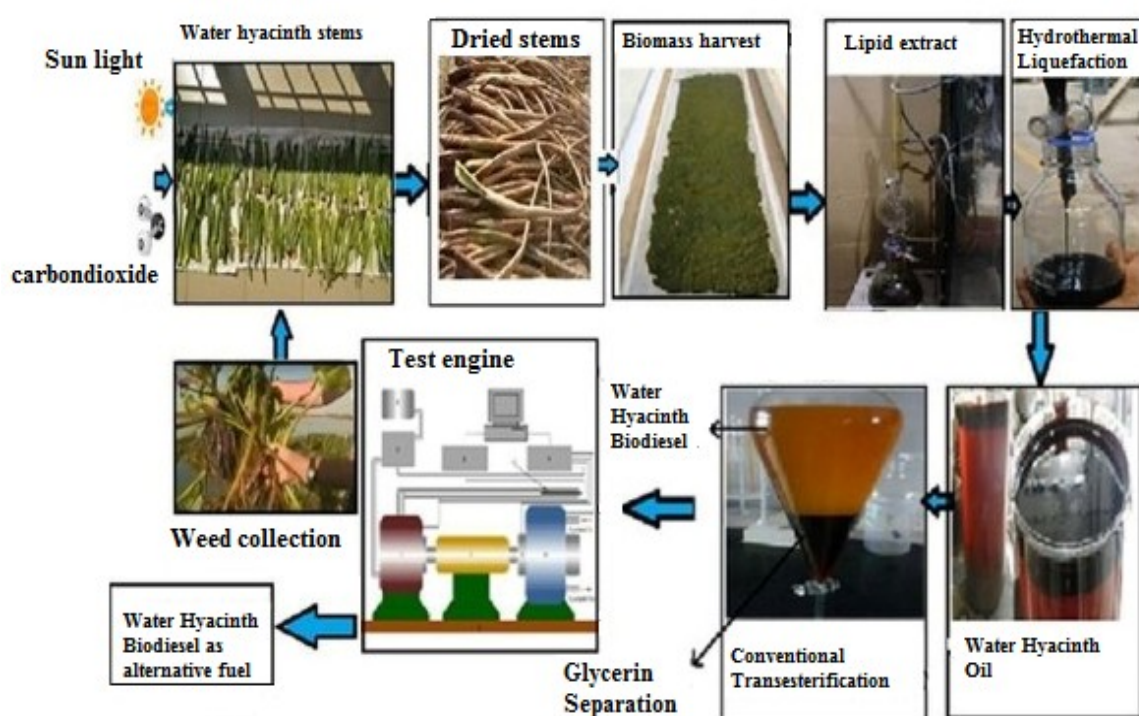
Figure 4: Schematic diagram of the experimental setup for biodiesel production.

A related study by Aswathy *et al.* (2010) (103) revealed that the plant has an excellent correlation with the standard parameters of the diesel available in the market (103) (Table 10). According to this report, water hyacinth biodiesel was mixed with petroleum diesel fuel at different volume proportions (10, 20, 30, 40, and 100%) and its properties were examined as per ASTM standards before it was used for diesel engines. The prepared test fuels were experimentally investigated in a single-cylinder

diesel engine at constant speed (1500 rev/min) for their combustion, performance, and emission features. The test results showed that 20% *E. crassipes* biodiesel and 80% diesel fuel blend was equivalent to the original diesel fuel in terms of thermal efficiency and smoke emissions. Generally, the displayed heat release and cylinder pressure by *E. crassipes* biodiesel were very close to those of ordinary diesel fuel (102).

Table 10: Fuel properties of blending stocks of *E. crassipes* (102).

No.	Fuel properties	Unit	Biodiesel standard		Diesel	Water hyacinth oil	Water hyacinth biodiesel				
			ASTM D 6751	DIN EN14214			B10	B20	B30	B40	B100
1	Density at 15 °C	kg/m^3	-	860-900	838	952	841	846	858	863	887
2	Kinematic viscosity at 40 °C	mm^2/s	1.9-6	3.5-5	2.76	26.4	2.92	2.86	3.18	3.37	3.96
3	Flash point	°C	>130	>120	68	246	74	98	125	148	212
4	Pour point	°C	-	-	-20	17	-3	-4	-1	0	7
5	Cetane number	-	>47	>51	48	44	47	47.4	48.6	49.3	52.5
6	Acid value	mg KOH/g	<0.8	<0.5	-	41	0.36	0.35	0.37	0.36	0.42
7	Water content	%	<0.03	<0.05	0.02	1.8	0.03	0.03	0.02	0.03	0.04
8	Ash content	%	<0.02	<0.02	0.01	0.96	0.01	0.01	0.01	0.01	0.01

CONCLUSION AND FUTURE PERSPECTIVES

This comprehensive review was compiled to evaluate the traditional uses, chemical constituents, pharmacological activity, and biodiesel production possibility of *E. crassipes* (water hyacinth) aiming to highlight the plant's potential to develop its limited therapeutic applications in Africa, especially in Ethiopia. Different phytochemicals isolated from the plant showed anticancer, antibacterial, antifungal, and anti-inflammatory activities. Previous reports revealed that the metabolites in water hyacinth contribute to significant biological activities, especially antioxidant and antibacterial properties. In this regard, further research may be needed to explore the possibility of evaluating the plant for radical scavenging activity and possibility of developing natural antioxidants from it. The plant also displayed promising antifungal activity against *A. flavus,* and the potential of using the leaves of the plant as biofungicides should be studied further. Similarly, the potential of n-butyl alcohol extract against *S. pyogenes, S.aureus,* and *E.coli* should be considered, and further research for natural antibacterial agents should be conducted. Moreover, several patents have described the pharmacological effects of the plant, but clinical applications are still rare and need further investigation. The plant can be considered as the best alternative to cope up with the progression of regional and global environmental change as well as the depletion of fossil fuels.

The ability of this plant to invade different kinds of water bodies across different geographical zones remains a challenge. In this regard, it is recommended to conduct molecular analysis of the plant growing in different water habitats and different geographical zones with due attention to examine the similarities in the genes across the different habitats that may help to genetically modify the plant to be less invasive. In addition, considering the biodiesel efficiency of the plant in situations where controlling the growth becomes a challenge and if facilities exist to utilize the potential of this plant, efforts should be geared toward harnessing the potential of the plant as an alternative energy source i.e., biodiesel production.

CONFLICT OF INTEREST

The authors declare that they have no competing interests to disclose.

ACKNOWLEDGMENTS

REFERENCES

1. Sindhu R, Binod P, Pandey A, Madhavan A, Alphonsa JA, Vivek N, et al. Water hyacinth a potential source for value addition: An overview. Bioresource Technology. 2017 Apr;230:152–62. <DOI>.

2. Maitera O, Khan M, James T. Phytochemical analysis and the chemotherapeutics of leaves and stem-bark of *Nauclea latifolia* grown in Hong, Adamawa State Nigeria. Asian Journal of Plant Science and Research. 2011;1(3):16–22.

3. Awasthi M, Kaur J, Rana S. Bioethanol production through water hyacinth, *Eichhornia crassipes* via optimization of the pretreatment conditions. International Journal of Emerging Technology and Advanced Engineering. 2013;3(3):42–6.

4. Kumar RS, Balasubramanian P, Govindaraj P, Krishnaveni T. Preliminary studies on phytochemicals and antimicrobial activity of solvent extracts of *Coriandrum sativum* L. roots (Coriander). Journal of Pharmacognosy and Phytochemistry. 2014;2(6).

5. Elenwo E, Akankali J. The Estimation of Potential Yield of Water Hyacinth: A Tool for Environmental Management and an Economic Resource for the Niger Delta Region. Journal of Sustainable Development Studies. 2016;9(2):115–37. <URL>.

6. Rodrigues A, Odero M, Hayombe P, Akuno W, Kerich D, Maobe I. Converting Water Hyacinth to Briquettes: A Beach Community Based Approach. IJSBAR. 2014;15(1):358–78. <URL>.

7. Chai TT, Ngoi JC, Wong FC. Herbicidal Potential of *Eichhornia crassipes* Leaf Extract against *Mimosa pigra* and *Vigna radiata*. International Journal of Agriculture & Biology. 2013;15:835–42. <URL>.

8. Thiripura Sundari M, Ramesh A. Isolation and characterization of cellulose nanofibers from the aquatic weed water hyacinth—*Eichhornia crassipes*. Carbohydrate Polymers. 2012 Jan;87(2):1701–5. <DOI>.

9. Mishra S, Maiti A. The efficiency of *Eichhornia crassipes* in the removal of organic and inorganic pollutants from wastewater: a review. Environ Sci Pollut Res. 2017 Mar;24(9):7921–37. <DOI>.

10. Saning A, Herou S, Dechtrirat D, Ieosakulrat C, Pakawatpanurut P, Kaowphong S, et al. Green and sustainable zero-waste conversion of water hyacinth (*Eichhornia crassipes*) into superior magnetic carbon composite adsorbents and supercapacitor electrodes. RSC Adv. 2019;9(42):24248–58. <DOI>.

11. Su W, Sun Q, Xia M, Wen Z, Yao Z. The Resource Utilization of Water Hyacinth (*Eichhornia crassipes* [Mart.] Solms) and Its Challenges. Resources. 2018 Aug 7;7(3):46. <DOI>.

12. Dersseh MG, Melesse AM, Tilahun SA, Abate M, Dagnew DC. Water hyacinth: review of its impacts on hydrology and ecosystem services—Lessons for management of Lake Tana. In: Extreme Hydrology and

Gebrehiwot H, Dekebo A, Endale M. JOTCSA. 2022; 9(3): 849-866.

REVIEW ARTICLE

Climate Variability [Internet]. Elsevier; 2019 [cited 2022 Jun 17]. p. 237–51. ISBN: 978-0-12-815998-9. <URL>.

13. Gaikwad RP, Gavande S. Major Factors Contributing Growth of Water Hyacinth in Natural Water Bodies. Internati Jour of Enginee Rese. 2017;6(6):304. <DOI>.

14. Degaga A. Water Hyacinth (*Eichhornia crassipes*) Biology and its Impacts on Ecosystem, Biodiversity, Economy and Human Wellbeing. J Life Sci Biomed. 2018;8(6):94–100.

15. Lata N, Dubey V. Preliminary phytochemical screening of *Eichhornia crassipes*: the world's worst aquatic weed. J Pharm Sci. 2010;3(6):1240–2. <URL>.

16. Aboul-Enein AM, Shanab SM, Shalaby EA, Zahran MM, Lightfoot DA, El-Shemy HA. Cytotoxic and antioxidant properties of active principals isolated from water hyacinth against four cancer cells lines. BMC Complement Altern Med. 2014 Dec;14(1):397. <DOI>.

17. Adegunloye D, Olosunde S, Omokanju A. Evaluation of ratio variation of water hyacinth (*Eichhornia crassipes*) on the production of pig dung biogas. Int Res J Biol Sci. 2013;2(3):44–8.

18. Amriani F. Physical and Biophysical Pretreatment of Water Hyacinth Biomass for Cellulase Enzyme Production. ChemBiochemEngQ. 2016 Jul 16;30(2):237–44. <DOI>.

19. Saratale RG, Cho SK, Ghodake GS, Shin HS, Saratale GD, Park Y, et al. Utilization of Noxious Weed Water Hyacinth Biomass as a Potential Feedstock for Biopolymers Production: A Novel Approach. Polymers. 2020 Jul 29;12(8):1704. <DOI>.

20. Setyaningsih L, Satria E, Khoironi H, Dwisari M, Setyowati G, Rachmawati N, et al. Cellulose extracted from water hyacinth and the application in hydrogel. IOP Conf Ser: Mater Sci Eng. 2019 Dec 1;673(1):012017. <DOI>.

21. Anuja S, Aggarwal N, Anita S, Anita Y. Beyond biocontrol: water hyacinth-opportunities and challenges. Journal of Environmental Science and Technology. 2016;9(1):26–48.

22. Villamagna A, Murphy B. Ecological and socio-economic impacts of invasive water hyacinth (*Eichhornia crassipes*): a review. Freshwater Biology. 2010;55(2):282–98.

23. Ayanda OI, Ajayi T, Asuwaju FP. *Eichhornia crassipes* (Mart.) Solms: Uses, Challenges, Threats, and Prospects. The Scientific World Journal. 2020 Jul 7;2020:1–12. <DOI>.

24. Asmare T, Demissie B, Nigusse AG, GebreKidan A. Detecting Spatiotemporal Expansion of Water Hyacinth (*Eichhornia crassipes*) in Lake Tana, Northern Ethiopia. J Indian Soc Remote Sens. 2020 May;48(5):751–64. <DOI>.

25. Balasubramanian D, Arunachalam K, Das AK, Arunachalam A. Decomposition and nutrient release of *Eichhornia crassipes* (Mart.) Solms. under different trophic conditions in wetlands of eastern Himalayan foothills. Ecological Engineering. 2012 Jul;44:111–22. <DOI>.

26. Jayanthi P, Lalitha P, Sripathi S. Phytochemical investigation of the extracts of *Eichhornia crassipes* and its solvent fractionates. J Pharm Sci. 2011;4(5):1405–6. <URL>.

27. Zhang Y, Shen Y, Zhang H, Wang L, Zhang H, Qian H, et al. Isolation, purification and identification of two antioxidant peptides from water hyacinth leaf protein hydrolysates (WHLPH). Eur Food Res Technol. 2018 Jan;244(1):83–96. <DOI>.

28. Lara-Serrano J, Rutiaga-Quiñones O, López-Miranda J, Fileto-Pérez H, Pedraza-Bucio F, Rico-Cerda J, et al. Physicochemical characterization of water hyacinth (*Eichhornia crassipes* (Mart.) Solms). Bioresources. 2016;11(3):7214–23.

29. Lata N, Dubey V. Quantification and identification of alkaloids of *Eichhornia crassipes*: the world's worst aquatic plant. J Phar Res. 2010;3:1229–31.

30. Tyagi T, Agarwal M. Phytochemical screening and GC-MS analysis of bioactive constituents in the ethanolic extract of *Pistia stratiotes* L. and *Eichhornia crassipes* (Mart.) solms. Journal of Pharmacognosy and Phytochemistry. 2017;6(1):195–206.

31. Lalitha P, Sripathi SK, Jayanthi P. Secondary Metabolites of *Eichhornia crassipes* (Waterhyacinth): A Review (1949 to 2011). Natural Product Communications. 2012 Sep;7(9):1934578X1200700. <DOI>.

32. Lata N, Huma A, Sumana D, Veenapani D, others. Antioxidants of *Eichhornia crassipes*: the world's worst aquatic plant. Journal of Pharmacy Research. 2010;3(9):2105–6.

33. Elvira K, Fachriyah E, Kusrini D. Isolation of Flavonoid Compounds from Eceng Gondok (*Eichhornia crassipes*) and Antioxidant Tests with DPPH (1,1-Diphenyl-2-Picrylhydrazyl) Method. J Kim Sains Apl. 2018 Oct 31;21(4):187–92. <DOI>.

34. Lata N, Veenapani D, others. Isolation of flavonoids from *Eichhornia crassipes*: the world's worst aquatic plant. Journal of Pharmacy Research. 2010;3(9):2116–8.

35. Ben Bakrim W, Ezzariai A, Karouach F, Sobeh M, Kibret M, Hafidi M, et al. *Eichhornia crassipes* (Mart.) Solms: A Comprehensive Review of Its Chemical Composition, Traditional Use, and Value-Added Products. Front Pharmacol. 2022 Mar 18;13:842511. <DOI>.

36. Mtewa A, Deyno S, Ngwira K, Lampiao F, Peter E, Ahovegbe L, et al. Drug-like properties of anticancer molecules elucidated from *Eichhornia crassipes*. Journal of

Pharmacognosy and Phytochemistry. 2018;7(5):2075–9. <DOI>.

37. Shanab S, Ameer M, Fekry A, Ghoneim A, Shalaby E. Corrosion resistance of magnesium alloy (AZ31E) as orthopaedic biomaterials in sodium chloride containing antioxidantly active compounds from *Eichhornia crassipes*. Int J Electrochem Sci. 2011;6:3017–35.

38. Shanab SMM, Shalaby EA, Lightfoot DA, El-Shemy HA. Allelopathic Effects of Water Hyacinth [*Eichhornia crassipes*]. Ahmed N, editor. PLoS ONE. 2010 Oct 8;5(10):e13200. <DOI>.

39. Fileto-Pérez HA, Rutiaga-Quiñones OM, Sytsma MD, Lorne IM, Luo W, Pankow JF, et al. GC/MS analysis of some extractives from *Eichhornia crassipes*. BioResources. 2015;

40. Kumar RS, Balasubramanian P, Govindaraj P, Krishnaveni T. Preliminary studies on phytochemicals and antimicrobial activity of solvent extracts of *Coriandrum sativum* L. roots (Coriander). Journal of Pharmacognosy and Phytochemistry. 2014;2(6).

41. Martins PF, de Melo MMR, Sarmento P, Silva CM. Supercritical fluid extraction of sterols from *Eichhornia crassipes* biomass using pure and modified carbon dioxide. Enhancement of stigmasterol yield and extract concentration. The Journal of Supercritical Fluids. 2016 Jan;107:441–9. <DOI>.

42. Silva RP, de Melo MMR, Silvestre AJD, Silva CM. Polar and lipophilic extracts characterization of roots, stalks, leaves and flowers of water hyacinth (*Eichhornia crassipes*), and insights for its future valorization. Industrial Crops and Products. 2015 Dec;76:1033–8. <DOI>.

43. Singh KS, Sawant SG, Prabha D, Kaminsky W, others. Stigmasterol from *Eichhornia crassipes* (water hyacinth): isolation, characterization and X-ray structure. Asian Journal of Chemistry. 2015;27(8):3028–30.

44. DellaGreca M, Previteira L, Zarrelli A. Structures of New Phenylphenalene-Related Compounds from *Eichornia crassipes* (Water Hyacinth). Tetrahedron. 2009; 65(39): 8206-8. <DOI>.

45. Kumar D, Karthik M, Rajakumar R. In-silico antibacterial activity of active phytocompounds from the ethanolic leaves extract of *Eichhornia crassipes* (Mart) Solms. against selected target pathogen *Pseudomonas fluorescens*. J Pharmacogn Phytochem. 2018;7:12–5.

46. Muthunarayanan V, Santhiya M, Swabna V, Geetha A. Phytodegradation of textile dyes by water hyacinth (*Eichhornia crassipes*) from aqueous dye solutions. International Journal of Environmental Sciences. 2011;1(7):1702.

47. Adelodun AA, Hassan UO, Nwachuckwu VO. Environmental, mechanical, and biochemical benefits of water hyacinth (*Eichhornia crassipes*). Environ Sci Pollut Res. 2020 Aug;27(24):30210–21. <DOI>.

48. Annie S, Raveen R, Paulraj M, Samuel T, Arivoli S. Screening of *Eichhornia crassipes* (Mart.) Solms (Pontederiaceae) crude leaf extracts for larvicidal efficacy against the filarial vector *Culex quinquefasciatus* say (Diptera: Culicidae). J Mosq Res. 2015;2:43–8.

49. Bochkov DV, Sysolyatin SV, Kalashnikov AI, Surmacheva IA. Shikimic acid: review of its analytical, isolation, and purification techniques from plant and microbial sources. J Chem Biol. 2012 Jan;5(1):5–17. <DOI>.

50. Tulika T, Mala A. Pharmaceutical potential of aquatic plant *Pistia stratiotes* (L.) and *Eichhornia crassipes*. Journal of Plant Science, Special Issue: Medicinal Plants. 2015;3:10–8.

51. Hussain Z, Khan KM, Perveen S, Zaman K, Hayat G, Karim A, et al. The Long Chain Alcohols of the n-hexane Fraction of Water Hyacinth (*Eichhornia crassipes*): Extraction, Estimation, GC-MS Analysis and Antimicrobial Activity. Journal of the Chemical Society of Pakistan. 2015;37(1).

52. Verma VK, Prakash O, Kumar RSR, Rani KV, Sehgal N. Water hyacinth (*Eichhornia crassipes*) leaves enhances disease resistance in *Channa punctata* from *Vibrio harveyi* infection. JoBAZ. 2021 Dec;82(1):6. <DOI>.

53. Bartfay WJ, Bartfay E, Johnson JG. Gram-Negative and Gram-Positive Antibacterial Properties of the Whole Plant Extract of Willow Herb (*Epilobium angustifolium*). Biological Research For Nursing. 2012 Jan;14(1):85–9. <DOI>.

54. Lavecchia T, Rea G, Antonacci A, Giardi MT. Healthy and Adverse Effects of Plant-Derived Functional Metabolites: The Need of Revealing their Content and Bioactivity in a Complex Food Matrix. Critical Reviews in Food Science and Nutrition. 2013 Jan;53(2):198–213. <DOI>.

55. Marasini BP, Baral P, Aryal P, Ghimire KR, Neupane S, Dahal N, et al. Evaluation of Antibacterial Activity of Some Traditionally Used Medicinal Plants against Human Pathogenic Bacteria. BioMed Research International. 2015;2015:1–6. <DOI>.

56. Valenzuela B, Imarai M, Torres R, Modak B. Immunomodulatory effects of the aromatic geranyl derivative filifolinone tested by the induction of cytokine expression. Developmental & Comparative Immunology. 2013 Dec;41(4):675–82. <DOI>.

57. Nugriani NO, Diah IW, ST, Yusri S, M.T SS. Antioxidant Stability Testing On Liquid And Powder *Eichhornia Crassipes* Extract. IOP Conf Ser: Mater Sci Eng. 2020 Jan 1;742(1):012019. <DOI>.

58. Islam S. In Vitro evaluation of Thrombolytic and Antioxidant Scavenging Activity of *Eichhornia crassipes.* SEU J Eng Sci. 2018;12(2):1.

59. Hamid HH, Ghaima K, Najem A. Photochemical, antioxidant and antibacterial activities of some extracts of water hyacinth (*Eichhornia crassipes*) leaves. Int J Adv Pharm Res. 2013;4:1847–51.

60. Aboul-Enein AM, Al-Abd AM, Shalaby E, Abul-Ela F, Nasr-Allah AA, Mahmoud AM, et al. *Eichhornia crassipes* (Mart) solms: From water parasite to potential medicinal remedy. Plant Signaling & Behavior. 2011 Jun;6(6):834–6. <DOI>.

61. Sanaa MS, Emad AS. Biological activities and anticorrosion efficiency of water hyacinth (*Eichhornia crassipes*). Journal of Medicinal Plants Research. 2012;6(23):3950–62.

62. Shehnaz B, Vijayalakshmi M. Antibacterial Activity of Methanolic Extract of the Flowers of *Eichhornia crassipes* (Mart.) Solms. Against Two Different Strains of Bacteria. Int J Pharm Bio Sci. 2016;7:1088–91.

63. Rufchaie R, Mirvaghefi A, Hoseinifar SH, Valipour A. Anti-microbial Activity of *Echhornia Crasippes* Aquatic and Hydromethanolic Leaves Extract. Journal of Fisheries. 2018;71(1):31–41.

64. Arismawati A, Ulfah N, Bargowo L. Inhibition Activity of Water Hyacinth Leaf Extract (*Eichornia Crassipes*) to the Growth of Subgingival Plaque Bacteria Colony. Mlu. 2021;21(1):552–6.

65. Baral B, Vaidya GS. Biological and chemical assessment of water hyacinth (*Eichhornia crassipes* (mart.) Solms.) of Phewa Lake, Nepal. Sci World. 1970 Jan 1;9(9):57–62. <DOI>.

66. Chang CC, Cheng W. Multiple dietary administrating strategies of water hyacinth (*Eichhornia crassipes*) on enhancing the immune responses and disease resistance of giant freshwater prawn, Macrobrachium rosenbergii. Aquac Res. 2016 Jan;47(1):140–52. <DOI>.

67. Gutiérrez-Morales A, Velázquez-Ordoñez V, Khusro A, Salem AZM, Estrada-Zúñiga ME, Salem MZM, et al. Anti-staphylococcal properties of *Eichhornia crassipes, Pistacia vera* , and *Ziziphus amole* leaf extracts: Isolates from cattle and rabbits. Microbial Pathogenesis. 2017 Dec;113:181–9. <DOI>.

68. Haggag MW, Abou El Ella SM, Abouziena HF. Phytochemical Analysis, Antifungal, Antimicrobial Activities and Application of *Eichhornia crassipes* Against Some Plant Pathogens. Planta daninha [Internet]. 2017 [cited 2022 Jun 17];35(0). <DOI>.

69. Hossain J, Khan A, Uddin MA. Antimicrobial Efficacy and Phytochemical Analysis of Three Aquatic Plant Species in Bangladesh. Bangla J Microbiol. 2019 Jan 15;35(1):7–11. <DOI>.

70. Jagathesan G, Rajiv P. Biosynthesis and characterization of iron oxide nanoparticles using *Eichhornia crassipes* leaf extract and assessing their antibacterial activity. Biocatalysis and Agricultural Biotechnology. 2018 Jan;13:90–4. <DOI>.

71. Joshi M, Kaur S. In vitro evaluation of antimicrobial activity and phytochemical analysis of *Calotropis procera, Eichhornia crassipes* and *Datura innoxia* leaves. Asian J Pharm Clin Res. 2013;6(5):25–8.

72. Kiristos TG, Kebede A, Chaithanya KK, Teka MZ. Evaluation of in vitro antibacterial potential of *Eichhornia crassipes* leaf extracts. Drug Invention Today. 2018;10(5).

73. Thombre R, Chitnis A, Kadam V, Bogawat Y, Colaco R, Kale A. A facile method for synthesis of biostabilized silver nanoparticles using *Eichhornia crassipes* (Mart.) Solms (water hyacinth). 2014;

74. Vadlapudi V. In vitro antimicrobial activity of methanolic extract of selected Indian medicinal plants. Pharmacophore. 2010;1(3):214–9.

75. Liu CC, Zhao GL, Li YN, Ding ZP, Liu QG, Li JL. Contribution of Phenolics and Flavonoids to Anti-Oxidat Activity and of Ethanol Extract from *Eichharnia crassipes.* AMR. 2010 Oct;156–157:1372–7. <DOI>.

76. Tulika T, Puneet P, Mala A. Qualitative phytochemical analysis and antioxidant activity of methonolic extract of *Eichhornia crassipes* (Mart.) Solms and *Pistia stratiotes* L. International Journal of Pharmacognosy and Phytochemical Research. 2017;9:632–6.

77. Jayanthi P, Lalitha P, Sujitha R, Thamaraiselvi A. Anti-inflammatory activity of the various solvent extracts of *Eichhornia crassipes* (Mart.) Solms. International Journal of PharmTech Research. 2013;5(2):641–5.

78. Rorong JA, Sudiarso S, Prasetya B, Polii-Mandang J, Suryanto E. Phytochemical analysis of eceng gondok (*Eichhornia crassipessolms*) of agricultural waste as biosensitizer for Ferri photoreduction. AGRIVITA, Journal of Agricultural Science. 2012;34(2):152–60.

79. Sharma AK, Sharma V, Sharma V, Sharma J, Singh R. Multifaceted potential of *Eichhornia crassipes* (Water Hyacinth) ladened with numerous value aided and therapeutic properties. Plant Archives. 2020;20(2):2059–65.

80. Lenora L, Kumara JS, Murugesanb S, Senthilkumarb N. Anticancer Activity of water hyacinth [*Eichhornia crassipes* (mart) solms] on human cervical cancer cell line. Octa Journal of Environmental Research. 2015;3(4):327–31.

81. Ali H, Lata N, Ahi J, Ganesh N. Evaluation of wound-healing activity of *Eichornia crassipes*: A novel approach. Drug Invention Today. 2010;2(3).

82. Thorat LJ, Nath BB. Effects of water hyacinth *Eichhornia crassipes* root extracts on midge *Chironomus ramosus* larvae: a preliminary note. Physiological Entomology. 2010 Dec;35(4):391–3. <DOI>.

83. Bote MA, Naik VR, Jagadeeshgouda KB. Review on water hyacinth weed as a potential bio fuel crop to meet collective energy needs. Materials Science for Energy Technologies. 2020;3:397–406. <DOI>.

84. Ohiagu FO, Chikezie PC, Chikezie CM, Enyoh CE. Anticancer activity of Nigerian medicinal plants: a review. Futur J Pharm Sci. 2021 Dec;7(1):70. <DOI>.

85. Turnipseed RK, Moran PJ, Allan SA. Behavioral responses of gravid *Culex quinquefasciatus, Aedes aegypti* , and *Anopheles quadrimaculatus* mosquitoes to aquatic macrophyte volatiles. Journal of Vector Ecology. 2018 Dec;43(2):252–60. <DOI>.

86. Bhattacharya A, Kumar P et al. Water hyacinth as a potential biofuel crop. Electronic Journal of Environmental, Agricultural and Food Chemistry. 2010;9(1):112–22.

87. Brandt A, Gräsvik J, Hallett JP, Welton T. Deconstruction of lignocellulosic biomass with ionic liquids. Green Chem. 2013;15(3):550. <DOI>.

88. Manyuchi MM, Mbohwa C, Muzenda E, Mutusva TN, Mpeta M. Degradation of Water Hyacinth (*Eichhornia crassipes*) to Vermicompost through Application of the Vermicomposting Technology. In: Proc Int Conf Ind Eng Oper Manag IEOM. 2019. p. 79–88.

89. Rezania S, Alizadeh H, Park J, Din MFM, Darajeh N, Ebrahimi SS, et al. Effect of various pretreatment methods on sugar and ethanol production from cellulosic water hyacinth. BioResources. 2019;14(1):592–606.

90. Sasmal S, Mohanty K. Pretreatment of Lignocellulosic Biomass Toward Biofuel Production. In: Kumar S, Sani RK, editors. Biorefining of Biomass to Biofuels [Internet]. Cham: Springer International Publishing; 2018 [cited 2022 Jun 18]. p. 203–21. (Biofuel and Biorefinery Technologies; vol. 4). <URL>.

91. Carreño Sayago UF, Rodríguez C. Design and Construction of a Biohydrogen and Bioethanol Production System from the Biomass of the *Eichhornia crassipes* [Internet]. ENGINEERING; 2018 May [cited 2022 Jun 18]. <URL>.

92. Nguyen Thi BT, Ong LK, Nguyen Thi DT, Ju YH. Effect of subcritical water pretreatment on cellulose recovery of water hyacinth (*Eichhornia crassipes*). Journal of the Taiwan Institute of Chemical Engineers. 2017 Feb;71:55–61. <DOI>.

93. Bayrakci AG, Koçar G. Second-generation bioethanol production from water hyacinth and duckweed in Izmir: A case study. Renewable and Sustainable Energy Reviews. 2014 Feb;30:306–16. <DOI>.

94. Bhattacharya A, Haldar S, Chatterjee P, others. Geographical distribution and physiology of water hyacinth (*Eichhornia crassipses*) the invasive hydrophyte and a biomass for producing xylitol. International Journal of ChemTech Research. 2015;7(4):1849–61.

95. Das A, Ghosh P, Paul T, Ghosh U, Pati BR, Mondal KC. Production of bioethanol as useful biofuel through the bioconversion of water hyacinth (*Eichhornia crassipes*). 3 Biotech. 2016 Jun;6(1):70. <DOI>.

96. Rodionova MV, Poudyal RS, Tiwari I, Voloshin RA, Zharmukhamedov SK, Nam HG, et al. Biofuel production: Challenges and opportunities. International Journal of Hydrogen Energy. 2017 Mar;42(12):8450–61. <DOI>.

97. Ruan T, Zeng R, Yin X, Zhang S, Yang Z, others. Water hyacinth (*Eichhornia crassipes*) biomass as a biofuel feedstock by enzymatic hydrolysis. BioResources. 2016;11(1):2372–80.

98. Sagar CV, Kumari NA. Sustainable biofuel production from water Hyacinth (*Eicchornia crassipes*). Int J Eng Trends Technol. 2013;4(10):4454–8.

99. Wang Z, Zheng F, Xue S. The Economic Feasibility of the Valorization of Water Hyacinth for Bioethanol Production. Sustainability. 2019 Feb 11;11(3):905. <DOI>.

100. Shanab SMM, Hanafy EA, Shalaby EA. Water Hyacinth as Non-edible Source for Biofuel Production. Waste Biomass Valor. 2018 Feb;9(2):255–64. <DOI>.

101. Merry M. Mitan N. Water hyacinth: Potential and Threat. Materials Today: Proceedings. 2019;19:1408–12. <DOI>.

102. Alagu K, Venu H, Jayaraman J, Raju VD, Subramani L, Appavu P, et al. Novel water hyacinth biodiesel as a potential alternative fuel for existing unmodified diesel engine: Performance, combustion and emission characteristics. Energy. 2019 Jul;179:295–305. <DOI>.

103. Aswathy US, Sukumaran RK, Devi GL, Rajasree KP, Singhania RR, Pandey A. Bio-ethanol from water hyacinth biomass: An evaluation of enzymatic saccharification strategy. Bioresource Technology. 2010 Feb;101(3):925–30. <DOI>.

An Iron(III)-S-methylthiosemicarbazone Complex: Synthesis, Spectral Characterization, and Antioxidant Potency Measured by CUPRAC and DPPH Methods

Büşra Kaya* iD

Istanbul University-Cerrahpasa, Faculty of Engineering, Department of Chemistry, 34320, Istanbul, Turkey.

Abstract: An iron(III) complex, $[Fe(L^1)Cl].H_2O$, was synthesized by template condensation reaction of 1,1,1-Trifluoroacetylacetone-S-methylthiosemicarbazone hydrogen iodide (L) and 2,3-dihydroxybenzaldehyde in the presence of iron(III) ions. The complex was characterized by IR, ESI MS and X-ray diffraction techniques. Free radical scavenging (FRS) ability and antioxidant capacity of the S-methylthiosemicarbazone and the iron(III) complex were evaluated through DPPH and CUPRAC methods, respectively. The complex exerted better than the S-methylthiosemicarbazone in both TEAC and FRS% values. In addition, iron(III) complex was found to be 3.1 times more antioxidant than the reference ascorbic acid according to the CUPRAC method.

INTRODUCTION

Iron plays a vital role in adjusting many redox processes essential for cell homeostasis and is also substantial for cellular respiration, oxygen carry, ATP production, heme and DNA synthesis (1,2). Research on iron-based complexes to discover chemotherapeutic ingredients is often preferred in medical chemistry (3). On the other side; thiosemicarbazones are a rising class of compounds that display marked and selective antitumor activity and can overcome resistance to standard chemotherapy (4–6). The metal complexes of thiosemicarbazones show variable binding properties and structural diversity, as well as promising anticancer activities (7–10). Especially, metal complexes of S-alkylthiosemicarbazones exert significant cytotoxic activity against various cancer cells (11–13). For instance, an iron(III) complex with an N_2O_2 donor S-methylthiosemicarbazone showed a significant cytotoxicity on HeLa and HT-29 cells (14). Another iron(III)-S-metylthiosemicarbazone complex with the same

donor atom set was cytotoxic in K562 cells at very low concentrations (15).

Free radicals are forms of atoms or molecules with unpaired electrons, which are unsteady and very reactive against chemical reactions (16). Under physiological conditions, specific organelles of the cell produce reactive oxygen species (ROS) as by-products of metabolism, normal respiration, and autoxidation of xenobiotics or as an outcome of stress associated with certain diseases (17,18). Therefore, it is necessary to investigate new antioxidants that can be effective in protecting organisms. Metal complexes are an alternative to the use of well-known antioxidants as they offer benefits such as variation in coordination geometry and number, and oxidation states that facilitate and support the redox processes involved in antioxidant effect (19).

Thiosemicarbazones and their metal complexes often exhibit useful antioxidant activity *in vitro* (20)**.** In recent years, antioxidant properties of some nickel(II), manganese(III) oxovanadium(IV),

iron(III) and zinc(II) complexes with S-alkylthiosemicarbazones have been reported (21–25). In a study; oxovanadium(IV), nickel(II) and iron(III) complexes of 3-hyroxysalicylaldehyde-S-methylthiosemicarbazone have been tested according to the CUPRAC method and observed that the iron(III) complex displayed a higher TEAC value than the other complexes (26). Another study showed that iron(III) complexes of S-alkylthiosemicarbazones have usable levels of inhibition against reactive oxygen species, H_2O_2, $O_2^{\circ -}$ and •OH (27).

To discover new iron(III) derivatives of S-alkylthiosemicarbazones with potent antioxidant activity, S-methylthiosemicarbazone (L) and its iron(III) complex [Fe(L^1)Cl].H_2O were synthesized. Since it is generally assumed that the antioxidant activity is related to the number of hydroxyl groups in the phenyl ring (16), it was aimed to increase the antioxidant activity by adding a hydroxyl group to the complex structure. The structural characterization of the complex was performed using elemental analysis, IR, ESI MS and X-ray diffraction techniques. The antioxidant potential of the S-methylthiosemicarbazone and iron(III) complex was screened in the scavenging activity of DPPH• and cupric ions (Cu^{2+}) reducing power (CUPRAC) *in vitro*.
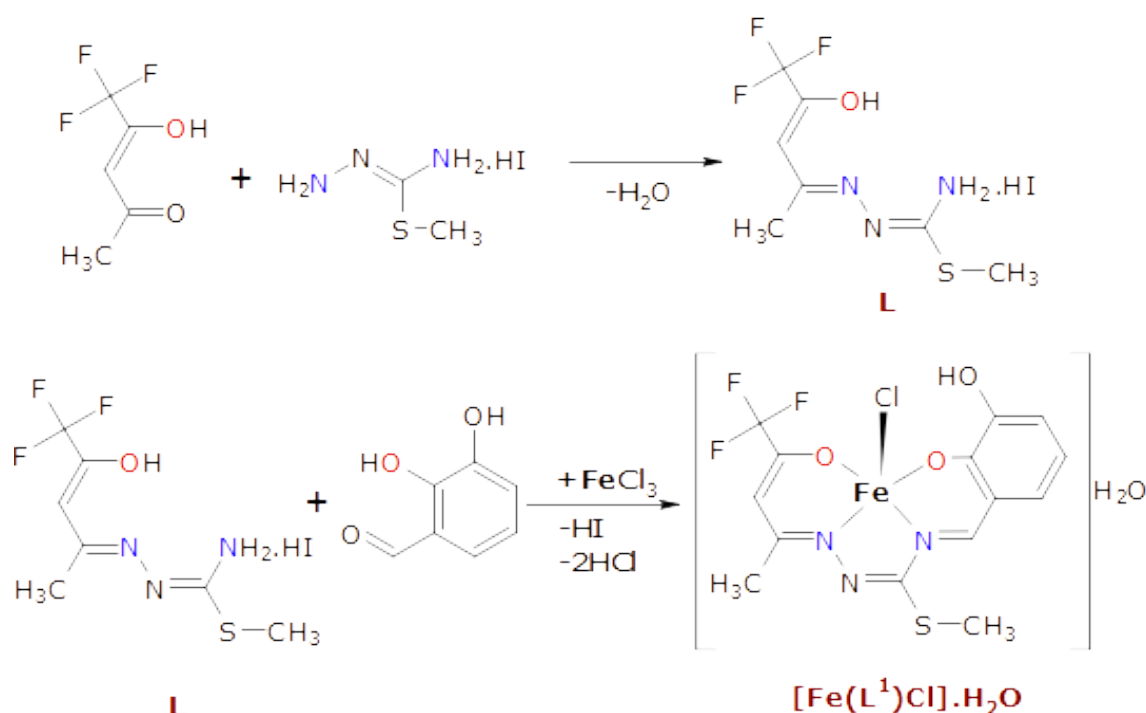
Figure 1: The synthesis of the iron(III) complex.

EXPERIMENTAL SECTION

Physical Measurements
Thermo Finnigan Flash EA 1112, Agilent Carry 630 FTIR, Varian UNITY INOVA 500 MHz NMR and Thermo Finnigan LCQ Advantage Max LC/MS were used for elemental, IR, NMR and ESI MS analysis, respectively. Magnetic moment measurement was performed using the Gouy technique with Sherwood Scientific's MK I model device at room temperature.

The crystallographic data for the suitable crystal of [Fe(L^1)Cl].H_2O was collected at room temperature with a D8-QUEST diffractometer equipped with graphite-monochromatic Mo-Kα radiation. Following procedures was used for analysis: solved by direct methods; SHELXS-2013 (28); refined by full-matrix least-squares methods; SHELXL-2013 (29); data collection: Bruker APEX2 (30); molecular graphics:

MERCURY (31); solution: WinGX (32). The crystallographic data of the complex are listed in Table 1 and selected bond distances and angles, in Table 2.

Synthesis
Starting material, 1,1,1-Trifluoro-acetylacetone-S-methylthiosemicarbazone hydrogen iodide (L), was prepared in accordance with a standard procedure reported earlier (33,34). Briefly, 1,1,1-Trifluoroacetylacetone and S-methylthiosemicarbazide hydrogen iodide were reacted in ethanol. The resulting cream colored compound was filtered and dried *in vacuo*. Elemental analysis and spectroscopic data for the thiosemicarbazone was confirmed its preparation.

Yield: 2.42 g, 65.0%; m.p. (°C): 149; Calc. for $C_7H_{11}N_3OSF_3I$ (M_r=369.14), %: C, 22.78; H, 3.00; N,

11.38; S, 13.04. Found, %: C, 22.51; H, 2.75; N, 11.43; S, 12.75. IR (cm^{-1}): $v_{as}(NH_2)$ 3352, $v_s(NH_2)$ 3250, $v(OH)$ 3040, ⌐(NH_2) 1641, $v(C=N)$ 1624, 1547. ^1H NMR (ppm): 9.84 (s, 2H, N*H$_2$*), 9.46 (s, 1H, O*H*), 3.70 (s, 2H, -C*H$_2$*-), 2.63 (s, 3H, S-C*H$_3$*), 2.12 (s, 3H, C-C*H$_3$*). m/z ESI MS (relative abundance%): [M-I] 242.0 (100%).

The iron(III) complex was synthesized using the literature methods (14,33). 1,1,1-Trifluoroacetylacetone-S-methylthiosemicarbazone hydrogen iodide (0.37 g, 1 mmol) and 2,3-dihydroxybenzaldehyde (0.14 g, 1 mmol) were dissolved in ethanol (10 mL) and the solution was added to a solution of $FeCl_3.6H_2O$ (0.27 g, 1 mmol) in ethanol (5 mL). Et_3N (0.1 mL) was added and the mixture was left to stand at room temperature for 6-8 hours. The solid was filtered off and recrystallized from a mixture of ethanol-dichloromethane (1:3).

Yield: 0.16 g, 35%. M.p. 275 °C. μ_{eff} (μ_B): 5.89. Anal. Calc. for $C_{14}H_{14}ClF_3FeN_3O_4S$ (468.64 g.mol^{-1}): C, 35.88; H, 3.01; N, 8.97; S, 6.84. Found: C, 35.53; H, 2.79; N, 8.71; S, 6.48%. IR: $v(OH)$ 3477-3442; $v(C=N^1)$ 1602; $v(N^2=C)$ 1578; $v(N^4=C)$ 1530. m/z ESI MS (relative abundance%): [M-H$_2$O-Cl] 415.1 (30.58%), 416.1 (6.51%), 417.2 (2.43%), [(M-H$_2$O-Cl)+CH$_3$OH] 446.5 (100%), 447.6 (16.30%), 448.5 (5.99%), [(M-H$_2$O-Cl)+CH$_3$OH+SCH$_3$] 492.9 (46.85%), 493.9 (9.76%), 494.8 (5.93%), [(M-H$_2$O)+Na+CH$_3$] 487.9 (27.52%), 488.9 (5.56%), 490.9 (2.71%).

Antioxidant Tests

1 mL of 1.10^{-4} M each compound was added to 2 mL of the DPPH (2,2-diphenyl-1-picrylhydrazyl) solution (4 mg/100 mL) and the final volume was completed to 4 mL using methanol. Reference solution was obtained by adding 2 mL of methanol to 2 mL of DPPH. The mixture was shaken and incubated. After 30 min absorbances were measured at 515 nm (35). The percentage of scavenging activity was calculated from the following equation: Radical scavenging activity(%) = [($A_{control}$ − A_{sample})/$A_{control}$] × 100.

CUPRAC (Cupric ion reducing antioxidant capacity) method was applied for determining cupric ions reducing potentials of the compounds (36). Briefly, 1 mL of each $CuCl_2$ (10 mM), neocuproine (Nc, 7.5 mM) and NH_4CH_3COO (1 M) solutions were added to the samples at 4.88-24.4 µM concentrations. Each of the volumes was adjusted to 4.1 mL with distilled water and incubated for 30 min. The increasing absorbance at 450 nm indicates the cupric reducing potential of the compounds. Trolox equivalent antioxidant capacities as TEAC values were calculated as the ratio of the molar absorption of each compound to that of trolox (ε_{trolox}: $1.58x10^4$ L mol^{-1} cm^{-1}).

RESULTS AND DISCUSSION

Synthesis and Structural Description

The thiosemicarbazone (L) was prepared by reacting 1,1,1-Trifluoroacetylacetone with S-methylthiosemicarbazide hydrogen iodide. The iron(III) complex, [Fe(L^1)Cl].H$_2$O, was synthesized by the reaction of equimolar ratio of 1,1,1-Trifluoroacetylacetone-S-methylthiosemicarbazone hydrogen iodide, the iron(III) salt (FeCl$_3$.6H$_2$O) and 2,3-dihydroxybenzaldehyde (Figure 1). The complex was obtained as black-looking crystals and it was soluble in solvents, such as CHCl$_3$, CH$_2$Cl$_2$, DMF, DMSO, and MeOH. The elemental analysis value and spectroscopic data were consistent with the proposed formulation of the iron(III) complex. The effective magnetic moment value of the complex was μ_{eff} = 5.89 μ_B, which corresponds to a high-spin state of iron(III) (37,38).

In the infrared spectra of the thiosemicarbazone, the $v_{as}(NH_2)$, $v_{as}(NH_2)$ and ⌐(NH_2) bands were observed at 3352, 3250 and 1641 cm^{-1}, respectively (Figure S3), were not present in the spectrum of the complex due to chelation. The band associated with the -OH bending mode at 3040 cm^{-1} was not seen in the spectrum of the complex because thiosemicarbazone is involved in complex formation with the deprotonated form. The $v(OH)$ bands of the 3-substituted hydroxyl group on the aromatic ring and one H$_2$O molecule in the complex structure were recorded around 3460 cm^{-1} (Figure S4). The C=N stretching bands of the thiosemicarbazone were observed at 1623 and 1541 cm^{-1}. After the formation of the complex, the $v(N^4=C)$ band of a new imine group formed by condensation of the thioamide nitrogen (N^4) and aldehyde was recorded at 1530 cm^{-1}.

The ESI MS data of the compounds were collected in positive ion mode using methanol (Figures. S1 and S2). For the thiosemicarbazone, the base peak (100% relative abundance) was registered at m/z 242 assigned to [M-I] structure. The monoisotopic mass of iron(III) complex, with the formula C$_{14}$H$_{14}$ClF$_3$FeN$_3$O$_4$S, is 467.97 Da and it was not seen prominently in the spectrum. The main peak of the complex was recorded at m/z 446.5 (100% relative abundance), along with a cluster of isotopes at m/z 447.6 and 448.5, which is related to [(M-H$_2$O-Cl) +CH$_3$OH]. The secondary noticeable peak was observed at m/z 492.9 (46.85%), attributed to [(M-H$_2$O-Cl)+CH$_3$OH+SCH$_3$], and it also showed isotope peaks at m/z 493.9 and 494.8. The cation adduct formation, [(M-H$_2$O)+Na+CH$_3$], was recorded in the range of m/z 487.9-490.9. The peak belonged to [M-H$_2$O-Cl] structure was recorded at m/z 415.1 (30.58% relative abundance) and it showed isotope peaks at m/z 416.1 and 417.2.
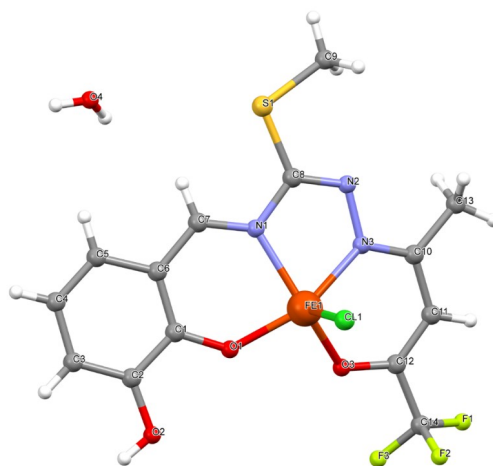
Figure 2: The molecular structure of [Fe(L^1)Cl].H$_2$O, showing the atom numbering scheme.

X-ray Analysis

The molecular structure of [Fe(L^1)Cl].H$_2$O is shown in Figure 2 with an atom numbering scheme. The asymmetric unit of complex [Fe(L^1)Cl].H$_2$O contains one Fe(III) ion, one L^1 ligand, one coordinated chlorine atom and one non-coordinated water molecule. The Fe(III) ion is coordinated by two oxygen [Fe1-O1= 1.893(2) Å and Fe1-O3= 1.935(3) Å] and two nitrogen atoms [Fe1-N1= 2.083(3) Å and Fe1-N3= 2.075(3) Å] from the thiosemicarbazidato structure and chlorine atom [Fe1-Cl1= 2.2114(13) Å]. The tau value, [τ =(β-α)/60, α and β being the two largest angles around the central atom], can be usefully used to estimate the degree of distortion from a square pyramidal to trigonal bipyramid structures. For an ideal square pyramidal geometry, the τ value is equal to zero, while it becomes one for a perfect trigonal bipyramidal geometry (39). The value of τ for the iron(III) ion is 0.09, indicating a distorted square pyramid. The molecules of [Fe(L^1)Cl].H$_2$O are connected by O-H⋯O and O-H⋯F hydrogen bonds (Table 3). The O4 atom of water molecule at (x, y, z) acts as a hydrogen-bond donor, via H4A atom, to O3^{ii} and F3^{ii} atoms, forming a R$_1^2$(5) ring. Similarly, the O4 atom at (x, y, z) acts as a hydrogen-bond donor, via H4B atom, to O1^{ii} and O2^{ii} atoms, forming a R$_1^2$(5) ring. The combination of hydrogen bonds produces edge-fused R$_1^2$(5), R$_2^2$(6) and R$_4^4$(8) rings (Figure 3).

Table 1: Crystal data and structure refinement parameters for [Fe(L^1)Cl].H$_2$O.

CCDC	2132527
Empirical formula	C$_{14}$H$_{14}$ClF$_3$FeN$_3$O$_4$S
Formula weight	468.64
Space group	P-1
Crystal system	Triclinic
a (Å)	7.928 (3)
b (Å)	8.744 (3)
c (Å)	14.269 (5)
$α$ (º)	97.039 (11)
$β$ (º)	94.454 (11)
$γ$ (º)	109.047 (9)
D_c (g cm^{-3})	1.691
V (Å^3)	920.6 (6)
μ (mm^{-1})	1.13
Z	2
Independent refls.	4578
Measured refls.	35138
S	1.12
R_{int}	0.047
R1/wR2	0.055/0.143
T$_{max}$/T$_{min}$	1.03/-0.43

Table 2: Selected bond distances (Å) and angles (º) for [Fe(L^1)Cl].H$_2$O.

Fe1-O1	1.893(2)	Fe1-O3	1.935(3)
Fe1-N3	2.075(3)	Fe1-N1	2.083(3)
Fe1-Cl1	2.2114(13)		
O1-Fe1-O3	92.96(11)	O1-Fe1-N3	149.45(12)
O3-Fe1-N3	87.52(12)	O1-Fe1-N1	86.99(11)
O3-Fe1-N1	143.46(12)	N3-Fe1-N1	75.02(11)
O1-Fe1-Cl1	106.66(9)	O3-Fe1-Cl1	107.63(10)
N3-Fe1-Cl1	102.24(9)	N1-Fe1-Cl1	107.33(9)
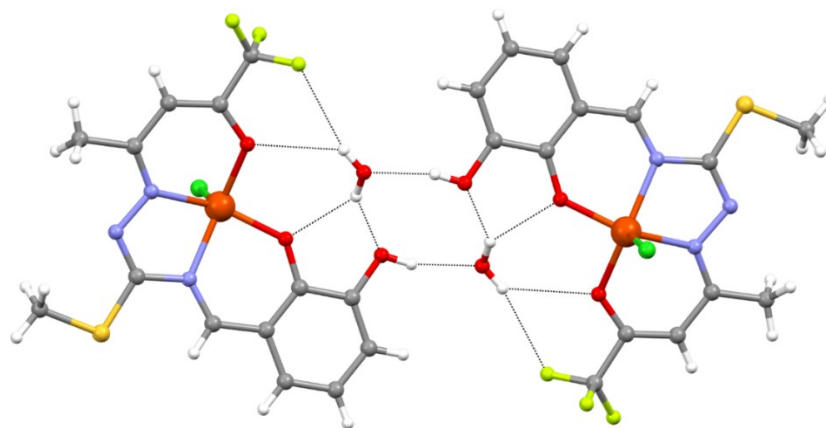
Figure 3: Crystal structure of [Fe(L^1)Cl].H$_2$O, showing the formation of R$_1^2$(5), R$_2^2$(6) and R$_4^4$(8) rings.

Table 3: Hydrogen-bond parameters for [Fe(L^1)Cl].H$_2$O (Å, º).

D-H···A	D-H	H···A	D···A	D-H···A
O2—H2···O4^i	0.82	1.94	2.740 (4)	164
O4—H4A···F3^{ii}	0.79 (7)	2.52 (7)	3.292 (6)	166
O4—H4A···O3^{ii}	0.79 (7)	2.57 (7)	3.136 (4)	130
O4—H4B···O1^{ii}	0.85 (7)	2.28 (7)	2.978 (4)	140
O4—H4B···O2^{ii}	0.85 (7)	2.25 (7)	3.009 (5)	149

Symmetry codes: (i) x−1, y−1, z; (ii) −x+1, −y+1, −z+1.

Antioxidant Properties

The DPPH radical is stable and commonly used for specifying the capability of an antioxidant agent (40). The result reveals that free radical (DPPH) scavenging activity follows the order: ascorbic acid > [Fe(L^1)Cl].H$_2$O > L (Table 4). According to this order, the iron complex is a more active radical scavenger than the free thiosemicarbazone (L). This might be due to the phenolic hydroxyl group in the complex structure. Based on the literature data, it was confirmed that the radical scavenging activities of the compounds were quite controlled by the number of phenolic hydroxyl groups (41,42). Among synthetic antioxidants, TBHQ with two hydroxyl groups has been shown to be a more potent antioxidant than BHA and BHT with one hydroxyl group (16). In a study, the DPPH assay showed that the ruthenium thiosemicarbazone complex is a more potent scavenger than the nickel thiosemicarbazone complex because it has two free hydroxyl groups (43). It was also reported that zinc(II) complexes containing four free hydroxyl groups showed remarkable scavenging activity (44).

Table 4: The free radical scavenging (FRS) activity as inhibition ratio %.

Compounds	FRS activity
L	39.65±2.43
[Fe(L^1)Cl].H$_2$O	66.77±1.44
Ascorbic acid	98.75±1.45

The CUPRAC method is based on the ability of a compound to reduce a [Cu(II)-Nc] complex to a [Cu(I)-Nc] complex. (19). The TEAC coefficients are given in Table 5. According to the results, the antioxidant capacity of both iron(III) complex and free thiosemicarbazone was superior to standard ascorbic acid. Especially, the TEAC value of the iron(III) complex was found to be 3.1 times higher than the value of ascorbic acid. Similar to the antiradical activity, the antioxidant capacity obtained for the iron(III) complex was also higher than for the free thiosemicarbazone.

In the literature, the antioxidant activity of the metal complexes was found to be higher (45,46) or lower (47,48) than the corresponding free ligands. The CUPRAC assay demonstrated that Zn(II), Co(II), Cu(II) and Ni(II) complexes of a chicoric acid ligand increased antioxidant properties compared to their free ligands (49). In another study, the antioxidant activity of the Zn(II) complex of chlorogenic acid ligand was tested and it was found that coordination with the metal nucleus increases the ability to reduce the ligand by about 1.5 times (50).

Table 5: The TEAC coefficients with regard to the CUPRAC assay.

Compounds	Molar absorptivity (L mol^{-1} cm^{-1})	TEAC$_{CUPRAC}$	Correlation coefficient (r)
L	3.6361 x 10^4	2.30 ± 0.15	0.9993
[Fe(L^1)Cl].H$_2$O	5.1590 x 10^4	3.27 ± 0.41	0.9977
Ascorbic acid	1.6590 x 10^4	1.05 ± 0.22	0.9989

CONCLUSION

The new iron(III) complex with S-methylthiosemicarbazone was synthesized and structurally confirmed. The crystal analysis showed that the complex had 6,5,6-membered chelate rings formed by coordination of the two oxygen and nitrogen atoms on the thiosemicarbazidato structure to the iron(III). The fifth coordination was completed with a chlorine atom, and coordination geometry around iron(III) could be defined as a distorted square pyramid.

The cupric ions (Cu^{2+}) reducing power (CUPRAC) and DPPH• scavenging activity of the synthesized S-methylthiosemicarbazone and iron(III) complex were studied. TEAC values showed that the iron(III) complex had a higher antioxidant capacity than the free thiosemicarbazone and ascorbic acid, and its DPPH radical scavenging ability was higher than that of the free thiosemicarbazone. The superior antioxidant properties of the iron(III) complex might be due to the presence of the hydroxyl group in the phenyl ring. Consequently, the complex with potent antioxidant activity is a promising component for

research related to oxidative stress-induced diseases and likely cancers.

CONFLICT OF INTEREST

The author declares no conflict of interest.

REFERENCES

1. Kalinowski DS, Stefani C, Toyokuni S, Ganz T, Anderson GJ, Subramaniam NV, et al. Redox cycling metals: Pedaling their roles in metabolism and their use in the development of novel therapeutics. Biochimica et Biophysica Acta (BBA) - Molecular Cell Research. 2016 Apr;1863(4):727–48. <DOI>.

2. Kalinowski DS, Richardson DR. The Evolution of Iron Chelators for the Treatment of Iron Overload Disease and Cancer. Pharmacol Rev. 2005 Dec;57(4):547–83. <DOI>.

3. Basu U, Roy M, Chakravarty AR. Recent advances in the chemistry of iron-based chemotherapeutic agents. Coordination Chemistry Reviews. 2020 Aug;417:213339. <DOI>.

4. Stacy AE, Palanimuthu D, Bernhardt PV, Kalinowski DS, Jansson PJ, Richardson DR. Structure–Activity Relationships of Di-2-pyridylketone, 2-Benzoylpyridine, and 2-Acetylpyridine Thiosemicarbazones for Overcoming Pgp-Mediated Drug Resistance. J Med Chem. 2016 Sep 22;59(18):8601–20. <DOI>.

5. Maqbool SN, Lim SC, Park KC, Hanif R, Richardson DR, Jansson PJ, et al. Overcoming tamoxifen resistance in oestrogen receptor-positive breast cancer using the novel thiosemicarbazone anti-cancer agent, DpC. Br J Pharmacol. 2020 May;177(10):2365–80. <DOI>.

6. Lui GYL, Kovacevic Z, Richardson V, Merlot AM, Kalinowski DS, Richardson DR. Targeting cancer by binding iron: Dissecting cellular signaling pathways. Oncotarget. 2015 Aug 7;6(22):18748–79. <DOI>.

7. Saswati S, Adão P, Majumder S, Dash SP, Roy S, Kuznetsov ML, et al. Synthesis, structure, solution behavior, reactivity and biological evaluation of oxidovanadium(iv / v) thiosemicarbazone complexes. Dalton Trans. 2018;47(33):11358–74. <DOI>.

8. Park KC, Fouani L, Jansson PJ, Wooi D, Sahni S, Lane DJR, et al. Copper and conquer: copper complexes of di-2-pyridylketone thiosemicarbazones as novel anti-cancer therapeutics. Metallomics. 2016;8(9):874–86. <DOI>.

9. Ohui K, Afanasenko E, Bacher F, Ting RLX, Zafar A, Blanco-Cabra N, et al. New Water-Soluble Copper(II) Complexes with Morpholine–Thiosemicarbazone Hybrids: Insights into the Anticancer and Antibacterial Mode of Action. J Med Chem. 2019 Jan 24;62(2):512–30. <DOI>.

10. Alcaraz R, Muñiz P, Cavia M, Palacios Ó, Samper KG, Gil-García R, et al. Thiosemicarbazone-metal complexes exhibiting cytotoxicity in colon cancer cell lines through oxidative stress. Journal of Inorganic Biochemistry. 2020 May;206:110993. <DOI>.

11. Kaya B, Kalındemirtaş FD, Ertik O, Yanardag R, Kuruca SE, Ülküseven B. New thiosemicarbazone-based Zinc(II) complexes. In vitro cytotoxicity competing with cisplatin on malignant melanoma A375 cells and its relation to neuraminidase inhibition. Chemico-Biological Interactions. 2022 Jan;351:109757. <DOI>.

12. Özerkan D, Ertik O, Kaya B, Kuruca SE, Yanardag R, Ülküseven B. Novel palladium (II) complexes with tetradentate thiosemicarbazones. Synthesis, characterization, in vitro cytotoxicity and xanthine oxidase inhibition. Invest New Drugs. 2019 Dec;37(6):1187–97. <DOI>.

13. Bal T, Atasever B, Solakoğlu Z, Erdem-Kuruca S, Ülküseven B. Synthesis, characterisation and cytotoxic properties of the N1,N4-diarylidene-S-methyl-thiosemicarbazone chelates with Fe(III) and Ni(II). European Journal of Medicinal Chemistry. 2007 Feb;42(2):161–7. <DOI>.

14. Kaya B, Yılmaz ZK, Şahin O, Aslim B, Tükenmez Ü, Ülküseven B. Structural analysis and biological functionalities of iron(III)– and manganese(III)–thiosemicarbazone complexes: in vitro anti-proliferative activity on human cancer cells, DNA binding and cleavage studies. J Biol Inorg Chem. 2019 May;24(3):365–76. <DOI>.

15. Bal-Demirci T, Congur G, Erdem A, Erdem-Kuruca S, Özdemir N, Akgün-Dar K, et al. Iron(iii) and nickel(ii) complexes as potential anticancer agents: synthesis, physicochemical and structural properties, cytotoxic activity and DNA interactions. New J Chem. 2015;39(7):5643–53. <DOI>.

16. Gulcin İ. Antioxidants and antioxidant methods: an updated overview. Arch Toxicol. 2020 Mar;94(3):651–715. <DOI>.

17. Haraguchi H. Antioxidative plant constituents. Bioactive compounds from natural sources. Taylor & Francis: London, UK; 2001. p. 337–78.

18. Anraku M, Gebicki JM, Iohara D, Tomida H, Uekama K, Maruyama T, et al. Antioxidant activities of chitosans and its derivatives in in vitro and in vivo studies. Carbohydrate Polymers. 2018 Nov;199:141–9. <DOI>.

19. Marchi RC, Campos IAS, Santana VT, Carlos RM. Chemical implications and considerations on techniques used to assess the in vitro antioxidant activity of coordination compounds. Coordination Chemistry Reviews. 2022 Jan;451:214275. <DOI>.

20. Balakrishnan N, Haribabu J, Dhanabalan AK, Swaminathan S, Sun S, Dibwe DF, et al. Thiosemicarbazone(s)-anchored water soluble mono- and bimetallic Cu(ii) complexes: enzyme-like activities, biomolecular interactions, anticancer property and real-time live cytotoxicity. Dalton Trans. 2020;49(27):9411–24. <DOI>.

21. İlhan-Ceylan B. Oxovanadium(IV) and Nickel(II) complexes obtained from 2,2'-dihydroxybenzophenone-S-methyl-thiosemicarbazone: Synthesis, characterization, electrochemistry, and antioxidant capability. Inorganica Chimica Acta. 2021 Mar;517:120186. <DOI>.

22. Poladian Q, Şahin O, Karakurt T, İlhan-Ceylan B, Kurt Y. A new zinc(II) complex with N2O2-tetradentate schiff-base derived from pyridoxal-S-methylthiosemicarbazone: Synthesis, characterization, crystal structure, DFT, molecular docking and antioxidant activity studies. Polyhedron. 2021 Jun;201:115164. <DOI>.

23. Eğlence-Bakır S. New nickel(II) complexes containing N2O2 donor thiosemicarbazones: Synthesis, characterization and antioxidant properties. Journal of Molecular Structure. 2021 Dec;1246:131121. <DOI>.

24. Kaya B, Şahin O, Bener M, Ülküseven B. Iron(III) and nickel(II) complexes with S-alkyl (n-C1-6)-thiosemicarbazidato ligands: Synthesis, structural characterization, and antioxidant features. Journal of Molecular Structure. 2018 Sep;1167:16–22. <DOI>.

25. Kaya B, Kaya K, Koca A, Ülküseven B. Thiosemicarbazide-based iron(III) and manganese(III) complexes. Structural, electrochemical characterization and antioxidant activity. Polyhedron. 2019 Nov;173:114130. <DOI>.

26. Bal-Demirci T, Şahin M, Kondakçı E, Özyürek M, Ülküseven B, Apak R. Synthesis and antioxidant activities of transition metal complexes based 3-hydroxysalicylaldehyde-S-methylthiosemicarbazone. Spectrochimica Acta Part A: Molecular and Biomolecular Spectroscopy. 2015 Mar;138:866–72. <DOI>.

27. Kalındemirtaş FD, Kaya B, Bener M, Şahin O, Kuruca SE, Demirci TB, et al. Iron(III) complexes based on tetradentate thiosemicarbazones: Synthesis, characterization, radical scavenging activity and in vitro cytotoxicity on K562, P3HR1 and JURKAT cells. Appl Organomet Chem [Internet]. 2021 Apr [cited 2022 Jun 22];35(4). <DOI>.

28. Sheldrick GM. A short history of SHELX. Acta Crystallogr A Found Crystallogr. 2008 Jan 1;64(1):112–22. <DOI>.

29. Sheldrick GM. Crystal structure refinement with SHELXL. Acta Crystallogr C Struct Chem. 2015 Jan 1;71(1):3–8. <DOI>.

30. Anonymous. APEX2. Bruker AXS, Inc., Wisconsin, USA; 2013.

31. Macrae CF, Sovago I, Cottrell SJ, Galek PTA, McCabe P, Pidcock E, et al. Mercury 4.0: from visualization to analysis, design and prediction. J Appl Crystallogr. 2020 Feb 1;53(1):226–35. <DOI>.

32. Farrugia LJ. WinGX and ORTEP for Windows: an update. J Appl Crystallogr. 2012 Aug 1;45(4):849–54. <DOI>.

33. Atasever Arslan B, Kaya B, Şahin O, Baday S, Saylan CC, Ülküseven B. The iron(III) and nickel(II) complexes with tetradentate thiosemicarbazones. Synthesis, experimental, theoretical characterization, and antiviral effect against SARS-CoV-2. Journal of Molecular Structure. 2021 Dec;1246:131166. <DOI>.

34. Gündüz MG, Kaya B, Özkul C, Şahin O, Rekha EM, Sriram D, et al. S-alkylated thiosemicarbazone derivatives: Synthesis, crystal structure determination, antimicrobial activity evaluation and molecular docking studies. Journal of Molecular Structure. 2021 Oct;1242:130674. <DOI>.

35. Sánchez-Moreno C, Larrauri JA, Saura-Calixto F. A procedure to measure the antiradical efficiency of polyphenols. J Sci Food Agric. 1998 Feb;76(2):270–6. <DOI>.

36. Apak R, Güçlü K, Özyürek M, Karademir SE. Novel Total Antioxidant Capacity Index for Dietary Polyphenols and Vitamins C and E, Using Their Cupric Ion Reducing Capability in the Presence of Neocuproine: CUPRAC Method. J Agric Food Chem. 2004 Dec 1;52(26):7970–81. <DOI>.

37. Leovac V, Divjakovic V, Cesljevic V, Fazlic R. Transition metal complexes with thiosemicarbazide-based ligand: Part 45 - Synthesis, crystal and molecular structure of [2,6-diacetylpyridine bis(S-methylisothiosemicarbazonato)]diazide-iron(III). J Serb Chem Soc. 2003;68(4–5):425–33. <DOI>.

38. Gullotti M, Casella L, Pasini A, Ugo R. Optically active complexes of Schiff bases. Part 3. Complexes of iron(III) with quadridentate Schiff bases derived from salicylaldehyde. J Chem Soc, Dalton Trans. 1977;(4):339. <DOI>.

39. Addison AW, Rao TN, Reedijk J, van Rijn J, Verschoor GC. Synthesis, structure, and spectroscopic properties of copper(II) compounds containing nitrogen–sulphur donor ligands; the crystal and molecular structure of aqua[1,7-bis(N-methylbenzimidazol-2'-yl)-2,6-dithiaheptane]copper(II) perchlorate. J Chem Soc, Dalton Trans. 1984;(7):1349–56. <DOI>.

40. Xie D, Gan T, Su C, Han Y, Liu Z, Cao Y. Structural characterization and antioxidant activity of water-soluble lignin-carbohydrate complexes (LCCs) isolated from wheat straw. International Journal of Biological Macromolecules. 2020 Oct;161:315–24. <DOI>.

41. Gülçin İ. Comparison of in vitro antioxidant and antiradical activities of L-tyrosine and L-Dopa. Amino Acids. 2007 Apr;32(3):431–8. <DOI>.

42. Mahendra raj K, Mruthyunjayaswamy BHM. Synthesis, spectroscopic characterization, electrochemistry and biological activity evaluation of some metal (II) complexes with ONO donor ligands containing indole and coumarin moieties. Journal of Saudi Chemical Society. 2017 Jan;21:S202–18. <DOI>.

43. Bal-Demirci T, Güveli Ş, Yeşilyurt S, Özdemir N, Ülküseven B. Thiosemicarbazone ligand, nickel(II) and ruthenium(II) complexes based on vitamin B6 vitamer: The synthesis, different coordination behaviors and antioxidant activities. Inorganica Chimica Acta. 2020 Mar;502:119335. <DOI>.

44. Andelescu AA, Cretu C, Sasca V, Marinescu S, Cseh L, Costisor O, et al. New heteroleptic Zn(II) and Cu(II) complexes with quercetine and N^N ligands. Polyhedron. 2018 Jun;147:120–5. <DOI>.

45. Buldurun K, Turan N, Savcı A, Çolak N. Synthesis, structural characterization and biological activities of metal(II) complexes with Schiff bases derived from 5-bromosalicylaldehyde: Ru(II) complexes transfer hydrogenation. Journal of Saudi Chemical Society. 2019 Feb;23(2):205–14. <DOI>.

46. Dimiza F, Raptopoulou CP, Psycharis V, Papadopoulos AN, Psomas G. Manganese(ii) complexes with the non-steroidal anti-inflammatory drugs naproxen and mefenamic acid: synthesis, structure, antioxidant capacity, and interaction with albumins and DNA. New J Chem. 2018;42(20):16666–81. <DOI>.

47. Hosseini-Yazdi SA, Mirzaahmadi A, Khandar AA, Mahdavi M, Rahimian A, Eigner V, et al. Copper, nickel and zinc complexes of a new water-soluble thiosemicarbazone ligand: Synthesis, characterization, stability and biological evaluation. Journal of Molecular Liquids. 2017 Dec;248:658–67. <DOI>.

48. Özdemir Ö. Bis-azo-linkage Schiff bases—Part(II): Synthesis, characterization, photoluminescence and DPPH radical scavenging properties of their novel luminescent mononuclear Zn(II) complexes. Journal of Photochemistry and Photobiology A: Chemistry. 2020 Apr;392:112356. <DOI>.

49. Świderski G, Jabłońska-Trypuć A, Kalinowska M, Świsłocka R, Karpowicz D, Magnuszewska M, et al. Spectroscopic, Theoretical and Antioxidant Study of 3d-

Transition Metals (Co(II), Ni(II), Cu(II), Zn(II)) Complexes with Cichoric Acid. Materials. 2020 Jul 11;13(14):3102. <DOI>.

50. Kalinowska M, Sienkiewicz-Gromiuk J, Świderski G, Pietryczuk A, Cudowski A, Lewandowski W. Zn(II) Complex of Plant Phenolic Chlorogenic Acid: Antioxidant, Antimicrobial and Structural Studies. Materials. 2020 Aug 24;13(17):3745. <DOI>.

An Iron(III)-S-methylthiosemicarbazone Complex: Synthesis, Spectral Characterization, and Antioxidant Potency Measured by CUPRAC and DPPH Methods

SUPPLEMENTARY INFORMATION

Büşra Kaya*

Istanbul University-Cerrahpasa, Faculty of Engineering, Department of Chemistry, 34320, Istanbul, Turkey.
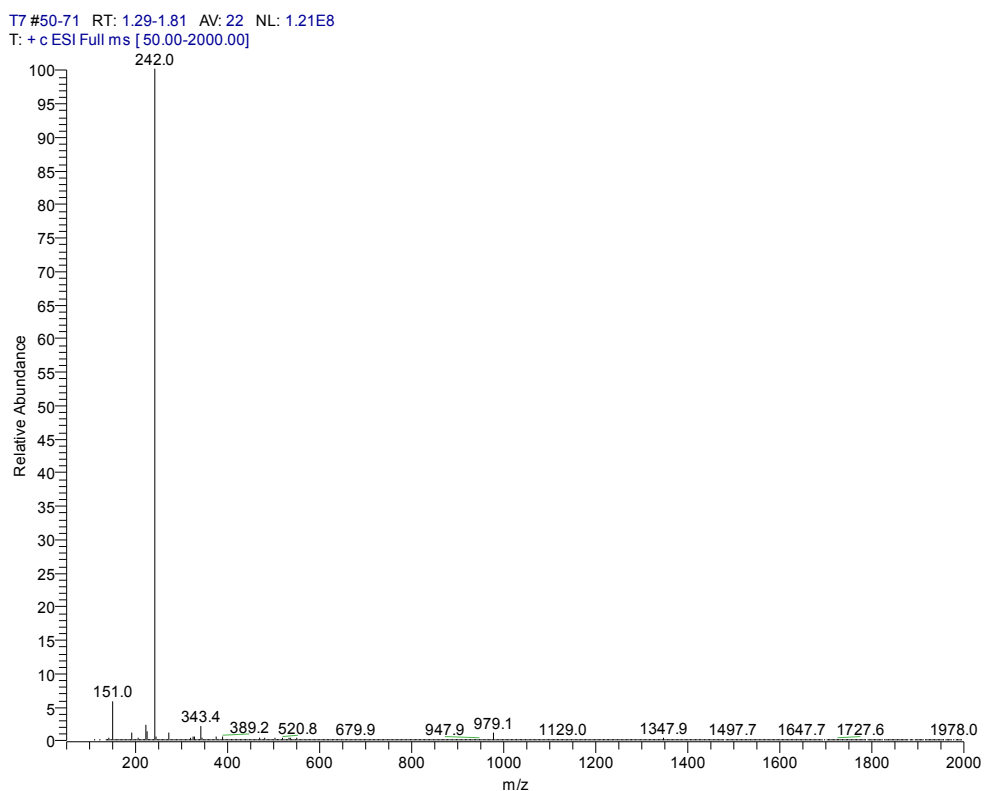
Figure S1: ESI MS of L in MeOH.
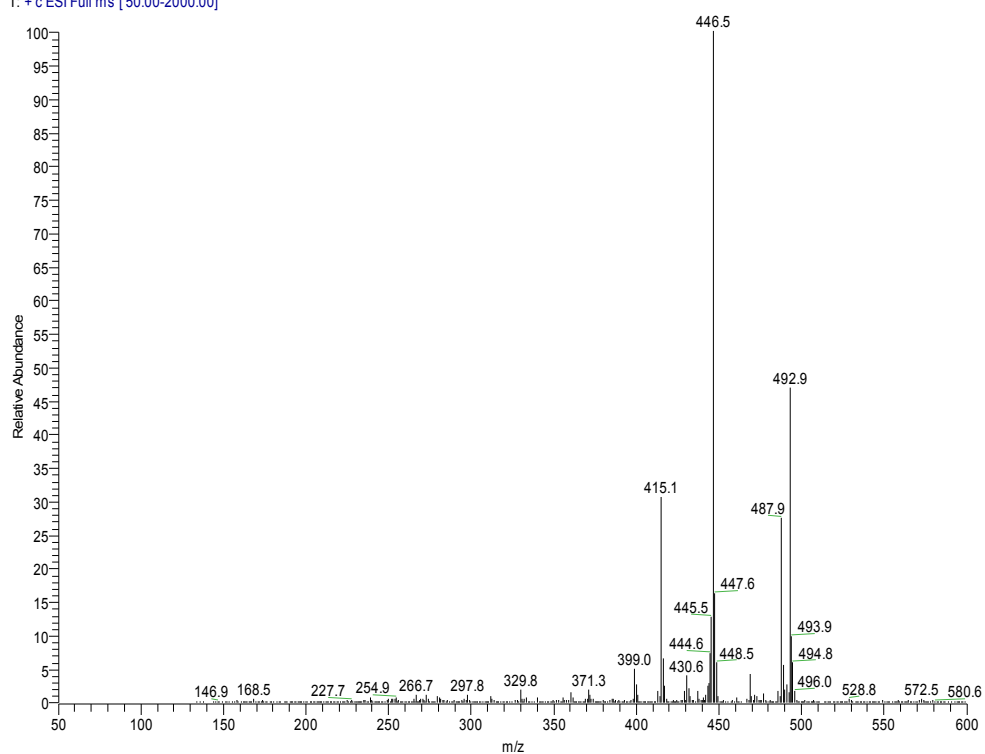
Figure S2: ESI MS of [Fe(L^1)Cl].H$_2$O in MeOH.
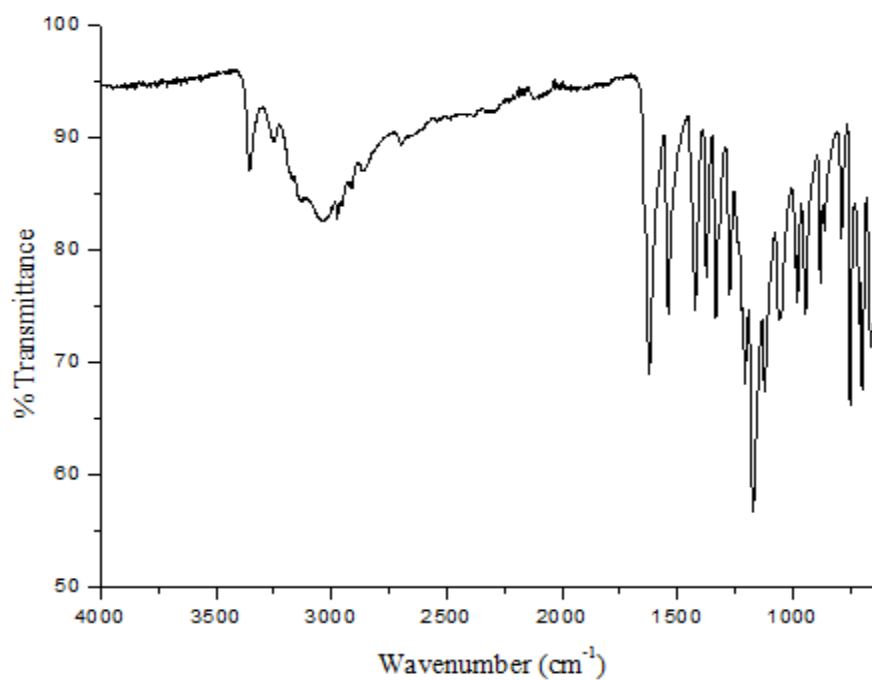
Figure S3: IR spectrum of L.
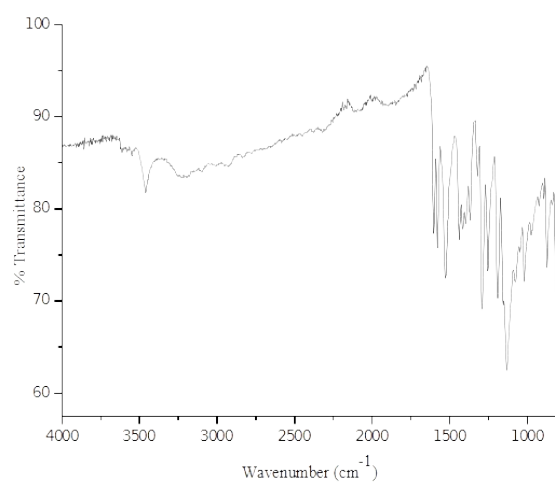
Figure S4: IR spectrum of $[Fe(L^1)Cl].H_2O$.
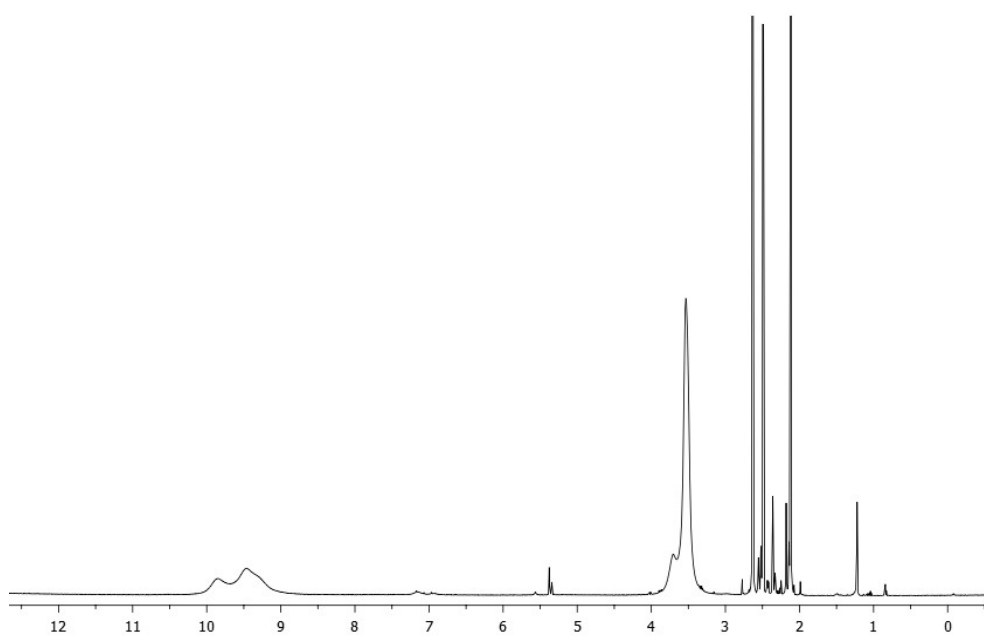
Figure S5: ^1H NMR spectrum of **L** in DMSO-d_6.

RESEARCH ARTICLE

Poly(MMA-co-MI) Nanocomposite with Modified Nano ZRP with KH570 Linker: Preparation, Characterization and Transparency Properties

Fariborz Atabaki*[1] [iD] **, Gholam Ali Koohmareh[2]** [iD] **and Samira Sarikhani[1]** [iD]
[1]Department of Chemistry, College of Science, Malek-ashtar University of Technology, Isfahan, Iran.
[2]Department of Chemistry, University of Isfahan, Isfahan, 81746-73441, Iran.

Abstract: In this study, zirconium phosphate was synthesized and modified with KH570 linker. It was then used to prepare several nanocomposites with different percent with poly (methyl methacrylate-co-N-2-methyl-4-nitro-phenylmaleimide) (Poly (MMA-co-MI)). The synthesized compounds were characterized by Fourier transform infrared spectroscopy (FTIR), X-ray diffraction (XRD), and field-emission scanning electron microscopy (FE-SEM). The particles size and structure determining showed nanoparticle are sheet and about 9-20 nm. Thermal stability of these compounds were evaluated by thermogravimetric analysis (TGA). The results showed adding nanoparticles to copolymer increased starting weight lost about 20 $^{\circ}$C and finishing weight lost about 90 $^{\circ}$C. The results of differential scanning calorimetry (DSC), showed that adding nanoparticles decreased the glass transition temperatures (T_g) of the copolymer. The transparency of these nanocomposites were examined by ultraviolet–visible (UV–Vis) spectroscopy. The results showed the best transparency refer to nanocomposites 0.5 to 1% of nanoparticles.

INTRODUCTION

The use of polymer nanocomposites has been recently paid much attention to applied and industrial researches. The polymeric matrices and nano fillers in nanocomposite structure have a special importance in determining their features and applications. Since the nanotechnology has been utilized to create materials with improving mechanical and physical properties, nanoparticles were added into the base of materials to form composite materials with unique physical and mechanical properties (1,2), such as the properties of polymers such as flexibility, optical clarity, and excellent dimensional stability of poly methyl methacrylate (PMMA), whereas inorganic materials show mechanical strength, thermal stability, and a high modulus (3-5).

PMMA is one of the common medical polymers employed widely in manufacturing various implants, especially in the fabrication of an ophthalmic intraocular lenses due to its mechanical properties, mould ability, and optical rehabilitation (6,7). Methyl methacrylate (MMA) has been used as a comonomer in several reports such as block copolymer with styrene (6,8,9), copolymerization with tricyclodecyl methacrylate (10), and copolymerization reaction with maleimide (11,12). In addition, the use of PMMA in the preparation of various nanocomposites with several additives such as SiO_2 (13), Clay (14), TiO_2 (15), ZrO_2 (16), MWCNT (17), and Al_2O_3 (18) has been reported.

The use of TiO_2 thin-films with high transmittance in the visible region as antibacterial coating could be effective for PMMA in ophthalmic applications (19,20). It was used with ZrO_2 nano particle for denture base applications, too (7,21).

Inorganic hybrid nanoparticles are highly attractive in both academic and industrial researches. They are able not only to combine the properties of both components, polymers and inorganic matter, but also provide unique and tuneable properties (22,23). One of the major issues in these materials is dispersing degree of particles into the polymer matrix and the interfacial property between the organic and inorganic components (24,25).

In order to enhance the stability of nanoparticles in the polymer matrix, surface modification of the nanoparticles is needed. It could be improved by introducing coupling agents or reactive functional groups onto the surface of nanoparticles (26).

Zirconium phosphate (ZrP) serves as nano filler in the polymeric interface, where their presence affects profoundly the chemical, mechanical, and thermal properties of the nanocomposite. It is acidic, inorganic cation exchange materials which usually presents a layered structure. There are various phases of ZrP that differ in their interlamellar spaces and their crystalline structure. Among all the ZrP phases, the most widely used are the α-phase and the γ-phase, whose crystal structures were elucidated by Clearfield and co-workers (27). Yamanaka and Hattori reported a mixed ɣ-zirconium phosphate (ɣ-ZrP) benzene phosphonate can be obtained by contacting ɣ-ZrP with benzene phosphoric acid. However, at that time ɣ-ZrP was formulated as $Zr(HPO_4)_2.2H_2O$ and its structure was believed erroneously to be similar to that of α-ZrP but with a different packing of the layers, so it was not possible to give a correct interpretation in order to experimental data (28). While layered ZrP micro-crystals might not be as ideal as porous materials, because of small hydroxyl accessibility, single-layer ZrP nano sheets from the exfoliation of its micro-crystals serve as an ideal candidate for post-grafting since after exfoliation, the hydroxyl groups are fully exposed and readily react with silane. The hydroxyl groups exist on both sides of nano sheets. After surface grafting, the obtained compounds are expected to possess a high density of functional groups, which are critical for high catalytic performance. Furthermore, the lateral dimension of ZrP nano sheets can be altered by tuning the synthetic conditions. Another major advantage of using ZrP nano sheets as the solid substrate is nano sheets can be uniformly dispersed in a wide range of polar solvents, leading to high catalytic efficiency, but meanwhile they can be easily separated from the dispersion system using centrifugation (29).

Modified silica nano particles -3-methacryloxypropyltrimethoxysilane- (KH-570 linker) can be attached to metallic surface by a condensation reaction resulting in a covalent bond and also cause a good interaction with PMMA to preparing nanocomposite (5). As N-2-methyl-4-nitro-phenylmaleimide (MI) was added in PMMA matrix to improve its thermal stability in previews work (30), in this research our goal is to modify nano ZrP with KH570 linker and make a nanocomposite based on this modified nanoparticles with poly(MMA-co-MI).

EXPERIMENTAL SECTION

Materials
Zirconium(IV) chloride (ZrCl₄, Aldrich), orthophosphoric acid (H₃PO₄, 85%, Aldrich), tetra-n-butylammonium hydroxide (TBA, Aldrich), nitric acid (Aldrich), KH-570 linker (γ-methacryloyloxypropyl trimethoxy silane, Aldrich), methyl methacrylate (Merck). Benzoyl peroxide (BPO, Merck), 2-methyl-4-nitroaniline (Merck), maleic anhydride (MA, Merck), ethyl acetate, and methanol were distilled over potassium hydroxide under vacuum.

Preparation of N-2-methyl-4-nitro-phenylmaleimide
MI was prepared according to our previous research (30). First, maleic anhydride (4.9 g, 0.05 mol) was dissolved in 15 mL of acetone. Then, a solution of 2-methyl-4-nitroaniline (7.6 g, 0.05 mol) in 15 mL of acetone was added dropwise under vigorous stirring. After complete addition, the mixture is stirred for 1 h. The solid (maleamic acid) which precipitated was filtered off (11.1 g, 89%, mp: 169-171 °C). Maleamic acid (10.0 g, 0.04 mol) was then dissolved in 15 mL of acetic anhydride with added 0.3 g of sodium acetate. The mixture was heated for 6 h under reflux. A cream solid is recovered (8.64 g, 93%. mp: 251–253 °C).

Preparation of Nanoparticle
In order to modify ZrP with KH-570 linker, first ZrP was synthesized and exfoliated with TBA according to reported procedures. It was then modified with KH-570 linker (Scheme 1).
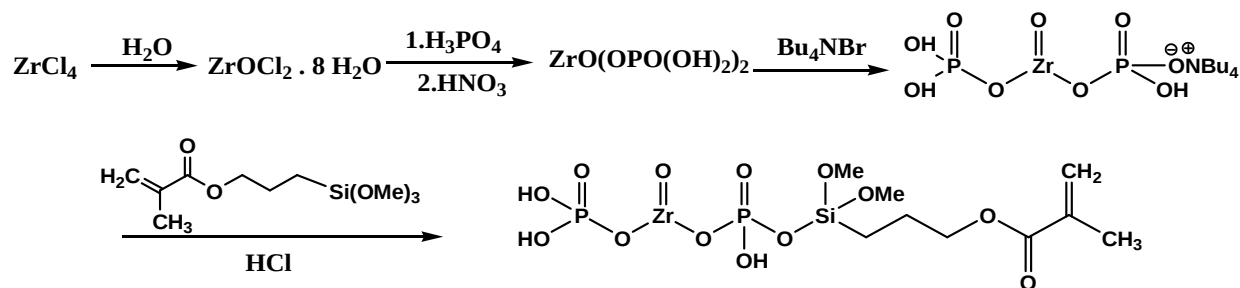
Preparation of zirconium phosphate (31,32)
Zirconium tetrachloride (4.66 g, 20 mmol) was dissolved in water (25 mL) and heated 100 °C, to make a saturated 2 M zirconium solution. Upon cooling, Zirconium oxychloride crystals (5.51 g, yield: 85.3%, mp: 149-152 °C) were formed. Zirconium oxychloride (5 g) was mixed with 50 mL of 6.0 M orthophosphoric acid solution in demineralized water (DMW) at 25 °C for 1 h and at 80 °C for 24 h. The precipitate was collected, followed by washing with DMW, and drying for 24 h in oven at 80 °C. This product was then treated with 20 mL (0.1 M) nitric acid solution for complete replacement of counter ions with H^+ ions at 25 °C for 1 h and was washed with DMW (7.12 g, yield:71.4%)

Reaction of ZrP with TBA (29)
The prepared ZrP (2.2 g in 10 mL of water) was reacted and exfoliated with TBA (10 mL of 0.5 M aqueous solution) in an ice bath for 6 h and at 25 °C for 18 h. The precipitate was smoothed and dried at 25 °C (1.8 g, yield: 81.8%, decomposed at 311 °C)

Modification of exfoliated ZrP with KH-570 linker
A solution of KH-570 linker (1 mL in 10 ml HCl 0.1 M) was added to a solution of exfoliated ZrP (1 g, in 5 mL of water) and spired at 65 °C for 1 h. The precipitate was collected (0.94 g, yield: 95.9%, mp>293 °C, XRF data acquired from the analyzer is (P, 18.2; Zr, 21.4; other 57.7), other is for elements smaller than Na such as C, O, H, Si; and calculated elemental analysis for $(ZrOPO(OH)OSi(OMe)_2(CH_2)_3OCOCCH_3CH_2)OPO(OH)_2)$ is (C, 20.89; H, 3.90; O, 40.19; P, 11.97; Si, 5.43; Zr, 17.63).
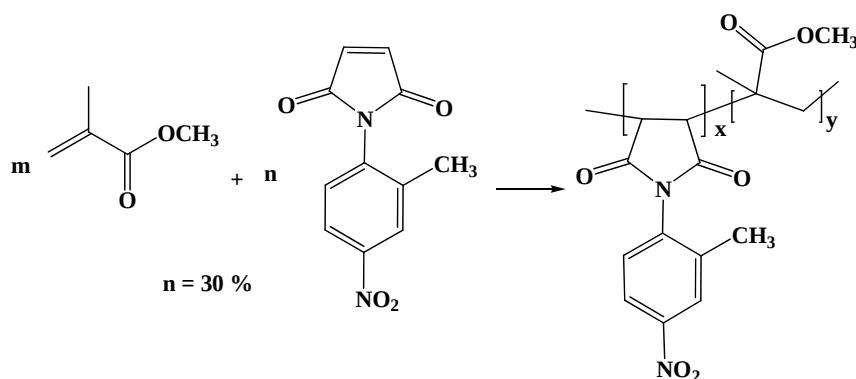
Scheme 1.

Synthesis of poly (MMA-co-MI)

In a 250 mL round bottomed flask, equipped with reflux condenser and nitrogen inlet tube, a solution of MMA (1.1 mL, 10 mmol), and MI (1 gr, 0.4 mmol) in ethyl acetate (6 mL) was prepared. BPO (0.02 g) was added and the reaction mixture was heated for 8h at 77 °C (reflux). The solution was then poured in methanol and the precipitate was washed with methanol and dried. (1.8 gr, yield: 85.7%, CHNS data acquired from the analyzer is (C, 58.49; H, 6.04; N, 5.58), and calculated elemental analysis for predicted copolymer is (C, 58.36; H, 5.91; N, 6.01; O, 29.73). Percentage of MI in copolymer is 27.8% (Scheme 2).

Scheme 2.

Preparation of Nanocomposite

A solution of synthesized copolymer (1 g) in ethyl acetate (10 mL) was prepared. A dispersion of modified nanoparticles (0.01 g) in ethyl acetate (5 mL) was sonicated for 20 min and was added to a prepared polymer solution and sonicated again for 20 min. The solution was then precipitated in methanol to afford 1% nanocomposite powder. Four other percentages were prepared according to the same procedure. In other reaction experiments, an in-situ nanocomposites were prepared by adding the appropriate nanoparticle amounts into monomers mixtures during polymerization reaction.

Characterization

FT-IR spectral data were recorded with a Bruker spectrometer in the range of 4000–400 cm^{-1} using KBr disks. SEM image of the electrospinning nanofibers was obtained through the scanning electron microscopy (SEM). The morphology of the pristine α-ZrP powder was also observed at an accelerating voltage of 5 kV. The chemical state of the surface was characterized by X-ray photoelectron spectroscopy Bruker model D8ADVANCE. TEM micrographs were obtained with an H-7500 transmission electron microscope (Philips 208 S 100 kW) at an accelerating voltage of 75 kV. Ultrathin sections were microtome at room temperature. Thermal stabilities were measured via thermogravimetric analysis in nitrogen with a TA Instruments model Q2000 at a heating rate of 20 °C min^{-1}. DSC was used to measure glass transition temperature using a TA Q2000 instrument in nitrogen atmosphere at the heating rate of 20 °C/min from 80 to 150 C and a cooling rate of 10 °C/min. The adsorption ability of Poly (MMA-co-MI)/nano (ZrP-KH570) was investigated by solution adsorption technique. For measuring transmittance in UV and visible area, 50 mg of nanocomposite was dissolved in 10 mL ethyl acetate, Ultraviolet-visible spectrophotometer model Photonix Ar 2015 was used. X-Ray Fluorescence analysis (XRF) was determined with XRF device model Niton from Thermo Company. Elemental analyses (CHNS) was determined by device model Vario EL Ш from Elementar Company.

RESULTS AND DISCUSSION

Characterization

Modified ZrP with KH-570 was prepared according to Scheme 1. FTIR spectra of these compounds are illustrated in Figure 1. For ZrP, the peaks locating at 3594, 3510 are due to the water molecules in the interlayer space of ZrP, 3164, and 1620 cm^{-1} are assigned as symmetric and bending vibrations of –

OH groups, respectively (29). The peaks at 3384, 1251 968 cm^{-1} are attributed to P–OH stretching vibrations or deformation vibrations. The strong bands in the range of 1000–1200 cm^{-1} are characteristic of PO$_4$ stretching vibrations and 597 cm^{-1} is ascribed to the vibration of Zr−O (33). After reaction of ZrP with TBA, no significant change was occurred and just the P-OH at 1200 cm^{-1} become broader, which was due to the presence of ammonium salt. After modification with KH-570 linker, a peak at 1745 cm^{-1} was appeared and confirmed presence of carbonyl group in the particles and 2957 cm^{-1} is ascribed to the asymmetric C–H stretching of SiOMe and The peaks at 980 cm^{-1} is attributed to C=C bending (34).

Figure 1: FTIR spectra of ZrP nano particles, ZrP modified by TBA and ZrP modified by KH-570 linker.

Solution polymerization of MMA with synthesized MI was led to poly (MMA-co-MI) due to Scheme 2. It was then sonicated with modified ZrP with KH-570 to prepare the related nanocomposites. Evaluation of the best technique for preparation of nanocomposite an in situ preparation during polymerization was also investigated. All of the polymers and composites were investigated using FTIR spectroscopy. (Figure 2).

The peaks of C=O (1727 cm^{-1}), CH3–O (1148, 1194 cm^{-1}), and C–O (1242, 1270 cm^{-1}) are consistent with those of PMMA as reported in the literature (35,36). And also the bands at 1782 cm^{-1} (C=O imide stretching), 1589 cm^{-1} (C=C aromatic stretching), 1530 and 1348 cm^{-1} (N=O stretching) show the maleimide units as mentioned in the literature and also peaks of nano particle that is discussed in Figure 1 (30,37,38).

Figure 2: FTIR spectra of poly (MMA-co-MI)–ZrP nanocomposites, poly (MMA-co-MI).

XRD analysis: It is known that ZrP has a clay-like layered structure, which can be characterized using XRD, with interlayer separation calculated from the Bragg equation. Figure 3(a–d) presents the XRD results. Sharpening the peaks of Figure 3b confirms the preparation of ammonium salts of nanoparticles compared to the peaks of Figure 3a. As shown in Figure 3d nanocomposite have both nanoparticles and PMMA background peak (39). The diffractogram of ZrP sample shows peaks at 2θ values: 7, 14, 23, 29, 40, 44, and 56. Reacted ZrP with TBA's spectrum shows same peaks, with a large difference in peak wide at 2θ: 7. Modified ZrP by KH-570's spectrum shows all peaks above except 44. According to Scherrer equation ($D = (0.9 \lambda)/ (\beta \cos \theta)$) the size of

crystals of nano particles can be determined. D is the mean size of the ordered (crystalline) domains, which may be smaller or equal to the particle size. λ is the X-ray wavelength (1.789 A°). β is the line broadening at half the maximum intensity (FWHM) in radian and θ is the Bragg angle. The results are summarized in Table 1 (40).

Table 1: Size of nano particles.

Nanoparticles	ZrP	ZrP-TBA	ZrP-KH
D(nm)	19.13	10.359	9.347
Used 2θ (°)	14	14	14

Figure 3: XRD results: (a) ZrP, (b) ZrP modified by TBA, (c) ZrP modified by KH-570 linker, (d) MMA-co-MI/ZrP 1% nanocomposite.

SEM micrographs: Figure 4 shows SEM micrographs of the ZrP modified by KH-570 linker and nanocomposites. Figure 4a confirms modified ZrP crystals sheet structure clearly. Figure 4b-d shows the good dispersion of nanoparticle in polymer layers. Figure 4e shows the undesirable accumulation of nanoparticle in nanocomposite 5%. It can make this composite unsuitable in some properties.
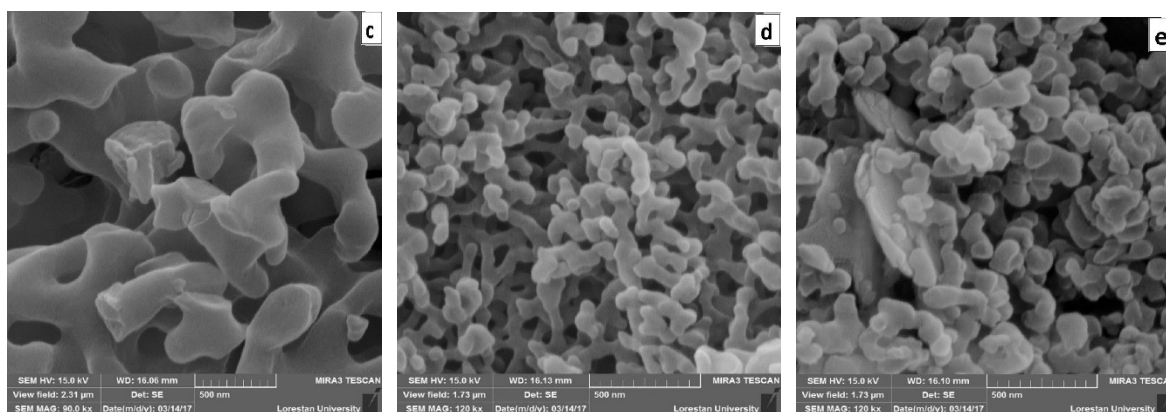
Figure 4: SEM micrographs of pristine ZrP nano particle (a) and poly (MMA-co-MI)/ZrP nanocomposite (b: 0.5%; c; 1%; d: 3%; e: 5%)

TEM micrographs: TEM micrographs of modified nano ZrP and nanocomposite are shown in Figure 5. As seen clearly, nanoparticles are evenly distributed in the polymer matrix.

Figure 5: TEM micrographs of (a) modified nano ZrP and (b) poly (MMA-co-MI)/ZrP nanocomposite.

The thermal decomposition of the pristine ZrP and modified ZrP nanoparticle were studied by TGA, DSC, DTG (Figure 6a-c). The range of two major weight losses of the pristine ZrP crystals are 95−170 and 430−590 °C. They refer to the loss of hydration water and condensation water in ZrP, respectively. Three major weight losses in 70−140, 320-440 and 490−600 °C range were observed in the modified ZrP by TBA. They correspond to the loss of hydration water, elimination of TBA and condensation water in ZrP-TBA. Two weight loss steps were observed in 85-185 and 470-620 °C in the modified ZrP by KH-570. First, it refers to the losing water and methoxy group, then losing methacrylate (29,41,42). Nanocomposites thermal properties and behaviour were investigated by TGA and DSC. The results are summarized in Table 2. The T_{10}, T_{50} and T_{max} were highlighted; T_{10} is the onset temperature, at which 10% degradation occurs, while T_{50} is the midpoint temperature, corresponding to 50% degradation.

T_{max} is the weight lost finishing temperature. The copolymer start losing weight at around 265 °C and when nanoparticles were added into its matrix, the temperature increase around 20 °C for starting weight loss of nanocomposites. The copolymer weight lost finishing around 576 °C while nanocomposites around 667 °C. It means improving the thermal stability. Nanocomposite's T_{10}, T_{50}, T_{max} and initiation weight lost temperature are more than PMMA nanocomposite. It shows good improvement of thermal stability nanocomposite than PMMA nanocomposite (43,44).

The eighth column shows time of using in-situ nanoparticles. As seen, adding ZrP nanoparticles to copolymer decrease amount of T_g, but the nanocomposite T_g are higher than PMMA nanocomposite. Also adding nanoparticle during polymerization have more effects on decrease of T_g.

Table 2: Sample designations; T_{max} and T_g of poly (MMA-co-MI)/ZrP-nanocomposite films measured from TGA and DSC curves.

Sample designation	PMMA-ZrP	Copolymer	CP/ZrP-1	CP/ZrP-3	CP/ZrP-5	CP/ZrP-7	In-situ nanocomposite
α-ZrP (w%)	1	0	1	3	5	7	1
$T_{10\%}$	284.5	327.52	328.1	318.02	321.51	318.79	334.7
$T_{50\%}$	367.6	369.96	360.07	360.46	359.11	361.82	378.5
T_{max} (°C)	488.2	576.18	667.6	679.06	669.0	674.22	691.5
T_g (°C)	96.1	133.7	113.85	114.11	115.2	115.35	106.6
Coal Productivity	2.87	15.30	11.51	12.04	15.74	15.09	12.25

Figure 6: a, b, c are TGA, DSC and DTG of the nanoparticle, respectively. d, e, f are TGA, DSC and DTG of the nanocomposite, respectively.

The transparency of the polymer and prepared nanocomposites were examined by UV-Vis spectroscopy. Figure 7 shows UV-Vis spectra of copolymer and nanocomposite solutions in EtOAc. The transparency of nanocomposite solutions 5 and 7% in 400 nm was about 11% which was not suitable. It reached to 73% that is near the copolymer transparency in nanocomposite solutions (3%). The best transparencies were observed in nanocomposites solutions 0.5, 1%, and in-situ, was 95% in 400 nm. All of the nanocomposites have more transmittance than PMMA nanocomposite except 5, 7%. Since nanocomposites 0.5 and 1% transmit the visible light as well as PMMA, they can be used whenever PMMA is used as a substitute for glass. Furthermore, nanocomposites do not transmit UV light so they can be used in sunglasses.

Figure 7: UV-Vis spectra of nanocomposite solutions.

CONCLUSION

A series of nanocomposites based on poly (MMA-co-MI) as a matrix and modified ZrP-KH570 was prepared and characterized by FTIR spectroscopy. The crystalline structure and the size of nanoparticles were confirmed by XRD. The surface morphology of these compounds, evaluated by SEM, were observed as sheet for nanoparticles. It was successfully dispersed in polymer matrix after sonication. The dispersion of nanoparticles into polymer matrix was also confirmed by TEM. Thermal analysis of nanoparticle was investigated.

The thermal stability of nanocomposites was examined by TGA and the results show that adding nanoparticle improve copolymer's thermal stability. Also, thermal behavior of these compounds, evaluated by DSC, shows a decrease in T_g after adding of nanoparticles into polymer matrix. It was probably due to location of nanoparticles between the polymer layers and so decrease interaction between polymer layers.

The results of transparency by UV-Vis spectroscopy showed that the best percent refer to nanocomposite 0.5 and 1% of nanoparticles. Nanocomposites absorb UV light well.

REFERENCES

1. Shafiee Hasani S, Ghazi Tabatabaei Z. Synthesis of Nanocomposites of Single-Wall Carbon Nanotubes Coated with ZnO Nanoparticles in a Matrix of Poly Methyl Methacrylate and Study of Its Optical Properties. Nashrieh Shimi va Mohandesi Shimi Iran. 2019;38(3):23–32.

2. Fatalla AA, Tukmachi MS, Jani GH. Assessment of some mechanical properties of PMMA/silica/zirconia nanocomposite as a denture base material. IOP Conference Series: Materials Science and Engineering. 2020 Nov;987(1):012031. <DOI>.

3. Tucureanu V, Matei A, Mihalache I, Danila M, Popescu M, Bita B. Synthesis and characterization of YAG:Ce,Gd and YAG:Ce,Gd/PMMA nanocomposites for optoelectronic applications. J Mater Sci. 2015 Feb;50(4):1883–90. <DOI>.

4. Singh AK, Prakash R, Pandey D. A comparative thermal, optical, morphological and mechanical properties studies of pristine and C15A nanoclay-modified PC/PMMA blends: a critical evaluation of the role of nanoclay particles as compatibilizers. RSC Adv. 2013;3(35):15411-20. <DOI>.

5. Schoth A, Wagner C, Hecht LL, Winzen S, Muñoz-Espí R, Schuchmann HP, et al. Structure control in PMMA/silica

hybrid nanoparticles by surface functionalization. Colloid Polym Sci. 2014 Oct;292(10):2427–37. <DOI>.

6. Gianotti V, Antonioli D, Sparnacci K, Laus M, Giammaria TJ, Ferrarese Lupi F, et al. On the Thermal Stability of PS- b -PMMA Block and P(S- r -MMA) Random Copolymers for Nanopatterning Applications. Macromolecules. 2013 Oct 22;46(20):8224–34. <DOI>.

7. Ali Sabri B, Satgunam M, Abreeza N, N. Abed A. A review on enhancements of PMMA Denture Base Material with Different Nano-Fillers. Jones IP, editor. Cogent Engineering. 2021 Jan 1;8(1):1875968. <DOI>.

8. Azimi HR, Rezaei M, Majidi F. The non-isothermal degradation kinetics of St–MMA copolymers. Polymer Degradation and Stability. 2014 Jan;99:240–8. <DOI>.

9. Teodorescu M. Free-radical copolymerization of methyl methacrylate with styrene in the presence of 2-mercaptoethanol II. Influence of methyl methacrylate/styrene ratio. European Polymer Journal. 2002 May;38(5):841–6. <DOI>.

10. Lin CT, Kuo SW, Huang CF, Chang FC. Glass transition temperature enhancement of PMMA through copolymerization with PMAAM and PTCM mediated by hydrogen bonding. Polymer. 2010 Feb;51(4):883–9. <DOI>.

11. Gevrek TN, Bilgic T, Klok HA, Sanyal A. Maleimide-Functionalized Thiol Reactive Copolymer Brushes: Fabrication and Post-Polymerization Modification. Macromolecules. 2014 Nov 25;47(22):7842–51. <DOI>.

12. Konsulov V, Grozeva Z, Tacheva J, Tachev K. Study of the copolymerization of n-(dichlorophenyl) maleimides with methyl methacrylate. Bulgarian chemical communications. 2009;41(1):31–8.

13. Sanchez FA, Redondo M, Olmos D, Kuzmanovic M, González-Benito J. A Near-Infrared Spectroscopy Study on Thermal Transitions of PMMA and PMMA/SiO 2 Nanocomposites. Macromol Symp. 2014 May;339(1):48–59. <DOI>.

14. Lerari D, Peeterbroeck S, Benali S, Benaboura A, Dubois Ph. Combining atom transfer radical polymerization and melt compounding for producing PMMA/clay nanocomposites. J Appl Polym Sci. 2011 Aug 5;121(3):1355–64. <DOI>.

15. Hosoda T, Yamada T. Effect of TiO 2 on morphology and mechanical properties of PVDF/PMMA blend films prepared by melt casting process. J Appl Polym Sci. 2014 Jul 5;131(13):1-10. <DOI>.

16. Akinci A, Sen S, Sen U. Friction and wear behavior of zirconium oxide reinforced PMMA composites. Composites Part B: Engineering. 2014 Jan;56:42–7. <DOI>.

17. Zanotto A, Luyt AS, Spinella A, Caponetti E. Improvement of interaction in and properties of PMMA-MWNT nanocomposites through microwave assisted acid treatment of MWNT. European Polymer Journal. 2013 Jan;49(1):61–9. <DOI>.

18. Hazim A, Abduljalil HM, Hashim A. Structural, Spectroscopic, Electronic and Optical Properties of Novel Platinum Doped (PMMA/ZrO2) and (PMMA/Al2O3) Nanocomposites for Electronics Devices. Trans Electr Electron Mater. 2020 Dec;21(6):550–63. <DOI>.

19. Su W, Wang S, Wang X, Fu X, Weng J. Plasma pre-treatment and TiO2 coating of PMMA for the improvement of antibacterial properties. Surface and Coatings Technology. 2010 Oct;205(2):465–9. <DOI>.

20. Yıldırım A, Acay H, Baran A. Synthesis and characterization of the molecularly imprinted composite as a novel adsorbent and its competition with non-imprinting composite for removal of dye. JOTCSA. 2021;8(2):609–22. <DOI>.

21. Zidan S, Silikas N, Alhotan A, Haider J, Yates J. Investigating the Mechanical Properties of ZrO2-Impregnated PMMA Nanocomposite for Denture-Based Applications. Materials. 2019 Apr 25;12(8):1344. <DOI>.

22. Yi C, Yang Y, Liu B, He J, Nie Z. Polymer-guided assembly of inorganic nanoparticles. Chem Soc Rev. 2020;49(2):465–508. <DOI>.

23. Adnan M, Dalod A, Balci M, Glaum J, Einarsrud MA. In Situ Synthesis of Hybrid Inorganic–Polymer Nanocomposites. Polymers. 2018 Oct 11;10(10):1129. <DOI>.

24. Hassanzadeh-Aghdam MK, Ansari R, Mahmoodi MJ, Darvizeh A. Effect of nanoparticle aggregation on the creep behavior of polymer nanocomposites. Composites Science and Technology. 2018 Jul;162:93–100. <DOI>.

25. Hamming LM, Qiao R, Messersmith PB, Catherine Brinson L. Effects of dispersion and interfacial modification on the macroscale properties of TiO2 polymer–matrix nanocomposites. Composites Science and Technology. 2009 Sep;69(11–12):1880–6. <DOI>.

26. Chau JLH, Hsieh CC, Lin YM, Li AK. Preparation of transparent silica–PMMA nanocomposite hard coatings. Progress in Organic Coatings. 2008 Jun;62(4):436–9. <DOI>.

27. Díaz A, Mosby BM, Bakhmutov VI, Martí AA, Batteas JD, Clearfield A. Self-Assembled Monolayers Based Upon a Zirconium Phosphate Platform. Chem Mater. 2013 Mar 12;25(5):723–8. <DOI>.

28. Alberti G, Vivani R, Biswas RK, Murcia-Mascarós S. Preparation and some properties of γ-zirconium phosphate benzenephosphonate. Reactive Polymers. 1993 May;19(1–2):1–12. <DOI>.

29. Zhou Y, Huang R, Ding F, Brittain AD, Liu J, Zhang M, et al. Sulfonic Acid-Functionalized α-Zirconium Phosphate Single-Layer Nanosheets as a Strong Solid Acid for Heterogeneous Catalysis Applications. ACS Appl Mater Interfaces. 2014 May 28;6(10):7417–25. <DOI>.

30. Atabaki F, Abdolmaleki A, Barati A. Free radical copolymerization of methyl methacrylate and N-2-methyl-4-nitro-phenylmaleimide: Improvement in the Tg of PMMA. Colloid Polym Sci. 2016 Feb;294(2):455–62. <DOI>.

31. Carter DP. Preparation of zirconium oxychloride [Internet]. US4256463A.1981 Available from: <URL> .

32. Baig U, Wani WA, Ting Hun L. Facile synthesis of an electrically conductive polycarbazole–zirconium(iv)phosphate cation exchange nanocomposite and its room temperature ammonia sensing performance. New J Chem. 2015;39(9):6882–91. <DOI>.

33. Barraclough C, Bradley D, Lewis J, Thomas I. 510. The infrared spectra of some metal alkoxides,

trialkylsilyloxides, and related silanols. Journal of the Chemical Society (Resumed). 1961;2601–5.

34. Matinlinna JP, Özcan M, Lassila LVJ, Vallittu PK. The effect of a 3-methacryloxypropyltrimethoxysilane and vinyltriisopropoxysilane blend and tris(3-trimethoxysilylpropyl)isocyanurate on the shear bond strength of composite resin to titanium metal. Dental Materials. 2004 Nov;20(9):804–13. <DOI>.

35. Zhang FA, Song C, Yu CL. Effects of preparation methods on the property of PMMA/SBA-15 mesoporous silica composites. J Polym Res. 2011 Nov;18(6):1757–64. <DOI>.

36. Licoccia S, Trombetta M, Capitani D, Proietti N, Romagnoli P, Di Vona ML. ATR–FTIR and NMR spectroscopic studies on the structure of polymeric gel electrolytes for biomedical applications. Polymer. 2005 Jun;46(13):4670–5. <DOI>.

37. Choudhary V, Mishra A. Studies on the copolymerization of methyl methacrylate and N-aryl maleimides. J Appl Polym Sci. 1996 Oct 24;62(4):707–12. <DOI>.

38. Lee SS, Ahn TO. Direct polymer reaction of poly(styrene-co-maleic anhydride): Polymeric imidization. J Appl Polym Sci. 1999 Feb 14;71(7):1187–96. <DOI>.

39. Shobhana E. X-Ray diffraction and UV-visible studies of PMMA thin films. International Journal of Modern Engineering Research. 2012;2(3):1092–5.
40. Patterson AL. The Scherrer Formula for X-Ray Particle Size Determination. Phys Rev. 1939 Nov 15;56(10):978–82. <DOI>.

41. Li X, Wang Z, Wu L, Tsai T. One-step in situ synthesis of a novel α-zirconium phosphate/graphene oxide hybrid and its application in phenolic foam with enhanced mechanical strength, flame retardancy and thermal stability. RSC Adv. 2016;6(78):74903–12. <DOI>.

42. Kozawa Y, Suzuki S, Miyayama M, Okumiya T, Traversa E. Proton conducting membranes composed of sulfonated poly(etheretherketone) and zirconium phosphate nanosheets for fuel cell applications. Solid State Ionics. 2010 Mar 11;181(5–7):348–53. <DOI>.

43. Carvalho HWP, Suzana AF, Santilli CV, Pulcinelli SH. Structure and thermal behavior of PMMA–polysilsesquioxane organic–inorganic hybrids. Polymer Degradation and Stability. 2014 Jun;104:112–9. <DOI>.

44. Hatanaka LC, Diaz A, Wang Q, Cheng Z, Mannan MS. Thermal Stability of Optically Transparent Alpha-Zirconium Phosphate/Poly(methyl methacrylate) Nanocomposites with High Particle Loading. Polymers and Polymer Composites. 2017 May;25(4):267–72. <DOI>.

New Bioactive Aromatic Indole Molecules with Monosaccharide Core

Israa Nadim Hamdi[1] , Salih Mahdi Salman[2]* iD, Luma Salman Abd[1]

[1]University of Diyala, College of Sciences, Department of Chemistry, Diyala, Iraq.
[2]University of Diyala, College of Medicine, Department of Chemistry, Diyala, Iraq.

Abstract: 1,1,2-trimethyl-1H-benzo[e]indole is an important heterocyclic compound, it is available in reasonable price and can easily be modified to make a good intermediate for synthesis of other derivatives. It can be used as a starting material for the synthesis of a new series of compounds by coupling with other biomolecules such as monosaccharide amines after a simple modification. The current work aims to synthesize new potentially bioactive compounds by coupling 1,1,2-trimethyl-1H-benzo[e]indole with one or two molecules of both 2-deoxy-2-amino-d-glucose and 6-deoxy-6-amino-d-glucose. The mono-substituted derivative were prepared in two steps, the first step is the functionalization reaction to create two reactions centers via the treatment of 1,1,2-trimethyl-1H-benzo[e]indole (**1**) with POCl₃ to produce 2-(1,1-dimethyl-1H-benzo[e]indol-2(3H)-ylidene) malonaldehyde (**2**) with two reaction centers represented by aldehyde groups, while in the second step the latter was coupled with two amino sugars. Four new molecules resulted from this reaction, two mono-substituted derivatives (**3**,**5**) when we apply the last reaction for a short time, while the di-substituted molecules (**4**,**6**) take long time for the same reaction conditions in order to overcome the steric hindrance at one reaction center. The purity and characterization of the target molecules were confirmed using spectroscopic methods including 1H NMR and 13C NMR. The synthesized compounds, especially the di-substituted derivatives, show a good biological activity as antibacterial and antifungal agents and they can find their way in medical application as they are soluble in water due to the presences of sugar moiety in their structures.

INTRODUCTION

There are many biologically active compounds synthesized and reported from different heterocyclic compounds. As the bacterial and fungi by the time may become more familiar with the known bioactive compounds, the need to modify and find new bioactive compounds to overcome this problem has become important and has a wide range of the scientific interest. 1,1,2-trimethyl-1H-benzo[e]indole is an aromatic heterocyclic compound modified by many chemists and scientists to produce other useful compounds and derivatives in many applications, including biological activity. Wen-Hai Zhan et al. reported the synthesis of cyanine dye derivatives (C-

Cy(1–4)) in which a coumarin moiety is attached to benzoindole via click chemistry (1). Yoichi Shimizu and coworkers, developed novel near-infrared NIR fluorophore-micelle complex probes. By using benzoindole for for synthesizing a novel lipophilic NIR fluorophores, which were encapsulated in an amphiphilic polydepsipeptide micelle "lactosome" (2), while Duanwen Shen and coworkers used the same material to develop near-infrared (NIR) dye that fluoresces at two different wavelengths (dichromic fluorescence, DCF) (3). Guillermo O. Menéndez and others presented water soluble and fluorescent biotinylated probe derived from a carbocyanine dye from benzoindole (4). Kaiquan Zhang et al. used benzoindole to developed a new type of fluorescent

probe (QcyCHO) featured with H_2S-triggered off-to-on near-infrared (NIR) fluorescence (5). Ludmila A. Oparina and coworkers reported the reaction of 3H-indoles with tertiary propargylic alcohols to give functionalized dihydrooxazolo[3,2-a]indoles (6). Nisha Narayanan and his team synthesized six squaraine dyes consisting of two different electron donor moiety including 1,1,2-trimethyl-1H-benzo[e]indole (7). Clare L. Lawrence et al. declared eighteen dyes were placed within classes based on their core subunit i.e. 2,3,3-trimethylindolenine, 1,1,2-trimethyl-1H-benzo[e]indole, or 2-methylben-zothiazole for antifungal activities (8). Kandasamy Ponnuvel et al. announced a merocyanine dye-based fluorescent probe have been synthesized for selective and sensitive detection of hypochlorous acid and imaging in live cells (9). Yury A. Sayapin and coworkers reported the synthesis of chemosensors based on 1H-indole, 1H-benzo[e]indole, and 1H-benzo[g]indole as fluorescence (10). Haribhau S. Kumbhar synthesized 1, 1, 2-trimethyl-1H benzo[e]indoline based β-enaminone boron complexes exhibited the intense fluorescence (11). Rasa Steponavičiūtė et al. reported the reaction of 1,1,2-trimethyl-1H-benzo[e]indole with acrylic acid and its derivatives was employed for the preparation of novel fluorescent building blocks (12). Rasa Steponavičiūtė was able to alkylate 1,1,2-trimethyl-1H-benzo[e]indole with bifunctional compounds, and investigated their chemical and optical properties (13). Waad Naim and coworkers presented the transparent and colorless dye-sensitized solar cells exceeding 75% average visible transmittance (14). Wang reported the synthesis of new benzo[e]indolinium cyanine dyes with two different fluorescence wavelengths (15). Xiangning Fang and coworkers provided a one-step condensation method for the synthesis of the fluorescent dye Indocyanine Green (ICG) with 92% yield using 1,1,2-trimethyl-1H-benzo[e]indole (16). In continuation with these efforts we aim to find a new modification for 1,1,2-trimethyl-1H-benzo[e]indole by functionalization and attaching two different amino glucose as mono and di-substitution targeting synthesis new bioactive derivatives for medical and pharmaceuticals application.

METHODOLOGY

Chemistry
Chemical and Solvents
All chemical, reagent and solvent were purchased from different companies and were used without any further purification.

NMR Spectroscopy and IR Spectrometry
The purity and characterization of the target compounds were done using spectroscopic methods including 1H and 13C NMR (Avance Neo Neo 400, Iran), IR spectrometer Perkin-Elmer Spectrum version 10.02 at the Department of Chemistry, Faculty of Science, Diyala University.

Programs and Software
Drawing the chemical structure and 2D investigation and finding were performed via ChemOffice Ultra 2006 (CambridgeSoft) and ChemSketch 2010 (Advanced Chemistry Development, lnc.).

Tools and Instruments
Follow up of the reactions performed via thin layer chromatography (TLC) using alumina plates (size 20×20 cm) percolated with silica gel and Fluorescence Analysis Cabinet Model CM-10 as a detector. The Stuart SMP10 electronic apparatus used to calculate the melting point of the final products (Department of Chemistry, Faculty of Sciences, University of Diyala).

General Methods
Functionalization
1,1,2-trimethyl-1H-benzo[e]indole (**1**) (1 eq.) was dissolved in about 15 mL of anhydrous dimethyl formamide (DMF) with cooling. Cooled solution of phosphorus oxytrichloride ($POCl_3$) in 15 mL of DMF added gradually to indole solution within about 30 min. at about 4 °C. The mixture was refluxed at about 85-90 °C. After about 4 h, TLC (3:1) n-hexane: ethyl acetate indicates the consumption of the starting material, the mixture poured into ice water and neutralized by sodium hydroxide (35% NaOH). Products precipitate, filtered off, washed with water, and dried in a 70 °C oven to give pale yellow crystals of 2-(1,1-dimethyl-1H-benzo[e]indol -2(3H)-ylidene) malonaldehyde (**2**) (17-19).

Coupling
Step1
2-(1,1-dimethyl-1H-benzo[e]indol-2(3H)-ylidene) malonaldehyde (**2**) (1 eq.) in 15-20 mL ethanol and solution of D-glucose amine (1 eq.) in 5-10 mL ethanol were mixed. Glacial acetic acid (1 mL) was added to the mixture before refluxing for about 10-12 hours. TLC 3:1 n-hexane: ethyl acetate indicates the end of the reaction in about 10-12 hours. The mono-substituted indole precipitate after reducing solvent, filtered, washed, and dried (20-22). Two derivatives were synthesized in this step:

(2S, 3S, 4R, 5S)-2-((E)-((E)-2-(1, 1-dimethyl-1H-benzo[e]indol-2(3H)-ylidene)-3 oxopropylidene) amino)-3, 4, 5, 6-tetrahydroxyhexanal (3)
2-(1,1-dimethyl-1H-benzo[e]indol-2(3H)-ylidene) malonaldehyde (**2**) (0.15 g, 0.00035 mmol) was coupled with 2-deoxy-2-amino-D-glucose according to general procedure mentioned in step-1 above to yield yellow crystals of (2S,3S,4R,5S)-2-((E)-((E)-2-(1,1-dimethyl-1H-benzo[e]indol-2(3H)-ylidene)-3 oxopropylidene) amino)-3,4,5,6-tetrahydroxyhexanal (**3**) (0.2 g, 0.00047 mmol, 83%) m.p. (208 °C). 1H NMR chemical shifts at (400 MHz, DMSO-d6, δ in ppm): δ = 13.46 (d, 1H, NH), 9.80 (s, 2H, -CH=O), 8.20 (d, 1H, -CH=N-), 8.04-7.17 (m, 6H, Ar-H), 5.65-3.19 (m, 10H, d-glucose-H) and 1.95 (s, 6H, 2x CH_3). The 13C-NMR spectra of this compound, exhibits the signals (100 MHz, DMSO-d6, δ

in ppm): δ =179.67 for 2CH=O, 133.01 for NH-CH=C, 156.66 for CH=N, 109.131 for Ar-C, 94.96 for O=C-C=C, 52.93 for CH₃-C-CH₃, 54-75 for d-glucose-C , 52.93 for CH₃CCH₃ and 22.29 for 2× CH₃. (For more details, see Figures S1 and S3).

(2S, 3S, 4R, 5S)-6-((E)-((E)-2-(1, 1-dimethyl-1H-benzo[e]indol-2(3H)-ylidene)-3 oxopropylidene) amino)-2, 3, 4, 5-tetrahydroxyhexanal (5)
2-(1,1-dimethyl-1H-benzo[e]indol-2(3H)-ylidene) malonaldehyde (2) (0.15 g, 000035 mmol) was coupled with 6-deoxy-6-amino-D-glucose according to general procedure mentioned in step-1 above to produce brown crystals of (2S,3S,4R,5S)-2-((E)-((2Z,3E)-2-(1,1-dimethyl-1H-benzo[e]indol-2(3H)-ylidene)-3-((2R,3R,4S,5R)-3,4,5,6-tetrahydroxy-1-oxohexan-2-ylimino) propylidene) amino)-3,4,5,6-tetrahydroxyhexanal (5) (0.21 g, 0.00049 mmol, 87%) m.p. (255 °C).1H NMR chemical shifts at (400 MHz, DMSO-d6, δ in ppm): δ = 13.46 (s, 1H, NH), 9.83 (s, 2H, -CH=O), 8.20 (d, 2H, -CH=N-), 7-8.5 (m, 6H, Ar-H, 2.88-5., 1.95 (s, 6H, 2x CH₃). The 13C-NMR spectra of this compound, exhibits the signals (100 MHz, DMSO-d6, δ in ppm): δ = 179.68 for 2CH=O, 133.01 for NH-CH=C, 156.77 for CH=N, 109-131 for Ar-, 89.34 for O=C-C=C, 54.94, for CH₃-C-CH₃, 61.75 for d-glucose-C, 54.93 for CH₃CCH₃ and 17.19 for 2× CH₃. (For more details see Supplementary Material)

Step 2
Mono-substituted indole (3) or (5) (1 eq.) in 15-20 mL ethanol of and solution of D-glucose amine (1 eq.) in 5-10 mL of ethanol were mixed. Glacial acetic acid (1 mL) was added to the mixture before refluxing for about 72 hours. TLC 3:1 n-hexane: ethyl acetate indicates the end of the reaction in about 10-12 hours. The di-substituted indole was precipitated after reducing solvent, filtered, washed, and dried. Two derivatives were synthesized in this step: -

(2S,3S,4R,5S)-2-((E)-((2Z,3E)-2-(1,1-dimethyl-1H-benzo[e]indol-2(3H)-ylidene)-3-((2R,3R,4S,5R)-3,4,5,6-tetrahydroxy-1-oxohexan-2-ylimino) propylidene) amino)-3,4,5,6-tetrahydroxyhexanal (4)
(2S,3S,4R,5S)-2-((E)-((E)-2-(1,1-dimethyl-1H-benzo[e]indol-2(3H)-ylidene)-3 oxopropylidene) amino)-3,4,5,6-tetrahydroxyhexanal (3) (0.15 g, 0.57 mmol) was further coupled with 2-deoxy-2-amino-D-glucose according to general procedure mentioned in step-2 to give orange crystals of (2S,3S,4R,5S)-2-((E)-((2Z,3E)-2-(1,1-dimethyl-1H-benzo [e] indol-2(3H)- ylidene) -3- ((2R,3R,4S,5R) -3,4,5,6-tetrahydroxy-1-oxohexan-2-ylimino) propylidene)amino)-3,4,5,6-tetrahydroxyhexanal (4) (0.155 g, 0.00026 mmol, 74%) m.p. (185 °C). 1H NMR chemical shifts at (400 MHz, DMSO-d6, δ in ppm): δ = 13.46 (s, 1H, NH), 9.79(s, 2H, -CH=O), 7.95 (d, 2H, -CH=N-), 6.60-8.18 (m, 6H, Ar-H), 2.58-4.85 (20H, d-glucose-H) (s, 5.23, 4H, CH₂OH) (m,3.61,8H, CH₂OH) ,(dd, 3.52,2H, CHOH, 1.94 (s, 6H, 2x CH₃) The 13C-NMR spectra of this

compound, exhibits the signals (100 MHz, DMSO-d6, δ in ppm): δ = 179.68 for 2CH=O, 137.86 for 2NH-CH=C, 133.01 for CH=N, 109.13-130.25 for Ar-C, 97.36 for O=C-C=C, 54.93, for CH₃-C-CH₃, 61.68-75.29 for d-glucose-C, 54,93 for CH₃CCH₃ and 22.28 for 2× CH₃ (For more details, see Figures S5 and S6).

(2S,3R,4S,5S)-6-((2E)-2-(1,1-dimethyl-1H-benzo[e]indol-2(3H)-ylidene)-3-((2R,3R,4S,5R)-2,3,4,5-tetrahydroxy-6-oxohexylimino)propylide-neamino)-2,3,4,5-tetrahydroxyhexanal (6)
(2S,3S,4R,5S)-2-((E)-((E)-2-(1,1-dimethyl-1H-benzo[e]indol-2(3H)-ylidene)-3-oxopropylidene) amino)-3,4,5,6-tetrahydroxyhexanal (5) (0.15 g, 0.00035 mmol) was further coupled with 2-deoxy-2-amino-D-glucose according to general procedure mentioned in step-2 to give greenish crystals of (2S,3R,4S,5S)-6-((2E)-2-(1,1-dimethyl-1H-benzo[e]indol-2(3H)-ylidene)-3-((2R,3R,4S,5R)-2,3,4,5-tetrahydroxy-6-oxohexylimino)propylide-neamino)-2,3,4,5-tetrahydroxyhexanal (6) (0.16 g, 0.00027 mmol, 76%) m.p. (193 °C). 1H NMR chemical shifts at (400 MHz, DMSO-d6, δ in ppm): δ = 13.46 (s, 1H, NH), 9.79 (s, 2H, -CH=O), 7.95 (d, 2H, -CH=N-), 6.61-8.17 (m, 6H, Ar-H), 2.58-4.87 (20H, d-glucose-H), 1.94 (s, 6H, 2x CH₃) The 13C-NMR spectra of this compound, exhibits the signals (100 MHz, DMSO-d6, δ in ppm): δ = 179.68 for 2CH=O, 137.86 for 2NH-CH=C, 133.01 for CH=N, 109.13-130.25 for Ar-C, 97.36 for O=C-C=C, (54.93), for CH₃-C-CH₃, 61.68-75.29 for d-glucose-C, 54,93 for CH₃CCH₃ and 22.28 for 2× CH₃ (For more details, see Figures S7 and S8).

Biological Activity
Material and Methods
Staphylococcus aureus and *Staphylococcus epidermidis* isolates were cultured on Blood agar and Mannitol salt agar. *Klebsiella pneumonia* and *Escherichia coli* isolates were cultured on MacConky agar and Eosin Methylene Blue agar, *Candida albicans* isolate was cultured on Sabouraud dextrose agar and candida chromogenic agar, to obtain pure isolates.

MacFarland turbidity standard
The preparing solution from the company (Biomeriex) was used in calibrating the number of bacterial cells, as it gives an approximate number of cells 1.5 x 10⁸ cells/mL.
1) Muller Hinton agar medium was prepared by dissolving 38 g of agar in 1 L of distilled water and sterilized in an autoclave at 121 °C and under pressure (15 pounds) for 15 minutes, cooled and poured into sterile dishes and kept in the refrigerator until use.

2) Determination the antimicrobial activity of the target compounds by agar well diffusion method as follows:

3) A number of bacterial colonies were transported by loop to prepare the suspended bacteria and put it

in tubes contain brain heart infusion broth to activate the bacteria. The tubes were incubated for (18 - 24) h at 37 °C. The suspended bacterium was compared to the standard MacFarland and solution (1.5 x 10^{8}) cells/mL. After that the bacteria suspended was spread by a sterile swab, it was spread on the plates containing Muller Hinton agar and then the plate was left for a while to dry.

4) Holes were made with a diameter of 5 mm in the culture media by using sterilized a cork borer 100 µL of the material were added to each hole individually by micropipette and one well represent the negative control by adding DMSO only. After then, the dishes were incubated at 37 °C for 24 h.

5) The effectiveness of each concentration was determined by measuring the diameter of the inhibition zone around each hole in mm (23-25).

RESULTS AND DISCUSSION

Synthesis
There are too many aromatic heterocyclic derivatives which are useful for many applications in all fields of the life one of them is 1,1,2-trimethyl-1H-

benzo[e]indole **1**, which is chosen as the starting material of the target synthesis for many reasons such as economy, availability, and accessibility. On the other hand, amino sugars, especially 2-deoxy-2-amino-D-glucose and 6-deoxy-6-amino-D-glucose are biochemical molecules chosen to attach with the heterocyclic starting material for the same reasons in addition their perfect chemical structures with multi hydroxyl group which may increase the solubility of the target compounds.

This coupling needs to modify the starting material to create new reaction centers, so that the functionalization of **1** was done via Vilsmeier-Haack reaction with of $POCl_3$ (phosphoryl chloride) in DMF to get **2** with two new reaction centers represented by aldehyde groups.

2 was coupled with the 2-deoxy-2-amino-D-glucose and 6-deoxy-6-amino-D-glucose via imines which are commonly called as Schiff bases or Schiff's bases to produce **5** respectively, with di-substituted amino sugar instead of expected di-substituted derivatives **4** and **6** in mild reaction conditions (Scheme 1) .
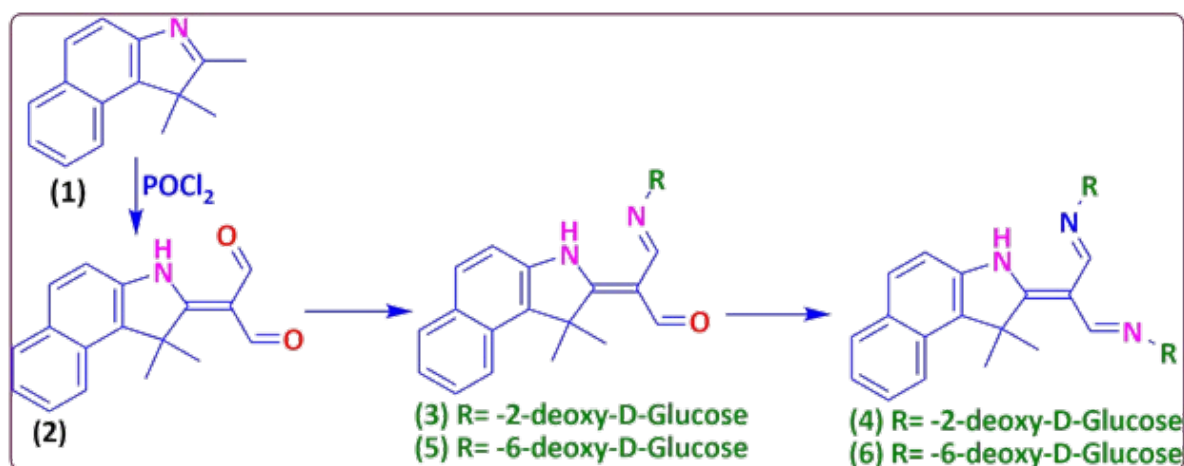
Scheme 1: Synthesis of mono and di-substituted heterocyclic derivatives.

In order to investigate the reasons for these unexpected products of the first step of the reaction, the 3D structure study of the precursor intermediate **2** shows that there is a steric hindrance at the aldehyde group close to the two methyl groups of the heterocyclic moiety, so the monosaccharide amine at the simple or mild conditions attach first the easy open aldehyde group away from the methyl group to produce the mono-substituted derivative as shown in Figure 1.
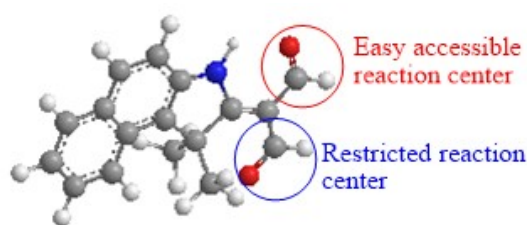

Figure 1: 3D structure of **2.**

Under hard conditions, it is possible to attach another amino monosaccharide to the hindered aldehyde group to yield compounds **4** and **6** respectively as shown in Scheme 1.
The purity and characterization of the mono-substituted derivatives **3** and **5** confirmed by IR , 1H NMR

and 13C NMR, proton NMR shows the chemical shift of the -NH at about 13-14 ppm, two aldehyde protons at about 8-9, -CH=N- at about 8-9, aromatic proton in between 7.0-8.5 ppm, the monosaccharides proton from 2-6 and the two methyl groups of the heterocyclic moiety at about 1-2 ppm (See Figures S1 and S2).

The 1H spectra of the di-sugar derivatives shows the chemical shift of the mentioned groups at the same positions with duplicated protons for sugar moieties and aldehyde groups, with appearance of the two -CH=N- proton chemical shifts. (See Figures S1 and S2)

13C NMR analysis confirms the structures as the number of carbon and the chemical shift fitting the suggested compounds, for the monosaccharide de-rivatives (**3**, **5**). The sugar aldehyde carbons appear at about 188 while indole aldehyde appears at 187, the 2NH-CH=C carbon list at 177-179, CH=N carbon located at about 153-155, aromatic carbons in be-tween 110-132, sugar carbons appear from about 50-75, CH_3-C-CH_3 carbon and the two groups of methyl for the indole moiety at about 20-22 (See Figures S3 and S4).

The new derivatives can either be represented by Fisher Projection structure or by Howarth formula as shown in Figure S6, Supplementary Material. The 1H NMR analysis above shows clearly the chemical shift of the aldehyde protons and the absence of $\alpha \wedge \beta$ configuration of the anomeric proton of glucose make the structure of the target compounds are compatible with Fisher projection rather than Howarth form (Figure 2).
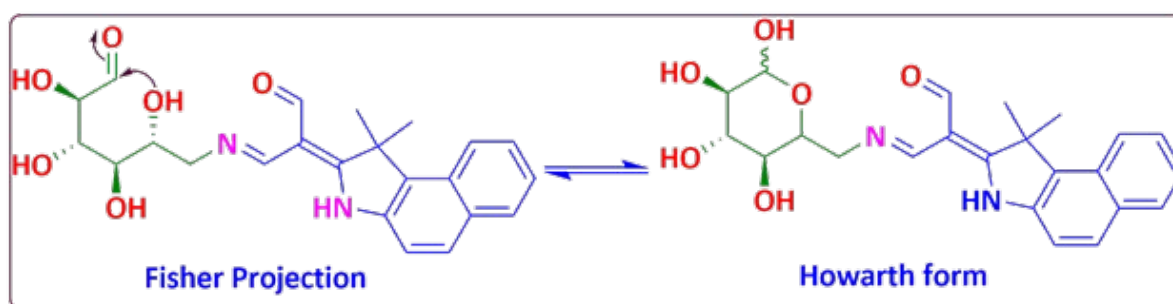

Figure 2: Fisher projection and Howarth form of compound (**5**).

The carbon and proton atoms number and their chemical shift of compounds **5** and **6**, are approxi-mately the same carbon and proton number and chemical shift with double integration for sugar moi-eties in compered to compounds **3** and **5** and disap-pearance of one CH=N group from compounds **5** and **6**. (See Figures S5, S6, S7, and S8).

Finally, we can confirm the sugar-indole derivative can be accessible easily with a very simple process and this reaction can improve the solubility which can make such derivatives suitable for many appli-cations especially in medical applications.

Biological Activity
The starting material and targets compounds were subjected to biological activity evaluation. The in-vestigation shows that the starting material 1, 1, 2-trimethyl-1H-benzo[e]indole (**1**) does not show any biological activity by its natural stand structure but, the attachments of the biochemical such as amino monosaccharides led to new molecules with differ-ent degrees of bioactivity. The modification of the starting material and attachment with 2-deoxy-2-amino -d-glucose and 6-deoxy-6-amino -d-glucose produced two new compounds **3** and **5**, the investigation of those molecules with two gram positive bacteria *Staphylococcus aureus* and *Staphylococcus epidermidis* only compound **3** showed a good biological activity with *Staphylococ-*

cus aureus while **5** is biologically inactive with this kind of bacteria, both of them showed inactivity with gram negative bacteria *Klebsiella pneumoniae* and *Escherichia coli* but, compounds **3** and **5** exist as a very good anti-fungal activity toward *Candida albicans.*

The modification of the precursor with two substitu-tion of 2-deoxy-2-amino -d-glucose and 6-deoxy-6-amino -d-glucose yield two compounds **4** and **6** which show a good activity with all mentioned bacterial except compound **5** show poor results with *Klebsiella pneumoniae* and both show a great anti-fungal activity toward *Candida albicans.*

As a conclusion, the modification of 1, 1, 2-trimethyl-1H-benzo[e]indole **1** with two amino sugar molecules could be useful and considerable methods for synthesis of new bioactive compounds which can participate in the field of medical and pharmaceuticals applications (Table 1).

CONCLUSION

Biological derivatives based on available, economic and biodegradable monosaccharide with aromatic indole can be easily accessible within two to three steps reaction in acceptable yields. The new deriva-tive show a good to moderate biological activity to-ward gram positive bacteria and gram negative bac-

teria, while they show activity toward fungi. It is possible for the new compounds in future to take the way in both medical and pharmaceuticals application to substitute the now known familiar for bacteria and fungi.

CONFLICT OF INTEREST

The researchers declare that there are no conflicts of interest regarding the current manuscript.

Table 1: The Biological Activity Investigation of Target Compounds.

No.	Gram Positive Bacteria								Gram Negative Bacteria								Fungi			
	S. aureus				*S. epidermidis*				*K. pneumoniae*				*E. coli*				*C. albicans*			
	1	2	3	4	1	2	3	4	1	2	3	4	1	2	3	4	1	2	3	4
1	R	R	R	R	R	R	R	R	R	R	R	R	R	R	R	R	R	R	R	R
3	16	14	13	R	R	R	R	R	R	R	R	R	R	R	R	R	26	24	24	23
4	15	14	13	11	R	R	R	R	R	R	R	R	R	R	R	R	27	24	24	22
5	15	15	14	13	16	11	R	R	R	R	R	R	13	11	R	12	26	23	22	22
6	18	18	17	R	15	14	14	11	12	11	11	12	16	16	14	18	27	23	21	20

Numbers indicate the diameter of the inhibition zone around each hole in mm.

REFERENCES

1. Zhan WH, Hua JL, Jin YH, Teng X, Tian H. The synthesis and characterization of novel coumarin-containing cyanine dyes via "Click" chemistry. Res Chem Intermed [Internet]. 2008 Feb [cited 2022 Jul 8];34(2–3):229–39. Available from: <URL>.

2. Shimizu Y, Temma T, Hara I, Yamahara R, Ozeki E ichi, Ono M, et al. Development of Novel Nanocarrier-Based Near-Infrared Optical Probes for In Vivo Tumor Imaging. J Fluoresc [Internet]. 2012 Mar [cited 2022 Jul 8];22(2):719–27. Available from: <URL>.

3. Shen D, Bai M, Tang R, Xu B, Ju X, Pestell RG, et al. Dual fluorescent molecular substrates selectively report the activation, sustainability and reversibility of cellular PKB/Akt activity. Sci Rep [Internet]. 2013 Dec [cited 2022 Jul 8];3(1):1697. Available from: <URL>.

4. Menéndez GO, Eva Pichel M, Spagnuolo CC, Jares-Erijman EA. NIR fluorescent biotinylated cyanine dye: optical properties and combination with quantum dots as a potential sensing device. Photochem Photobiol Sci [Internet]. 2013 [cited 2022 Jul 8];12(2):236–40. Available from: <URL>.

5. Zhang K, Meng J, Bao W, Liu M, Wang X, Tian Z. Mitochondrion-targeting near-infrared fluorescent probe for detecting intracellular nanomolar level hydrogen sulfide with high recognition rate. Anal Bioanal Chem [Internet]. 2021 Feb [cited 2022 Jul 8];413(4):1215–24. Available from: <URL>.

6. Oparina L, Kolyvanov N, Ushakov I, Mal'kina A, Vashchenko A, Trofimov B. Metal- and Solvent-free Synthesis of Functionalized Dihydrooxazolo[3,2-a]indoles by One-Pot Tandem Assembly of 3H-Indoles and Propargylic Alcohols. Synthesis [Internet]. 2019 Mar [cited 2022 Jul 8];51(06):1445–54. Available from: <URL>.

7. Narayanan N, Karunakaran V, Paul W, Venugopal K, Sujathan K, Kumar Maiti K. Aggregation induced Raman scattering of squaraine dye: Implementation in diagnosis of cervical cancer dysplasia by SERS imaging. Biosensors and Bioelectronics [Internet]. 2015 Aug [cited 2022 Jul 8];70:145–52. Available from: <URL>.

8. Lawrence CL, Okoh AO, Vishwapathi V, McKenna ST, Critchley ME, Smith RB. N-alkylated linear heptamethine polyenes as potent non-azole leads against Candida albicans fungal infections. Bioorganic Chemistry [Internet]. 2020 Sep [cited 2022 Jul 8];102:104070. Available from: <URL>.

9. Ponnuvel K, Ramamoorthy J, Sivaraman G, Padmini V. Merocyanine Dye-Based Fluorescent Chemosensor for Highly Selective and Sensitive Detection of Hypochlorous Acid and Imaging in Live Cells. ChemistrySelect [Internet]. 2018 Jan 10 [cited 2022 Jul 8];3(1):91–5. Available from: <URL>.

10. Sayapin YA, Gusakov EA, Tupaeva IO, Karlutova OY, Dubonosova IV, Tkachev VV, et al. 1H-indole-based chemosensors for the sequential recognition of Hg2+ and CN− ions. Tetrahedron [Internet]. 2021 Mar [cited 2022 Jul 8];84:132030. Available from: <URL>.

11. Kumbhar HS, Gadilohar BL, Shankarling GS. Synthesis and spectroscopic study of highly fluorescent β-enaminone based boron complexes. Spectrochimica Acta Part A: Molecular and Biomolecular Spectroscopy [Internet]. 2015 Jul [cited 2022 Jul 8];146:80–7. Available from: <URL>.

12. Steponavičiūtė R, Martynaitis V, Bieliauskas A, Šačkus A. Synthesis of new fluorescent building blocks via the microwave-assisted annulation reaction of 1,1,2-trimethyl-1H-benzo[e]indole with acrylic acid and its derivatives. Tetrahedron [Internet]. 2014 Mar [cited 2022 Jul 8];70(11):1967–74. Available from: <URL>.

13. Steponavičiūtė R. Alkylation of 1,1,2-Trimethyl-1H-benzo[e]indole with bifunctional compounds, synthesis of phenyl substituted indolo[2,1-b][1,3]benzoxazines and investigation of chemical and optical properties [Internet] [Doctoral dissertation]. [Lithuania]: Lithuanian University of Health Sciences; 2014. Available from: <URL>.

14. Naim W, Novelli V, Nikolinakos I, Barbero N, Dzeba I, Grifoni F, et al. Transparent and Colorless Dye-Sensitized Solar Cells Exceeding 75% Average Visible Transmittance. JACS Au [Internet]. 2021 Apr 26 [cited 2022 Jul 8];1(4):409–26. Available from: <URL>.

15. Wang Q. New benzo[e]indolinium cyanine dyes with two different fluorescence wavelengths. Dyes and Pigments [Internet]. 2003 Nov [cited 2022 Jul 8];59(2):163–72. Available from: <URL>.

16. Fang X, Liu W, Wu X, Zhou W, Chen J, Liu X, et al. One-step condensation synthesis and characterizations of indocyanine green. Results in Chemistry [Internet]. 2021 Jan [cited 2022 Jul 8];3:100092. Available from: <URL>.

17. Khezri M, Afghan A, Roohi L, Baradarani MM. Vilsmeier-Haack Reaction with 2,3,3-Trimethyl-3H-benzo[g]indole and Its Conversion into 2-(1-aryl-1H-pyrazol-4-yl)-3,3-dimethyl-3H-benzo[g]indoles. Org Chem Res [Internet]. 2016 Sep [cited 2022 Jul 8];2(2). Available from: <URL>.

18. Roohi L, Afghan A, Baradarani M. Vilsmeier-Haack reagent-a facile synthesis of 2,4-chloro-3,3-dimethyl-7-phenoxyindolin-2-ylidenemalonaldehyde and transformation into different heterocyclic compounds. Curr Chem Lett [Internet]. 2013;Current Chemistry Letters:187–96. Available from: <URL>.

19. Nimbarte VD, Wirmer-Bartoschek J, Gande SL, Alshamleh I, Seibert M, Nasiri HR, et al. Synthesis and in Vitro Evaluation of Novel 5-Nitroindole Derivatives as c-Myc G-Quadruplex Binders with Anticancer Activity. ChemMedChem [Internet]. 2021 May 18 [cited 2022 Jul 8];16(10):1667–79. Available from: <URL>.

20. Berber N. Synthesis of New Schiff Base Compounds and Identification of Their Structures. Adıyaman University Journal of Science [Internet]. 2020 Jun 30 [cited 2022 Jul 8]; Available from: <URL>.

21. Halawa AH, El-Gilil SMA, Bedair AH, Shaaban M, Frese M, Sewald N, et al. Synthesis, biological activity and molecular modeling study of new Schiff bases incorporated with indole moiety. Zeitschrift für Naturforschung C [Internet]. 2017 Oct 26 [cited 2022 Jul 8];72(11–12):467–75. Available from: <URL>.

22. Liu H, Chu ZW, Xia DG, Cao HQ, Lv XH. Discovery of novel multi-substituted benzo-indole pyrazole schiff base derivatives with antibacterial activity targeting DNA

gyrase. Bioorganic Chemistry [Internet]. 2020 Jun [cited 2022 Jul 8];99:103807. Available from: <URL>.

23. Selvakumar N, editor. Standard operating procedure for mycobacteriology laboratory. Tuberculosis Research Centre, ICMR; 2010.

24. Vargahese N, editor. Microbiology Laboratory Manual. Kerala Agricultural University; 2014.

25. Karim A. Effect of Tris-EDTA and ascorbate in increasing antibiotic activity against bacteria isolated from otitis media [Doctoral dissertation]. [Baghdad]: Al-Nahrain University; 2005.

New Bioactive Aromatic Indole Molecules with Monosaccharide Core

Israa Nadim Hamdi Mahmsood, Salih Mahdi Salman*, Luma Salman Abd
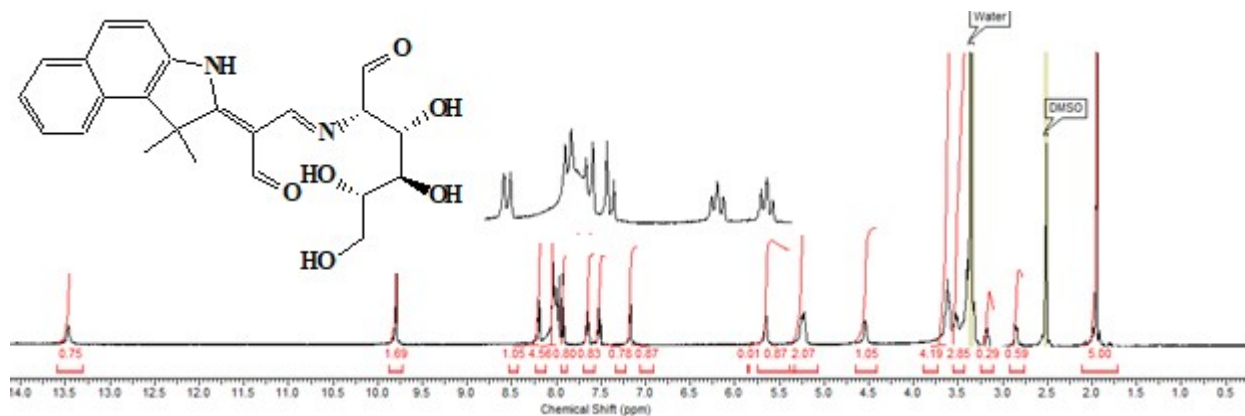
Supporting Material

Figure S1: 1H NMR Spectrum for (2S,3S,4R,5S)-2-((E)-((E)-2-(1,1-dimethyl-1H-benzo[e]indol-2(3H)-yli-dene)-3-oxopropylidene) amino)-3,4,5,6-tetrahydroxyhexanal (**3**).

Figure S2: 1H NMR for (2R,3S,4R,5R)-6-((E)-((E)-2-(1,1-dimethyl-1H-benzo [e]indol-2(3H)-ylidene)-3-oxopropylidene) amino)-2,3,4,5-tetrahydroxyhexanal (**5**).

Figure S3: 13C NMR Spectrum for (2S,3S,4R,5S)-2-((E)-((E)-2-(1,1-dimethyl-1H-benzo[e]indol-2(3H)-yli-dene)-3-oxopropylidene) amino)-3,4,5,6-tetrahydroxyhexanal (**3**).
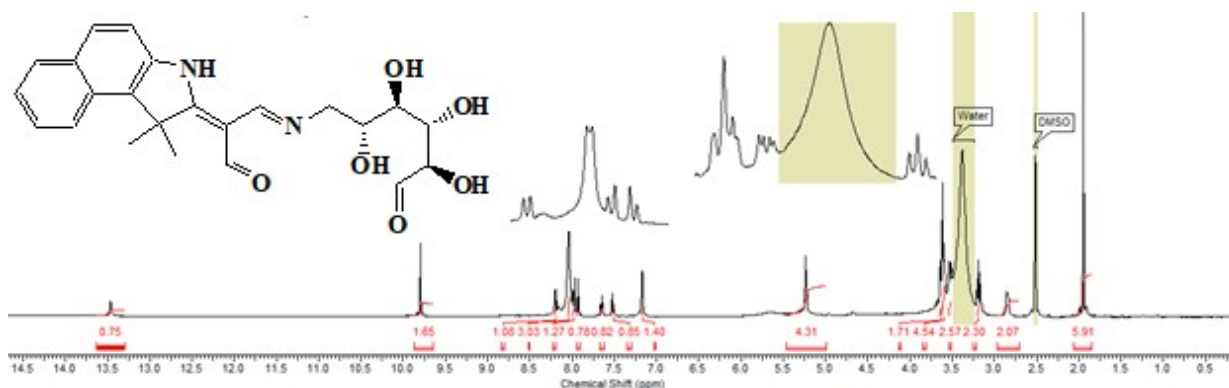
Figure S4: 13C NMR Spectrum for (2R,3S,4R,5R)-6-((E)-((E)-2-(1,1-dimethyl-1H-benzo [e]indol-2(3H)-ylidene)-3-oxopropylidene) amino)-2,3,4,5-tetrahydroxyhexanal (**5**).
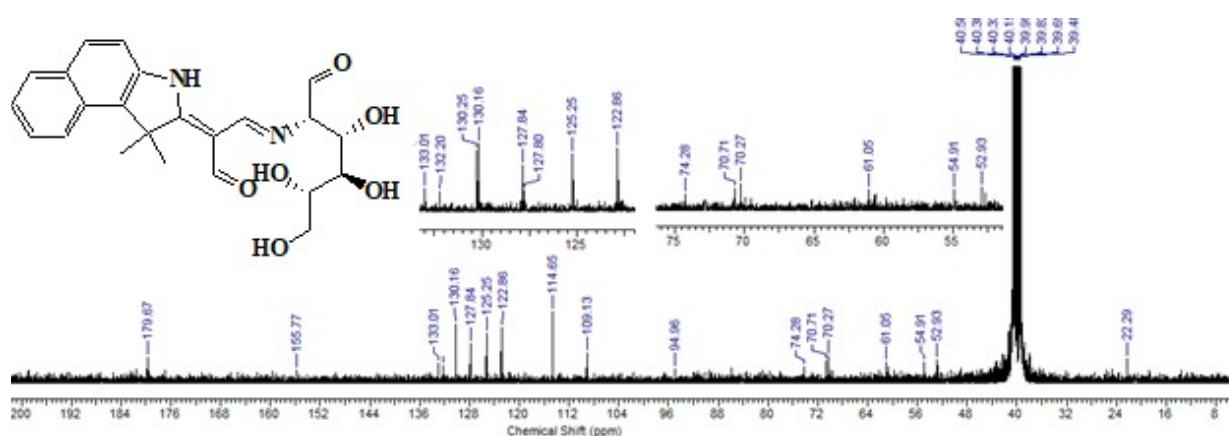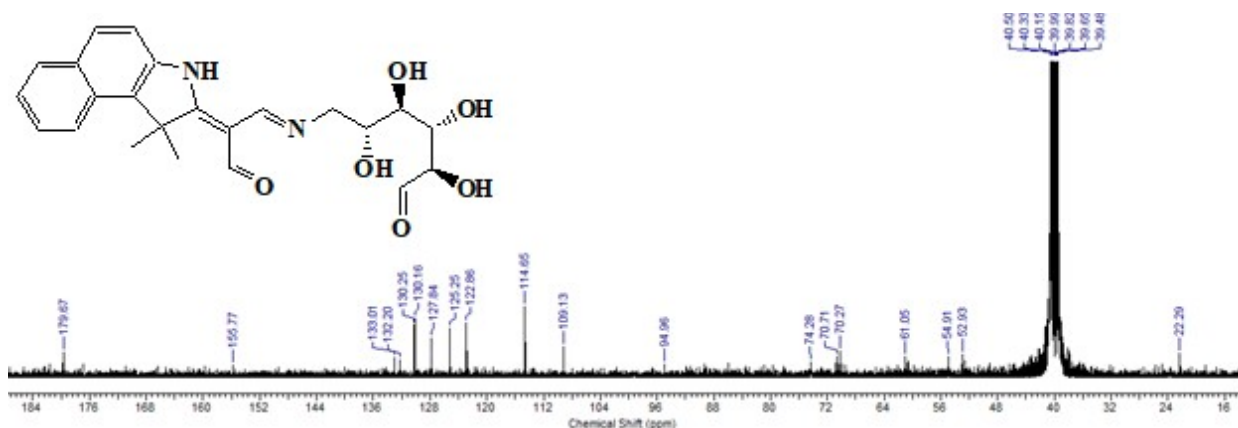

Figure S5: 1H NMR Spectrum for Compound (2S,3S,4R,5S)-2-((E)-((2Z,3E)-2-(1,1-dimethyl-1H-benzo[e]indol-2(3H)-ylidene)-3-((2R,3R,4S,5R)-3,4,5,6-tetrahydroxy-1-oxohexan-2-ylimino) propylidene) amino) -3,4,5,6-tetrahydroxyhexanal (4).
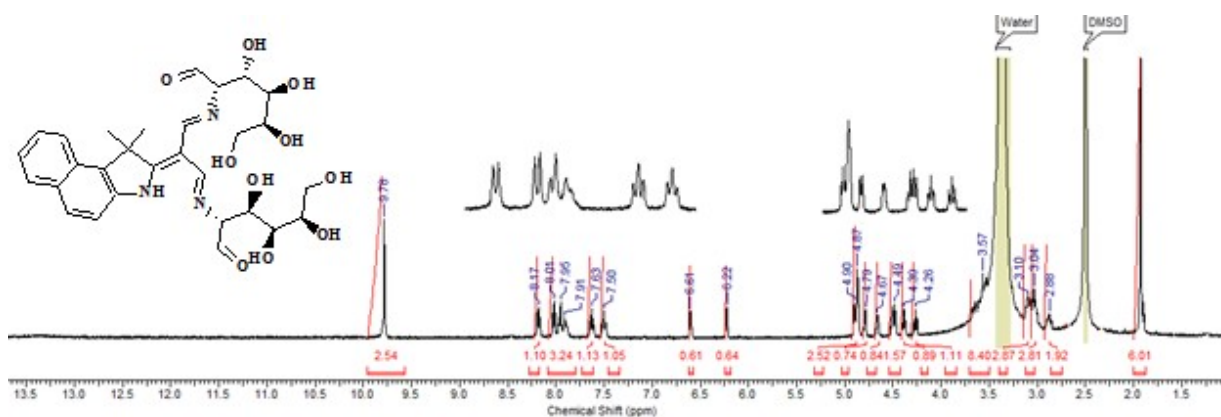

Figure S6: 13C NMR Spectrum for compound (2S,3S,4R,5S)-2-((E)-((2Z,3E)-2-(1,1-dimethyl-1H-benzo[e]indol-2(3H)-ylidene)-3-((2R,3R,4S,5R)-3,4,5,6-tetrahydroxy-1-oxohexan-2-ylimino) propylidene) amino) -3,4,5,6-tetrahydroxyhexanal (**4**)

Figure S7: 1H NMR Spectrum for compound(2S,3R,4S,5S)-6-((2E)-2-(1,1-dimethyl-1H-benzo[e]indol-2(3H)-ylidene)-3-((2R,3R,4S,5R)-2,3,4,5-tetrahydroxy-6 oxohexylimino) propylideneamino) -2,3,4,5-tetrahydroxyhexanal (**6**).

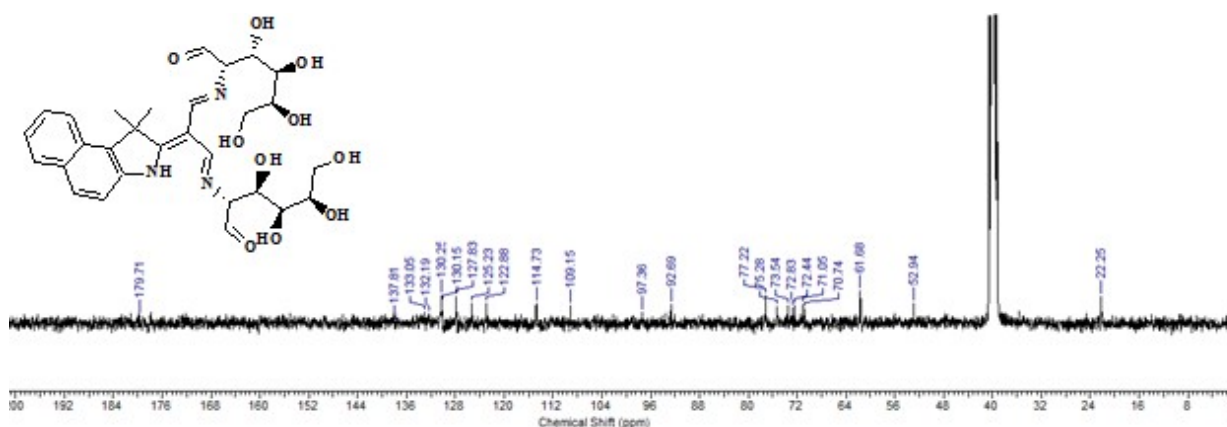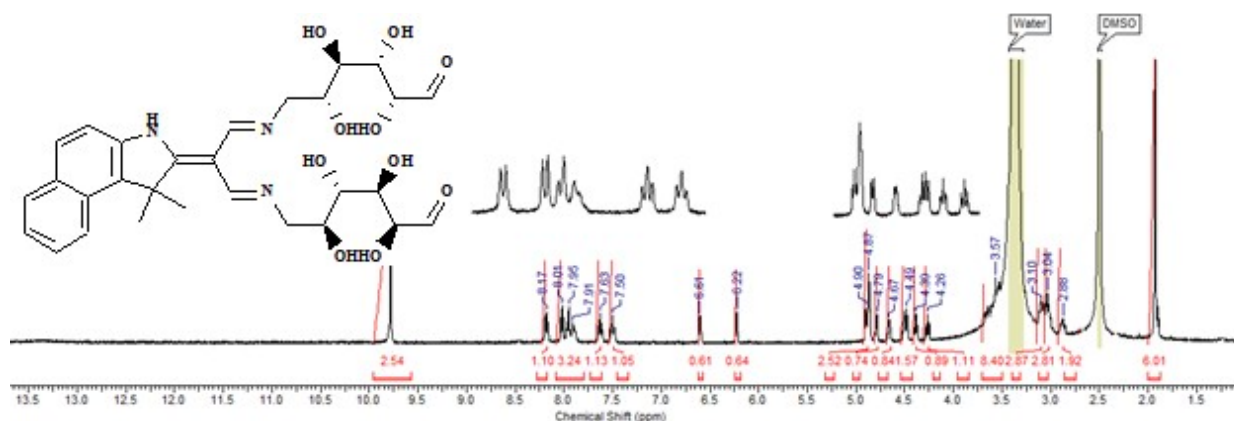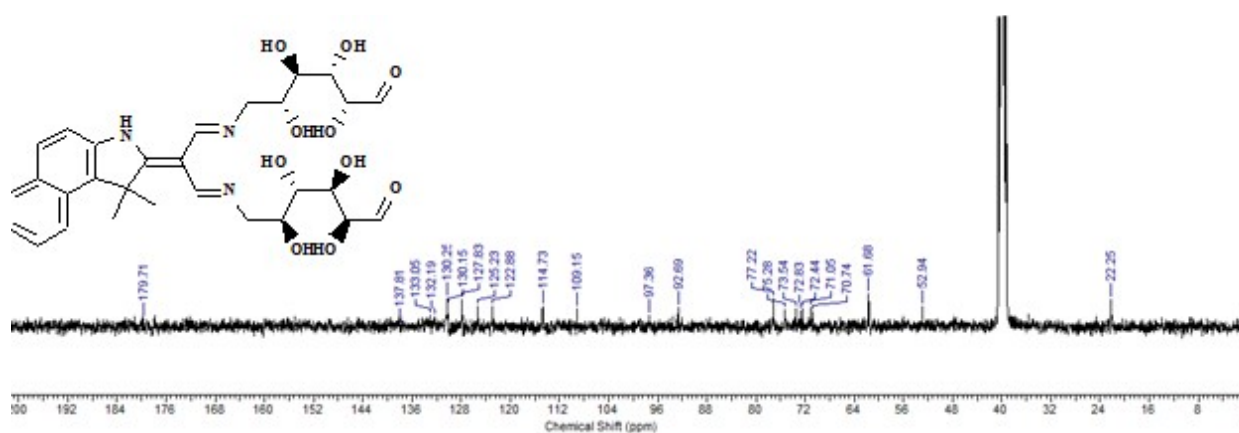**Fig-ure S8:** 13C NMR Spectrum for compound (2S,3R,4S,5S)-6-((2E)-2-(1,1-dimethyl-1H-benzo[e]indol-2(3H)-ylidene)-3-((2R,3R,4S,5R)-2,3,4,5-tetrahydroxy-6 oxohexylimino) propylideneamino) -2,3,4,5-tetrahydroxyhexanal [6].

The Effects on Some Parameters of Microbiological and Physicochemical Research of Zeolite and Zeolite Filtered Water from Rhodope Mountains, Bulgaria

Teodora P. Popova[1] (iD) , **Ignat Ignatov[2]*** (iD) , **Nedyalka Valcheva[3]** (iD) , **Alexander I. Ignatov[2]** (iD)

[1] University of Forestry, Faculty of Veterinary Medicine, 10 Kl. Ohridski Blvd., Sofia 1756, Bulgaria
[2] Scientific Research Center of Medical Biophysics, Sofia, Bulgaria
[3] Trakia University, Stara Zagora, Bulgaria

Abstract: The physicochemical composition and antibacterial effect of aqueous zeolite infusion (spring zeolite water Sevtopolis with zeolite from deposit Beli plast, Bulgaria), obtained for 12 and 36 hours, were tested. Ordinance No. 9/2001, Official State Gazette, issue 30, and Decree No.178/23.07.2004 regarding the quality of water intended for drinking and household purposes were applied to study the physicochemical composition. *Staphylococcus aureus*-ATCC and TSA-MRSA, and *Escherichia coli* ATCC were used in the studies. Both tested zeolite waters reduced the amounts of viable *E. coli* and *S. aureus* cells even when they were in high concentrations (10^6 cells/mL). The effect of the 36-hour infusion was better, under the influence of which, after 60 minutes, the number of live bacteria of both tested species decreased by almost half compared to the initial amounts. Slightly higher sensitivity to two zeolite waters was shown by *E. coli*, whose cells were reduced to about 35% after two hours of exposure to both zeolite waters tested. However, about 20% of the cells of the tested bacteria survived even after 96 hours of exposure to these waters. Only in *E. coli* no growth was found after 96 hours of exposure to 12 hours of zeolite water. These results show the effectiveness of zeolite for water purification from Gram-positive and Gram-negative bacteria, as well as prospects for using zeolite water as a prophylactic and auxiliary treatment for bacterial infections.

INTRODUCTION

Scientific research shows that in areas where there is zeolite, the mineral, with its antimicrobial properties and physicochemical composition of zeolite water, can benefit public health and longevity (1-5). Zeolite is used in filtration systems for water purification (6,7). In Southern Bulgaria, there are six zeolite deposits in the Rhodope Mountains. They are located in the northeastern Rhodopes. These are Beli Plast, Most, Gorna Krepost, Golobradovo, Lyaskovets and Beliat Bair.

Clinoptilolite and modernite are the primary zeolite materials in them. In this area, the water passes through zeolite layers.

Zeolites are aluminosilicate members of the family of microporous solids, known as "molecular sieves" and consist mainly of silicon, aluminum, and others. They have a porous structure that can hold a wide variety of cations, such as Na^+, K^+, Ca^{2+}, Mn^{2+}, and others. These positive ions are relatively weakly bound and can be easily replaced by others in contact solution. Some of the most common mineral

zeolites are analzyme, chabazite, stilbit, clinoptilolite, hyulandite, natrolite and phillipsite. These cations exchanged zeolites have different acidity and catalyze several acids catalyzes (8, 9). Because zeolites are microporous aluminosilicate minerals, they are often used as adsorbents and catalysts. Zeolite is a non-toxic, three-dimensionally porous, crystalline, hydrated aluminosilicate with natural adsorbent and ion exchange properties, which removes harmful microbes as well as dispersed insoluble and soluble toxins from drinking water. Zeolite has been used since the Maya civilization for water purification and decontamination (10, 11). Nowadays, creating a simple flow filter made of zeolite-cotton packing in a tube (ZCT) provides a solution as an inexpensive device for removing heavy metal ions from contaminated water with high adsorption efficiency. After flowing through the setup packed with 10 g of zeolite-cotton, 65 mL 1000 ppm Cu^{2+} solution is purified down to its safety limit (<1 ppm) (12). ZCT can be used for disinfection by introducing Ag-exchanging zeolite-cotton for silver ion exchanging by incorporating them into a commercial dental adhesive and investigating the inhibition of biofilm formation at the tooth-restoration margin (13).

Zeolites for industrial use are also produced synthetically. This is done by heating aqueous alumina and silica solutions with sodium hydroxide. Equivalent reagents include sodium aluminate and sodium silicate. Synthetic zeolites have some key advantages over their natural counterparts. Synthetic materials are produced in a homogeneous, phase pure state. It is also possible to obtain zeolite structures that do not occur in nature. As the main raw materials used for producing zeolites are silicon and aluminum, one of the most common mineral components on earth, the potential for supplying zeolites is practically unlimited (14). This allows their widespread use as ion exchanger means for domestic and commercial water purification, softening, and more. In chemistry, zeolites are used to separate molecules (only molecules of certain sizes and shapes can be omitted) and as molecule traps so that they can be analyzed. Zeolites are also widely used as catalysts and sorbents. Their well-defined pore structure and regulated acidity make them highly active in a wide variety of reactions (15). Their application as filter additives in aquariums for the adsorption of ammonia and other nitrogen compounds is also very useful. Due to the adsorption properties of zeolites for calcium, they may effectively reduce calcium in hard water (1). Recently, studies have been presented on a new type of zeolite, finding that it helps increase eggplant yields by supplying potassium, calcium, and iron ions to the soil (16). This zeolite has a good content of nutrients necessary for plants and physical properties for water retention, making it an important clay mineral for agricultural and industrial purposes.

The research and development of many biochemical and biomedical applications of zeolites, particularly the naturally occurring species heulandite, clinoptilolite, and chabazite, continues. (18). In the present work, the authors performed physicochemically and *in vitro* studies to test the antibacterial properties of zeolite waters with zeolite from deposit Beli Plast (Figure 1) (17-20).

Figure 1: Zeolite, Beli plast, Bulgaria. Natural deposit,"Zeolitni gabi".

The water used for the research was spring water "Sevtopolis" (21). It was obtained via filtration with zeolite from Beli plast, Bulgaria. The physicochemical parameters of that zeolite and the water that filtered through it, as well as their antimicrobial effects, have not yet been studied. We have selected some of the most important conditionally pathogenic Gram-positive (*S. aureus*) and Gram-negative (*E. coli*) bacteria of great importance in the infectious pathology of animals and humans. The effects on them would be indicative of other similar microorganisms.

The study aims to show with microbiological and physicochemical parameters that zeolite has the potential for important positive effects on public health and environmental cleanliness in the areas where it is used.

MATERIALS AND METHODS

Zeolite
The effect of aqueous infusions of zeolite water was obtained by soaking 50 g of zeolite from Beli plast (Bulgaria) in the form of granules (0.5 cm in diameter) in 500 mL of zeolite water for 12 and 36 hours at room temperature 20 ± 0.5 °C.

Chemical composition of Zeolite from Beli plast (Bulgaria)
Table 1 illustrates the chemical composition of the tested zeolite in % (w/w).

Table 1. The chemical composition of zeolite from Beli plast (Bulgaria) in % (w/w)

No.	Chemical component	Content, % (w/w)
1	SiO_2	66.6
2	Al_2O_3	11.41
3	Fe_2O_3	0.8
4	MgO	0.06
5	TiO_2	0.15
5	CaO	2.80
6	Na_2O	0.22
7	K_2O	2.9

Physical indicators. The physical and chemical indicators are pH, oxidation-reduction potential (ORP), and temperature of zeolite waters were measured using Manual multi-parameter analyzer Consort C1010 (Consort bvba, Belgium) for pH, mV, and temperature measurement).

Microorganisms. Suspensions with a concentration of 10^7 cells.mL^{-1} of two strains of Staphylococcus aureus - ATCC-6538 and TSA-MRSA, as well as Escherichia coli ATCC-8739 were used in the studies. The suspensions were prepared in sterile saline by the Mc Ferland standard optical method.

Nutrient media.
Mueller Hinton agar (BUL BIO NCIPD - Sofia) was used to obtain 24-hour cultures of the tested strains, as well as solid selective media (Antisel - Sharlau Chemie SA, Spain) to determine the effect of the tested zeolite waters for antimicrobial activity: Eosin Methylene Blue agar for *E. coli* and Chapman Stone agar for *S. aureus*.

Methods for determination of microbiological indicators from Bulgarian State Standard
1. Methods for evaluating microbiological indicators according to Ordinance No. 9/2001, Official State Gazette, issue 30, and decree No. 178/23.07.2004 about the quality of water intended for drinking purposes.
2. Method for determination of *Escherichia coli* and coliform bacteria – BDSEN ISO 9308-1: 2004;

3. Method for determination of enterococci – BDS EN ISO 7899-2;
4. Method for determination of sulfite reducing spore anaerobes – BDS EN 26461-2: 2004;
5. Method for determination of the total number of aerobic and facultative anaerobic bacteria – BDS EN ISO 6222: 2002;
6. Method for determination of *Pseudomonas aeruginosa* – BDS EN ISO 16266: 2008.
7. Determination of coli – titre by fermentation method – Ginchev's method
Determination of coli – bacteria over Endo's medium – membrane method.
8. Determination of sulfite reducing anaerobic bacteria (*Clostridium perfringens*) – membrane method.
The number of the isolated bacteria was presented in colony-forming units per mL (CFU.mL^{-1}) of the tested waters (22).

Methods for physicochemical analysis.
The physicochemical analysis was performed according to Ordinance No. 9/2001, Official State Gazette, issue 30, and Decree No. 178/23.07.2004 regarding the quality of water intended for drinking and household purposes. The following methods are applied (Ordinance No. 9/2001) (22):

The determination of color was according to Rublyovska Scale – the method by Bulgarian State Standard (BDS) 8451: 1977;

Method for determining smell at 20°C — method BDS 8451: 1977 technical device – glass mercury thermometer, conditions No. 21;

Method for determination of turbidity - EN ISO 7027, with technical device turbidimeter type TURB 355 IR ID No 200807088;

Method for determination of pH – BDS 3424: 1981, technical device pH meter type UB10 ID NoUB10128148;

Method for determination of oxidisability – BDS 3413: 1981;

Method for determination of chlorides – BDS 3414: 1980;

Method for determination of nitrates – Validated Laboratory Method (VLM) – NO_3 – No. 2, technical device photometer "NOVA 60 A" ID No. 08450505;

Method for determination of nitrites – VLM NO_2 – No. 3, technical device photometer "NOVA 60 A" ID No. 08450505;

Method for determination of ammonium ions – VLM – NH_4 – No. 1, technical device photometer "NOVA 60 A" ID No. 08450505;

Method for determination of general hardness – BDS ISO 6058;

Method for determination of sulfates – VLM – SO_4 – No. 4, technical device photometer "NOVA 60 A" ID No. 08450505;

Method for determination of calcium – BDS ISO 6058;

Method for determination of magnesium – BDS 7211: 1982;

Method for determination of phosphates – VLM - PO_4 – No. 5, technical device photometer "NOVA 60 A" ID No 08450505;

Method for determination of manganese – VLM – Mn – No. 7, technical device photometer "NOVA 60 A" ID № 08450505;

Method for determination of iron – VLM – Fe – No. 6, technical device photometer "NOVA 60 A" ID No. 08450505;

Method for determination of fluorides – VLM – F – No. 8, technical device photometer "NOVA 60 A" ID No. 08450505;

Method for determining electrical conductivity – BDS EN 27888, technical device – conductivity meter inoLab cond 720 ID No 11081137.

Experimental staging
To 4.5 mL of a 12-hour as well as 36-hour zeolite water, 0.5 mL of a suspension of the corresponding bacterial strain was added at a concentration of 10^7 cells. mL^{-1}, reaching a final concentration of 10^6 cells/mL for each species and strain of microorganisms used. The following controls were placed - 12 and 36-hour zeolite water without microorganisms, as well as bacteria without zeolite water. After different time intervals for exposure to zeolite waters (15 min, 30 min, 60 min, 120 min, 24 h, and 96 h), cultures were made from each of the samples on Eosin Methylene Blue selective agar medium for the Gram-negative bacteria and Chapman Stone agar for S. aureus in order to determine the antimicrobial activity of the tested waters against E. coli and S. aureus. After culturing at 37 °C for 18-24, the growth of the tested bacteria was reported, as well as that of the set controls. Colonies formed were counted, and the results were calculated in colony-forming units/mL $(CFU.mL^{-1})$ as a percentage of the growth of untreated controls of the strains, which were considered 100 %.

Statistical analysis. The results were processed mathematically, and the arithmetic mean (AV) and standard deviation (SD) were found. Student's t-test analysis for independent samples was applied to test the statistical dependence and reliability of the results. The significance of the results was defined at a significance level of $P<0.05$. Microsoft®Office Professional Plus Excel 2013 (15.0.4569.15060) was used for the calculations.

RESULTS AND DISCUSSION

Physicochemical analysis of spring water with zeolite filtration "Sevtopolis"
Table 2 illustrates physicochemical parameters of spring water with zeolite filtration "Sevtopolis" according to Ordinance No. 9/2001. The research is with the document (Laboratory Alimenti Omnilab, Plovdiv, Bulgaria, No. 10838, 22.02.2021)

Table 2. Physicochemical parameters of spring water with zeolite filtration "Sevtopolis"

Controlled parameter	Measuring unit	Maximum Limit Value	Spring water with zeolite filtration "Sevtopolis"
1. pH	pH values	≥ 6,5 and ≤ 9,5	6.91±0.1
2. Electrical conductivity	$\mu S.L^{-1}$	2000	278 ±8.3
3. Color	Chromaticity Values	Acceptable	Acceptable
4. Turbidity	FNU	Acceptable	Acceptable
5. Odor	force	Acceptable	Acceptable
6. Calcium (Ca^{2+})	mg. L^{-1}	150	34.8±3.5
7. Magnesium (Mg^{2+})	mg. L^{-1}	80	8.26±0.83
8. Zinc (Zn^{2+})	mg. L^{-1}	4.0	<2.0
9. Manganese (Mn^{2+})	$\mu g. L^{-1}$	50	<10.0
10. Sodium (Na^+)	mg. L^{-1}	200	13.85±1.4
11. Potassium (K^+)	mg. L^{-1}	-	3.57±0.36
12. Nitrites (NO_2^-)	mg. L^{-1}	0.5	<0.05
13. Nitrates (NO_3^-)	mg. L^{-1}	50	11.80±0.12
14. Sulfates (SO_4^{2-})	mg. L^{-1}	250	41.40±0.41
15. Ammonium (NH_4^+)	mg. L^{-1}	0.5	<0.013
16. Chlorine (Cl^-)	mg. L^{-1}	0.3-0.4	0.018
17. Iron (Fe)	$\mu g. L^{-1}$	200	<5.0
18. Selenium (Se)	$\mu g. L^{-1}$	10	<2.0
19. Antimony (Sb)	mg. L^{-1}	5	<2.7
20. Aluminum (Al)	$\mu g. L^{-1}$	200	<40.00
21. Lead (Pb)	$\mu g. L^{-1}$	10	<2.0
22. Boron (B)	mg. L^{-1}	1	<0.02
23. Arsenic (As)	$\mu g. L^{-1}$	10	<2.0
24. Chromium (Cr)	$\mu g. L^{-1}$	50	<10.0
25. Cadmium (Cd)	$\mu g. L^{-1}$	5	<1.0
26. Copper (Cu)	mg. L^{-1}	2	<0.08
27. Nickel (Ni)	$\mu g. L^{-1}$	20	<4.0
28. Mercury (Hg)	$\mu g. L^{-1}$	1	<0.5

The physical parameters of pH and ORP of the studied zeolite waters at room temperature 20° C are presented in Table 3.

Table 3. Physical indicators of the tested zeolite water

Zeolite water	pH	ORP (mV)
12 h	6.76 ± 0,1	0.7 ± 2.52
36 h	6.5 ± 0,04	32.3 ± 0.58

As can be seen from the data in the table, the zeolite water obtained for 12 and 36 hours have a slightly acid reaction and a neutral to slightly high ORP. A lower pH and a higher ORP indicated the water obtained for a longer time (36 h) compared to that obtained for 12 h. The differences between both waters for pH were statistically significant (P <0.05), as well as for ORP (P <0.01).

The results of the studies performed to determine the sensitivity of the used strains of *E. coli* and *S. aureus* to zeolite waters, tested at a final concentration of 10^6 cells.mL^{-1} by the suspension method, are presented in Table 4. Bacterial growth was defined as the percentage compared to growth of zeolite-free bacterial controls, which were considered 100%.

The data indicated that the two tested aqueous infusions of zeolite exhibited an antimicrobial effect, although it was not strongly pronounced. After 30 minutes of exposure, they reduced the amount of viable *E. coli* and *S. aureus* cells even when they were in high concentrations (10^6 cells.mL^{-1}). The effect of the 36-hour infusion was better, under the influence of which, after 60 minutes, the number of live bacteria of the two tested species decreased by almost half compared to the initial amounts. Slightly higher sensitivity to the zeolite waters was shown by *E. coli*, whose cells were reduced to about 35% after two hours of exposure to both zeolite waters tested. *S. aureus* cells were reduced to a lesser extent under the action of 12 h zeolite water. However, about 20% of the cells of the tested bacteria survived even after 96 hours of exposure to these waters. Only in *E. coli* no growth was found after 96 hours of exposure to 12 h zeolite water.

Table 4 and figures 3 and 4 illustrate the antimicrobial effect of 12 h zeolite water and 36 h

zeolite water against *S. aureus,* and *E. coli* strains in   suspensions with a density 10^6 cells. mL^{-1}

Table 4. Antimicrobial effect of 12 h zeolite water and 36 h zeolite water against *S. aureus* and *E. coli* strains in suspensions with a density 10^6 cells. mL^{-1}

| Time of action	Growth of the strains (% of CFU.mL^{-1}) after different intervals of exposure to zeolite waters			
	S. aureus		*E. coli*	
	12 h	36 h	12 h	36 h
15 min	100.0 ±10.0	100.0 ±10.0	100.0 ±10.0	100.0 ±10.0
30 min	77.5 ±4.3	80.0 ±0.0	82.5 ±3.5	87.5 ±2.5
60 min	62.5 ±8.3	55.0 ±5.0	55.0 ±5.0	52.5 ±2.5
120 min	50.0 ±10.0	35.0 ±5.0	35.0 ±5.0	32.5 ±2.5
24 h	50.0 ±10.0	35.0 ±5.0	32.5 ±2.5	30.0 ±0.0
96 h	22.0 ±0.0	20.0 ±10.0	0	18.0 ±10.0
Untreated controls	100.0 ±10.0	100.0 ±10.0	100.0 ±10.0	100.0 ±10.0
Control without bacteria	0	0	0	0
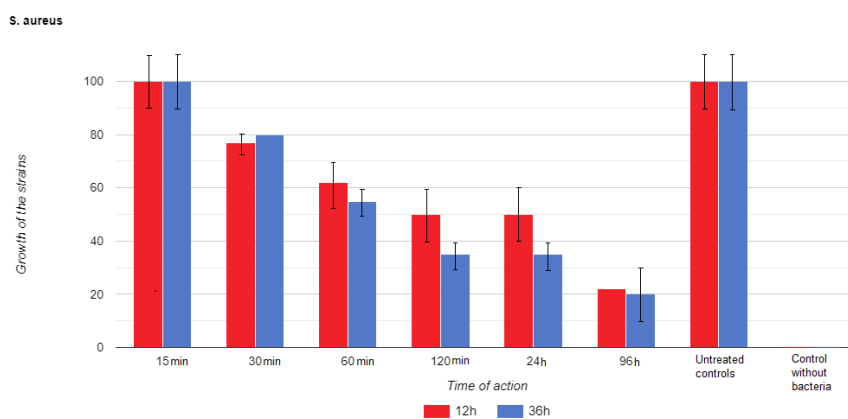
Figure 2: Antimicrobial effect of 12 h zeolite water and 36 h zeolite water against *S. aureus* and strains in suspensions with a density 10^6 cells. mL^{-1}
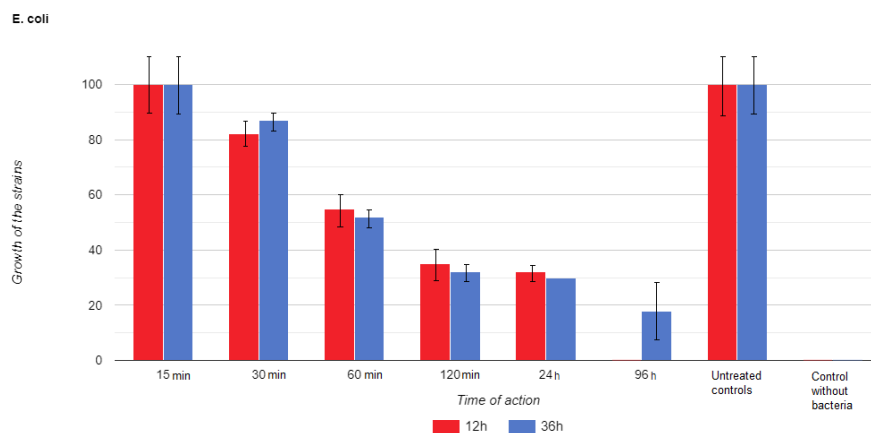

Figure 3: Antimicrobial effect of 12 h zeolite water and 36 h zeolite water against *E. coli* strains in suspensions with a density 10^6 cells. mL^{-1}

Microbiological research of this standard was performed by Bulgarian authors (23-26). Data from many of them show that silver ions enhance the antimicrobial properties of zeolite (27, 28). The research was performed with *in vitro* antimicrobial effect of fabric softeners containing silver zeolite on *S. aureus, Pseudomonas aeruginosa,* and *Candida albicans* (29). The studies demonstrated the inhibitory action of silver-zeolite-containing samples on *S. aureus*, including MRSA, as well as on *C. albicans* (30). In studies of the Mexican silver zeolite mineral clinoptilolite - heulandite demonstrated that it eliminated pathogenic microorganisms *E. coli* and *Streptococcus faecalis* from the water after 2 hours of contact (31). Silver ZCT exhibits antibacterial properties by completely purifying *E. coli*-contaminated water from the bacterial cells as it flows through the device (7). The zeolite water filter is a sustainable, natural solution for purifying drinking water and wastewater (32). Zeolite filters have many pores, so they not only trap particles between the grains but absorb them into their pores. This is partly done by zeolite minerals' ability to cation exchange, whereby they absorb positive ions from water (i.e., dissolved metals, sodium, ammonia, etc.). Also, due to its high pore density, zeolite has a highly effective surface and can trap high concentrations of contaminants before the filter needs to be cleaned. For these reasons, it can be used successfully to treat drinking water, wastewater, radioactive water, freshwater aquaculture, and others (33). The zeolite formulas can be combined with various materials used to manufacture medical devices, surfaces, textiles, or household items where antimicrobial properties are required.

Our research also shows that zeolite can be used to reduce the bacterial water content even when it is significant.

CONCLUSIONS

By examining the physicochemical and antimicrobial properties of zeolite, the study shows that it positively affects public health and environmental cleanliness in the areas where it is distributed.

The tested zeolite water, obtained for 12 and 36 hours, reduced the amount of viable *E. coli* and *S. aureus* cells even when they were in high concentration (10^6 cells/mL). *E. coli* showed a higher sensitivity to these waters' action than *S. aureus*.

REFERENCES

1. Tinteri C, Potenza M, Rizzetto R. Antimicrobial efficacy and longevity of silver+ zeolite incorporating preinsulated ducts installed in real healthcare settings. J prev med hyg. 2012;53(4):177–80.

2. Ernst WG. Overview of naturally occurring Earth materials and human health concerns. Journal of Asian Earth Sciences [Internet]. 2012 Oct [cited 2022 Jul 12];59:108–26. Available from: <URL>.

3. Ignatov I, Mosin O, Bauer E. Carbonaceous Fullerene Containing Mineral Shungite and Aluminosilicate Mineral Zeolite. Mathematical Model and Practical Application of Water Solution of Shungite and Zeolite. Journal of Medicine, Physiology and Biophysics. 2014;4:27–44.

4. Ibrahim SS, Salem NY. Insecticidal efficacy of nano zeolite against Tribolium confusum (Col., Tenebrionidae) and Callosobruchus maculatus (Col., Bruchidae). Bulletin of the National Research Centre. 2019;43(1):1–8.

5. Peixoto P, Guedes JF, Rombi E, Fonseca AM, Aguiar CA, Neves IC. Metal Ion–Zeolite Materials against Resistant Bacteria, MRSA. Ind Eng Chem Res [Internet]. 2021 Sep 8 [cited 2022 Jul 12];60(35):12883–92. Available from: <URL>.

6. Luo J, Lindsey S. The use of pine bark and natural zeolite as biofilter media to remove animal rendering process odours. Bioresource Technology [Internet]. 2006 Sep [cited 2022 Jul 12];97(13):1461–9. Available from: <URL>.

7. Chen W, Acharya D, Liu Z, Yi X, Xiao Y, Tang X, et al. Mechanistic insights of selective syngas conversion over Zn grafted on ZSM-5 zeolite. Catal Sci Technol [Internet]. 2020 [cited 2022 Jul 12];10(24):8173–81. Available from: <URL>.

8. Marakatti VS, Rao PVC, Choudary NV, Ganesh GS, Shah G, Maradur SP, et al. Influence of Alkaline Earth Cation Exchanged X-Zeolites Towards <I>Ortho</I>-Selectivity in Alkylation of Aromatics: Hard-Soft-Acid-Base Concept. adv porous mat [Internet]. 2014 Dec 1 [cited 2022 Jul 12];2(4):221–9. Available from: <URL>.

9. Marakatti VS, Halgeri AB. Metal ion-exchanged zeolites as highly active solid acid catalysts for the green synthesis of glycerol carbonate from glycerol. RSC Adv [Internet]. 2015 [cited 2022 Jul 12];5(19):14286–93. Available from: <URL>.

10. Flanigen EM. Chapter 2 Zeolites and Molecular Sieves an Historical Perspective. In: Studies in Surface Science and Catalysis [Internet]. Elsevier; 1991 [cited 2022 Jul 12]. p. 13–34. Available from: <URL>.

11. Tankersley KB, Dunning NP, Carr C, Lentz DL, Scarborough VL. Zeolite water purification at Tikal, an ancient Maya city in Guatemala. Sci Rep [Internet]. 2020 Dec [cited 2022 Jul 12];10(1):18021. Available from: <URL>

12. Chen X, Yu L, Zou S, Xiao L, Fan J. Zeolite Cotton in Tube: A Simple Robust Household Water Treatment Filter for Heavy Metal Removal. Sci Rep [Internet]. 2020 Dec [cited 2022 Jul 12];10(1):4719. Available from: <URL>.

13. Li W, Qi M, Sun X, Chi M, Wan Y, Zheng X, et al. Novel dental adhesive containing silver exchanged EMT zeolites against cariogenic biofilms to combat dental caries. Microporous and Mesoporous Materials [Internet]. 2020 Jun [cited 2022 Jul 12];299:110113. Available from: <URL>.

14. Rollmann L, Valyocsik E, Shannon R. Zeolite Molecular Sieves. In: Murphy D, Interrante L, editors. Inorganic

Syntheses. New York: Wiley and Sons, Inc.; 1995. p. 227–34.

15. Bhatia S. Zeolite Catalysts: Principles and applications. Boca Raton: CRC Press; 1989. 304 p.

16. Yasir A, Janabi N. Discovered a new type of zeolite and tested on some chemical properties of soil and plant yield. Plant Archives. 2020;Supp 1:1978–82.

17. Djurova E, Stefanova I, Gradev G. Geological, mineralogical and ion exchange characteristics of zeolite rocks from Bulgaria. Journal of Radioanalytical and Nuclear Chemistry, Articles [Internet]. 1989 Apr [cited 2022 Jul 12];130(2):425–32. Available from: <URL>.

18. Petrova N, Mizota T, Fujiwara K. Hydration Heats of Zeolites For Evaluation of Heat Exchangers. Journal of Thermal Analysis and Calorimetry [Internet]. 2001 [cited 2022 Jul 12];64(1):157–66. Available from: <URL>.

19. Yanev Y, Cochemé JJ, Ivanova R, Grauby O, Burlet E, Pravchanska R. Zeolites and zeolitization of acid pyroclastic rocks from paroxysmal Paleogene volcanism, Eastern Rhodopes, Bulgaria. njma [Internet]. 2006 Aug 18 [cited 2022 Jul 12];182(3):265–83. Available from: <URL>.

20. Nikolov A, Rostovsky I, Nugteren H. Geopolymer materials based on natural zeolite. Case Studies in Construction Materials [Internet]. 2017 Jun [cited 2022 Jul 12];6:198–205. Available from: <URL>.

21. Ignatov I. Aluminosilicate Mineral Zeolite. Interaction of Water Molecules in Table and Mountain Zeolite Water Sevtopolis from Bulgaria. Journal of Medicine, Physiology and Biophysics. 2017;31:41–5.

22. Anonymous. Methods for evaluation of physicochemical indicators according to Ordinance No. 9 / 2001. 2004 Jul. (Official State Gazette).

23. Popova T, Petrova T, Kaleva M, Karadzhov S. Comparative study of the effect of electrochemically activated water solutions on Pseudomonas aeruginosa. Acta Microbiologica Bulgarica. 2018;34(3):160–4.

24. Popova TP, Petrova TE, Petrichev M, Valyova M. Action of activated waters on plants after adverse chemical effects, imitating acid rain. Bulgarian Journal of Agriculture Science. 2019;25(4):638–45.

25. Popova T, Ignatov I, Huether F, Petrova T. Antimicrobial activity of colloidal nanosilver 24 ppm in vitro. Bulgarian Chemical Communications. 2021;53(3):365–70.

26. Popova T, Ignatov I. In vitro Antimicrobial activity of colloidal nano silver. Bulg J Vet Med. 2021;

27. Kwakye-Awuah B, Williams C, Kenward MA, Radecka I. Antimicrobial action and efficiency of silver-loaded zeolite X. J Appl Microbiol [Internet]. 2008 May [cited 2022 Jul 12];104(5):1516–24. Available from: <URL>.

28. Matsuura T, Abe Y, Sato Y, Okamoto K, Ueshige M, Akagawa Y. Prolonged antimicrobial effect of tissue conditioners containing silver-zeolite. Journal of Dentistry [Internet]. 1997 Sep [cited 2022 Jul 12];25(5):373–7. Available from: <URL>.

29. Odabaş ME, Çinar Ç, Akça G, Araz İ, Ulusu T, Yücel H. Short-term antimicrobial properties of mineral trioxide aggregate with incorporated silver-zeolite: MTA with incorporated silver-zeolite. Dental Traumatology [Internet]. 2011 Jun [cited 2022 Jul 12];27(3):189–94. Available from: <URL>.

30. Abe Y, Ishii M, Takeuchi M, Ueshige M, Tanaka S, Akagawa Y. Effect of saliva on an antimicrobial tissue conditioner containing silver-zeolite. J Oral Rehabil [Internet]. 2004 Jun [cited 2022 Jul 12];31(6):568–73. Available from: <URL>.

31. Rivera-Garza M, Olguín MT, García-Sosa I, Alcántara D, Rodríguez-Fuentes G. Silver supported on natural Mexican zeolite as an antibacterial material. Microporous and Mesoporous Materials [Internet]. 2000 Oct [cited 2022 Jul 12];39(3):431–44. Available from: <URL>.

32. Nicholas N. How is zeolite water treatment media used in water and wastewater treatment? [Internet]. Water onine. 2019. Available from: <URL>.

33. Demirci S, Ustaoğlu Z, Yılmazer GA, Sahin F, Baç N. Antimicrobial Properties of Zeolite-X and Zeolite-A Ion-Exchanged with Silver, Copper, and Zinc Against a Broad Range of Microorganisms. Appl Biochem Biotechnol [Internet]. 2014 Feb [cited 2022 Jul 12];172(3):1652–62. Available from: <URL>.

Synthesis and Biological Evaluation of Furyl-Carboxamide Derivatives as Potential Anticancer Agents

Aymen Al-Sammarra'e[1] (iD), **Manal M. Al-Najdawi[1]*** (iD),
Maysaa M. Saleh[1] (iD), **Yusuf M. Al-Hiari[2]** (iD), **and Rabab Al-Bashiti[3]** (iD)

[1]Isra University, Department of Applied Pharmaceutical Sciences and Clinical Pharmacy, Amman 11622, Jordan.
[2]University of Jordan, Department of Pharmaceutical Sciences, Amman 11942, Jordan.
[3]University of Jordan, Department of Chemistry, Amman 11942, Jordan.

Abstract: Topoisomerase II (Top-II) is an essential therapeutic target in cancer treatment owing to its overexpression in a wide variety of cancerous cells, including colorectal and breast cancer. Significant efforts have been made to discover and develop competitive inhibitors of the Top-II enzyme as potential anticancer agents. Herein, molecular modeling was employed to identify a new series of furyl-2-carboxamide derivatives as potential anticancer agents. Compounds **3**, **5**, and **7** were synthesized and characterized with the aid of several spectroscopic techniques, such as FT-IR, NMR, and mass spectroscopy, as well as elemental analysis. The anticancer activity properties of compounds **3**, **5**, and **7** were evaluated *in vitro* using an MTT assay in a human colorectal HCT-116 cell line with different concentration dilutions. The results indicate that the anthraquinone compound **3** is 1.3-1.6 times more potent against human colon cancer HCT-116 cells than the pyridine and benzophenone compounds **7** and **5**, respectively, which reveals the importance of the anthraquinone moiety in exerting the inhibitory activity of the compound. Our findings recommend that further optimization of this series would benefit colon cancer treatment.

*Corresponding author. E-mail: manal.najdawi@iu.edu.jo.

INTRODUCTION

In developing countries, cancer is a multifaceted illness leading cause of death. Cancer kills one in every eight people worldwide, making it the second most common cause of death in the United States and Europe, behind only heart disease (1). According to estimates, 15 million new cancer patients will be diagnosed each year by 2020 (2). Surgeons created new cancer treatment methods in the last decades of the twentieth century by combining both surgeries, chemotherapy and/or radiation. In the last years, the use of multiple chemotherapy medications has resulted in the successful and effective treatment of various cancers. Anticancer drug resistance is a complicated process that occurs as drug targets shift and new chemotherapy agents have progressed rapidly and effectively (3). The essential pharmacophore of heterocyclic plays a role in the production of pharmacologically active chemical structures. Sulfur, nitrogen, and oxygen-containing in heterocyclic nuclei as therapeutic agents are an essential part of the processing of drug discovery, investigation, and development (6). Some of the synthesized compounds with the heterocyclic group showed a significant cytotoxic activity as compared to a reference control (7). For that reason, there is a growing need to identify suitable druggable

macromolecules that can be targeted selectively by antitumor agents in cancer cells. In an effort to find unique targets for anticancer agents, the Top II inhibitors have been demonstrated as plausible ones, which have been proved to play a crucial role in the pathology of cancer.

In this work, we tailored the backbone of 2-furoyl chloride to probe the effect of introducing benzophenone, anthraquinone, and pyridine on the accommodating Top-II binding pocket. The prospective derivatives were synthesized to investigate their structure-activity relationship (SAR) and improve their inhibitory activity as anticancer compounds.

MATERIALS AND METHODS

General synthetic procedure
Three novel derivatives of *2-furan-carboxamide N-(9,10-dioxo-9,10-dihydroanthracen-2-yl), N-(2-Benzoylphenyl), and N-(pyridine-2-yl)* were synthesized by fusion at high temperature, in which 2-furoyl chloride **1** was thoroughly mixed with 2-aminoanthraquinone **2**, 2-aminobenzophenone **4** and 2-aminopyridine **6** derivatives, respectively, and refluxed at 120 °C for 18 h. Then 1,4-dioxane was added, and the mixture was stirred for an additional 24 h at room temperature (8). The resulting products were filtered and recrystallized from chloroform/methanol to give the desired compounds **3**, **5**, and **7** (Scheme 1). ^{1}H NMR, ^{13}C NMR, IR, and MS analysis were used to confirm the structures of the target compounds.

Analytical procedures
Apparatus SMP10 (Stone, Staffordshire, UK). ^{1}H NMR and ^{13}C NMR spectra were collected on a Varian Oxford NMR300 spectrometer (Santa Clara, CA, USA). The samples were dissolved in CDCl$_3$ at a content of 0:3 – 0:7 wt-% and placed in 5-mm NMR tubes. High-resolution (HR) mass spectra were measured in the negative ion mode using the electrospray ion trap (ESI) technique by collision-induced dissociation on a Bruker Apex-4 (Tesla) instrument (Bremen, Germany). The samples were dissolved in acetonitrile, diluted in spray solution (methanol/water, 5:4.9, v/v+0.1-part formic acid), and infused using a syringe pump with a flow rate of 2 μL/min. External calibration was done using an arginine cluster in the mass range *m/z* 175 – 871.

Infrared (IR) spectra were recorded on a Shimadzu 8400F FT-IR spectrophotometer (Kyoto, Japan). The samples were dissolved in CHCl$_3$ and analyzed as thin solid films using NaCl plates or KBr discs (Merck, Darmstadt, Germany). Thin-layer chromatography (TLC) was performed on aluminum plates pre-coated with fluorescent silica gel, and the spots were visualized by UV light at 254 and/or 360 nm.

2-Furan-carboxamide N-(9,10-dioxo-9,10-dihydroanthracen-2-yl) 3
2-Furoyl chloride **1** (0.43 g, 3.45 mmol) was treated with 2-aminoanthraquinone **2** (0.40 g, 1.8 mmol) and processed as described in general procedure section. Recrystallization afforded the *title compound* (0.554 g, 97.54%) as a brown-green solid; Rf: 0.58 (chloroform : methanol, 9.8 : 0.2); m.p.: 285 °C (decomposed); ^{1}H-NMR (300 MHz, DMSO-d_6): rotamers δ = 10.66 (s, 1H, NHCO), 8.52 (br s, 1H, Ar-H, H$_3$-furan), 8.21 (d, 1H, Ar-H), 8.19-8.07, d, 8.06-7.83, m; 7.40, d, 7.35, s, 7.29-7.27, d, (8H, Ar-H); ^{13}C-NMR (DMSO-d_6) rotomers: δ = 182.80 (CO-ketone), 181.67 (CO-ketone), 156.97 (CONH), 147.2776, 146.9122 (CH-Ar), 144.7427, 134.9315 (CH-Ar), 134.6143, 134.3856, 133.5075, 128.6764, 128.5715, 127.1481, 127.0549 (CH-Ar), 125.0627 (CH-Ar), 117.3430, 116.3521, 112.8203 ppm; IR: 3497 (CONH), 2921 (C-H aromatic), 1689, 1734 (ketone), 1282 (C-O). HRMS (ESI, positive mode): *m/z* (M$^+$ + H$^+$): Found 318.07608 (C$_{19}$H$_{12}$N$_1$O$_4$) requires 317.30.
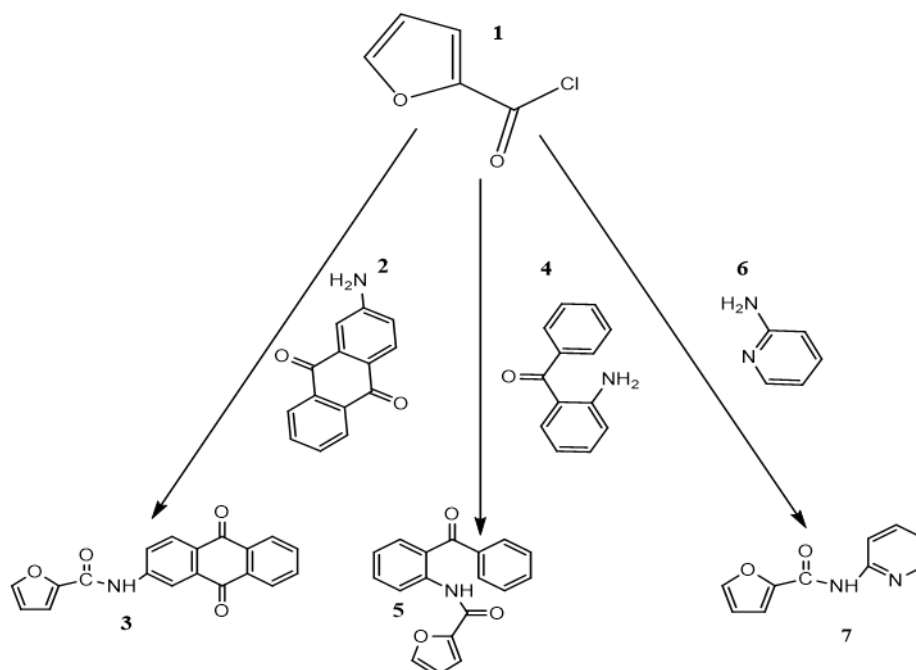
N-(2-Benzoylphenyl)-2-furan-2-carboxamide
2-Aminobenzophenone **4** (0.35 g, 1.77 mmol) and 2-furoylchloride **1** (0.43 g, 4.19 mmol) were mixed and processed as described in general procedure section. Recrystallization afforded the *title compound* (0.238 g, 46.2%) as a pale yellow solid; Rf: 0.8 (chloroform:methanol, 9.8:0.2); m.p.: 117 °C; ^{1}H-NMR (500 MHz, DMSO-d_6): δ = 10.99 (br s, 1H, NHCO), 8.0474 (br s, 1H, Ar-H-2'), 8.0312 (d,1H, Ar-H-6'), 7.6718 (s, 1H, Ar-H-5), 7.6570 (d, 2H, Ar-H-2''&6''), 7.6261 (dd,1H, Ar-H-4''), 7.6107 (d, 2H, Ar-H-3''&5''), 7.5930 (m, 1H, Ar-H-5'), 7.5753 (d, 1H, Ar-H-4'), 7.5609 (d, 1H, Ar-H-3), 7.4785 (d, 1H, Ar-H-4), 7.1539 (d, 1H, Ar-H-4), 6.6238 (d, 1H, Ar-H-4); ^{13}C-NMR (125 MHz, DMSO-d_6): δ = 197.2320 (CO-ketone), 156.4341 (CONH), 147.6107 (C-2), 146.4400 (C-5), 137.9514 (C-1'), 137.7469 (C-1''), 133.3220 (C-3'), 133.0372 (C-2'), 131.9800 (C-2''&6''), 130.1420 (C-6'), 128.7292 (C-3''&5''), 128.5554 (C-4''), 124.2936 (C-5'), 123.4369 (C-4'), 115.7523 (C-3), 112.8763 (C-4) ppm. IR: 3340 (CONH), 3086 (C-H aromatic), 1612 (ketone), 1435 (C=C aromatic); HRMS (ESI, positive mode): *m/z* (M$^+$ + H$^+$): Found 292.09682 (C$_{18}$H$_{14}$N$_1$O$_3$) requires 291.31.

N-(Pyridine-2-yl) furan-2-carboxamide 7
2-Furylchloride **1** (0.43 g, 4.19 mmol) was added to 2-aminopyridine **6** (0.42 g, 4.46 mmol) and processed as described in general procedure section. Recrystallization afforded a white brown crystal solid (0.155 g, 18.5%); Rf: 0.13 (chloroform:methanol, 9.8:0.2); m.p.: 223 °C (decomposed); ^{1}H-NMR (300 MHz, DMSO-d_6): δ = 12.0217 (br s, 1 H, NHCO), 8.4473 (d, 1H, Ar-H), 8.2207 (s, 1H, Ar-H), 8.0172 (s, 1H, Ar-H), 7.8940 (d, 1H, Ar-H), 7.4229 (m, 3H, Ar-H), 7.0094 (dd, 1H, Ar-H), 6.7292 (dd, 1H, Ar-H); ^{13}C-NMR (DMSO-d_6): rotamers δ = 157.5104

Al-Sammarra'e et al. JOTCSA. 2022; 9(3):909-918.

RESEARCH ARTICLE

(CONH), 149.5901 (CH-Ar), 148.2859 (CH-Ar), 146.0175 (CH-Ar), 144.3656 (CH-Ar), 142.2762 (CH-Ar), 120.7421 (CH-Ar), 118.4750 (CH-Ar), 116.6861 (CH-Ar), 113.0626 (CH-Ar) ppm; IR (thin film): v = 3344 (NHCO), 2950 (C-H aromatic), 1327 (C=C aromatic), 1073 (CO) cm^{-1}; HRMS (ESI, positive mode): m/z (M$^+$ + H$^+$): Found 189.06585 ($C_{10}H_9N_2O_2$) requires 188.93.

Scheme 1: Preparation of 2-furan-carboxamide N-(9,10-dioxo-9,10-dihydroanthracen-2-yl) **3**, N-(3-ben-zoylphenyl)-2-furamide **5** and N-(pyridine-2-yl) furan-2-carboxamide **7**.

Experimental Section
MTT assay was purchased from (Bioworld/USA, CN: 42000092-3), Human carcinoma HCT-116 (colorectal) cell line was sourced from the American Type Culture Collection (ATCC, USA, CN: 302007, CCL-247™) and stored in liquid nitrogen. All other chemicals (fine super grade) were purchased from Across Organics (Amman, Jordan).

MTT assay: measuring cell viability
The method has been described previously by (9) and was adapted from Mosmann (10). MTT [3-(4,5-dimethylthiazol-2-yl)-2,5-diphenyltetrazolium bromide] reagent was used to evaluate the antiproliferative activity of compounds **3**, **5**, and **7** on human cancer colorectal HCT-116 cell line. The carcinoma cells were maintained in RPMI-1640 medium supplemented with 10% (v/v) heat-inactivated fetal bovine serum (FBS), 1% L-glutamine (100X) and 1% penicillin-streptomycin (100X). The cells were seeded into 96-well plates at a density of 3×10^3 per well (180 µL per well) and allowed to adhere for 24 hrs at 37 °C/5% CO$_2$. Agent top stock solutions (10 mM in DMSO) were then freshly made. Serial dilutions were prepared in the same media as mentioned above for addition to colon cancer cells. Control wells received vehicle alone (20 µL per well). Final test agent concentrations in the wells were; 0.01, 0.05, 0.1, 0.5, 1, 5, 10, 50 and 100 µM. The final concentration of DMSO in the wells never ex-

ceeded 1%. Vehicle control assays were performed (0.0001-1% DMSO). Experimental plates were incubated for a further 72 hrs period at 37 °C/5% CO$_2$. Cell viability was recorded at the time of agent addition (T$_0$), and after 72 hrs exposure: following the addition of MTT solution (2 mg/mL in PBS: 50 µL per well), experimental plates were incubated for 3 hrs to allow reduction of MTT by viable cells to insoluble dark purple formazan crystals. The supernatant in each well was then aspirated, and cellular formazan was solubilized by the addition of DMSO (150 µL per well). Absorbance was read at a wavelength of 550 nm using a Shimadzu UV-1601 spectrophotometer plate reader. The measured intensity is proportional to metabolic activity, which correlates with viable cell numbers. Estimated GI$_{50}$ values (test agent concentrations that inhibit cell growth by 50%) were calculated using Microsoft Excel 2010 software. Results are expressed as the mean of three independent experiments (n = 8 per trial) (10).

RESULTS AND DISCUSSION

Growth inhibitory and cytotoxic effect of the synthesized furyl carboxamide derivatives
The antiproliferative activities of the furyl carboxamide derivatives **3**, **5**, and **7** plus the known anticancer drug Doxorubicin (9) were evaluated *in vitro* using MTT assay (9-10) against human carcinoma

colorectal HCT-116 cell line. Colorectal carcinoma is the third most common cancer and caused more than 935,173 deaths globally in 2020 (11). Thus, developing new therapies for such malignant diseases represents a severely unmet need.

The concentrations at which cell growth is inhibited by 50% (GI_{50}) after 72 hrs exposure of cells to furyl carboxamide derivatives **3**, **5**, **7**, and Doxorubicin were obtained from dose-response curves after considering the initial optical density acquired at the time of treatment. GI_{50} values are presented in Table 1, while Figure 1 shows the structure of Doxorubicin as a reference drug used as an antiproliferation-active compound (12).

Table 1: Growth inhibitory activity of compounds **3**, **5**, **7**, and Doxorubicin against human colorectal carcinoma HCT-116 cell line. GI_{50} values are represented as mean±standard deviation of at least three independent experiments (n = 8 per trial).

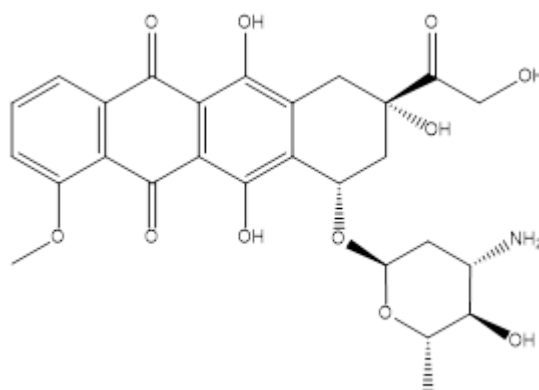| Compound	GI_{50} (µM) ± S.D.
	HCT-116 Cell Line
3	23.3 ± 1.3
5	36.6 ± 2.8
7	30.5 ± 8.4
Doxorubicin	0.190 ± 0.065

Figure 1: Structure of doxorubicin (11).

As can be deduced from the table, the three compounds **3**, **5**, and **7** show significant and almost identical cellular growth inhibitory activity against human carcinoma colon HCT-116 cell line in the examined concentration range (0.01-100 µM). The highest growth inhibitory activity against colon cancer cells is shown by compound **3**, which contains the anthraquinone core structure like Doxorubicin, with a GI_{50} value of 23.3 µM, followed by compound **7**, containing pyridine moiety, and compound **5**, containing benzophenone structure, with GI_{50} values of 30.5 µM and 36.6 µM, respectively. The results indicate that the anthraquinone compound **3** is 1.3-1.6 times more potent against human colon cancer HCT-116 cells than the pyridine and benzophenone compounds **7** and **5**, respectively.

On a direct comparison of compound **3** with Doxorubicin, it can be deduced that Doxorubicin has potent growth inhibitory (GI50 = 0.190 µM) and antitumor activity of 122-fold greater than anthraquinone compound **3** against human colon cancer HCT-116 cell line, as shown in Figures 2 and 3.
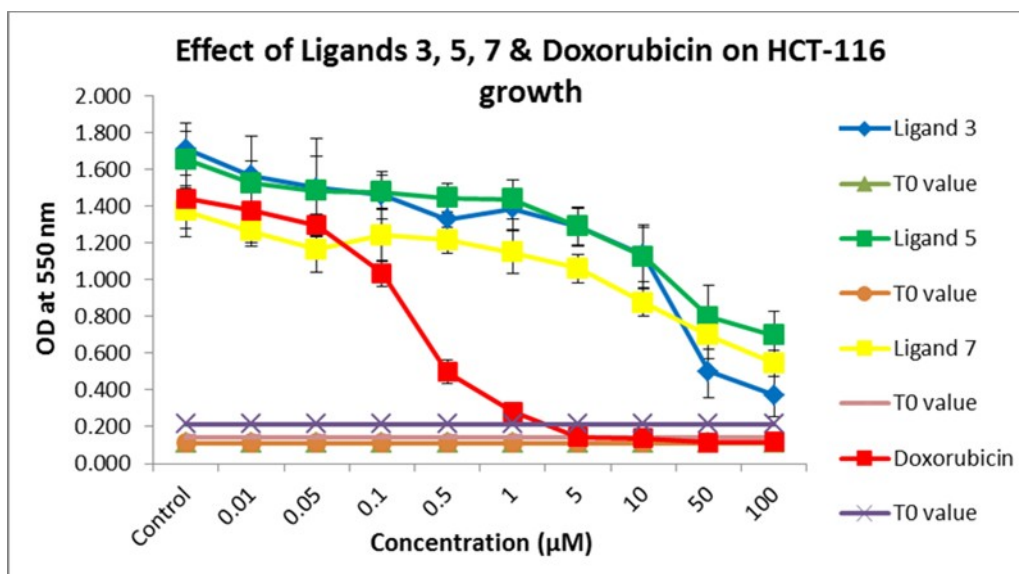
Figure 2: Dose-response curves that show the growth inhibitory effects of compounds 3, 5, 7, and Doxorubicin against human colorectal carcinoma HCT-116 cell line cell. Values are mean±SD, n = 8, graphs are representative of experiments performed on at least three separate occasions.

Figure 3: Dose-response curves that show the growth inhibitory effects of compound **3** & Doxorubicin against human colorectal carcinoma HCT-116 cell line cell. Values are mean ± SD, n = 8, graphs representative of experiments performed on at least three separate occasions.
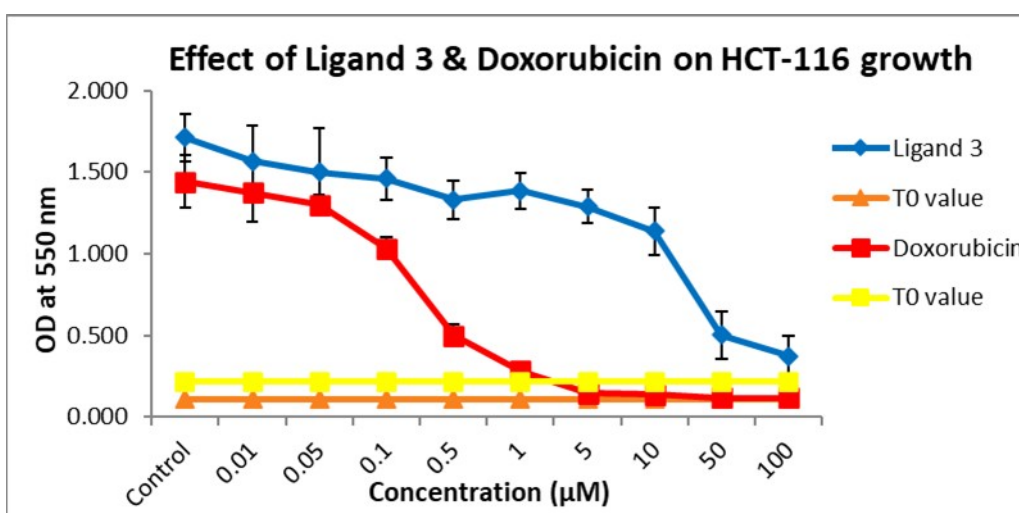
Induced-Fit Docking (IFD)

In order to investigate the anticancer activity of compounds **3**, **5**, and **7** in the HCT-116 cell line, molecular docking simulations were performed using Biovia Discovery Studio (DS) and Schrodinger (Schro) software with CDOCKER Algorithm. Both compound **3** and Doxorubicin were docked to the binding site of the topoisomerase II crystal structure (PDB ID: 6CA8) to investigate the nature of their binding interactions with topoisomerase II targeted enzyme. The x-ray diffraction structure of topoisomerase II (PDB ID: 6CA8) with a resolution of 2.33 Å was obtained from RCSB website. Figures **4**, **5**, and **6** show the nature of interactions between the

synthesized compound **3** and Doxorubicin with the binding site of the topoisomerase II enzyme.

It is clearly seen that our synthesized compound **3** is well docked inside the binding pocket of Top-II but interacts with amino acid residues different than those that Doxorubicin interacts with, except LYS A:747 residue. Compound **3** showed hydrogen bonds with ARG:737 and THR A:791 as well as π-π stacking with GLN: 790, π-alkyl bond with PRO A:748 and LYS A:747, Van der Waals interactions with HIS A783, GLY A749 and SER A:787, and π-lone pair TYR A:733. However, Doxorubicin showed hydrogen bonds with LYS A:747, GLU A:878, GLN

913

A:750, GLY A:801, LYS A:953, and GLY A:820, carbon-hydrogen bond with ASN A:890, and π-alkyl bond PHE A:799.

From Figures 4 and 5, we realize that the compound inhibition mechanisms follow in both hydrophobic and hydrogen bonding interactions with the enzyme understudy. Also, the strength of the inhibitor's interaction with Top-II is a reflection to the frequency of hydrogen bonds exist between the inhibitor and binding pocket. In addition, from Figure 6, it is obviously seen that the binding pocket of Doxorubicin is different from that of compound **3**, which implicates the strength of binding interaction of both compounds. The docking score is a negative value that describes the tightness (binding affinity) of the drug-target interactions and is reported as the free energy of binding in kcal/mol.

The results showed a correlation between the docking score (-33.416 kcal/mol) of compound **3** with the number of hydrogen bond, hydrophobic, and π-π stacking interactions present in the compounds under study. However, the docking score of Doxorubicin was (-150.329 kcal/mol), which corresponds to the number of hydrogen bond, hydrophobic and π-π stacking interactions.

The comparison between the growth inhibitory activities (GI$_{50}$ values) of compounds **3** and **5** revealed that the fixation of the 2-phenyl ring is more favorable. Many furan-like compounds with various structures have been studied previously for their cytotoxic activities. However, our present understanding of the relationships between their chemical structures and anticancer properties is still very limited. The structural modifications of the furyl-2-carboxamide derivatives primarily focused on the alteration of the lipophilic part along with their substituents and conformational restriction of the biphenyl ring to give rigid cyclic analogs.

DISCUSSION

Furan carboxamides were chosen in this work since they are novel and provide reasonable antioxidant activity as their counterpart analog as indole carboxamide (14). In addition, furan and other privileged structure such as pyridazine, pyridazine as a privileged structure (15), quinoline (16), pyran (17), and other heterocyclic structures have been investigated as the scaffold and a core for potential anticancer agents. Therefore, it is important to keep searching for a potent anticancer agent with remarkable selectivity and lower toxicity. Therefore, we chose to evaluate the furan scaffold as an anticancer. Many procedures have been performed to synthesize the proposed compounds, but the fusion method showed superior yield, which was adopted for the three compounds, as shown in Scheme 1.

From the results in Table 1, it was found that compound **3** showed moderate antitumor activity comparable to that of Doxorubicin. Anthraquinone derivative exhibited better anticancer activity than benzophenone and pyridine derivatives which supports a previous study (14) where this compound showed encouraging antioxidant activity using DPPH *in vitro* test, which could explain its effect as a potential anticancer agent. On the other hand, its structure may be considered as conformationally constrained congeners of Doxorubicin that would bind to the receptor similarly, which implicates its activity to inhibit cancer cell growth via multiple mechanisms, including DNA cross-linking by disrupting topoisomerase II and free radical generation damaging the cell membrane, proteins, and DNA.
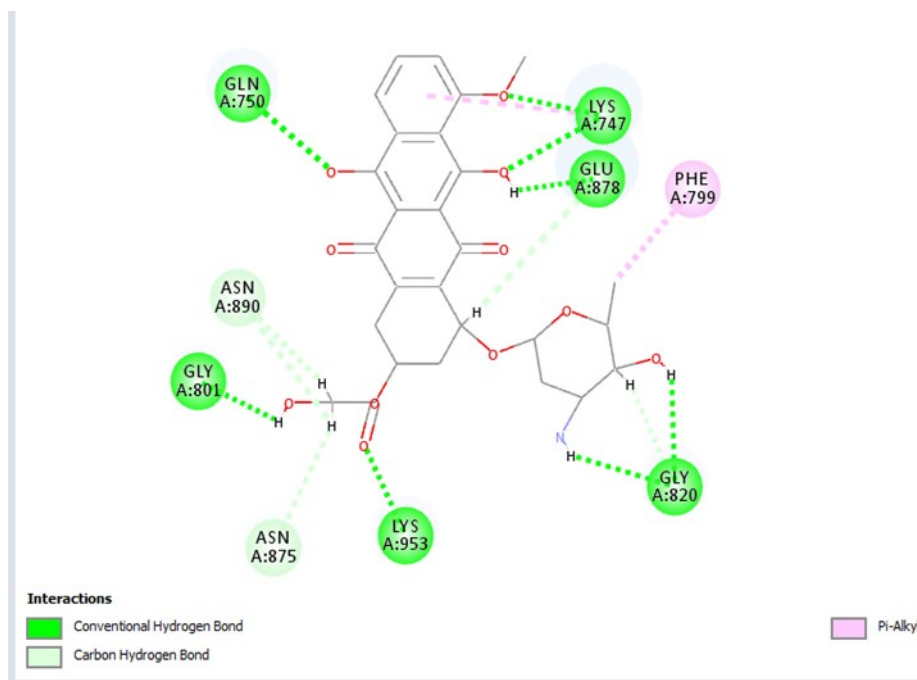
Figure 4: 2D interaction of compound **3** with the binding site of topoisomerase II.
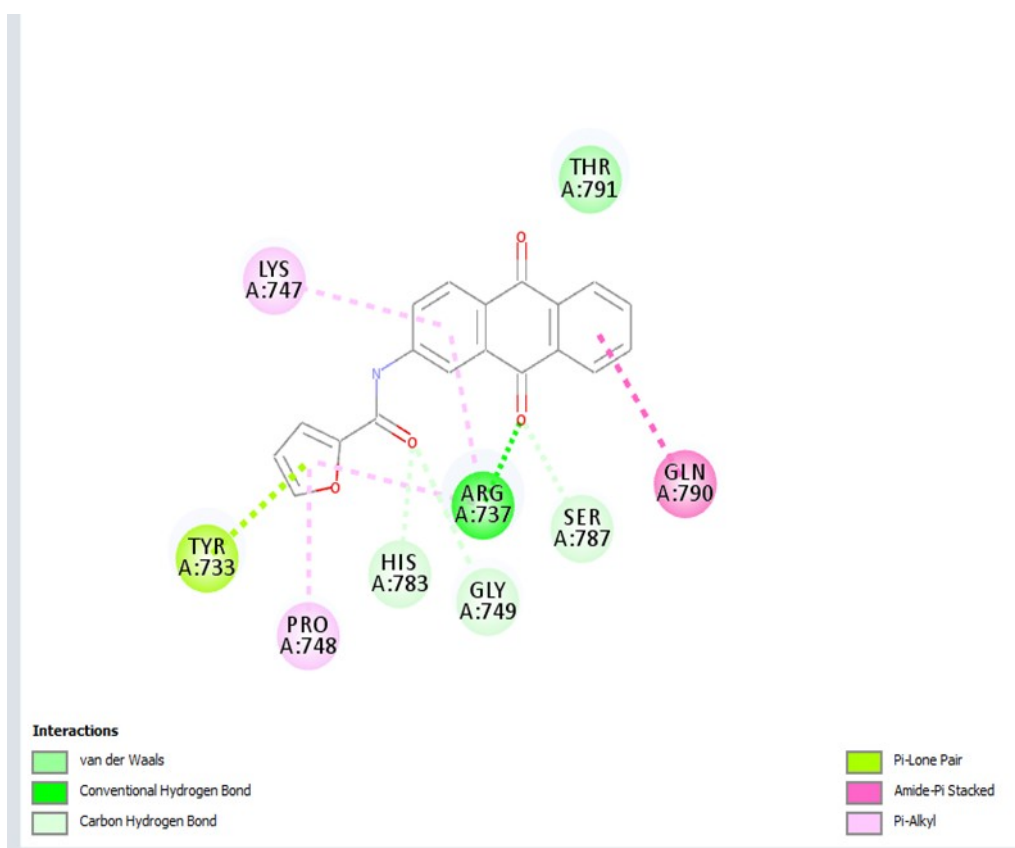

Figure 5: 2D interaction of Doxorubicin with the binding site of topoisomerase II.
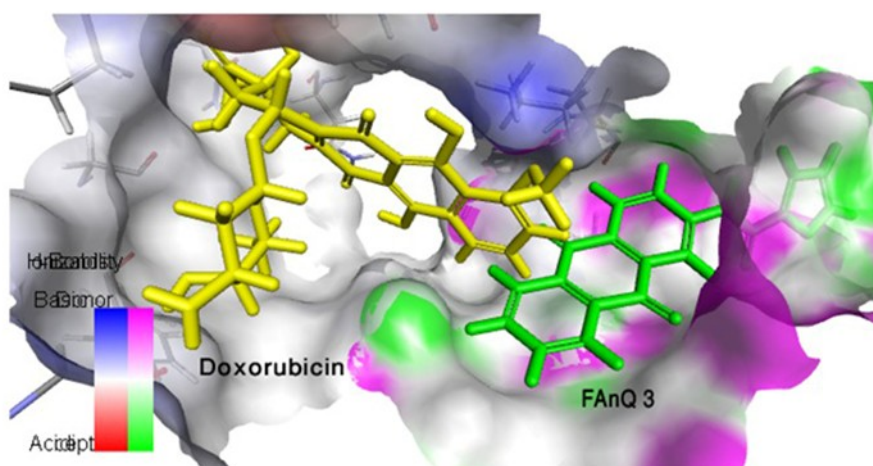
Figure 6: 3D interactions of Doxorubicin and compound **3** with the topoisomerase II enzyme binding site.

CONCLUSION

In this work, we provided a series of new 2-furyl carboxamide derivatives **3**, **5**, and **7** as cytotoxic agents against human colorectal cancer cells and found that compound **3** showed the best antiproliferative activities towards the HCT116 cell line. Compound **3** had a rigid shape structure like Doxorubicin which would affect the binding affinity to the receptor. Furthermore, the prediction results of the physicochemical properties of compound **3** demonstrated that it might be an essential scaffold for future structural design in developing highly efficient antiproliferative agents.

REFERENCES

1. Kumar S, Narasimhan B. Therapeutic potential of heterocyclic pyrimidine scaffolds. Chemistry Central Journal [Internet]. 2018 Dec [cited 2022 Jul 19];12(1):38. Available from: <URL>.

2. WHO. Cancer [Internet]. Cancer. 2022 [cited 2022 Jul 19]. Available from: <URL>.

3. Sweidan K, Sabbah DA, Bardaweel S, Dush KA, Sheikha GA, Mubarak MS. Computer-aided design, synthesis, and biological evaluation of new indole-2-carboxamide derivatives as PI3Kα/EGFR inhibitors. Bioorganic & Medicinal Chemistry Letters [Internet]. 2016 Jun [cited 2022 Jul 19];26(11):2685–90. Available from: <URL>.

4. Sayed M, Kamal El-Dean AM, Ahmed M, Hassanien R. Synthesis of some heterocyclic compounds derived from indole as antimicrobial agents. Synthetic Communications [Internet]. 2018 Feb 16 [cited 2022 Jul 19];48(4):413–21. Available from: <URL>.

5. Irfan A, Batool F, Zahra Naqvi SA, Islam A, Osman SM, Nocentini A, et al. Benzothiazole derivatives as anticancer agents. Journal of Enzyme Inhibition and Medicinal Chemistry [Internet]. 2020 Jan 1 [cited 2022 Jul 19];35(1):265–79. Available from: <URL>.

6. Ohba M, Oka T, Ando T, Arahata S, Ikegaya A, Takagi H, et al. Discovery and Synthesis of Heterocyclic Carboxamide Derivatives as Potent Anti-norovirus Agents. Chem Pharm Bull [Internet]. 2016 [cited 2022 Jul 19];64(5):465–75. Available from: <URL>.

7. Kassem AF, Nassar IF, Abdel-Aal MT, Awad HM, El-Sayed WA. Synthesis and Anticancer Activity of New ((Furan-2-yl)-1,3,4-thiadiazolyl)-1,3,4-oxadiazole Acyclic Sugar Derivatives. Chem Pharm Bull [Internet]. 2019 Aug 1 [cited 2022 Jul 19];67(8):888–95. Available from: <URL>.

8. Al-Najdawi M, Hiari Y, Qirim T, Shattat G, Al-Zweri M, Sheikha GA. Synthesis and Pharmacological Evaluation of Novel Unsubstituted Indole-Anthraquinone Carboxamide Derivatives as Potent Antihyperlipidemic Agents. Zeitschrift für Naturforschung C [Internet]. 2014 Feb 1 [cited 2022 Jul 19];69(1–2):21–8. Available from: <URL>.

9. Saleh MM. Development of a New Series of Bis-triazoles as Antitumour Agents [PhD thesis]. [UK]: University of Nottingham; 2014.

10. Mosmann T. Rapid colorimetric assay for cellular growth and survival: Application to proliferation and cytotoxicity assays. Journal of Immunological Methods [Internet]. 1983 Dec [cited 2022 Jul 19];65(1–2):55–63. Available from: <URL>.

11. Saleh MM, Laughton CA, Bradshaw TD, Moody CJ. Development of a series of bis-triazoles as G-quadruplex ligands. RSC Adv [Internet]. 2017 [cited 2022 Jul 19];7(75):47297–308. Available from: <URL>.

12. Martin M, Ramos-Medina R, Bernat R, García-Saenz JA, del Monte-Millan M, Alvarez E, et al. Activity of docetaxel, carboplatin, and doxorubicin in patient-derived triple-negative breast cancer xenografts. Sci Rep [Internet]. 2021 Dec [cited 2022 Jul 19];11(1):7064. Available from: <URL>.

13. IARC. Cancer Today [Internet]. Cancer Today. 2020. Available from: <URL>.

14. Najdawi M. The synthesis of novel heterocyclic carboxamide derivatives and evaluation of their antihyperlipidemic and antioxidant activity [Internet] [PhD Thesis]. [Amman, Jordan]: Jordan university/ department of pharmacy; 2011. Available from: <URL>.

15. He ZX, Gong YP, Zhang X, Ma LY, Zhao W. Pyridazine as a privileged structure: An updated review on anticancer activity of pyridazine containing bioactive molecules. European Journal of Medicinal Chemistry [Internet]. 2021 Jan [cited 2022 Jul 19];209:112946. Available from: <URL>.

16. Musiol R. An overview of quinoline as a privileged scaffold in cancer drug discovery. Expert Opinion on Drug Discovery [Internet]. 2017 Jun 3 [cited 2022 Jul 19];12(6):583–97. Available from: <URL>.

17. Kumar D, Sharma P, Singh H, Nepali K, Gupta GK, Jain SK, et al. The value of pyrans as anticancer scaffolds in medicinal chemistry. RSC Adv [Internet]. 2017 [cited 2022 Jul 19];7(59):36977–99. Available from: <URL>.

RESEARCH ARTICLE

Isotherm and Thermodynamic Studies on the Removal of Gelatin-Stabilized Silver Nanoparticles from Water by Activated Carbon

Aysenur Ceryan[1] iD **, Nurettin Eltugral[2*]** iD

[1]Bolu Abant Izzet Baysal University, Department of Property Protection and Security, Bolu, 14030, Turkey
[2]Karabük University, Department of Medical Engineering, Karabük, 78050, Turkey.

Abstract: Gelatin-stabilized silver nanoparticles (AgNPs) with a particle size of 6.9 (±3.2) nm were synthesized and employed in nanoparticle adsorption onto activated carbon (AC). Subsequently, the synthesized AgNPs and the adsorbed nanoparticles onto the AC (AgNP@AC) were characterized by various techniques including UV–Vis spectrophotometry, transmission electron microscopy (TEM), scanning electron microscopy (SEM), Fourier transform infrared spectroscopy (FT–IR) and X–ray diffraction (XRD). AgNPs possessed colloidal stability at a wide pH interval ranging between 4 and 13. Adsorption was studied batch-wise as a function of initial nanoparticle concentration (4–14 mg L^{-1}), temperature (298–323 K), pH (4–13) and adsorbent dosage (0.01–0.05 g). Adsorption isotherms were investigated by fitting the data to different isotherm models including Langmuir, Freundlich, Temkin, and Dubinin–Radushkevich (D–R). Error analysis indicated that the adsorption is well described by the Langmuir model with a monolayer adsorption capacity of 10.36 mg g^{-1} for 0.05 g AC at pH 7 and 323 K. Thermodynamic parameters such as enthalpy (66.77 kJ mol^{-1}), entropy (232.92 J mol^{-1} K^{-1}), and Gibbs free energy (–8.31 kJ mol^{-1}) indicated that the process is endothermic, favorable and spontaneous through physical interactions.

INTRODUCTION

Silver nanoparticles (AgNPs) have been a focus research field by scientists from different disciplines due to their unique properties which has opened new capabilities in a wide range of applications (1). Silver nanoparticles (AgNPs) have already been utilized in many fields including medical equipments, textile industry, water treatment, ventilation and air conditioning systems, cosmetics, and sport equipments as they possess high antibacterial activity (2,3).

Nano-silver can be prepared according to a common method which involves wet chemical synthesis where a silver salt precursor is reduced in the presence of a stabilizer (3). The most commonly considered agents for reducing silver salt are sodium borohydride (NaBH$_4$) (4), citrate (5), ascorbic acid (6), dimethylformamide (DMF) (7,8), and oleylamine (9).

Colloidal instability of AgNPs against aggregation has been encountered as a common problem for many applications. This problem may end up with the formation of large aggregates which causes the blockage of the active surface area, thus limiting the unique antibacterial and catalytic properties (3). Therefore, to avoid this problem and improve colloidal stability as well as the availability of AgNPs for further applications, their surface is needed to be protected. For this purpose, there are many types of chemicals such as surface-active agents which are also called surfactants (10,11), synthetic polymers,

i.e. polyvinyl pyrrolidone (PVP) (12), polyvinyl alcohol (PVA) (13), polyethylene glycol (PEG) (14), polymethyl methacrylate (PMMA) (15), and dendrimers (16). Additionally, natural polymers such as chitosan (17,18), polysaccharides, and gelatin are potentially preferred for the stabilization of AgNPs (19–22). These ligands prevent nanoparticles from being aggregated in the surrounding atmosphere and are also heavily important in determining the particle size and shape in colloidal systems (23,24).

Activated carbons (ACs) have a relatively porous structure and large surface area, which can act as a host structure, as well as they consist of amines, phenols, nitrobenzene, and other types of cationic functional groups on its surface. The adsorption capacity of ACs can be estimated based on these chemical functionalities. The incorporation of silver nanoparticles onto ACs has gained a greater choice of interest for use as the host material in wastewater treatment, air purification, and removal of organic and inorganic contaminants (25,26).

In a previous report, adsorption of AgNPs modified by using different types of ligands onto AC was studied to investigate the ligand type on the adsorption performance (27). Since ligands are surrounding the active metal surface, they play an important role in nanoparticle interaction with the outside world. Gelatin is an excellent coating material to produce nanoparticles that show high endurance and stability in a wide range of pH. Since gelatin-stabilized nanoparticles could can a long-term aggregation resistance in aqueous media including natural aquatic ecosystems, their removal from wastewaters might be challenging and this appears to be a scientific concern. Therefore, in this study, it is aimed to investigate the adsorption of gelatin-stabilized AgNPs onto AC. In that regard, gelatin-stabilized AgNPs were synthesized and employed in nanoparticle adsorption onto AC. Batchwise adsorption studies were conducted between AgNPs and the AC as a function of initial nanoparticle concentration (4–14 mg L^{-1}), temperature (298–323 K), pH (4–13), and adsorbent dosage (0.01–0.05 g). Adsorption isotherms were investigated by fitting the data to different isotherm models including Langmuir, Freundlich, Temkin, and Dubinin–Radushkevich (D–R). The resulting nano–silver–AC product (AgNPs@AC) was characterized by several techniques including UV–vis, TEM, SEM, XRD, and FTIR.

EXPERIMENTAL SECTION

Materials and methods
Silver nitrate (AgNO₃, 99.0%), sodium borohydride (NaBH₄, 98.0%), ammonia (NH₃, 25–30%), sodium carbonate (Na₂CO₃), and gelatin were purchased from Sigma-Aldrich. NaOH, HCl (37%), NaHCO₃, phenolphthalein, and methyl orange were purchased from Merck. AC was purchased from Nanografi. All reagents were of analytical grade and used as

received. Ultrapure water was used for the preparation of all samples during the experiments.

The pH of the samples was adjusted using a Mettler Toledo model pH meter by adding either 0.1 M HCl or NaOH. The prepared AgNPs colloids were checked for their optical properties and long-term stability by collecting absorbance spectra on a double beam UV–vis spectrophotometer (Agilent Cary 60 UV–vis Spectrophotometer). All the spectra were recorded between 700 and 300 nm. The crystal structure of the prepared samples were analyzed through the X–ray diffraction (XRD by Rigaku). Morphology of the synthesized nanoparticles was studied using a transmission electron microscope (TEM by Jeol 2100F RTEM 200 kV). Structural and morphological properties of AgNPs@AC was investigated through a SEM device (by Carl Zeiss Ultra Plus Gemini FESEM at accelerating voltage in the range of 5–10 kV, equipped with an energy-dispersive X–ray (EDX) spectrometer). Identification of organic groups were performed on a FTIR spectrometer (FTIR by Bruker Alpha Platinum FTIR–ATR spectrometer equipped with a single reflection diamond ATR accessory). X-ray and FT–IR analysis of the AgNPs were done on the solid powder form of the product by evaporating its water content.

Synthesis of Silver Nanoparticles
Silver nanoparticles were synthesized according to the Tollens' method (28). Accordingly, aqueous solutions of AgNO₃ (20 mL, 2.5×10^{-3} M), NH₃ (20 mL, 1.25×10^{-2} M), and NaOH (10 mL, 5×10^{-2} M) were mixed thoroughly under constant stirring to obtain $[Ag(NH_3)_2]^+$ complex under basic conditions. Then, 2.5 %(w/w) 1.25 gr of gelatin was added and finally, a freshly prepared aqueous solution of NaBH₄ (5 mL, 0.1 M) was added dropwise yielding a yellow-brownish color of solution which indicated the AgNPs formation. The resulting mixture was further stirred for 20 min at ambient temperature and kept dark throughout the experiments. The pH of the prepared stock nanoparticle solution was measured to be 11.5. Nanoparticle molar concentration was expressed in terms of silver content and it was 9.1×10^{-4} M (98 mg L^{-1}) for the stock nanoparticle solution. A representative absorbance spectrum of a diluted nanoparticle solution (1.8×10^{-4} M) was given in Figure 1(a).

Identification of surface groups of the AC
Bohem titration method (29) was employed for characterizing the surface functional groups and the acidity of the AC as described in our previous work (27). In this regard, 0.1 g of the AC was mixed with NaOH, NaHCO₃, and Na₂CO₃ (each, 50 mL, 0.1 N), respectively, and agitated for 36 h at room temperature. Then, carbon was filtered off and 10 mL of each supernatant was titrated with 0.1 N HCl in the presence of phenolphthalein and methyl orange indicators. Thus, acidic groups on the AC was calculated. NaOH neutralizes carboxylic, lactonic, and phenolic groups, Na₂CO₃ neutralizes carboxylic and lactonic groups, and NaHCO₃ neutralizes

carboxylic groups present on the AC. Similarly, 1 g of the AC was mixed with 0.1 N HCl (50 mL, 0.1 N) and agitated for 36 h at room temperature to determine total basicity. Then, 10 mL of the supernatant was titrated against 0.1N NaOH to calculate the number of basic groups.

Adsorption Studies

In the present study, 10-mL solutions of AgNPs, each having a concentration and a pH in the range of 3–15 mg L^{-1}, and 4–12, respectively were prepared by diluting the stock AgNPs to the proper concentration and changing the pH (4, 7, 10 and 12) with 0.1 M HCl or NaOH. To each of the prepared nanoparticle solution, 0.05 g of AC was added and agitated at room temperature for 24 h of equilibrium contact time at a low rpm. After that, the supernatant was first filtered off through a filtering paper (M&Nagel–125 mm) followed by a syringe filter (0.45 µm pore size). The supernatant liquids were checked for their nanoparticle content by collecting absorbance spectra at a wavelength of 415 nm. The same procedure was employed to study the effect of temperature and adsorbent dosage.

The nanoparticle concentrations (in silver content) were determined by plotting a calibration curve by recording the absorbance for diluted nanoparticles samples of known concentrations having absorbance in the range of 0.1–0.5 at a wavelength of 415 nm. The adsorbed nanoparticle concentration (q_e, mg g^{-1}) on the AC was calculated using the following equation;

$$q_e = \frac{(C_o - C_e)V}{m} \qquad (1)$$

Where C_o is the initial concentration of AgNPs, C_e (mg L^{-1}) is the equilibrium concentration of the nanoparticles in the aqueous phase, V (L) is the volume of the solution, m (g) is the mass of AC@AgNPs, and q_e (mg g^{-1}) is the calculated amount of nanoparticle concentration adsorbed onto the AC. Additionally, the percent adsorbed amount *(%R)* was obtained by the equation:

$$\%R = \frac{(C_o - C_e)}{C_o} \, x \, 100 \qquad (2)$$

RESULTS AND DISCUSSION

Characterization of silver nanoparticles

Silver nanoparticles were synthesized according to the Tollens' process (28). This process is based on the reduction of silver complex, [Ag(NH$_3$)$_2$]$^+$ in alkaline media using suitable reducing agents. In our study, sodium borohydride (NaBH$_4$) was used as a reducing agent. NaBH$_4$ is one of the most powerful reducing agents used in nanoparticle synthesis. For example, its reduction of power is large enough to reduce iron salts to iron nanoparticles (30). Gelatin, a natural polymer, was used as a stabilizer to protect the highly active metal surface at the nanoscale.

Figure 1(a) shows the UV–vis absorption spectra obtained after diluting the stock nanoparticle solution. AgNPs exhibits a narrow absorbance band at 415 nm as a result of surface plasmon resonance (31). Silver nanoparticles of spherical shape have a characteristic absorbance band 410 and 430 nm with an average particle size of 6 and 30 nm, respectively (3,32). A representative TEM image of nanoparticles is shown in Figure 1(b). The average particle size calculated from TEM results is 6.9 (±3.2) nm. Our findings from TEM analysis were in good agreement with UV analysis.
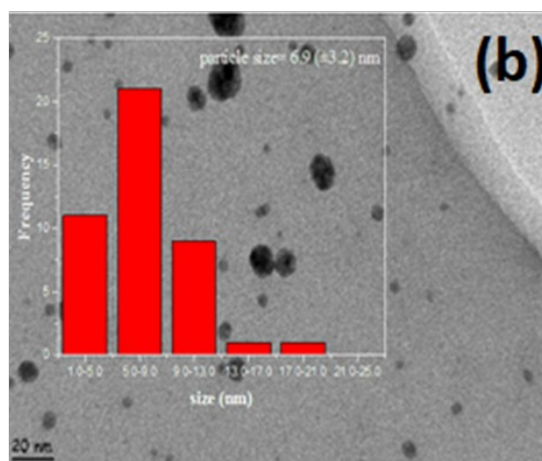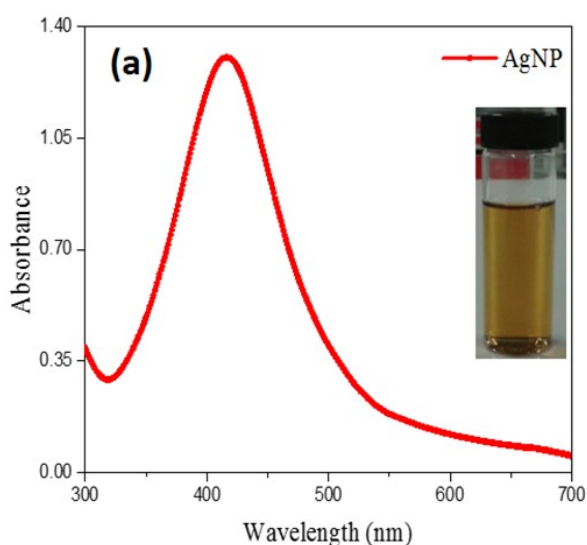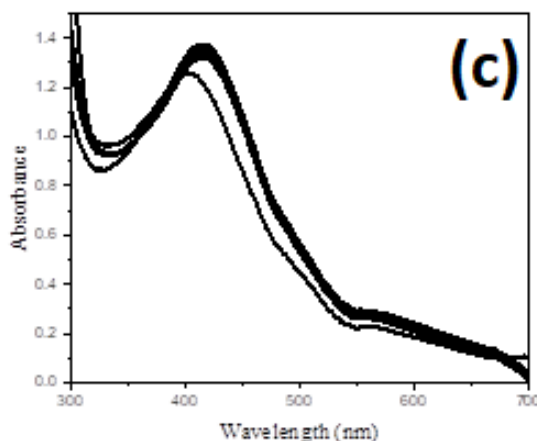
Figure 1: (a) UV–vis spectrum of gelatin-stabilized AgNPs (1.8×10^{-4} M); inset is a photo of nanoparticle solution, (b) TEM and size distribution histogram of the synthesized nanoparticles and (c) AgNP UV–vis spectra at different pH values.

Spectrophotometric investigations show that AgNPs are stable over months as reported previously (33). The extinction coefficient of 7171.9 M^{-1} cm^{-1} at the wavelength of 415 nm was obtained as the slopes of absorbance vs concentration plots (see supplementary information, Figure S1((a) and (b)). As it can be understood from the linearity of the plot and the correlation coefficient value≈1, it shows that the absorbance values of different concentrations of AgNP at 415 nm give good correlations with the Lambert–Beer law (34,35).

The influence of gelation on the colloidal stability of the AgNPs was investigated against the pH. For this purpose, the pH of diluted AgNPs solutions was adjusted to different pH values (2, 5, 7, 9, 11, and 13) by adding either 0.1 M HCl or 0.1 M NaOH. Then absorbance spectra of the resulting samples were recorded. Figure 1(c) shows that AgNPs exhibits similar absorbance spectra over a wide range of pH except pH 2.

Nitrogen atoms of the amine groups in gelatin covalently interact with the metal surface and attach themselves to the metal core thus stabilizing the nanoparticle. Gelatin can have different charges at different pH values owing to the carboxylic and amine groups in its structure. In the acidic media, amine groups are positively charged while carboxyl groups remain the same. At high pH values, carboxyl groups lose the hydrogen and become negatively charged while amine groups remain the same. Since the carboxyl groups of gelatin become negatively charged, the nanoparticle surface gains a negative charge as well, thus preventing the particles from interacting with each other by electrostatic repulsion. However, at low pH values, amine groups that interact with the metal in the acidic environment become positively charged. Although, the covalent interaction between the nitrogen atom and the metal surface is impaired, this time it is expected that gelatin surrounds and stabilizes the metal core as a result of the electrostatic interaction between the positively charged amino groups and metal's surface electrons. A proposed model for gelatin-stabilized AgNPs under acidic or alkali media is shown in Fig. 2.

When the carboxyl groups do not carry a net charge, there will be no electrostatic repulsion between the particles, which can cause the particles to interact with each other and collapse in the solution by forming aggregates. The sudden change in the absorbance profile of AgNPs at pH 2 is attributed to the aforementioned effect, inconsistent with the result in the literature (3).
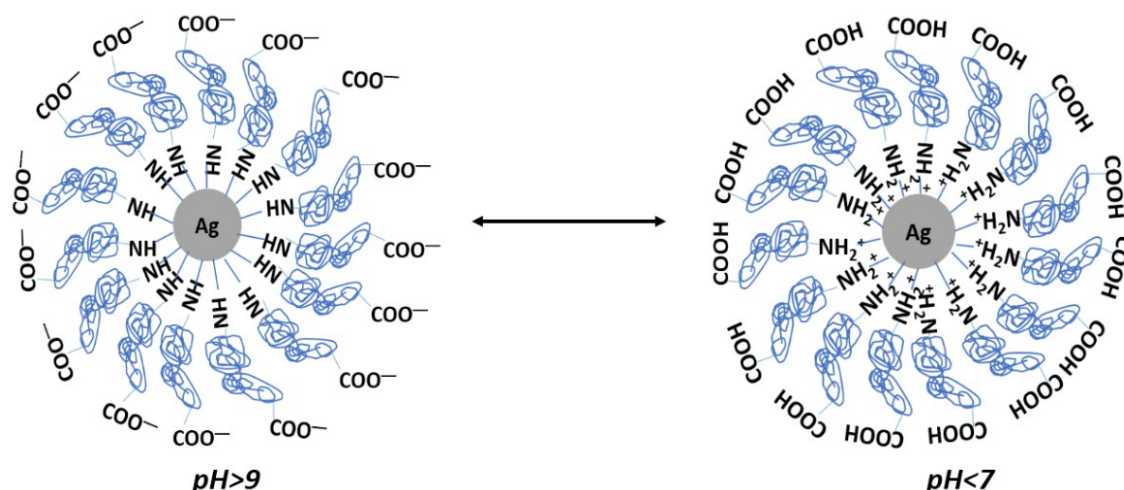
Figure 2: A schematic model for gelatin-stabilized AgNPs under acidic and basic media.

Gelatin is an amphiphilic molecule and the isoelectric point for gelatin is approximately 8.5 (between 7–9) (36). This means that the negative and positive charges on the molecule are in balance between the pH of 7 and 9. The presence of negative charges on the surface ensures that the nanoparticles are colloidally stable against aggregation and precipitation. Colloidal stability lasts as long as there exists a negative charge on the particle surface over a pH range.

Characterization of AgNPs@AC
Figure 4 shows an SEM image of AgNPs adsorbed onto the surface of AC. The SEM image shows that AgNPs are deposited on the entire surface of the AC with sizes range between 50–140 nm. The nanoparticle surface is coated with gelatin which mainly regulates the interaction between the nanoparticle and adsorbent (32). Therefore, it is claimed that gelatin functional groups can interact with the surface functional groups of AC during the formation of AgNPs@AC.
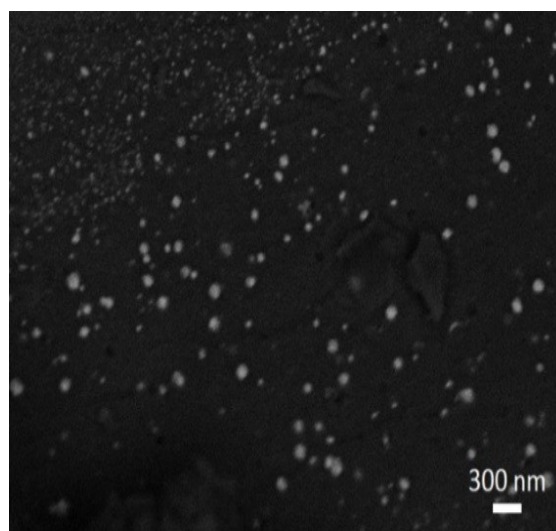
Figure 3: SEM image of AgNP@AC.

The functional groups of the sole AgNPs and AgNPs@AC were examined using FTIR spectra (see Figure S2). First of all, when the IR spectrum of gelatin is examined, the peak between 3400–3200 cm^{-1} is assigned to the peptide bond by N–H stretching, whereas, the peak around 3100–2800 cm^{-1} corresponds to C–H stretching. The peak 1660–1600 cm^{-1} is assigned to the stretching of C=O

attached to peptide unit. Two peaks around 1565–1500 cm^{-1} and 1450–1300 cm^{-1} can be attributed to C–N–H and C–H bending of the amino group of gelatin. (37). AgNPs possess a similar FTIR spectrum to that of gelatin except for peak intensities, and the band between 3400–3200 cm^{-1} is observed to broaden. We attribute the observed broadening to be the consequence of the interaction of peptide

amine groups with the active metal surface. Besides, FTIR of AgNPs does not display a new peak other than that of gelatin which indicates no chemical bonding occurs between gelatin and silver atoms (38).

For the functional groups of AC, a broad peak positioned between 2500–3000 cm^{-1} indicates the stretching vibrations of the –OH on the carboxyl group while the peak centered at 1500–1330 cm^{-1} is designated to C=C stretching of aromatic rings. The peak at 1000–1180 cm^{-1} could be attributed to C–O stretching.

When AgNPs were doped on the AC, nanoparticles could be traced in the FTIR spectrum by observing the N–H band of the gelatin stabilized–AgNPs that appeared between 1500–2000 cm^{-1}. The intensity of the FTIR peaks of the AgNPs seemed to decrease. These findings indicate that AgNP was successfully adsorbed to the AC surface.

The XRD patterns of AgNP, AC and AgNP@AC are shown in Figure S3. XRD pattern of AgNP shows major characteristic peaks with 2θ values 37.3º, 43.5º, 64.8º, and 77.3º which are assigned to (111),

(200), (220), and (311) lattice planes of the face-centered cubic structure of metallic Ag (39–41). The broad and reduced intensity of peaks that the diffractograms displayed are due to smaller particle size and high concentration of the gelation layer at the surface of the metallic core (42). AC has a broad XRD pattern without any sharp and intense peaks since it is an amorphous structure (43,44). AgNP@AC yielded almost the same XRD pattern as that of AgNPs which means that there is no significant change in AgNPs (44,45).

Table 1 summarizes the amount of functional surface groups of AC using the Boehm titration method. The obtained data show that AC has both basic and acidic properties (46). Acidic groups such as phenol and carboxyl are not expected to release their acidic protons under acidic pH values. However, basic surface groups such as amine, chromene, and pyrene are protonated and the carbon surface can have a positive charge. A negative charge on the carbon surface may refer to the decomposition of acidic regions such as carboxyl and phenol, which release their protons under basic pH conditions (47).

Table 1: Amount of groups on the surface of activated carbon.

Surface Groups (meq g^{-1})					
Sample	Carboxylic	Lactonic	Phenolic	Acidic	Basic
Activated carbon	0.400	0.550	2.150	3.100	0.300

Effect of AgNP initial concentration and temperature

The effect of initial AgNP concentration and temperature on the efficiency of its adsorption onto 0.05 g AC was investigated by varying the initial concentration at 298, 308, and 323 K, and the results are shown in Figure 8. The percentage amount of AgNP adsorbed on the AC was observed to decrease with increasing nanoparticle concentration (Figure 4(a)). When the amount of AC is fixed, the decrease in the adsorption percentage is probably due to the saturation of the active binding sites on the AC surface at higher AgNP

concentrations. However, the amount of AgNP adsorbed per AC unit mass (q_e) was observed to increase as the AgNP concentration increases (Figure 4(b)). AgNP concentration provides an important driving force to overcome mass transfer resistance for AgNP transfer between nanoparticle solution and AC surface (48,49). In this process, AgNP first encounters the AC boundary layer. It then diffuses to the AC boundary surface layers and subsequently into the pores. Additionally, an increase in percentage adsorption occurred with an increase in temperature.
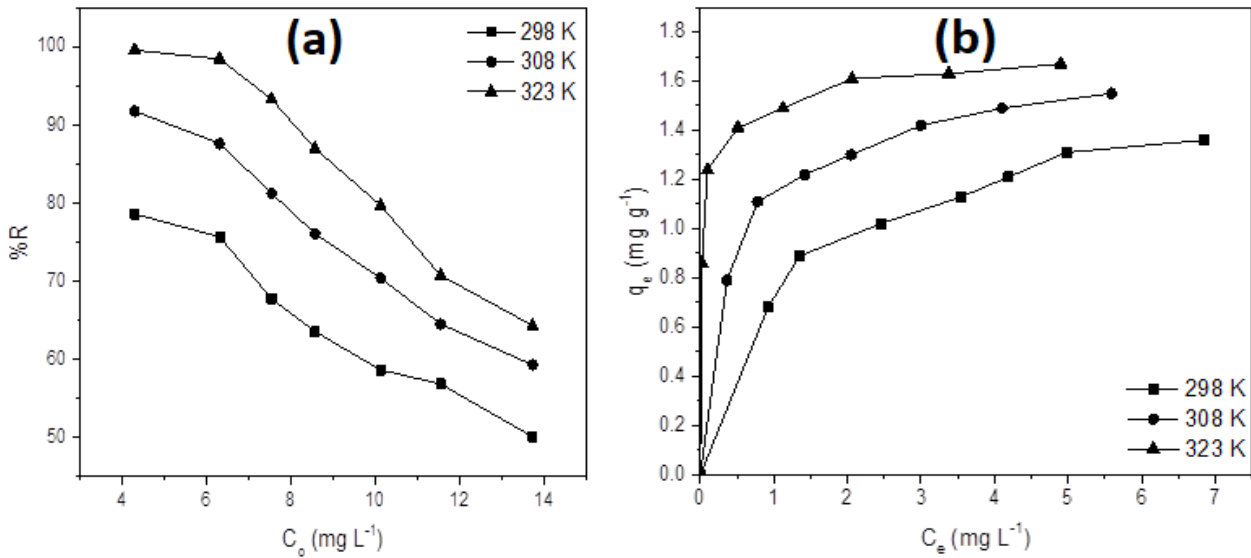
Figure 4: (a) Effect of initial nanoparticle concentration, and (b) temperature on the AgNP@AC adsorption (AgNP concertation: 4–14 mg L^{-1}, pH 7, AC dosage: 0.05 g).

The temperature increase was observed to promote AgNP adsorption, which is typical for endothermic adsorption. The increase in AgNP adsorption with temperature can be explained by the increase in the AgNP mobility thus increasing the number of active binding sites on the AC surface for adsorption as a result of the enlargement of the AC pores (50).
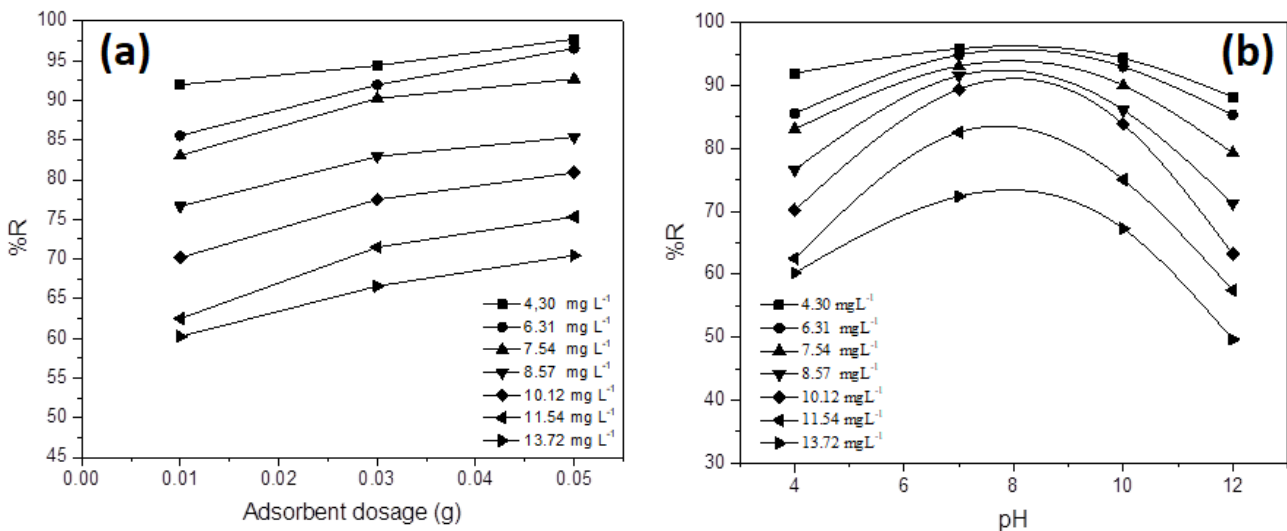
Figure 5: (a) Effect of dosage on AgNP@AC adsorption (AgNP concentration: 4–14 mg L^{-1}, pH 7, 298 K) (b) Effect of pH on AgNP@AC adsorption (AgNP concentration: 4–14 mg L^{-1}, AC dosage: 0.05 g, 298 K).

Effect of Adsorbent Dosage
The amount of adsorbent is an important factor in determining the capacity of the adsorbent for a certain concentration of AgNP solution in adsorption studies (50). AgNP@AC adsorption was investigated as a function of AC dose for AgNP in the concentration range of 4.30–13.72 mg L^{-1} and the results are given in Figure 5 (a). It was observed

that the adsorption capacity increased after the dosage of the adsorbent is increased due to the greater accessibility of surface binding sites with an increased dosage of the adsorbent. This can be explained by increasing of the available sites with increasing adsorbent dosage for the interaction with the AgNP in solution and lead to increases in the removal efficiency of the nanoparticles. On the other hand, the amount of AgNP adsorbed per unit mass of AC has decreased as the adsorbent dosage increased (51).

Many factors affect adsorption by increasing the amount of adsorbent. The first and most important factor is that the binding sites remain unoccupied without any saturation during the adsorption. This is because as the amount of adsorbent increases, there is less increase in adsorption resulting from the lower adsorptive capacity utilization of the adsorbent (52). The second factor is the aggregation of sorbent particles at higher doses, which leads to a decrease in surface area and an increase in the diffusion path length. Finally, the third factor, particle interactions at high sorbent dosages may cause some of the loosely bound AgNP to desorb from the AC surface (53).

Effect of pH
The nanoparticle surface functional groups, as well as the AC surface nature, can be very sensitive to the solution pH, and therefore, it can directly affect the surface binding during the adsorption process (28). In this study, the effect of pH was investigated in the range of 4–12, at room temperature, for the nanoparticle concentration range of 4.30–13.72 mg L^{-1} for 0.05 g of AC. The results shown in Figure 5(b) suggest that the pH of the solution significantly alters the adsorption. The pH dependence of adsorption can be explained by the isoelectric point, pH$_{IEP}$ that is the pH at which a molecule carries no net charge (50).

pH$_{IEP}$ can be used as an index for positive or negative loading capability and can be controlled according to the pH of the solution. This phenomenon is basically due to the presence of functional groups present on both the nanoparticles and the activated carbon. Those functional groups show different ionization/dissociation by the influence of the pH. Namely, if the solution pH is lower than pH$_{IEP}$, the sorbent surface acts as a positive surface, and vice versa. Besides, the observed pH effect is also closely related to AgNP surface chemistry (54).

The pH$_{IEP}$ for AgNP solution is in the range of 7–9, and it is in the range of 2–3 for the studied AC. Accordingly, in the adsorption process, which takes place at pH 4 and 7 AgNP is well adsorbed to the AC surface since the AgNP surface was negative while the AC surface was positively charged. When the pH of the medium was in the range of 7–10, AgNP has partially negative and positive charges on its surface due to its pH$_{IEP}$ value. When pH shifts towards 10,

the amount of nanoparticle uptake decreases due to the decrease of electrostatic attraction forces. Finally, strong repulsive electrostatic forces from the surfaces at pH 12, where both AgNP and AC surface are negative, also decreases the adsorption (55). But hydrophobic interactions provide an important driving force for AgNP uptake onto the AC surface (55).

Adsorption Isotherms
Adsorption isotherms are widely utilized methods while studying the equilibrium of the adsorption. Various isotherm equations have been derived to determine adsorption properties and understand the driving forces behind the process. Four important models of Langmuir, Freundlich, Temkin, and Dubinin–Raduskevich (D–R) isotherms derived from the equations were applied to this study.

Langmuir isotherm
Langmuir isotherm is based on the assumption that the adsorption process takes place in certain homogeneous regions on the adsorbent, that when AgNP is attached somewhere on the AC surface, no further adsorption can occur in that region, and the adsorption process is single-layered (56). Experimental data were evaluated with Langmuir isotherm to determine whether the adsorption event is a monolayer. Langmuir isotherm is expressed by the linear equation given below;

$$\frac{C_e}{q_e} = \frac{1}{K_L q_m + \frac{1}{q_m}} C_e \qquad (3)$$

where; q_m is the maximum amount of absorption (mg g^{-1}), q_e is the amount of substance at equilibrium (mg g^{-1}), K_L is the Langmuir equilibrium constant (L mg^{-1}), C_e is the nanoparticle concentration remained in solution at equilibrium (mg L^{-1}) (57). Besides, the further characteristics of Langmuir isotherm can be described by a factor, separation factor, which is defined by the following equation

$$R_L = \frac{1}{1 + K_L \cdot C_e} \qquad (4)$$

The R_L value indicates the nature of the adsorption which is favorable when $0 < R_L < 1$.

Freundlich Isotherm
The Freundlich isotherm equation used to describe the multi-layered adsorption systems of the adsorption process is shown linearly as follows (57).

$$ln q_e = ln K_f + ln \frac{1}{n} C_e \qquad (5)$$

Where K_f (L g^{-1}) is the Freundlich absorption constant related to adsorption capacity and

represents the quantity of nanoparticle adsorbed onto the adsorbent. q_e is the amount of substance adsorbed per unit of adsorbent at equilibrium (mg g^{-1}), n is Freundlich absorption constant, and for $n > 1$ a physical adsorption is favored. Furthermore, the *1/n* value indicates the heterogeneity and ranges between 0 and 1. For heterogeneous surfaces, this value approaches 0 (58).

Temkin Isotherm
In an absorption process, the heat of absorption and indirect adsorbent-adsorbate interactions were studied by Temkin and Pyzhev. The Temkin isotherm equation is given as

$$q_e = B \ln \left(K_T \right) + B \ln \left(C_e \right) \qquad (6)$$

$$B = \frac{RT}{b_T} \qquad (7)$$

Where K_T is the equilibrium binding constant (L g^{-1}) of the Temkin isotherm, b_T is the Temkin isotherm constant, R is defined as the ideal gas constant (8.314 J mol^{-1} K^{-1}), and B is defined as the adsorption heat constant (J mol^{-1}) (59).

Dubinin–Radushkevich (D–R) isotherm
Dubinin–Radushkevich isotherm is generally used to express the adsorption mechanism on a heterogeneous surface with Gaussian energy distribution (60). The relation expressing this isotherm is shown in eq. (8) (61).

$$\ln q_e = \ln q_s + \left(K_{DR} \right) + \mathcal{E}^2 \qquad (8)$$

Where, q_e is expressed as equilibrium adsorbent amount (mg g^{-1}), q_s is adsorption saturation capacity (mg g^{-1}), K_{DR} Dubinin-Radushkevich isotherm constant related to the adsorption energy (mol^2 J^2), $\mathcal{E}$ Dubinin-Radushkevich constant (61). This constant can be expressed as

$$\mathcal{E} = RT \ln \left(1 + \frac{1}{C_e} \right) \qquad (9)$$

where; R represents the ideal gas constant (8.314 J mol^{-1} K^{-1}), T is absolute temperature (K), C_e is adsorbent equilibrium concentration (mg L^{-1}) (61).

This approach can usually be calculated by the following correlation with the mean free energy, E for adsorption, and the E value gives information on whether the adsorption is chemical or physical (61).

$$E = \sqrt{\frac{1}{2 K_{DR}}} \qquad (10)$$

If E value is less than 8 kJ mol^{-1}, the interaction between adsorbate-adsorbent is physical. If on the contrary, it is greater than 8 kJ mol^{-1}, adsorption refers to a chemical interaction (62).

Langmuir, Freundlich, Temkin, and Dubinin-Radushkevich isotherms of AgNP@AC adsorption processes at different pHs (4,7,10 and 12) are shown in Figure 6. Also, isotherms were carried out at different temperatures and adsorbent amounts. Isotherm parameters and correlation coefficients (R^2) obtained from the plots are summarized in Tables 2 and 3. The Langmuir isotherm parameters, K_L, and qm were obtained from the slope and intercept respectively from the plot shown in Figure 6 (a). The compatibility of experimental data was also evaluated by applying different temperatures and AC amounts. The records given in Tables 2 and 3 indicate that AgNP@AC Langmuir isotherms are observed to be linear throughout the entire concentration range and high correlation coefficients (R^2) are obtained. The high R^2 values indicate the applicability of the experimental data to the Langmuir model, which represents the single-layered adsorption (63). Furthermore, the separation factor, R_L obtained from recorded data according to Equation (4) ranges between 0 and 1. This indicates that the adsorption of AgNPs onto AC is favorable.

Also, the increase in qe with the increase in temperature confirms that the nature of their adsorption is endothermic, as mentioned above in the effect of temperature on adsorption. Since K_L constant is considered as an equilibrium constant in adsorption processes, an increase of K_L with temperature increases indicates that the equilibrium shifts to the right (Table 2) (64). Freundlich isotherm parameters such as K_F and n were obtained from the slope and intercept of the lnq_e–lnC_e linear plots shown in Fig. 6(b) (58). As R^2 values of Freundlich isotherms are lower than that of Langmuir isotherms, it is suggested that AgNP@AC adsorption does not fit the Freundlich isotherm model which suggests multilayered adsorption (57).
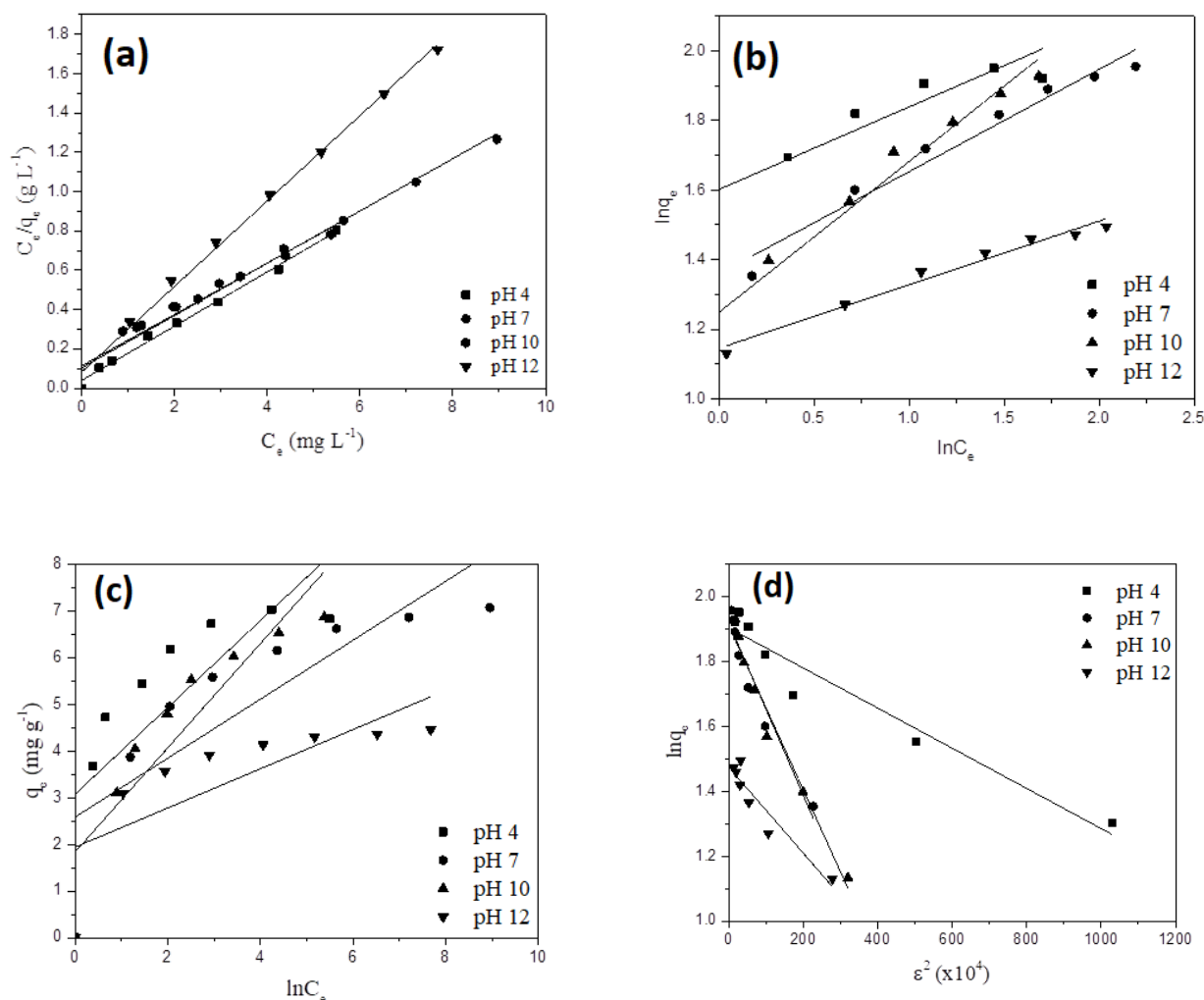
Figure 6: Isotherm plots of AgNP@AC adsorption (a) Langmuir, (b) Freundlich, (c) Temkin and (d) Dubinin–Radushkevich (AgNP concentration: 4–14 mg L^{-1}, pH: 4–12, AC dosage: 0.05 g, 298 K).

In the AgNP@AC adsorption study, the heat of adsorption and the interaction between adsorbent–adsorbate were evaluated using the Temkin isotherm. Temkin isotherm plots, shown in Figure 6(c), were obtained from the studies which were carried out at different pH values at 298 K. Temkin isotherm parameters, B and K_T were obtained from the slope and the intercept, respectively (58). The heat of adsorption is expected to decrease by increasing the temperature, and the reaction of adsorption takes place exothermically (64). From the results given in Tables 2 and 3, one can see that Temkin isotherm parameters increase as the temperature increases which suggests that the adsorption process is endothermic. It can be stated that the type of adsorption is physical adsorption involving electrostatic and Van der Waals interactions between AgNP and AC since the B values are less than 84 kJ mol^{-1} (54). But the high correlation coefficient (R^2) could not be obtained from Temkin isotherms. Therefore, those

parameters obtained from Temkin isotherms cannot provide definite results for AgNP@AC adsorption.

Equilibrium adsorption data were fitted using D–R isotherm which suggests whether the AgNP@AC adsorption process is physical or chemical (61). This isotherm is more general than the Langmuir isotherm because there is no need to assume a hypothetical surface or a constant adsorption potential (65).

It is known that Langmuir and Freundlich isotherm constants do not give any idea for the adsorption mechanism. Consequently, equilibrium data were evaluated by D–R isotherm to understand the type of adsorption. By applying the experimental data to the D–R equation, the D–R isotherms at different pH values at 298 K are shown in Figure 6(d). K_{DR} and q_s D–R parameters were calculated from the slope and intercept of the plots, respectively (Tables 2 and 3) (59). E values (the mean free energy for adsorption)

were calculated using Equation (9) (61,65). E values for AgNP were found to be 1 – 8 kJ mol^{-1}. This reveals that the adsorption mechanism for AgNP@AC adsorption is physical. However, the R^2 values obtained from D–R isotherms are low, as, in Freundlich and Temkin isotherms, there is no definite conclusion about the AgNP@AC adsorption process from parameters obtained from D–R isotherms. According to the R^2 values obtained from various isotherms, it can be stated that the AgNP@AC adsorption process is defined best with the Langmuir model.

Thermodynamic Study
Thermodynamic parameters such as Gibbs free energy $(\Delta G°)$, enthalpy $(\Delta H°)$, and entropy $(\Delta S°)$ change were calculated from the equations given below to examine whether the adsorption process is endothermic or exothermic, and its behavior thermodynamically.

$$\Delta G° = -RT \ln K_L \quad \cdot \quad (11)$$

Where, R is the universal gas constant (8.314 J mol^{-1} K^{-1}), T absolute temperature (K), and K_L is the thermodynamic equilibrium constant. Negative $\Delta G°$ values indicate the feasibility and spontaneous

occurrence of the adsorption process. The enthalpy $(\Delta H°)$ and entropy $(\Delta S°)$ changes are determined by the Van't Hoff equation given below.

$$\ln K_L = \frac{\Delta S°}{R - \dfrac{\Delta H°}{RT}} \quad (12)$$

According to the equation, the lnK_L vs. $1/T$ graph was obtained and is shown in Figure 7. The thermodynamic parameters $\Delta H°$ and $\Delta S°$ are calculated from the slope and intercept, respectively (59). The calculated thermodynamic parameters are given in Table 4. The positive values of $\Delta H°$ indicate that AgNP@AC adsorption is endothermic. The positive values of the $\Delta S°$ values indicate the nano–silver affinity towards the activated carbon as well as the increased irregularity at the solid/solution interface during the adsorption process. The negative $\Delta G°$ values indicate the feasibility and spontaneity of the adsorption. In general, $\Delta G°$ of physical adsorption is lower than that of chemical adsorption. While the magnitude of physical adsorption varies between -20 – 0 kJ mol^{-1}, it is between -80 – -400 kJ mol^{-1} for chemical adsorption (66).
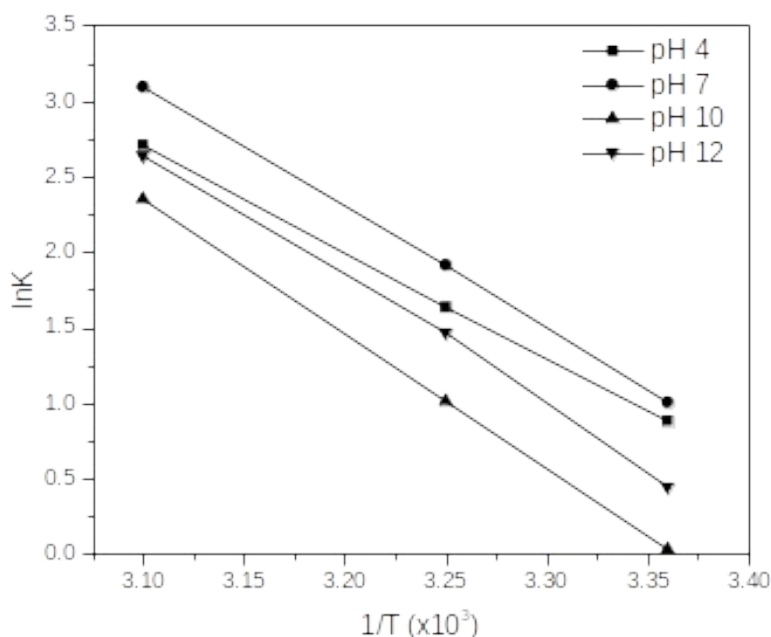
Figure 7: Van't Hoff plots for staining AgNP@AC adsorption at different pH values.

Also, the adsorption process can be classified to some extent by $\Delta H°$ as physical adsorption or chemical adsorption. A change of enthalpy <84 kJ mol^{-1} represents physisorption and values between 84 and 420 kJ mol^{-1} are considered (54).

Considering both the $\Delta G°$ and $\Delta H°$ values for the AgNP@AC adsorption process, it suggests that single layer adsorption occurs at different temperatures and conditions by means of a physical process.

Table 2: Isotherm parameters and correlation coefficients calculated by various isotherm models for AgNP@AC adsorption (AgNP concentration: 4–14 mgL^{-1}, pH: 4–12, AC dosage: 0.05 g, 298–323 K).

Isotherm	Parameter	Value of parameters											
		pH 4			pH 7			pH 10			pH 12		
	Temparature (K)	298	308	323	298	308	323	298	308	323	298	308	323
Langmuir	q_m (mg g^{-1})	7.48	7.91	9.23	7.89	9.11	10.36	7.00	8.50	9.07	4.81	7.16	7.20
	K_L (L mg^{-1})	2.42	5.14	15.04	2.74	6.79	22.11	1.03	2.76	4.35	1.56	10.51	14.00
		0.08	0.02	0.02	0.04	0.01	0.02	0.12	0.10	0.02	0.02	0.04	0.12
	R^2	0.997	0.999	0.999	0.997	0.999	0.999	0.997	0.999	0.999	0.999	0.999	0.999
Freundlich	K_F (L mg^{-1})	4.96	6.02	7.91	3.88	7.84	9.42	3.48	5.43	7.64	3.14	5.4	6.1
	N	4.21	5.4	8.64	3.4	7.18	8.12	2.3	4.13	8.26	5.46	543	8.53
	R^2	0.942	0.907	0.845	0.966	0.965	0.953	0.972	0.984	0.975	0.978	0.864	0.836
Temkin	B	1.258	1.083	0.826	1.596	0.885	0.885	2.203	1.422	0.805	0.690	0.996	0.679
	K_T (L mg^{-1})	57.15	300	17206	10.42	8134	64263	1.275	50.19	15656	91.1	251	9200
	b_T	1969	2364	3251	1552	2893	3034	1178	1801	3336	3590	2571	3950
	R^2	0.961	0.940	0.890	0.989	0.956	0.985	0.995	0.998	0.992	0.987	0.899	0.862
D-R	q_s (mg g^{-1})	6.72	7.45	9.05	1.916	8.13	9.66	6.68	7.32	8.31	4.34	6.84	7.1
	K_{DR} (mol^2 J^2)	6.E-08	3.E-08	1.E-08	3.E-07	5.E-09	5.E-09	2.E-07	6.E-08	7.E-09	1.E-07	5.E-08	2.E-08
	E (kJ mol^{-1})	2.9	4.0	7.1	1.3	1.5	1.7	2.2	2.9	7.45	2.2	3.2	5.0
	R^2	0.946	0.902	0.997	0.947	0.813	0.967	0.9629	0.916	0.922	0.927	0.989	0.988

Table 3: Isotherm parameters and correlation coefficients calculated by various isotherm models for AgNP@AC adsorption (AgNP concentration: 4–14 mgL^{-1}, pH: 4–12, AC dosage: 0.01–0.03–0.05 g, 298 K).

Isotherm	Parameter	Value of parameters											
		pH 4			pH 7			pH 10			pH 12		
	Adsorbent (g)	0.01	0.03	0.05	0.01	0.03	0.05	0.01	0.03	0.05	0.01	0.03	0.05
Langmuir	q_m (mg g^{-1})	10.52	9.52	7.48	10.73	9.91	7.89	10.33	9.84	7.00	7.49	6.63	4.81
	K_L (L mg^{-1})	2.82	2.29	2.42	1.02	1.21	2.74	0.71	0.94	1.03	0.30	0.65	1.56
	R_L	0.03	0.04	0.08	0.05	0.08	0.04	0.12	0.10	0.12	0.31	0.19	0.12
	R^2	0.998	0.999	0.997	0.999	0.999	0.997	0.999	0.999	0.997	0.999	0.999	0.999
Freundlich	K_F (L mg^{-1})	7.26	0.71	4.96	7.68	0.75	3.88	7.60	7.70	3.48	2.10	6.01	3.14
	N	3.52	6.46	4.21	3.99	5.86	3.4	7.10	4.82	2.3	2.16	28.25	5.46
	R^2	0.931	0.988	0.942	0.972	0.965	0.966	0.992	0.961	0.972	0.983	0.980	0.978
Temkin	B	1.938	2.032	1.258	1.722	1.134	1.596	0.949	1.389	2.203	1.797	0.187	0.690
	K_T (L mg^{-1})	49.1	32.05	57.15	101.3	1819	10.42	3557	296.5	1.275	2.45	1.E+14	91.1
	b_T	1278	1219	1969	1439	2185	1552	3610	1784	1178	1379	13249	3590
	R^2	0.978	0.973	0.961	0.993	0.992	0.989	0.996	0.990	0.995	0.999	0.965	0.987
D-R	q_s (mg g^{-1})	11.52	9.25	6.72	9.24	8.96	1.92	8.40	8.86	6.68	5.24	6.17	4.34
	K_{DR} (mol^2 J^2)	5.E-08	6.E-08	6.E-08	3.E-08	9.E-09	3.E-07	9.E-09	2.E-08	2.E-07	6.E-07	6.E-10	1.E-07
	E (kJ mol^{-1})	3.16	6.24	2.9	6.67	7.45	1.3	5.45	5.00	2.20	0.91	1.87	2.20
	R^2	0.981	0.984	0.946	0.946	0.939	0.947	0.879	0.952	0.9629	0.956	0.871	0.927

Table 4: Thermodynamic parameters for AgNP@AC adsorption (AgNP concentration: 4–14 mg L^{-1}, pH: 4–12, AC dosage: 0.05 g).

pH	K_L	T (K)	$\Delta G°$ (kJ mol^{-1})	$\Delta H°$ (kJ mol^{-1})	$\Delta S°$ (Jmol^{-1} K^{-1})	R^2
4	2.42	298	-2.19			
	5.14	308	-4.19	58.53	203.70	0.9999
	15.04	323	-7.28			
7	2.74	298	-2.49			
	6.79	308	-4.50	66.77	232.92	0.9970
	22.11	323	-8.31			
10	1.03	298	-0.08			
	2.76	308	-2.59	74.21	249.33	0.9999
	10.51	323	-6.32			
12	1.56	298	-1.11			
	4.35	308	-3.77	69.78	328.35	0.9971
	14.00	323	-7.09			

CONCLUSION

AgNPs were synthesized by using gelatin as a capping agent. Colloidal stability of AgNPs was checked at pHs of 2–13. AgNPs displayed colloidal stability at pHs ranging from 4 to 13. The stability of the nanoparticles was observed to weaken at a pH of 2. AgNP adsorption onto AC was examined and found to be influenced by experimental parameters including initial nanoparticle concentration, temperature, pH, and adsorbent dosage. Adsorption percentage decreased with increased initial nanoparticle concentration. However, qe value seemed to increase per AC mass as nanoparticle concentration increased. Temperature increase promoted AgNP adsorption onto AC. The amount of adsorbed AgNP per unit mass of AC decreases as adsorbent dosage increases. Adsorption isotherms were investigated by fitting the data to different isotherm models including Langmuir, Freundlich, Temkin, and Dubinin–Radushkevich (D–R). Results suggest that the adsorption is well described by the Langmuir model. Thermodynamic studies indicated that the adsorption is endothermic, favorable, and spontaneous. Our findings reveal that gelatin–stabilized AgNPs can be successfully removed from water using AC.

CONFLICT OF INTEREST

Authors declare that they have no conflict of interest.

ACKNOWLEDGMENTS

REFERENCES

1. García-Barrasa J, López-De-luzuriaga JM, Monge M. Silver nanoparticles: Synthesis through chemical methods in solution and biomedical applications. Cent Eur J Chem. 2011;9(1):7–19. <DOI>.

2. Calderón-Jiménez B, Johnson ME, Montoro Bustos AR, Murphy KE, Winchester MR, Baudrit JRV. Silver nanoparticles: Technological advances, societal impacts, and metrological challenges. Front Chem. 2017;5(Feb):1–26. <DOI>.

3. Sivera M, Kvitek L, Soukupova J, Panacek A, Prucek R, Vecerova R, et al. Silver nanoparticles modified by gelatin with extraordinary pH stability and long-term antibacterial activity. PLoS One. 2014;9(8). <DOI>.

4. Seoudi R, Shabaka A, El Sayed ZA, Anis B. Effect of stabilizing agent on the morphology and optical properties of silver nanoparticles. Phys E Low-Dimensional Syst Nanostructures. 2011;44(2):440–7. <DOI>.

5. Alarcon EI, Bueno-Alejo CJ, Noel CW, Stamplecoskie KG, Pacioni NL, Poblete H, et al. Human serum albumin as protecting agent of silver nanoparticles: Role of the protein conformation and amine groups in the nanoparticle stabilization. J Nanoparticle Res. 2013;15(1). <DOI>.

6. Salgueiriño-Maceira V, Correa-Duarte MA, Farle M, López-Quintela MA, Sieradzki K, Diaz R. Synthesis and characterization of large colloidal cobalt particles. Langmuir. 2006;22(4):1455–8. <DOI>.

7. Campos AM, Raymundo-Pereira PA, Cincotto FH, Canevari TC, Machado SAS. Sensitive determination of the endocrine disruptor bisphenol

A at ultrathin film based on nanostructured hybrid material SiO2/GO/AgNP. J Solid State Electrochem. 2016;20(9):2503–7. <DOI>.

8.   Mdluli PS, Revaprasadu N. An improved N,N-dimethylformamide and polyvinyl pyrrolidone approach for the synthesis of long silver nanowires. J Alloys Compd. 2009;469(1–2):519–22. <DOI>.

9.   Kashiwagi Y, Yamamoto M, Nakamoto M. Facile size-regulated synthesis of silver nanoparticles by controlled thermolysis of silver alkylcarboxylates in the presence of alkylamines with different chain lengths. J Colloid Interface Sci. 2006;300(1):169–75. <DOI>.

10.   Brust M, Kiely CJ. Some recent advances in nanostructure preparation from gold and silver particles: A short topical review. Colloids Surfaces A Physicochem Eng Asp. 2002;202(2–3):175–86. <DOI>.

11.   Bunge SD, Boyle TJ, Headley TJ. Synthesis of coinage-metal nanoparticles from mesityl precursors. Nano Lett. 2003;3(7):901–5. <DOI>.

12.   Pastoriza-Santos I, Liz-Marzán LM. Formation of PVP-protected metal nanoparticles in DMF. Langmuir. 2002;18(7):2888–94. <DOI>.

13.   Ahmad M Bin, Lim JJ, Shameli K, Ibrahim NA, Tay MY. Synthesis of silver nanoparticles in chitosan, gelatin and chitosan/gelatin bionanocomposites by a chemical reducing agent and their characterization. Molecules. 2011;16(9):7237–48. <DOI>.
14.   Jia Z, Sun H, Gu Q. Preparation of Ag nanoparticles with triethanolamine as reducing agent and their antibacterial property. Colloids Surfaces A Physicochem Eng Asp. 2013;419:174–9. <DOI>.

15.   Xiong Y, Luo G, Chen C, Yuan H, Shen Q, Li M. In situ synthesis of zero-valent silver nanoparticles in polymethylmethacrylate under high temperature. Appl Surf Sci. 2012;258(15):5822–6. <DOI>.

16.   Sun X, Dong S, Wang E. One-step preparation and characterization of poly(propyleneimine) dendrimer-protected silver nanoclusters. Macromolecules. 2004;37(19):7105–8. <DOI>.

17.   Long Y, Ran X, Zhang L, Guo Q, Yang T, Gao J, et al. A method for the preparation of silver nanoparticles using commercially available carboxymethyl chitosan and sunlight. Mater Lett. 2013;112:101–4. <DOI>.

18.   Moussa SH, Tayel AA, Alsohim AS, Abdallah RR. Botryticidal activity of nanosized silver-chitosan composite and its application for the control of gray mold in strawberry. J Food Sci. 2013;78(10):1589–94. <DOI>.

19.   Oluwafemi OS, Lucwaba Y, Gura A, Masabeya M, Ncapayi V, Olujimi OO, et al. A facile completely "green" size tunable synthesis of maltose-reduced silver nanoparticles without the use of any accelerator. Colloids Surfaces B Biointerfaces. 2013;102:718–23. <DOI>.

20.   Lee C, Zhang P. Facile synthesis of gelatin-protected silver nanoparticles for SERS applications. J Raman Spectrosc. 2013;44(6):823–6. <DOI>.

21.   Darroudi M, Khorsand Zak A, Muhamad MR, Huang NM, Hakimi M. Green synthesis of colloidal silver nanoparticles by sonochemical method. Mater Lett. 2012;66(1):117–20. <DOI>.

22.   Zamiri R, Azmi BZ, Ahangar HA, Zamiri G, Husin MS, Wahab ZA. Preparation and characterization of silver nanoparticles in natural polymers using laser ablation. Bull Mater Sci. 2012;35(5):727–31. <DOI>.

23.   Cushing BL, Kolesnichenko VL, O'Connor CJ. Recent advances in the liquid-phase syntheses of inorganic nanoparticles. Chem Rev. 2004;104(9):3893–946. <DOI>.

24.   Evanoff DD, Chumanov G. Synthesis and optical properties of silver nanoparticles and arrays. ChemPhysChem. 2005;6(7):1221–31.<DOI>.

25.   Valdés H, Sánchez-Polo M, Rivera-Utrilla J, Zaror CA. Effect of ozone treatment on surface properties of activated carbon. Langmuir. 2002;18(6):2111–6. <DOI>.

26.   Fabris D, Garg V, Sapag K, Oliveira LCA, Rios RVRA, Lago RM. Activated carbon / iron oxide magnetic composites for the adsorption of contaminants in water. 2002;40:2177–83. <DOI>.

27.   Eltugral N, Simsir H, Karagoz S. Preparation of nano-silver-supported activated carbon using different ligands. Res Chem Intermed. 2016;42(3):1663–76.<DOI>.

28.   Panáček A, Kvítek L, Prucek R, Kolář M, Večeřová R, Pizúrová N, et al. Silver colloid nanoparticles: Synthesis, characterization, and their antibacterial activity. J Phys Chem B. 2006;110(33):16248–53. <DOI>.

29.   Boehm HP. Chemical Identification of Surface Groups. Adv Catal. 1966;16(C):179–274. <DOI>.

30.   Teng H, Xu S, Zhao C, Lv F, Liu H. Removal of Hexavalent Chromium from Aqueous Solutions by Sodium Dodecyl Sulfate Stabilized Nano Zero-Valent Iron: A Kinetics, Equilibrium, Thermodynamics Study. Sep Sci Technol. 2013;48(11):1729–37. <DOI>.

31.   Maity D, Kanti Bain M, Bhowmick B, Sarkar J, Saha S, Acharya K, et al. In situ synthesis, characterization, and antimicrobial activity of silver nanoparticles using water soluble polymer. J Appl Polym Sci. 2011;122(4):2189–96. <u><DOI></u>.

32.   Srinivasan NR, Shankar PA, Bandyopadhyaya R. Plasma treated activated carbon impregnated with silver nanoparticles for improved antibacterial effect in water disinfection. Carbon N Y. 2013;57(22):1–10. <u><DOI></u>.

33.   Peña-González CE, Pedziwiatr-Werbicka E, Shcharbin D, Guerrero-Beltrán C, Abashkin V, Loznikova S, et al. Gold nanoparticles stabilized by cationic carbosilane dendrons: Synthesis and biological properties. Dalt Trans. 2017;46(27):8736–45.<u><DOI></u>.

34.   El-Shishtawy RM, Asiri AM, Al-Otaibi MM. Synthesis and spectroscopic studies of stable aqueous dispersion of silver nanoparticles. Spectrochim Acta - Part A Mol Biomol Spectrosc. 2011;79(5):1505–10. <u><DOI></u>.

35.   Ho CM, Yau SKW, Lok CN, So MH, Che CM. Oxidative dissolution of silver nanoparticles by biologically relevant oxidants: A kinetic and mechanistic study. Chem - An Asian J. 2010;5(2):285–93. <u><DOI></u>.

36.   Dickinson E, Lopez G. Comparison of the emulsifying properties of fish gelatin and commercial milk proteins. J Food Sci. 2001;66(1):118–23. <u><DOI></u>.

37.   Hashim DM, Man YBC, Norakasha R, Shuhaimi M, Salmah Y, Syahariza ZA. Potential use of Fourier transform infrared spectroscopy for differentiation of bovine and porcine gelatins. Food Chem. 2010;118(3):856–60.<u><DOI></u>.

38.   Solanki PR. Gelatin Nanoparticles as a Delivery System for Proteins. J Nanomedicine Res. 2015;2(1):2–4.<u><DOI></u>.

39.   Shende S, Ingle AP, Gade A, Rai M. Green synthesis of copper nanoparticles by Citrus medica Linn. (Idilimbu) juice and its antimicrobial activity. World J Microbiol Biotechnol. 2015;31(6):865–73.<u><DOI></u>.

40.   Usman MS, El Zowalaty ME, Shameli K, Zainuddin N, Salama M, Ibrahim NA. Synthesis, characterization, and antimicrobial properties of copper nanoparticles. Int J Nanomedicine. 2013;8:4467–79. <u><DOI></u>.

41.   Pandey S, Goswami GK, Nanda KK. Green synthesis of biopolymer-silver nanoparticle nanocomposite: An optical sensor for ammonia detection. Int J Biol Macromol. 2012;51(4):583–9.<u><DOI></u>.

42.   Wang X, Chen Y. A new two-phase system for the preparation of nearly monodisperse silver nanoparticles. Mater Lett. 2008;62(28):4366–8. <u><DOI></u>.

43.   Das D, Samal DP, BC M. Preparation of Activated Carbon from Green Coconut Shell and its Characterization. J Chem Eng Process Technol. 2015;06(05).<u><DOI></u>.

44.   Tuan TQ, Son N Van, Dung HTK, Luong NH, Thuy BT, Anh NT Van, et al. Preparation and properties of silver nanoparticles loaded in activated carbon for biological and environmental applications. J Hazard Mater. 2011;192(3):1321–9. <u><DOI></u>.

45.   Karthik C, Radha K V. Silver nanoparticle loaded activated carbon: An escalated nanocomposite with antimicrobial property. Orient J Chem. 2016;32(1):735–41. <u><DOI></u>.

46.   Chun Y, Sheng G, Chiou GT, Xing B. Compositions and sorptive properties of crop residue-derived chars. Environ Sci Technol. 2004;38(17):4649–55. <u><DOI></u>.

47.   Ridder DJ de. Adsorption of organic micropollutants onto activated carbon and zeolites. Vol. P.hD, Water management academic press. 2012. <u><DOI></u>.

48.   Senthilkumaar S, Varadarajan PR, Porkodi K, Subbhuraam C V. Adsorption of methylene blue onto jute fiber carbon: Kinetics and equilibrium studies. J Colloid Interface Sci. 2005;284(1):78–82. <u><DOI></u>.

49.   Zhu HY, Fu YQ, Jiang R, Jiang JH, Xiao L, Zeng GM, et al. Adsorption removal of congo red onto magnetic cellulose/Fe3O4/activated carbon composite: Equilibrium, kinetic and thermodynamic studies. Chem Eng J. 2011;173(2):494–502. <u><DOI></u>.

50.   Ghaedi M, Sadeghian B, Pebdani AA, Sahraei R, Daneshfar A, Duran C. Kinetics, thermodynamics and equilibrium evaluation of direct yellow 12 removal by adsorption onto silver nanoparticles loaded activated carbon. Chem Eng J. 2012;187:133–41. <u><DOI></u>.

51.   Garg VKKR, Gupta R. Dyes Pigments. Remov malachite green Dye from aqueous Solut by Adsorpt using agro-industry waste a case study Prosopis cineraria. 2004;62:1–10. <u><DOI></u>.

52.   Honeyman BD, Santschi PH. Metals in aquatic systems. Environ Sci Technol. 1988;22(8):862–71.<u><DOI></u>.

53.   Manohar DM, Anoop Krishnan K, Anirudhan TS. Removal of mercury(II) from aqueous solutions and chlor-alkali industry wastewater using 2-mercaptobenzimidazole-clay. Water Res. 2002;36(6):1609–19. <u><DOI></u>.

54. Al-Degs YS, El-Barghouthi MI, El-Sheikh AH, Walker GM. Effect of solution pH, ionic strength, and temperature on adsorption behavior of reactive dyes on activated carbon. Dye Pigment. 2008;77(1):16–23. <DOI>.

55. Norde W, Lyklema J. Thermodynamics of protein adsorption. Theory with special reference to the adsorption of human plasma albumin and bovine pancreas ribonuclease at polystyrene surfaces. J Colloid Interface Sci. 1979;71(2):350–66.<DOI>.

56. Bhatnagar A, Sillanpää M. Removal of natural organic matter (NOM) and its constituents from water by adsorption – A review. Chemosphere. 2017;166:497–510. <DOI>.

57. Jalil AA, Triwahyono S, Adam SH, Rahim ND, Aziz MAA, Hairom NHH, et al. Adsorption of methyl orange from aqueous solution onto calcined Lapindo volcanic mud. J Hazard Mater. 2010;181(1–3):755–62. <DOI>.

58. Ng C, Losso JN, Marshall WE, Rao RM. Freundlich adsorption isotherms of agricultural by-product-based powdered activated carbons in a geosmin-water system. Bioresour Technol. 2002;85(2):131–5. <DOI>.

59. Da A. Adsorption- from theory to practice. 2001;93(1–3):135–224. <DOI>.

60. Foo KY, Hameed BH. Insights into the modeling of adsorption isotherm systems. Chem Eng J. 2010;156(1):2–10. <DOI>.

61. Sogut E, Caliskan N. Isotherm and kinetic studies of Pb(II) adsorption on raw and modified diatomite by using non-linear regression method. Fresenius Environ Bull. 2017;26(4):2721–9. <DOI>.

62. Günay A, Arslankaya E, Tosun I. Lead removal from aqueous solution by natural and pretreated clinoptilolite: Adsorption equilibrium and kinetics. J Hazard Mater. 2007;146(1–2):362–71. <DOI>.

63. Özer A, Özer D, Özer A. The adsorption of copper(II) ions on to dehydrated wheat bran (DWB): Determination of the equilibrium and thermodynamic parameters. Process Biochem. 2004;39(12):2183–91. <DOI>.

64. Nekouei F, Nekouei S, Tyagi I, Gupta VK. Kinetic, thermodynamic and isotherm studies for acid blue 129 removal from liquids using copper oxide nanoparticle-modified activated carbon as a novel adsorbent. J Mol Liq. 2015;201:124–33.<DOI>.

65. Kilislioglu A, Bilgin B. Thermodynamic and kinetic investigations of uranium adsorption on amberlite IR-118H resin. Appl Radiat Isot. 2003;58(2):155–60. <DOI>.

66. Weil KG. M. J. Jaycock, G. D. Parfitt: Chemistry of Interfaces. Ellis Horwood Limited Publishers, Chichester 1981. Berichte der Bunsengesellschaft für Phys Chemie. 1981;85(9):718–718.<DOI>.

SUPPLEMENTARY MATERIAL

Isotherm and Thermodynamic Studies on the Removal of Gelatin-stabilized Silver Nanoparticles from Water by Activated Carbon
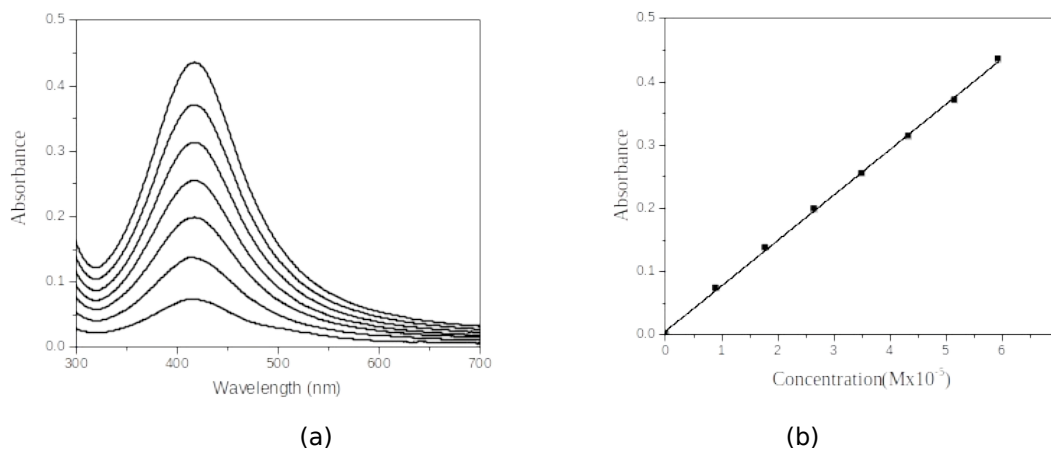
Aysenur Ceryan[1], Nurettin Eltugral[2*]

(a)   (b)

Figure S1: UV-Vis absorbance spectra and b) Lambert-Beer plot of AgNP solutions at different concentrations (9.0×10^{-6} - 6.0×10^{-5} M).
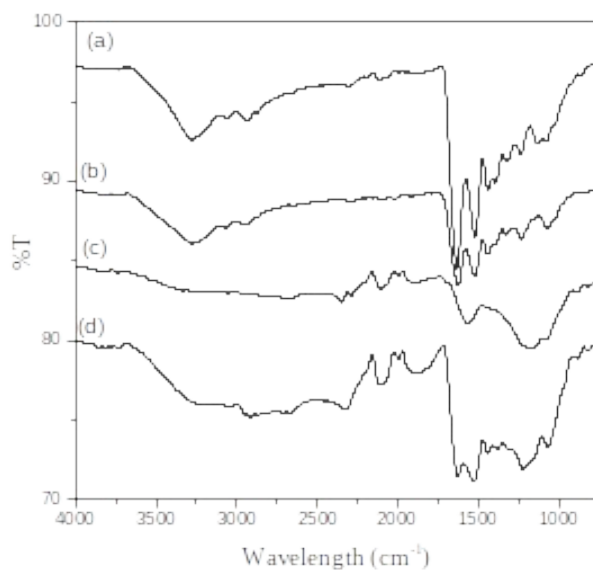

Figure S2: FTIR spectrum of a) Gelatin, b) AgNP, c) AC, and d) AgNP@AC
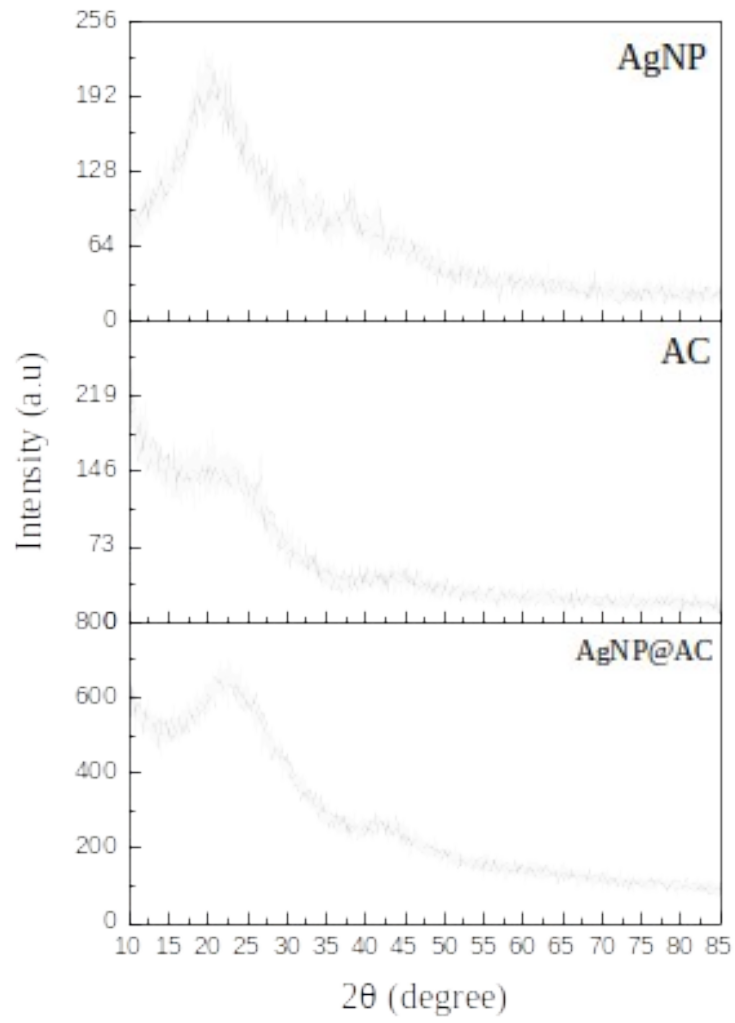
Figure S3: XRD diffraction patterns of AgNP, AC, and AgNP@AC.

Biodiesel Production from Waste Frying Oil using Catalysts Derived from Waste Materials

Welela Meka Kedir[1*] iD **, Tsegaye Girma Asere[2]** iD

[1]Mattu University, Department of Chemistry, Mattu, Ethiopia
[2]Jimma University, Department of Chemistry, Jimma, Ethiopia

Abstract: Domestic resources such as vegetable oil, animal fats, tallows, and waste frying oil are common raw materials for making biodiesel. In contrast to ordinary diesel, biodiesel helps to reduce CO_2 emissions. This study aimed to produce biodiesel using waste frying oil in the presence of suitable solid waste-derived heterogeneous catalysts. Firstly, CaO/K_2O catalyst was synthesised using eggshells and banana peels. Then, the pre-prepared catalyst (CaO/K_2O) modified with ZnO was utilized for biodiesel production. The prepared catalyst and biodiesel were characterized using X-ray diffraction (XRD) and FTIR spectroscopy. The AOAC and ASTM standard methods were employed to analyze the physicochemical properties of oils and biodiesel. The catalytic efficiency of CaO/K_2O and CaO/K_2O-ZnO tested for the transesterification of purified oil to biodiesel at the catalyst weight (1-7 % wt), temperature (60-80°C), and methanol to oil ratios ranging from 3:1 to 12:1. The highest biodiesel yield (92%) obtained when 5 % wt CaO/K_2O catalyst used. However, a 95% yield resulted when using a 3 % wt CaO/K_2O-ZnO catalyst load in 2 h with a methanol to oil (v/v) ratio of 9:1 at 65°C. The study revealed that waste frying oil is a good source of biodiesel which could replace nonrenewable energy in the future. The catalysts made from solid waste could also replace an expensive chemical catalyst.

INTRODUCTION

Renewable energy generation has been prioritized globally due to the energy and global warming crises (1). Currently, fossil fuel represents 88% of total world energy consumption and is the largest energy source (2). Non-renewable fossil fuels contribute approximately 52% of CO_2 emissions to the atmosphere and are the sources of other greenhouse gases (3). Various renewable resources are considered alternative fossil fuels, including wind, solar, geothermal, wave energy, and biofuel (4, 5). Biodiesel is sold as a diesel engine supplement fuel among various alternative fuels (6). Its advantages are renewability, degradability, non-toxic nature, and compatibility with other energy sources (5, 7).

However, the current biodiesel production uses edible oils, which are more expensive than petroleum-based fuels (8). In addition to the high feedstock cost of biodiesel production, the absence of economically and technically viable technology affects its efficient production (9, 10). Thus, using non-edible oil as a biodiesel source may alleviate the existing problems (11, 12).

Transesterification of oil with alcohol with suitable homogeneous or heterogeneous catalysts yielded fatty acid methyl ester or biodiesel (13). The Common used homogeneous catalysts for the transesterification processes are NaOH, KOH, and CH_3ONa, which have high catalytic activity (14). However, separating, purifying, and reusing them is challen-

ging (7). Various heterogeneous catalysts for biodiesel generation have been developed, including zeolite, alkali earth metal oxides, KF/YAl$_2$O$_3$, and sodium aluminate (12). However, due to the high cost of catalyst manufacturing, only selective heterogeneous catalysts are used in industry (15). The wise use of waste material as a heterogeneous catalyst can minimize overall biodiesel production costs. CaO and K$_2$O are common catalysts for biodiesel production because they are abundant in nature, low cost, and show high activity (1). Therefore, this study aimed to produce biodiesel using waste frying oil in the presence of suitable solid waste-derived heterogeneous catalysts.

MATERIAL AND METHODS

Study Area and Study Period
Heterogeneous catalyst preparation, waste frying oil refining, and biodiesel production were carried out at Mattu University, College of Natural and Computational Sciences, Department of Chemistry. The physicochemical properties of the catalysts, oil, and biodiesel were studied by using various analytical techniques. The XRD of catalysts and FTIR analysis of oil and biodiesel were carried out at Jimma University, Institute of Technology, Department of Material Sciences.

Chemicals
Chemicals used for this study include chloroform (99%) and methanol (99.99%) from Blulax, India. Glacial acetic acid, potassium iodide, sodium bisulfate, hydrochloric acid, ammonium chloride, ammonium hydroxide, starch, and phenolphthalein indicator, distilled water, hanus solution, ethanol, ferric chloride, sodium thiosulfate, potassium hydroxide, and sodium hydroxide were used for the physicochemical analysis of oil and biodiesel.

Apparatus and Instrument
Apparatus such as titration flask, burets (300 and 500 mm), pestle, and mortar, filter paper, weighing balances, oven, beakers, funnels, Erlenmeyer flasks, magnetic stirrer, crucible dish, water bath, aluminum foil, refrigerator, and rotary evaporator, muffle furnace, and thermometer were used. Instruments such as refractometer, conductometry, pH meter, XRD, and FTIR were used.

Sample Collection
Eggshell, banana peel, and waste frying oil samples were collected from Mattu town, Ilubabara Zone, South-West Ethiopia. A purposive sampling technique was adopted during sample collection.

Purification of Waste Frying Oil
The collected waste frying oil was allowed to pass through the micron-sized holes sieve to remove any solid particles. The filtrate was poured into a separatory funnel. It was followed by adding 40 mL of hot water to remove salt and other soluble particles. The separated oil was put into the oven at 105 °C to remove water. The purified oil was cooled to room temperature and then in a water bath for further analysis and biodiesel production (16).

Catalyst Preparation
The eggshell and banana peel samples were sliced and then washed using hot distilled water (40 °C) to remove waxy material and dirt particles.

Preparation of CaO
The raw waste eggshell is the source of CaCO$_3$ because it converts to CaO when calcined. A 50 g eggshell was dried overnight at 100 °C using an oven. Then, it was powdered and calcined for three hours in a furnace at 900 °C (17). The received CaO catalyst was kept in an airtight container for further use.

Preparation of K$_2$O
A 50 g banana peel was washed, sliced, and dried at 90 °C in an oven for 48 hours. The dried sample was powdered and calcined at 750 °C for 3 hours (17). The obtained K$_2$O catalyst was collected and stored in an airtight container for future use.

Preparation of CaO/K$_2$O
After separate preparation of CaO from the eggshell and K$_2$O from the banana peel, their mixture (1:1 ratio) is immersed in 10 mL of distilled water to form a solution. The solution was continuously stirred at 25 °C for 3 hours, and the obtained product was dried for 24 hours at 80 °C. Then, it was calcined for 5 hours at 500 °C (11). The received product was denoted as CaO/K$_2$O.

CaO/K$_2$O/ZnO Catalyst
A wet impregnation method was used to prepared CaO/K$_2$O/ZnO catalyst by mixing CaO/K$_2$O catalysts from (eggshells and banana peels) with ZnO in a ratio of 1:1:1 (CaO:K$_2$O:ZnO). The mixtures were immersed in distilled water (10 mL). Then, the solution was stirred for 3 hours continuously at room temperature, and the recevied product was dried for 24 hours at 80 °C (11). Next, the obtained material was calcined for 5 hours at 500 °C and the resulting catalyst was denoted as CaO/K$_2$O/ZnO.

Transesterification of Purified Oil Using CaO/K$_2$O and CaO/K$_2$O/ZnO Catalyst
The transesterification process was conducted according to the method reported in Khan H.M, et al. 2020 (18) with minor modifications. In a 250 mL two-necked flat bottom flask equipped with a reflux condenser, 20 mL of the purified oil was added, then stirred at 600 rpm for all test runs. The oil was heated at 105 °C for 5 minutes in a heating mantle to evaporate water and other volatile contaminants. A mixture of the oil and a calcined catalyst (1, 3, 5, and 7 % wt.) was stirred at 600 rpm. An oil to methanol ratio was 1:3 to 1:12. Each experiment was allowed to continue at a temperature of 65–80 °C. When the reaction completed, the solution was cooled, and centrifuged or filtered to separate the catalyst. The spent catalyst was regenerated by

treating it with methanol. The filtrate mixture was then placed in a separatory funnel for 10 minutes to separate the layers. Methyl esters and unconverted triglycerides make up the top layer. Glycerol, excess methanol, soap generated during the process, and some entrained methyl esters were found in the lower layer. The excess methanol was removed by distillation before the fatty acid methyl esters (FAME) percent analysis. The percentage yield of biodiesel was calculated using Equation 1 (19).

$$\text{Biodiesel yield \%} = \frac{\text{weight of Biodiesel}}{\text{weight of oil used}} \times 100$$

(Eq. 1)

Biodiesel Purification
The obtained biodiesel was rinsed with distilled water after removing the glycerol layer. The mixture was stirred using mechanical stirring for 10 minutes. The stirring was turned off after 10 minutes, and the water was left to settle for two days. At this point, the process was complete, and the clear crystal product was biodiesel (11, 17).

Physicochemical Analysis of Waste Frying Oil, Purified Oil, and Biodiesel
The physicochemical properties of waste frying oil (WFO), purified oil (PO), and biodiesel were ana-lyzed following the AOAC official method (969.17). The common physicochemical properties include acid value (AV), refractive index (RI), iodine value (IV), saponification value (SV), density, free fatty acid (FFA), moisture content, ash content, pH, and cetane number (20, 21). The biodiesel was also subjected to ASTM standard fuel characterization. Density, flash point, pour point, and cloud point measurements of the ethyl esters produced were made following ASTM D6751 standards.

pH
A 3 g sample of oil or biodiesel was placed in a clean, dry 25 mL beaker, and 15 mL of hot distilled water was slowly poured and stirred. It was cooled in a cold water bath. The pH meter electrode was calibrated with buffer solution and immersed in the sample, and the pH value was recorded (21).

Moisture content
The AOAC official method (969.17) was employed to determine the moisture content. The oil/biodiesel was weighed and dried for 24 hours at 105 °C in an oven. The final weight was taken and recorded (20). The moisture content was calculated by using Equation 2.

$$\text{Moisture (\%)} = \frac{\text{Initial weight of oil - Final weight of oil}}{\text{Initial weight of oil}} \times 100$$

(Eq. 2)

Ash content
2 g of oil or biodiesel sample was added to a crucible dish. The crucible contained the sample was heated carefully in the muffle furnace at 775 °C for 25 minutes until all carbonaceous materials were disappeared. Then the crucible was cooled at room temperature in a desiccator (20). The ash content was calculated using Equation 3.

$$\text{Ash} (\%) = \frac{W_3 - W_1}{W_2} \times 100$$

(Eq. 3)

Where, W_1= weight of crucible dish, W_2=weight of oil sample, W_3=Weight the sample plus the crucible dish after calcination.

Acid value (AV)
A 2 g of oil/ biodiesel sample was mixed with neutral ethyl alcohol (30 mL); after boiling for 2 minutes in a water bath, the mixture was titrated with KOH solution (0.1 N) using phenolphthalein as an indicator (20). The AV was calculated by using equation 4.

$$\text{Acid value} = \frac{V \times N \times 56.1}{W}$$ (Eq. 4)

Where, V is the volume in mL of standard KOH used, N is the normality of the KOH solution, and W is the weight in g of the sample.

Determination of free fatty acid (%)
The acid values of the oil samples were used to calculate the percentage of free fatty acid of the samples (20) by using Equation 5.

$$\text{FFA (\%)} = \frac{\text{Acid value}}{2}$$

(Eq. 5)

Peroxide value (PV)
1 g of oil or biodiesel was placed in a conical flask. Then, 30 mL of glacial acetic acid/chloroform (3:2 v/v) was added. The mixture was shaken until the sample was dissolved. Then, 1 mL of saturated potassium iodide solution was added, followed by 0.5 mL of starch indicator solution. 0.1 M $Na_2S_2O_3$ (sodium thiosulfate) was used to titrate the solution until the dark blue color vanished. The PV was determined by using Equation 6 (20).

$$PV = \frac{Titer \times N \times 1000}{\text{weight of the sample}}$$ (Eq. 6)

Where, titer is the mL of $Na_2S_2O_3$ used (blank corrected), and N is the normality of sodium thiosulfate solution.

Determination of iodine value (IV)
1 g of sample was placed in a 250-mL conical flask, followed by adding 30 mL of Hanus iodine solution and mixing. Then, the mixture was kept in the drawer for 30 minutes. The mixture was titrated against 0.14 M $Na_2S_2O_3$ until the solution became light yellow. After the addition of a starch indicator (1%, 2 mL), the titration continued until the blue colors disappeared (20). A similar procedure was employed to determine the blank solution. The IV was calculated by using Equation 7.

$$IV = \frac{(B-S) \times N \times 12.69}{\text{Weight of sample}} \qquad \text{(Eq. 7)}$$

Where, B is the volume in mL of standard $Na_2S_2O_3$ solution required for the blank, S is the volume in mL of standard $Na_2S_2O_3$ solution required for the sample, and N is the normality of the standard $Na_2S_2O_3$ solution.

Saponification value (SV)
The AOAC official method (920.160) was used to determine the saponification value (SV). A 2.5 g of oil or biodiesel sample was heated with alcoholic potassium hydroxide (25 mL, 0.5%) for 30 minutes. The resulting solution was cooled and titrated with an HCl solution (0.5 N) using phenolphthalein as an indicator. The same volume of alcoholic KOH solution without oil was treated as a blank (20). The SV was calculated by using Equation 8.

$$SV = \frac{(B-S) \times N \times 56.1}{\text{Weight of sample}} \qquad \text{(Eq. 8)}$$

Where, B is the volume in mL of standard hydrochloric acid required for the blank; S is the volume in mL of standard hydrochloric acid required for the sample; and N is the normality of the standard hydrochloric acid.

Cetane number (CN)
The calculated SV and IV were employed to calculate the cetane number (CN), which is the capacity of fatty acid methyl esters as a fuel to burn quickly after injection. The greater the value, the better the quality of the ignition. Cetane number is among the crucial factors must be considered when choosing fatty acid methyl esters for biodiesel production (21). The CN was determined by using Equation 9.

$$\text{Cetane Number (\%)} = 46.3 + \frac{5458}{SV - 0.225 \times IV} \qquad \text{(Eq. 9)}$$

Where, SV is the saponification value, and IV is the iodine value.

Refractive index (RI)
An Abbé Refractometer (NYRL-3-Leica Mark, Leica Inc., Buffalo, New York) was used to determine the refractive index of the oil or biodiesel sample (20).

Density
The mass of an empty container weighed using a digital weighing balance to estimate the density of the biodiesel. A 5 mL of the produced biodiesel was added to the pre-weighed container and weighed again. The mass of mass of the biodiesel was calculated by subtructing the mass of the empty container from the mass of the container plus the biodiesel (20). The density was then determined by dividing the sample mass by its volume.

Determination of the Cloud Point
A few drops of biodiesel was poured right into a test tube. Then a thermometer was inserted into the test tube. The setup was put on a beaker containing ice. After a few minutes, the biodiesel was discovered to form a cloud of gel. The temperature at which the biodiesel form a cloud of gel record (22).

Determination of the pour point
The same setup as in the cloud point test was immersed in the ice and left to solidify. The test tube was withdrawn and inverted after the biodiesel form a solid, and the solid was closely examined until it began to flow. The temperature at which the solid biodiesel begin to flow was considered its pour point (22).

Determination of the flash point
A few drops of biodiesel were poured into a flask with a branch opening fitted with a cork. A thermometer was inseted into the flask through the cork with caution the thermometer tip not to contact the bottom of the flask. The biodiesel contained flask produced fume upon heating. The temperature at which the fume ignites considered as the flashpoint temperature (22).

Characterization of Synthesized Catalyst, Purified Oil, and Biodiesel
XRD measuremnts of the prepared catalysts (K_2O/CaO and K_2O/CaO/ZnO) performed to determine their composition and phase. FTIR spectroscopy was used to determine the functional groups present in the biodiesel.

RESULTS AND DISCUSSION

Physicochemical Analysis of Frying Oils
The oxidative breakdown of lipids is accelerated by repeated heating of the oil, creating dangerous reactive oxygen species and decreasing the frying oil's natural antioxidant content (23). The quality of biodiesel depends on the quality of oil used to produce it. The quality of the oil depends on its physi-cochemical properties. Thus, it is crucial to determine the physicochemical properties of the oil to prepare good quality biodiesel.

Physical Properties of Frying Oil
The physicochemical properties of waste frying oil and purified oil were determined to evaluate their suitability for biodiesel production. Table 1 summarizes the obtained results.

Table 1: Physical properties of oils.

Physical properties	Local oil (Hayat)	WFO	PO	AOAC Standard (20)
Moisture (%)	0.2	0.3	0.1	≤ 0.3
Ash (%)	NS	0.2	0.012	0.015
pH at 25 °C	6.5	5	6.32	5-7
Density g/ml) 25 °C	NS	0.644	0.510	0.840
Odor	Agreeable	Unpleasant	Agreeable	Agreeable
State at 25 °C	Smooth-S	Viscous-L	liquid	liquid
Conductivity (µS/cm)	-	0.04	0.5	NS
RI (at 25 °C (nD)	1.4665	1.443	1.3453	1.4694
Color	White-yellowish	Reddish-brown	yellowish	yellowish

WFO= waste frying oil, PO= purified oil, NS=not specified, S=solid

The percentage moisture content of purified oil (0.1%) was lower than waste frying oil (0.3%), but the moisture content of WFO was higher than the raw un-frying oil (0.2%). The higher moisture content can cause difficulties such as water accumulation and growth of microbes in fuel handling and storage, as well as inappropriate post-processing treatment (24). The low moisture content of purified oil samples may improve their storability and suitability (25). The ash value refers to the amount of solid material left behind when the oil burns. The results showed that the WFO samples have a significant amount of ash compared to PO; it indicates a high amount of solid materials left over after frying (25). In addition, the ash value of WFO (0.2%) is much higher than the AOAC standard (0.015) (20). The RI value of oils varies depending on molecular weight, fatty acid chain length, unsaturation, and conjugation. The RI value of the purified oil (1.3453) was lower than that of unpurified oil (1.443). This lower RI of PO can be explained as the oxidation of double bonds of the oil during frying and then up on treatment with hot water reduces the oil unsaturation. The pH of WFO is lower than that of PO (Table 1). The higher pH of PO may be due to the removal of some free fatty acids during the purification. The lower density of PO (0.510 g/mL) indicates that the WFO (0.644 g/mL) had lost some soluble particles upon treatment.

Chemical Properties of Frying Oil
Table 2 gives the chemical properties of WFO and PO oils like AV, FFA, SV, IV, and PV. The acid values (mg/KOH/g) of WFO and PO were 8.42 and 5.61, respectively. The acid values of both WFO and PO oils were higher than the value in the AOAC standard (20). The increase in acid value on WFO may be due to the formation of small monomeric acids and FFA on thermal oxidation. The saponification values (mg/KOH/g) of WFO and PO were 213.2 and 190, respectively (Table 2), where these values are in good agreement with the value given in the AOAC standard (20). The higher the SV of WFO could be due to the presence of lower molecular weight fatty acid in glycerides than that of PO (11). The iodine value (IV) measures the degree of unsaturation in fatty acids. In general, the degree of polymerization increases as the IV of unsaturated fatty acids increases (26).

Table 2: Chemical properties of waste frying and purified oil.

Chemical Properties	Local oil (Hayat)	WFO	PO	AOAC Standard (20)
Acid value(mg/KOH/g)	3	8.42	5.61	≤4.00
% FFA (mg/KOH/g)	1.5	4.208	2.805	≤1.304
Saponification value (mg/g)	190	213.2	190	≥ 180
Iodine value (g/100g)	90	76	69	80-100
Peroxide value (meqO$_2$/kg)	10	13	8	2-10

WFO=waste frying oil, PO=purified oil

The IV of WFO (76 g/100 g) was higher than that of PO (69 g/100 g), but the IV of WFO and PO were less than the AOAC standard. Similarly, the peroxide value of WFO (13 meq/kg) was higher than that of PO (8 meq O$_2$/kg). PV is the most widely used test for determining the state of oxidation in fats and oils. It also indicates the fats/oil's rancidity or degree of oxidation, not its stability. The PV value of WFO was higher than the maximum limit of the AOAC standard (2-10 meq O$_2$/kg), but PO was within the range of the AOAC standard (20). The high PV of WFO may be due to the high moisture content of oil since increased moisture content increases PV.

Physicochemical Properties of Catalysts
Table 3 gives the physicochemical properties of banana peels, eggshells, and the prepared catalysts. The pH values of the raw and the synthesized materials were in the alkaline range (Table 3). The percentage moisture content of banana peels (50%) was higher than that of the eggshell (20%). The ash content of the catalysts was 42% (C.E. S) to 45% (ZnO/B.P /E.S). The highest ash content of the ZnO/B.P/E.S may be due to the impregnation of ZnO.

Table 3: Physicochemical properties of the catalyst.

Physical properties	BP	ES	C.B.P	C.E.S	ZnO/B.P /E.S
pH	9.91	9.33	11.9	8.5	11.81
Moisture content (%)	50	20	-	-	-
Ash content (%)	44	43	42	42	45
Conductivity (µs/cm)	3.5	4.6	2.5	3	2.7
Colour	Black	White	Black	White-black	Bluish
Calcination T(°C)	-	-	700	900	500
Calcination time (h)	-	-	3	3	5

B.P = banana peel, E.S = eggshell, C.B.P= Calcined banana peel, C.E.S= Calcined eggshell

Transesterification of Purified Oils
The transesterification of purified oil was evaluated under the conditions of catalyst weight (1–7 % wt.), temperature 60–80 °C, and methanol to oil ratio of 3:1 to 12:1. For the CaO/K$_2$O catalyst; the highest biodiesel yield (92%) obtained for a 9:1 methanol to oil ratio, at 5% wt catalyst load in 3 h at 65 °C. However, with CaO/K$_2$O-ZnO catalyst, the methanol/oil molar ratio of 9:1 resulted in the highest biodiesel yield (95%) with a 3 % wt catalyst load in 2 h at 65 °C. It means that incorporating ZnO into CaO/K$_2$O catalyst can facilitate the conversion of oil to FAME (biodiesel) and shorten the reaction time. This study resulted in a higher yield of biodiesel (95%) compared to the previously reported by Zuleta et al. (26), which claimed that 2% wt. K$_2$O/CaO-Zinc oxide catalyst showed the highest activity

with a FAME yield of 81% at a 15:1 methanol to oil ratio at a temperature of 60 °C in 4 h. The observed yield difference may be due to the difference in the amount of ZnO presented in the catalyst, the size and purity level of the catalysts.

Effect of Reaction Parameters on the Biodiesel Yield
The parameters that affect biodiesel yield: the methanol to oil ratio, the catalyst load, catalyst reusability, temperature, and reaction time evaluated; the obtained results are given in Figures 1, 2, 3, 4, and 5, respectively.

Effect of Methanol/Purified Oil Ratio
Figure 1 illustrates the influence of the methanol/oil ratio on the formation of methyl ester. The highest

FAME yields were obtained (95%) for 6:1 and 9:1 using CaO/K$_2$O-ZnO (3% wt.), but a 92% yield was obtained using CaO/K$_2$O (5% wt), a 9:1 methanol to oil ratio in 3 h. However, the FAME yield was lower for both CaO/K$_2$O and CaO/K$_2$O-ZnO catalysts in the 3:1 and 12:1 methanol to oil ratios. These indicate that the optimum methanol to oil ratio was 9:1. The results contradicted the one reported by Madhuvil-akku and Piraman (27), the optimum methanol to oil ratio for FAME production is 6:1. This disagreement may be due to the difference in the catalyst, the oil quality, and the reaction condition. On the other hand, the results of this study were in agreement with the results reported by Refaat (28), who prepared biodiesel from waste cooking oil at an optimum 9:1 oil to methanol ratio.
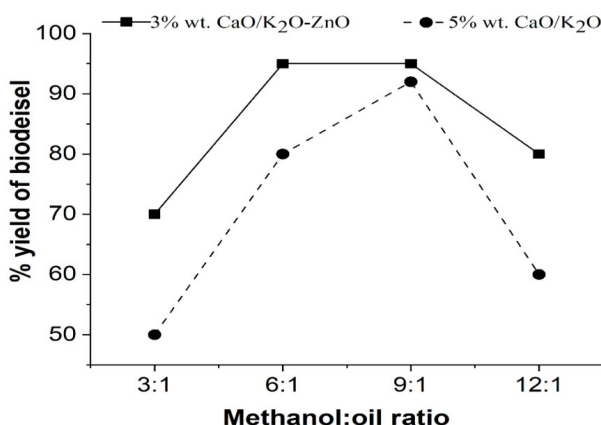

Figure 1: Effect of methanol to oil on biodiesel yield with time 3 h and temperature 65 °C.

Effect of Temperature on Biodiesel Yield

The effect of temperature on the yield of FAME was evaluated using a 9:1 methanol to oil ratio at a fixed reaction time (3 h). At lower temperatures, the FAME conversion efficiency was very low. The temperature around the boiling point of alcohol resulted in the maximum FAME yield. Therefore, 65 °C was the optimum temperature with 95% and 92% FAME yields for CaO/K$_2$O-ZnO (3% wt) and CaO/K$_2$O (5% wt.) catalysts, respectively. The FAME yields decreased as the temperature increased to 80 °C (Figure 2). It may be due to the methanol in the vapor form (beyond its boiling point) less interacting with the oil. The result of this study agrees with the previously reported data by Birla A, et al. 2012 (29) and stated that the reaction temperature must be lower than the boiling point of the alcohol to avoid loss of alcohol through vaporization. Therefore, alcoholysis of vegetable oils is usually carried out at atmospheric pressure at the boiling point of the alcohol.
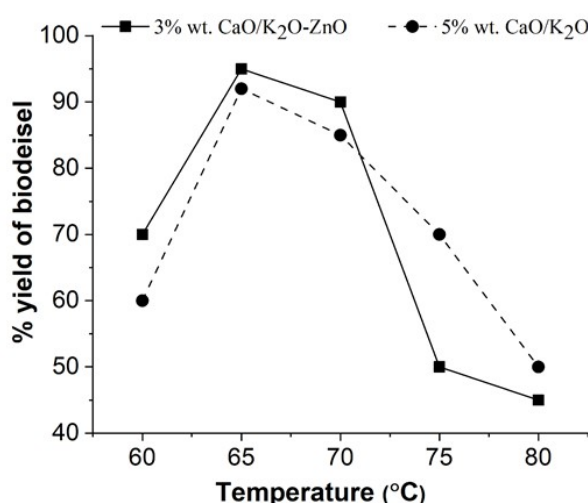

Figure 2: Effect of temperature on biodiesel yield with 9:1 methanol to oil ratio in 3 h.

Effect of Catalyst Load on Biodiesel Yield

The effect of catalyst load on the biodiesel production was evaluated for both CaO/K$_2$O-ZnO and CaO/K$_2$O catalysts with a 9:1 methanol to oil ratio in

3 h reaction time by varying the doses from 1 to 7% wt, keeping the temperature at 65 °C. Figure 3 shows the obtained results. The ZnO doped catalyst

(1%) converted 60% of the oil into FAME, but as the catalyst load increased to 3% wt, the conversion oil to FAME reached 95%.
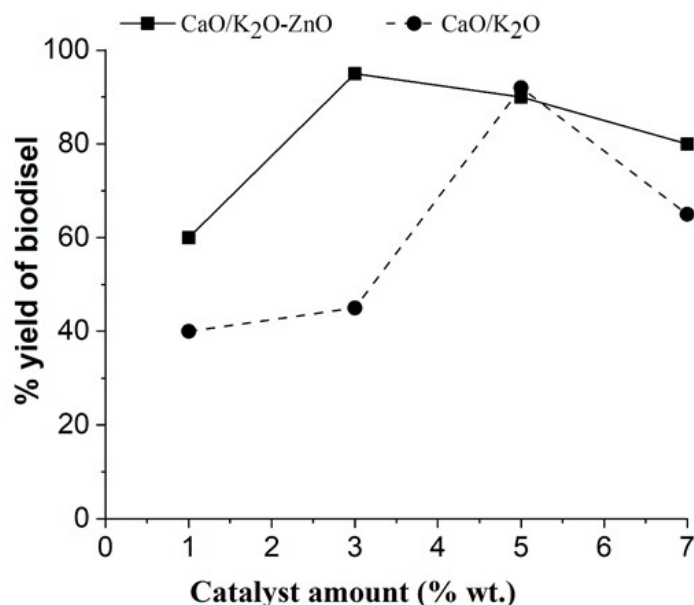

Figure 3: Effect of catalyst load on biodiesel yield with a 9:1 methanol/oil ratio for 3 h at 65 °C.

The result indicates that a 3% CaO/K_2O-ZnO catalyst was sufficient to convert 95% oil to biodiesel with a 9:1 methanol to oil ratio in 3 h. The catalyst without ZnO converts 92% of oil to biodiesel (FAME) with a 9:1 methanol to oil ratio in 3 h. In the previous report, the percentage yield of biodiesel from *Citrullus vulgaris* seeds oil using NaOH as a catalyst was only 70% (19). This variation may be due to the higher amount of NaOH (0.13 g) employed may convert oil to soap rather than biodiesel. Further, increasing the catalyst amount does not increase the yield but may add to the production cost and make the separation process more complex (29).

The Effect of Reaction Time (h) on Biodiesel Yields
The effect of reaction time on the biodiesel formation evaluated using CaO/K_2O-ZnO (3% wt.),and CaO/K_2O (5% wt.) catalysts at constant temperat-

ure (65 °C), methanol to oil ratio of 9:1. Figure 4 illustrates the effect of reaction time on the conversion of oil to biodiesel. The conversion of the oil to biodiesel using either catalyst increased up to 3 h. However, the CaO/K_2O-ZnO catalyst reached 95% conversion in 2 h. These indicate that modifying CaO/K_2O catalyst using ZnO can improve the biodiesel yield and shorten the reaction time. As the reaction time goes beyond 3 h, the conversion of oil to biodiesel decrease for CaO/K_2O-ZnO and CaO/K_2O catalysts. Therefore, a reaction time of 3 h is assumed to be an optimum time for the maximum biodiesel yield for CaO/K_2O-ZnO (3% wt.) and CaO/K_2O (5% wt.) catalysts using methanol and an oil ratio of 9:1 molar ratio at 65 °C. The effective conversion of oil to FAME in a short time using the prepared catalysts is favorable for industrial applications (5).
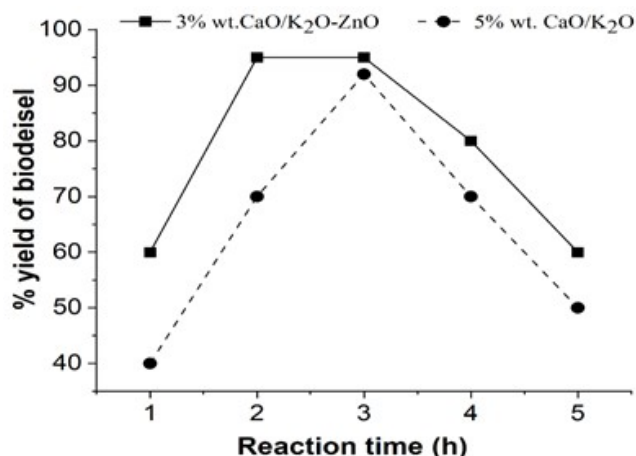
Figure 4: Effect of reaction time (h) on biodiesel yield with 9:1 methanol to oil ratio.

The Effect of Catalysts Reusability on Biodiesel Yields

The reuse of CaO/K_2O and CaO/K_2O-ZnO catalysts in the transesterification PO was evaluated at optimum conditions. Figure 5 shows the obtained results. The spent catalyst was separated using filter paper and washed with methanol. Then, the dried adsorbent was re-activated with a muffle furnace at 500 °C for reuse. The CaO/K_2O-ZnO catalyst resulted in a high yield (95%) of biodiesel in the first cycle, and the catalyst without ZnO converted 92% of the oil to biodiesel. The result was consistent with the previously reported by Navas, M. B. et al. (30); the recycling test of catalyst 0.5 Zn/Mg in the transesterification of castor oil showed a higher yield than in the first cycle.
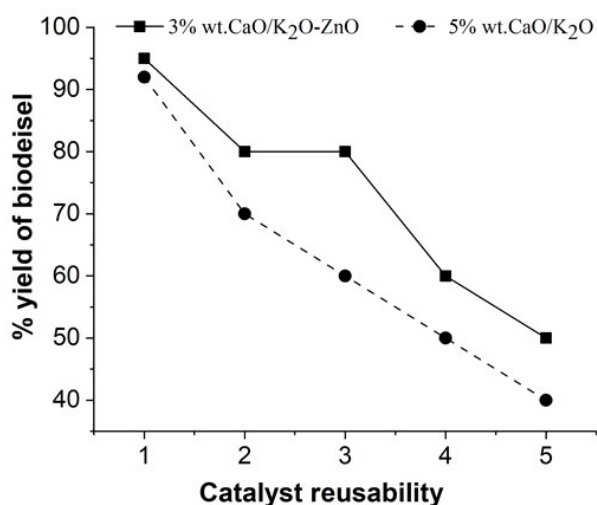

Figure 5: Effect of catalyst reusability on biodiesel yield with methanol: oil of 9:1 for 3 h at 65 °C.

After the first cycle, the percentage yield of biodiesel decreased until the fourth cycle. That is, the efficiency of both catalysts decreased when they were used repetitively. The 3% wt CaO/K_2O-ZnO catalyst could convert 80% of oil to biodiesel in up to 3 cycles. However, the biodiesel conversion efficiency of the CaO/K_2O catalyst declined to 60% in the 3rd cycle. These indicate that modifying CaO/K_2O catalyst with ZnO can improve both the biodiesel yield and durability of the catalyst. The decrease in efficiency of a catalyst for successive cycles in the conversion of oil to biodiesel is because of the active site metal ion leaching into the reaction medium. Bond cleavage and the formation of Ca^{2+} and CH_3O^- ions and leaching into the alcoholic phase are responsible for the loss of active sites (5).

Physicochemical Analysis of Biodiesel

Biodiesel was produced from waste frying oil using 3% wt CaO/K_2O-ZnO and 5% wt CaO/K_2O catalysts. Tables 4 and 5 present the physical and chemical properties of the biodiesel.

Physical Properties of Biodiesel

The physical properties of biodiesel: moisture (%), ash (%), pH, and density (g/cm^3) at 25 °C, cloud point, flash point, and RI are depicted in Table 4. The moisture content of biodiesel prepared using 3% wt CaO/K_2O-ZnO (0.2%) was a lower moisture

content than that of using 5% wt CaO/K_2O (0.5%). The lower moisture content of biodiesel improves its storability and adaptability for long-term preservation (31). The percentage ash content of BPO using CaO/K_2O catalyst (0.02%) was higher than the biodiesel obtained from CaO/K_2O-ZnO (3% wt.)

(0.01%). However, the ash content of produced biodiesels was higher than the ASTM-D6751 standard. The density and refractive index of the prepared biodiesel matched the standard. However, the flash point of the synthesized biodiesel was higher than the standard.

Table 4: Physical properties of biodiesel from 9:1 methanol to oil a period of 3 h.

Physicochemical	BPO using CaO/K_2O (5% wt.)	BPO using CaO/K_2O-ZnO (3% wt.)	Standard [ASTM D6751], (21,29)
Moisture (%)	0.5	0.2	0.050
Ash (%)	0.02	0.01	0.01
pH	5.20	6.35	6.99
Density g/cm^{3}25°C	0.88	0.88	0.82-0.90
Color	Yellowish	Yellowish	Yellowish
Cloud point	1.1	1.2	-3-12
Pour point	1.5	2	-5-10
Flash point	198	150	130
RI(at 25 °C(nD)	1.459	1.457	1.45

BPO= Biodiesel from purified oil, RI = Refractive index.

Chemical properties of Biodiesel

The chemical properties such as AV (mg/KOH/g), %FFA (mg/KOH/g), IV (g/100g), SV (mg/g), PV, and CN were depicted in Table 5. The AV reflects how much lubrication has degraded. A higher AV in the fuel supply system and the internal combustion engine might cause severe corrosion (4, 32). Both the American and European Standards permit a maximum of 0.8 mg KOH/g acid and a minimum of 0.5 mg KOH/g acid. In this study, the AV of the biodiesel was 0.6 and 0.4 mg KOH/g, and the free fatty value was 0.3 and 0.2 mg KOH/g, CaO/K_2O (5 % wt.) and CaO/K_2O-ZnO (3% wt.) catalysts re-

spectively, which is closer to the ASTM-D6751 standard. The %FFA of BPO using CaO/K_2O-ZnO (3% wt.) was lower than BPO using CaO/K_2O (5% wt.), but both BPO using CaO/K_2O (5% wt.) and BPO using CaO/K_2O-ZnO (3% wt.) were less than the ASTM D6751 standard. The iodine value of BPO using CaO/K_2O (5% wt.) and BPO using CaO/K_2O-ZnO (3% wt.) were 77 and 80, respectively. The iodine value of BPO was less than the iodine value of oil from the previously reported study, which is 104 g/100 g. The observed variation may be due to the oil type and the amount of catalyst used (33).

Table 5: Chemical properties of biodiesel from 9:1 methanol to oil a period of 3 h.

Physicochemical	BPO using CaO/K_2O (5% wt.)	BPO using CaO/K_2O-ZnO (3% wt.)	Standard [ASTM D6751], (21,29)
Acid value (mg/KOH/g)	0.6	0.4	$\leq$0.8
%FFA(mg/KOH/g)	0.3	0.2	2.5
Iodine value (g/100g)	77	80	80-106
Saponification value (mg/g)	127.6	182.3	150.1
PV (meq O_2/kg)	4	3	8
Cetane number	79	96.1	$\geq$50

BPO=biodiesel from waste purified oil, PV =peroxide value

Saponification value (SV) indicates the average molecular weight of triglycerides. The lower the SV, the larger the molecular weight of fatty acids in the glycerides (33). The SV of BPO using CaO/K_2O (5% wt) and CaO/K_2O-ZnO (3% wt) were 127.6 and 182.3, respectively. These values are not consistent with the previously reported by Ogunkunle and Ahmed

(34), 167 mg of KOH g/L. The amount of PV in fats indicates primary oxidation and rancidity in oil. The peroxide value increased with increasing moisture content. The PV of BPO using CaO/K_2O (5% wt.) and CaO/K_2O-ZnO (3% wt.) was 4 and 3, respectively. The peroxide value for BPO using CaO/K_2O (5% wt) was higher than that of BPO using

CaO/K$_2$O-ZnO (3% wt). However, the peroxide values of both BPO using CaO/K$_2$O (5% wt) and BPO using CaO/K$_2$O-ZnO (3% wt.) were less than the ASTM-D6751 Standard. The low peroxide and acid values indicate good quality of the biodiesel.

Characterization of Oils, Biodiesels, and Catalyst
The FTIR analysis of PO was only determined because WFO showed a lower potential to make biodiesel. X-ray diffraction spectroscopy (XRD) was em-

ployed to characterize the synthesized catalysts CaO/K$_2$O and CaO/K$_2$O-ZnO that converted oils to biodiesel.

FTIR Characterization of Purified Oil
The FTIR spectra of purified oil showed a peak aaround 3500 cm^{-1} and an intense peak at 2900 cm^{-1} due to OH (emulsified water) and CH$_3$ (sp^3) stretching, respectively, as depicted in Figure 6. The high-intensity peak at 1700 cm^{-1} is assigned to the carbonyl stretching (C=O stretching) of the oil.
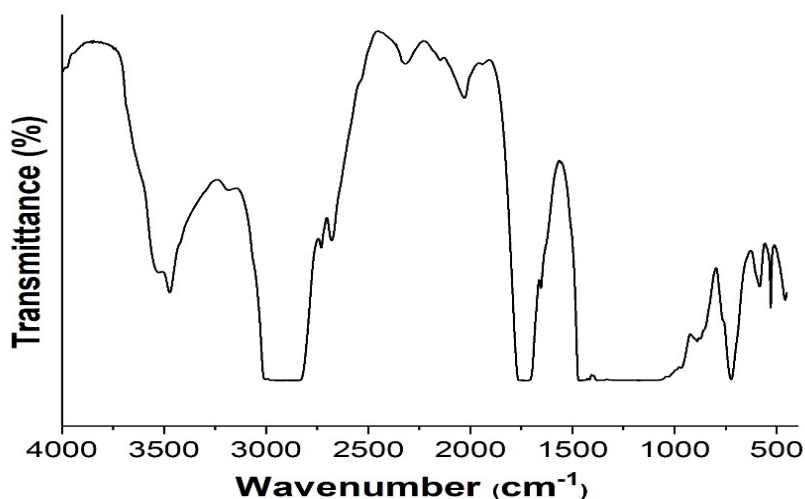

Figure 6: FTIR spectra of purified oil.

FTIR Characterization of Biodiesel
Figure 7 depicts the FTIR spectra of biodiesel from the purified oil. The strong band around 3400 cm^{-1} indicates the OH stretching of the residue alcohol in the biodiesel. Medium intense peaks around 2900 cm^{-1} and 2800 cm^{-1} indicate the presence of CH$_2$

and CH$_3$ groups. The medium peak at 1650 cm^{-1} indicates carbonyl (C=O) stretching of the ester. The peaks at 1416-1470 cm^{-1} were assigned for CH bending of sp^3 carbon. The intense peak around 1100 cm^{-1} indicates the presence of C-O stretching of the ester functional group (35, 36).
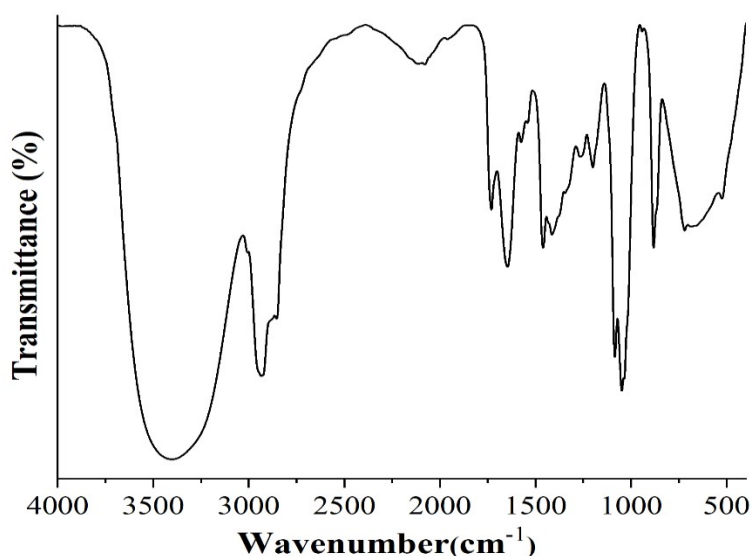

Figure 7: FTIR characterization of biodiesel.

Powder XRD Analysis of Catalysts
The crystalline structures of the prepared CaO/K$_2$O and CaO/K$_2$O-ZnO heterogeneous catalysts were

characterized by using XRD. Figures 8 and 9 shows the obtained results. At a 2 theta angle, the diffraction patterns were recorded in the range of 10º to

90º with a scanning speed of 4º min^{-1} at ambient temperature.

XRD Pattern of CaO/K$_2$O Catalyst

The powder XRD patterns of CaO show that the intensified and narrowed peaks at 2θ angles of 17.5°, 26.3°, 28.13°, 33.5°, 37.3°, 47.1°, and 53.8°, respectively. The K$_2$O impregnation into the CaO catalyst surface (1:1, 5 % wt.) revealed a second peak of intensity at 2θ angles of 23.05°, 25.10°, 28.60º, 33.2°, 40.7º, and 48.90° which assigned to the presence of K$_2$O on the surface of the catalyst, respectively (JCPDS File No. 47-1701; 77-2176) (39). The result matched the (JCPDS File No. 37-1497) and the previous study data (38, 39). However, the observed shift in 2θ degree may be due to the effect of K$_2$O on the crystal surface of the calcium oxide catalyst (Figure 8). The result indicates that the heterogeneous catalyst, CaO/K$_2$O, was successfully produced, and the narrow band indicates the smaller crystalline size of the catalyst (Figure 8).
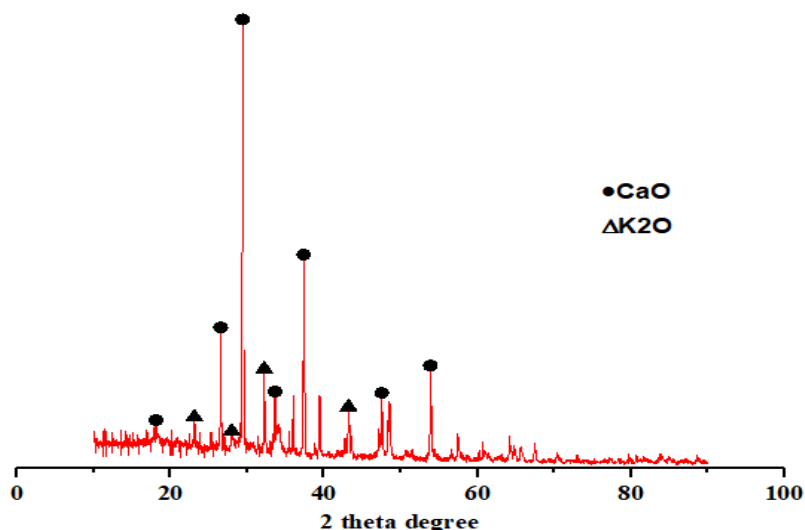

Figure 8: XRD pattern CaO/K$_2$O catalyst.

XRD Pattern of CaO/K$_2$O/ZnO Catalyst

Figure 9 shows the XRD patterns of the prepared catalyst by using a mixture of CaO/K$_2$O and modified with ZnO. After impregnating ZnO into the prepared CaO/K$_2$O catalyst, some of the peaks of CaO and K$_2$O vanished, and others shifted to the higher 2θ value, indicating that the ZnO affects the crystal structure of the CaO/K$_2$O catalyst.
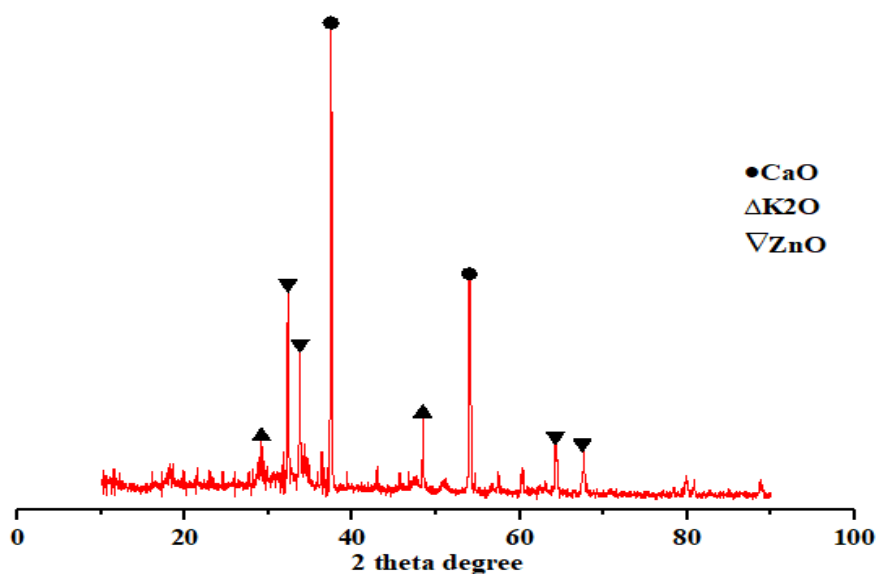

Figure 9: XRD pattern CaO/K$_2$O-ZnO catalyst.

The peak of CaO 2θ at 28.13° in Figure 8 shifted to 37.3°, which may be due to the addition of ZnO affecting the crystal structure of CaO/K$_2$O (Figure 9). The peak at 2θ values of 28.607° and 48.8° corres-

pond to K_2O, similar to peaks observed in the previous report (39). The XRD result showed that the 2θ value of ZnO at 31.6°, 34.52°, 47.31°, 66.21°, and 67.6°, indicating that the ZnO was in the wurtzite hexagonal phase. The shift in the 2θ value on the ZnO peak may be due to the impact of CaO and K_2O.

CONCLUSION

In this study, biodiesel is produced from waste frying oil after purification. Catalysts such as eggshells (CaO) and banana peels (K_2O) were prepared and employed for biodiesel production. The methanol to oil ratios of 6:1 and 9:1 resulted in the highest biodiesel yield (95%) than 3:1 and 12:1 using CaO/K_2O-ZnO catalyst (3% wt), but 9:1 gave the highest product (92%) for the CaO/K_2O at 5% wt catalyst load. It is conceivable to deduce that both catalysts were effective at a 9:1 methanol to oil ratio and yielded the highest biodiesel. The catalyst prepared from eggshell and banana peels (CaO/K_2O) was most effective at a 5% wt load and converted around 92% of the oil to biodiesel. After modification of the CaO/K_2O catalyst with ZnO, the percentage yield of biodiesel increased to 95%. The CaO/K_2O and CaO/K_2O-ZnO were effective up to four cycles resulting in 60 and 50% biodiesel yield, respectively. Transesterification of purified oil with CaO/K_2O-ZnO (3% wt.) and CaO/K_2O (5%) wt.) catalysts at 65 °C produced the highest yield.

REFERENCES

1. Faruque MO, Razzak SA, Hossain MM. Application of Heterogeneous Catalysts for Biodiesel Production from Microalgal Oil—A Review. Catalysts [Internet]. 2020 Sep 7 [cited 2022 Jun 16];10(9):1025. Available from: <URL>.

2. Azócar L, Ciudad G, Heipieper HJ, Navia R. Biotechnological processes for biodiesel production using alternative oils. Appl Microbiol Biotechnol [Internet]. 2010 Oct [cited 2022 Jun 16];88(3):621–36. Available from: <URL>.

3. El Sherbiny SA, Refaat AA, El Sheltawy ST. Production of biodiesel using the microwave technique. Journal of Advanced Research [Internet]. 2010 Oct [cited 2022 Jun 16];1(4):309–14. Available from: <URL>.

4. Lani N.S., Ngadi N., Taib M.R. Parametric study on the transesterification reaction by using cao/silica catalyst. Chemical Engineering Transactions [Internet]. 2017 Apr [cited 2022 Jun 16];56:601–6. Available from: <URL>.

5. Win TT, Khine MM. Synthesis and Characterization of CaO and KF Doped CaO (KF/CaO) Derived from Chicken Eggshell Waste as Heterogeneous Catalyst in Biodiesel Production. ASRJETS [Internet]. 2017;38(2):134–51. Available from: <URL>.

6. Kalligeros S, Zannikos F, Stournas S, Lois E, Anastopoulos G, Teas C, et al. An investigation of using biodiesel/marine diesel blends on the performance of a stationary diesel engine. Biomass and Bioenergy [Internet]. 2003 Feb [cited 2022 Jun 16];24(2):141–9. Available from: <URL>.

7. Thangaraj B, Solomon PR, Muniyandi B, Ranganathan S, Lin L. Catalysis in biodiesel production—a review. Clean Energy [Internet]. 2019 Feb 27 [cited 2022 Jun 16];3(1):2–23. Available from: <URL>.

8. Changmai B, Vanlalveni C, Ingle AP, Bhagat R, Rokhum SL. Widely used catalysts in biodiesel production: a review. RSC Adv [Internet]. 2020 [cited 2022 Jun 16];10(68):41625–79. Available from: <URL>.

9. Lee AF, Bennett JA, Manayil JC, Wilson K. Heterogeneous catalysis for sustainable biodiesel production *via* esterification and transesterification. Chem Soc Rev [Internet]. 2014 [cited 2022 Jun 16];43(22):7887–916. Available from: <URL>.

10. Navas MB, Ruggera JF, Lick ID, Casella ML. A sustainable process for biodiesel production using Zn/Mg oxidic species as active, selective and reusable heterogeneous catalysts. Bioresour Bioprocess. 2020;7:4.

11. Demirbas A, Bafail A, Ahmad W, Sheikh M. Biodiesel production from non-edible plant oils. Energy Exploration & Exploitation [Internet]. 2016 Mar [cited 2022 Jun 16];34(2):290–318. Available from: <URL>.

12. Bach U, Lupo D, Comte P, Moser JE, Weissörtel F, Salbeck J, et al. Solid-state dye-sensitized mesoporous TiO2 solar cells with high photon-to-electron conversion efficiencies. Nature [Internet]. 1998 Oct [cited 2022 Jun 16];395(6702):583–5. Available from: <URL>.

13. Li Y, Jiang Y. Preparation of a palygorskite supported KF/CaO catalyst and its application for biodiesel production *via* transesterification. RSC Adv [Internet]. 2018 [cited 2022 Jun 16];8(29):16013–8. Available from: <URL>.

14. Sivasamy A, Cheah KY, Fornasiero P, Kemausuor F, Zinoviev S, Miertus S. Catalytic Applications in the Production of Biodiesel from Vegetable Oils. ChemSusChem [Internet]. 2009 Apr 20 [cited 2022 Jun 16];2(4):278–300. Available from: <URL>.

15. Birla A, Singh B, Upadhyay SN, Sharma YC. Kinetics studies of synthesis of biodiesel from waste frying oil using a heterogeneous catalyst derived from snail shell. Bioresource Technology [Internet]. 2012 Feb [cited 2022 Jun 16];106:95–100. Available from: <URL>.

16. Ismail SA, Ali RFM. Physico-chemical properties of biodiesel manufactured from waste frying oil using domestic adsorbents. Science and Technology of Advanced Materials [Internet]. 2015 Jun 20 [cited 2022 Jun 16];16(3):034602. Available from: <URL>.

17. Mansir N, Hwa Teo S, Lokman Ibrahim M, Yun Hin TY. Synthesis and application of waste egg shell derived CaO supported W-Mo mixed oxide catalysts for FAME production from waste cooking oil: Effect of stoichiometry. Energy Conversion and Management [Internet]. 2017 Nov [cited 2022 Jun 16];151:216–26. Available from: <URL>.

18. Khan HM, Iqbal T, Ali CH, Yasin S, Jamil F. Waste quail beaks as renewable source for synthesizing novel catalysts for biodiesel production. Renewable Energy [Internet]. 2020 Jul [cited 2022 Jun 16];154:1035–43. Available from: <URL>.

19. Efavi JK, Kanbogtah D, Apalangya V, Nyankson E, Tiburu EK, Dodoo-Arhin D, et al. The effect of NaOH catalyst concentration and extraction time on the yield and properties of Citrullus vulgaris seed oil as a potential biodiesel feed stock. South African Journal of Chemical Engineering [Internet]. 2018 Jun [cited 2022 Jun 16];25:98–102. Available from: <URL>.

20. David F, Matton P. AOAC official methods of Oils and Fats. In: Nutrition & Food Science. 2011. p. 38–43.

21. Sahasrabudhe SN, Rodriguez-Martinez V, O'Meara Meghan, Farkas BE. Density, viscosity, and surface tension of five vegetable oils at elevated temperatures: Measurement and modeling. International Journal of Food Properties [Internet]. 2017 Dec 29 [cited 2022 Jun 16];1–17. Available from: <URL>.

22. Gunstone FD, editor. Vegetable oils in food technology: composition, properties and uses. 2. ed. Oxford: Wiley-Blackwell; 2011. 353 p.

23. Amsalu H, Wondimnew T, Mateos T, Fekadie M, Bogale G. The Effect of Palm Oil-Fried Street Kokor on Liver and Kidney Biomarkers of Swiss Albino Mice. Wertz PW, editor. Journal of Lipids [Internet]. 2020 Dec 4 [cited 2022 Jun 16];2020:1–5. Available from: <URL>.

24. Gnanaprakasam A, Sivakumar VM, Surendhar A, Thirumarimurugan M, Kannadasan T. Recent Strategy of Biodiesel Production from Waste Cooking Oil and Process Influencing Parameters: A Review. Journal of Energy [Internet]. 2013 [cited 2022 Jun 16];2013:1–10. Available from: <URL>.

25. Saeed M, Shola E. Extraction and physico chemical properties of some edible seed oils sampled in Kano metropolis, Kano state. Bayero J Pure App Sci [Internet]. 2016 Jun 2 [cited 2022 Jun 16];8(2):239. Available from: <URL>.

26. Zuleta EC, Baena L, Rios LA, Calderón JA. The oxidative stability of biodiesel and its impact on the deterioration of metallic and polymeric materials: a review. J Braz Chem Soc [Internet]. 2012 Dec [cited 2022 Jun 16];23(12):2159–75. Available from: <URL>.

27. Madhuvilakku R, Piraman S. Biodiesel synthesis by TiO2–ZnO mixed oxide nanocatalyst catalyzed palm oil transesterification process. Bioresource Technology [Internet]. 2013 Dec [cited 2022 Jun 16];150:55–9. Available from: <URL>.

28. Refaat AA. Biodiesel production using solid metal oxide catalysts. Int J Environ Sci Technol [Internet]. 2011 Dec [cited 2022 Jun 16];8(1):203–21. Available from: <URL>.

29. Hamester MRR, Balzer PS, Becker D. Characterization of calcium carbonate obtained from oyster and mussel shells and incorporation in polypropylene. Mat Res [Internet]. 2012 Feb 14 [cited 2022 Jun 16];15(2):204–8. Available from: <URL>.

30. Navas MB, Ruggera JF, Lick ID, Casella ML. A sustainable process for biodiesel production using Zn/Mg oxidic species as active, selective and reusable heterogeneous catalysts. Bioresour Bioprocess [Internet]. 2020 Dec [cited 2022 Jun 16];7(1):4. Available from: <URL>.

31. Patel A, Arora N, Sartaj K, Pruthi V, Pruthi PA. Sustainable biodiesel production from oleaginous yeasts utilizing hydrolysates of various non-edible lignocellulosic biomasses. Renewable and Sustainable Energy Reviews [Internet]. 2016 Sep [cited 2022 Jun 16];62:836–55. Available from: <URL>.

32. Che Hamzah NH, Khairuddin N, Siddique BM, Hassan MA. Potential of Jatropha curcas L. as Biodiesel Feedstock in Malaysia: A Concise Review. Processes [Internet]. 2020 Jul 6 [cited 2022 Jun 16];8(7):786. Available from: <URL>.

33. Atabani AE, Silitonga AS, Badruddin IA, Mahlia TMI, Masjuki HH, Mekhilef S. A comprehensive review on biodiesel as an alternative energy resource and its characteristics. Renewable and Sustainable Energy Reviews [Internet]. 2012 May [cited 2022 Jun 16];16(4):2070–93. Available from: <URL>.

34. Ogunkunle O, Ahmed NA. Overview of Biodiesel Combustion in Mitigating the Adverse Impacts of Engine Emissions on the Sustainable Human–Environment Scenario. Sustainability [Internet]. 2021 May 13 [cited 2022 Jun 16];13(10):5465. Available from: <URL>.

35. Banerjee S, Kumar S, Mandal A, Naiya TK. Design of novel chemical solvent for treatment of waxy crude. International Journal of Oil, Gas and Coal Technology. 2017;15(4):363–79.

36. Schönemann A, Edwards HGM. Raman and FTIR microspectroscopic study of the alteration of Chinese tung oil and related drying oils during ageing. Anal Bioanal Chem [Internet]. 2011 May [cited 2022 Jun 16];400(4):1173–80. Available from: <URL>.

37. Istadi I, Mabruro U, Kalimantini BA, Buchori L, Anggoro DD. Reusability and Stability Tests of Calcium Oxide Based Catalyst (K2O/CaO-ZnO) for Transesterification of Soybean Oil to Biodiesel. Bull Chem React Eng Catal [Internet]. 2016 Mar 10 [cited 2022 Jun 16];11(1):34. Available from: <URL>.

38. Taufiq-Yap YH, Lee HV, Hussein MZ, Yunus R. Calcium-based mixed oxide catalysts for methanolysis of Jatropha curcas oil to biodiesel. Biomass and Bioenergy [Internet]. 2011 Feb [cited 2022 Jun 16];35(2):827–34. Available from: <URL>.

39. Navas MB, Ruggera JF, Lick ID, Casella ML. A sustainable process for biodiesel production using Zn/Mg oxidic species as active, selective and reusable heterogeneous catalysts. Bioresour Bioprocess [Internet]. 2020 Dec [cited 2022 Jul 19];7(1):4. Available from: <URL>.

RESEARCH ARTICLE

QSAR Studies on Nitrobenzene Derivatives using Hyperpolarizability and Conductor-like Screening Model as Molecular Descriptors

A. N. Alias[*] iD , Z. M. Zabidi iD

Faculty of Applied Sciences, Universiti Teknologi MARA Perak Branch Tapah Campus, 35400 Tapah Road Malaysia

Abstract: Nitrobenzene derivatives are organic compounds that have been widely synthesized and used in chemical industries such as the polymer industry, lumber preservatives, textile industry, pesticides, and warlike weapons industry. The rapid growth of nitrobenzene derivatives in the industry requires research into the effects of toxicity in the environment. Quantitative structure-activity relationship (QSAR) models were useful in understanding how chemical structure relates to the toxicology of chemicals. In the present study, we report quantum molecular descriptors using conductor-like screening model (COs) area, the linear polarizability, first and second order hyperpolarizability for modelling the toxicology of the nitro substituent on the benzene ring. All the molecular descriptors were performed using semi-empirical PM6 approaches. The QSAR model was developed using stepwise multiple linear regression. We found that the stable QSAR modelling of toxicology of the benzene derivatives used second order hyper-polarizability and COs area, which satisfied the statistical measures. Second order hyperpolarizability shows the best QSAR model with the value of $R^2 = 89.493\%$, $r^2 = 68.7\%$ and $r_{cv}^2 = 87.52\%$. We also found that the substitution of functional group in the nitrobenzene derivative for second order hyperpolarizability has the same sequence which was the γ ortho < γ meta < γ para. These has made that the second order hyperpolarizability was the best descriptors for QSAR model.

INTRODUCTION

Nitro substituent on the benzene ring (nitrobenzene derivatives) constitutes an organic compound that has been widely synthesized and used in the chemical industry. Nitrobenzene derivatives have been used as depolymerizing agents in the polymer industry to lower molecular weight (1). Nitrobenzene derivatives have also been shown to be good as a lumber preservative (2). The textile industry uses nitrobenzene derivatives- in the manufacturing and processing of textiles, particularly in the wet processing of textiles (3). Modern pesticides typically contain a nitrobenzene derivative as their active ingredient, which protects plants and crops (4). Nitrobenzene-based explosives, which are often low in sensitivity and great in performance, have been utilized in warlike weapons as one sort of explosive (5).

Nitro group substituents show strong electron-withdrawing effects. It also belongs to the chemical class of compounds with bioactivation (6). Therefore, nitro substituents in benzene are responsible for a number of toxicities and adverse environmental effects (7). The rapid use of these chemicals necessarily requires knowledge of their effects on human and environmental safety and health. For example, o-nitrophenols are toxic to plants, fish, and many other organisms. They can accumulate in the food chain, pose potential risks to both human health and the environment (8). Nitrobenzene derivative has also been linked to carcinogenesis, mutagenesis, skin sensitization, and hepatotoxicity (9). Therefore, the useful understanding of this material on the mechanism and action of toxicity is still going strong (10-12).

The biological properties of organic materials are strongly related to their geometrical and electronic structures. Studies of quantitative structure activity relationships (QSAR) are one of the most important fields in computational chemistry because they can be used to investigate the relationships between biological activity and organic materials. A QSAR is a mathematical representation of biological activity in terms of numerical molecular descriptors. Each numerical molecular descriptor must be invariant to represent the molecular structure. The molecular descriptors are the physical and chemical characteristics of molecules, such as topological index, 3D-molecular geometrical information, thermodynamics descriptors, quantum-chemical descriptors, and constitution descriptors (13). In a wide range of applications, QSAR enables faster and more cost-effective models for new molecular designs. In QSAR, partitioning properties are typically utilized as descriptors. However, the availability and veracity of experimental data limit their application.

The quantum molecular descriptors provide an alternative for molecular descriptors. The quantum molecular descriptors are more accurate and detailed description to relate with biological activity (14). The quantum molecular descriptors using ab initio model Hamiltonian calculation such multiconfiguration self-consistent field, Moller-Plesset theory of variation or correlated pair many-electron theory (15). As an alternative to ab initio methods, density function theory and semi-empirical quantum chemistry method are practicable for molecular

descriptors. The net atomic charges, the HOMO-LUMO energy gap, chemical hardness, and chemical potential, in particular, have been used to correlate with various biological activities (16,17). Chemical hardness and chemical potential are strongly influenced by HOMO and LUMO energies (18,19). These energies need to consider electronic reorganization in the excited state, which may often lead to conceptually incorrect results for the prediction of QSAR (17).

Semiempirical methods are based on Hartree–Fock formalism omit some molecular integral calculations. For instance, the approximation of zero differential overlap (ZDO) reduces the number of multicenter integrals. Numerous approaches have been introduced to improve the calculation's accuracy, including CNDO, NDDO, INDO, and MINDO (20). Semiempirical methods also have been widely used in the application of QSAR/QSPR because they are significantly faster than ab initio and DFT approaches, particularly for large molecule calculations. Several software, such as MOPAC, AMPAC, SPARTAN, and VAMP, has been developed to perform these semi-calculations. Wang et. al. has implemented semi-empirical method using MOPAC software to investigate toxicity endpoints for a wide range of compound (21). Adinin et al. also used the same software to generate quantum molecular descriptors of physicochemical properties of isothiocyanate antimicrobials (22).

The purpose of the present work was to study the polarizability, first and second order hyperpolarizability as molecular descriptors for modeling the toxicology of the nitro substituent on the benzene ring (nitrobenzene derivatives). Dipole moment is an important aspect in determining how a chemical reaction affects in the biological system. Polarizability, hyperpolarizability, and the surface of charge dispersion are both related to dipole moment. A conductor-like screening model (COs) area as a new class of molecular descriptors is also introduced in this paper. To the best of our knowledge, there are no studies using these descriptors for modeling the toxicology of the nitrobenzene derivatives. We performed our calculation using well-established semiempirical electronic structure program known as MOPAC. The semi-empirical quantum chemical calculation was based on the self-consistent field method to calculate the electronic and molecular orbital properties.

These calculations were much faster than ab initio and less time-consuming.

METHOD AND CALCULATION

$$W(E) = W(0) - \mu_{i0}E_i - \frac{1}{2!}\alpha_{ij}E_iE_j - \frac{1}{3!}\beta_{ijk}E_iE_jE_k - \frac{1}{4!}\gamma_{ijkl}E_iE_jE_kE_l - \cdots$$

(Eq. 1)

where μ_{i0} is a component of dipole moment and α_{ij} is a tensor linear polarizability and α_{ij} is a tensor linear polarizability. The parameters β_{ijk} and γ_{ijkl} in Eq. 1 are the components of the first and second order hyperpolarizability. The ijkl suffixes denote as Cartesian component

Calculation of the Quantum Molecular Descriptors

Molecular hyperpolarizability is primarily related to their role in nonlinear optics. Polarizability is related to a molecule's energy in an external field. The energy as a function of the external field (E) can be expressed as a power series as

implying over the X, Y, and Z axes. The component of the total dipole moment can be obtained using the derivation of energy with respect to the field. The series of molecular dipole moments can be written as (1).

$$\mu_i(E) = \mu_{i0} + \alpha_{ij}E_i + \frac{1}{2!}\beta_{ijk}E_iE_k + \frac{1}{3!}\gamma_{ijkl}E_jE_kE_l + \cdots$$

(Eq. 2)

The expression in (Eq. 2) represents the response of a dipole moment to an applied electric field of third order in the field. The coefficient on α_{ij}, β_{ijk} and γ_{ijkl} can be obtained using finite field or perturbation method. In this calculation we implemented finite field method by Kurtz et al. (23). The value of linear polarizability was a tensor diagonal vector in x, y or z and it is given by Eq. 3 (23).

$$\alpha = (\alpha_{xx} + \alpha_{yy} + \alpha_{zz}) / 3 \qquad (Eq. 3)$$

The average of first order hyperpolarizability, β and second order (γ) hyperpolarizability for the interest value at 0.25 eV were given by Eq. 2 and 3, respectively.

$$\beta = (\beta_{xxx} + \beta_{yyy} + \beta_{xzz}) \qquad (Eq. 4)$$

$$\gamma = 1/5 \ [\ (\ \gamma_{xxxx} + \gamma_{yyyy} + \gamma_{zzzz}) \ + 2(\gamma_{xxyy} + \gamma_{xxzz} + \gamma_{yyzz} \ (Eq. 5)$$

Conductor-like screening model (COs) area is related with the surface charge densities on the adjacent segments. The surface charge of a molecule is distributed on the molecule's interface. The charge distribution causes the localized charge distribution on the surface. The localized charge in the molecule may disrupt the Coulombic interaction, which 'screens' the polarization in the molecule. As a result, the screening is dependent on charge localization and molecular polarizability (16). The COs area is an effective area of the screening surface. We use the Klamt algorithm, which has been modified

from the dielectric polarized continuum mode, to calculate the COs area (24).

The molecular structures were generated using Avogadro version 1.2.0. Next, the geometric optimization was performed using the force field method MMFF94s with a step per update of 4. In this work, we use the parameterization of parametric method 6 (PM6) as the integration method (25). All the calculations were calculated using Semi-empirical MOPAC2016, Version: 21.002 James J. P. Stewart software. MOPAC programs implement the value and components of dipole moments, conductor-like screening model (COs) area, polarizability (α), first order (β) and second order (γ) hyperpolarizability (23). In the QSAR calculation, the linear polarizability constant was calculated using 0.25 eV.

Experimental Data

For the present work, we chose a data set of aquatic toxicity of benzene derivatives of ciliated protozoan *Tetrahymena pyriformis* which was retrieved from Fatemi and Malekzadeh (27). Toxicity is represented in terms of $\log(1/IGC_{50})$, where "IGC_{50}" refers to a concentration that inhibits growth for two days at 50 percent of its normal rate. In this study, a total of 120 nitrobenzene derivatives were investigated. The nitrobenzene derivatives compounds and their corresponding $\log(1/IGC_{50})$ values are listed in Table S1.

Statistical Analysis
Multiple linear Regression: The quantum molecular descriptors (input data) were normalized using Eq. 6.

$$I_i = \frac{I_x - I_{min}}{I_{max} - I_{min}}$$

(Eq. 6)

where I_x unnormalized input data, I_{max} was the maximum value of the sample, and I_{min} was the minimum value of value of the sample (28). The structure-toxicity models were developed using multiple linear regression, which was a simple approach for modelling the linear relationship between independent and dependent variables by fitting the linear equation. The Simple Linear Regression equation was stated as in Equation 7:

$$y = b_o + b_1 x_1 + ... + b_n x_2$$

(Eq. 7)

where b_o was the intercept; b_1 and b_n was coefficient; x_1 and x_n was the independent descriptors, and y was the predictive (calculated) values. The multiple regression was calculated using the stepwise selection method with an alpha to enter and remove value of 0.25. We perform regression using the statistical software Minitab. The plot of observed vs. calculated toxicity with a 95% prediction index was plotted using Minitab.

Model evaluation and validation: The R^2 was the coefficient of determination, which describes how much of the variability of dependent y was explained by the independent variable of x. In other words, r^2 indicates how well the model predicts the variance of the independent variable explained. The value of R^2 (also called Pearson's r) was computed using equation (8).

$$R^2 = 1 - \frac{\Sigma(y_i - \hat{y})^2}{\Sigma(y_i - \bar{y})^2}$$

(Eq. 8)

where y is the y is the observed response variable, $\hat{y}$ was prediction (calculated) value, $\bar{y}$ was the mean value of y. Another indicator we use in this work was r^2 value which was a dimensionless goodness-of-fit indicator between linear graph of $y_{exp.}$ and $y_{cal.}$. The Variance Inflation Factor (VIF) was a measure of the indicator for multi-collinearity, commonly stated as:

$$VIF = \frac{1}{1 - R^2}$$

(Eq. 9)

where R^2 was the correlation coefficient calculated form Equation (9). Table 1 shows the rule for interpreting the value of VIF (29).

Table 1: VIF interpretation.

VIF value	Condition
VIF = 1	Not correlated
1 < VIF ≤ 5	The related model is acceptable
5 < VIF < 10	The multicollinearity is substantial
VIF ≥ 10	The related model is unstable, and recheck is necessary

Internal validation was accomplished through the employment of leave-one-out cross validation. The dataset was divided into two sets as training set and test set. This procedure was carried out by leaving one sample from the data set and using the other data samples as the training set, while the testing sample was included in the data set. The procedure was repeated until all data samples had been used as the testing set. The square of cross-validation coefficient (q^2) for LOO-CV is calculated using Eq. 10.

$$q^2 = 1 - \frac{\sum_{i=1}^{training}(y_i - \hat{y}_i)^2}{\sum_{i=1}^{training}(y_i - \bar{y})^2}$$

(Eq. 10)

where y_i, $\hat{y}_i$, and $\bar{y}$ are, respectively, the measured, predicted, and averaged values of the respective testing set.

The developed model was validated further in order to assess its prediction competency using the test and training sets. The k-fold cross validation technique is also useful for

validating QSAR models (30). The k-fold cross validation procedure can give an optimized prediction performance in QSAR (31). The k-fold cross-validation the resampling the data to determine the ability of predictive models. The dataset was divided randomly into k-partition with equal size of segments of fold for training and test set of data. The recommended value for k was 10 (32). In our work, we used 10-fold to holdout with an iteration process of 10 times. The training dataset was commanded to make predictions about the data in the validation fold. Thus, we have used the parameters of the k-fold cross-validated correlation coefficient (r_{cv}^2) for regression validation.

RESULTS

In this work, non-linear optical properties of molecules have been used, that was, polarizability, first and second order hyperpolarizability. The molecular descriptor of polarizability involves three components: α_{xx}, α_{yy} and α_{zz}. The perturbed external electrical field for first order hyperpolarizability involved β_{xxx}, β_{xyy}, β_{xzz}, β_{yxx}, β_{yyy}, β_{yzz}, β_{zxx}, β_{zyy} and β_{zzz}. While the perturbed external electrical field for second order hyperpolarizability involved γ_{xxxx}, γ_{yyyy}, γ_{zzzz}, γ_{xxyy}, γ_{xxzz}, γ_{yyxx}, γ_{yyzz}, γ_{zzxx}, and γ_{zzyy}. Polarizability and hyperpolarizability were related to the coordinate axis of molecular

polarization. The calculated polarizability, first order and second hyperpolarizability, conductor-like screening model (COs) area, and dipole moment molecule using MOPAC were tabulated in supplementary Table S1-S3. The quantum molecular descriptors were implemented into the QSAR relationship using stepwise selection regression. In the stepwise regression method, polarizability, first and second order hyperpolarizability, and constant reassessment via their partial F (or t) statistics. The linear regression for polarizability was given in Equation (8).

$$\log(1/IGC_{50}) = 1.223\ \alpha_{xx} + 1.547\ \alpha_{yy}$$
(Eq. 8)

$$n = 70,\ R^2 = 89.21\%,\ s = 0.3590,\ F = 280.99,\ q^2 = 0.677065.$$

The stepwise regression indicates two polarizability descriptors were significant. However, the value of VIF for α_{xx} and α_{yy} was more than 5 (6.70). This modeling equation was too highly correlated, which means multicollinearity was substantial. Figure 1(a) shows the correlation between the experimental and calculated values of $\log(1/IGC_{50})$ obtained from α_{xx} and α_{yy}. The plot shows the r^2 of experimental and calculated $\log(1/IGC_{50})$ was 67.7%. Figure 1(b) shows the residual plot versus the calculated value.

Figure 1: Plot of (left) experiment vs calculated $\log(1/IGC_{50})$ using linear polarizability. (Right) the residual plot with the calculated value.

The molecular descriptor for first order hyperpolarizability calculated from semi-empirical calculation has nine descriptors. The stepwise regression method determined the five values of descriptors that were significant

to the toxicology of benzene derivatives. The QSAR relationship obtained was given by Eq. 9.

$$\log (1/IGC_{50}) = 1.216\, \beta_{xxx} + 0.763\, \beta_{xzz} + 1.107\, \beta_{yyy} + 0.992\, \beta_{zyy} \quad \text{(Eq. 9)}$$

$n = 70$, $R^2 = 59.79\%$, $s = 0.70337$, $F = 24.53$, $q^2 = 0.0784$.

The VIF value for β_{xxx}, β_{xzz}, β_{yyy}, β_{zyy} were 1.52, 1.27, 1.46 and 1.27 respectively. The plot of experimental vs calculated $(1/IGC_{50})$ using first order hyper-polarizability is shown in Figure 1(b). The r^2 value using first order hyper-polarizability as molecular descriptor was 5.9%.

The second order hyperpolarizability calculated from semi-empirical calculation also has nine descriptors. There were four values of descriptors that were significant to the toxicology of benzene derivatives. The second order hyperpolarizability relationship yields an equation:

$$\log (1/IGC_{50}) = 1.203\, \gamma_{yyyy} + 0.587\, \gamma_{zzzz} + 1.247\, \gamma_{xxzz} - 1.276\, \gamma_{yyxx} \quad \text{(Eq. 10)}$$

$n = 70$, $R^2 = 89.493\%$, $s = 0.359559$, $F = 140.52$, $q^2 = 0.68453$

with the VIF value for γ_{yyyy}, γ_{zzzz}, γ_{xxzz} and γ_{yyxx} were 2.31, 1.29, 4.91 and 3.01 respectively. The plot of experimental vs calculated $(1/IGC_{50})$ using first order hyper-polarizability is shown in Figure 3 and the r^2 value of this plot was 68.7%.
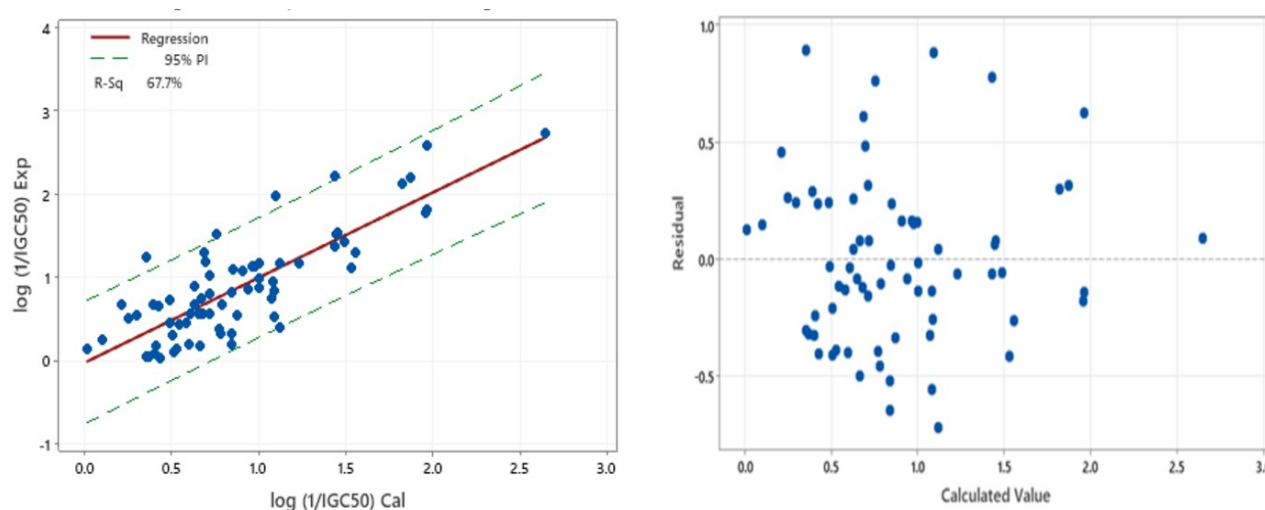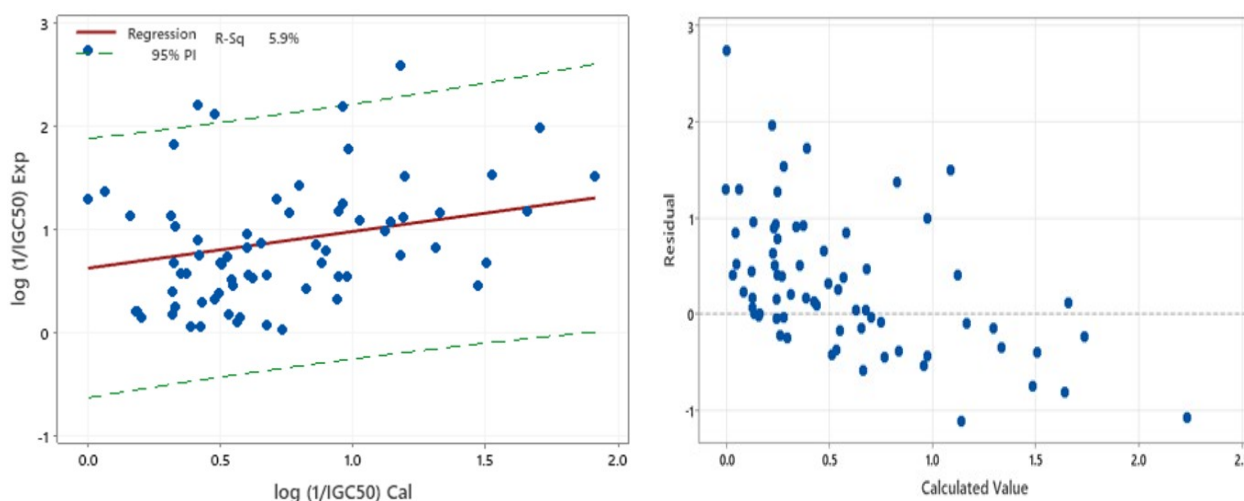

Figure 2: Plot of (left) experiment vs calculated $\log(1/IGC_{50})$ using first order hyperpolarizability. (Right) the residual plot with the calculated value.
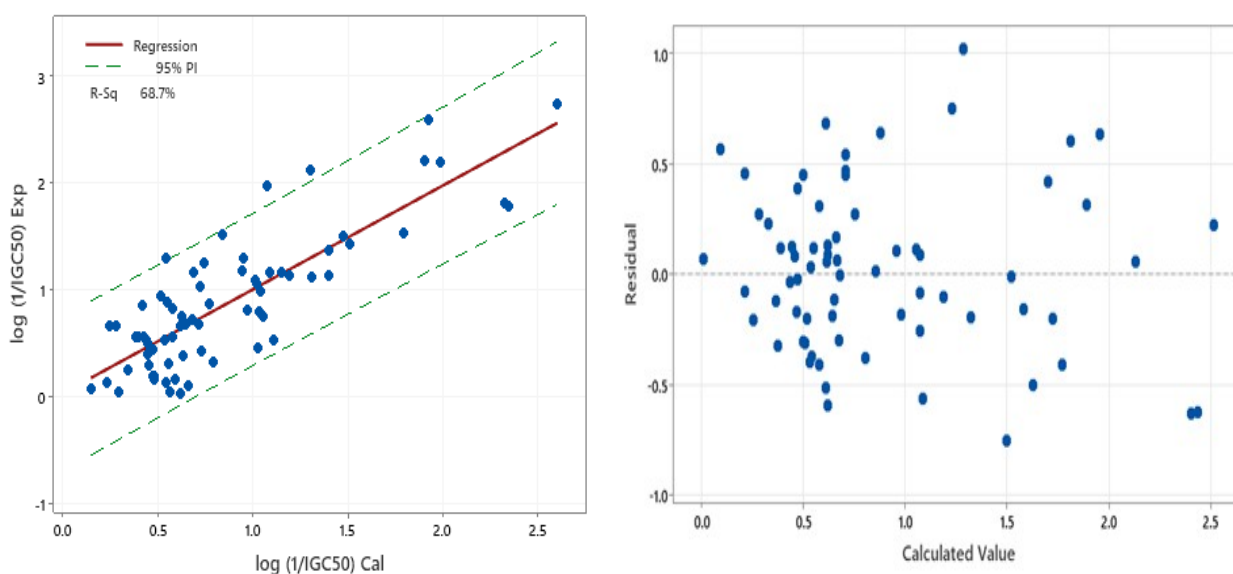

Figure 3. Plot of (left) experiment vs calculated $\log(1/IGC_{50})$ using second order hyperpolarizability. (Right) the residual plot with the calculated value.

The relationship between conductor-like screening model (COs) area and dipole moment with toxicology has been tested. In semiempirical calculation, two types of dipole moment were identified: the dipole moment net charge density and the hybrid. Only the dipole moment net charge density (μ_c) correlated well with COs area, indicating a good correlation with toxicology. The relationship was given by:

$$\log (1/IGC_{50}) = -0.264\,\mu_c + 2.335\,\text{Cos} \tag{Eq. 11}$$

$n = 70$, $R^2 = 87.04\%$, $s = 0.3935$, $F = 228.26$, $q^2 = 0.615627$.

Both the Cos area and μ_c have a VIF value of 3.06. The plot of experimental vs calculated ($1/IGC_{50}$) using Cos area and dipole moment net charge density is shown in Figure 4. The r^2 value for this plot was 61.4%.
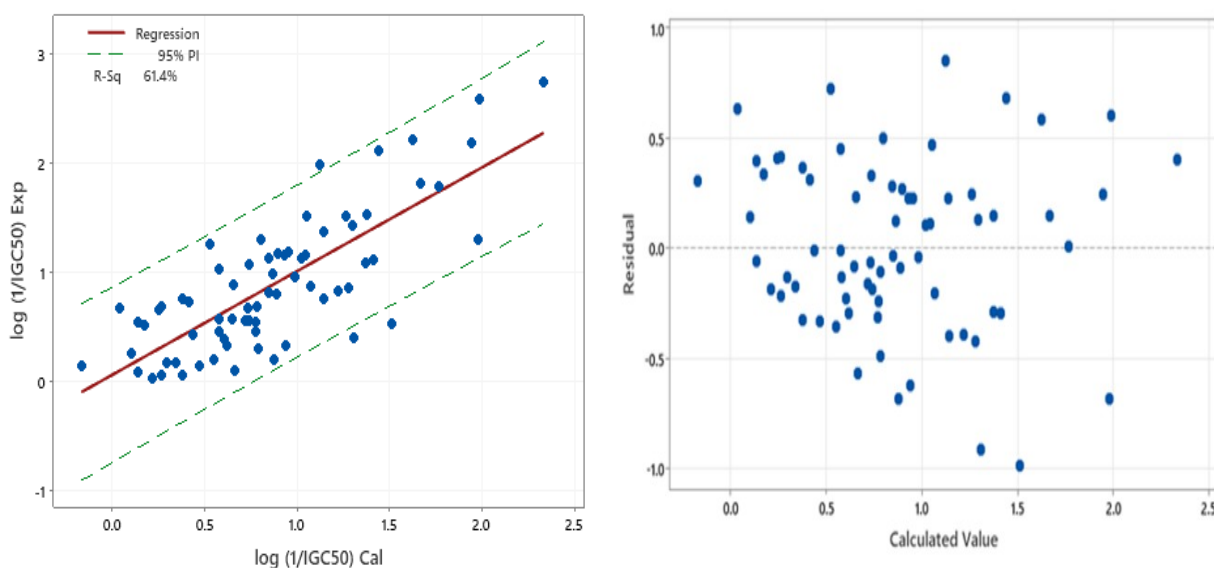

Figure 4: Plot of (left) experiment vs calculated $\log(1/IGC_{50})$ using Cos and dipole moment; (right) the residual plot with the calculated value.

The k-fold cross-validation has been used to check the stability of the QSAR model. A acceptable range of relative deviation of the r^2_{cv} of k-fold cross-validation with r^2 was ±2% (33). The values of r^2_{cv} for polarizability, first and second order hyper-polarizability were 88.78%, 55.2% and 87.52% respectively. While the value of r^2_{cv} for Cos area and dipole moment net charge density was 86.71%. All model relative deviation were in the acceptance range except for second order hyper-polarizability. The F value for polarizability, second order hyper-polarizability, Cos area and dipole moment net charge density has a value greater than 95, which has good levels of significance (34). In addition, the fitting of the experimental and calculated ($1/IGC_{50}$) has an r^2 value for polarizability, second order hyper-polarizability, Cos area, and dipole moment net charge density greater than 0.6 (34). The results also show that the q^2 for all descriptors except first order hyperpolarizability has a value greater than 0.5, which was the acceptance range for the QSAR model. Since

the VIF of α_{xx} and α_{yy} was 6.70 the multicollinearity was substantial. Therefore, the stable QSAR modeling for toxicology of benzene derivatives used second order hyper-polarizability, COs area and dipole moment net charge density as molecular descriptors, which satisfied the statistical measures.

DISCUSSION

The toxicology of the nitrobenzene derivative elaborated QSAR model reveals that the electronic properties such as polarizability, hyper-polarizability, dipole moment, and conductor-like screening model (COs) area have an impact on this study. In quantum molecular calculations, the polarizability, hyper-polarizability, and dipole moment were calculated based on the non-linear optical properties of molecules whose induced frequency energy that we used to represent the external electric field was 0.25 eV. The interaction dipole moment of a molecule with the field was dependent on the permanent dipole moment, polarizability (α), first order

hyper-polarizability (β) and second order hyper-polarizability (γ). The linear response of electronic charge distribution can be described by linear polarizability. Molecular linear polarizability was related to charge distribution in the molecules. The linear polarizability was very closely linked to intermolecular forces, electronic interaction inside the molecule, and chemical reactivity, among other things (35). Tandon et al. also reported that linear polarizability has a good correlation with chemical-biological activity of anaesthetics and drugs for blocking activities (36). Furthermore, hydrophobicity was found to be directly related to molecular linear polarizability (37).

The expected relationship between substituent properties and calculated first order hyperpolarizabilities will be seen to require a more detailed electronic population analysis. The first order hyperpolarizability has showed a low stability model with a value of r^2 = 59.79%. The first order hyperpolarizability also showed low stability and aquatic toxicity of hydrocarbons (EC_{50}) to aquatic organisms (16).

The conductor-like screening model (COs) area with molecular dipole moment net charge density was a surprisingly good fit for toxicity. The COs area was proportional to the surface charge densities of the surrounding segments of molecules. It was the effective area of the screening surface of the charge density on a van der Waals-like surface. The screening surface was correlated to the perturbation of Coulombic interaction in the molecule. The screening surface was dependent on the localization of charge and the polarizability of the molecule (16). While, molecular polarization was contributed by electronic charge, molecular vibration, and rotation, which reflect the molecular dipole moment.

In QSAR, the effect of substitution in the nitrobenzene structure was of great importance to obtain the best molecular descriptor. To confirm the influence of molecular structure on this nitrobenzene, we have performed a comparison of polarizability, hyperpolarizability, and COs area to the meta, ortho, and para-substituents for aniline (NH_3), phenol (OH), chloro, bromo, methyl (CH_3), fluoro, nitrile (CN) and methoxy (OCH_3) as shown in Figure 5. As seen clearly, the effect of meta, ortho, and para-substituents has significant changes to linear polarizability, second order hyperpolarizability, and COs area. The value of linear polarizability has the sequence α ortho < α meta < α para except for fluorobenzene and nitroanisole. For the second order hyperpolarizability, all the nitrobenzene has the same sequence that was the γ ortho < γ meta < γ para. This has made that the second order hyperpolarizability has the highest value of r^2. The COs area of nitrobenzene has the sequence COs ortho < COs para < Cos meta except for nitroaniline, nitroanisole, fluoronitrobenzene and nitrobenzeldehyde. Fluoronitrobenzene and nitrobenzaldehyde have nearly the same value of COs area for meta and para. While the sequence of the substituents from anisole to nitrobenzene was para < ortho < meta. For the first order hyperpolarizability, the substitutional of functional groups was difficult to expect. This might be due to the substitutional of para, meta, or ortho inducing the charge transfer effect in the first order hyperpolarizability calculation (38). This means there was no suitable sequence of the substitutional of para, meta, or ortho. In this case, the first order hyperpolarizability was not a good molecular descriptor for QSAR because it was too high.
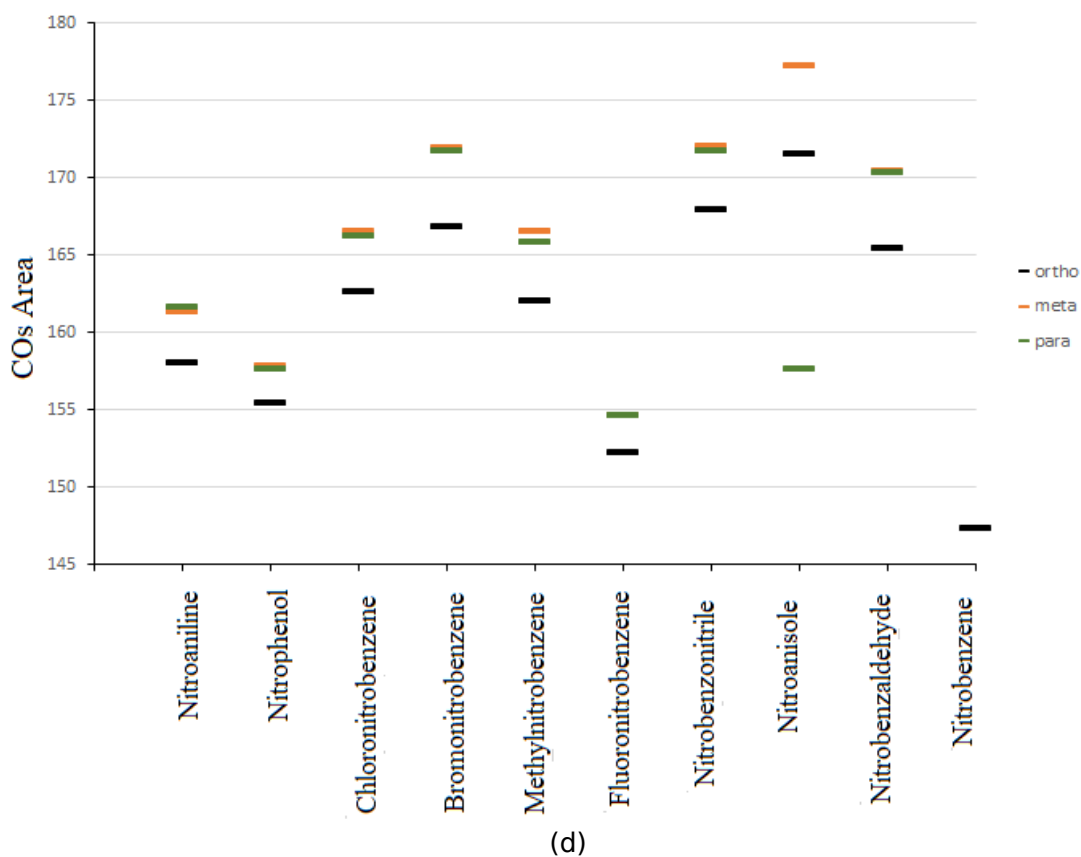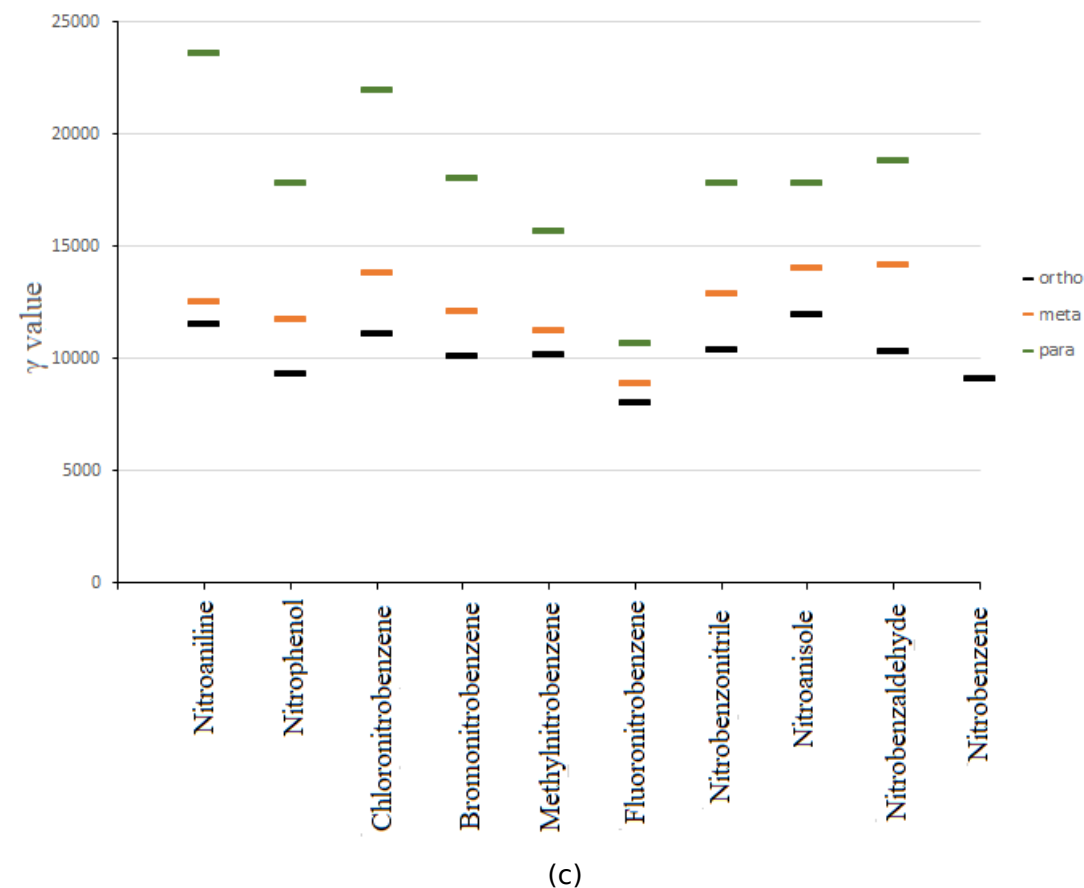
(a)

(b)

(c)

(d)
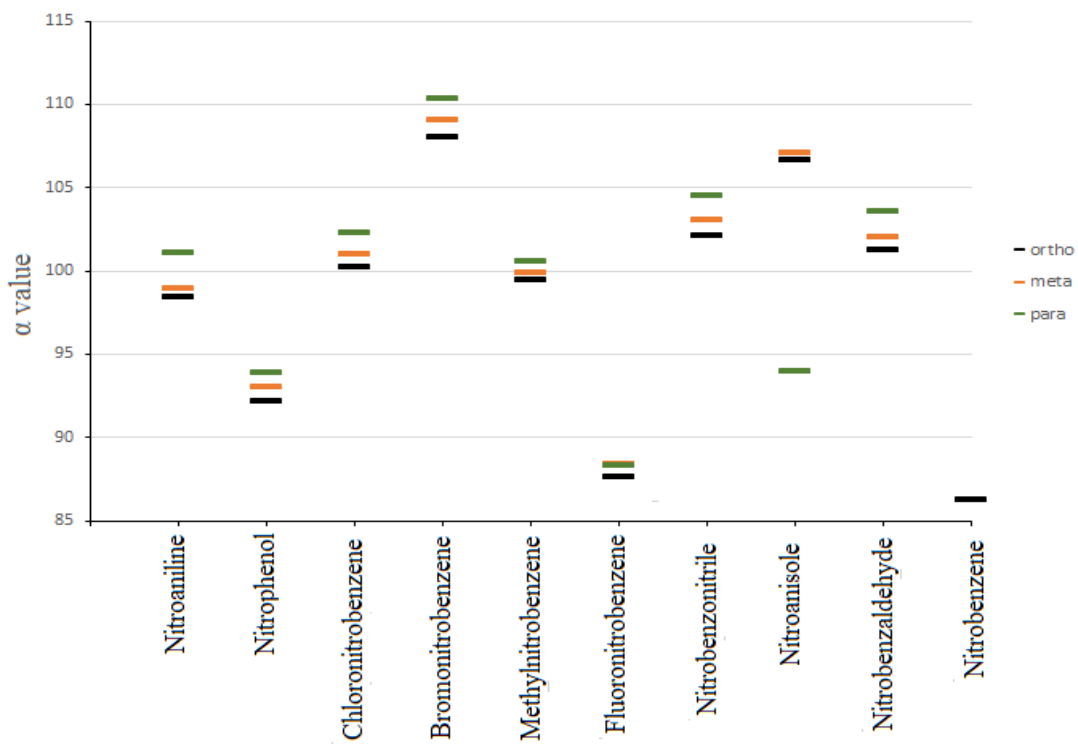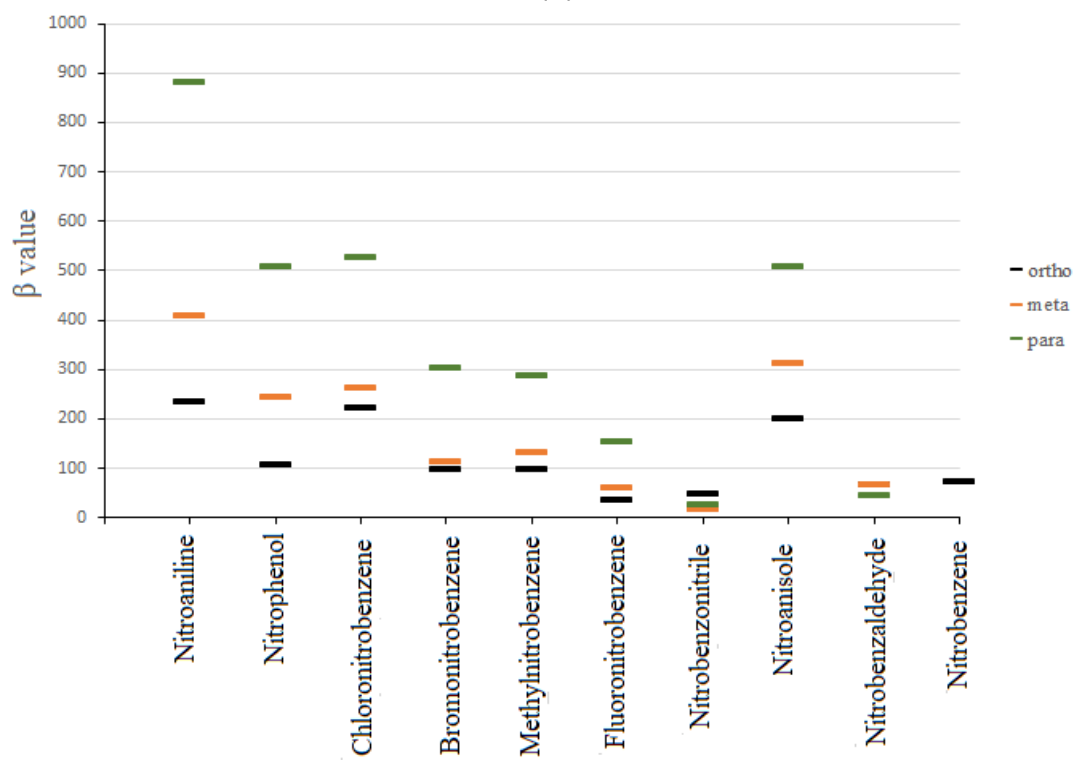
Figure 5 The value of (a) α, (b) β, (c) γ and (d) COs area of ortho, meta and para-substituted nitrobenzenes calculated using PM6 .

CONCLUSION

The work we have used linear polarizability, first and second order hyperpolarizability and conductor-like screening model (COs) area as molecular descriptors for QSAR of nitrobenzene derivative. In this work we use stepwise regression which fit the suitable variables in QSAR model. Second order hyperpolarizability shows the best QSAR model with the value of R^2 = 89.493%, r^2 = 68.7% and r_{cv}^2 = 87.52%. We also found that the substitutional of functional group in the nitrobenzene derivative for second order hyperpolarizability has the same sequence which was the γ ortho < γ meta < γ para. These has made that the second order hyperpolarizability was the best descriptors for QSAR model.

CONFLICT OF INTEREST

No conflict of interest in this work.

ACKNOWLEDGMENTS

REFERENCES

1. Ayub R, Raheel A. High-Value Chemicals from Electrocatalytic Depolymerization of Lignin: Challenges and Opportunities. IJMS. 2022 Mar 29;23(7):3767. <DOI>.

2. Hagiopol C. Chapter 3: The tree fractionation: the extraction of natural polyphenols. CHENG K, Hagiopol C, editors. S.l.: ELSEVIER; 2021. 33–84 p. ISBN: 978-0-12-822205-8.

3. Manickam P, Vijay D. Chapter 2 - Chemical hazards in textiles. In: Muthu S, editor. Chemical Management in Textiles and Fashion. Woodhead Publishing; 2021. p. 19–52.

4. Oladele JO, Oyeleke OM, Akindolie BO, Olowookere BD, Oladele OT. Vernonia amygdalina Leaf Extract Abates Oxidative Hepatic Damage and Inflammation Associated with Nitrobenzene in Rats. Jordan Journal of Biological Sciences. 2021;14(3):463–9.

5. Siqueira Soldaini Oliveira R, Borges I. Correlation Between Molecular Charge Properties and Impact Sensitivity of Explosives: Nitrobenzene Derivatives. Prop, Explos, Pyrotech. 2021 Feb;46(2):309–21. <DOI>.

6. Xavier JA, Silva TL, Torres-Santos EC, de Vasconcelos CC, Boane A, dos Santos RA, et al. Unveiling the relevance of the redox character of nitroaromatic and nitroheteroaromatic compounds as potential medicines. Current Opinion in Electrochemistry. 2021 Oct;29:100740. <DOI>.

7. Adhikari C, Mishra B kumar. Quantitative Structure-Activity Relationships of Aquatic Narcosis: A Review. CAD. 2018 Mar 21;14(1):7–28. <DOI>.

8. Kadam VV, Balakrishnan RM, Ponnan Ettiyappan J, Thomas NS, D Souza SA, Parappan S. Sensing of p-nitrophenol in aqueous solution using zinc oxide quantum dots coated with APTES. Environmental Nanotechnology, Monitoring & Management. 2021 Dec;16:100474. <DOI>.

9. Nepali K, Lee HY, Liou JP. Nitro-Group-Containing Drugs. J Med Chem. 2019 Mar 28;62(6):2851–93. <DOI>.

10. Ji Z, Ji Y, Ding R, Lin L, Li B, Zhang X. DNA-templated silver nanoclusters as an efficient catalyst for reduction of nitrobenzene derivatives: a systematic study. Nanotechnology. 2021 Feb 19;32(19):195705. <DOI>.

11. Rajak SK, others. QSAR study in terms of conceptual density functional theory based descriptors in predicting toxicity of nitrobenzenes towards Tetrahymena pyriformis. Indian Journal of Chemical Technology (IJCT). 2022;28(4):467–72.

12. Bilal M, Bagheri AR, Bhatt P, Chen S. Environmental occurrence, toxicity concerns, and remediation of recalcitrant nitroaromatic compounds. Journal of Environmental Management. 2021 Aug;291:112685. <DOI>.

13. Shaker B, Ahmad S, Lee J, Jung C, Na D. In silico methods and tools for drug discovery. Computers in Biology and Medicine. 2021 Oct;137:104851. <DOI>.

14. Wang L, Ding J, Pan L, Cao D, Jiang H, Ding X. Quantum chemical descriptors in quantitative structure–activity relationship models and their applications. Chemometrics and Intelligent Laboratory Systems. 2021 Oct;217:104384. <DOI>.

15. Dahmani R, Manachou M, Belaidi S, Chtita S, Boughdiri S. Structural characterization and QSAR modeling of 1,2,4-triazole derivatives as α-glucosidase inhibitors. New J Chem. 2021;45(3):1253–61. <DOI>.

16. Alias AN, Zabidi ZM, Zakaria NA, Mahmud ZS, Ali R. Biological Activity Relationship of Cyclic and

Noncyclic Alkanes Using Quantum Molecular Descriptors. OJAppS. 2021;11(08):966–84. <DOI>.

17. Karelson M, Lobanov VS, Katritzky AR. Quantum-Chemical Descriptors in QSAR/QSPR Studies. Chem Rev. 1996 Jan 1;96(3):1027–44. <DOI>.

18. Wady A, Khalid M, Alotaibi M, Ahmed Y. Synthesis, characterization, DFT calculations, and catalytic epoxidation of two oxovanadium(IV) Schiff base complexes. Journal of the Turkish Chemical Society Section A: Chemistry. 2022 Jan 17;9(1):163–208. <DOI>.

19. Yunusa U, Umar U, Idriss S, Ibrahim A, Abdullahi T. Experimental and DFT Computational Insights on the Adsorption of Selected Pharmaceuticals of Emerging Concern from Water Systems onto Magnetically Modified Biochar. Journal of the Turkish Chemical Society Section A: Chemistry. 2021 Nov 11;8(4):1179–96. <DOI>.

20. Gieseking RLM. A new release of MOPAC incorporating the INDO /S semiempirical model with CI excited states. J Comput Chem. 2021 Feb 15;42(5):365–78. <DOI>.

21. Wang S, Zhang X, Gui B, Xu X, Su L, Zhao YH, et al. Comparison of modes of action between fish, cell and mitochondrial toxicity based on toxicity correlation, excess toxicity and QSAR for class-based compounds. Toxicology. 2022 Mar;470:153155. <DOI>.

22. Andini S, Araya-Cloutier C, Lay B, Vreeke G, Hageman J, Vincken JP. QSAR-based physicochemical properties of isothiocyanate antimicrobials against gram-negative and gram-positive bacteria. LWT. 2021 Jun;144:111222. <DOI>.

23. Kurtz HA, Stewart JJP, Dieter KM. Calculation of the nonlinear optical properties of molecules. J Comput Chem. 1990 Jan;11(1):82–7. <DOI>.

24. Klamt A. The COSMO and COSMO-RS solvation models. WIREs Comput Mol Sci. 2011 Sep;1(5):699–709. <DOI>.

25. Hostaš J, Řezáč J, Hobza P. On the performance of the semiempirical quantum mechanical PM6 and PM7 methods for noncovalent interactions. Chemical Physics Letters. 2013 May;568–569:161–6. <DOI>.

26. Stewart J. MOPAC2016. Colorado Springs, CO; 2016.

27. Fatemi MH, Malekzadeh H. Prediction of Log(IGC 50) −1 for Benzene Derivatives to Ciliate Tetrahymena pyriformis from Their Molecular Descriptors. BCSJ. 2010 Mar 15;83(3):233–45. <DOI>.

28. Osaghi B, Safa F. QSPR study on the boiling points of aliphatic esters using the atom-type-based AI topological indices. Rev Roum Chim. 2019;64(2):183–9.

29. Mustapha A, Shallangwa G, Ibrahim MT, Bello AU, Ebuka DA, Uzairu A, et al. QSAR studies on some C14-urea tetrandrine compounds as potent anti-cancer against Leukemia cell line (K562). Journal of the Turkish Chemical Society, Section A: Chemistry. 2018 Dec 25;5(3):1391–402. <DOI>.

30. Majumdar S, Basak SC. Editorial: Beware of Naïve q2, use True q2: Some Comments on QSAR Model Building and Cross Validation. CAD. 2018 Mar 21;14(1):5–6. <DOI>.

31. Rakhimbekova A, Akhmetshin TN, Minibaeva GI, Nugmanov RI, Gimadiev TR, Madzhidov TI, et al. Cross-validation strategies in QSPR modelling of chemical reactions. SAR and QSAR in Environmental Research. 2021 Mar 4;32(3):207–19. <DOI>.

32. Toma C, Manganaro A, Raitano G, Marzo M, Gadaleta D, Baderna D, et al. QSAR Models for Human Carcinogenicity: An Assessment Based on Oral and Inhalation Slope Factors. Molecules. 2020 Dec 29;26(1):127. <DOI>.

33. Baumann D, Baumann K. Reliable estimation of prediction errors for QSAR models under model uncertainty using double cross-validation. J Cheminform. 2014 Dec;6(1):47. <DOI>.

34. Veerasamy R, Rajak H, Jain A, Sivadasan S, Varghese CP, Agrawal RK. Validation of QSAR models-strategies and importance. Int J Drug Des Discov. 2011;3:511–9.

35. Goel H, Yu W, Ustach VD, Aytenfisu AH, Sun D, MacKerell AD. Impact of electronic polarizability on protein-functional group interactions. Phys Chem Chem Phys. 2020;22(13):6848–60. <DOI>.

36. Tandon H, Ranjan P, Chakraborty T, Suhag V. Polarizability: a promising descriptor to study chemical–biological interactions. Mol Divers. 2021 Feb;25(1):249–62. <DOI>.

37. Zhu T, Chen W, Singh RP, Cui Y. Versatile in silico modeling of partition coefficients of organic compounds in polydimethylsiloxane using linear and nonlinear methods. Journal of Hazardous Materials. 2020 Nov;399:123012. <DOI>.

38. Zyss J. Hyperpolarizabilities of substituted conjugated molecules. II. Substituent effects and respective σ–π contributions. The Journal of Chemical Physics. 1979 Apr;70(7):3341–9. <DOI>.

QSAR Studies on Nitrobenzene Derivatives using Hyperpolarizability and Conductor-like Screening Model as Molecular Descriptors

A. N. Alias[*] iD **, Z. M. Zabidi** iD

Supplementary Material

Name	βxxx	βxyy	βxzz	βyxx	βyyy	βyzz	βzxx	βzyy	βzzz
3-nitrobenzaldehyde	-107.406	-8.13873	6.95055	-194.685	220.2986	4.03478	-0.02997	-0.09594	0.02021
3-Nitroaniline	-277.812	-266.894	2.33934	143.1703	265.0084	-4.05664	0.28304	0.05348	0.0436
2-Nitroaniline	-442.042	237.1784	-0.52997	154.073	174.0243	2.22041	-0.3837	-0.6019	-0.00824
4-NITROBENZAMIDE	164.2175	33.43775	3.63387	-19.7175	-12.1311	13.45701	-0.02028	0.00584	0.1242
4-Nitrobenzyl alcohol	576.203	-119.842	1.09036	48.86409	-57.7258	-1.51291	-4.62689	-0.50518	-5.99972
Methyl 4-nitrobenzoate	157.5613	14.80136	9.99508	-27.0893	43.80339	17.92242	-0.04126	0.27467	0.24997
4-nitrobenzaldehyde	20.61401	-86.3345	10.05155	-19.8487	-26.9678	-2.31037	-0.06159	-0.00429	-0.00595
3-Nitroanisole	322.8077	161.1222	6.96617	81.23778	91.75077	-14.115	-0.42497	0.23712	0.07669
2-nitrobenzaldehyde	13.05212	-24.4508	-6.92444	4.71585	-117.046	5.02317	-0.25362	-0.50811	-0.01777
4-Fluoronitrobenzene	409.4995	-155.675	1.92477	0.00661	-0.09222	-0.00478	0.13113	0.04254	0.00252
3-Nitroacetophenone	-44.2635	-5.72725	2.12282	-210.932	224.3482	10.72745	0.02065	0.0544	-0.00386
4-Nitrophenetole	1618.209	-278.852	5.22649	-135.926	17.04215	-7.79467	0.86974	-0.16206	0.18803
4-Nitroanisole	-1081.34	246.6922	-9.89709	-10.7317	-24.6004	-2.15571	-0.56548	-0.25527	0.03636
4-Nitrobenzyl chloride	348.5093	-155.854	25.27714	-0.74771	0.42059	0.1246	-38.5231	16.44961	33.71734
4-Ethylnitrobenzene	645.8094	-167.319	11.35641	10.68836	-6.49552	-0.08176	-16.753	11.32412	2.18177
2-Nitrobiphenyl	-153.951	15.49075	-7.68834	10.40523	110.5113	41.5736	-4.5394	-12.6303	10.59206
5-Hydroxy-2-nitrobenzaldehyde	-732.208	147.4603	0.38729	-291.476	205.6326	-10.0762	-0.12093	-0.17876	-0.00092
6-Chloro-2,4-dinitroaniline	-1024.71	372.4929	-3.08485	397.0051	201.6174	-9.91456	0.61227	-0.341	0.14031
3-Nitrobenzonitrile	40.1177	2.08986	-17.3495	-172.788	169.8454	7.87914	-0.12241	0.00357	-0.00777
4-Nitrobenzonitrile	149.9968	-126.313	20.69014	0.04503	0.20171	0.00431	0.00016	0.00033	-0.00001
2-Amino-4-chloro-5-nitrophenol*	-1096.98	-161.256	3.10006	-870.765	231.7681	-5.38898	31.29405	15.44982	5.08301
2,3-Dinitrophenol *	-167.69	116.9766	-46.6554	-191.413	-288.537	-68.9416	37.64876	11.50439	6.6923

Name	βxxx	βxyy	βxzz	βyxx	βyyy	βyzz	βzxx	βzyy	βzzz
3-Nitrophenol *	233.4414	109.0344	6.17516	44.31182	159.3321	-0.52827	-0.52827	0.01679	-0.00208
2,6-Dinitrophenol *	-184.652	-48.288	-4.23249	274.0526	-401.894	-5.62201	0.08114	0.24699	-0.00921
4-Methyl-2-nitrophenol *	21.19537	-7.77141	-11.522	-204.721	119.7415	-6.07916	-0.00979	0.00271	0.00663
2-Nitrophenol*	180.5037	-215.828	-1.38299	-73.9181	-93.1267	-4.23917	-0.03343	-0.02707	0.00405
2-Chloromethyl-4-nitrophenol*	-927.516	-78.3501	-6.02087	-485.373	221.0804	-20.1294	-0.11388	-0.15094	0.08312
2,5-Dinitrophenol *	456.3495	-157.247	3.65367	49.96321	116.1203	12.25693	0.43926	0.08193	-0.02202
2-Nitroresorcinol*	-479.639	288.2737	4.99292	17.79195	-45.3904	-6.34166	0.0459	0.03576	-0.00274
3-Nitro-2-xylene	-259.731	9.47801	-2.34206	-82.7347	205.6168	-10.2414	-0.02697	-0.02249	0.02534
2,6-dimethylnitrobenzene	-69.3849	154.0333	31.85578	1.80146	-2.36372	0.41409	1.33912	0.49623	-0.84623
2,3-dimethylnitrobenzene	-210.093	-0.08592	9.32443	-62.4941	196.671	-9.34246	-11.763	1.83536	-0.80275
2-methyl-3-chloronitrobenzene	-294.951	-89.6077	12.57144	-5.31444	230.5288	-2.03959	-26.6933	3.74238	-0.38834
2-methylnitrobenzene	-280.128	154.0435	-7.43852	43.10892	46.09325	-1.67936	-0.12252	0.39051	-0.27098
2-chloronitrobenzene	-16.2558	191.1657	14.84702	140.4117	175.9841	0.39656	6.2425	-41.7044	0.15244
2-methyl-5-chloronitrobenzene	-252.408	-134.867	-2.99171	64.57506	-119.748	2.66624	9.63111	-6.45379	-1.02694
2,4,5-trichloronitrobenzene	-519.396	-121.814	15.63978	407.1055	-78.3658	-0.59776	10.00321	-34.0882	0.3478
2,5-dichloronitrobenzene	-47.779	-43.399	3.07005	-85.1452	-11.6088	-3.29785	0.65462	-9.21405	-0.10206
6-chloro-1,3-dinitrobenzene	776.1823	-76.3143	20.55704	-316.231	167.4616	7.78888	13.83512	24.09994	0.46451
nitrobenzene	-227.147	107.65	-2.70756	-0.00286	-0.25499	-0.0021	0.01385	-0.02581	-0.00092
3-methylnitrobenzene	-207.598	-13.2319	5.58666	-61.3692	109.5199	-3.35465	0.05627	-0.04426	0.02192
1,3-dinitrobenzene	-0.80821	-0.28553	0.00261	-188.243	222.5985	-1.76682	-0.64097	0.04371	-0.00515
3,4-dichloronitrobenzene	-958.72	-75.853	-3.4705	-182.164	304.0829	-1.56579	0.10785	-0.01365	0.00143
4-methylnitrobenzene	662.188	-180.748	-2.77864	-10.731	-0.06797	3.95765	-0.18072	-0.08166	0.01305
1,4-dinitrobenzene	0.22225	-0.02254	0.00351	0.04947	0.0793	-0.00089	0.0239	0.01609	-0.00304
4-chloronitrobenzene	1024.197	-154.696	4.9467	-0.13816	-0.11031	-0.0016	0.09985	-0.00281	0.00781
2,3,5,6-tetrachloronitrobenzene	0.32491	-0.86776	0.01726	-38.0493	-172.688	1.37661	0.12494	-0.03103	-0.01338
6-methyl-1,3-dinitrobenzene	-275.782	87.76645	0.83589	-338.917	220.994	2.40858	3.00765	-1.02092	-0.48669
3-chloronitrobenzene	293.9259	100.183	1.05459	28.32126	157.9507	-1.33774	0.18775	-0.05016	0.00803
2-bromonitrobenzene	221.647	-65.817	-4.45118	57.10785	-105.418	-3.88547	-0.15725	0.17946	0.0017
3-bromonitrobenzene	112.2158	77.32627	-3.02739	-76.5724	112.0591	-3.18281	0.0472	-0.04491	0.00029

Name	βxxx	βxyy	βxzz	βyxx	βyyy	βyzz	βzxx	βzyy	βzzz
4-bromonitrobenzene	636.1428	-131.777	-1.34632	0.14062	-0.41076	-0.00084	0.02408	0.02996	0.00119
2,4,6-trimethylnitrobenzene	487.2197	-240.514	-41.4805	-9.0686	3.38915	4.35927	-1.02309	-0.50699	0.06539
5-methyl-1,2-dinitrobenzene	182.9819	-122.835	-65.9328	-132.798	-30.9037	-18.1088	-21.2979	10.37502	-2.78741
2,4-dichloronitrobenzene	922.6029	-275.532	4.68841	264.341	196.2572	5.52379	0.23118	0.32871	-0.00996
3,5-dichloronitrobenzene	171.2097	255.2306	2.14095	1.95536	-3.56673	-0.04293	0.02372	-0.07608	-0.00909
6-iodo-1,3-dinitrobenzene	459.143	-162.182	-0.25996	-9.86538	65.73475	-3.92581	-0.07814	0.41036	0.01076
2,3,4,5-tetrachloronitrobenzene	699.5292	78.39559	1.69574	367.8519	230.0996	5.559	-0.12905	0.3356	-0.01229
2,3-dichloronitrobenzene	330.074	121.9904	1.76158	34.03553	465.7443	1.31138	-0.01351	0.12179	0.01527
2,5-dibromonitrobenzene	-62.8901	74.86594	-0.51253	39.59764	-4.23922	1.76134	-0.13096	0.09024	0.00876
1,2-dichloro-4,5-dinitrobenzene	534.0062	289.3468	-0.0491	0.90223	-0.55667	-0.0491	-0.83199	-0.41753	-0.19002
3-methyl-4-bromonitrobenzene	575.4357	-52.5483	-8.91783	-29.4821	121.2631	-3.12227	0.05273	-0.03945	0.00855
2,3,4-trichloronitrobenzene	1011.229	-120.032	3.93728	-26.9388	592.7289	3.07087	-0.24504	0.1254	-0.0093
2,4,6-trichloronitrobenzene	976.7745	-450.077	5.18579	-0.49055	0.95889	-0.01732	-0.04162	-0.18462	0.00464
3,5-dinitrobenzyl alcohol	-234.518	94.46671	-3.67346	116.539	4.2354	-2.2517	-5.65075	16.67305	-5.36324
3,4-dinitrobenzyl alcohol	-136.287	77.06394	66.54098	56.60117	27.28624	10.45835	-6.13512	4.7163	2.21966
1,2-dinitrobenzene	-134.112	-98.0993	-65.3709	-28.3669	20.48465	-2.12874	-0.68789	-3.04461	-2.91564
2,4,6-trichloro-1,3-dinitrobenzene	4.59865	3.75504	0.63119	-678.306	485.1152	33.27589	12.18542	-1.818	-6.60903
2,3,5,6-tetrachloro-1,4-dinitrobenzene	-0.16924	-0.04236	0.00414	0.26336	0.00638	-0.01492	-0.09023	0.1211	-0.00218
2,4,5-trichloro-1,3-dinitrobenzene	691.7179	-6.27857	7.33992	310.2391	-107.273	44.42341	12.45873	-15.707	-1.48189